APPLIED COMPUTATIONAL ELECTROMAGNETICS SOCIETY JOURNAL

Special Issue on ACES 2018 Conference in Denver: Part 2

Guest Editor:
Branislav M. Notaros

February 2019
Vol. 34 No. 2
ISSN 1054-4887

The ACES Journal is abstracted in INSPEC, in Engineering Index, DTIC, Science Citation Index Expanded, the Research Alert, and to Current Contents/Engineering, Computing & Technology.

The illustrations on the front cover have been obtained from the research groups at the Department of Electrical Engineering, The University of Mississippi.

FEBRUARY 2019 REVIEWERS: REGULAR PAPERS

Ahmed Abdelrahman
Sami Barmada
Nayanatara Chandrasekaran
John Daniel
Han Guo
Mourad Ibrahim
Amir Jafargholi
Branislav Notaros
Xuezhe Tian

THE APPLIED COMPUTATIONAL ELECTROMAGNETICS SOCIETY JOURNAL

Vol. 34 No. 2 February 2019

SPECIAL ISSUE ON ADVANCED COMPUTATIONAL ELECTROMAGNETIC METHODOLOGIES AND TECHNIQUES

SPECIAL ISSUE ON NEW DESIGNS OF ANTENNAS AND RF, MICROWAVE, AND WIRELESS STRUCTURES AND SYSTEMS

SPECIAL ISSUE ON CUTTING-EDGE MODELING AND APPLICATIONS OF ELECTROMAGNETIC DEVICES AND FIELDS

Surface Integral Computation for the Higher Order Surface Integral Equation Method of Moments

Sanja B. Manić and Branislav M. Notaroš

Electrical & Computer Engineering Department
Colorado State University, Fort Collins, CO, USA
smanic@colostate.edu, notaros@colostate.edu

Abstract ─ This paper presents extraction technique applied to the double higher order surface integral equation method of moments and discusses the numerical results compared with previously implemented extraction method and numerical Gauss-Legendre integration.

Index Terms ─ Double higher order method of moments, integral accuracy, integration extraction technique, surface integral equation.

I. INTRODUCTION

This paper presents our ongoing study of convergence behavior of near-singular (potential) and near-hypersingual (field) integrals for double higher order large-domain surface integral equation method of moments (SIE-MoM). The fast and accurate integral computation that will effectively give the MoM matrix entries is essential in the computational electromagnetics (CEM). The main challenge arises with small source-to-field distances which often occur in microstrip and printed circuit design but are part of almost any model analysis. The technique for integral evaluation presented here uses the singularity extraction method. The analytically evaluated integral of the principal singular part is computed over a parallelogram which surface is defined to be similar to the surface of the generalized quadrilateral in the near area of the singular point. Numerical integrals over parallelogram and quadrilateral are using Gauss-Legendre quadrature formula.

II. THE METHOD

A. 2D double higher order (DHO) integrals

In the DHO SIE-MoM the 2D surface integrals are defined on the Lagrange-type generalized curved parametric quadrilateral MoM-SIE surface elements (in Fig. 1) defined in the parametric *u*-*v* domain as [1]:

$$\mathbf{r}(u,v)=\sum_{k=0}^{K_u}\sum_{l=0}^{K_v}\mathbf{r}_{kl}u^k v^l \ , \quad \text{for } -1\le u,v\le 1, \qquad (1)$$

where $\mathbf{r}_{kl}$ are vector coefficients and K_u and K_v are geometrical orders (K_u, $K_v \ge 1$). The current is approximated by higher order polynomial basis functions [1] leading to 2D integrals over the quadrilateral having the following form:

$$I_{ij}^{\mathrm{s}}=\int_{-1}^{1}\int_{-1}^{1}\frac{u^i v^j e^{-\mathrm{j}\beta R}}{4\pi R}\mathrm{d}u\mathrm{d}v \ , \ I_{ij}^{\mathrm{hs}}=\int_{-1}^{1}\int_{-1}^{1}\frac{u^i v^j (1+\mathrm{j}\beta R)e^{-\mathrm{j}\beta R}}{4\pi R^3}\mathrm{d}u\mathrm{d}v \ , \quad (2)$$

where s and hs represent singular and hypersingular integrals respectively, *i* and *j* are arbitrary polynomial orders of the basis functions, β is propagation coefficient, *f* is the operating frequency, ε and μ are permittivity and permeability of the dielectric medium respectively and *R* is the distance of the source point from the field point.

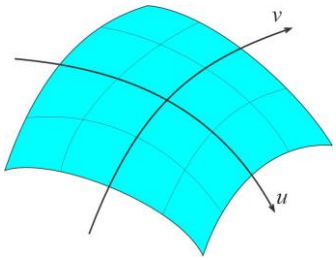

Fig. 1. Quadrilateral element.

B. Parallelogram for the extraction technique

The quadrilateral element and the parallelogram constructed at projection point (u_0, v_0) are shown in Fig. 2. The distance of the point on the parallelogram and singular point is defined as:

$$R_p^2=d^2+a_u^2\Delta u^2+a_v^2\Delta v^2+2a_u a_v\cos\alpha\Delta u\Delta v \ , \qquad (3)$$

where a_u, a_v and cosα are computed to take into account the curvature of the quadrilateral element, $\Delta u = u\text{-}u_0$, $\Delta v = v\text{-}v_0$ and *d* is the distance between singular point and the close point projection on the quadrilateral element.

C. Taylor's expansion and analytic integration

The relation between quadrilateral and parallelogram parametric surfaces is given by:

$$R(u,v)^2=R_P^2(u,v)+t(u,v) \ , R(u,v)=R_P\sqrt{1+x(u,v)} \ , \quad (4)$$

where $x(u,v) = t(u,v)/R_\mathrm{p}^2(u,v)$. The singular and

Submitted On: September 28, 2018
Accepted On: January 1, 2019

hypersingular parts of integrands for the integration over the parallelogram are represented through Taylor's expansion over x having in mind (4). Analytical integrals are computed by dividing parallelogram into triangles and using recursive formulas similarly to the procedure described in [2].

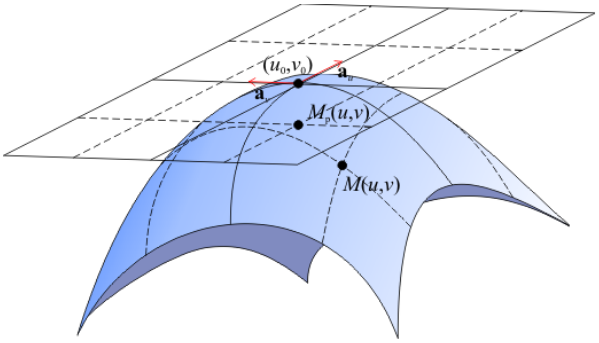

Fig. 2. Quadrilateral patch and parallelogram constructed at projected point.

D. Projected points outside of the patch

For the case of large and negative $2a_u a_v \cos\alpha \Delta u \Delta v$ contribution in (3), $|x(u,v)|$ becomes large because $R_p^2(u,v)$ is taking a small value. As a result, the Taylor's expansion over x does not approximate the (hyper) singular function well. In this situation, when the projection point is outside of the element domain, the parallelogram is constructed using parameters at the closest point, i.e., the most singular point on the quadrilateral. For the large values of $|x(u,v)|$, the patch is divided into four parts and the extraction method is applied to each part separately (example in Fig. 5).

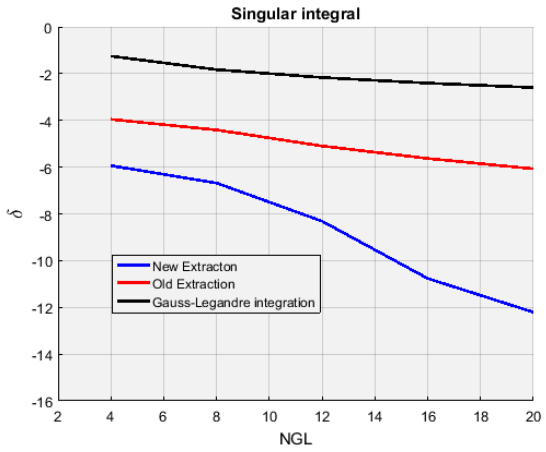

Fig. 3. Singular integral convergence for u_0 = 0.1, v_0=-0.1 and i=0, j=0 orders of the basis function.

III. RESULTS

The results shown in Figs. 3-5 are computed for second order curvilinear patch (one of the six patches modeling 1 m radius sphere) shown in Fig. 2. The integral convergence is obtained for d=5e-7 and β=0.77546 and results are compared to Gauss-Legendre numerical integration and previously implemented traditional (old) extraction technique.

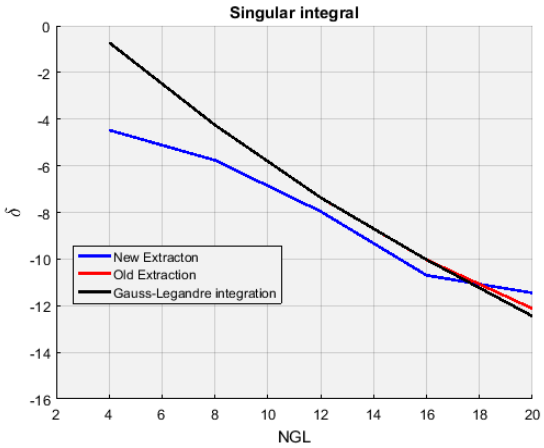

Fig. 4. Singular integral convergence for u_0 = 0.1, v_0=-0.1 and i=6, j=6 orders of the basis function.

The NGL label on the graphs represents the square root of the number of Gauss-Legendre points used for the numerical integration over quadrilateral or parallelogram. The relative convergence error is computed as $\delta = \log_{10}\left|I - \tilde{I}\right| / \left|\tilde{I}\right|$, where $\tilde{I}$ is the integral obtained using described extraction method with high value of Gauss-Legendre points and I represents the integrals as function of NGL.

Results in Fig. 5 are computed for the point described in part D of previous section and the improvement in convergence is shown for the divided patch method.

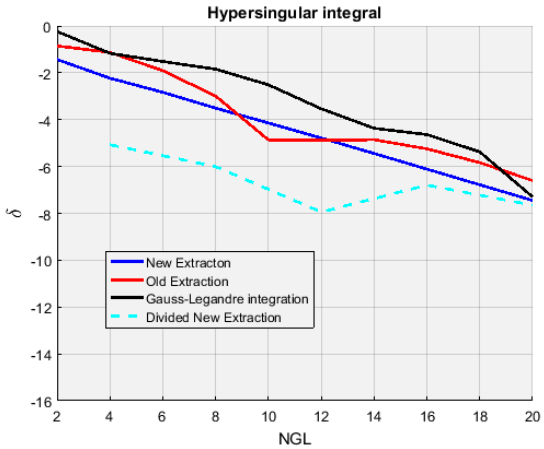

Fig. 5. Hypersingular integral convergence comparison for u_0 = 1.1, v_0=1.1 and i=0, j=0 orders of the basis function. Patch is divided at (0.8, 0.8) point in u-v domain.

IV. CONCLUSION

New extraction method is introduced and the method is verified with results. The convergence improvement is shown compared to the traditional extraction technique as well as further improvements achieved by dividing the patch. The convergence improvement is due the integral of the difference of the two functions defined over the constructed parallelogram and quadrilateral being accurately evaluated with small number of integration points.

AKNOWLEDGMENT

This work was supported by the National Science Foundation under Grant ECCS-1646562.

REFERENCES

[1] M. Djordjevic and B. M. Notaros, "Double higher order method of moments for surface integral equation modeling of metallic and dielectric antennas and scatterers," *IEEE Transactions on Antennas and Propagation*, vol. 52, no. 8, pp. 2118-2129, August 2004.

[2] S. Jarvenpaa, M. Taskinen, and P. Yla-Oijala, "Singularity subtraction technique for high-order polynomial vector basis functions on planar triangles," *IEEE Transactions on Antennas and Propagation*, vol. 54, no. 1, pp. 42-49, January 2006.

Millimeter-wave Frequency FDTD Simulation for Error Vector Magnitude of Modulated Signals

Joseph Elliott Diener
Colorado School of Mines
Golden, USA
jdiener@mines.edu

Jeanne Quimby
National Institute of Standards and Technology
Boulder, USA
jeanne.quimby@nist.gov

Kate A. Remley
National Institute of Standards and Technology
Boulder, USA
kate.remley@nist.gov

Atef Z. Elsherbeni
Colorado School of Mines
Golden, USA
aelsherb@mines.edu

***Abstract*—At millimeter frequencies, a simulation of propagating complex modulated signals through an environmental channel can be computationally prohibitive using the finite difference time domain method. A transfer function approach known as the "grid impulse response" method uses a delta-function as a source signal to solve for the transfer function of the finite difference time domain grid. Once the transfer function of the channel is known, any number of source signals of differing lengths, such as those involving M-ary quadrature amplitude modulation may be used to estimate the propagation of a complex modulated signal through the environmental channel. Numerical investigations show that the maximum error between the two approaches can be very small. Simple environmental channels are used to present the error vector magnitude at mmWave frequencies obtained from the grid impulse response method.**

***Keywords*—EVM, FDTD, QAM.**

I. Introduction

Modern millimeter-wave communication systems have complex hardware and modulation schemes that can be modeled using finite difference time domain (FDTD) directly by propagating the source signal through a simulated channel. Using the full FDTD approach will be a computationally-demanding task for dense FDTD grids propagating long-duration signals due to the gridding requirements based on the very small wavelengths found at millimeter-wave frequencies. Authors in [1-2] show that transfer functions derived from the system response to a delta-function source signal can be used to predict the response of the 1D FDTD grid for an arbitrary input. Perrin *et al*. use a similar technique to predict the grid response in 3D [3]. We extend this previous work into the millimeter-wave frequencies and show numerically that a delta-function excitation of the grid can be used to obtain the transfer function of the FDTD grid. Once obtained, the transfer function can be used to solve for the signal received at any grid point when the source is excited by an arbitrary source signal. This approach is known as the grid impulse response (GIR) method. We will show the use of the GIR method to calculate the distortion of a modulated signal using error-vector-magnitude as the metric of distortion.

II. The Transfer Function and Grid Impulse Response

We define the transfer function of the FDTD grid as,

$$T(\omega) = \frac{F(\,RX(t)\,)}{F(\,TX(t)\,)}\,, \tag{1}$$

where F is the fast Fourier transform, RX is the time-domain sampled signal at a point of interest in the FDTD grid, TX is the source signal used to excite the FDTD grid, and $T(\omega)$ is the transfer function. It is often more convenient to work with the time domain representation of the transfer function, the grid impulse response (GIR) given by:

$$GIR(t) = F^{-1}(T\,(\omega)\,)\,. \tag{2}$$

Note that for a delta-function source signal incident on the FDTD grid, the GIR is directly obtained by sampling the grid, $GIR(t) = RX(t)$. Once the GIR is found, any signal of interest can be solved at the RX sampling point by convolution, given by:

$$RX_{calculated}(t) = GIR(t) * TX_{arbitrary}(t)\,, \tag{3}$$

where * indicates convolution, and $RX_{calculated}$ is the predicted signal obtained from the arbitrary signal source $TX_{arbitrary}$. This formulation is most useful in solving for signals where the number of time steps needed to inject the signal into the grid is much larger than the number of time steps needed for the GIR to converge.

III. Numerical Demonstration of Accuracy

We used an M-ary quadrature amplitude modulation (M-QAM) signal to examine the accuracy of the GIR method. The FDTD code from [5] is used for all simulations, run in single precision. A source transmitting an M-QAM signal is placed in free-space terminated in either convolutional perfectly matched layer (CPML) [6] or perfect electrical conductor (PEC) boundaries. The signal is a 16-QAM modulation, 10 GSym/s, with five symbol durations. The CPML is eight cells thick. A simulation using the full FDTD approach and another using the GIR method are compared. The signals at a given point of interest in space as a function of time-step are recorded for both methods. The received signal from the full-length simulation RX_{full} is compared with the predicted signal from the GIR method. The signals are compared with an error metric defined by,

$$Error = \left|RX_{full} - RX_{GIR}\right|. \tag{4}$$

RX_{full} has its maximum amplitude normalized to 1, and RX_{GIR} is normalized using the same normalization constant. The free space propagation case is shown in the solid line in Fig. 1. At 500 time steps, the jump in the figure is due to the arrival of the

Submitted On: September 30, 2018
Accepted On: October 3, 2018

transmitted signal at the receiver. The signal difference previous to this time step is due to numeric noise. The GIR determination uses 1816 time steps. Through time step 1816, the error is less than 10^{-6}. At time step 1817, the error increases by ~10x, with a maximum error of approximately 10^{-3} from time step 1888 and beyond. Thus, for time steps less than or equal to the number of time steps used in the full FDTD simulation, the GIR method will capture the grid response with the error of a predicted signal $< 10^{-6}$. For time steps after this point, the error will reflect the degree to which the long-term GIR has been captured. When the GIR has begun to converge, the error for future time steps is relatively low ($\sim 10^{-3}$), and will be reduced further when the grid is sampled for more time steps. When the long-term GIR has not been captured, the error for future time steps will be large. This is shown in the dashed line in Fig. 1, where the CPML boundaries are replaced with PEC walls to simulate a metal enclosure shown by the Box results. Through the time step of the GIR simulation, the response of the grid is captured well ($< 10^{-6}$ error). The maximum error very quickly approaches 0.5 for time steps after this point, corresponding to essentially no agreement between predicted and actual signals. This is due to the resonant nature of the box, and shows the transfer function method can fail when used inappropriately.

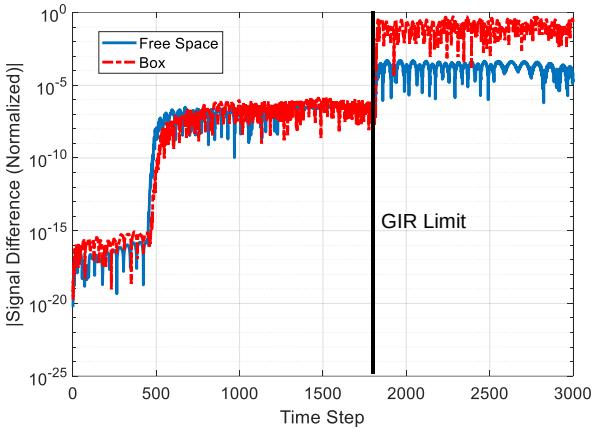

Fig. 1. Error between full-length FDTD simulation, and predicted response using the GIR method. Dashed line shows the PEC box case, while the solid line shows the free-space case. Truncated at 3000 timesteps for clarity.

IV. Error Vector Magnitude Calculation

The GIR method is an excellent compromise between accuracy and computational expense for determining distortion in a modulated signal from a channel. By creating a modulated signal and convolving with the GIR, the effects of the channel will be seen on the received signal. This can show channel effects such as path loss, power delay profile, and the error vector magnitude (EVM) [4] introduced by the channel. Application of the technique to an EVM calculation is shown using two identical dipole antennas operating at 90 GHz as a TX/RX pair in a free-space channel and in a channel with an infinite ground plane below the antennas. The distance between the two antennas is swept through 0.12 m. A 1000 symbol, duration 16-QAM signal is the excitation and the signal is post-processed to yield the EVM. The mean EVM is shown in Fig. 2. The ground-bounce case shows significantly increased distortion resulting from the reflected signal, with two distinct peaks appearing. These peaks are not present in the free-space case, and so are solely attributable to the reflected signal from the ground-plane.

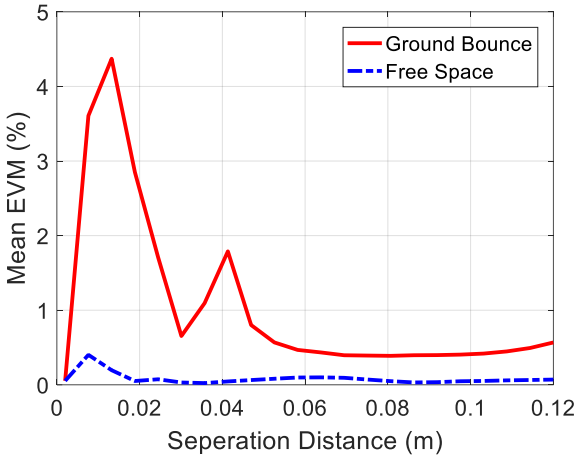

Fig. 2. EVM for a dipole-dipole case using 16-QAM signal, with results calculated by the GIR. Distinct peaks are seen from ground-bounce effects.

V. Conclusion

We have shown that the use of transfer functions in the full 3D FDTD grid can obtain long-term grid responses wit accuracy less than $< 10^{-6}$. An understanding of the error in such an approach has been introduced, showing clear cases where the GIR is not satisfactory. Through the use of the transfer function of the grid, simulations of the modulated signals can be solved rapidly, and channel effects on the EVM of the signal seen directly.

References

[1] J. B. Schneider and C. L. Wagner, "FDTD dispersion revisited: Faster-than-light propagation," in IEEE Microwave and Guided Wave Letters, vol. 9, no. 2, pp. 54-56, Feb. 1999.

[2] J. P. Bérenger, "Propagation and Aliasing of High Frequencies in the FDTD Grid," in IEEE Transactions on Electromagnetic Compatibility, vol. 58, no. 1, pp. 117-124, Feb. 2016.

[3] E. Perrin, C. Guiffaut, A. Reineix, and F. Tristant, "Using Transfer Function Calculation and Extrapolation to Improve the Efficiency of the Finite-Difference Time-Domain Method at Low Frequencies," in IEEE Transactions on Electromagnetic Compatibility, vol. 52, no. 1, pp. 173-178, Feb. 2010.

[4] M. Mckinley, K. A. Remley, M. Mylinshi, and J. S. Kenney, "EVM Calculation for Broadband Modulated Signals," in ARFTG Microwave Measurement Conference, Orlando, FL, 2004.

[5] A. Z. Elsherbeni and V. Demir, The Finite Difference Time Domain Method for Electromagentics with MATLAB Simulations. Second edition, ACES Series on Computational Electromagnetics and Engineering, SciTech Publishing, an Imprint of IET, Edison, NJ, 2015.

[6] J. A. Roden and S. D. Gedney, "Convolutional PML (CPML): An efficient FDTD implementation of the CFS-PML for arbitrary media," Microw. Opt. Technol. Lett., vol 27, pp 334-339, 2000.

Hierarchical Universal Matrices for Sensitivity Analysis by Curvilinear Finite Elements

László Levente Tóth
Chair for Electromagnetic Theory
Saarland University
D-66123 Saarbrücken, Germany
l.toth@lte.uni-saarland.de

Romanus Dyczij-Edlinger
Chair for Electromagnetic Theory
Saarland University
D-66123 Saarbrücken, Germany
edlinger@lte.uni-saarland.de

***Abstract*—A new method for calculating the geometric sensitivities of curvilinear finite elements is presented. Approximating the relevant metric tensors by hierarchical orthogonal polynomials enables the sensitivity matrices to be integrated analytically. The resulting numerical method is based on pre-calculated universal matrices and achieves significant savings in computer runtime over conventional techniques based on numerical integration. Moreover, there exists a representation limit for the geometry, i.e., the degree of basis functions fully determines a critical order of the geometry expansion, beyond which the derivatives of the finite-element matrices will remain constant. To validate the suggested approach, a numerical example is presented.**

***Keywords*—curvilinear, eigenvalues, finite elements, hierarchical, sensitivity, universal matrix.**

I. Introduction

Higher-order finite elements (FEs) are attractive because they yield exponential convergence in case of smooth fields. However, to harvest their full potential, curvilinear boundaries must be taken into account. Typically, the resulting metric terms do not admit analytical integration of the FE matrices. Numerical integration is possible, though computationally expensive. An alternative is polynomial interpolation or approximation of the metric terms followed by exact integration. The resulting algorithms [1], [2] achieve significant savings in computer runtime, by utilizing pre-calculated universal matrices (UMs) [3]. Applications such as sensitivity analysis and gradient-based optimization require not only the FE matrices but also their derivatives with respect to the parameters [4], [5]. This paper presents a procedure for computing such derivatives at low computational cost. It employs hierarchical UMs and applies to both straight-sided and curvilinear FEs. The method will be demonstrated by reference to the $\boldsymbol{H}(\mathrm{curl})$ shape functions of [6].

II. Model Problem

Consider a cavity resonator Ω whose boundary Γ_E is a perfect electric conductor (PEC). Maxwell's equations lead to the following eigenvalue problem (EVP) for the modal electric field $\boldsymbol{E}$ and the corresponding free-space wavenumber k:

$$\nabla \times \left(\boldsymbol{\mu}_r^{-1} \nabla \times \boldsymbol{E}\right) - k^2 \boldsymbol{\varepsilon}_r \boldsymbol{E} = \boldsymbol{0} \qquad \text{in } \Omega, \tag{1a}$$

$$\hat{\boldsymbol{n}} \times \boldsymbol{E} = \boldsymbol{0} \qquad \text{in } \Gamma_E. \tag{1b}$$

Herein $\boldsymbol{\mu}_r$ and $\boldsymbol{\varepsilon}_r$ denote the relative magnetic permeability and electric permittivity, respectively. The weak formulation of the EVP (1) reads:

$$\int_\Omega \nabla \times \boldsymbol{E} \cdot \boldsymbol{\mu}_r^{-1} \nabla \times \boldsymbol{w} \,\mathrm{d}\boldsymbol{x} - k^2 \int_\Omega \boldsymbol{E} \cdot \boldsymbol{\varepsilon}_r \boldsymbol{w} \,\mathrm{d}\boldsymbol{x} = 0 \quad \forall \boldsymbol{w} \in \boldsymbol{H}_E(\mathrm{curl}; \Omega, \Gamma_E). \tag{2}$$

FE discretization using a set of $\boldsymbol{H}(\mathrm{curl})$ basis functions $\boldsymbol{w}_a^m$, where $(\cdot)^m$ indicates the polynomial degree, leads to the algebraic EVP:

$$\left(\boldsymbol{S} - k^2 \boldsymbol{T}\right) \boldsymbol{v} = \boldsymbol{0}, \tag{3}$$

with eigenvector $\boldsymbol{v}$. Herein the stiffness matrix $\boldsymbol{S}$ and the mass matrix $\boldsymbol{T}$ are given by:

$$[\boldsymbol{S}^{mn}]_{aq} = \int_\Omega \nabla \times \boldsymbol{w}_a^m \cdot \boldsymbol{\mu}_r^{-1} \nabla \times \boldsymbol{w}_q^n \,\mathrm{d}\boldsymbol{x}, \tag{4a}$$

$$[\boldsymbol{T}^{mn}]_{aq} = \int_\Omega \boldsymbol{w}_a^m \cdot \boldsymbol{\varepsilon}_r \boldsymbol{w}_q^n \,\mathrm{d}\boldsymbol{x}. \tag{4b}$$

Provided that $\boldsymbol{\mu}_r, \boldsymbol{\varepsilon}_r \in \mathbb{R}^+$ and both matrices are real symmetric, $\boldsymbol{S}$ and $\boldsymbol{T}$ is positive definite. Let $\boldsymbol{S}$ and $\boldsymbol{T}$ depend smoothly on a parameter τ, and let the considered eigenvalue k_i^2 be of multiplicity one. Then, according to [7], the sensitivity of k_i^2 with respect to τ is given by:

$$\frac{\partial}{\partial \tau} k_i^2 = \boldsymbol{v}_i^T \left(\frac{\partial}{\partial \tau} \boldsymbol{S} - k_i^2 \frac{\partial}{\partial \tau} \boldsymbol{T} \right) \boldsymbol{v}_i, \tag{5}$$

provided that the eigenvectors are normalized according to:

$$\boldsymbol{v}_i^T \boldsymbol{T} \boldsymbol{v}_i = \boldsymbol{I}. \tag{6}$$

Thus, sensitivity analysis requires the considered eigenpair $(k_i^2, \boldsymbol{v}_i)$ as well as the matrix derivatives $\frac{\partial}{\partial \tau}\boldsymbol{S}$ and $\frac{\partial}{\partial \tau}\boldsymbol{T}$.

III. Hierarchical Universal Matrices

In an unstructured mesh, FEs of different sizes and shapes are present. It is customary to compute the contributions of a single FE Ω_e, i.e., the element matrices $\boldsymbol{S}_e$ and $\boldsymbol{T}_e$, from a reference domain $\widehat{\Omega}_e$ equipped with local coordinates $\boldsymbol{\varphi}$. Let $\widehat{\boldsymbol{w}}_a^m(\boldsymbol{\varphi})$ denote the basis functions on $\widehat{\Omega}_e$ and $\boldsymbol{J}(\boldsymbol{\varphi})$ the

Submitted On: September 29, 2018
Accepted On: October 3, 2018

Jacobian of the geometry mapping. By means of the metric tensors $\widehat{\boldsymbol{\Lambda}}^1(\boldsymbol{\varphi})$ and $\widehat{\boldsymbol{\Lambda}}^2(\boldsymbol{\varphi})$ defined by:

$$\widehat{\boldsymbol{\Lambda}}^1 = |\boldsymbol{J}|\boldsymbol{J}^{-T}\boldsymbol{\varepsilon}_r\boldsymbol{J}^{-1}, \tag{7a}$$

$$\widehat{\boldsymbol{\Lambda}}^2 = |\boldsymbol{J}|^{-1}\boldsymbol{J}\boldsymbol{\mu}_r^{-1}\boldsymbol{J}^{T}, \tag{7b}$$

the element matrices $\boldsymbol{S}_e$ and $\boldsymbol{T}_e$ take the form:

$$[\boldsymbol{S}_e^{mn}]_{aq} = \int_{\widehat{\Omega}_e} \nabla_\varphi \times \widehat{\boldsymbol{w}}_a^m \cdot \widehat{\boldsymbol{\Lambda}}^2 \nabla_\varphi \times \widehat{\boldsymbol{w}}_q^n \,\mathrm{d}\boldsymbol{\varphi}, \tag{8a}$$

$$[\boldsymbol{T}_e^{mn}]_{aq} = \int_{\widehat{\Omega}_e} \widehat{\boldsymbol{w}}_a^m \cdot \widehat{\boldsymbol{\Lambda}}^1 \widehat{\boldsymbol{w}}_q^n \,\mathrm{d}\boldsymbol{\varphi}. \tag{8b}$$

In [3] a hierarchical basis of scalar polynomials $b_l^k(\boldsymbol{\varphi})$ which are pairwise orthogonal on $\widehat{\Omega}_e$ was introduced:

$$\int_{\widehat{\Omega}_e} b_l^k(\boldsymbol{\varphi}) b_i^p(\boldsymbol{\varphi}) \,\mathrm{d}\boldsymbol{\varphi} = \begin{cases} 1 & \text{for } (k,l) = (p,i), \\ 0 & \text{else.} \end{cases} \tag{9}$$

Here $(\cdot)^k$ gives the polynomial order, and $(\cdot)_l$ denotes functions of same order. Expanding $\widehat{\boldsymbol{\Lambda}}^{(\cdot)}$ in the basis $\{b_l^k\}$ leads to:

$$\widehat{\boldsymbol{\Lambda}}^{(\cdot)}(\boldsymbol{\varphi}) = \sum_{k=0}^{\infty} \sum_{l=1}^{L(k)} \widehat{\boldsymbol{\Lambda}}_{kl}^{(\cdot)} b_l^k(\boldsymbol{\varphi}), \qquad \boldsymbol{\varphi} \in \widehat{\Omega}, \tag{10}$$

wherein $\widehat{\boldsymbol{\Lambda}}_{kl}$ stands for a constant matrix-valued coefficient and $L(k)$ for the number of homogeneous polynomials of order k. Thanks to orthonormality (9), the calculation of $\widehat{\boldsymbol{\Lambda}}_{kl}$ reduces to:

$$\widehat{\boldsymbol{\Lambda}}_{kl} = \int_{\widehat{\Omega}} \widehat{\boldsymbol{\Lambda}}(\boldsymbol{\varphi}) b_l^k \,\mathrm{d}\boldsymbol{\varphi}. \tag{11}$$

In the general case, the evaluation of (11) requires numerical integration. Note that this is the only source of error in the proposed method.

Eq. (10) yields a polynomial representation for (8), which hereby becomes accessible to analytical integration. We thus have:

$$\boldsymbol{S}^{mn} = \sum_{k=0}^{m+n-2} \sum_{l=1}^{L(k)} \sum_{i,j} \left[\widehat{\boldsymbol{\Lambda}}_{kl}^2\right]_{ij} \boldsymbol{S}_{ijl}^{mnk}, \tag{12a}$$

$$\boldsymbol{T}^{mn} = \sum_{k=0}^{m+n} \sum_{l=1}^{L(k)} \sum_{i,j} \left[\widehat{\boldsymbol{\Lambda}}_{kl}^1\right]_{ij} \boldsymbol{T}_{ijl}^{mnk}, \tag{12b}$$

wherein $\boldsymbol{S}_{ijl}^{mnk}$ and $\boldsymbol{T}_{ijl}^{mnk}$ are metric-independent UMs. They are independent of the geometry and need to be computed only once. The UMs inherit the hierarchical structure of the basis functions [6]. Thanks to orthogonality, the results of the truncated sums in (12) are exact; see [3].

IV. Universal Matrices for Sensitivity Analysis

When the geometry is parameterized by τ, the Jacobian $\boldsymbol{J}$ and, in consequence, the metric tensors $\boldsymbol{\Lambda}^{(\cdot)}$ become τ dependent, whereas the $\widehat{\boldsymbol{w}}_a^m(\boldsymbol{\varphi})$ remain unchanged. In view of (7) and (8), the derivatives of the element matrices read:

$$\frac{\partial}{\partial\tau}[\boldsymbol{S}_e^{mn}]_{aq} = \int_{\widehat{\Omega}_e} \nabla_\varphi \times \widehat{\boldsymbol{w}}_a^m \cdot \frac{\partial}{\partial\tau}\widehat{\boldsymbol{\Lambda}}^2 \nabla_\varphi \times \widehat{\boldsymbol{w}}_q^n \,\mathrm{d}\boldsymbol{\varphi}, \tag{13a}$$

$$\frac{\partial}{\partial\tau}[\boldsymbol{T}_e^{mn}]_{aq} = \int_{\widehat{\Omega}_e} \widehat{\boldsymbol{w}}_a^m \cdot \frac{\partial}{\partial\tau}\widehat{\boldsymbol{\Lambda}}^1 \widehat{\boldsymbol{w}}_q^n \,\mathrm{d}\boldsymbol{\varphi}. \tag{13b}$$

The structure of (13) implies that $\frac{\partial}{\partial\tau}\boldsymbol{S}$ and $\frac{\partial}{\partial\tau}\boldsymbol{T}$ may be constructed from UMs too, by a method similar to Section III: The polynomial expansions of $\frac{\partial}{\partial\tau}\boldsymbol{\Lambda}^{(\cdot)}$ in terms of b_l^k read:

$$\frac{\partial}{\partial\tau}\widehat{\boldsymbol{\Lambda}}^{(\cdot)}(\boldsymbol{\varphi}) = \sum_{k=0}^{\infty} \sum_{l=1}^{L(k)} \frac{\partial}{\partial\tau}\widehat{\boldsymbol{\Lambda}}_{kl}^{(\cdot)} b_l^k(\boldsymbol{\varphi}), \qquad \boldsymbol{\varphi} \in \widehat{\Omega}. \tag{14}$$

Substituting the series expansion (14) for the derivatives of the metric tensors in (13) leads to polynomial representations which, again, allow for analytical integration. We arrive at:

$$\frac{\partial}{\partial\tau}\boldsymbol{S}^{mn} = \sum_{k=0}^{m+n-2} \sum_{l=1}^{L(k)} \sum_{i,j} \left[\frac{\partial}{\partial\tau}\widehat{\boldsymbol{\Lambda}}_{kl}^2\right]_{ij} \boldsymbol{S}_{ijl}^{mnk}, \tag{15a}$$

$$\frac{\partial}{\partial\tau}\boldsymbol{T}^{mn} = \sum_{k=0}^{m+n} \sum_{l=1}^{L(k)} \sum_{i,j} \left[\frac{\partial}{\partial\tau}\widehat{\boldsymbol{\Lambda}}_{kl}^1\right]_{ij} \boldsymbol{T}_{ijl}^{mnk}. \tag{15b}$$

Eq. (15) provides an efficient procedure for computing the matrix derivatives, based on the same UMs as (12). It can be shown that metric expansions of order $m+n-2$ and $m+n$ for $\boldsymbol{S}$ and $\boldsymbol{T}$, respectively, yield exact results; see the Appendix for a detailed derivation. Hence, the maximum order of the metric expansion required in the general curvilinear case is:

$$k = 2p-2 \qquad \text{for } \frac{\partial}{\partial\tau}\boldsymbol{S}, \tag{16a}$$

$$k = 2p \qquad \text{for } \frac{\partial}{\partial\tau}\boldsymbol{T}. \tag{16b}$$

A. Sensitivity with Respect to Geometry Parameters

Let the geometry be described by $\boldsymbol{H}^1$ interpolatory FE basis functions $L_i(\boldsymbol{\varphi})$, using the parameter-dependent locations of the element nodes $\boldsymbol{r}_i(\tau)$ as interpolation points. By denoting the matrix of node coordinates by $\boldsymbol{R}(\tau)$ and the vector of basis functions by $\boldsymbol{L}(\boldsymbol{\varphi})$, the position vector $\boldsymbol{x}(\tau)$ takes the form:

$$\boldsymbol{x}(\tau) = \boldsymbol{f}(\tau,\boldsymbol{\varphi}) = \sum_i \boldsymbol{r}_i(\tau) L_i(\boldsymbol{\varphi}) = \boldsymbol{R}(\tau)\boldsymbol{L}(\boldsymbol{\varphi}). \tag{17}$$

Thus, the derivative of the Jacobian reads:

$$\frac{\partial}{\partial\tau}\boldsymbol{J} = \frac{\partial}{\partial\tau}\nabla_\varphi \boldsymbol{f}^T = \left[\nabla_\varphi \boldsymbol{L}^T\right]\left[\frac{\partial}{\partial\tau}\boldsymbol{R}^T\right], \tag{18}$$

and the derivatives of the metric tensors $\widehat{\mathbf{\Lambda}}^1$ and $\widehat{\mathbf{\Lambda}}^2$, which are needed in (13), are obtained by:

$$\frac{\partial}{\partial\tau}\widehat{\mathbf{\Lambda}}^1 = \widehat{\mathbf{\Lambda}}^1 \operatorname{tr}\left[\boldsymbol{J}^{-1}\frac{\partial}{\partial\tau}\boldsymbol{J}\right] - |\boldsymbol{J}|\left(\boldsymbol{J}^{-T}\frac{\partial \boldsymbol{J}^T}{\partial\tau}\boldsymbol{J}^{-T}\boldsymbol{\varepsilon}_r\boldsymbol{J}^{-1}\right) - |\boldsymbol{J}|\left(\boldsymbol{J}^{-T}\boldsymbol{\varepsilon}_r\boldsymbol{J}^{-1}\frac{\partial \boldsymbol{J}}{\partial\tau}\boldsymbol{J}^{-1}\right), \tag{19a}$$

$$\frac{\partial}{\partial\tau}\widehat{\mathbf{\Lambda}}^2 = |\boldsymbol{J}|^{-1}\left(\frac{\partial \boldsymbol{J}}{\partial\tau}\boldsymbol{\mu}_r^{-1}\boldsymbol{J}^T + \boldsymbol{J}\boldsymbol{\mu}_r^{-1}\frac{\partial \boldsymbol{J}^T}{\partial\tau}\right) - \widehat{\mathbf{\Lambda}}^2 \operatorname{tr}\left[\boldsymbol{J}^{-1}\frac{\partial}{\partial\tau}\boldsymbol{J}\right]. \tag{19b}$$

B. Computational Cost

In the following, $N(p)$ denotes the number of scalar polynomials up to order p and $G(p)$ the number of interpolation points of a quadrature method for the reference tetrahedron which is exact for polynomials up to order p; see [8].

With the present method, computing the derivatives of the element matrices involves two steps: The first is the k-th order expansion of the metric tensors according to (10) and (11), respectively. This is computationally cheap and will not be further considered.

The second step is the actual calculation of $\frac{\partial}{\partial\tau}\boldsymbol{S}$ and $\frac{\partial}{\partial\tau}\boldsymbol{T}$. Since the polynomial expansions for the metric tensors allow (13) to be integrated analytically with the help of UMs, the numbers of scaled matrix additions $A_{\boldsymbol{S}}$ and $A_{\boldsymbol{T}}$ are solely determined by the number of metric coefficients $\widehat{\mathbf{\Lambda}}_{kl}$ in (10) and (14): Each metric tensor is a symmetric 3×3 matrix, with six independent entries. Hence, the number of coefficients is $6N(k)$, and we have:

$$A_{\boldsymbol{S}} = 6N(k) \overset{(16a)}{=} 6N(2p-2) \qquad \text{for } \frac{\partial}{\partial\tau}\boldsymbol{S}, \tag{20a}$$

$$A_{\boldsymbol{T}} = 6N(k) \overset{(16b)}{=} 6N(2p) \qquad \text{for } \frac{\partial}{\partial\tau}\boldsymbol{T}. \tag{20b}$$

Further optimizations are possible by exploiting the fact that, thanks to the hierarchical structure of the considered FE basis functions, many of the integrals (13) are of lower order.

For comparison, consider methods that compute the element matrices $\frac{\partial}{\partial\tau}\boldsymbol{S}$ and $\frac{\partial}{\partial\tau}\boldsymbol{T}$ by numerical integration in the curvilinear case. Eq. (13) implies that the quadrature rule ought to be exact for polynomials of order $2(p-1)+k$ and $2p+k$, respectively. Thus, the resulting numbers of scaled matrix additions, $A_{\boldsymbol{S}}^{num}$ and $A_{\boldsymbol{T}}^{num}$, are:

$$A_{\boldsymbol{S}}^{num} = 6G(2p+k-2) \overset{(16a)}{=} 6G(4p-4), \tag{21a}$$

$$A_{\boldsymbol{T}}^{num} = 6G(2p+k) \overset{(16b)}{=} 6G(4p). \tag{21b}$$

Table I and Table II compare the numerical cost of the UM-based scheme (20) and numerical integration (21), for the $\frac{\partial}{\partial\tau}\boldsymbol{S}$ and $\frac{\partial}{\partial\tau}\boldsymbol{T}$ matrix, respectively. The quadrature method of [8] is used. The superiority of the suggested approach is evident.

TABLE I
NUMBER OF SCALED MATRIX ADDITIONS FOR THE STIFFNESS MATRIX

Method	FE Order	Order of Metric Expansion k						
	p	0	1	2	3	4	5	6
Num.	1	6	6	24	48	84	84	144
integ.	2	24	48	84	84	144	216	276
	3	84	84	144	216	276	366	486
This	1	6	6	6	6	6	6	6
work	2	6	24	60	60	60	60	60
	3	6	24	60	120	210	210	210

TABLE II
NUMBER OF SCALED MATRIX ADDITIONS FOR THE MASS MATRIX

Method	FE Order	Order of Metric Expansion k						
	p	0	1	2	3	4	5	6
Num.	1	24	48	84	84	144	216	276
integ.	2	84	84	144	216	276	366	486
	3	144	216	276	366	486	654	840
This	1	6	24	60	60	60	60	60
work	2	6	24	60	120	210	210	210
	3	6	24	60	120	210	336	504

V. NUMERICAL EXAMPLE

We consider a lossless spherical resonator, with the material properties of free space and a perfect electric conductor on its outer boundary. The radius r of the sphere depends on a parameter τ,

$$r(\tau) = (1+\tau)r_0, \tag{22}$$

wherein the nominal radius r_0 is taken to be r_0 = 1 m. The goal is to compute the sensitivity of the resonance eigenvalue k^2 of the dominant mode with respect to τ.

To avoid technicalities with the analysis of convergence rates due to eigenvalues of higher multiplicity, only one quarter of the structure is modeled. Thereby, the symmetry planes are taken to be perfect magnetic conductors. The structure is discretized into 512 tetrahedra, using piecewise 3rd order polynomials for the element shapes. The reference values for the numerical studies below have been obtained from analytical calculations [9].

Fig. 1 presents the relative error in the sensitivity of the dominant eigenvalue: High-order FEs yield the optimal rate of convergence only if the curvilinear boundary is approximated well enough, i.e., if the approximation orders of the metric tensors $\widehat{\mathbf{\Lambda}}^1$ and $\widehat{\mathbf{\Lambda}}^2$ are chosen correctly. It is also interesting to see that approximation by constant metrics (k = 0) performs much better than conventional interpolation by straight-sided tetrahedra.

Fig. 2 demonstrates that increasing the metric approximation beyond a FE-order specific limit does not improve the solution, because the FE matrices are sharp already. Beyond this point, the error in the solution is solely due to the approximation properties of the FE basis.

Since the fields are smooth, the rate of convergence of the eigenvalue sensitivity $\frac{\partial}{\partial \tau} k^2$ is expected to be exponential in the mesh parameter h. The rates obtained from the authors' numerical data, for metric expansion order $k = 6$, are of order $\mathcal{O}(h^{2.04p})$ and $\mathcal{O}(h^{2.07p})$ for basis function order $p = 2$ and $p = 3$, respectively.

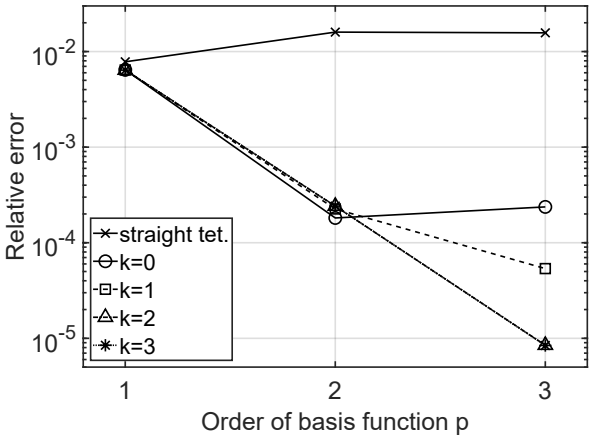

Fig. 1. Relative error in sensitivity of dominant eigenvalue k^2 versus order of FE basis p. Parameter: order of metric approximation k.

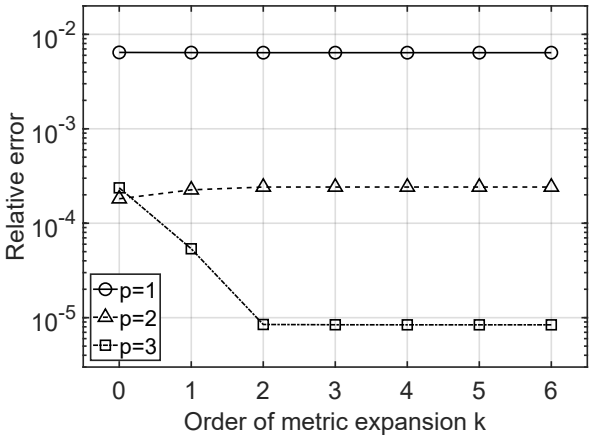

Fig. 2. Relative error in sensitivity of dominant eigenvalue k^2 versus order of metric approximation k. Parameter: order of FE basis p.

VI. Conclusions

An improved method for computing the sensitivity of FE solutions with respect to geometric parameters has been presented. Its key feature is the use of orthogonal hierarchical polynomial expansions for the metric terms present in the FE matrices. This allows the element matrices and their derivatives to be obtained from precomputed universal matrices, even in the curvilinear case. In consequence, the computational costs of the the proposed method are lower than those of traditional methods which use numerical integration. Moreover, it has been shown that there exists a critical order of the metric expansion, which is determined by the degree of the FE basis functions, beyond which the FE matrices and their derivatives will remain constant.

The validity of the suggested approach has been demonstrated by a numerical example, for the sensitivity of resonance wavenumbers.

VII. Appendix

Substituting the hierarchical expansion (14) for the metric tensors in (13) leads to UMs of the form:

$$[\boldsymbol{S}_{ijl}^{mnk}]_{aq} = \int_{\widehat{\Omega}_e} [\nabla_\varphi \times \widehat{\boldsymbol{w}}_a^m]_i \, b_l^k \, [\nabla_\varphi \times \widehat{\boldsymbol{w}}_q^n]_j \, \mathrm{d}\boldsymbol{\varphi}, \tag{23a}$$

$$[\boldsymbol{T}_{ijl}^{mn}]_{aq} = \int_{\widehat{\Omega}_e} [\widehat{\boldsymbol{w}}_a^m]_i \, b_l^k \, [\widehat{\boldsymbol{w}}_q^n]_j \, \mathrm{d}\boldsymbol{\varphi}. \tag{23b}$$

Let $\mathcal{P}^q$ denote the space of scalar polynomials of order q on $\widehat{\Omega}_e$. The products of (the curl of) the basis functions in (23) are readily seen to satisfy:

$$[\nabla_\varphi \times \widehat{\boldsymbol{w}}_a^m]_i \, [\nabla_\varphi \times \widehat{\boldsymbol{w}}_q^n]_j \in \mathcal{P}^{m+n-2}, \tag{24a}$$

$$[\widehat{\boldsymbol{w}}_a^m]_i \, [\widehat{\boldsymbol{w}}_q^n]_j \in \mathcal{P}^{m+n}. \tag{24b}$$

Expressing these in the hierarchical basis $\{b_l^p\}$ yields:

$$[\nabla_\varphi \times \widehat{\boldsymbol{w}}_a^m]_i \, [\nabla_\varphi \times \widehat{\boldsymbol{w}}_q^n]_j = \sum_p^{m+n-2} \sum_i \sigma_i^p b_i^p, \tag{25a}$$

$$[\widehat{\boldsymbol{w}}_a^m]_i \, [\widehat{\boldsymbol{w}}_q^n]_j = \sum_p^{m+n} \sum_i \tau_i^p b_i^p, \tag{25b}$$

with constant coefficients σ_i^p and τ_i^p. In consequence, the entries of the UMs of (23) take the form:

$$[\boldsymbol{S}_{ijl}^{mn}]_{aq} = \sum_p^{m+n-2} \sum_i \sigma_i^p \int_{\widehat{\Omega}_e} b_i^p b_l^k \, \mathrm{d}\boldsymbol{\varphi}, \tag{26a}$$

$$[\boldsymbol{T}_{ijl}^{mn}]_{aq} = \sum_p^{m+n} \sum_i \tau_i^p \int_{\widehat{\Omega}_e} b_i^p b_l^k \, \mathrm{d}\boldsymbol{\varphi}. \tag{26b}$$

Thanks to orthogonality (9), the integrals in (26a) vanish for $k > m + n - 2$ and those in (26b) for $k > m + n$. This completes the proof of (16).

References

[1] D. Villeneuve and J. P. Webb, "Hierarchical universal matrices for triangular finite elements with varying material properties and curved boundaries," International Journal for Numerical Methods in Engineering, vol. 44, no. 2, pp. 215–228, 1999.

[2] D. A. O. Beig, J. Wang, Z. Peng, and J. F. Lee, "A universal array approach for finite elements with continuously inhomogeneous material properties and curved boundaries," IEEE Transactions on Antennas and Propagation, vol. 60, no. 10, pp. 4745–4756, Oct. 2012.

[3] L. L. Tóth and R. Dyczij-Edlinger, "Universal finite-element matrices for curvilinear tetrahedra with continuously varying material properties," in Kleinheubacher Tagung, 2017, p. 32. [Online]. Available: https://www.kh2017.de/KH2017 book of abstracts.pdf.

[4] H. Akel and J. P. Webb, "Design sensitivities for scattering-matrix calculation with tetrahedral edge elements," IEEE Transactions on Magnetics, vol. 36, no. 4, pp. 1043–1046, July 2000.

[5] M. R. Abdelhafez and M. A. Swillam, "Efficient sensitivity analysis approach based on finite element solutions of photonic structures," Optics Communications, vol. 313, pp. 430–435, 2014.

[6] P. Ingelström, "A new set of H(curl)-conforming hierarchical basis functions for tetrahedral meshes," IEEE Transactions on Microwave Theory and Techniques, vol. 54, no. 1, pp. 106–114, Jan. 2006.
[7] R. B. Nelson, "Simplified calculation of eigenvector derivatives," AIAA Journal, vol. 14, no. 9, pp. 1201–1205, 1976.
[8] L. Zhang, T. Cui, and H. Liu, "A set of symmetric quadrature rules on triangles and tetrahedra," Journal of Computational Mathematics, vol. 27, no. 1, pp. 89–96, 2009.
[9] R. Harrington, Time-Harmonic Electromagnetic Fields, ser. IEEE Press Series on Electromagnetic Wave Theory. Wiley, pp. 264–273, 2001.

A DC to HF Volume PEEC Formulation Based on Hertz Potentials and the Cell Method

Riccardo Torchio, Piergiorgio Alotto, Paolo Bettini, Dimitri Voltolina, and Federico Moro
Dipartimento di Ingegneria Industriale
Università di Padova
Padova, Italy
riccardo.torchio@studenti.unipd.it

***Abstract*—A new Partial Element Equivalent Circuit formulation based on Hertz potentials and the Cell Method is presented. Conductive, dielectric, and magnetic linear-homogeneous media are considered by means of conduction, polarization, and magnetization current densities. The use of edge unknowns leads to reduce system size with respect to typical face-based approaches.**

I. Introduction

A large body of literature shows that integral methods are particularly suited to the solution of high frequency electromagnetic problems (EM) involving large domains with the characteristics of vacuum. In particular, the Partial Element Equivalent Circuit (PEEC) method has been shown to be well suited for the analysis of electromagnetic devices, such as printed circuit boards and antennas. The aim of this work is to present a novel 3-D Hertz-PEEC formulation, including conductive, dielectric, and magnetic media. This approach is based on the theory of Hertz potentials [1] and magnetization currents for the magnetic media [2], [3], while in literature Amperian currents [4] or the magnetization [5] are applied. The discretization of the formulation is obtained by means of the Cell Method (CM) [6] and the current density vector, which is the only unknown, is expanded by Whitney face functions [7]. The proposed approach leads to a unified treatment of magnetic and dielectric media which can be handled with a single set of robust and efficient semi-analytical integration routines. The approach is thus capable of solving EM problems over a larger frequency range compared to extant PEEC approaches for magnetic media [5]. Furthermore, the formulation uses edge unknowns, leading to the reduction of the linear system size with respect to other approaches.

II. Integral Formulation

Conductive, dielectric, and magnetic domains Ω_c, Ω_d, and Ω_m (with boundaries Γ_c, Γ_d, and Γ_m, respectively) are considered in the formulation. The domains have no intersection and their disjoint union is $\Omega = \Omega_c \sqcup \Omega_d \sqcup \Omega_m$.

When conductive, dielectric, and magnetic media are considered, the following constitutive relations can be introduced:

$$\begin{aligned} \mathbf{J}_f = \sigma\mathbf{E} \ in\ \Omega_c, \qquad \mathbf{D} = \varepsilon_0\mathbf{E} + \mathbf{P} \ in\ \Omega_d, \\ \mathbf{B} = \mu_0\mathbf{H} + \mu_0\mathbf{M} \ in\ \Omega_m, \end{aligned} \tag{1}$$

where $\mathbf{J}_f$ is the conduction current density, $\mathbf{E}$ and $\mathbf{H}$ are the electric and the magnetic field, $\mathbf{D}$ is the electric displacement and $\mathbf{B}$ is the magnetic flux density, σ is the conductivity, ε_0 and μ_0 are the vacuum permittivity and permeability. The polarization $\mathbf{P}$ and the magnetization $\mathbf{M}$ are introduced as equivalent sources in vacuum, so the effects of dielectric and magnetic media are taken into account. With the introduction of (1), following the approach and notation of [8] (chap. 5, 7), Maxwell's equations in frequency domain can be re-written in a more symmetric form, avoiding the use of $\mathbf{D}$ and $\mathbf{B}$:

$$\begin{aligned} \nabla\cdot\mathbf{E} &= \varepsilon_0{}^{-1}(\varrho_f + \varrho_p), & -\nabla\times\mathbf{E} &= \mathbf{J}_{m^*} + i\omega\mu_0\mathbf{H}, \\ \nabla\cdot\mathbf{H} &= \mu_0{}^{-1}\varrho_{m^*}, & \nabla\times\mathbf{H} &= \mathbf{J}_f + \mathbf{J}_p + i\omega\varepsilon_0\mathbf{E}, \end{aligned} \tag{2}$$

where ϱ_f is the free electric charge density, $\mathbf{J}_p = i\omega\mathbf{P}$ and $\varrho_p = -\nabla\cdot\mathbf{P}$ are the polarization current and bound dielectric charge densities, $\mathbf{J}_{m^*} = i\omega\mu_0\mathbf{M}$ is the magnetization current density and $\varrho_{m^*} = -\nabla\cdot\mu_0\mathbf{M}$ is the bound magnetic charge density. As shown in [1] and [9], it is possible to write the electric field $\mathbf{E}$ and the magnetic field $\mathbf{H}$ as:

$$\begin{aligned} \mathbf{E} &= -(i\omega)^2\boldsymbol{\Pi}_e - \nabla\varphi_e - \varepsilon_0{}^{-1}\nabla\times(i\omega\boldsymbol{\Pi}_m) + \mathbf{E}_0, \\ \mathbf{H} &= -(i\omega)^2\boldsymbol{\Pi}_m - \nabla\varphi_m + \mu_0{}^{-1}\nabla\times(i\omega\boldsymbol{\Pi}_e) + \mathbf{H}_0, \end{aligned} \tag{3}$$

where $\boldsymbol{\Pi}_e$ and $\boldsymbol{\Pi}_m$ are the Hertz electric and magnetic vector potentials, φ_e and φ_m are electric and magnetic scalar potentials and $\mathbf{E}_0$ and $\mathbf{H}_0$ are imposed sources.

By defining $\mathbf{A}_e = i\omega\boldsymbol{\Pi}_e$, and $\mathbf{A}_m = i\omega\boldsymbol{\Pi}_m$ as "new" electric and magnetic vector potentials, applying Lorenz gauge, $\nabla\cdot\mathbf{A}_e = -i\omega\varepsilon_0\mu_0\varphi_e$, $\nabla\cdot\mathbf{A}_m = -i\omega\varepsilon_0\mu_0\varphi_m$, and letting (3) into (2), four partial differential equations can be obtained:

$$\begin{aligned} \Box\mathbf{A}_e &= \mu_0\mathbf{J}_e, & \Box\varphi_e &= \varepsilon_0{}^{-1}(\varrho_f + \varrho_p), \\ \Box\mathbf{A}_m &= \varepsilon_0\mathbf{J}_{m^*}, & \Box\varphi_m &= \mu_0{}^{-1}\varrho_{m^*}, \end{aligned} \tag{4}$$

where $\mathbf{J}_e = \mathbf{J}_f$ in Ω_c and $\mathbf{J}_e = \mathbf{J}_p$ in Ω_d, $\Box = (i\omega)^2\frac{1}{c^2} - \nabla^2$ is the d'Alembert operator and c is the speed of light. The solution of the first equation of (4) is:

$$\mathbf{A}_e(\mathbf{r}_y) = \mu_0\int_\Omega \mathbf{J}_e(\mathbf{r}_x)g(\mathbf{r}_x,\mathbf{r}_y)dr_x, \tag{5}$$

where $\mathbf{r}_y$ is the field point, $\mathbf{r}_x$ is the integration point and $g(\mathbf{r}_x,\mathbf{r}_y) = \frac{e^{-i\omega c^{-1}|\mathbf{r}_y-\mathbf{r}_x|}}{|\mathbf{r}_y-\mathbf{r}_x|}$ is the scalar retarded free space Green function. The solution of the other three equations in (4) is obtained likewise (5).

Submitted On: September 27, 2018
Accepted On: January 1, 2019

III. Cell Method Discretization

The electric domains Ω_c and Ω_d are discretized into primal tetrahedral grids $\mathcal{G}_{\Omega_c}$ and $\mathcal{G}_{\Omega_d}$, consisting of n_c, n_d nodes, e_c, e_d edges, f_c, f_d faces, and v_c, v_d volumes. Then, dual grids $\tilde{\mathcal{G}}_{\Omega_c}$ and $\tilde{\mathcal{G}}_{\Omega_d}$ can be obtained by taking the barycentric subdivision of $\mathcal{G}_{\Omega_c}$ and $\mathcal{G}_{\Omega_d}$ [10]. The same approach can be applied to the magnetic domain Ω_m, but in this case $\tilde{\mathcal{G}}_{\Omega_m}$ is chosen to be made up of tetrahedral elements, while $\mathcal{G}_{\Omega_m}$ is obtained by its barycentric subdivision. The following incidence matrices can be obtained: $\mathbf{G}_{\Omega_\alpha}$ (edges to nodes), $\mathbf{C}_{\Omega_\alpha}$ (faces to edges), and $\mathbf{D}_{\Omega_\alpha}$ (volumes to faces), on $\mathcal{G}_{\Omega_\alpha}$, where $\alpha = c, d, m$ indicates the domain. Dual matrices can be obtained for $\tilde{\mathcal{G}}^a_{\Omega_\alpha}$, i.e., $\tilde{\mathbf{G}}^a_{\Omega_\alpha}$, $\tilde{\mathbf{C}}^a_{\Omega_\alpha}$, $\tilde{\mathbf{D}}^a_{\Omega_\alpha}$, where the superscript a indicates that the matrix is *augmented* [10]. To build the CM formulation, following arrays of degrees of freedom are introduced:

- $\mathbf{j_e} = (j_{e_i})$ on faces $f_i \in \mathcal{G}_{\Omega_c}$, $j_{e_i} = \int_{f_i} \mathbf{J}_e \cdot d\mathbf{S}$,
- $\tilde{\mathbf{j}}_{\mathbf{m}^*} = (\tilde{j}_{m^*_i})$ on faces $\tilde{f}_i \in \tilde{\mathcal{G}}_{\Omega_m}$, $\tilde{j}_{m^*_i} = \int_{\tilde{f}_i} \mathbf{J}_{m^*} \cdot d\mathbf{S}$,
- $\mathbf{h} = (h_i)$ on edges $e_i \in \mathcal{G}_{\Omega_m}$, $h_i = \int_{e_i} \mathbf{H} \cdot d\mathbf{l}$,
- $\tilde{\mathbf{e}} = (\tilde{e}_i)$ on edges $\tilde{e}_i \in \tilde{\mathcal{G}}_{\Omega_c \sqcup \Omega_d}$, $\tilde{e}_i = \int_{\tilde{e}_i} \mathbf{E} \cdot d\mathbf{l}$,
- $\mathbf{a}_m = (a_{m_i})$ on edges $e_i \in \mathcal{G}_{\Omega_m}$, $a_{m_i} = \int_{e_i} \mathbf{A}_m \cdot d\mathbf{l}$,
- $\tilde{\mathbf{a}}_e = (\tilde{a}_{e_i})$ on edges $\tilde{e}_i \in \tilde{\mathcal{G}}_{\Omega_c \sqcup \Omega_d}$, $\tilde{e}_i = \int_{\tilde{e}_i} \mathbf{A}_e \cdot d\mathbf{l}$,
- $\tilde{\boldsymbol{\phi}}_e = (\tilde{\phi}_{e_i})$ on nodes $\tilde{n}_i \in \tilde{\mathcal{G}}_{\Omega_c \sqcup \Omega_d}$, $\tilde{\phi}_{e_i} = \varphi_e(\mathbf{r}_{n_i})$,
- $\boldsymbol{\phi}_m = (\phi_{m_i})$ on nodes $n_i \in \mathcal{G}_{\Omega_m}$, $\phi_{m_i} = \varphi_m(\mathbf{r}_{n_i})$.

The coupling between the domains is enforced by weakly imposing (1):

$$\begin{aligned} \int_{\Omega_c \sqcup \Omega_d} \mathbf{w}_i^f \cdot \big(\rho_e \mathbf{J}_e(\mathbf{r}) - \mathbf{E}(\mathbf{r})\big) d\mathbf{r} = 0, \\ \int_{\Omega_m} \mathbf{w}_i^f \cdot \big(\rho_{m^*} \mathbf{J}_{m^*}(\mathbf{r}) - \mathbf{H}(\mathbf{r})\big) d\mathbf{r} = 0, \end{aligned} \tag{6}$$

where $\rho_e = (\sigma_c)^{-1}$ in Ω_c and $\rho_e = (i\omega\varepsilon_0(\varepsilon_r - 1))^{-1}$ in Ω_d, $\rho_{m^*} = (i\omega\mu_0(\mu_r - 1))^{-1}$, $\mathbf{w}_i^f$ is the Whitney face basis function. By expanding $\mathbf{J}_e$ and $\mathbf{J}_{m^*}$ with $\mathbf{w}_i^f$ and letting (3) into (6), the following system is obtained:

$$\begin{bmatrix} \mathbf{Z}_{11} & \mathbf{Z}_{12} \\ \mathbf{Z}_{21} & \mathbf{Z}_{22} \end{bmatrix} \begin{bmatrix} \mathbf{j}_e \\ \tilde{\mathbf{j}}_{m^*} \end{bmatrix} = \begin{bmatrix} \tilde{\mathbf{e}}_0 \\ \mathbf{h}_0 \end{bmatrix}, \tag{7}$$

where:

- $\mathbf{Z}_{11} = \mathbf{R}_e + i\omega\mathbf{L}_e - \frac{1}{i\omega}\tilde{\mathbf{G}}^a_{\Omega_c \sqcup \Omega_d} \mathbf{P}_e \mathbf{D}^a_{\Omega_c \sqcup \Omega_d}$,
- $\mathbf{Z}_{12} = \mathbf{M}_{1/\varepsilon_0} \mathbf{C}_{\Omega_c \sqcup \Omega_d} \mathbf{L}_{\mathbf{em}}$,
- $\mathbf{Z}_{21} = -\mathbf{M}_{1/\mu_0} \tilde{\mathbf{C}}_{\Omega_m} \mathbf{L}_{\mathbf{me}}$,
- $\mathbf{Z}_{22} = \mathbf{R}_m + i\omega\mathbf{L}_m - \frac{1}{i\omega}\tilde{\mathbf{G}}^a_{\Omega_m} \mathbf{P}_m \mathbf{D}^a_{\Omega_m}$.

$\mathbf{R}$, $\mathbf{L}$, and $\mathbf{P}$ are the "traditional" PEEC resistance, inductance and potential matrices, respectively, $\mathbf{L}_{\mathbf{em}}$ and $\mathbf{L}_{\mathbf{me}}$ are "inductance" matrices representing the coupling between electric and magnetic domains, whereas $\mathbf{M}_{1/\varepsilon_0}$ and $\mathbf{M}_{1/\mu_0}$ are mass matrices. Then, the system can be solved by applying a change of variables (from faces to edges of the mesh) and a projection into a reduced set of equations [4].

IV. Numerical Results

The 3-D Hertz-PEEC code has been developed with MATLAB® for the system assembly and data handling, while MEX-FORTRAN functions combined with OpenMP libraries have been adopted for the computation of the matrix coefficients and post-processing.

The code has been validated on several benchmarks, including the case, shown here, of two spheres with 1m radius, a dielectric one ($\varepsilon_r = 2$) and a magnetic one ($\mu_r = 10$) placed 3m apart on the y-axis and excited by a linearly polarized plane wave $\mathbf{E_0} = e^{-ik_0 x}\mathbf{u}_z$. Where $k_0 = 2\pi f\sqrt{\varepsilon_0\mu_0}$, $f = 30$MHz. The magnitude of the real and imaginary part of the scattered electric field has been compared with the Radio-Frequency module of COMSOL® with good agreement (Fig. 1). Small discrepancies are due to the sphere meshes required by PEEC and FEM, the intrinsic differences of the two approaches, and the numerical post processing adopted for PEEC.

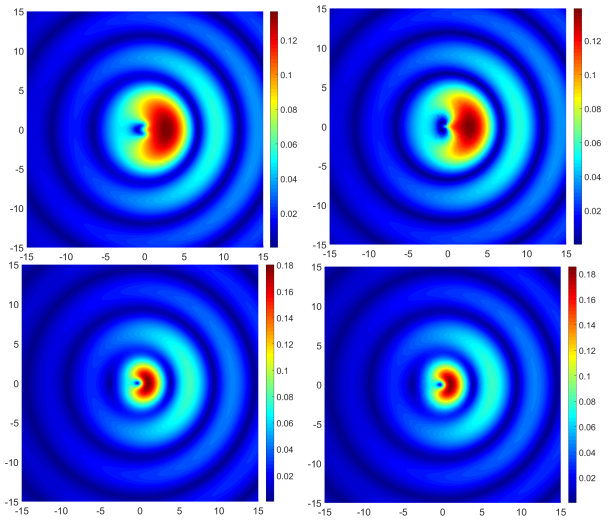

Fig. 1. Scattered Electric Field magnitude V/m, xz-plane, dimensions in m. Left: 3-D PEEC-Hertz. Right: COMSOL®. Top: $\Re$ part. Bottom: $\Im$ part.

References

[1] A. Nisbet, "Herzian electromagnetic potentials and associated gauge transformation," Proceedings of the Royal Society of London A: Mathematical, Physical and Engineering Sciences, 1955.

[2] A. G. Polimeridis, et al., "On the computation of power in volume integral equation formulations," in IEEE Trans. on Antennas and Propag., vol. 63, no. 2, pp. 611-620, Feb. 2015.

[3] J. Markkanen, et al., "Discretization of volume integral equation formulations for extremely anisotropic materials," in IEEE Trans. on Antennas and Propag, vol. 60, no. 11, pp. 5195-5202, Nov. 2012.

[4] R. Torchio, et al., "A 3–D PEEC formulation based on the cell method for full wave analyses with conductive, dielectric, and magnetic media," in IEEE Trans. Magn., 2017.

[5] D. Romano and G. Antonini, "Quasi-static partial element equivalent circuit models of linear magnetic materials," in IEEE Trans. Magn., vol. 51, no. 7, pp. 1-15, July 2015.

[6] F. Freschi and M. Repetto, "A general framework for mixed structured/unstructured PEEC modelling," Applied Computational Electromagnetic Society Journal, vol. 23, no. 3, pp. 200-206, 2008.

[7] J. Siau, et al., "Volume integral formulation using face elements for electromagnetic problem considering conductors and dielectrics," in IEEE Trans. on Electromag. Compat., vol. 58, no. 5, pp. 1587-1594, Oct. 2016.

[8] R. M. Fano, L. J. Chu, and R. B. Adler, *Electromagnetic Fields, Energy, and Forces*. M.I.T. Press, 1960.

[9] J. A. Stratton, *Electromagnetic Theory*. M.I.T. Press, 1941.

[10] L. Codecasa, "Refoundation of the cell method using augmented dual grids," IEEE Trans. Magn., vol. 50, no. 2, Art. ID 7012204, Feb. 2014.

Adjoint Methods for Uncertainty Quantification in Applied Computational Electromagnetics: FEM Scattering Examples

Cameron L. Key [1], Aaron P. Smull [1], Donald J. Estep [2], Troy D. Butler [3], and Branislav M. Notaroš [1]

[1] Electrical & Computer Engineering Department, Colorado State University, Fort Collins, CO
camkey@rams.colostate.edu, aarons24@hotmail.com, notaros@colostate.edu

[2] Department of Statistics, Colorado State University, Fort Collins, CO
Donald.Estep@colostate.edu

[3] Department of Mathematical and Statistical Sciences, University of Colorado Denver, Denver, CO
troy.butler@ucdenver.edu

Abstract **—** We present methods for quantifying uncertainty and discretization error of numerical electromagnetics solvers based on adjoint operators and duality. We briefly introduce the concept of the adjoint operator and describe applications of adjoint solutions for predicting and analyzing numerical error and approximating sensitivity of a given quantity of interest to a given parameter. Forward solutions are based on the higher order finite element method (FEM).

Index Terms **—** Adjoint methods, computational electromagnetics, finite element method, scattering; radar, sensitivity analysis, uncertainty quantification.

I. INTRODUCTION

Computational error estimation, model sensitivity prediction, and optimization are growing areas of interest in the field of computational electromagnetics. While full wave numerical methods using the finite element method (FEM) are ubiquitous in the field, analyzing solutions from these methods is challenging due to geometric discretization error, field order expansion error, and lengthy computation times. Problems requiring numerical methods typically lack analytical solutions, making computational error difficult to discern from measurement error when comparing model results to real-world data where error analysis is desired. Meanwhile, prohibitive computation times make techniques like Monte-Carlo simulation computationally untenable where model sensitivity analysis and optimization are desired.

This paper focuses on an application of adjoint methods toward sensitivity analysis for computational electromagnetics problems. Specifically, it presents an example of an application of an adjoint operator to quantify sensitivity of a quantity of interest (QoI) to perturbations in an input parameter. We use the sensitivity information to predict the QoI over the parameter domain. The computational modeling, both for forward and reverse solutions, in the given example was performed using a double-higher-order FEM solver [1].

II. THE ADJOINT SOLUTION AND ITS APPLICATIONS

To define the adjoint operator for a given problem, we first put the problem in variational form. If the problem is nonlinear, we use the integral Mean Value Theorem to write the problem in linear form. For the illustrative dielectric scatterer problem, we consider the solution of the Dirichlet boundary value problem:

Find $\mathbf{E}^{sc} \in \mathrm{H}^1$ (the space of L^2 functions with L^2 first derivatives) such that the variational formulation of the following holds:

$$\nabla\times\bar{\bar{\mu}}_r^{-1}\nabla\times\mathrm{E}^{sc}-k_0^2\bar{\bar{\varepsilon}}_r\,\mathrm{E}^{sc}=-\nabla\times\bar{\bar{\mu}}_r^{-1}\nabla\times\mathrm{E}^{inc}+k_0^2\bar{\bar{\varepsilon}}_r\,\mathrm{E}^{inc}, \quad (1a)$$

$$n\times\mathrm{E}^{sc}=0, \quad (1b)$$

where the former equation holds through the volume of the domain and the latter holds on the boundary of the domain. This may be stated in linear operator form as:

$$L\mathbf{v}=\mathbf{f}. \quad (2)$$

The adjoint operator of L is then the operator L^* which satisfies:

$$\langle\mathbf{u}, L\mathbf{v}\rangle=\langle L^*\mathbf{u}, \mathbf{v}\rangle, \quad (3)$$

with angle brackets denoting the L^2 inner product between two vectors. The adjoint problem may then be formulated as:

$$L^*\mathbf{v}=\mathbf{p}, \quad (4)$$

where $\mathbf{p}$ denotes a vector representation of a linear functional defining a QoI. A solution for one such adjoint problem is presented in Fig. 1 for scattering from a 1m-radius lossy dielectric sphere with relative permittivity

Submitted On: September 30, 2018
Accepted On: January 1, 2019

ε_r=2.25-1i. Here, the incident wave was chosen to arrive from $\theta = 90°$, $\phi = 0°$ and was modeled to be θ-polarized at 300 MHz with unit electric field amplitude. Figure 2 shows the magnitude of the adjoint solution.

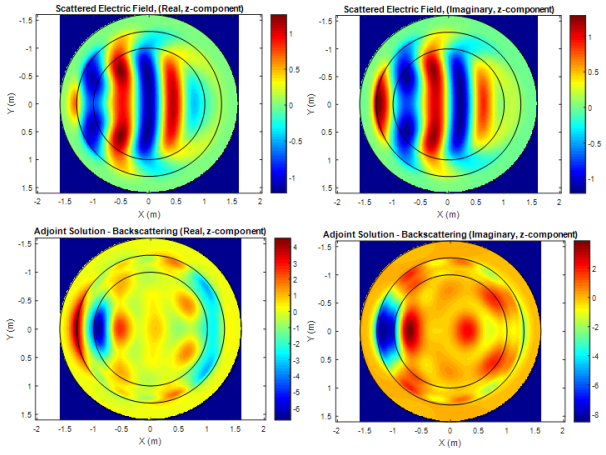

Fig. 1. Solutions to the scattering problem for a lossy dielectric sphere of ε_r=2.25-1i and radius 1 meter in free space. Domain terminated with perfectly matched layer with perfect electric conductor (PEC) exterior boundary. Incident wave was chosen to arrive from $\theta = 90°$, $\phi = 0°$ and θ-polarized at 300 MHz with unit electric field amplitude. Solutions to the adjoint problem are given below the corresponding forward solution.

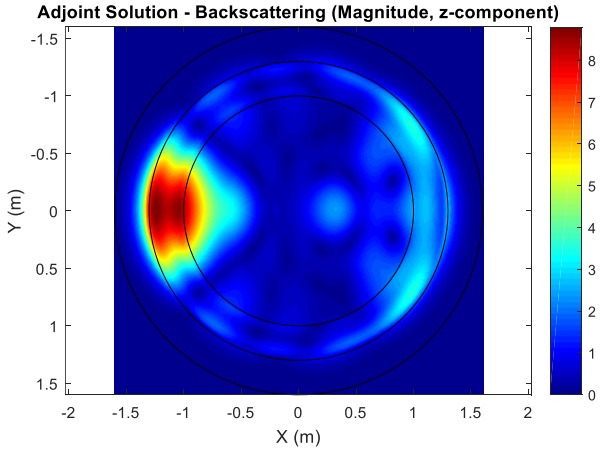

Fig. 2. Magnitude of the *z*-component of the adjoint solution for the problem described in Fig. 1. The areas most affecting the backscattered field lie in the region facing the radar receiver and the Arago spot. Z = 0 cross section is given.

III. FURTHER RESULTS AND DISCUSSION

Given the forward and adjoint solutions at a nominal value of a parameter, values of a desired QoI may be approximated linearly around this parameter value using the adjoint to estimate the derivative of the QoI at the parameter. In [2], this approach is used to construct piecewise linear approximations to the QoI response over the parameter domain in the higher-order parameter sampling method (HOPS). In Fig. 3, we show HOPS results for a 1D analogue of the problem described in Fig. 1. Here, the QoI is the amplitude of the reflected field, and the parameter is the radius of the dielectric scatterer.

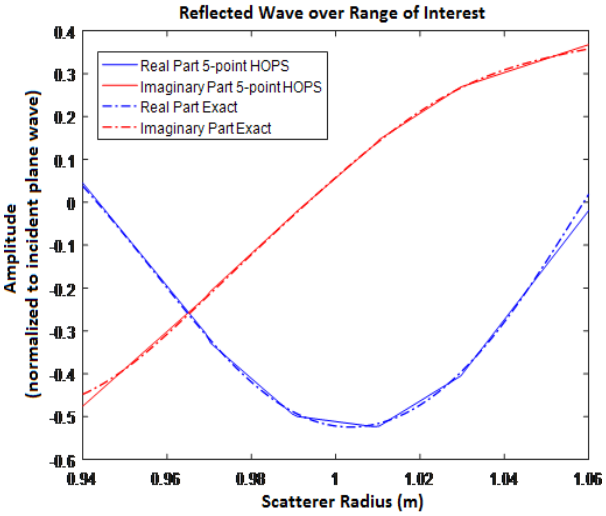

Fig. 3. Amplitude of reflected field calculated using HOPS on adjoint information generated from 1-D higher-order FEM solutions to a lossy dielectric scatterer problem. QoI is amplitude of reflected field and parameter of interest is dielectric scatterer radius.

Figure 4 gives another illustrative example for the same QoI, in this case with respect to the parameter of scatterer conductivity. In both Figs. 3 and 4, we also plot the exact QoI response for which HOPS exhibits excellent agreement. For multiple parameters, we can similarly reconstruct gradient information about the QoI using adjoint solutions. This gradient information allows for faster optimization methods to be employed to optimize a QoI with respect to a set of input parameters. Such information can also be used to reconstruct the underlying relationship between the desired QoI and the given set of input parameters, as shown in Fig. 3 and Fig. 4. An adjoint solution, as given in Fig. 2, may also be used directly to determine areas in the computational domain most affecting some QoI. As expected, for the spherical lossy dielectric scatterer in Fig. 1 the magnitude of the adjoint solution is highest in the region facing the radar receiver and the so-called "Arago Spot" at the center of the opposite face.

Further work will concern utilizing such information for targeted mesh refinement and higher field-order expansion to improve forward solutions.

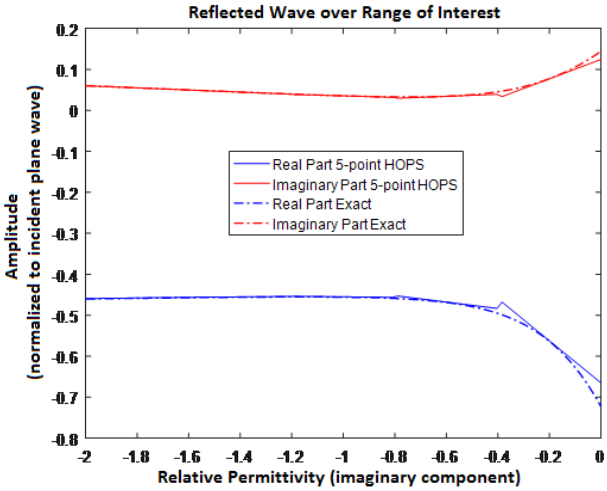

Fig. 4. Amplitude of reflected field calculated using HOPS on adjoint information generated from 1-D Galerkin FEM solutions to a lossy dielectric scatterer problem. QoI is chosen as the magnitude of the reflected field. This is shown with respect to changes in conductivity of the lossy scatterer.

ACKNOWLEDGEMENT

This work was supported by the US Air Force Research Laboratory, CREATE SENTRi, Riverside Research Institute, under contract FA8650-14-D-1725 (6F1957).

REFERENCES

[1] M. M. Ilic and B. M. Notaros, "Higher order hierarchical curved hexahedral vector finite elements for electromagnetic modeling," *IEEE Transactions on Microwave Theory and Techniques*, 51(3), pp. 1026-1033, 2003.

[2] D. Estep and D. Neckels, "Fast and reliable methods for determining the evolution of uncertain parameters in differential equations," *Journal of Computational Physics*, 213(2), pp. 530-556, 2006.

Impact of Flat Radomes on Amplitude-Only Direction Finding Performance

Muhannad A. Al-Tarifi and Dejan S. Filipovic
Department of Electrical, Computer, and Energy Engineering
University of Colorado Boulder
Boulder, CO USA
muhannad.altarifi@colorado.edu, dejan.filipovic@colorado.edu

***Abstract*—We investigate the impact of placing a thin flat radome in front of an amplitude-only direction finding (AODF) antenna system. The considered system consists of two identical Ka-band, air-filled horn antennas squinted off boresight by 30° for direction finding (DF) error within ±0.82°/dB over a field-of-view (FoV) from -20° to +20°. Computational results with various radome materials, thicknesses, and placements indicate that it is possible to maintain excellent DF performance if radome is properly designed and located.**

Keywords—amplitude only direction finding, antenna radome, horn antennas, millimeter-wave antennas.

I. Introduction

Radomes are often desired to provide mechanical and environmental protection of antenna front-ends in air-borne warfare, communication, and sensing applications. A properly-designed radome should provide the required protection with minimal influence on electrical performance [1]. The design challenge varies with the acceptable compromise between the level of protection and electrical transparency as allowed for a specific application. In amplitude-only direction finding (AODF) systems, any alteration of radiation performance is carried to the DF performance in terms of accuracy, field of view (FoV), and bandwidth. Therefore, a careful radome design is essential in order to avoid any degradation of radiation patterns, such as rippling and beamwidth instability.

In this paper we investigate the effect of thin, flat radomes on AODF antenna system operating in the Ka band (26.5–40 GHz). The system consists of two nearly-sectoral horn antennas squinted off in the H-plane to provide two differential beams suitable for low-error DF over -20°–20° FoV. The plane-wave analysis suggests that lower radome permittivity and thickness entails minimal degradation of radiation and, thus, DF performance. This is computationally validated by full-wave simulation in HFSS [2] with the radome placed flush over horn aperture. However, since the radome exists in the near field of the antenna, it is found that far-field performance can also be controlled by adjusting the separation between the radome and horn aperture. Subsequently, excellent DF performance can be maintained with thicker radome sheets.

II. Horn and System Configurations

Fig. 1 shows the configuration and far-field performance of a stand-alone, nearly H-sectoral horn antenna designed for smooth and stable H-plane patterns over the entire Ka band. By squinting two horns off in the H-plane, two distinctive beams suitable for DF scanning are produced. Fig. 2 shows an AODF front-end system with 30° squinted antennas. The direction finding function (DFF), in dB, is the difference between voltage amplitudes at antenna ports or, alternatively, the difference between realized gains of the generated beams. The quality of DFF is determined by its slope (dB/°), shown in Fig. 3, which is inversely proportional to DF errors (°/dB). As seen, the minimum slope is 0.61 dB/°, which corresponds to a maximum DF error of ±0.82°/dB. The purpose is to maintain similar or close DF performance after radome is introduced.

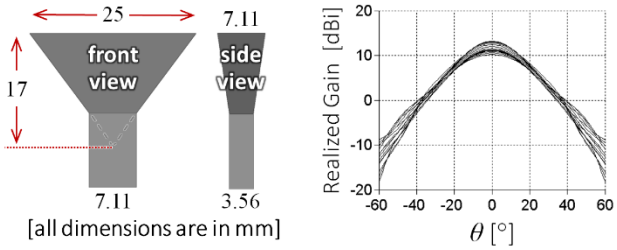

Fig. 1. Configuration of a stand-alone horn antenna (left) and its H-plane radiation patterns (right, 15 curves, 26–40 GHz, 1-GHz step).

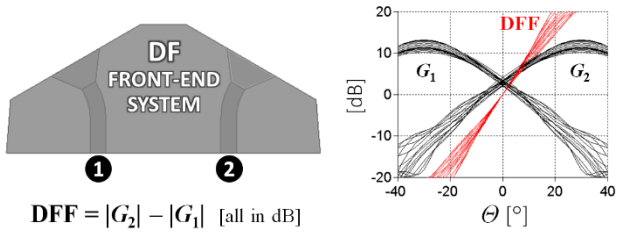

Fig. 2. AODF configuration (left) and DFF performance (right).

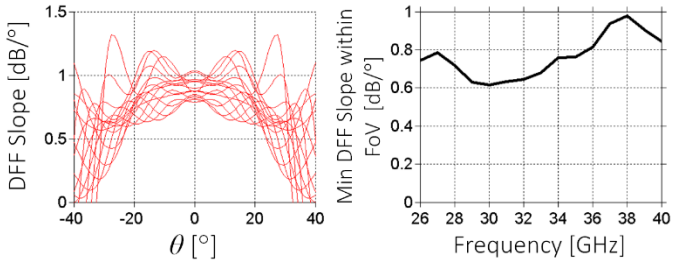

Fig. 3. DFF slope (left) and its minimum in -20°–20° FoV (right).

This research is supported by the Office of Naval Research (ONR) award # N00014-15-1-2111.
Submitted On: September 30, 2018
Accepted On: October 3, 2018

III. Radome Permittivity and Thickness

Initially, the permittivity and thickness of radome are investigated by means of full-wave simulations with various radome types. Specifically, three, commercially-available, dielectric sheets are considered: Rogers RO5880 (ε_r = 2.2) of 0.125-mm thickness, Kapton (ε_r = 3.5) of 0.125-mm thickness, and SHEERGARD™ SX-12 (ε_r = 2.35) of 0.4-mm thickness. All of these sheets are placed flush to the horn aperture, and computational results are presented in Fig. 4 as curves of minimum DFF slope. It is found that the RO5880 radome maintains the best DF performance compared to the higher permittivity Kapton sheet and to the thicker SX-12 composite. This result is expected because thinner and lower permittivity sheets correspond to lower reflection coefficients as analytically predicted by plane-wave analysis of the stand-alone radome [3]. Fig. 5 shows that the RO5880 sheet reflects much less energy compared to Kapton and SX-12; therefore, the total DF performance resembles more closely to the originally designed system with no radome.

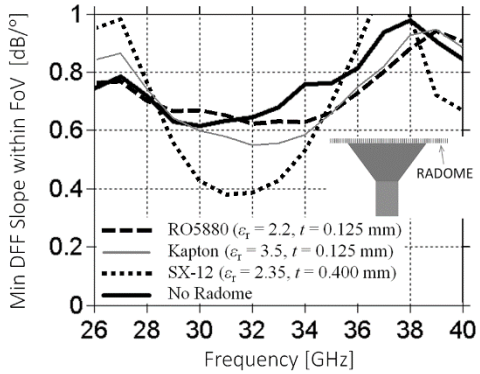

Fig. 4. Minimum DFF slope after applying various radome sheets flush to horn aperture.

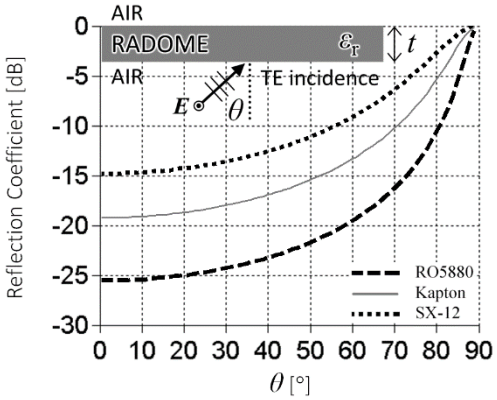

Fig. 5. Reflection coefficient amplitude of a TE plane wave impinging upon various radome sheets.

It is worth to mention that the outcome from the preceding investigation is typically conflicting with mechanical durability that requires more dense radome material (i.e., higher ε_r), higher thickness, or both. Half-wavelength radomes and sandwich arrangements [4] are common choices to increase radome durability at the expense of limiting the bandwidth or field of view, especially for low-error DF applications. Nevertheless, designing radomes based solely on plane-wave analysis ignores the fact that the radome exists at the near field of the antenna and that there might be additional effects of the radome other than energy reflection. Thus, a computational study of radome location is essential in order to choose the best placement of a desired durable radome sheet (such as SX-12).

IV. Radome Separation

Fig. 6 shows DF performance with an SX-12 radome placed at a separation distance *S* from the horn aperture. It is evident that performance varies significantly with *S*, which should not be the case if the plane-wave analysis is an accurate approximation of radome effect. The shown results demonstrate that it is possible to maintain a very high DF accuracy if the SX-12 sheet is placed 5mm away from horn aperture. Despite the added installation complexity (a foam sheet is needed for separation), this radome arrangement presents a more durable choice than a thinner RO5880 flush to the horn. Since radome placement primarily affects the near-field distribution, a new computational study is required when any modification is applied to antenna structure, radome material, or AODF geometry and performance requirement.

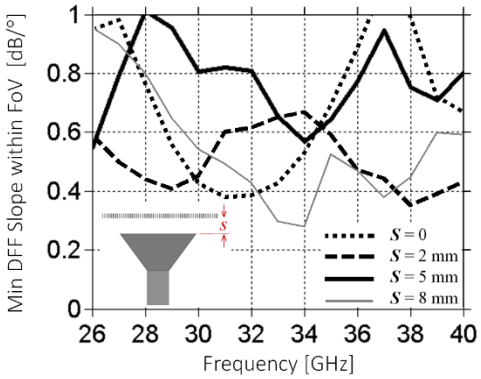

Fig. 6. Minimum DFF slope after applying SX-12 radome at a separation distance *S* from horn aperture.

V. Conclusion

Impact of placing a flat radome in front of an amplitude-only direction finding system is investigated. While thinner, lower-permittivity radomes are preferred, it is still possible to maintain decent DF performance using thicker radomes if it is separated properly from the antenna aperture.

References

[1] D. J. Kozakoff, Analysis of Radome-Enclosed Antennas. Norwood, MA: Artech House, 1997.

[2] Ansoft Inc. High Frequency Structure Simulation (HFSS). Accessed on Nov. 2017. [Online]. Available: http://www.ansys.com

[3] W. C. Chew, Waves and Fields in Inhomogeneous Media. New York: Van Nostrand, 1990, pp. 49-53.

G. A. E. Crone, A. W. Rudge, and G. N. Taylor, "Design and performance of airborne radomes: A review," Proc. Inst. Elect. Eng., pt. F, vol. 128, pp. 451-463, Dec. 1981.

Efficient Multiphysics and Multiscale FDTD Methods for Terahertz Plasmonic Devices

Shubhendu Bhardwaj
Electrical and Computer Engineering
Florida International University
10555 W. Flagler Street, Miami, FL, USA
sbhardwa@fiu.edu

***Abstract*—Modeling terahertz plasmonic devices is a multiphysics and multiscale problem. Due to high mesh density in the electron transport regions, the simulation times are long. In this work, we develop hybrid coupled finite difference time domain (FDTD) methods for fast design of terahertz plasmonic devices. The methods employ implicit solution (using Alternate Direction Implicit), coupled with hydrodynamic modeling for plasmonic applications. The theory, simulation and time-improvement related results will be presented at the conference.**

***Keywords*—FDTD, graphene, HEMT, hydrodynamic, plasmonic modeling, terahertz.**

I. INTRODUCTION

2D electron-gas based terahertz electronics has gained interest for terahertz operations such as mixing and detection. Underlying phenomenon in these devices is plasma-wave oscillations in the 2D electron gas (2DEG) channel [1]. These 2DEG based devices can be modeled using multiphysics modeling tool that integrates the electromagnetic propagation effects and electron transport effects within the devices [2]. This is often accomplished using finite difference time domain (FDTD) based coupled models that integrate hydrodynamic equations in their solution.

A typical 2DEG-channel has an electron density of 10^{11} to $10^{13} cm^{-2}$. Therefore, the plasmonic wavelengths would be 10 to 1000 times smaller than that the free-space. This requires a mesh-size in the order of $\lambda/5000$. As per Courant-Friedrich-Levy (CFL) condition, FDTD time-step for this simulation is 10^{-17}s. This results in long simulations times using traditional FDTD coupled hydrodynamic equations.

In this work, the time-efficiency of the traditional FDTD based model [2] is improved using unconditionally stable FDTD algorithms. First, we present Alternating Direction Implicit (ADI) FDTD method [3] coupled with hydrodynamic equations for terahertz plasmonic applications. Secondly, an iterative-ADI based FDTD method [4] coupled with hydrodynamic equations, is presented for efficient yet accurate modeling. These methods are referred to as ADI-FDTD-HD and it-ADI-FDTD-HD, respectively.

II. GOVERNING EQUATIONS FOR MULTIPHYSICS MODELING

Solution requires modeling of electrodynamic fields via:

$$\nabla \times \vec{H} = \frac{\partial \vec{D}}{\partial t} + \vec{J} + \sigma \vec{E}, \quad \text{and} \tag{1}$$

$$\nabla \times \vec{E} = -\frac{\partial \vec{B}}{\partial t} - \sigma^* \vec{H}. \tag{2}$$

For 2D TE$_Z$ solution, electric field $\vec{E} = \hat{x}E_x + \hat{y}E_y$ is used. Electrical and magnetic conductivity parameters, i.e., σ and σ^*, are used for the modeling of anisotropic, perfectly matched layer surrounding the domain. Electron transport in the channel is modelled via hydrodynamic equations, given by,

$$\frac{\partial n_{sh}}{\partial t} + \frac{\partial j}{\partial x} = 0, \quad \text{and} \tag{3}$$

$$\frac{\partial j}{\partial t} + v\frac{\partial j}{\partial x} + \frac{j\partial v}{\partial x} = -\frac{qnE_x}{m_e} - \frac{j}{\tau} - \frac{KT}{m_e}. \tag{4}$$

Here n_{sh} is the sheet carrier density, j (= $n_{sh}v$) is the sheet current and v is the electron velocity within the 2DEG channel. τ refers to the momentum relaxation time and m_e is the effective electron mass. q = 1.6×10−19 C is the charge-magnitude of a single electron. T is the electron temperature in the channel and K is the Boltzmann constant.

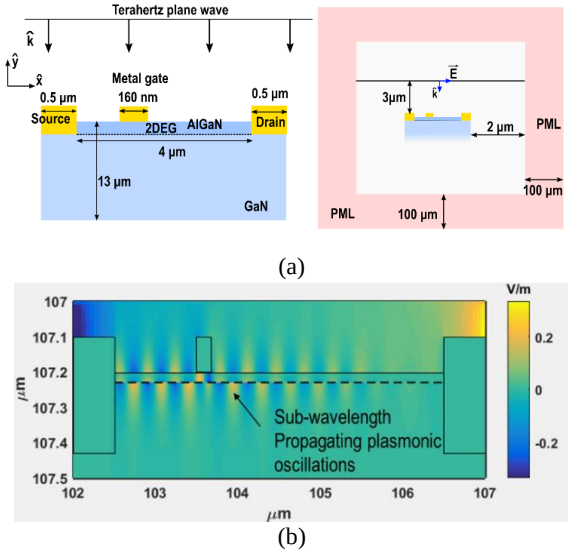

Fig. 1. GaN/AlGaN High Electron Mobility Transistor (HEMT) model used for the performance evaluation of the algorithms. Left: Schematic showing device-dimensions and excitation-method. Right: Simulation domain and position of PML boundaries. (b) Plasmonic field obtained at t=3ps, propagating away from discontinuity.

Submitted On: September 1, 2018
Accepted On: October 3, 2018

III. ADI-FDTD-HD AND IT-ADI-FDTD-HD METHODS

Note that solution of hydrodynamic equations is carried by upwind discretization, similar to prior work in [2] and will not be discussed here. The distinction of this work, use of ADI-FDTD and it-ADI-FDTD methods, is briefly explained in the following.

A. ADI-FDTD-HD Method

The ADI-FDTD approach uses a splitting-operator applied on the electrodynamic equations to yield an implicit form of difference equations [3, 4]. Notably, these equations are tridiagonal and can be solved at a small computational cost. In the meantime, the time-steps can be arbitrarily large, reducing the simulation-times. In ADI-FDTD method, the accuracy is perturbed by a second order terms (which is truncated so as to achieve a tridiagonal system of linear implicit equations [5]). This error term (so-called splitting error or truncation error) is proportional to Δt^2 and second order spacial derivative of field [3] (Δt is the time-step).

B. Iterative ADI-FDTD-HD Method

The iterative method uses the basic ADI-FDTD method with added iterative corrections to correct ignored Δt^2 term [4]. Note that it-ADI-FDTD and ADI-FDTD are both O(Δt^2) accurate. However, iterative method has more accuracy due to correction of additionally truncated term of the ADI method. The added iterations come at some time-cost, but overall performance is maintained over the traditional FDTD-HD method.

IV. PERFORMANCE COMPARISON

For performance bench-marking, we modeled a gallium nitride (GaN) based High Electron Mobility Transistor (HEMT) device under the influence of an incident terahertz plane-wave excitation (freq. = 5 THz) (Fig. 1). A small gate discontinuity is used for coupling of the incident terahertz waves to the 2DEG channel. The channel and media parameters are chosen as $n_{sh} = 5 \times 10^{12}\ cm^{-2}$, $\epsilon_r = 9.5$, $m_e = 0.2m_o$ and $\tau = 1.14$ ps (considering low temperature operation). The cell-size along *x*-axis was chosen to be $\Delta x = 4$ nm in the channel area. The minimum mesh of $\Delta y = 1$ nm was used in vertical direction. For outside the channel regions, non-uniform meshing scheme was used, resulting in 1460 and 740 cells respectively in the horizontal and vertical directions. Simulation is allowed to run for 3 ps.

For comparison, the obtained channel-currents are plotted in Fig. 2. The simulation-cases considered here are *CN*=300, <*CN*=300, *it*=3>, <*CN*=300, *it*=7>. Here *CN* refers to Courant Number and *it* refers to the number of iterations used for the iterative case. That is, *CN*=300 case is for ADI-FDTD-HD algorithm and rest are for it-ADI-FDT-HD method. As shown in the plot, in ADI-FDTD-HD method the solution diverges from the reference data, however errors are recovered by adding more and more iterations. Specifically, for 7 iterations the solution converges to the reference solution. Here, the reference solution corresponds to the Yee's FDTD method [6]. Comparison of total simulation times for various scenarios are shown in Table I. As shown *CN*=300, *it*=7 case takes only half of total simulation time taken by the original reference case. Thus, high degree of accuracy if achieved with almost 50% decrease in simulation times. Note that CPU-time for ADI-FDTD-HD cases may also be calculated by simply dividing the it-ADI-FDTD-HD's CPU time by corresponding *it* count. A more rigorous analysis and results are can be referred from [7].

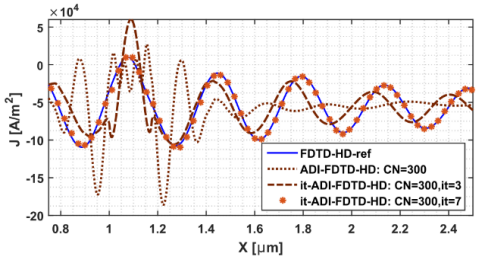

Fig. 2. Channel current at 3 ps calculated using reference (FDTD-HD) and proposed ADI-FDTD and it-ADI-FDTD schemes.

Table I. TIME COMPARISON FOR IT-ADI-FDTD-HD METHODS

`	ΔT (s)	CPU-Time Per Time-Step (s)	CPU-Time Total (Hrs)
FDTD-HD	3.24×10^{-18}	0.35	90
it-ADI-FDTD-HD (*CN*=100, *it*=2)	3.24×10^{-16}	15.17	39.14
it-ADI-FDTD-HD (*CN*=200, *it*=4)	6.48×10^{-16}	30.25	19.16
it-ADI-FDTD-HD (*CN*=300, *it*=7)	9.72×10^{-16}	53.11	43.64

V. CONCLUSIONS

We have proposed efficient method for multiphysics modeling using iterative-ADI-FDTD methods. For the devices under consideration, the total simulation time was reduced by a factor of 0.42 using it-ADI-FDTD-HD method, while nominal 3% error was registered. Overall, we maintained the accuracy-levels with significant time-cost advantages as compared to traditional explicit-FDTD modeling.

REFERENCES

[1] M. Dyakonov and M. Shur, "Detection, mixing, and frequency multiplication of terahertz radiation by two-dimensional electronic fluid," IEEE Transactions on Electron Devices, vol. 43, no. 3, pp. 380–387, Mar. 1996.

[2] S. Bhardwaj, N. K. Nahar, S. Rajan, and J. L. Volakis, "Numerical analysis of terahertz emissions from an ungated hemt using full-wave hydrodynamic model," IEEE Transactions on Electron Devices, vol. 63, no. 3, pp. 990–996, 2016.

[3] T. Namiki, "A new FDTD algorithm based on alternating-direction implicit method," IEEE Transactions on Microwave Theory and Techniques, vol. 47, no. 10, pp. 2003–2007, 1999.

[4] S. Wang, F. L. Teixeira, and J. Chen, "An iterative ADI-FDTD with reduced splitting error," IEEE Microwave and Wireless Components Letters, vol. 15, no. 2, pp. 92–94, 2005.

[5] S. G. Garcia, Tae-Woo Lee and S. C. Hagness, "On the accuracy of the ADI-FDTD method," in IEEE Antennas and Wireless Propagation Letters, vol. 1, pp. 31-34, 2002.

[6] Allen Taflov and S. C. Hagness. "Computational Electrodynamics: the finite-difference time-domain method," Artech House, 2005.

[7] S. Bhardwaj, F. L. Teixeira, and J. L. Volakis, "Fast modeling of terahertz plasma-wave devices using unconditionally stable FDTD methods," in IEEE Journal on Multiscale and Multiphysics Computational Techniques, vol. 3, pp. 29-36, 2018.

Numerical Validation of a Boundary Element Method with Electric Field and Its Normal Derivative as the Boundary Unknowns*

Johannes Markkanen[1], Alex J. Yuffa[2], and Joshua A. Gordon[2]

[1]Max Planck Institute for Solar System Research, Göttingen, 37077, Germany
markkanen@mps.mpg.de

[2]National Institute of Standards and Technology, Boulder, CO 80305, USA
alex.yuffa@nist.gov, josh.gordon@nist.gov

Abstract – We recently developed a surface integral equation method where the electric field and its normal derivative are chosen as the boundary unknowns. After reviewing this formulation, we present preliminary numerical calculations that show good agreement with the known results. These calculations are encouraging and invite the further development of the numerical solution.

Index Terms – Boundary element method, electromagnetic scattering, surface integral equations.

I. INTRODUCTION

We have recently formulated a frequency domain surface integral equation method [1] that is applicable to penetrable closed surface scatterers. The method has several unique applications and advantages over the standard Stratton–Chu formulation as discussed in [1]. In our formulation, we choose the electric field (E-field) and its normal derivative as the boundary unknowns. This choice leads to 12 scalar unknowns on the surface of the scatterer; for each homogeneous region we have three scalar unknowns associated with the E-field and three scalar unknowns associated with its normal derivative. Similar to a typical surface integral equation formulation, our formulation is also based on the Green's theorem (Green's second identity). This formulation leads to *six* scalar equations, and thus it must be supplemented with *six* additional constraints in order to have the same number of equations as unknowns. Three of these constraints come from the well-known continuity condition of the E-field across an interface and the other three come from the recently derived continuity condition for the normal derivative of the E-field [1–3].

In this paper, we numerically solve the above discussed equations for several scatterers and compare our results to the results obtained via other methods. We also comment on the choice of the basis functions in the Galerkin's method and its effects on numerical convergence.

II. FORMULATION REVIEW

Consider a scatterer with permittivity $\overset{2}{\epsilon}$ and permeability $\overset{2}{\mu}$. The space surrounding the scatterer is assumed to be lossless with permittivity $\overset{1}{\epsilon}$ and permeability $\overset{1}{\mu}$, i.e., $\{\overset{1}{\epsilon},\overset{1}{\mu}\} \in \mathbb{R}$. If we apply the Green's second identity to the scatterer and the surrounding space, then, after setting the observation point on the surface of the scatterer, we obtain:

$$\overset{\text{inc}}{\boldsymbol{E}}(\widetilde{S}) - \fint_{\Sigma}\left[\overset{1}{G}\frac{\partial \overset{1}{\boldsymbol{E}}}{\partial N} - \overset{1}{\boldsymbol{E}}\frac{\partial \overset{1}{G}}{\partial N}\right]\mathrm{d}S = \frac{1}{2}\overset{1}{\boldsymbol{E}}(\widetilde{S}), \quad (1a)$$

and

$$\fint_{\Sigma}\left[\overset{2}{G}\frac{\partial \overset{2}{\boldsymbol{E}}}{\partial N} - \overset{2}{\boldsymbol{E}}\frac{\partial \overset{2}{G}}{\partial N}\right]\mathrm{d}S = \frac{1}{2}\overset{2}{\boldsymbol{E}}(\widetilde{S}), \quad (1b)$$

where $\overset{\text{inc}}{\boldsymbol{E}}$ is the incident E-field, $\fint$ denotes the Cauchy principal value integral, Σ denotes the surface of the scatterer, $\frac{\partial}{\partial N}$ denotes the normal derivative, G is the free-space Green's function, and $\widetilde{S}$ is the observation point on Σ. In (1), the overset digit indicates if the quantity is associated with the scatterer or the surrounding space, e.g., $\overset{2}{\boldsymbol{E}}$ is the E-field just inside the scatterer. In the Gaussian unit system, the continuity condition for the E-field across an interface can be written as [1]:

$$\overset{2}{\boldsymbol{E}} = \overset{r}{\epsilon}{}^{-1}\left(\boldsymbol{N}\cdot\overset{1}{\boldsymbol{E}}\right)\boldsymbol{N} + \left(\boldsymbol{S}^{\alpha}\cdot\overset{1}{\boldsymbol{E}}\right)\boldsymbol{S}_{\alpha}, \quad (2a)$$

and the continuity condition for its normal derivative as [1]:

$$\frac{\partial \overset{2}{\boldsymbol{E}}}{\partial N} = \overset{r}{\mu}\left(\frac{\partial \overset{1}{\boldsymbol{E}}}{\partial N} - \nabla^{\alpha}\left[\left(\boldsymbol{N}\cdot\overset{1}{\boldsymbol{E}}\right)\boldsymbol{S}_{\alpha} - \left(\boldsymbol{S}_{\alpha}\cdot\overset{1}{\boldsymbol{E}}\right)\boldsymbol{N}\right]\right) + \nabla^{\alpha}\left[\left(\boldsymbol{N}\cdot\overset{2}{\boldsymbol{E}}\right)\boldsymbol{S}_{\alpha} - \left(\boldsymbol{S}_{\alpha}\cdot\overset{2}{\boldsymbol{E}}\right)\boldsymbol{N}\right], \quad (2b)$$

*U.S. Government work not protected by U.S. copyright.

Submitted On: September 26, 2018
Accepted On: December 28, 2018

where $\overset{r}{\mu} = \overset{2}{\mu} / \overset{1}{\mu}$, $\overset{r}{\epsilon} = \overset{2}{\epsilon} / \overset{1}{\epsilon}$, $\boldsymbol{N}$ is the unit-normal pointing out of the scatterer, $\boldsymbol{S}_\alpha$ is the surface covariant basis [4], and ∇^α is the contravariant surface derivative [4]. Notice that (2) is written in the Einstein summation convention where the Greek indices range from 1 to 2. Substituting (2) into (1b) and using Gauss's theorem in two dimensions yields [1]:

$$\begin{aligned}\frac{1}{2}\overset{2}{\boldsymbol{E}}(\widetilde{S}) =& \fint_\Sigma \left[\overset{r}{\mu}\overset{2}{G}\frac{\partial \overset{1}{\boldsymbol{E}}}{\partial N} - \overset{1}{\boldsymbol{E}}\frac{\partial \overset{2}{G}}{\partial N}\right] \mathrm{d}S \\ &+ \left(\overset{r}{\mu} - \overset{r}{\epsilon}^{-1}\right) \fint_\Sigma \left(\boldsymbol{N}\cdot\overset{1}{\boldsymbol{E}}\right) \boldsymbol{\nabla}\overset{2}{G}\, \mathrm{d}S \\ &+ (1-\overset{r}{\mu}) \fint_\Sigma \left(\overset{1}{\boldsymbol{E}}\cdot\boldsymbol{\nabla}\overset{2}{G}\right) \boldsymbol{N}\, \mathrm{d}S, \end{aligned} \tag{3a}$$

where

$$\overset{2}{\boldsymbol{E}} = \overset{1}{\boldsymbol{E}} + \left(\overset{r}{\epsilon}^{-1} - 1\right)\left(\boldsymbol{N}\cdot\overset{1}{\boldsymbol{E}}\right)\boldsymbol{N}. \tag{3b}$$

Equations (3) and (1a) form a set of *six* scalar integral equations with *six* scalar unknowns, namely, $\overset{1}{\boldsymbol{E}}$ and $\frac{\partial}{\partial N}\overset{1}{\boldsymbol{E}}$. This is the set of the integral equations that we numerically solve in the next section.

III. NUMERICAL CALCULATIONS

We discretize the scatterers with flat triangular elements and construct a basis for the E-field and its normal derivative. We use piecewise constant basis functions for each component associated with the triangular surfaces. Thus, the number of unknowns is six times the number of the triangular elements. Furthermore, we use Galerkin's method to discretize the equations. In other words, the test and basis functions are identical. It is worth noting that the basis functions *do not* enforce any continuity conditions for the E-field or its normal derivative along the surface. Hence, it is clear that we cannot obtain an optimal convergence rate. Moreover, we anticipate that the sharp wedges may also cause some difficulties. Finding a better set of basis functions is an interesting question for future research.

The integral equation set given by (3) and (1a) contains singular integrals. The gradient of the Green's function has the strongest singularity, and we decompose it into the normal and surface derivative parts. With the help of integration by parts, the latter one reduces to an integral over a triangular surface and a closed integral over the triangle's edges. We evaluate these integrals using the standard singularity extraction technique [5] in which the singular part is calculated analytically and the remaining part is calculated numerically. We solve the resulting system of equations for the boundary unknowns iteratively with the generalized minimal residual GMRES method with the tolerance of 10^{-5}.

To assess the method, we compare the radar cross-section (RCS) of a sphere in free-space meshed by 940 flat triangular patches with the Mie series solution. Figure 1 shows the RCS of a dielectric sphere with $\overset{1}{k}\rho = 1$, $\overset{2}{\epsilon} = 4$, and $\overset{2}{\mu} = 1$, where ρ is the radius of the sphere and Fig. 2 shows the RCS of a lossy sphere with $\overset{1}{k}\rho = 4$, $\overset{2}{\epsilon} = -2 + \mathrm{i}$, and $\overset{2}{\mu} = 1$. From the figures, we see that our solution agrees well with the Mie series solution in both the dielectric case and the lossy case. More specifically, the L^2-norm relative error of the far-field $\|\boldsymbol{E}\|^2$ integrated over a solid angle is 4.832×10^{-3} for Fig. 1 and 9.360×10^{-3} for Fig. 2. In general, the accuracy of the solution depends on the shape, size, electric permittivity, and discretization of the scatterer. The current discretization scheme leads to a less accurate solution with respect the mesh density than the conventional Poggio–Miller–Chan–Harringto–Wu–Tsai (PMCHWT) formulation discretized with the RWG functions. This is not surprising because our basis functions are not the most optimal. This is discussed in more detail in Section IV.

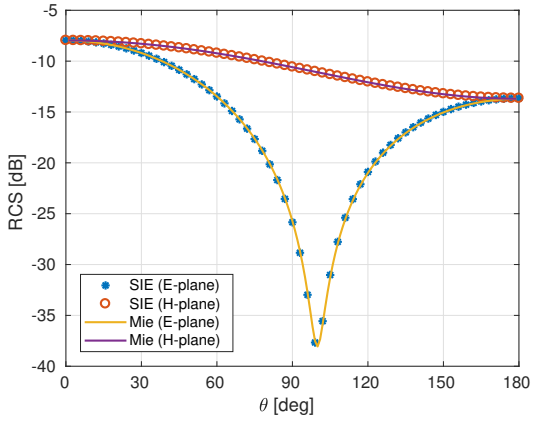

Fig. 1. (Color online) Comparison of the dielectric sphere's RCS as a function of the scattering angle θ computed via the surface integral equation (SIE) method with the Mie series solution.

Next, we investigate the stability of the method with respect to the element size. Because our formulation contains only weakly singular integrals, we expect the condition number of the system matrix to be almost independent of the element size. To demonstrate this, we discretize a cube with and without mesh refinement on edges as shown in Fig. 3. The condition number for the equally triangulated cube equals 117 and for the refined cube it equals 178. In the case of the PMCHWT formulation, the corresponding numbers are 1.0×10^5 and 1.3×10^6, respectively. Hence, the formulation based on the field and its normal derivative is much more stable than the standard surface integral equation formulation without any regularization technique.

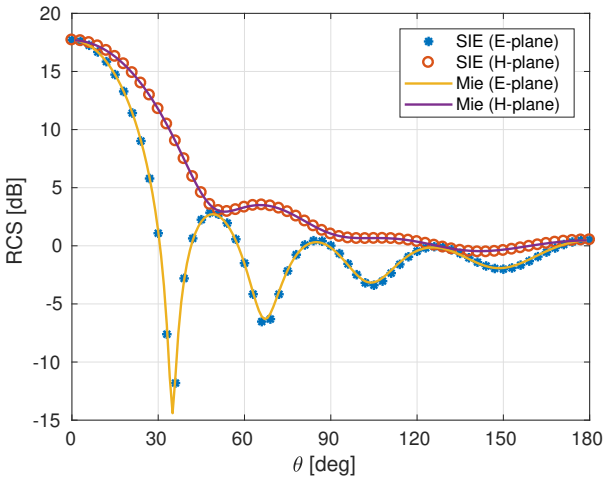

Fig. 2. (Color online) Comparison of the lossy sphere's RCS as a function of the scattering angle θ computed via the surface integral equation (SIE) method with the Mie series solution.

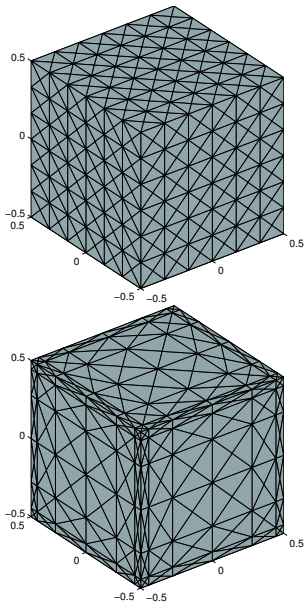

Fig. 3. The discretization of a cube with and without mesh refinements is shown. The condition number associated with the left-hand side cube is 117 and the condition number associated with the right-hand side cube is 178.

Finally, in Fig. 4 we compare the radar cross-section of a dielectric cube computed via our formulation to the standard PMCHWT formulation with the RWG basis and testing functions. We see that the two solutions approach each other with the decreasing element size.

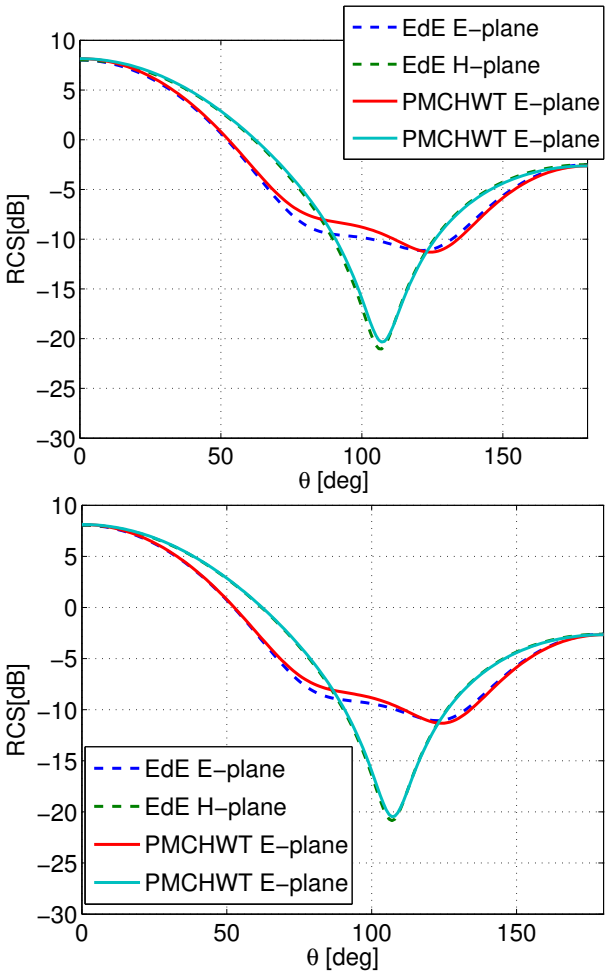

Fig. 4. Scattering by a cube discretized with 432 (top) and 1200 (bottom) triangular elements computed by the new formulation (dash lines) and by the standard PMCHWT formulation (solid lines).

IV. DISCUSSION

We have shown that the discretization scheme using the piecewise constant functions and Galerkin's testing gives a reasonable accuracy for scattering problems involving large and smooth scatterers. However, particularly at low frequencies, the discretization scheme results in low accuracy. This is because we have not exactly enforced the zero divergence condition on the boundary surface. The zero divergence condition can be enforced by requiring that (4) holds on each surface patch. Namely, we require that: [1]

$$\int_{\Pi_i} \boldsymbol{N} \cdot \frac{\partial \boldsymbol{E}}{\partial N} \mathrm{d}S = \int_{\Pi_i} (\boldsymbol{N} \cdot \boldsymbol{E}) W_\alpha^\alpha \mathrm{d}S - \int_{\partial \Pi_i} n^\alpha (\boldsymbol{S}_\alpha \cdot \boldsymbol{E}) \mathrm{d}C, \quad (4)$$

where W_α^α is the mean curvature tensor, n^α is the tangential surface vector perpendicular to $\partial\Pi_i$, and Π_i is the support of ith basis function. In the case of a smooth surface, the last term on the right-hand side cancels with the adjacent surface patches. Thus, in this case, the normal components of the basis functions can be combined such that the divergence of the surface field is exactly zero. In the case of a non-smooth surface, the last term on the right-hand side does not cancel with the neighbouring surface patches and therefore must be computed explicitly. This requires using basis functions spanning a proper function space for the tangential field. Such basis functions are outside the scope of this paper and were not used in the present work.

V. CONCLUSIONS

We numerically tested a recently formulated surface integral equation method where the electric field and its normal derivative are chosen as the boundary unknowns. The preliminary results presented here are in agreement with the Mie series solution for both dielectric and lossy spheres. Furthermore, the method seems to be viable for numerical computations and may be further improved if we employ basis functions that enforce the continuity conditions.

REFERENCES

[1] A. J. Yuffa and J. Markkanen, "A 3-D tensorial integral formulation of scattering containing intriguing relations," *IEEE Transactions on Antennas and Propagation*, vol. 66, no. 10, pp. 5274–5281, Oct. 2018.

[2] J. DeSanto and A. Yuffa, "A new integral equation method for direct electromagnetic scattering in homogeneous media and its numerical confirmation," *Waves in Random and Complex Media*, vol. 16, no. 4, pp. 397–408, Nov. 2006.

[3] J. A. DeSanto, "A new formulation of electromagnetic scattering from rough dielectric interfaces," *Journal of Electromagnetic Waves and Applications*, vol. 7, no. 10, pp. 1293–1306, Jan. 1993.

[4] P. Grinfeld, *Introduction to Tensor Analysis and the Calculus of Moving Surfaces*, Springer, New York, 2013.

[5] S. Järvenpää, M. Taskinen, and P. Ylä-Oijala, "Singularity subtraction technique for high-order polynomial vector basis functions on planar triangles," *IEEE Transactions on Antennas and Propagation*, vol. 54, no. 1, pp. 42–49, 2006.

Johannes Markkanen received the D.Sc. degree in Electromagnetics from the Department of Radio Engineering, Aalto University, Espoo, Finland, in 2013. From 2014 to 2018, he was a Post-Doctoral Researcher with the Department of Physics, University of Helsinki, Helsinki, Finland. He is currently a Post-Doctoral Researcher with the Max Planck Institute for Solar System Research, Göttingen, Germany. His current research interests include computational methods in electromagnetics and thermophysics with an emphasis on planetary science applications.

Alex J. Yuffa received the B.Sc. degree (Hons.) in Mathematical and Computer Sciences, the B.Sc. degree (Hons.) in Engineering Physics, and the M.Sc. and Ph.D. degrees in Applied Physics from the Colorado School of Mines, Golden, CO, USA. In 2013, he joined the U.S. Army Research Laboratory, Adelphi, MD, USA, first as an ORAU PostDoctoral Research Fellow and then as a Physical Scientist. In 2016, he joined the National Institute of Standards and Technology, Boulder, CO, USA, as a Physicist. His research has been highlighted in *Optics and Photonics News magazine* and featured on the covers of *Optics and Photonics News magazine* and *Applied Optics journal*.

Joshua A. Gordon received the Doctorate degree in Optics and Electromagnetics from the College of Optical Sciences, University of Arizona, Tucson, AZ, USA. He is a Physicist in the Electromagnetics Division at the National Institute of Standards and Technology, Boulder, CO, USA. His current research areas investigate new technologies for electric field measurements which include robotic based antenna metrology systems, optical techniques for antenna alignment, and atom-based electric-field sensing.

Ray Tracing Using Shooting-Bouncing Technique to Model Mine Tunnels: Theory and Verification for a PEC Waveguide

Blake A. Troksa, Cam L. Key, Forest B. Kunkel, Slobodan V. Savić, Milan M. Ilić, and Branislav M. Notaroš

Department of Electrical & Computer Engineering
Colorado State University, Fort Collins, CO, USA
blake.troksa@gmail.com, camkey@rams.colostate.edu, forestkunkel@gmail.com, ssavic@@etf.bg.ac.rs, milanilic@etf.bg.ac.rs, notaros@colostate.edu

***Abstract*—**We present a shooting-bouncing approach to ray-tracing as applied to signal propagation modeling in electrically large waveguides, such as underground mine tunnels at wireless communication frequencies. The method is verified for a dominant-mode rectangular metallic waveguide excited by a dipole antenna.

Keywords*—communications, computational electromagnetics, high-frequency, microwave, ray tracing, signal propagation, waveguide.*

I. INTRODUCTION

This paper addresses application of computational electromagnetics (CEM) to signal propagation modeling in underground mines. One of our main approaches to the wireless propagation analysis of underground mines, which is an extremely challenging CEM problem, relies primarily on shooting-bouncing rays (SBR) ray-tracing (RT).

Using traditional full-wave EM solvers for microwave frequencies in an underground mine may prove impractical in many cases due to computation run time required, as well as memory requirements, depending on the particular technique employed. Ray-tracing provides a significant decrease in computational run time for these electrically large structures. Ray-tracing methods enable propagation modeling in very complicated scenarios such as railway stations, and they can provide useful prediction of signal loss characteristics [1,4].

II. RAY TRACING THEORY

The shooting-bouncing rays approach in RT involves launching a set of test rays in all directions in which propagation from the source can be expected. These rays are then traced through the scene, and their intersections with objects in the scene recorded. This method is described in detail in [1]. The electric field at a desired location in the scene is then found by employing an ideal plane wave approximation for each ray. Then, using the reflection coefficients based on surface parameters for each reflection, the final electric field at the desired observation point can be approximated due to each ray path between the source and observation point [3]. This process may be repeated for several observation points to produce a 2D or 3D field profile at a desired location in the scene.

When a 2D field profile is desired, we discretize the plane of the desired field profile into a grid of uniform pixels or grid blocks. The complex-valued field vectors of all rays intersecting a given block are added to approximate the total field at that block due to the given source and scene geometry. This process naturally approximates interference. While this introduces phase and magnitude error, the error can be minimized by ensuring the grid blocks are small relatively to the wavelength, and that a large number of rays are used, such that each block has a sufficiently high sample density to accurately approximate the field.

The shooting-bouncing approach to ray-tracing is advantageous because it is conveniently parallelizable which allows for efficient and expeditious computations. This is essential because it enables analysis of problems that require very high ray counts to achieve sufficient sample density for field convergence. Another benefit to the acceleration (by parallelization) of ray-tracing is that larger structures can be evaluated for signal propagation characteristics more easily and more quickly. This technique may be further accelerated by reducing the total cost of ray to facet (environment objects) intersection tests. The rays that propagate in this model interact with environment objects that cause the rays to be reflected. These interactions with the environment can be optimized using space-partitioning trees that efficiently store and access obstacles located in the environment (similar to a binary search tree) [1,2].

III. RESULTS AND DISCUSSION

Testing of the ray-tracing method we developed was conducted on a perfect electric conductor (PEC) rectangular waveguide. This scene was chosen because of the ability to compare with an analytic solution for verification. The waveguide dimensions are chosen to be 0.5842 m × 0.2921 m, and the waveguide was excited with a Hertzian dipole antenna of unit peak field magnitude and frequency 350 MHz. The observation plane was placed 50 cm from the source. Operation frequency was chosen to only propagate the dominant TE_{10} mode in this waveguide.

This waveguide embodies a very challenging case for ray-tracing, as it is PEC, so all reflections must be considered (this is a completely convex scene), and it is not electrically very large, as convenient in ray-tracing technique.

Submitted On: September 29, 2018
Accepted On: January 1, 2019

The analytical solution for the dominant mode in the rectangular PEC waveguide states that the electric field should be uniform in the direction parallel to the short axis of the waveguide, and vary with a half-cosine in the axis parallel with the long axis of the waveguide. Figure 1 shows the result of the ray-tracing method on this scene.

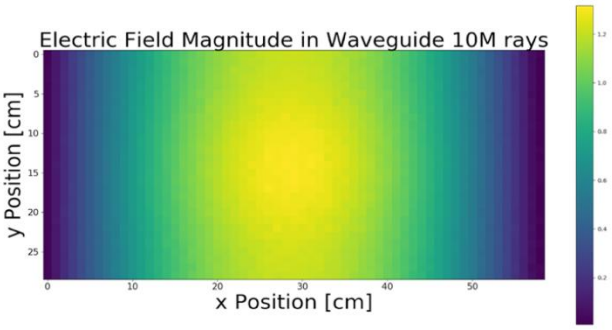

Fig. 1. Magnitude of the electric field for the waveguide excited with a Hertzian dipole at 350 MHz. The cutoff frequency for the waveguide is 256 MHz, which only allows propagation of the TE_{10} mode.

We observe in Fig. 1 the expected trends along both axes. The magnitude varies only slightly along *y* for any *x* coordinate in the waveguide, and the magnitude is peaked in *x* at the center of the waveguide, and is relatively symmetrical about the center of the waveguide.

The final electric field is found by summing a discrete number of uniform plane waves at the observation plane. The number of rays that intersect the observation plane determines the number of plane waves. The solution generated by a ray-tracing method should converge to the analytical solution as the number of rays increases. Figure 2 shows the electric field magnitudes for a cross section of the waveguide for varying numbers of rays.

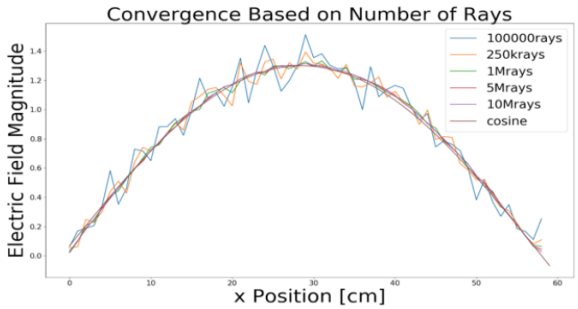

Fig. 2. Electric field magnitude in the cross section of the waveguide, with the waveguide parameters and excitation frequency remaining identical to Fig. 1. The number of rays was varied from 100 thousand rays to 10 million rays.

We observe from Fig. 2 the expected convergence of the ray tracing results with increasing the number of rays in the simulation. As the number of rays increases, the cross-section magnitude begins to smoothen to a cosine. The analytical solution states the electric field should be zero at the walls of the waveguide. The ray-tracing method results in a symmetrical offset of approximately 0.2 units on the edges. The offset is a result of the loss of accuracy from sending a finite number of rays resulting in a finite sampling density.

Each ray is terminated after a given number of reflections; if it did not reach the observation plane within the reflection limit, it will not contribute to a field at observation location. The solution should converge as the number of permissible reflections increases, as each additional ray that intersects the observation plane increases the sampling density. Figure 3 shows the cross-sectional magnitude for varying number of reflections.

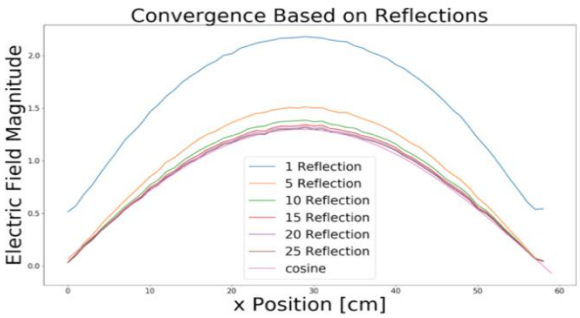

Fig. 3. Electric field magnitude based on the reflection order. The waveguide parameters remain identical to Fig. 1. The reflection order allowed varied from 1 to 25.

We observe from Fig. 3 a good convergence of the ray tracing results to the offset cosine as reflection order increases. The error is worst for low reflection order, and best for high reflection order, as expected.

ACKNOWLEDGMENT

This work was supported by the National Science Foundation under Grant ECCS-1646562.

REFERENCES

[1] M. F.Cátedra and J. Perez, C*ell Planning for Wireless Communications*. Norwood, MA, USA: Artech House, 1999.

[2] T. S. Rappaport, S. Y. Seidel, and K. R. Schaubach, "Site-specific propagation for PCS system design," in *Wireless Personal Communications*, M. J. Feuerstein and T. S. Rappaport, eds., Boston: Kluwer Academic Publishers, pp. 281-315, 1993.

[3] B. M. Notaros, *Electromagnetics*. New Jersey: PEARSON Prentice Hall; 2010.

[4] X. Zhang, N. Sood, J. Siu, and C. D. Sarris, "A Hybrid Ray-Tracing/Vector Parabolic Equation Method for Propagation Modeling in Train Communication Channels," in IEEE Transactions on Antennas and Propagation, vol. 64, no. 5, May 2016.

Micromagnetic Model Simulation of Spin-Torque Oscillator and Write Head for Microwave-Assisted Magnetic Recording – Spin Injection Layer with In-Plane Anisotropy –

Yasushi KANAI and Ryo ITAGAKI
Department of Information and Electronics Engineering
Niigata Institute of Technology
Kashiwazaki, Japan
kanai@iee.niit.ac.jp, r_itagaki@cc.niit.ac.jp

Simon GREAVES and Hiroaki MURAOKA
Research Institute of Electrical Communication (RIEC)
Tohoku University
Sendai, Japan
{simon, muraoka}@riec.tohoku.ac.jp

***Abstract*—Micromagnetic simulations were carried out to obtain stable oscillation of a spin transfer torque oscillator (STO) inserted into the gap between the main pole and trailing shield of a write head. We assumed a spin injection layer with in-plane anisotropy. Results show that reducing the magnetostatic interaction between the write head and the STO is the key to obtaining stable STO oscillation.**

Keywords—micromagnetic simulations, microwave-assisted magnetic recording, spin-torque oscillator, write head.

I. INTRODUCTION

Microwave-assisted magnetic recording (MAMR) [1] is one candidate for next-generation perpendicular magnetic recording [2]. Stable oscillation is one of the most important factors for spin-torque oscillators (STO) used in a MAMR system. We performed micromagnetic simulations and found that the oscillation states of the isolated (without write head), and integrated (with write head), STO models were different, i.e., stable STO oscillations were hard to obtain primarily due to the magnetostatic interactions between the STO and write head [3].

In this paper, we investigate STOs utilizing a spin injection layer (SIL) with in-plane anisotropy [4]. We also introduce a STO tilted with respect to the medium plane, along with a tilted main pole – trailing shield gap (tilted STO) to reduce the magnetostatic interactions between the STO and write head. Results show that the SIL with in-plane anisotropy worked well when the STO was isolated. Whilst the integrated STO only worked when the tilted STO was used.

II. CALCULATION MODEL

A micromagnetic model analysis was carried out considering a STO utilizing transmission spin torque. We used the commercial micromagnetic software (Fujitsu, EXAMAG v.2.1, http://www.fujitsu.com/global/about/resources/news/press-releases/2015/0324-01.html).

In Fig. 1, the isolated STO, without write head, used for the calculations is shown. A double-layered STO was used, with a non-magnetic interlayer (IL) placed between the field generation layer (FGL) and SIL. Table I lists the main parameters of the FGL and SIL that were used unless stated otherwise in Sections III and IV. We modelled both soft and hard, in-plane magnetic SILs. A uniform external field and uniform injected current were assumed along the z-axis over the STO volume. The STO was divided into cubes with 2.5 nm sides. Note that we modeled an STO with 20 nm × 20 nm area as it rotated stably with low injected current density, *J*, and low external field.

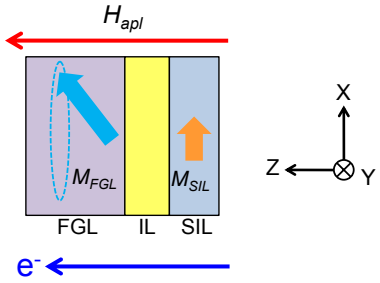

Fig. 1. STO model used for the calculations. Double-layered STO with transmission spin torque utilized.

TABLE I. MAIN PARAMETERS OF FGL AND SIL USED IN THE CALCULATIONS

	FGL	SIL
$4\pi M_s$	20 kG	6 kG
H_k (*) in-plane	31.4 Oe	31.4 Oe, 20 kOe
α	0.02	0.02
Exchange, A	2.5×10^{-6} erg/cm	0.75×10^{-6} erg/cm
Thickness	10 nm	2 nm
P_o = 0.5, Width × height = 20 nm × 20 nm, Inter layer = 2 nm		

* H_k: anisotropy field

The authors acknowledge the financial support from JSPS Kaken-hi (16K06321) and Advance Storage Research Consortium (ASRC); software support from JSOL, Japan.

Submitted On: September 13, 2018
Accepted On: January 1, 2019

III. Results – Isolated STO –

In Fig. 2, FGL rotations under a 1 GHz, external field are shown for soft and hard SILs, where the horizontal axis is the time. The results are shown from t = 0, initial state. The left vertical axis shows M/M_s for the in-plane (M_y) and perpendicular-to-the-plane (M_z) components of the FGL magnetization averaged over the FGL volume, i.e., the FGL magnetization rotated perfectly in the x-y plane when M_y/M_s = 1. As can be seen, the FGL rotated well for both soft (H_k = 31.4 Oe) and hard (H_k = 20 kOe) SIL materials with in-plane anisotropy, which was quite different from STOs utilizing SILs with perpendicular anisotropy [3].

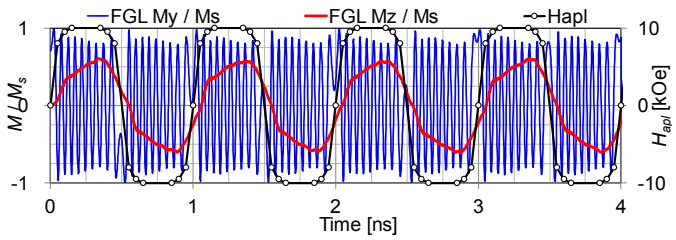

(a) SIL H_k = 31.4 Oe (in-plane)

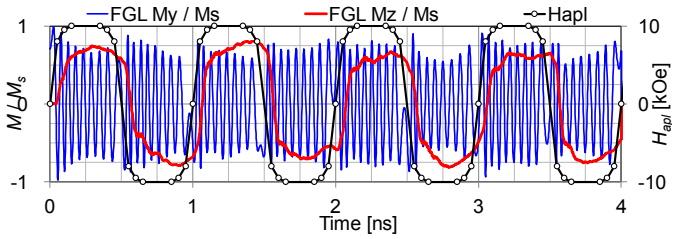

(b) SIL H_k =20 kOe (in-plane)

Fig. 2. FGL rotations vs. time for soft and hard SILs. $J = 3.0\times10^8$ A/cm^2.

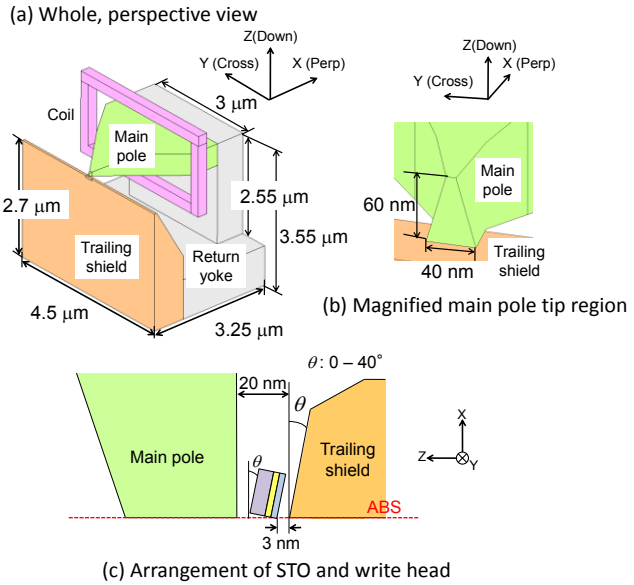

Fig. 3. Schematics of write head and STO integrated into the tilted MP–TS gap used in the calculations.

IV. Results – Integrated STO –

In Fig. 3, the STO was integrated into the main pole and trailing shield (MP–TS) gap of the write head. We considered both perpendicular STOs (STO perpendicular to the medium plane (parallel to ABS)), and tilted STOs (STO tilted to the medium plane). In the tilted STO, the magnetostatic interactions between the STO and the write head were smaller than the perpendicular STO. The STOs had the same parameters shown in Table I.

In Fig. 4, FGL rotations vs. time are shown for the perpendicular and tilted STOs when a 1 GHz coil current was applied. It is seen that the perpendicular STO did not rotate stably, while the tilted STO worked quite well. It is also seen that the oscillation state of the integrated STO was quite different from isolated one. This shows that an integrated STO utilizing an SIL with in-plane anisotropy works only when used in a tilted MP-TS gap.

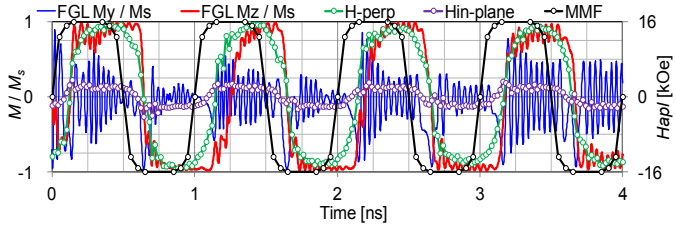

(a) Perpendicular STO: θ = 0°

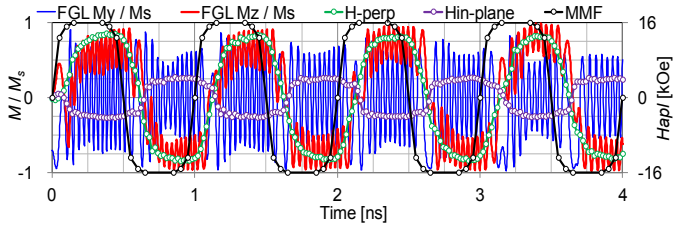

(b) Tilted STO: θ = 40°

Fig. 4. FGL rotations vs. time. Integrated perpendicular and tilted STO models. Applied MP-TS gap fields to FGL are also shown. $J = 3.0\times10^8$ A/cm^2, SIL H_k = 20 kOe (in-plane).

References

[1] J.-G. Zhu, X. Zhu, and Y. Tang, "Microwave assisted magnetic recording," IEEE Trans. on Magn., vol. 44, no. 1, pp. 125-131, Jan. 2008.

[2] Energy-assisted Recording Technology, [Online.] Available: https://play.vidyard.com/JZLozr2ujb2jR964BaFNPW

[3] Y. Kanai, R. Itagaki, S. Greaves, and H. Muraoka, "Micromagnetic model analysis of various spin torque oscillators with write head for microwave-assisted magnetic recording," IEEE Trans. on Magn., vol. 53, no. 11, Nov. 2017. Art. no. 3001105.

H. Sepeheri-Amin, S. Bosu, C. Abert, Y. Sakuraba, S. Kasai, M. Hayashi, D. Suess, and K. Hono, "Design and development of spin-torque-oscillator for microwave assisted magnetic recording," The Magnetic Recording Conference, E2, Tsukuba, Japan, Aug. 2017.

Nano-Optical Couplers for Efficient Power Transmission Along Sharply Bended Nanowires

Aşkın Altınoklu and Özgür Ergül
Department of Electrical and Electronics Engineering
Middle East Technical University
Ankara, Turkey
ozergul@metu.edu.tr

***Abstract*—We consider nano-optical couplers that consist of optimal arrangements of nanoparticles to improve the transmission abilities of nanowire systems with sharp bends. Previously, it was shown that absence/existence of nanoparticles in a given grid can be optimized such that the power transmission can significantly be increased without curving the bend. In this contribution, we present a detailed investigation and analysis of coupler performances to critical geometric parameters. While the designed couplers are robust against fabrication errors, numerical results demonstrate a remarkable dependency of coupler characteristics to particle types, as well as to bending geometry, due to strong plasmonic interactions at short distances. These findings further support the need for case-dependent optimization that must be performed efficiently and accurately via full-wave simulations.**

I. Introduction

Nanowires are natural components of nano-optical systems as they enable long-distance transmission of electromagnetic power via surface plasmons [1]–[7]. When they are straight, smooth, and perfectly aligned, nanowires have excellent transmission abilities for long distances with respect to the operating wavelength [2],[6]. When they are bended, however, reflection and diffraction at the bend regions may significantly reduce the efficiency [3]. To alleviate this problem, nano-optical couplers can be used to improve the power transmission, especially when curved bending is not desired for efficient usage of the available space. Recently, we showed that robust couplers involving nanoparticles can be designed such that transmission can be improved significantly even through very sharp corners [7]. The designs were obtained via optimization with genetic algorithms (GAs) supported by full-wave solutions with surface integral equations and the multilevel fast multipole algorithm (MLFMA) [8].

It is well known that plasmonic properties of metals at optical frequencies lead to complex interactions and very different responses to excitations, in comparison to the behaviors of metals at the lower (radio and microwave) frequencies. For example, when nanostructures are close to each other, the extraordinary coupling between them leads to useful abilities, particularly for energy harvesting, focusing, and optical sensing. At the same time, these strong interactions may increase the sensitivity of designs to geometric properties. In this contribution, we further investigate nano-optical couplers and their optimal designs to improve the power transmission through sharp corners. We show that the designed couplers are quite stable against fabrication errors, while particle geometries and bending shapes can significantly change their performances. Hence, a new optimization may be required depending on the case, while the optimization trials must be performed accurately for estimating the actual performances of candidate couplers. In the following section, we briefly introduce the simulation and optimization environment, followed by the description of the optimization problems in Section III. Then, Section IV presents optimization results and detailed analysis, before our concluding remarks in Section V.

II. Simulation and Optimization Environment

The transmission problems involving nanowires and couplers (nanoparticles) are modeled as three-dimensional structures and formulated by using surface integral equations in the frequency domain. There are diverse choices for the formulation [9]–[11], while we prefer the electric and magnetic current combined-field integral equation (JMCFIE) [12] or the modified combined tangential formulation (MCTF) [13] for fast and accurate solutions depending on the frequency. The surfaces and integral equations are discretized by using triangles and the Rao-Wilton-Glisson functions. The complex permittivity values of the metals are extracted from experimental data [14]. The problems are solved iteratively, while the required matrix-vector multiplications are performed via MLFMA. In addition, electromagnetic interactions in plasmonic media (e.g., inside

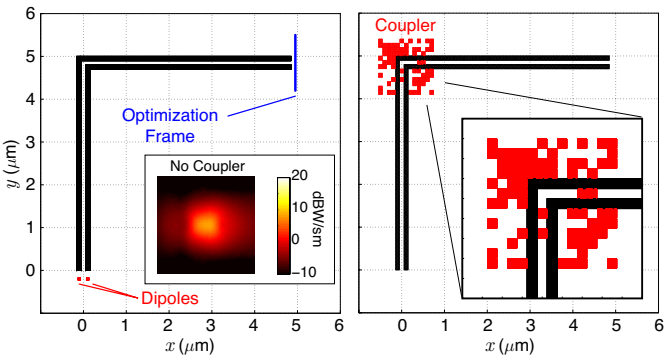

Fig. 1. An optimization problem involving a transmission line (a pair of Ag nanowires) with a 90° sharp bend. An optimal coupler that consists of $90 \times 90 \times 90$ nm cubic nanoparticles is also depicted.

Submitted On: October 9, 2018
Accepted On: October 21, 2018

nanowires) are truncated to improve the efficiency without sacrificing the accuracy [15].

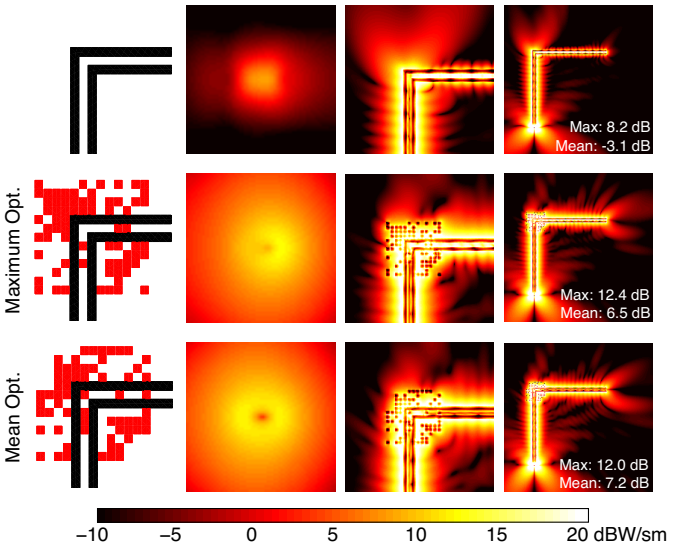

Fig. 2. Optimization results (couplers and power density distributions) when the maximum power density and the mean power density inside the output frame are maximized.

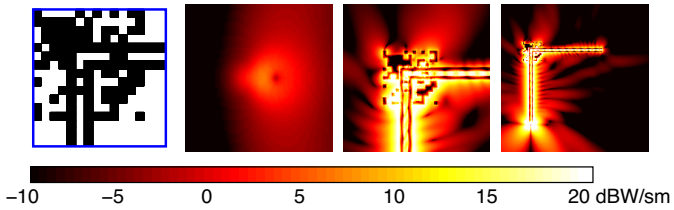

Fig. 3. Power density distribution when the nearby nanoparticles in the optimal design (Fig. 2) are combined.

III. Coupler Optimization Problems

We consider transmission lines involving nanowires with sharp (e.g., 90°) bends. As shown in Fig. 1, a given transmission line is excited from one side and the power density is observed inside an output frame at the other side. A coupler is designed and located at the corner such that the power density (either its maximum or its mean) at the output is maximized. Optimization problems are solved by employing GAs, while the required trials are performed as three-dimensional simulations via the MLFMA implementation. The couplers are designed by considering an initial grid of nanoparticles and deciding which particles need to be kept/extracted to maximize the cost functions (e.g., maximum/mean of the power density at the output). The GA implementation is integrated with the MLFMA implementation by employing dynamic accuracy control [16] in order the reduce the optimization time. In addition, embarrassing parallelism is used by assigning simultaneous MLFMA solutions to multiple cores.

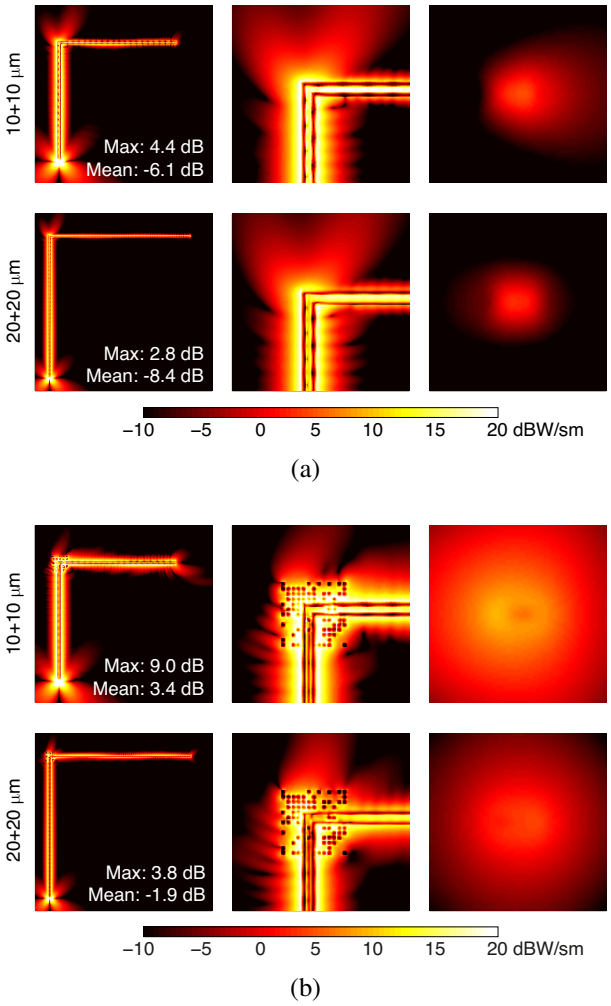

Fig. 4. Power density distributions when the length of the nanowires is $10+10$ μm and $20+20$ μm: (a) Without a coupler and (b) with the coupler in Fig. 2 designed for $5+5$ μm nanowires.

IV. Optimization Results and Coupler Analysis

As optimization results in this paper, the main geometry that we consider is a pair of $5+5=10$ μm silver nanowires with 90° sharp bends at the middle, as shown in Fig. 1. Each nanowire has a 0.1×0.1 μm square cross section. The transmission line is excited by a pair of Hertzian dipoles located on one side at 0.2 μm from the nanowires. The output frame is selected as a 1.3×1.3 μm square area at 0.1 μm distance from the nanowires. The frequency in the results of this paper is selected as 250 THz, at which the relative permittivity of Ag is approximately $-60.8+4.31i$. As a typical result, Fig. 1 also depicts the power density inside the output frame when no coupler is used. Most couplers are designed by using a total of 13×13 Ag cubes with $90\times 90\times 90$ nm dimensions and 10 nm face-to-face distances, while we also consider other types of geometries. In general, each optimization is performed by using GAs for 200 generations on pools of 40 individuals, leading to a total of 8000 simulations per optimization (omitting duplicate individuals).

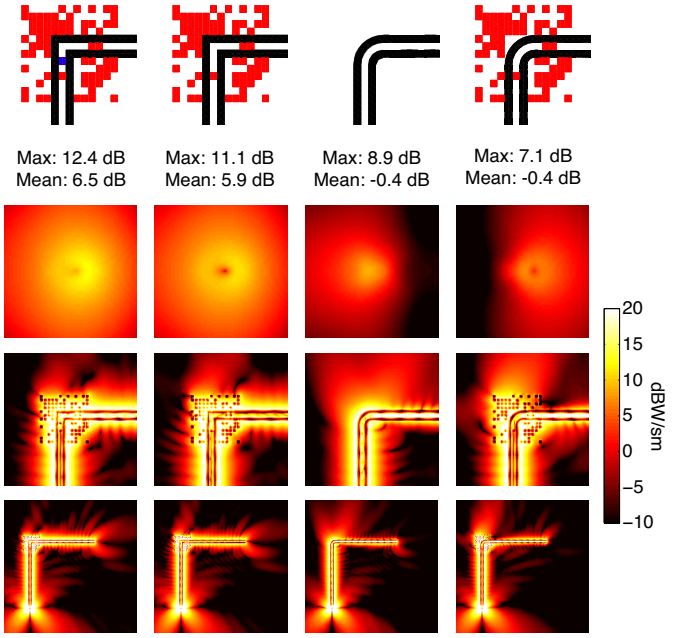

Fig. 5. Using the coupler, which is designed for a sharp bend (Fig. 2), for a curved bend with 0.4 μm radius of curvature.

A. Maximum Versus Mean Optimization

Depending on the application, the maximum or the mean of the power density at the output can be optimized. It is remarkable that coupler designs can significantly be different depending on the optimization target, while the achievable power values are often close to each other. Fig. 2 presents two optimization results when the maximum of the power density (second row) and the mean of the power density (third row) inside the output frame are maximized. The no-coupler case is also shown in the first row for comparisons. In addition to power density distributions inside the output frame (second column) and in the coupler region (third column), a general view is shown for each case (fourth column), while the coupler designs are presented in the first column. We observe that the power transmission can significantly be improved by using effective couplers. Specifically, the maximum power density (in dBW/sm) can be increased from 8.2 dB to 12.4 dB, while the mean power density can be increased from -3.1 dB to 7.2 dB. We also note that optimization of the maximum power density leads to 6.5 dB mean power density. Similarly, the maximum power density reaches 12.0 dB if the mean power density is maximized. In the following sections, we consider the optimization of the maximum power density (specifically the coupler in the second row of Fig. 2), while this selection does not change the interpretation of the results and conclusions.

B. Combination of Nanoparticles

Once an optimization is completed and an optimal design is found, one may question whether the nanoparticles must be kept as separated (as designed) or they can be combined (without any distance between them) as much as possible. This is particularly interesting since such a combination may simplify the fabrication process. As an example, Fig. 3 presents the results when the nearby nanoparticles (cubes) in the optimal design shown in Fig. 2 are combined. Comparing the results, we observe that the performance of the coupler significantly deteriorates. A close examination in the bending region shows that the coupler with combined nanoparticles operates very differently with cavities, in comparison to the well-designed interactions between separated nanoparticles in the original design.

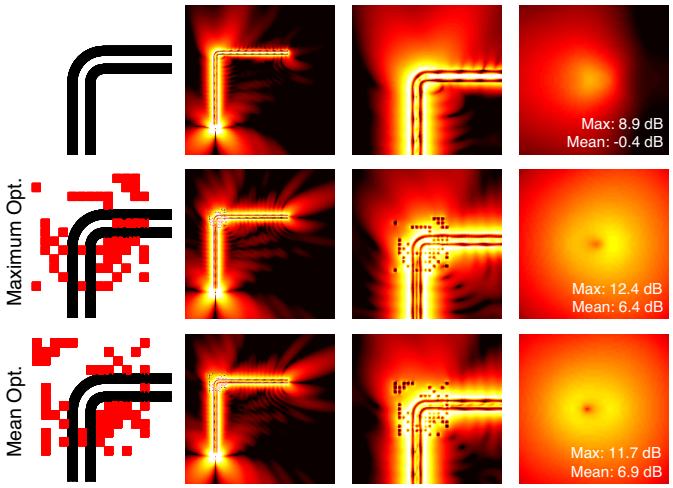

Fig. 6. Optimization results (couplers and power density distributions) when the maximum power density and the mean power density inside the output frame are maximized for curved nanowires.

C. Performance of Couplers for Different Nanowire Lengths

The coupler designs presented in this paper are obtained for a specific length of nanowires, i.e., for $5 + 5$ μm. On the other hand, they can still perform well for other lengths, particularly for longer nanowires. As two examples, Fig. 4 depicts power density distributions for $10 + 10$ μm and $20+20$ μm nanowires with sharp bends at the middle. Without a coupler, the maximum power density inside the output frame drops to 4.4 dB and 2.6 dB, respectively, from 8.2 dB for the original ($5 + 5$ μm) case. Similarly, the mean power density values are found to be -6.1 dB and -8.4 dB. Using the coupler shown in Fig. 2, the maximum power density is kept at 9.0 dB for $10+10$ μm nanowires and 3.8 dB for $20+20$ μm nanowires, while the corresponding mean power density values are 3.4 dB and -1.9 dB, respectively. Investigating the power density distributions in the coupler region, we observe that the coupler operates similarly, by reducing the escaping power and guiding the incoming wave through the bend, for different nanowire lengths. It can be an advantage to use the same coupler design for different nanowire lengths, while it is also possible to repeat optimization trials for different nanowire lengths (but this becomes computationally difficult for longer nanowires).

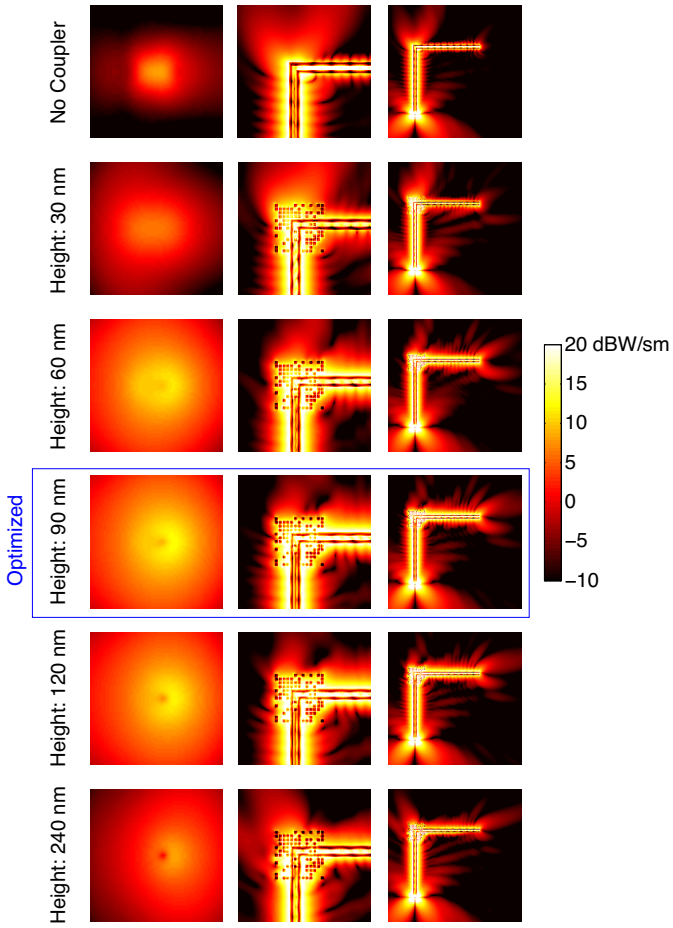

Fig. 7. Power density distributions when the height of the particles is changed to 30 nm, 60 nm, 120 nm, and 240 nm for the coupler design in Fig. 2 involving $90 \times 90 \times 90$ nm cubes.

D. Effect of Curving

It is well known that curving the bends can significantly improve the power transmission along bended nanowires, while our studies show that the radius of curvature must be very large (at the cost of reduced compactness of the bending region) to compete with the designed couplers. It may be possible to use a coupler for a curved bend; but, the optimization must be repeated due to the sensitivity of coupler designs to the geometry of bends. As an example, Fig. 5 presents the results when the coupler in Fig. 2 is used for a curved bend with 0.4 μm radius of curvature. In order to use the design, one of the cubes must be extracted since it coincides with one of the curved nanowire. Since this cube is a critical one, its removal leads to a remarkable decrease in the maximum/mean power density to $11.1/5.9$ dB (from $12.4/6.5$ dB). These values are still much better than only curving, leading to 8.9 dB maximum and -0.4 dB mean power density values. But, a major problem occurs when the coupler is used for the curved bend. The maximum power density decreases to 7.1 dB (even below the value for the case of sharp bend without a coupler), while the mean power density stays at -0.4 dB (no improvement in comparison to only curving). These results show that, if the geometry of the bend is changed, even to make it better by curving, optimization must be repeated.

As an example to optimization trials for curved nanowires, Fig. 6 presents the results when couplers are designed for 0.4 μm radius of curvature. It can be observed that the optimization of the maximum power density leads to $12.4/6.4$ dB maximum/mean power density in the output frame, while these values are $11.7/6.9$ dB when the mean power density is maximized. Hence, once again, the designed couplers significantly improve the power transmission, in comparison to the no-coupler (but curved) case, i.e., $8.9/-0.4$ dB. On the other hand, the results are not better than those obtained for sharply bended with couplers. This, in fact, shows the overall success of the designed couplers, particularly for the sharp case, which can improve the power transmission to high levels such that curving does not provide an improvement anymore.

E. Sensitivity to Particle Geometries

Naturally, the electromagnetic characteristics of a coupler strongly depends on the geometry of its particles. On the other hand, the designed couplers in this study are quite resistant to fabrication errors and deformations, as long as the general shape of the particles does not change. As an example, Fig. 7 presents power density distributions when the height of the particles in the optimized coupler in Fig. 2 is changed. While the original cubes have $90 \times 90 \times 90$ nm dimensions, we make their height 30 nm, 60 nm, 120 nm, and 240 nm. We observe that decreasing/increasing the height to $60/120$ nm has little effect on the efficiency of the coupler. A relatively poor performance is obtained when the height is changed to 30 nm (one third of the original), while the power transmission even for this case is not worse than the one without a coupler. Increasing the height to 240 nm also leads to visible deterioration in the performance of the coupler, while it still provides improved transmission in comparison to the no-coupler case.

In order to investigate realistic fabrication errors that may cause corrugations on particle surfaces, we consider the results for deformed cubes in Fig. 8. For the coupler design in Fig. 2, the discretization nodes (used for numerical simulations) are shifted randomly in the x, y, and z directions, while the shift in each direction is limited to ± 2 nm. In addition to each cube, nanowires are also deformed using a similar approach. Uniform distribution is used for the randomly generated shift distances. Fig. 8 shows the histogram of the shift distances, as well as the obtained power density distributions, for two different trials. It can be observed that corrugations have little effects on the coupler characteristics. While these results demonstrate the robustness of the coupler design, we emphasize that the cubes are not allowed to touch each other in these trials, which may have disastrous effects as shown in the combination example above (see Fig. 3).

Despite they can be robust against fabrication errors, as well as to modifications in simple geometric parameters such as the height of particles, the particle geometry significantly affects

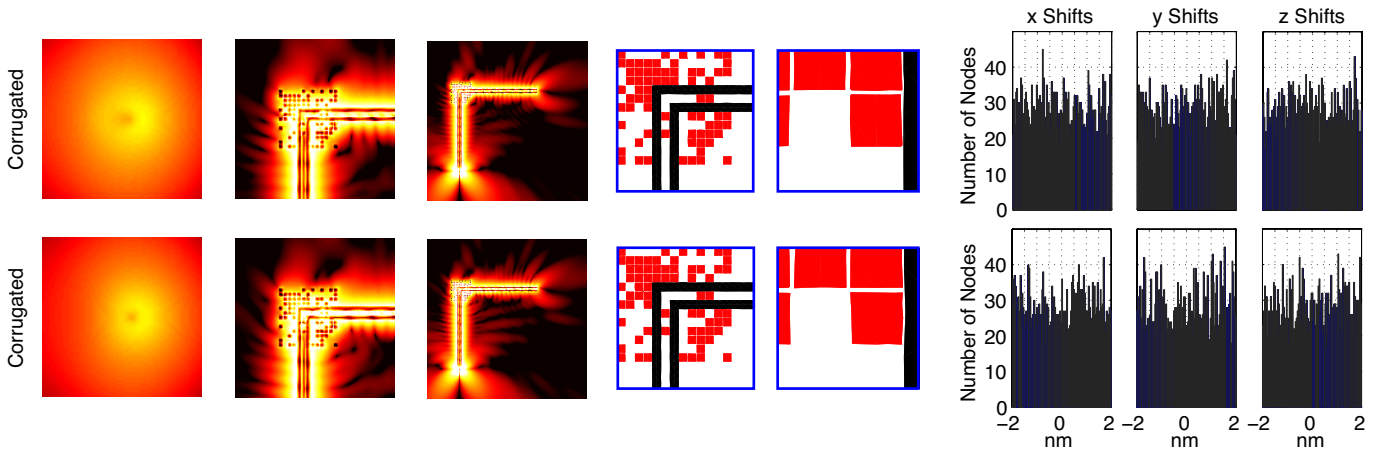

Fig. 8. Power density distributions when the coupler particles (cubes) and the nanowires are deformed for the coupler design in Fig. 2. Two different trials (rows) are shown.

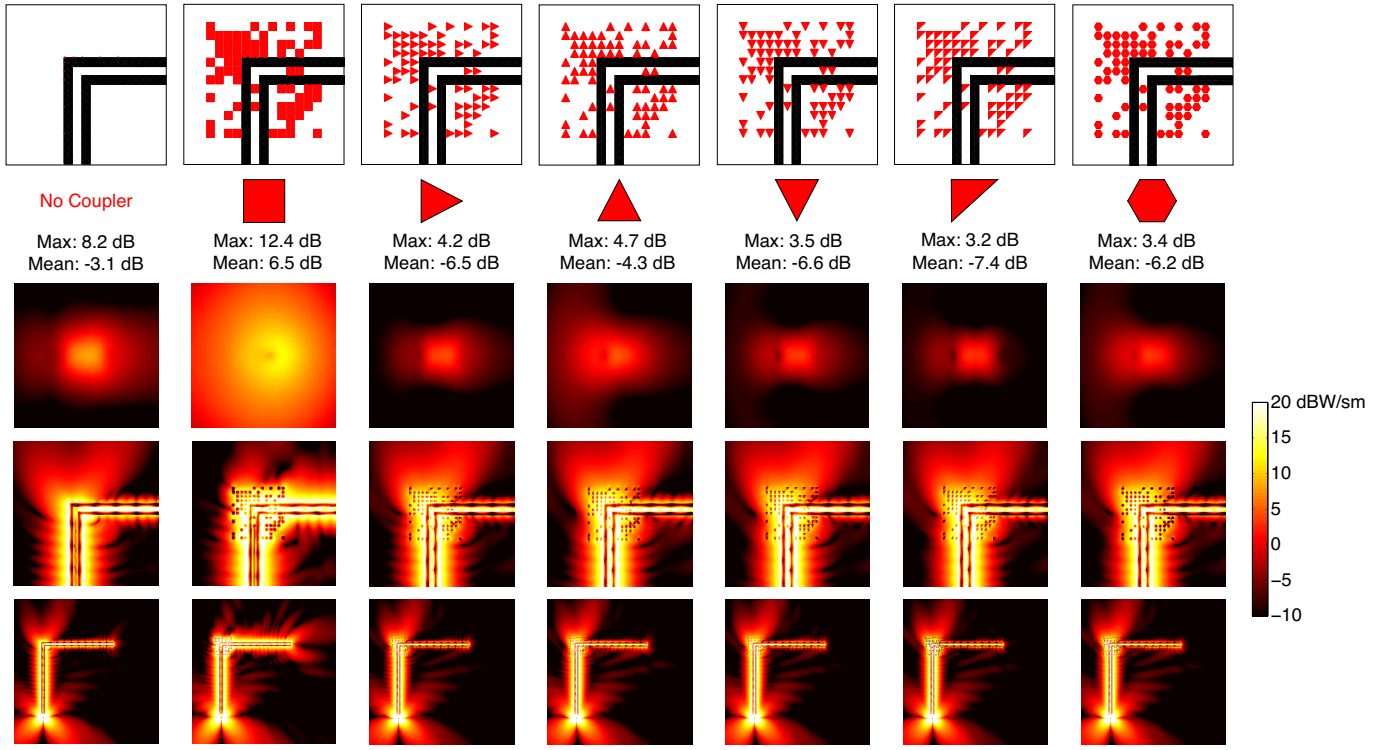

Fig. 9. Using an optimal arrangement of cubic particles (coupler design in Fig. 2) for different particle geometries.

the characteristics and performances of nano-optical couplers. As a demonstration, Fig. 9 presents the results when an optimal coupler arrangement obtained for cubic particles (Fig. 2) is used for different particle shapes (prisms). Specifically, we test the arrangement for five different particles with different cross sections (height is kept at 90 nm). We observe that the transmission performance significantly drops, i.e., the coupler design becomes useless, when employing different particles instead of cubes. In fact, such couplers make the transmission worse compared to the no-coupler case.

F. Optimization for Different Particle Shapes

In this work, using cubes to design effective couplers is not an arbitrary choice. Our studies with different shapes consistently show that the cube is one of the best geometries when a regular grid is used, while other geometries are also possible. As shown above, directly changing the particle geometry for an optimized arrangement leads to very poor results. But, it is possible to use alternative shapes by optimization. For example, Fig. 10 presents four different couplers with different types of nanoparticles when an optimization is performed for each particle type to increase the maximum power density

in the output frame. Specifically, in addition to the coupler with cubic particles in Fig. 2, we consider triangular and hexagonal prisms, again in 13×13 arrangements. It can be observed that the maximum power density can significantly be increased (compared to the no-coupler case) for all particle types, while the optimal arrangement of nanoparticles strongly depends on the particle type. As mentioned above, cubic particles lead to a larger value for the mean power density, while the performances are similar for the maximum power density. Although not shown here, optimization of the mean power density using alternative particles leads to relatively low maximum power density values in comparison to the results with cubic particles.

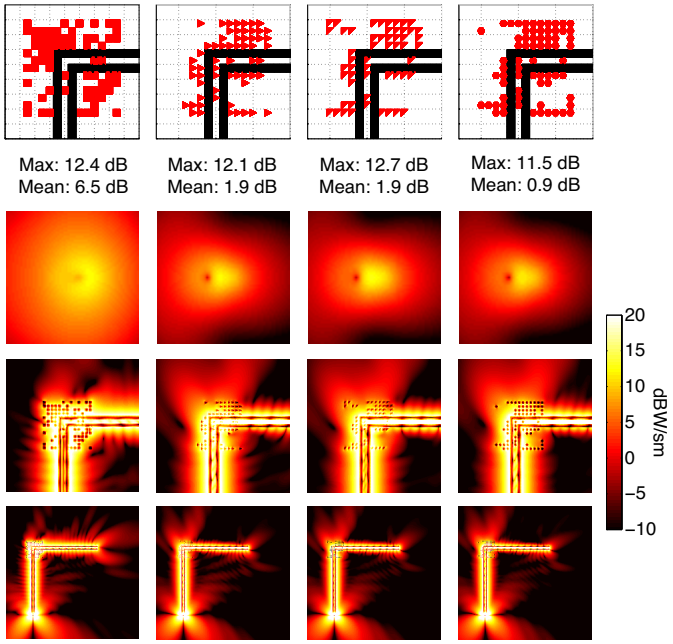

Fig. 10. Power density distributions when four designed couplers involving different types of nanoparticles are used.

V. Concluding Remarks

In this paper, we provide a detailed analysis of nano-optical couplers that are designed for improving the power transmission along sharply bended nanowires. The designs are obtained via GAs, while the optimization trials are performed accurately and efficiently by using MLFMA. All results demonstrate the effectiveness of the couplers that can significantly maximize the output power. Numerical results also show that the designed couplers maintain their performances for different nanowire lengths and they are robust against fabrication errors (different heights and surface corrugations), while they are sensitive to the main geometry of particles. In addition, the particles need to be separated, as designed, without physical contacts between them. It is possible to design couplers with different particle shapes, while cubic particles provide the best results for compact (e.g., 13×13) regular arrangements. Despite their relatively small sizes, the couplers are so effective that curving within the coupler region does not further improve the power transmission.

Acknowledgement

This work was supported by the Scientific and Technical Research Council of Turkey (TUBITAK) under the Research Grant 118E243 and by the Turkish Academy of Sciences (TUBA) in the framework of the Young Scientist Award Program.

References

[1] X. Wang, C. J. Summers, and Z. L. Wang, "Large-scale hexagonal-patterned growth of aligned ZnO nanorods for nano-optoelectronics and nanosensor arrays," Nano Lett., vol. 4, no. 3, pp. 423–426, Jan. 2004.
[2] A. W. Sanders, et al., "Observation of plasmon propagation, redirection, and fan-out in silver nanowires," Nano Lett., vol. 6, no. 8, pp. 1822–1826, Jun. 2006.
[3] W. Wang, et al., "Light propagation in curved silver nanowire plasmonic waveguides," Nano Lett., vol. 11, no. 4, pp. 1603–1608, Mar. 2011.
[4] S. M. Bergin, et al., "The effect of nanowire length and diameter on the properties of transparent, conducting nanowire films," Nanoscale, vol. 4, no. 6, pp. 1996–2004, Feb. 2012.
[5] Y. Huang, et al., "Nanowire-supported plasmonic waveguide for remote excitation of surface-enhanced Raman scattering," Light: Science and Applications, vol. 3, no. 199, Aug. 2014.
[6] H. A. Şatana, B. Karaosmanoğlu, and Ö. Ergül, "A comparative study of nanowire arrays for maximum power transmission," in Nanowires, K. Maaz, Ed. InTech, 2017.
[7] Y. E. Tunçyürek, B. Karaosmanoğlu, and Ö. Ergül, "Computational design of optical couplers for bended nanowire transmission lines," ACES J., vol. 32, no. 7, pp. 562–568, Jul. 2017.
[8] Ö. Ergül and L. Gürel, The Multilevel Fast Multipole Algorithm (MLFMA) for Solving Large-Scale Computational Electromagnetics Problems. Wiley-IEEE, 2014.
[9] Ö. Ergül and L. Gürel, "Comparison of integral-equation formulations for the fast and accurate solution of scattering problems involving dielectric objects with the multilevel fast multipole algorithm," IEEE Trans. Antennas Propag., vol. 57, no. 1, pp. 176–187, Jan. 2009.
[10] M. G. Araujo, et al., "Comparison of surface integral equation formulations for electromagnetic analysis of plasmonic nanoscatterers," Opt. Exp., vol. 20, no. 8, pp. 9161–9171, Apr. 2012.
[11] D. M. Solis, J. M. Taboada, and F. Obelleiro, "Surface integral equation method of moments with multiregion basis functions applied to plasmonics," IEEE Trans. Antennas Propag., vol. 63, no. 5, pp. 2141–2152, May 2015.
[12] P. Ylä-Oijala, M. Taskinen, and S. Järvenpää, "Surface integral equation formulations for solving electromagnetic scattering problems with iterative methods," Radio Sci., vol. 40, no. 6002, Dec. 2005.
[13] B. Karaosmanoğlu, A. Yılmaz, and Ö. Ergül, "A comparative study of surface integral equations for accurate and efficient analysis of plasmonic structures," IEEE Trans. Antennas Propag., vol. 65, no. 6, pp. 3049–3057, Jun. 2017.
[14] P. B. Johnson and R. W. Christy, "Optical constants of the noble metals," Phys. Rev. B, vol. 6, no. 12, pp. 4370–4379, Dec. 1972.
[15] B. Karaosmanoğlu, et al., "Solutions of plasmonic structures using the multilevel fast multipole algorithm," Special Issue on Challenges in RF and Microwave Defense Engineering, Int. J. RF Microwave Comput.-Aided. Eng., vol. 26, no. 4, pp. 335–341, May 2016.
[16] C. Önol, A. Üçüncü, and Ö. Ergül, "Efficient multilayer iterative solutions of electromagnetic problems using approximate forms of the multilevel fast multipole algorithm," IEEE Antennas Wireless Propag. Lett., vol. 16, pp. 3253–3256, 2017.

3D Diagonalization and Supplementation of Maxwell's Equations in Fully Bi-anisotropic and Inhomogeneous Media Part I: Proof of Existence by Construction

A. R. Baghai-Wadji [1,2]

[1]Electrical Engineering Department
University of Cape Town, Cape Town, 7701, South Africa
alireza.baghai-wadji@uct.ac.za

[2]College of Science
Xi'an University of Science and Technology, Xi'an, Shaanxi, 710054, China

Abstract − Consider the Maxwell's curl equations in fully bi-anisotropic and inhomogeneous media in three dimensional (x, y, z) spatial Cartesian coordinates. Let the media be characterized by 3×3 permittivity, electro-magnetic coupling, magneto-electric coupling, and permeability matrices $\boldsymbol{\varepsilon}^{3\times3}(x, y, z)$, $\boldsymbol{\xi}^{3\times3}(x, y, z)$, $\boldsymbol{\zeta}^{3\times3}(x, y, z)$, and $\boldsymbol{\mu}^{3\times3}(x, y, z)$, respectively. Assume a harmonic time-dependence according to $\exp(-j\omega t)$. The prime objective in this paper is to establish that the Maxwell's electrodynamic equations jointly with the constitutive equations can be diagonalized, leading to the $\mathcal{D}-$, and the associated supplementary $\mathcal{S}-$forms. A finitary algorithm involving ''structural,'' ''differential,'' and ''material'' matrices has been proposed, and the existence of the $\mathcal{D}-$ and $\mathcal{S}-$forms proved by construction. In the accompanying paper (Part II) the internal consistency of the $\mathcal{D}-$ and $\mathcal{S}-$forms has been shown, by proving their sharp equivalence with Maxwell's and constitutive equations.

Index Terms − Bi-anisotropic and inhomogeneous media, diagonalization, Maxwell's equations, supplementaion.

I. INTRODUCTION

A. Background and motivation

Recognizing patterns in the structure of fundamental equations in mathematical physics, identifying commonalities between seemingly different areas in physics, and the dream of unifying schemes have ever since been the driving force for many original work in science and engineering. In pursuit of casting light on fundamentals, it is also hoped that more systematized and efficient algorithms for the numerical solution of increasingly more challenging problems will emerge. This paper focuses on the two (governing) Maxwell's curl equations in fully bi-anisotropic and inhomogeneous media characterized by four 3×3 constitutive matrices, in three dimensional (3D) spatial Cartesian coordinates. The method is based on ''unpacking'' the governing and constitutive equations, and identifying irreducible ''structural,'' ''differential,'' and ''material'' matrices, which not entirely coincidentally exhibit intriguing properties. The occurrence of identity matrices of varying dimensions simplifies and systematizes the derivations and provides clues to the deeper understanding of the underlying equations in mathematical physics in general. In particular, the factorization of the identity matrix into structurally complex forms can be viewed as an enabling instrument to peer into the fabric of the governing- and constitutive equations in a myriad of ways. On the other hand, the appearance of the 2×2 null matrix, as the ''complement'' to the identity matrix simplifies the calculations.

The diagonalized $(\mathcal{D})$ and supplementary $(\mathcal{S})-$forms offer benefits from epistemological, theoretical, and numerical points of view. In the course of investigating other fundamental equations in mathematical physics, these features have been discussed in greater length and will not be repeated here [1]-[6]. It merely should be pointed out that the $\mathcal{D}-$form in spectral domain corresponds to an algebraic eigenvalue problem. The calculation of a given problem's eigenpairs is quintessential to obtaining Green's functions, and, as demonstrated in earlier works, [1] and [2], to developing regularization techniques for dealing with singularities of any order, and thus to analyzing the near- and far-fields. The existence of supplementary equations is a new result, which allows factorizing the fields and minimizing the complexity and cost of computations by relegating ex-

Submitted On: October 16, 2018
Accepted On: October 23, 2018

pensive computations to post-processing processes. It turns out that the $\mathcal{D}-$ and $\mathcal{S}-$forms are both required for proving their sharp equivalence with the originating governing and constitutive equations, and thus their internal consistency. The accompanying paper (Part II, [7]) focuses on the details using the ''Occam's razor.''

Diagonalization can be carried out in a variety of ways, each aimed at illuminating certain desired features of the governing and constitutive equations, and of the resulting $\mathcal{D}-$ and $\mathcal{S}-$forms. The description of a strictly formal and ''automatic'' procedure would require considerably more space. (The stringent approach was detailed in the author's tutorial presentations at previous ACES conferences and recorded in the ACES proceedings.) The current self-sufficient presentation is compact and permits the reader to focus on the essentials and appreciate interrelationships.

B. Organization of the paper

The remaining sections are organized as follows. Section II ''unpacks'' Maxwell's curl equations in component form in the $(x, y, z)-$Cartesian coordinates and prepares them for further analysis by introducing normalized variables. Section III introduces the ''essential,'' ''nonessential,'' and ''auxiliary'' field variables. In the process three ''structural,'' and two ''differential'' matrices are identified, which play key roles in obtaining the $\mathcal{D}-$ and $\mathcal{S}-$forms. Section IV focuses on the factorization of the constitutive equations, identifying four characteristic ''material'' matrices. Using the developed preparatory tools, Section V constructs the $\mathcal{D}-$ and $\mathcal{S}-$forms. Section VI concludes the paper.

II. GOVERNING AND CONSTITUTIVE EQUATIONS

Consider Maxwell's electrodynamic equations with the field variables having the conventional meaning,

$$\nabla \times \mathbf{H} = \frac{\partial \mathbf{D}}{\partial t} + \mathbf{J}, \tag{1a}$$

$$\nabla \times \mathbf{E} = -\frac{\partial \mathbf{B}}{\partial t}. \tag{1b}$$

Consider the constitutive equation in fully bianisotropic and inhomogenous media characterized by 3×3 material matrices $\boldsymbol{\varepsilon}^{3\times3}(x, y, z)$, $\boldsymbol{\xi}^{3\times3}(x, y, z)$, $\boldsymbol{\zeta}^{3\times3}(x, y, z)$, and $\boldsymbol{\mu}^{3\times3}(x, y, z)$,

$$\mathbf{D} = \boldsymbol{\varepsilon}^{3\times3}(x, y, z)\mathbf{E} + \boldsymbol{\xi}^{3\times3}(x, y, z)\mathbf{H}, \tag{2a}$$

$$\mathbf{B} = \boldsymbol{\zeta}^{3\times3}(x, y, z)\mathbf{E} + \boldsymbol{\mu}^{3\times3}(x, y, z)\mathbf{H}. \tag{2b}$$

Assume a harmonic time-dependence according to $\exp(-j\omega t)$, and ''unpack'' the Eqs. (1):

$$\begin{bmatrix} 0 & -\partial_z & \partial_y \\ \partial_z & 0 & -\partial_x \\ -\partial_y & \partial_x & 0 \end{bmatrix} \begin{bmatrix} H_1 \\ H_2 \\ H_3 \end{bmatrix} = -j\omega \begin{bmatrix} D_1 \\ D_2 \\ D_3 \end{bmatrix} + \begin{bmatrix} J_1 \\ J_2 \\ J_3 \end{bmatrix}, \tag{3a}$$

$$\begin{bmatrix} 0 & -\partial_z & \partial_y \\ \partial_z & 0 & -\partial_x \\ -\partial_y & \partial_x & 0 \end{bmatrix} \begin{bmatrix} E_1 \\ E_2 \\ E_3 \end{bmatrix} = j\omega \begin{bmatrix} B_1 \\ B_2 \\ B_3 \end{bmatrix}. \tag{3b}$$

For notational convenience, divide each of the above equations by $j\omega$ and introduce the ''velocities'' $\tilde{x} = j\omega x$, $\tilde{y} = j\omega y$, and $\tilde{z} = j\omega z$. Thus, $\partial_x/(j\omega) = \partial_{\tilde{x}}$, $\partial_y/(j\omega) = \partial_{\tilde{y}}$, $\partial_z/(j\omega) = \partial_{\tilde{z}}$. Furthermore,, introduce the ''charges'' $\tilde{J}_1 = J_1/(j\omega)$, $\tilde{J}_2 = J_2/(j\omega)$, and $\tilde{J}_3 = J_3/(j\omega)$. Write Eqs. (3) component-wise, and employ the introduced ''velocities'' and the ''charges,''

$$-\partial_{\tilde{z}}H_2 + \partial_{\tilde{y}}H_3 = -D_1 + \tilde{J}_1, \tag{4a}$$

$$\partial_{\tilde{z}}H_1 - \partial_{\tilde{x}}H_3 = -D_2 + \tilde{J}_2, \tag{4b}$$

$$-\partial_{\tilde{y}}H_1 + \partial_{\tilde{x}}H_2 = -D_3 + \tilde{J}_3, \tag{4c}$$

$$-\partial_{\tilde{z}}E_2 + \partial_{\tilde{y}}E_3 = B_1, \tag{4d}$$

$$\partial_{\tilde{z}}E_1 - \partial_{\tilde{x}}E_3 = B_2, \tag{4e}$$

$$-\partial_{\tilde{y}}E_1 + \partial_{\tilde{x}}E_2 = B_3. \tag{4f}$$

III. ESSENTIAL-, NONESSENTIAL-, AND AUXILIARY VARIABLES

The main objective in this paper is the diagonalization and supplementation of the governing and constitutive equations with respect to the arbitrarily chosen $\tilde{z}-$axis. To this end, the first step consists of identifying the ''essential-,'' ''nonessential-'', and ''auxiliary'' field variables. When diagonalizing with respect to $\tilde{z}$, the field variables associated with $\partial_{\tilde{z}}$ are referred to as the ''essential'' field variables. Inspecting Eqs. (4) it is easily seen that the electromagnetic field components E_1, E_2, H_1, and H_2 are accompanied by $\partial_{\tilde{z}}$. The remaining components E_3 and H_3 are referred to as the ''nonessential'' field components. Equations involving $\partial_{\tilde{z}}E_1$, $\partial_{\tilde{z}}E_2$, $\partial_{\tilde{z}}H_1$, and $\partial_{\tilde{z}}H_2$, are, respectively, (4e), (4d), (4b), and (4a). The Eqs. (4c) and (4f) do not involve the partial derivative $\partial_{\tilde{z}}$. Next, reshuffle the order of the Eqs. (4) to reflect the successive appearances of the terms $\partial_{\tilde{z}}E_1$, $\partial_{\tilde{z}}E_2$, $\partial_{\tilde{z}}H_1$, and $\partial_{\tilde{z}}H_2$, and subdivide the Eqs. (4) into the systems of equations,

$$\partial_{\tilde{z}}E_1 - \partial_{\tilde{x}}E_3 = B_2, \tag{5a}$$

$$-\partial_{\tilde{z}}E_2 + \partial_{\tilde{y}}E_3 = B_1, \tag{5b}$$

$$\partial_{\tilde{z}}H_1 - \partial_{\tilde{x}}H_3 = -D_2 + \tilde{J}_2, \tag{5c}$$

$$-\partial_{\tilde{z}}H_2 + \partial_{\tilde{y}}H_3 = -D_1 + \tilde{J}_1, \tag{5d}$$

$$-\partial_{\tilde{y}} H_1 + \partial_{\tilde{x}} H_2 = -D_3 + \tilde{J}_3, \quad (6a)$$
$$-\partial_{\tilde{y}} E_1 + \partial_{\tilde{x}} E_2 = B_3. \quad (6b)$$

Bringing the terms accompanied by $\partial_{\tilde{z}}$ to the R.H.S. and rearranging,

$$B_2 + \partial_{\tilde{x}} E_3 = \partial_{\tilde{z}} E_1, \quad (7a)$$
$$-B_1 + \partial_{\tilde{y}} E_3 = \partial_{\tilde{z}} E_2, \quad (7b)$$
$$-D_2 + \partial_{\tilde{x}} H_3 + \tilde{J}_2 = \partial_{\tilde{z}} H_1, \quad (7c)$$
$$D_1 + \partial_{\tilde{y}} H_3 - \tilde{J}_1 = \partial_{\tilde{z}} H_2, \quad (7d)$$

$$D_3 = \partial_{\tilde{y}} H_1 - \partial_{\tilde{x}} H_2 + \tilde{J}_3, \quad (8a)$$
$$B_3 = -\partial_{\tilde{y}} E_1 + \partial_{\tilde{x}} E_2. \quad (8b)$$

Inspecting Eqs. (7) it is seen that the components of the fields $\mathbf{D}$ and $\mathbf{B}$ are not accompanied by any partial derivatives at all. The components of $\mathbf{D}$ and $\mathbf{B}$ are referred to as the ''auxiliary'' field components, and, in the framework of diagonalization and supplementation, they have to be eliminated from the equations. It should also be noted that Eqs. (7) containing the $\partial_{\tilde{z}}-$derivative, involve the components D_1, D_2, B_1, and B_2. On the other hand, Eqs. (8) not containing the $\partial_{\tilde{z}}-$derivative, involve the components D_3 and B_3. In virtue of these findings the following representations for (7) and (8), respectively, offer themselves:

$$\underbrace{\begin{bmatrix} 0 & 0 & 0 & 1 \\ 0 & 0 & -1 & 0 \\ 0 & -1 & 0 & 0 \\ 1 & 0 & 0 & 0 \end{bmatrix}}_{\mathbf{P}^{4\times 4}} \underbrace{\begin{bmatrix} D_1 \\ D_2 \\ B_1 \\ B_2 \end{bmatrix}}_{\mathbf{\Phi}_c^{\parallel}} + \underbrace{\begin{bmatrix} \partial_{\tilde{x}} & 0 \\ \partial_{\tilde{y}} & 0 \\ 0 & \partial_{\tilde{x}} \\ 0 & \partial_{\tilde{y}} \end{bmatrix}}_{\mathbf{Q}_c^{4\times 2}} \underbrace{\begin{bmatrix} E_3 \\ H_3 \end{bmatrix}}_{\mathbf{\Psi}_c^{\perp}}$$
$$+ \underbrace{\begin{bmatrix} 0 & 0 \\ 0 & 0 \\ 0 & 1 \\ -1 & 0 \end{bmatrix}}_{\mathbf{P}^{4\times 2}} \underbrace{\begin{bmatrix} \tilde{J}_1 \\ \tilde{J}_2 \end{bmatrix}}_{\tilde{\mathbf{J}}_c^{\parallel}} = \partial_{\tilde{z}} \underbrace{\begin{bmatrix} E_1 \\ E_2 \\ H_1 \\ H_2 \end{bmatrix}}_{\mathbf{\Psi}_c^{\parallel}}, \quad (9a)$$

$$\underbrace{\begin{bmatrix} D_3 \\ B_3 \end{bmatrix}}_{\mathbf{\Phi}_c^{\perp}} = \underbrace{\begin{bmatrix} 0 & 0 & \partial_{\tilde{y}} & -\partial_{\tilde{x}} \\ -\partial_{\tilde{y}} & \partial_{\tilde{x}} & 0 & 0 \end{bmatrix}}_{\mathbf{Q}_c^{2\times 4}} \underbrace{\begin{bmatrix} E_1 \\ E_2 \\ H_1 \\ H_2 \end{bmatrix}}_{\mathbf{\Psi}_c^{\parallel}}$$
$$+ \underbrace{\begin{bmatrix} 1 \\ 0 \end{bmatrix}}_{\mathbf{P}^{2\times 1}} \underbrace{\tilde{J}_3}_{\tilde{J}_c^{\perp}}. \quad (9b)$$

Using the introduced matrices and vectors, as indicated in Eqs. (9), the following compact forms can be established, which build the basis for our analysis,

$$\mathbf{P}^{4\times 4}\mathbf{\Phi}_c^{\parallel} + \mathbf{Q}_c^{4\times 2}\mathbf{\Psi}_c^{\perp} + \mathbf{P}^{4\times 2}\tilde{\mathbf{J}}_c^{\parallel} = \partial_{\tilde{z}}\mathbf{\Psi}_c^{\parallel}, \quad (10a)$$
$$\mathbf{\Phi}_c^{\perp} = \mathbf{Q}_c^{2\times 4}\mathbf{\Psi}_c^{\parallel} + \mathbf{P}^{2\times 1}\tilde{J}_c^{\perp}. \quad (10b)$$

Comments: The matrices $\mathbf{P}^{4\times 4}$, $\mathbf{P}^{4\times 2}$, and $\mathbf{P}^{2\times 1}$ in (9) are ''universal structural'' matrices, in the sense that their structures are independent of the diagonalization with respect to $\tilde{x}$, $\tilde{y}$, or $\tilde{z}$. The matrices $\mathbf{Q}_c^{4\times 2}$ and $\mathbf{Q}_c^{2\times 4}$ (and their counterparts $\mathbf{Q}_a^{4\times 2}$ and $\mathbf{Q}_a^{2\times 4}$, and $\mathbf{Q}_b^{4\times 2}$ and $\mathbf{Q}_b^{2\times 4}$) are matrix differential operators, possessing an ''intriguing'' property, as will be shown in Part II, [7]. The field vector $\mathbf{\Psi}_c^{\parallel}$ (along with its counterparts $\mathbf{\Psi}_a^{\parallel}$ and $\mathbf{\Psi}_b^{\parallel}$) is an ''essential'' field vector. The essential field vectors $\mathbf{\Psi}_c^{\parallel}$, $\mathbf{\Psi}_a^{\parallel}$, and $\mathbf{\Psi}_b^{\parallel}$, respectively, arise in the $\mathcal{D}_c-$, $\mathcal{D}_a-$, and $\mathcal{D}_b-$forms. Their associated field vectors $\mathbf{\Psi}_c^{\perp}$, $\mathbf{\Psi}_a^{\perp}$, and $\mathbf{\Psi}_b^{\perp}$, are ''nonessential'' field vectors. The nonessential field vectors $\mathbf{\Psi}_c^{\perp}$, $\mathbf{\Psi}_a^{\perp}$, and $\mathbf{\Psi}_b^{\perp}$, respectively, arise in the $\mathcal{S}_c-$, $\mathcal{S}_a-$, and $\mathcal{S}_b-$forms. Furthermore, $\mathbf{\Phi}_c^{\parallel}$ and $\mathbf{\Phi}_c^{\perp}$ (along with their counterparts $\mathbf{\Phi}_a^{\parallel}$ and $\mathbf{\Phi}_a^{\perp}$, and $\mathbf{\Phi}_b^{\parallel}$ and $\mathbf{\Phi}_b^{\perp}$) are auxiliary field vectors. Auxiliary vectors must be eliminated from the $(\mathcal{D}_c, \mathcal{S}_c)-$, $(\mathcal{D}_a, \mathcal{S}_a)-$, and $(\mathcal{D}_b, \mathcal{S}_b)-$forms.

IV. CONSTITUTIVE EQUATIONS

''Unpacking'' the constitutive Eqs. (2a) and (2b), leads to:

$$\begin{bmatrix} D_1 \\ D_2 \\ D_3 \end{bmatrix} = \begin{bmatrix} \varepsilon_{11} & \varepsilon_{12} & \varepsilon_{13} \\ \varepsilon_{21} & \varepsilon_{22} & \varepsilon_{23} \\ \varepsilon_{31} & \varepsilon_{32} & \varepsilon_{33} \end{bmatrix} \begin{bmatrix} E_1 \\ E_2 \\ E_3 \end{bmatrix} + \begin{bmatrix} \xi_{11} & \xi_{12} & \xi_{13} \\ \xi_{21} & \xi_{22} & \xi_{23} \\ \xi_{31} & \xi_{32} & \xi_{33} \end{bmatrix} \begin{bmatrix} H_1 \\ H_2 \\ H_3 \end{bmatrix}, \quad (11)$$

$$\begin{bmatrix} B_1 \\ B_2 \\ B_3 \end{bmatrix} = \begin{bmatrix} \zeta_{11} & \zeta_{12} & \zeta_{13} \\ \zeta_{21} & \zeta_{22} & \zeta_{23} \\ \zeta_{31} & \zeta_{32} & \zeta_{33} \end{bmatrix} \begin{bmatrix} E_1 \\ E_2 \\ E_3 \end{bmatrix} + \begin{bmatrix} \mu_{11} & \mu_{12} & \mu_{13} \\ \mu_{21} & \mu_{22} & \mu_{23} \\ \mu_{31} & \mu_{32} & \mu_{33} \end{bmatrix} \begin{bmatrix} H_1 \\ H_2 \\ H_3 \end{bmatrix}, \quad (12)$$

respectively. The aforementioned categorization (grouping) of the field vectors suggests partitioning

Eqs. (11) and (12), respectively, into:

$$\begin{bmatrix} D_1 \\ D_2 \end{bmatrix} = \begin{bmatrix} \varepsilon_{11} & \varepsilon_{12} \\ \varepsilon_{21} & \varepsilon_{22} \end{bmatrix} \begin{bmatrix} E_1 \\ E_2 \end{bmatrix} + \begin{bmatrix} \varepsilon_{13} \\ \varepsilon_{23} \end{bmatrix} E_3 + \begin{bmatrix} \xi_{11} & \xi_{12} \\ \xi_{21} & \xi_{22} \end{bmatrix} \begin{bmatrix} H_1 \\ H_2 \end{bmatrix} + \begin{bmatrix} \xi_{13} \\ \xi_{23} \end{bmatrix} H_3, \quad (13a)$$

$$D_3 = \begin{bmatrix} \varepsilon_{31} & \varepsilon_{32} \end{bmatrix} \begin{bmatrix} E_1 \\ E_2 \end{bmatrix} + \varepsilon_{33} E_3 + \begin{bmatrix} \xi_{31} & \xi_{32} \end{bmatrix} \begin{bmatrix} H_1 \\ H_2 \end{bmatrix} + \xi_{33} H_3, \quad (13b)$$

$$\begin{bmatrix} B_1 \\ B_2 \end{bmatrix} = \begin{bmatrix} \zeta_{11} & \zeta_{12} \\ \zeta_{21} & \zeta_{22} \end{bmatrix} \begin{bmatrix} E_1 \\ E_2 \end{bmatrix} + \begin{bmatrix} \zeta_{13} \\ \zeta_{23} \end{bmatrix} E_3 + \begin{bmatrix} \mu_{11} & \mu_{12} \\ \mu_{21} & \mu_{22} \end{bmatrix} \begin{bmatrix} H_1 \\ H_2 \end{bmatrix} + \begin{bmatrix} \mu_{13} \\ \mu_{23} \end{bmatrix} H_3, \quad (14a)$$

$$B_3 = \begin{bmatrix} \zeta_{31} & \zeta_{32} \end{bmatrix} \begin{bmatrix} E_1 \\ E_2 \end{bmatrix} + \zeta_{33} E_3 + \begin{bmatrix} \mu_{31} & \mu_{32} \end{bmatrix} \begin{bmatrix} H_1 \\ H_2 \end{bmatrix} + \mu_{33} H_3. \quad (14b)$$

Equations (13) and (14) can be written more compactly in the forms:

$$\begin{bmatrix} D_1 \\ D_2 \end{bmatrix} = \begin{bmatrix} \varepsilon_{11} & \varepsilon_{12} & \xi_{11} & \xi_{12} \\ \varepsilon_{21} & \varepsilon_{22} & \xi_{21} & \xi_{22} \end{bmatrix} \begin{bmatrix} E_1 \\ E_2 \\ H_1 \\ H_2 \end{bmatrix} + \begin{bmatrix} \varepsilon_{13} & \xi_{13} \\ \varepsilon_{23} & \xi_{23} \end{bmatrix} \begin{bmatrix} E_3 \\ H_3 \end{bmatrix}, \quad (15a)$$

$$D_3 = \begin{bmatrix} \varepsilon_{31} & \varepsilon_{32} & \xi_{31} & \xi_{32} \end{bmatrix} \begin{bmatrix} E_1 \\ E_2 \\ H_1 \\ H_2 \end{bmatrix} + \begin{bmatrix} \varepsilon_{33} & \xi_{33} \end{bmatrix} \begin{bmatrix} E_3 \\ H_3 \end{bmatrix}, \quad (15b)$$

and

$$\begin{bmatrix} B_1 \\ B_2 \end{bmatrix} = \begin{bmatrix} \zeta_{11} & \zeta_{12} & \mu_{11} & \mu_{12} \\ \zeta_{21} & \zeta_{22} & \mu_{21} & \mu_{22} \end{bmatrix} \begin{bmatrix} E_1 \\ E_2 \\ H_1 \\ H_2 \end{bmatrix} + \begin{bmatrix} \zeta_{13} & \mu_{13} \\ \zeta_{23} & \mu_{23} \end{bmatrix} \begin{bmatrix} E_3 \\ H_3 \end{bmatrix}, \quad (16a)$$

$$B_3 = \begin{bmatrix} \zeta_{31} & \zeta_{32} & \mu_{31} & \mu_{32} \end{bmatrix} \begin{bmatrix} E_1 \\ E_2 \\ H_1 \\ H_2 \end{bmatrix} + \begin{bmatrix} \zeta_{33} & \mu_{33} \end{bmatrix} \begin{bmatrix} E_3 \\ H_3 \end{bmatrix}. \quad (16b)$$

Combining (15a) with (16a),

$$\underbrace{\begin{bmatrix} D_1 \\ D_2 \\ B_1 \\ B_2 \end{bmatrix}}_{\boldsymbol{\Phi}_c^{\parallel}} = \underbrace{\begin{bmatrix} \varepsilon_{11} & \varepsilon_{12} & \xi_{11} & \xi_{12} \\ \varepsilon_{21} & \varepsilon_{22} & \xi_{21} & \xi_{22} \\ \zeta_{11} & \zeta_{12} & \mu_{11} & \mu_{12} \\ \zeta_{21} & \zeta_{22} & \mu_{21} & \mu_{22} \end{bmatrix}}_{\mathbf{M}_c^{4\times 4}} \underbrace{\begin{bmatrix} E_1 \\ E_2 \\ H_1 \\ H_2 \end{bmatrix}}_{\boldsymbol{\Psi}_c^{\parallel}} + \underbrace{\begin{bmatrix} \varepsilon_{13} & \xi_{13} \\ \varepsilon_{23} & \xi_{23} \\ \zeta_{13} & \mu_{13} \\ \zeta_{23} & \mu_{23} \end{bmatrix}}_{\mathbf{M}_c^{4\times 2}} \underbrace{\begin{bmatrix} E_3 \\ H_3 \end{bmatrix}}_{\boldsymbol{\Psi}_c^{\perp}}. \quad (17)$$

Employing the "material" matrices $\mathbf{M}_c^{4\times 4}$ and $\mathbf{M}_c^{4\times 2}$, and the fields $\boldsymbol{\Phi}_c^{\parallel}$, $\boldsymbol{\Psi}_c^{\parallel}$, and $\boldsymbol{\Psi}_c^{\perp}$, as indicated in (17),

$$\boldsymbol{\Phi}_c^{\parallel} = \mathbf{M}_c^{4\times 4} \boldsymbol{\psi}_c^{\parallel} + \mathbf{M}_c^{4\times 2} \boldsymbol{\Psi}_c^{\perp}. \quad (18)$$

Similarly, combining (15b) with (16b),

$$\underbrace{\begin{bmatrix} D_3 \\ B_3 \end{bmatrix}}_{\boldsymbol{\Phi}_c^{\perp}} = \underbrace{\begin{bmatrix} \varepsilon_{31} & \varepsilon_{32} & \xi_{31} & \xi_{32} \\ \zeta_{31} & \zeta_{32} & \mu_{31} & \mu_{32} \end{bmatrix}}_{\mathbf{M}_c^{2\times 4}} \underbrace{\begin{bmatrix} E_1 \\ E_2 \\ H_1 \\ H_2 \end{bmatrix}}_{\boldsymbol{\Psi}_c^{\parallel}} + \underbrace{\begin{bmatrix} \varepsilon_{33} & \xi_{33} \\ \zeta_{33} & \mu_{33} \end{bmatrix}}_{\mathbf{M}_c^{2\times 2}} \underbrace{\begin{bmatrix} E_3 \\ H_3 \end{bmatrix}}_{\boldsymbol{\Psi}_c^{\perp}}. \quad (19)$$

Employing the "material" matrices $\mathbf{M}_c^{2\times 4}$ and $\mathbf{M}_c^{2\times 2}$, and the fields $\boldsymbol{\Phi}_c^{\perp}$, $\boldsymbol{\Psi}_c^{\parallel}$, and $\boldsymbol{\Psi}_c^{\perp}$, as indicated in (19),

$$\boldsymbol{\Phi}_c^{\perp} = \mathbf{M}_c^{2\times 4} \boldsymbol{\Psi}_c^{\parallel} + \mathbf{M}_c^{2\times 2} \boldsymbol{\Psi}_c^{\perp}. \quad (20)$$

Preliminary summary: For easy reference, the governing equation dressed in the forms in (10), and the material equations formulated in the forms (18) and (20), are summarized below:

$$\mathbf{P}^{4\times4}\mathbf{\Phi}_c^{\parallel} + \mathbf{Q}_c^{4\times2}\mathbf{\Psi}_c^{\perp} + \mathbf{P}^{4\times2}\tilde{\mathbf{J}}_c^{\parallel} = \partial_{\tilde{z}}\mathbf{\Psi}_c^{\parallel}, \tag{21a}$$

$$\mathbf{\Phi}_c^{\perp} = \mathbf{Q}_c^{2\times4}\mathbf{\Psi}_c^{\parallel} + \mathbf{P}^{2\times1}\tilde{J}_c^{\perp}, \tag{21b}$$

$$\mathbf{\Phi}_c^{\parallel} = \mathbf{M}_c^{4\times4}\mathbf{\Psi}_c^{\parallel} + \mathbf{M}_c^{4\times2}\mathbf{\Psi}_c^{\perp}, \tag{21c}$$

$$\mathbf{\Phi}_c^{\perp} = \mathbf{M}_c^{2\times4}\mathbf{\Psi}_c^{\parallel} + \mathbf{M}_c^{2\times2}\mathbf{\Psi}_c^{\perp}. \tag{21d}$$

The governing Eqs. (21a) and (21b), and the constitutive Eqs. (21c) and (21d), express the set of electromagnetic field components $(E_1, E_2, E_3, H_1, H_2, H_3)$ in terms of the essential $\mathbf{\Psi}_c^{\parallel} = [E_1, E_2, H_1, H_2]^T$ and nonessential field components $\mathbf{\Psi}_c^{\perp} = [E_3, H_3]^T$. Furthermore, the differential operators are factorized into the $(\partial_{\tilde{x}}, \partial_{\tilde{y}})-$dependent operators $\mathbf{Q}_c^{2\times4}$ and $\mathbf{Q}_c^{4\times2}$ and the partial derivative $\partial_{\tilde{z}}$. It should also be noted that in addition to the essential- and nonessential field components, the auxiliary field components $\mathbf{\Phi}_c^{\parallel} = [D_1, D_2, B_1, B_2]^T$ and $\mathbf{\Phi}_c^{\perp} = [D_3, B_3]^T$ appear in the equations. Within the developed framework, auxiliary field variables must be eliminated from the Eqs. (21). The rationale for this stems from the fact that the auxiliary field components are, by definition, not accompanied by any spatial partial derivatives. The elimination of the auxiliary field components leads to the desired diagonalized $\mathcal{D}_c-$ and the associated supplementary $\mathcal{S}_c-$forms. The next section presents the details involved in the manipulations. Thereby, the individual steps will be explicated and the results interpreted.

V. THE $\mathcal{D}_c-$ AND THE ASSOCIATED $\mathcal{S}_c-$FORMS

Substituting (21c) into (21a), and equating the terms at the R.H.S. of (21d) and (21b),

$$\mathbf{P}^{4\times4}\left\{\mathbf{M}_c^{4\times4}\mathbf{\Psi}_c^{\parallel} + \mathbf{M}_c^{4\times2}\mathbf{\Psi}_c^{\perp}\right\} + \mathbf{Q}_c^{4\times2}\mathbf{\Psi}_c^{\perp} + \mathbf{P}^{4\times2}\tilde{\mathbf{J}}_c^{\parallel} = \partial_{\tilde{z}}\mathbf{\Psi}_c^{\parallel}, \tag{22a}$$

$$\mathbf{M}_c^{2\times4}\mathbf{\Psi}_c^{\parallel} + \mathbf{M}_c^{2\times2}\mathbf{\Psi}_c^{\perp} = \mathbf{Q}_c^{2\times4}\mathbf{\Psi}_c^{\parallel} + \mathbf{P}^{2\times1}\tilde{J}_c^{\perp}. \tag{22b}$$

The nonessential field vector $\mathbf{\Psi}_c^{\perp}$ must be eliminated from (22a) to obtain the $\mathcal{D}_c-$form. To this effect (22b) is employed, which is preferably rewritten in the form,

$$\mathbf{M}_c^{2\times2}\mathbf{\Psi}_c^{\perp} = \left(-\mathbf{M}_c^{2\times4} + \mathbf{Q}_c^{2\times4}\right)\mathbf{\Psi}_c^{\parallel} + \mathbf{P}^{2\times1}\tilde{J}_c^{\perp}. \tag{23}$$

A. Physical realizability condition

In view of (23) it is immediate that for expressing $\mathbf{\Psi}_c^{\perp}$ in terms of $\mathbf{\Psi}_c^{\parallel}$ and the source term $\tilde{J}_c^{\perp}$, the existence of the inverse of $\mathbf{M}_c^{2\times2}$ must be assumed. Consequently,

$$\det\left\{\mathbf{M}_c^{2\times2}\right\} = \det\begin{bmatrix} \varepsilon_{33} & \xi_{33} \\ \zeta_{33} & \mu_{33} \end{bmatrix}, \tag{24a}$$

$$= \varepsilon_{33}\mu_{33} - \zeta_{33}\xi_{33} \neq 0. \tag{24b}$$

To obtain the $\mathcal{S}_c-$ and $\mathcal{D}_c-$forms it is merely required that the condition stipulated in (24b) is valid.

B. The $\mathcal{S}_c-$form

Multiplying (23) by $\left[\mathbf{M}_c^{2\times2}\right]^{-1}$ from the L.H.S.,

$$\mathbf{\Psi}_c^{\perp} = \left[\mathbf{M}_c^{2\times2}\right]^{-1}\left(-\mathbf{M}_c^{2\times4} + \mathbf{Q}_c^{2\times4}\right)\mathbf{\Psi}_c^{\parallel} + \left[\mathbf{M}_c^{2\times2}\right]^{-1}\mathbf{P}^{2\times1}\tilde{J}_c^{\perp}. \tag{25}$$

This is the desired $\mathcal{S}_c-$form. It expresses the nonessential field components $\mathbf{\Psi}_c^{\perp}$ in terms of the essential field components $\mathbf{\Psi}_c^{\parallel}$ and the source term $\tilde{J}_c^{\perp}$: given $\tilde{J}_c^{\perp}$, once $\mathbf{\Psi}_c^{\parallel}$ has been determined, the nonessential field vector $\mathbf{\Psi}_c^{\perp}$ can be obtained according to the inexpensive post-processing step expressed in (25).

C. The $\mathcal{D}_c-$form

Focus on (22a) and pull the $\mathbf{\Psi}_c^{\perp}-$terms together,

$$\mathbf{P}^{4\times4}\mathbf{M}_c^{4\times4}\mathbf{\Psi}_c^{\parallel} + \left(\mathbf{P}^{4\times4}\mathbf{M}_c^{4\times2} + \mathbf{Q}_c^{4\times2}\right)\mathbf{\Psi}_c^{\perp} + \mathbf{P}^{4\times2}\tilde{\mathbf{J}}_c^{\parallel} = \partial_{\tilde{z}}\mathbf{\Psi}_c^{\parallel}. \tag{26}$$

Substituting (25) into (26) allows the elimination of the nonessential field vector $\mathbf{\Psi}_c^{\perp}$,

$$\mathbf{P}^{4\times4}\mathbf{M}_c^{4\times4}\mathbf{\Psi}_c^{\parallel} + \left(\mathbf{P}^{4\times4}\mathbf{M}_c^{4\times2} + \mathbf{Q}_c^{4\times2}\right)\left\{\left[\mathbf{M}_c^{2\times2}\right]^{-1} \times \left(-\mathbf{M}_c^{2\times4} + \mathbf{Q}_c^{2\times4}\right)\mathbf{\Psi}_c^{\parallel} + \left[\mathbf{M}_c^{2\times2}\right]^{-1}\mathbf{P}^{2\times1}\tilde{J}_c^{\perp}\right\} + \mathbf{P}^{4\times2}\tilde{\mathbf{J}}_c^{\parallel} = \partial_{\tilde{z}}\mathbf{\Psi}_c^{\parallel}. \tag{27}$$

Factoring out the $\mathbf{\Psi}_c^{\parallel}-$terms and rearranging lead to the $\mathcal{D}_c-$form,

$$\left\{\mathbf{P}^{4\times4}\mathbf{M}_c^{4\times4} + \left(\mathbf{P}^{4\times4}\mathbf{M}_c^{4\times2} + \mathbf{Q}_c^{4\times2}\right) \times \left[\mathbf{M}_c^{2\times2}\right]^{-1}\left(-\mathbf{M}_c^{2\times4} + \mathbf{Q}_c^{2\times4}\right)\right\}\mathbf{\Psi}_c^{\parallel} + \left(\mathbf{P}^{4\times4}\mathbf{M}_c^{4\times2} + \mathbf{Q}_c^{4\times2}\right)\left[\mathbf{M}_c^{2\times2}\right]^{-1}\mathbf{P}^{2\times1}\tilde{J}_c^{\perp} + \mathbf{P}^{4\times2}\tilde{\mathbf{J}}_c^{\parallel} = \partial_{\tilde{z}}\mathbf{\Psi}_c^{\parallel}. \tag{28}$$

This is the desired $\mathcal{D}_c-$form, involving the essential field vector $\mathbf{\Psi}_c^{\parallel}$ and the sources terms $\tilde{J}_c^{\perp}$ and $\tilde{\mathbf{J}}_c^{\parallel}$.

VI. CONCLUSION

Maxwell's electrodynamic equations were considered in fully bi-anisotropic and inhomogeneous media in three spatial dimensions. A harmonic time dependence according to $\exp(-j\omega t)$ and an $(x, y, z)-$Cartesian coordinate system were assumed. It was rigorously established that the Maxwell's equations along with the constitutive equations can be transformed into the diagonalized $(\mathcal{D}-)$ and the associated supplementary $(\mathcal{S}-)$forms. To this end, three ''structural,'' two ''differential,'' and four ''material,'' matrices were introduced and their properties discussed. It was shown that the conditions $\varepsilon_{ii}\mu_{ii} - \xi_{ii}\zeta_{ii} \neq 0$ $(i = 1, 2, 3)$ suffice to construct the $\mathcal{D}-$ and $\mathcal{S}-$forms. It was alluded to the fact that the derived forms play eminent roles in developing regularization techniques for dealing with infinities arising in computational electromagnetics and calculating the near- and far-fields. The utilitarian properties of the $\mathcal{D}-$ and $\mathcal{S}-$forms have been detailed in the author's earlier works [1]-[6]. The proof of their sharp equivalence with the combined Maxwell's and constitutive equations, and, thus, their internal consistency, has been provided in the accompanying paper, [7].

REFERENCES

[1] A. R. Baghai-Wadji, ''3-D electrostatic charge distribution on finitely thick busbars in micro acoustic devices: Combined regularization in the near- and far-field,'' IEEE Transactions on Ultrasonics, Ferroelectrics, and Frequency Control (UFFC), vol. 62, no. 6, June 2015, pp. 1132-1144.

[2] A. R. Baghai-Wadji, ''Dyadic universal functions and simultaneous near-field/far-field regularization of elasto-dynamic dyadic Green's functions for 3D mass-loading analysis in micro-acoustic devices,'' IEEE Transactions on UFFC, vol. 63, no. 10, October 2016, pp. 1563-1574.

[3] A. R. Baghai-Wadji, ''3D Thermo-acousto-electric diagonalized and supplementary equations in fully tri-anisotropic and inhomogeneous media, Part I: Proof of existence by construction,'' IEEE Journal on Multiscale and Multiphysics Computational Techniques (JMMCT), vol. 3, 2018, pp.149-158.

[4] A. R. Baghai-Wadji, ''3D Thermo-acousto-electric diagonalized and supplementary equations in fully tri-anisotropic and inhomogeneous media, Part II: Relative proof of consistency,'' IEEE Journal on Multiscale and Multiphysics Computational Techniques (JMMCT), vol. 3, 2018, pp. 159-166.

[5] A. R. Baghai-Wadji, ''Diagonalizability of Thermo Electromagnetic Equations in Inhomogeneous and Fully Tri-anisotropic Media,'' Proc. Applied Computational Electromagnetics Society Symposium (ACES), 2018, pp.1-2.

[6] A. R. Baghai-Wadji, ''The Path from Monadic to Tetradic Green's Functions,'' Proc. International Conference on Electromagnetics in Advanced Applications (ICEAA), 2018, pp.1-4.

[7] A. R. Baghai-Wadji, ''3D diagonalization and supplementation of Maxwell's equations in fully bi-anisotropic and inhomogeneous media, Part II: Relative proof of consistency,'' ACES Journal, this issue.

Alireza Baghai-Wadji is Professor and Convener of the ECE Program at University of Cape Town (UCT), South Africa. Previously, he was Assistant Dean (internationalization) in the Faculty of Engineering and the Built Environment at UCT. Serving as a high-level foreign expert Visiting Professor (Vis. Prof.), he was on sabbatical at Xian University of Science and Technology, Xian, Shaanxi, China, in the period 15 July 2017 - 15 July 2018. He received his M.Sc., Ph.D., and D.Sc. in 1984, 1987 and 1994, respectively, from Vienna University of Technology (TU-Wien), Austria. In 2003 he was awarded D.Sc. from Aalto University (AU), Finland. In August 2017 he was bestowed an Honorary Professorship at Amity University, Uttar Pradesh, New Delhi, India. He was 2005-2012 Prof., Discipline Head, and International Representative at RMIT University, Australia. He was 1979-2005 at TU-Wien: Assoc. Prof. (1997-2005), Docent (1994-1997), Assist. Prof. (1988-1994), Res. Fellow (1984-1988), and Res. Assoc. (1979-1983). He has worked on five continents accumulating vast experience in both academia and high-tech industry: Distinguished Vis. Prof. at Beijing Institute of Technology, China (Jan. 2014, Dec. 2013, Nov. 2012, Nov. 2011, Nov. 2010); Vis. Prof. at AU (Jan. 2009); Vis. Scientist at the Max Planck Ins. (Quantum Optics), Germany (July 2009, Nov 2009 - Jan 2010); Consultant (Cons.) to EPCOS, Germany (2004-2012); Vis. Prof. at AU for one-and-a-half year (1999, 2000, and 2004); Nokia Fellow, Helsinki (2000); Vis. Prof. at the Ins. for High Perf. Comp. and a Senior Mem. of the Ins. for Math. Sci. in Singapore (Jan., Feb., Oct., Nov. 2003). He was three times the recipient of the prestigious Austrian Kurt Goedel Res. Fellowship enabling him to spend a total of ten months at the University of California, Irvine, USA (1990, 1991, and 1992); he was Adj. Prof. at the Arizona State University, USA (1995-2004); Principal Eng. Cons. at Motorola, USA (1994-1999); Principal Eng. Cons. with CTS, USA (1999-2000); Principal Eng. Cons. with Siemens Matsushita, Austria (1990-1994); Cons. with Siemens, Germany (1983- 1990). He was Director of the Aerospace and Aviation Electronics Prog. at The Sir Lawrence Wackett Aerospace Centre, Australia (2007 and 2008). He is an Honorary Mem. and Fellow of The Electromagnetics Academy, USA and has been listed in Who is Who in Electromagnetics, USA. Since 1997 he has been an Assoc. Ed. for IEEE-UFFC Transactions. He was twice a guest ed. for the IEEE-UFFC Transactions. He has more than 200 publications in peer reviewed journals and conference proceedings, and has delivered more than 120 invited speeches internationally. He is the owner of one patent in USA. He has instructed 30 half-day or full-day short courses sponsored by IEEE or ACES since 1994.

3D Diagonalization and Supplementation of Maxwell's Equations in Fully Bi-anisotropic and Inhomogeneous Media Part II: Relative Proof of Consistency

A. R. Baghai-Wadji [1,2]

[1]Electrical Engineering Department
University of Cape Town, Cape Town, 7701, South Africa
alireza.baghai-wadji@uct.ac.za

[2]College of Science
Xi'an University of Science and Technology, Xi'an, Shaanxi, 710054, China

Abstract – Consider fully bi-anisotropic and inhomogeneous media supporting the electromagnetic wave propagation. Assume an $(x, y, z)-$Cartesian coordinate system and a harmonic time-dependence according to $\exp(-j\omega t)$. In the accompanying paper (Part I) it was shown that the Maxwell's equations can be diagonalized with respect to the $z-$axis, resulting in the $\mathcal{D}_c-$form. Furthermore, the existence of the associated supplementary matrix equation, the $\mathcal{S}_c-$form, was demonstrated rigorously. In the present paper ''structural,'' ''differential,'' and ''material'' matrices have been introduced to explicate the $(\mathcal{D}_a, \mathcal{S}_a)-$, $(\mathcal{D}_b, \mathcal{S}_b)-$, and $(\mathcal{D}_c, \mathcal{S}_c)-$forms, relative to the $x-$, $y-$, and $z-$axes, respectively. As the pinnacle of the theory, it has thoroughly been established that the derived combined $(\mathcal{D}_c, \mathcal{S}_c)-$forms are sharply equivalent with the joint Maxwell's and constitutive equations, and thus internally consistent. The presented proof is relative in the sense that its validity hinges on the consistency of Maxwell's equations and the material realizability conditions.

Index Terms – Bi-anisotropic and inhomogeneous media, diagonalization, Maxwell's equations, supplementation.

I. INTRODUCTION

Natural laws in their originally-conceived manifestations, and more generally, the process of theory construction, occasionally mirror the contents of experiments and their underlying assumptions. The Maxwell's curls equations offer themselves as an archetypical example. They explicate the Faraday's and Ampere's experiments, in an awe-inspiringly elegant manner, and expose the intricately interwoven links between them. On the other hand, not only in logic, but also in mathematics and physics, when constructing theories, one is concerned with the internal consistency of formulations and equations, beside the existence and uniqueness of their solutions. In the 1930's several other epistemologically groundbreaking ideas emerged, e.g., completeness, consistency, provability, and computability, [1], promoting the concepts of, e.g., finitary algorithms, and down the road, complexity and optimality of algorithms for obtaining accurate, robust, and accelerated numerical solutions to engineering problems. In the context of Maxwell's equations, a fundamental question arises as to whether Maxwell's equations' necessarily-heuristic nature renders them, as they stand, optimal for theorizing, algorithms design and computations. Concerning theorizing and algorithm design, the answer depends on the specificities of the theoretical investigations one might be interest in. However, when ''taming'' infinities and dealing with divergences in computations, the diagonalized $(\mathcal{D}-)$ and supplementary $(\mathcal{S}-)$ forms are considerably more adequate, for reasons substantiated in [2] and [3], and the references therein. This paper completes the exposition in [2] and proves the internal consistency of the $\mathcal{D}-$ and $\mathcal{S}-$forms by showing the sharp equivalence of the $\mathcal{D}-$ and $\mathcal{S}-$forms with the Maxwell's and constitutive equations.

The paper has been organized as follows. Section II starts with introducing three ''universal structural'' matrices. The attribute ''universal'' points to the fact that the introduced matrices are independent of the spatial direction along which the diagonalization and the associated supplementation take place: the structural matrices are the same, irrespective of which pairs $(\mathcal{D}_a, \mathcal{S}_a)$, $(\mathcal{D}_b, \mathcal{S}_b)$, or $(\mathcal{D}_c, \mathcal{S}_c)$ are constructed. The attribute ''structural'' alludes the fact that the entries of

Submitted On: October 16, 2018
Accepted On: October 23, 2018

the matrices, being 0 or 1, merely serve as place holders. Following a discussion of the properties of the structural matrices, a theorem has been stated which formalizes and completes the results obtained in [2]. The expressions for the diagonalized- and supplemented forms with respect to the $x-$axis have been stated, and the counterparts with respect to the $y-$ and $z-$axes have been obtained by cyclic permutations of indices and variables. The theorem comprises Parts I, II, and III, which are dedicated to $(\mathcal{D}_a, \mathcal{S}_a)$, $(\mathcal{D}_b, \mathcal{S}_b)$, and $(\mathcal{D}_c, \mathcal{S}_c)$, respectively. In each part the corresponding matrix differential operators and material matrices have been defined and their properties explained. A reference to the proof in [2] completes this section. Section III proves the internal consistency of the diagonalized- and supplementary equations in terms of the $(\mathcal{D}_c, \mathcal{S}_c)-$forms. Section IV concludes the paper.

II. 3D DIAGONALIZATION AND SUPPLEMENTATION OF MAXWELL'S EQUATIONS

It is assumed that the reader is acquainted with the notation introduced in [2]. Define the following ''universal structural'' matrices:

$$\mathbf{P}^{4\times4} = \begin{bmatrix} 0 & 0 & 0 & 1 \\ 0 & 0 & -1 & 0 \\ 0 & -1 & 0 & 0 \\ 1 & 0 & 0 & 0 \end{bmatrix}, \tag{1a}$$

$$\mathbf{P}^{4\times2} = \begin{bmatrix} 0 & 0 \\ 0 & 0 \\ 0 & 1 \\ -1 & 0 \end{bmatrix}, \tag{1b}$$

$$\mathbf{P}^{2\times1} = \begin{bmatrix} 1 \\ 0 \end{bmatrix}. \tag{1c}$$

The following relationships do not play any direct role in the diagonalization- and supplementation processes. Nevertheless, their underpinning unified connection to identity matrices deserves to be mentioned,

$$\left(\mathbf{P}^{4\times4}\right)^T\left(\mathbf{P}^{4\times4}\right) = \begin{bmatrix} 1 & 0 & 0 & 0 \\ 0 & 1 & 0 & 0 \\ 0 & 0 & 1 & 0 \\ 0 & 0 & 0 & 1 \end{bmatrix} = \mathbb{I}^{4\times4}, \tag{2a}$$

$$\left(\mathbf{P}^{4\times2}\right)^T\left(\mathbf{P}^{4\times2}\right) = \begin{bmatrix} 1 & 0 \\ 0 & 1 \end{bmatrix} = \mathbb{I}^{2\times2}, \tag{2b}$$

$$\left(\mathbf{P}^{2\times1}\right)^T\left(\mathbf{P}^{2\times1}\right) = \begin{bmatrix} 1 \end{bmatrix} = \mathbb{I}^{1\times1}. \tag{2c}$$

Here, $\mathbb{I}^{N\times N}$ refers to the $N\times N$ identity matrix.

Theorem: Consider the Maxwell's equations in fully bi-anisotropic and inhomogeneous media.

Part A: Define the matrix differential operators:

$$\mathbf{Q}_a^{2\times4} = \begin{bmatrix} 0 & 0 & \partial_{\tilde{z}} & -\partial_{\tilde{y}} \\ -\partial_{\tilde{z}} & \partial_{\tilde{y}} & 0 & 0 \end{bmatrix}, \tag{3a}$$

$$\mathbf{Q}_a^{4\times2} = \begin{bmatrix} \partial_{\tilde{y}} & 0 \\ \partial_{\tilde{z}} & 0 \\ 0 & \partial_{\tilde{y}} \\ 0 & \partial_{\tilde{z}} \end{bmatrix}. \tag{3b}$$

Observe the ''intriguing'' interplay between the entries of the matrices $\mathbf{Q}_a^{2\times4}$ and $\mathbf{Q}_a^{4\times2}$ leading to,

$$\mathbf{Q}_a^{2\times4}\mathbf{Q}_a^{4\times2} = \begin{bmatrix} 0 & 0 \\ 0 & 0 \end{bmatrix} = \mathbb{O}^{2\times2}. \tag{4}$$

Here $\mathbb{O}^{2\times2}$ refers to the 2×2 null matrix.

Define the following material-specific matrices:

$$\mathbf{M}_a^{4\times4} = \begin{bmatrix} \varepsilon_{22} & \varepsilon_{23} & \xi_{22} & \xi_{23} \\ \varepsilon_{32} & \varepsilon_{33} & \xi_{32} & \xi_{33} \\ \zeta_{22} & \zeta_{23} & \mu_{22} & \mu_{23} \\ \zeta_{32} & \zeta_{33} & \mu_{32} & \mu_{33} \end{bmatrix}, \tag{5a}$$

$$\mathbf{M}_a^{4\times2} = \begin{bmatrix} \varepsilon_{21} & \xi_{21} \\ \varepsilon_{31} & \xi_{31} \\ \zeta_{21} & \mu_{21} \\ \zeta_{31} & \mu_{31} \end{bmatrix}, \tag{5b}$$

$$\mathbf{M}_a^{2\times4} = \begin{bmatrix} \varepsilon_{12} & \varepsilon_{13} & \xi_{12} & \xi_{13} \\ \zeta_{12} & \zeta_{13} & \mu_{12} & \mu_{13} \end{bmatrix}, \tag{5c}$$

$$\mathbf{M}_a^{2\times2} = \begin{bmatrix} \varepsilon_{11} & \xi_{11} \\ \zeta_{11} & \mu_{11} \end{bmatrix}. \tag{5d}$$

Define the essential, $\mathbf{\Psi}_a^{\parallel}$, and its associated nonessential, $\mathbf{\Psi}_a^{\perp}$, field vectors according to,

$$\mathbf{\Psi}_a^{\parallel} = [E_2, E_3, H_2, H_3]^T, \tag{6a}$$

$$\mathbf{\Psi}_a^{\perp} = [E_1, H_1]^T. \tag{6b}$$

Then, the following $\mathcal{D}_a-$ and $\mathcal{S}_a-$forms hold valid.

The $\mathcal{D}_a-$form:

$$\begin{aligned}&\Big\{\mathbf{P}^{4\times4}\mathbf{M}_a^{4\times4}+\left(\mathbf{P}^{4\times4}\mathbf{M}_a^{4\times2}+\mathbf{Q}_a^{4\times2}\right)\\&\times\left[\mathbf{M}_a^{2\times2}\right]^{-1}\left(-\mathbf{M}_a^{2\times4}+\mathbf{Q}_a^{2\times4}\right)\Big\}\mathbf{\Psi}_a^{\parallel}\\&+\left(\mathbf{P}^{4\times4}\mathbf{M}_a^{4\times2}+\mathbf{Q}_a^{4\times2}\right)\left[\mathbf{M}_a^{2\times2}\right]^{-1}\mathbf{P}^{2\times1}\tilde{J}_a^{\perp}\\&+\mathbf{P}^{4\times2}\tilde{\mathbf{J}}_a^{\parallel}=\partial_{\tilde{x}}\mathbf{\Psi}_a^{\parallel}.\end{aligned}\tag{7}$$

The $\mathcal{S}_a-$form:

$$\begin{aligned}\mathbf{\Psi}_a^{\perp}&=\left[\mathbf{M}_a^{2\times2}\right]^{-1}\left(-\mathbf{M}_a^{2\times4}+\mathbf{Q}_a^{2\times4}\right)\mathbf{\Psi}_a^{\parallel}\\&+\left[\mathbf{M}_a^{2\times2}\right]^{-1}\mathbf{P}^{2\times1}\tilde{J}_a^{\perp}.\end{aligned}\tag{8}$$

Part B: Define the matrix differential operators $\mathbf{Q}_b^{2\times4}$ and $\mathbf{Q}_b^{4\times2}$, the material matrices $\mathbf{M}_b^{4\times4}$, $\mathbf{M}_b^{4\times2}$, $\mathbf{M}_b^{2\times4}$, and $\mathbf{M}_b^{2\times2}$, and the field vectors $\mathbf{\Psi}_b^{\parallel}$ and $\mathbf{\Psi}_b^{\perp}$, by performing the cyclic permutations $\tilde{x}\rightarrow\tilde{y}$, $\tilde{y}\rightarrow\tilde{z}$, $\tilde{z}\rightarrow\tilde{x}$, $1\rightarrow2$, $2\rightarrow3$, $3\rightarrow1$, and $a\rightarrow b$.

Matrix differential operators $\mathbf{Q}_b^{2\times4}$ and $\mathbf{Q}_b^{4\times2}$:

$$\mathbf{Q}_b^{2\times4}=\begin{bmatrix}0&0&\partial_{\tilde{x}}&-\partial_{\tilde{z}}\\-\partial_{\tilde{x}}&\partial_{\tilde{z}}&0&0\end{bmatrix},\tag{9a}$$

$$\mathbf{Q}_b^{4\times2}=\begin{bmatrix}\partial_{\tilde{z}}&0\\\partial_{\tilde{x}}&0\\0&\partial_{\tilde{z}}\\0&\partial_{\tilde{x}}\end{bmatrix}.\tag{9b}$$

The following relationship holds valid,

$$\mathbf{Q}_b^{2\times4}\mathbf{Q}_b^{4\times2}=\mathbb{O}^{2\times2}.\tag{10}$$

Material matrices $\mathbf{M}_b^{4\times4}$, $\mathbf{M}_b^{4\times2}$, $\mathbf{M}_b^{2\times4}$, and $\mathbf{M}_b^{2\times2}$:

$$\mathbf{M}_b^{4\times4}=\begin{bmatrix}\varepsilon_{33}&\varepsilon_{31}&\xi_{33}&\xi_{31}\\\varepsilon_{13}&\varepsilon_{11}&\xi_{13}&\xi_{11}\\\zeta_{33}&\zeta_{31}&\mu_{33}&\mu_{31}\\\zeta_{13}&\zeta_{11}&\mu_{13}&\mu_{11}\end{bmatrix},\tag{11a}$$

$$\mathbf{M}_b^{4\times2}=\begin{bmatrix}\varepsilon_{32}&\xi_{32}\\\varepsilon_{12}&\xi_{12}\\\zeta_{32}&\mu_{32}\\\zeta_{12}&\mu_{12}\end{bmatrix},\tag{11b}$$

$$\mathbf{M}_b^{2\times4}=\begin{bmatrix}\varepsilon_{23}&\varepsilon_{21}&\xi_{23}&\xi_{21}\\\zeta_{23}&\zeta_{21}&\mu_{23}&\mu_{21}\end{bmatrix},\tag{11c}$$

$$\mathbf{M}_b^{2\times2}=\begin{bmatrix}\varepsilon_{22}&\xi_{22}\\\zeta_{22}&\mu_{22}\end{bmatrix}.\tag{11d}$$

Field vectors $\mathbf{\Psi}_b^{\parallel}$ and $\mathbf{\Psi}_b^{\perp}$:

$$\mathbf{\Psi}_b^{\parallel}=[E_3,E_1,H_3,H_1]^T,\tag{12a}$$

$$\mathbf{\Psi}_b^{\perp}=[E_2,H_2]^T.\tag{12b}$$

Then the following $\mathcal{D}_b-$ and $\mathcal{S}_b-$forms hold valid.

The $\mathcal{D}_b-$form:

$$\begin{aligned}&\Big\{\mathbf{P}^{4\times4}\mathbf{M}_b^{4\times4}+\left(\mathbf{P}^{4\times4}\mathbf{M}_b^{4\times2}+\mathbf{Q}_b^{4\times2}\right)\\&\times\left[\mathbf{M}_b^{2\times2}\right]^{-1}\left(-\mathbf{M}_b^{2\times4}+\mathbf{Q}_b^{2\times4}\right)\Big\}\mathbf{\Psi}_b^{\parallel}\\&+\left(\mathbf{P}^{4\times4}\mathbf{M}_b^{4\times2}+\mathbf{Q}_b^{4\times2}\right)\left[\mathbf{M}_b^{2\times2}\right]^{-1}\mathbf{P}^{2\times1}\tilde{J}_b^{\perp}\\&+\mathbf{P}^{4\times2}\tilde{\mathbf{J}}_b^{\parallel}=\partial_{\tilde{y}}\mathbf{\Psi}_b^{\parallel}.\end{aligned}\tag{13}$$

The $\mathcal{S}_b-$form:

$$\begin{aligned}\mathbf{\Psi}_b^{\parallel}&=\left[\mathbf{M}_b^{2\times2}\right]^{-1}\left(-\mathbf{M}_b^{2\times4}+\mathbf{Q}_b^{2\times4}\right)\mathbf{\Psi}_b^{\parallel}\\&+\left[\mathbf{M}_b^{2\times2}\right]^{-1}\mathbf{P}^{2\times1}\tilde{J}_b^{\perp}.\end{aligned}\tag{14}$$

Part C: Define the matrix differential operators $\mathbf{Q}_c^{2\times4}$ and $\mathbf{Q}_c^{4\times2}$, the material matrices $\mathbf{M}_c^{4\times4}$, $\mathbf{M}_c^{4\times2}$, $\mathbf{M}_c^{2\times4}$, and $\mathbf{M}_c^{2\times2}$, and the field vectors $\mathbf{\Psi}_c^{\parallel}$ and $\mathbf{\Psi}_c^{\perp}$, by performing the cyclic permutations $\tilde{x}\rightarrow\tilde{y}$, $\tilde{y}\rightarrow\tilde{z}$, $\tilde{z}\rightarrow\tilde{x}$, $1\rightarrow2$, $2\rightarrow3$, $3\rightarrow1$, and $b\rightarrow c$.

Operator matrices $\mathbf{Q}_c^{2\times4}$ and $\mathbf{Q}_c^{4\times2}$:

$$\mathbf{Q}_c^{2\times4}=\begin{bmatrix}0&0&\partial_{\tilde{y}}&-\partial_{\tilde{x}}\\-\partial_{\tilde{y}}&\partial_{\tilde{x}}&0&0\end{bmatrix},\tag{15a}$$

$$\mathbf{Q}_c^{4\times2}=\begin{bmatrix}\partial_{\tilde{x}}&0\\\partial_{\tilde{y}}&0\\0&\partial_{\tilde{x}}\\0&\partial_{\tilde{y}}\end{bmatrix}.\tag{15b}$$

The following relationship holds valid,

$$\mathbf{Q}_c^{2\times4}\mathbf{Q}_c^{4\times2}=\mathbb{O}^{2\times2}.\tag{16}$$

Material matrices $\mathbf{M}_c^{4\times4}$, $\mathbf{M}_c^{4\times2}$, $\mathbf{M}_c^{2\times4}$, and $\mathbf{M}_c^{2\times2}$:

$$\mathbf{M}_c^{4\times4} = \begin{bmatrix} \varepsilon_{11} & \varepsilon_{12} & \xi_{11} & \xi_{12} \\ \varepsilon_{21} & \varepsilon_{22} & \xi_{21} & \xi_{22} \\ \zeta_{11} & \zeta_{12} & \mu_{11} & \mu_{12} \\ \zeta_{21} & \zeta_{22} & \mu_{21} & \mu_{22} \end{bmatrix}, \quad (17a)$$

$$\mathbf{M}_c^{4\times2} = \begin{bmatrix} \varepsilon_{13} & \xi_{13} \\ \varepsilon_{23} & \xi_{23} \\ \zeta_{13} & \mu_{13} \\ \zeta_{23} & \mu_{23} \end{bmatrix}, \quad (17b)$$

$$\mathbf{M}_c^{2\times4} = \begin{bmatrix} \varepsilon_{31} & \varepsilon_{32} & \xi_{31} & \xi_{32} \\ \zeta_{31} & \zeta_{32} & \mu_{31} & \mu_{32} \end{bmatrix}, \quad (17c)$$

$$\mathbf{M}_c^{2\times2} = \begin{bmatrix} \varepsilon_{33} & \xi_{33} \\ \zeta_{33} & \mu_{33} \end{bmatrix}. \quad (17d)$$

Field vectors $\mathbf{\Psi}_c^{\parallel}$ and $\mathbf{\Psi}_c^{\perp}$:

$$\mathbf{\Psi}_c^{\parallel} = [E_1, E_2, H_1, H_2]^T, \quad (18a)$$
$$\mathbf{\Psi}_c^{\perp} = [E_3, H_3]^T. \quad (18b)$$

Then the following $\mathcal{D}_c-$ and $\mathcal{S}_c-$forms hold valid.

The $\mathcal{D}_c-$form:

$$\Big\{\mathbf{P}^{4\times4}\mathbf{M}_c^{4\times4} + \left(\mathbf{P}^{4\times4}\mathbf{M}_c^{4\times2} + \mathbf{Q}_c^{4\times2}\right) \times \left[\mathbf{M}_c^{2\times2}\right]^{-1}\left(-\mathbf{M}_c^{2\times4} + \mathbf{Q}_c^{2\times4}\right)\Big\}\mathbf{\Psi}_c^{\parallel} + \left(\mathbf{P}^{4\times4}\mathbf{M}_c^{4\times2} + \mathbf{Q}_c^{4\times2}\right)\left[\mathbf{M}_c^{2\times2}\right]^{-1}\mathbf{P}^{2\times1}\tilde{J}_c^{\perp} + \mathbf{P}^{4\times2}\tilde{\mathbf{J}}_c^{\parallel} = \partial_{\tilde{z}}\mathbf{\Psi}_c^{\parallel}. \quad (19)$$

The $\mathcal{S}_c-$form:

$$\mathbf{\Psi}_c^{\perp} = \left[\mathbf{M}_c^{2\times2}\right]^{-1}\left(-\mathbf{M}_c^{2\times4} + \mathbf{Q}_c^{2\times4}\right)\mathbf{\Psi}_c^{\parallel} + \left[\mathbf{M}_c^{2\times2}\right]^{-1}\mathbf{P}^{2\times1}\tilde{J}_c^{\perp}. \quad (20)$$

Proof: The constructions of the $\mathcal{D}_c-$ and $\mathcal{S}_c-$forms, expressed in Eqs. (19) and (20), respectively, were performed in exhaustive and painstaking detail in [2], rigorously proving the claims in Part III. The proofs of Parts I and II follow from the proof of Part III by successive cyclic permutations as mentioned above.

III. ON THE CONSISTENCY OF THE $\mathcal{D}_c-$ AND $\mathcal{S}_c$ FORMS

In this section it is rigorously shown that the derived $\mathcal{D}_c-$ and $\mathcal{S}_c-$forms are, taken jointly, sharply equivalent with the originating governing and constitutive equations, and thus internally consistent.

Theorem: The $\mathcal{D}_c-$ and $\mathcal{S}_c-$forms given in Eqs. (19) and (20), respectively, are, taken together, sharply equivalent with Maxwell's equations and constitutive relationships, and thus internally consistent.

Proof: The $\mathcal{D}_c-$ and $\mathcal{S}_c-$forms given in Eqs. (19) and (20), respectively, are the starting point. Writing the $\mathcal{D}_c-$form more explicitly,

$$\mathbf{P}^{4\times4}\mathbf{M}_c^{4\times4}\mathbf{\Psi}_c^{\parallel} + \left(\mathbf{P}^{4\times4}\mathbf{M}_c^{4\times2} + \mathbf{Q}_c^{4\times2}\right) \times \left[\mathbf{M}_c^{2\times2}\right]^{-1}\left(-\mathbf{M}_c^{2\times4} + \mathbf{Q}_c^{2\times4}\right)\mathbf{\Psi}_c^{\parallel} + \left(\mathbf{P}^{4\times4}\mathbf{M}_c^{4\times2} + \mathbf{Q}_c^{4\times2}\right)\left[\mathbf{M}_c^{2\times2}\right]^{-1}\mathbf{P}^{2\times1}\tilde{J}_c^{\perp} + \mathbf{P}^{4\times2}\tilde{\mathbf{J}}_c^{\parallel} = \partial_{\tilde{z}}\mathbf{\Psi}_c^{\parallel}. \quad (21)$$

Rewriting the $\mathcal{S}_c-$form,

$$\left[\mathbf{M}_c^{2\times2}\right]^{-1}\left(-\mathbf{M}_c^{2\times4} + \mathbf{Q}_c^{2\times4}\right)\mathbf{\Psi}_c^{\parallel} = \mathbf{\Psi}_c^{\perp} - \left[\mathbf{M}_c^{2\times2}\right]^{-1}\mathbf{P}^{2\times1}\tilde{J}_c^{\perp}. \quad (22)$$

Using (22) for the term in the second line in (21),

$$\mathbf{P}^{4\times4}\mathbf{M}_c^{4\times4}\mathbf{\Psi}_c^{\parallel} + \left(\mathbf{P}^{4\times4}\mathbf{M}_c^{4\times2} + \mathbf{Q}_c^{4\times2}\right) \times \left(\mathbf{\Psi}_c^{\perp} - \left[\mathbf{M}_c^{2\times2}\right]^{-1}\mathbf{P}^{2\times1}\tilde{J}_c^{\perp}\right) + \left(\mathbf{P}^{4\times4}\mathbf{M}_c^{4\times2} + \mathbf{Q}_c^{4\times2}\right)\left[\mathbf{M}_c^{2\times2}\right]^{-1}\mathbf{P}^{2\times1}\tilde{J}_c^{\perp} + \mathbf{P}^{4\times2}\tilde{\mathbf{J}}_c^{\parallel} = \partial_{\tilde{z}}\mathbf{\Psi}_c^{\parallel}. \quad (23)$$

Terms associated with $\tilde{J}_c^{\perp}$ drop off,

$$\mathbf{P}^{4\times4}\mathbf{M}_c^{4\times4}\mathbf{\Psi}_c^{\parallel} + \left(\mathbf{P}^{4\times4}\mathbf{M}_c^{4\times2} + \mathbf{Q}_c^{4\times2}\right)\mathbf{\Psi}_c^{\perp} + \mathbf{P}^{4\times2}\tilde{\mathbf{J}}_c^{\parallel} = \partial_{\tilde{z}}\mathbf{\Psi}_c^{\parallel}. \quad (24)$$

Rewriting and factoring out $\mathbf{P}^{4\times4}$,

$$\mathbf{P}^{4\times4}\underbrace{\left(\mathbf{M}_c^{4\times4}\mathbf{\Psi}_c^{\parallel} + \mathbf{M}_c^{4\times2}\mathbf{\Psi}_c^{\perp}\right)}_{=\mathbf{\Phi}_c^{\parallel}} + \mathbf{Q}_c^{4\times2}\mathbf{\Psi}_c^{\perp} + \mathbf{P}^{4\times2}\tilde{\mathbf{J}}_c^{\parallel} = \partial_{\tilde{z}}\mathbf{\Psi}_c^{\parallel}. \quad (25)$$

Recognizing the indicated term in (25) to be equal to $\mathbf{\Phi}_c^{\parallel}$ (defined in [2]),

$$\mathbf{P}^{4\times4}\mathbf{\Phi}_c^{\parallel} + \mathbf{Q}_c^{4\times2}\mathbf{\Psi}_c^{\perp} + \mathbf{P}^{4\times2}\tilde{\mathbf{J}}_c^{\parallel} = \partial_{\tilde{z}}\mathbf{\Psi}_c^{\parallel}. \quad (26)$$

Multiplying (20) from the L.H.S. by $\mathbf{M}_c^{2\times2}$,

$$\mathbf{M}_c^{2\times2}\mathbf{\Psi}_c^{\perp} = \left(-\mathbf{M}_c^{2\times4} + \mathbf{Q}_c^{2\times4}\right)\mathbf{\Psi}_c^{\parallel} + \mathbf{P}^{2\times1}\tilde{J}_c^{\perp}. \quad (27)$$

Rearranging (27),

$$\underbrace{\mathbf{M}_c^{2\times4}\mathbf{\Psi}_c^{\parallel} + \mathbf{M}_c^{2\times2}\mathbf{\Psi}_c^{\perp}}_{=\mathbf{\Phi}_c^{\perp}} = \mathbf{Q}_c^{2\times4}\mathbf{\Psi}_c^{\parallel} + \mathbf{P}^{2\times1}\tilde{J}_c^{\perp}. \quad (28)$$

Recognizing the indicated term in (28) as $\mathbf{\Phi}_c^{\perp}$ (defined in [2]),

$$\mathbf{\Phi}_c^{\perp} = \mathbf{Q}_c^{2\times4}\mathbf{\Psi}_c^{\parallel} + \mathbf{P}^{2\times1}\tilde{J}_c^{\perp}. \quad (29)$$

Taking the derivative with respect to $\tilde{z}$ of both sides, unpacking $\mathbf{\Phi}_c^{\perp}$ and $\mathbf{\Psi}_c^{\parallel}$, and noting $\tilde{J}_c^{\perp} = \tilde{J}_3$,

$$\partial_{\tilde{z}}\begin{bmatrix} D_3 \\ B_3 \end{bmatrix} = \partial_{\tilde{z}}\mathbf{Q}_c^{2\times4}\begin{bmatrix} E_1 \\ E_2 \\ H_1 \\ H_2 \end{bmatrix} + \partial_{\tilde{z}}\mathbf{P}^{2\times1}\tilde{J}_3. \quad (30)$$

Using the commutativity relationships,

$$\partial_{\tilde{z}}\mathbf{Q}_c^{2\times4} = \mathbf{Q}_c^{2\times4}\partial_{\tilde{z}}, \quad (31a)$$
$$\partial_{\tilde{z}}\mathbf{P}^{2\times1} = \mathbf{P}^{2\times1}\partial_{\tilde{z}}, \quad (31b)$$

equation (30) transforms into,

$$\partial_{\tilde{z}}\begin{bmatrix} D_3 \\ B_3 \end{bmatrix} = \mathbf{Q}_c^{2\times4}\partial_{\tilde{z}}\begin{bmatrix} E_1 \\ E_2 \\ H_1 \\ H_2 \end{bmatrix} + \mathbf{P}^{2\times1}\partial_{\tilde{z}}\tilde{J}_3. \quad (32)$$

Remembering the definition $\mathbf{\Psi}_c^{\parallel} = [E_1, E_2, H_1, H_2]^T$, [2], and considering (26), Eq. (32) reads,

$$\partial_{\tilde{z}}\begin{bmatrix} D_3 \\ B_3 \end{bmatrix} = \mathbf{Q}_c^{2\times4}\left\{\mathbf{P}^{4\times4}\begin{bmatrix} D_1 \\ D_2 \\ B_1 \\ B_2 \end{bmatrix} + \mathbf{Q}_c^{4\times2}\begin{bmatrix} E_3 \\ H_3 \end{bmatrix} + \mathbf{P}^{4\times2}\begin{bmatrix} \tilde{J}_1 \\ \tilde{J}_2 \end{bmatrix}\right\} + \mathbf{P}^{2\times1}\partial_{\tilde{z}}\tilde{J}_3. \quad (33)$$

Here, $\mathbf{\Phi}_c^{\parallel}$, $\mathbf{\Psi}_c^{\perp}$, and $\tilde{\mathbf{J}}_c^{\parallel}$ have been unpacked for greater clarity. Written more explicitly,

$$\partial_{\tilde{z}}\begin{bmatrix} D_3 \\ B_3 \end{bmatrix} = \mathbf{Q}_c^{2\times4}\mathbf{P}^{4\times4}\begin{bmatrix} D_1 \\ D_2 \\ B_1 \\ B_2 \end{bmatrix} + \mathbf{Q}_c^{2\times4}\mathbf{Q}_c^{4\times2}\begin{bmatrix} E_3 \\ H_3 \end{bmatrix} + \mathbf{Q}_c^{2\times4}\mathbf{P}^{4\times2}\begin{bmatrix} \tilde{J}_1 \\ \tilde{J}_2 \end{bmatrix} + \mathbf{P}^{2\times1}\partial_{\tilde{z}}\tilde{J}_3. \quad (34)$$

In (16) it was established that $\mathbf{Q}_c^{2\times4}\mathbf{Q}_c^{4\times2} = \mathbb{O}^{2\times2}$, with $\mathbb{O}^{2\times2}$ being the 2×2 null matrix. Thus (34) reads,

$$\partial_{\tilde{z}}\begin{bmatrix} D_3 \\ B_3 \end{bmatrix} = \mathbf{Q}_c^{2\times4}\mathbf{P}^{4\times4}\begin{bmatrix} D_1 \\ D_2 \\ B_1 \\ B_2 \end{bmatrix} + \mathbf{Q}_c^{2\times4}\mathbf{P}^{4\times2}\begin{bmatrix} \tilde{J}_1 \\ \tilde{J}_2 \end{bmatrix} + \mathbf{P}^{2\times1}\partial_{\tilde{z}}\tilde{J}_3. \quad (35)$$

Considering,

$$\mathbf{Q}_c^{2\times4}\mathbf{P}_c^{4\times4} = \begin{bmatrix} 0 & 0 & \partial_{\tilde{y}} & -\partial_{\tilde{x}} \\ -\partial_{\tilde{y}} & \partial_{\tilde{x}} & 0 & 0 \end{bmatrix}\begin{bmatrix} 0 & 0 & 0 & 1 \\ 0 & 0 & -1 & 0 \\ 0 & -1 & 0 & 0 \\ 1 & 0 & 0 & 0 \end{bmatrix}, \quad (36a)$$

$$= \begin{bmatrix} -\partial_{\tilde{x}} & -\partial_{\tilde{y}} & 0 & 0 \\ 0 & 0 & -\partial_{\tilde{x}} & -\partial_{\tilde{y}} \end{bmatrix}, \quad (36b)$$

and

$$\mathbf{Q}_c^{2\times4}\mathbf{P}_c^{4\times4} = \begin{bmatrix} 0 & 0 & \partial_{\tilde{y}} & -\partial_{\tilde{x}} \\ -\partial_{\tilde{y}} & \partial_{\tilde{x}} & 0 & 0 \end{bmatrix}\begin{bmatrix} 0 & 0 \\ 0 & 0 \\ 0 & 1 \\ -1 & 0 \end{bmatrix}, \quad (37a)$$

$$= \begin{bmatrix} \partial_{\tilde{x}} & \partial_{\tilde{y}} \\ 0 & 0 \end{bmatrix}, \quad (37b)$$

and using the definition $\mathbf{P}^{2\times1} = [1, 0]^T$, (35) reads,

$$\partial_{\tilde{z}}\begin{bmatrix} D_3 \\ B_3 \end{bmatrix} = \begin{bmatrix} -\partial_{\tilde{x}} & -\partial_{\tilde{y}} & 0 & 0 \\ 0 & 0 & -\partial_{\tilde{x}} & -\partial_{\tilde{y}} \end{bmatrix}\begin{bmatrix} D_1 \\ D_2 \\ B_1 \\ B_2 \end{bmatrix} + \begin{bmatrix} \partial_{\tilde{x}} & \partial_{\tilde{y}} \\ 0 & 0 \end{bmatrix}\begin{bmatrix} \tilde{J}_1 \\ \tilde{J}_2 \end{bmatrix} + \begin{bmatrix} 1 \\ 0 \end{bmatrix}\partial_{\tilde{z}}\tilde{J}_3. \quad (38)$$

Multiplying out,

$$\begin{bmatrix} \partial_{\tilde{z}} D_3 \\ \partial_{\tilde{z}} B_3 \end{bmatrix} = \begin{bmatrix} -\partial_{\tilde{x}} D_1 - \partial_{\tilde{y}} D_2 \\ -\partial_{\tilde{x}} B_1 - \partial_{\tilde{y}} B_2 \end{bmatrix} + \begin{bmatrix} \partial_{\tilde{x}} \tilde{J}_1 + \partial_{\tilde{y}} \tilde{J}_2 \\ 0 \end{bmatrix} + \begin{bmatrix} \partial_{\tilde{z}} \tilde{J}_3 \\ 0 \end{bmatrix}. \quad (39)$$

Writing component-wise,

$$\begin{aligned} \partial_{\tilde{z}} D_3 &= -\partial_{\tilde{x}} D_1 - \partial_{\tilde{y}} D_2 \\ &\quad +\partial_{\tilde{x}} \tilde{J}_1 + \partial_{\tilde{y}} \tilde{J}_2 + \partial_{\tilde{z}} \tilde{J}_3, \quad (40a) \\ \partial_{\tilde{z}} B_3 &= -\partial_{\tilde{x}} B_1 - \partial_{\tilde{y}} B_2. \quad (40b) \end{aligned}$$

Rearranging, remembering the definitions $\partial_{\tilde{x}} = \partial_x/j\omega$, $\partial_{\tilde{y}} = \partial_y/j\omega$, and $\partial_{\tilde{z}} = \partial_z/j\omega$, introduced in [2], assuming $\omega \neq 0$, and multiplying by $j\omega$,

$$\begin{aligned} \mathrm{div}\mathbf{D} &= \mathrm{div}\tilde{\mathbf{J}}, \quad (41a) \\ \mathrm{div}\mathbf{B} &= 0. \quad (41b) \end{aligned}$$

Remembering the definition of $\tilde{\mathbf{J}} = \mathbf{J}/(j\omega)$, [2],

$$\mathrm{div}\mathbf{D} = \mathrm{div}\frac{1}{j\omega}\mathbf{J}. \quad (42)$$

Multiplying by $j\omega(\neq 0)$,

$$j\omega \mathrm{div}\mathbf{D} = \mathrm{div}\mathbf{J}. \quad (43)$$

Considering the electric charge conservation law,

$$\mathrm{div}\mathbf{J} + \frac{\partial \rho}{\partial t} = 0, \quad (44)$$

and recalling the $\exp(-j\omega t)$ time-harmonic assumption, Eq. (44) can equivalently be written in the form,

$$\mathrm{div}\mathbf{J} = j\omega\rho. \quad (45)$$

Thus, Eq. (43) results in,

$$j\omega \mathrm{div}\mathbf{D} = j\omega\rho. \quad (46)$$

Dividing by $j\omega(\neq 0)$,

$$\mathrm{div}\mathbf{D} = \rho. \quad (47)$$

Summarizing our results, it can be stated that by assuming the charge conservation law, Eq. (44), and using the derived $\mathcal{D}_c-$ and $\mathcal{S}_c-$forms, Maxwell's divergence equations have been established,

$$\begin{aligned} \mathrm{div}\mathbf{D} &= \rho, \quad (48a) \\ \mathrm{div}\mathbf{B} &= 0. \quad (48b) \end{aligned}$$

This completes the relative proof of the internal consistency of the drived $\mathcal{D}_c-$ and the associated $\mathcal{S}_c-$forms, in virtue of their sharp equivalence with the originating Maxwell's equations and the constitutive equations, characterizing fully bi-anisotropic and inhomogeneous media.

IV. CONCLUSION

In the accompanying paper, [2], it was shown that the Maxwell's equations in fully bi-anisotropic and inhomogeneous media can be diagonalized resulting in the $\mathcal{D}-$form. In addition, the existence of an associated supplementary equation, the $\mathcal{S}-$form, was demonstrated. In this work it was stringently proved that the derived $(\mathcal{D}, \mathcal{S})-$forms are internally consistent, based on the fact that they are sharply equivalent with the originating Maxwell's equations and constitutive relationships. A relative consistency proof was presented which proceeded along the following line of argument: (i) It is a known fact that the Maxwell's curl equations together with the electric charge conservation law imply the Maxwell's divergence equations. (ii) Within the framework of the classical electrodynamics it is assumed that the Maxwell's equations are self-consistent (internal consistency). (iii) Employing the $\mathcal{D}-$ and the $\mathcal{S}-$forms constructed in [2], and utilizing the charge conservation law, this paper established the Maxwell's divergence equations. (iv) The sharp equivalence of the $\mathcal{D}-$ and the $\mathcal{S}-$forms with Maxwell's curl equations, and the consistency of Maxwell's curl equations, imply the consistency of the $\mathcal{D}-$ and $\mathcal{S}-$forms. The discussion in [3] provides a glimpse on possible wide-ranging implications of the proposed theoretical framework.

REFERENCES

[1] B. J. Copeland, C. J. Posy, and O. Shagrir, Eds., ''Computability - Turing, Gödel, Church, and Beyond,'' The MIT Press, Cambridge, Massachusetts, London, England, 2015.

[2] A. R. Baghai-Wadji, ''3D Diagonalization and supplementation of Maxwell's equations in fully bi-anisotropic and inhomogeneous media, Part I: Proof of existence by construction,'' ACES Journal, this issue.

[3] A. R. Baghai-Wadji, ''The Path from Monadic to Tetradic Green's Functions,'' Proc. International Conference on Electromagnetics in Advanced Applications (ICEAA), 2018, pp. 1-4.

Alireza Baghai-Wadji: For a biography, please refer to the accompanying paper, [2], in this issue.

3D Diagonalization and Supplementation of Electrostatic Field Equations in Fully Anisotropic and Inhomogeneous Media Proof of Existence and Consistency

A. R. Baghai-Wadji [1,2]

[1]Electrical Engineering Department
University of Cape Town, Cape Town, 7701, South Africa
alireza.baghai-wadji@uct.ac.za

[2]College of Science,
Xi'an University of Science and Technology, Xi'an, Shaanxi, 710054, China

Abstract – Consider Maxwell's homogeneous curl equation $\nabla \times \mathbf{E} = 0$ for the electric field vector $\mathbf{E}$ and the inhomogeneous divergence equation $\nabla \cdot \mathbf{D} = \rho$ for the dielectric displacement vector $\mathbf{D}$ and the charge density function ρ in the static limit. Assume an $(x, y, z)-$Cartesian coordinate system. Consider the constitutive equation $\mathbf{D} = \boldsymbol{\varepsilon}\ \mathbf{E}$, with the 3×3 position-dependent positive-definite permittivity matrix $\boldsymbol{\varepsilon}(x, y, z)$ modeling fully anisotropic and inhomogeneous dielectric media. This paper proves that $\nabla \times \mathbf{E} = 0$ and $\nabla \cdot \mathbf{D} = \rho$ along with $\mathbf{D} = \boldsymbol{\varepsilon}\ \mathbf{E}$ are diagonalizable with respect to the arbitrarily chosen $z-$axis leading to the $\mathcal{D}_c-$form. The existence of an associated supplementary equation, the $\mathcal{S}_c-$form, has also been demonstrated. Finally, it is shown that the constructed $(\mathcal{D}_c, \mathcal{S}_c)-$forms are sharply equivalent with the originating set of equations $\nabla \times \mathbf{E} = 0$, $\nabla \cdot \mathbf{D} = \rho$, and $\mathbf{D} = \boldsymbol{\varepsilon}\ \mathbf{E}$, and, thus, internally consistent. The proof scheme is relative in the sense that its validity hinges on the consistency of Maxwell's equations in the static limit and the material realizability conditions.

Index Terms – Anisotropic and inhomogeneous dielectric media, diagonalization, electrostatic field, supplementation.

I. INTRODUCTION

In the accompanying paper, [1], Maxwell's electrodynamic equations in linear fully bi-anisotropic and inhomogeneous media were analyzed. It was demonstrated that the governing $(\mathcal{G})$ and constitutive $(\mathcal{C})$ equations can be diagonalized $(\mathcal{D}-$form$)$ with reference to any arbitrary direction in space. Furthermore, it was shown that there exists a unique supplementary equation $(\mathcal{S}-$form$)$ associated with the $\mathcal{D}-$form. The existence of $(\mathcal{D}, \mathcal{S})-$forms was established by construction. In [2], it was rigorously proved that the constructed $(\mathcal{D}, \mathcal{S})-$forms are sharply equivalent with the originating set of equations $(\mathcal{G}, \mathcal{C})$. Assuming the consistency of $(\mathcal{G}, \mathcal{C})$, it was then concluded that the $(\mathcal{D}, \mathcal{S})-$forms are internally consistent. The present paper considers Maxwell's $\nabla \times \mathbf{E} = 0$ and $\nabla \cdot \mathbf{D} = \rho$ equations in the electrostatic limit. Fully anisotropic and inhomogeneous dielectric media characterized by the 3×3 position-dependent positive-definite permittivity matrix $\boldsymbol{\varepsilon}(x, y, z)$ have been assumed. The constitutive equation $\mathbf{D}= \boldsymbol{\varepsilon}\mathbf{E}$ relates the dielectric displacement vector $\mathbf{D}$ to the electric field vector $\mathbf{E}$. Rigorous proofs of existence and internal consistency of the $(\mathcal{D}, \mathcal{S})-$forms substantially refine the related discussion in [3]. The merits of the $(\mathcal{D}, \mathcal{S})-$forms have been alluded to in [1] and [2], and the references therein, and will not be repeated here. Nonetheless one outstanding feature of the $\mathcal{D}-$form deserves mentioning: the $\mathcal{D}-$form automatically gives rise to the ''interface conditions.'' This fundamental property has been detailed in [3]. Despite the fact that the paper is self-sufficient, the reader would most likely benefit from acquainting themselves with the contents of [1] and [2].

The paper has been organized as follows. The brief Section II fixes the overall notation. Section III explains the construction of the $(\mathcal{D}, \mathcal{S})-$forms, by stating and proving a theorem. Section IV is devoted to the consistency analysis of the constructed $(\mathcal{D}, \mathcal{S})-$forms. Thereby, a second theorem will be stated and a relative proof will be provided. Sections III and IV consider the $z-$axis as the direction along which the diagonalization is performed. The letter ''c,'' used as a suffix or superscript, signifies the fact that the chosen direction has been the $z-$axis. In the Appendix the formulae corresponding to the $x-$, $y-$, and the $z-$axes have been

Submitted On: October 16, 2018
Accepted On: October 23, 2018

summarized. Correspondingly, the formulae have been equipped with the letters ''a,'' ''b,'' and ''c.'' The ''a-'' and ''b-'' related formulae have been obtained from the formulae derived in Sections III and IV, by cyclic permutations $1 \to 2$, $2 \to 3$, $3 \to 1$, $a \to b$, $b \to c$, $c \to a$. Section V concludes the paper.

II. MAXWELL'S EQUATIONS IN THE STATIC LIMIT

Consider the set of equations $(\mathcal{G}, \mathcal{C})$,

$$\nabla \times \mathbf{E} = 0, \tag{1a}$$
$$\nabla \cdot \mathbf{D} = \rho, \tag{1b}$$
$$\mathbf{D} = \boldsymbol{\varepsilon}(x, y, z)\mathbf{E}. \tag{1c}$$

A sufficient condition for $\nabla \times \mathbf{E} = 0$ to be valid is:

$$\mathbf{E} = -\nabla\varphi, \tag{2}$$

with $\varphi(x, y, z)$ being the electric potential function. Utilizing matrix notation and ''unpacking'' the Eqs. (2), (1b) and (1c), respectively,

$$E_1 = -\partial_x\varphi, \tag{3a}$$
$$E_2 = -\partial_y\varphi, \tag{3b}$$
$$E_3 = -\partial_z\varphi, \tag{3c}$$

$$\partial_x D_1 + \partial_y D_2 + \partial_z D_3 = \rho, \tag{4}$$

$$D_1 = \varepsilon_{11}E_1 + \varepsilon_{12}E_2 + \varepsilon_{13}E_3, \tag{5a}$$
$$D_2 = \varepsilon_{21}E_1 + \varepsilon_{22}E_2 + \varepsilon_{23}E_3, \tag{5b}$$
$$D_3 = \varepsilon_{31}E_1 + \varepsilon_{32}E_2 + \varepsilon_{33}E_3. \tag{5c}$$

III. 3D DIAGONALIZATION AND SUPPLEMENTATION ALONG THE $Z-$AXIS

Consider the governing Eqs. (3) and (4) along with the constitutive Eqs. (5). Focus on the $z-$axis. The objective in this section is to prove, by construction, the existence of the diagonalized $(\mathcal{D}_c)$ and the associated supplementary $(\mathcal{S}_c)$ forms, with $(\mathcal{D}_c, \mathcal{S}_c)$ being sharply equivalent with the originating set of equations $(\mathcal{G}, \mathcal{C})$. Recall that the suffix ''c'' signifies the $z-$axis. Not surprisingly, the partial derivative ∂_z shall play a significant role in the presented arguments and derivations. Diagonalization with respect to the $x-$ and $y-$axes are specified by the suffixes ''a'' and ''b,'' respectively, with ∂_x and ∂_y being the main players.

Theorem: The set of equations $(\mathcal{G}, \mathcal{C})$ can uniquely be transformed into the $(\mathcal{D}_c, \mathcal{S}_c)-$forms.

Proof: The strategy for proofing the existence of the $\mathcal{D}_c-$ and $\mathcal{S}_c-$forms amounts to constructing them. The first step in obtaining the $\mathcal{D}_c-$ and $\mathcal{S}_c-$forms is to identify field components which are accompanied by ∂_z. Simple inspection shows that these are φ, Eq. (3c), and D_3, Eq. (4). The proof requires partitioning the field variables into certain categories, introduced next.

Essential field variables: Field variables accompanied by ∂_z are referred to as the ''essential'' field variables. In the current context, these are φ and D_3.

Nonessential field variables: The remaining two components of $\mathbf{D}$; i.e., D_1, and D_2, are referred to as the ''nonessential'' field variables.

Auxiliary field variables: Equations (5) do not involve any spatial derivatives. More importantly, the spatial derivatives of the components of $\mathbf{E}$ do not arise in neither the governing nor the constitutive equations. Fields of this kind are referred to as the ''auxiliary'' field variables.

In the $(\mathcal{D}, \mathcal{S})-$framework, auxiliary field variables must be eliminated at once. This requirement prompts substituting (3) into (5),

$$D_1 = -\varepsilon_{11}\partial_x\varphi - \varepsilon_{12}\partial_y\varphi - \varepsilon_{13}\partial_z\varphi, \tag{6a}$$
$$D_2 = -\varepsilon_{21}\partial_x\varphi - \varepsilon_{22}\partial_y\varphi - \varepsilon_{23}\partial_z\varphi, \tag{6b}$$
$$D_3 = -\varepsilon_{31}\partial_x\varphi - \varepsilon_{32}\partial_y\varphi - \varepsilon_{33}\partial_z\varphi. \tag{6c}$$

In virtue of the positive-definiteness of $\boldsymbol{\varepsilon}$, $\varepsilon_{ii} \neq 0$ $(i = 1, 2, 3)$. Dividing (6c) by ε_{33} and rearranging,

$$\left(-\frac{\varepsilon_{31}}{\varepsilon_{33}}\partial_x - \frac{\varepsilon_{32}}{\varepsilon_{33}}\partial_y\right)\varphi - \frac{1}{\varepsilon_{33}}D_3 = \partial_z\varphi. \tag{7}$$

Introducing the operators,

$$\mathcal{L}^c_{11} = -\frac{\varepsilon_{31}}{\varepsilon_{33}}\partial_x - \frac{\varepsilon_{32}}{\varepsilon_{33}}\partial_y, \tag{8a}$$
$$\mathcal{L}^c_{12} = -\frac{1}{\varepsilon_{33}}, \tag{8b}$$

equation (7) can be written compactly,

$$\mathcal{L}^c_{11}\varphi + \mathcal{L}^c_{12}D_3 = \partial_z\varphi. \tag{9}$$

This completes the construction of the first of the two equations which constitute the $\mathcal{D}_c-$form.

To obtain the missing counterpart, rewrite (4),

$$\left[\begin{array}{cc} -\partial_x & -\partial_y \end{array}\right] \left[\begin{array}{c} D_1 \\ D_2 \end{array}\right] + \rho = \partial_z D_3. \tag{10}$$

For this equation to qualify as a $\mathcal{D}_c-$form, the non-essential field variables D_1 and D_2 must be expressed in terms of the essential field variables φ and D_3. To this end, consider (6a) and (6b) and eliminate the term $\partial_z\varphi$ from their R.H.S. Fortunately, an expression for $\partial_z\varphi$ in terms of φ and D_3 is already available, Eq. (9). Substituting for $\partial_z\varphi$ from (9) into (6a) and (6b),

$$\begin{aligned} D_1 &= -\varepsilon_{11}\partial_x\varphi - \varepsilon_{12}\partial_y\varphi \\ &\quad -\varepsilon_{13}\left(\mathcal{L}^c_{11}\varphi + \mathcal{L}^c_{12}D_3\right), \end{aligned} \tag{11a}$$

$$\begin{aligned} D_2 &= -\varepsilon_{21}\partial_x\varphi - \varepsilon_{22}\partial_y\varphi \\ &\quad -\varepsilon_{23}\left(\mathcal{L}^c_{11}\varphi + \mathcal{L}^c_{12}D_3\right). \end{aligned} \tag{11b}$$

Or, equivalently,

$$\begin{aligned} \left[\begin{array}{c} D_1 \\ D_2 \end{array}\right] &= \left[\begin{array}{c} -\varepsilon_{11}\partial_x - \varepsilon_{12}\partial_y - \varepsilon_{13}\mathcal{L}^c_{11} \\ \\ -\varepsilon_{21}\partial_x - \varepsilon_{22}\partial_y - \varepsilon_{23}\mathcal{L}^c_{11} \end{array}\right]\varphi \\ &\quad + \left[\begin{array}{c} -\varepsilon_{13}\mathcal{L}^c_{12} \\ \\ -\varepsilon_{23}\mathcal{L}^c_{12} \end{array}\right] D_3. \end{aligned} \tag{12}$$

Employing the explicit expressions for $\mathcal{L}^c_{11}$ and $\mathcal{L}^c_{12}$, Eqs. (8),

$$\begin{aligned} &\left[\begin{array}{c} D_1 \\ D_2 \end{array}\right] \\ &= \left[\begin{array}{c} -\left(\varepsilon_{11} - \frac{\varepsilon_{13}\varepsilon_{31}}{\varepsilon_{33}}\right)\partial_x - \left(\varepsilon_{12} - \frac{\varepsilon_{13}\varepsilon_{32}}{\varepsilon_{33}}\right)\partial_y \\ \\ -\left(\varepsilon_{21} - \frac{\varepsilon_{23}\varepsilon_{31}}{\varepsilon_{33}}\right)\partial_x - \left(\varepsilon_{22} - \frac{\varepsilon_{23}\varepsilon_{32}}{\varepsilon_{33}}\right)\partial_y \end{array}\right]\varphi \\ &+ \left[\begin{array}{c} \frac{\varepsilon_{13}}{\varepsilon_{33}} \\ \\ \frac{\varepsilon_{23}}{\varepsilon_{33}} \end{array}\right] D_3. \end{aligned} \tag{13}$$

Introducing operators $\mathcal{A}^c_{ij}$ $(i,j=1,2)$,

$$\mathcal{A}^c_{11} = -\left(\varepsilon_{11} - \frac{\varepsilon_{13}\varepsilon_{31}}{\varepsilon_{33}}\right)\partial_x - \left(\varepsilon_{12} - \frac{\varepsilon_{13}\varepsilon_{32}}{\varepsilon_{33}}\right)\partial_y, \tag{14a}$$

$$\mathcal{A}^c_{12} = \frac{\varepsilon_{13}}{\varepsilon_{33}}, \tag{14b}$$

$$\mathcal{A}^c_{21} = -\left(\varepsilon_{21} - \frac{\varepsilon_{23}\varepsilon_{31}}{\varepsilon_{33}}\right)\partial_x - \left(\varepsilon_{22} - \frac{\varepsilon_{23}\varepsilon_{32}}{\varepsilon_{33}}\right)\partial_y, \tag{14c}$$

$$\mathcal{A}^c_{22} = \frac{\varepsilon_{23}}{\varepsilon_{33}}, \tag{14d}$$

equation (13) can be written compactly,

$$\left[\begin{array}{c} D_1 \\ D_2 \end{array}\right] = \left[\begin{array}{cc} \mathcal{A}^c_{11} & \mathcal{A}^c_{12} \\ \\ \mathcal{A}^c_{21} & \mathcal{A}^c_{22} \end{array}\right] \left[\begin{array}{c} \varphi \\ D_3 \end{array}\right]. \tag{15}$$

This concludes the construction of the supplementary equations, the $\mathcal{S}_c-$form, expressing the nonessential components D_1 and D_2 in terms of the essential variables φ and D_3.

Substitute (15) into (10) to eliminate the nonessential field variables D_1 and D_2,

$$\begin{aligned} &\left[\begin{array}{cc} -\partial_x & -\partial_y \end{array}\right] \left[\begin{array}{cc} \mathcal{A}^c_{11} & \mathcal{A}^c_{12} \\ \\ \mathcal{A}^c_{21} & \mathcal{A}^c_{22} \end{array}\right] \left[\begin{array}{c} \varphi \\ D_3 \end{array}\right] \\ &\quad + \rho = \partial_z D_3. \end{aligned} \tag{16}$$

Defining the composite operators $\mathcal{L}^c_{21}$ and $\mathcal{L}^c_{22}$,

$$\mathcal{L}^c_{21} = -\partial_x\mathcal{A}^c_{11} - \partial_y\mathcal{A}^c_{21}, \tag{17a}$$

$$\mathcal{L}^c_{22} = -\partial_x\mathcal{A}^c_{12} - \partial_y\mathcal{A}^c_{22}, \tag{17b}$$

(16) leads to the second equation of the $\mathcal{D}_c-$form,

$$\left[\begin{array}{cc} \mathcal{L}^c_{21} & \mathcal{L}^c_{22} \end{array}\right] \left[\begin{array}{c} \varphi \\ D_3 \end{array}\right] + \rho = \partial_z D_3. \tag{18}$$

Combining (9) with (18),

$$\left[\begin{array}{cc} \mathcal{L}^c_{11} & \mathcal{L}^c_{12} \\ \\ \mathcal{L}^c_{21} & \mathcal{L}^c_{22} \end{array}\right] \left[\begin{array}{c} \varphi \\ D_3 \end{array}\right] + \left[\begin{array}{c} 0 \\ \rho \end{array}\right] = \partial_z \left[\begin{array}{c} \varphi \\ D_3 \end{array}\right]. \tag{19}$$

This completes the construction of the $\mathcal{D}_c-$form.

IV. THE INTERNAL CONSISTENNCY OF THE $\mathcal{D}_c-$ AND $\mathcal{S}_c-$FORMS

Theorem: The constructed $\mathcal{D}_c-$ and $\mathcal{S}_c-$forms, Eqs. (19) and (15), respectively, are internally consistent.

Proof: The proof strategy consists of demonstrating that $(\mathcal{D}_c, \mathcal{S}_c)$ is sharply equivalent with $(\mathcal{G}, \mathcal{C})$: The derivation of $(\mathcal{D}_c, \mathcal{S}_c)$ exclusively requires the entirety of $(\mathcal{G}, \mathcal{C})$. Conversely, $(\mathcal{G}, \mathcal{C})$ can exclusively be obtained from the entirety of $(\mathcal{D}_c, \mathcal{S}_c)$.

Consider the $\mathcal{S}_c-$form, Eq. (15). Apply the operator $[\partial_x \;\; \partial_y]$ from the L.H.S.,

$$\left[\begin{array}{cc} \partial_x & \partial_y \end{array}\right] \left[\begin{array}{c} D_1 \\ D_2 \end{array}\right]$$

$$= \left[\begin{array}{cc} \partial_x & \partial_y \end{array}\right] \left[\begin{array}{cc} \mathcal{A}^c_{11} & \mathcal{A}^c_{12} \\ \mathcal{A}^c_{21} & \mathcal{A}^c_{22} \end{array}\right] \left[\begin{array}{c} \varphi \\ D_3 \end{array}\right], \tag{20a}$$

$$= \left[\begin{array}{cc} \underbrace{\partial_x \mathcal{A}^c_{11} + \partial_y \mathcal{A}^c_{21}}_{-\mathcal{L}^c_{21}} & \underbrace{\partial_x \mathcal{A}^c_{12} + \partial_y \mathcal{A}^c_{22}}_{-\mathcal{L}^c_{22}} \end{array}\right] \left[\begin{array}{c} \varphi \\ D_3 \end{array}\right]. \tag{20b}$$

In view of definition equations (17), and recognizing the appearance of the operators $-\mathcal{L}^c_{21}$ and $-\mathcal{L}^c_{22}$ in (20b), as indicated,

$$\left[\begin{array}{cc} \partial_x & \partial_y \end{array}\right] \left[\begin{array}{c} D_1 \\ D_2 \end{array}\right] = - \left[\begin{array}{cc} \mathcal{L}^c_{21} & \mathcal{L}^c_{22} \end{array}\right] \left[\begin{array}{c} \varphi \\ D_3 \end{array}\right]. \tag{21}$$

Considering (18); i.e., the second equation of the $\mathcal{D}_c-$form, the R.H.S. of (21) equals $\rho - \partial_z D_3$. Thus, (21) results in,

$$\partial_x D_1 + \partial_y D_2 = \rho - \partial_z D_3. \tag{22}$$

Or, written more compactly,

$$\nabla \cdot \mathbf{D} = \rho. \tag{23}$$

Fact 1: *The second equation of the $\mathcal{D}_c-$form and both equations of the $\mathcal{S}_c-$form allow reproducing the Maxwell's divergence equation for* $\mathbf{D}$.

Next consider the first equation of the $\mathcal{D}_c-$form, (9), which in view of the definition equations of $\mathcal{L}^c_{11}$ and $\mathcal{L}^c_{12}$, given in Eqs. (8), leads to,

$$\left(-\frac{\varepsilon_{31}}{\varepsilon_{33}}\partial_x - \frac{\varepsilon_{32}}{\varepsilon_{33}}\partial_y\right)\varphi - \frac{1}{\varepsilon_{33}} D_3 = \partial_z \varphi. \tag{24}$$

Multiply both sides of (24) by ε_{33}, and rearrange,

$$D_3 = -\varepsilon_{31}\partial_x\varphi - \varepsilon_{32}\partial_y\varphi - \varepsilon_{33}\partial_z\varphi. \tag{25}$$

Define the electric field components E_i $(i = 1, 2, 3)$,

$$E_1 = -\partial_x \varphi, \tag{26a}$$
$$E_2 = -\partial_y \varphi, \tag{26b}$$
$$E_3 = -\partial_z \varphi, \tag{26c}$$

which are sufficient for the validity of $\nabla \times \mathbf{E} = 0$. Then, (25) leads to,

$$D_3 = \varepsilon_{31}E_1 + \varepsilon_{32}E_2 + \varepsilon_{33}E_3. \tag{27}$$

Fact 2: *The first equation of the $\mathcal{D}_c-$form together with the sufficient conditions for the validity of Maxwell's curl equation for the electric field* $(\nabla \times \mathbf{E} = 0)$ *allow reproducing the third constitutive equation.*

Comment: Thus far Maxwell's equations $\nabla \times \mathbf{E} = 0$ and $\nabla \cdot \mathbf{D} = \rho$ and the third of the constitution equations have been reconstructed. The reconstruction of the first- and the second constitutive equations will complete the proof of the sharp equivalence of the $(\mathcal{D}_c, \mathcal{S}_c)-$forms with the originating governing and constitutive equations $(\mathcal{G}, \mathcal{C})$.

Consider the $\mathcal{S}_c-$form, Eq. (15). Consider the explicit expressions for the operators $\mathcal{A}^c_{ij}$ $(i, j = 1, 2)$, (14). "Unpacking" $\mathcal{A}^c_{ij}$, leads to,

$$\begin{aligned} D_1 &= -\left(\varepsilon_{11} - \frac{\varepsilon_{13}\varepsilon_{31}}{\varepsilon_{33}}\right)\partial_x\varphi \\ &\quad -\left(\varepsilon_{12} - \frac{\varepsilon_{13}\varepsilon_{32}}{\varepsilon_{33}}\right)\partial_y\varphi + \frac{\varepsilon_{13}}{\varepsilon_{33}} D_3, \end{aligned} \tag{28}$$

$$\begin{aligned} D_2 &= -\left(\varepsilon_{21} - \frac{\varepsilon_{23}\varepsilon_{31}}{\varepsilon_{33}}\right)\partial_x\varphi \\ &\quad -\left(\varepsilon_{22} - \frac{\varepsilon_{23}\varepsilon_{32}}{\varepsilon_{33}}\right)\partial_y\varphi + \frac{\varepsilon_{23}}{\varepsilon_{33}} D_3. \end{aligned} \tag{29}$$

Rearranging (28) and (29),

$$\begin{aligned} D_1 = &-\varepsilon_{11}\partial_x\varphi - \varepsilon_{12}\partial_y\varphi \\ &+ \varepsilon_{13}\left\{\underbrace{\left[\frac{\varepsilon_{31}}{\varepsilon_{33}}\partial_x + \frac{\varepsilon_{32}}{\varepsilon_{33}}\partial_y\right]}_{=-\mathcal{L}^c_{11}}\varphi + \underbrace{\left[\frac{1}{\varepsilon_{33}}\right]}_{=-\mathcal{L}^c_{12}} D_3\right\}, \end{aligned} \tag{30}$$

$$\begin{aligned} D_2 = &-\varepsilon_{21}\partial_x\varphi - \varepsilon_{22}\partial_y\varphi \\ &+ \varepsilon_{23}\left\{\underbrace{\left[\frac{\varepsilon_{31}}{\varepsilon_{33}}\partial_x + \frac{\varepsilon_{32}}{\varepsilon_{33}}\partial_y\right]}_{=-\mathcal{L}^c_{11}}\varphi + \underbrace{\left[\frac{1}{\varepsilon_{33}}\right]}_{=-\mathcal{L}^c_{12}} D_3\right\}, \end{aligned} \tag{31}$$

where the operators $-\mathcal{L}^c_{11}$ and $-\mathcal{L}^c_{12}$ have been identified, as indicated. Simplifying,

$$\begin{aligned} D_1 = &-\varepsilon_{11}\partial_x\varphi - \varepsilon_{12}\partial_y\varphi \\ &- \varepsilon_{13}\underbrace{[\mathcal{L}^c_{11}\varphi + \mathcal{L}^c_{12}D_3]}_{=\partial_z\varphi}, \end{aligned} \tag{32}$$

$$\begin{aligned} D_2 = &-\varepsilon_{21}\partial_x\varphi - \varepsilon_{22}\partial_y\varphi \\ &- \varepsilon_{23}\underbrace{[\mathcal{L}^c_{11}\varphi + \mathcal{L}^c_{12}D_3]}_{=\partial_z\varphi}. \end{aligned} \tag{33}$$

Recognizing the first equation of the $\mathcal{D}_c-$form, Eq. (9), as indicated in (32) and (33),

$$D_1 = -\varepsilon_{11}\partial_x\varphi - \varepsilon_{12}\partial_y\varphi - \varepsilon_{13}\partial_z\varphi, \quad (34a)$$
$$D_2 = -\varepsilon_{21}\partial_x\varphi - \varepsilon_{22}\partial_y\varphi - \varepsilon_{23}\partial_z\varphi. \quad (34b)$$

Together with the stipulated conditions (26),

$$D_1 = \varepsilon_{11}E_1 + \varepsilon_{12}E_2 + \varepsilon_{13}E_3, \quad (35a)$$
$$D_2 = \varepsilon_{21}E_1 + \varepsilon_{22}E_2 + \varepsilon_{23}E_3. \quad (35b)$$

Fact 3: *The two equations of the $\mathcal{S}_c-$form, the first equation of the $\mathcal{D}_c-$form, and the sufficient conditions for the validity of $\nabla \times \mathbf{E} = 0$; i.e., $E_1 = -\partial_x\varphi$, $E_2 = -\partial_y\varphi$, and $E_3 = -\partial_z\varphi$, were used to reconstruct the second- and the third constitutive equations.*

Consequently, in virtue of (35) and (27) the complete set of constitutive equations has been reconstructed,

$$\mathbf{D} = \boldsymbol{\varepsilon}\mathbf{E}. \quad (36)$$

The analyses in Sections III and IV complete the proof of the sharp equivalence of the constructed $(\mathcal{D}_c, \mathcal{S}_c)-$forms with the Maxwell's electrostatic equations and the constitutive equations in fully anisotropic and inhomogeneous media. Consequently, postulating the consistency of the Maxwell's equations in the electrostatic limit along with the material realizability conditions, it can be inferred that the constructed $(\mathcal{D}_c, \mathcal{S}_c)-$forms are internally consistent. This completes the proof of existence of the $(\mathcal{D}_c, \mathcal{S}_c)-$forms and the relative proof of their internal consistency.

V. CONCLUSION

Governing $(\mathcal{G})$ and constitutive $(\mathcal{C})$ equations in mathematical physics can be diagonalized $(\mathcal{D}-$form) with respect to any chosen direction in space. The fact that there also exists an accompanying dual supplementary equation $(\mathcal{S}-$form) associated with the $\mathcal{D}-$form is a recent result. This paper focused on the important electrostatic limit, by considering fully-anisotropic and inhomogeneous dielectrics in three spatial dimensions. It completes the $(\mathcal{D}, \mathcal{S})-$treatment of the Maxwell's electrodynamic equations presented in [1] and [2]. Furthermore, it substantiates the discussion in [3] by rigorously discussing the consistency of the derived $(\mathcal{D}, \mathcal{S})-$forms. Selecting the $z-$axis, it was rigorously established that the system of $(\mathcal{G}, \mathcal{C})$ equations can be partitioned into the $(\mathcal{D}, \mathcal{S})-$forms. It was also demonstrated that the $(\mathcal{D}, \mathcal{S})-$forms are sharply equivalent with the $(\mathcal{G}, \mathcal{C})$ equations and thus internally consistent. In carrying out the proofs it was required that diagonal entries of the permittivity matrix $\boldsymbol{\varepsilon}$ must be non-zero, a condition which in virtue of the positive-definiteness of $\boldsymbol{\varepsilon}$ is satisfied. The diagonalization and supplementation of magneto-static fields will be rigorously treated in an upcoming work.

VI. APPENDIX

Diagonalization and Supplementation with respect to the $x-$axis:

A. Operator matrix entries for the $\mathcal{S}_a-$form

$$\mathcal{A}^a_{11} = -\left(\varepsilon_{22} - \frac{\varepsilon_{21}\varepsilon_{12}}{\varepsilon_{11}}\right)\partial_y - \left(\varepsilon_{23} - \frac{\varepsilon_{21}\varepsilon_{13}}{\varepsilon_{11}}\right)\partial_z, \quad (37a)$$
$$\mathcal{A}^a_{12} = \frac{\varepsilon_{21}}{\varepsilon_{11}}, \quad (37b)$$
$$\mathcal{A}^a_{21} = -\left(\varepsilon_{32} - \frac{\varepsilon_{31}\varepsilon_{12}}{\varepsilon_{11}}\right)\partial_y - \left(\varepsilon_{33} - \frac{\varepsilon_{31}\varepsilon_{13}}{\varepsilon_{11}}\right)\partial_z, \quad (37c)$$
$$\mathcal{A}^a_{22} = \frac{\varepsilon_{31}}{\varepsilon_{11}}, \quad (37d)$$

$$\begin{bmatrix} D_2 \\ D_3 \end{bmatrix} = \begin{bmatrix} \mathcal{A}^a_{11} & \mathcal{A}^a_{12} \\ \mathcal{A}^a_{21} & \mathcal{A}^a_{22} \end{bmatrix} \begin{bmatrix} \varphi \\ D_1 \end{bmatrix}. \quad (38)$$

B. Operator matrix entries for the $\mathcal{D}_a-$form

$$\mathcal{L}^a_{11} = -\frac{\varepsilon_{12}}{\varepsilon_{11}}\partial_y - \frac{\varepsilon_{13}}{\varepsilon_{11}}\partial_z, \quad (39a)$$
$$\mathcal{L}^a_{12} = -\frac{1}{\varepsilon_{11}}, \quad (39b)$$
$$\mathcal{L}^a_{21} = -\partial_y\mathcal{A}^a_{11} - \partial_z\mathcal{A}^a_{21}, \quad (39c)$$
$$\mathcal{L}^a_{22} = -\partial_y\mathcal{A}^a_{12} - \partial_z\mathcal{A}^a_{22}, \quad (39d)$$

$$\begin{bmatrix} \mathcal{L}^a_{11} & \mathcal{L}^a_{12} \\ \mathcal{L}^a_{21} & \mathcal{L}^a_{22} \end{bmatrix} \begin{bmatrix} \varphi \\ D_1 \end{bmatrix} + \begin{bmatrix} 0 \\ \rho \end{bmatrix} = \partial_x \begin{bmatrix} \varphi \\ D_1 \end{bmatrix}. \quad (40)$$

Diagonalization and Supplementation with respect to the $y-$axis:

C. Operator matrix entries for the $\mathcal{S}_b-$form

$$\mathcal{A}^b_{11} = -\left(\varepsilon_{33} - \frac{\varepsilon_{32}\varepsilon_{23}}{\varepsilon_{22}}\right)\partial_z - \left(\varepsilon_{31} - \frac{\varepsilon_{32}\varepsilon_{21}}{\varepsilon_{22}}\right)\partial_x, \tag{41a}$$

$$\mathcal{A}^b_{12} = \frac{\varepsilon_{32}}{\varepsilon_{22}}, \tag{41b}$$

$$\mathcal{A}^b_{21} = -\left(\varepsilon_{13} - \frac{\varepsilon_{12}\varepsilon_{23}}{\varepsilon_{22}}\right)\partial_z - \left(\varepsilon_{11} - \frac{\varepsilon_{12}\varepsilon_{21}}{\varepsilon_{22}}\right)\partial_x, \tag{41c}$$

$$\mathcal{A}^b_{22} = \frac{\varepsilon_{12}}{\varepsilon_{22}}, \tag{41d}$$

$$\begin{bmatrix} D_3 \\ D_1 \end{bmatrix} = \begin{bmatrix} \mathcal{A}^b_{11} & \mathcal{A}^b_{12} \\ \mathcal{A}^b_{21} & \mathcal{A}^b_{22} \end{bmatrix} \begin{bmatrix} \varphi \\ D_2 \end{bmatrix}. \tag{42}$$

D. Operator matrix entries for the $\mathcal{D}_b-$form

$$\mathcal{L}^b_{11} = -\frac{\varepsilon_{23}}{\varepsilon_{22}}\partial_z - \frac{\varepsilon_{21}}{\varepsilon_{22}}\partial_x, \tag{43a}$$

$$\mathcal{L}^b_{12} = -\frac{1}{\varepsilon_{22}}, \tag{43b}$$

$$\mathcal{L}^b_{21} = -\partial_z\mathcal{A}^b_{11} - \partial_x\mathcal{A}^b_{21}, \tag{43c}$$

$$\mathcal{L}^b_{22} = -\partial_z\mathcal{A}^b_{12} - \partial_x\mathcal{A}^b_{22}, \tag{43d}$$

$$\begin{bmatrix} \mathcal{L}^b_{11} & \mathcal{L}^b_{12} \\ \mathcal{L}^b_{21} & \mathcal{L}^b_{22} \end{bmatrix} \begin{bmatrix} \varphi \\ D_2 \end{bmatrix} + \begin{bmatrix} 0 \\ \rho \end{bmatrix} = \partial_y \begin{bmatrix} \varphi \\ D_2 \end{bmatrix}. \tag{44}$$

Diagonalization and Supplementation with respect to the $z-$axis:

E. Operator matrix entries for the $\mathcal{S}_c-$form

$$\mathcal{A}^c_{11} = -\left(\varepsilon_{11} - c\frac{\varepsilon_{13}\varepsilon_{31}}{\varepsilon_{33}}\right)\partial_x - \left(\varepsilon_{12} - \frac{\varepsilon_{13}\varepsilon_{32}}{\varepsilon_{33}}\right)\partial_y, \tag{45a}$$

$$\mathcal{A}^c_{12} = \frac{\varepsilon_{13}}{\varepsilon_{33}}, \tag{45b}$$

$$\mathcal{A}^c_{21} = -\left(\varepsilon_{21} - \frac{\varepsilon_{23}\varepsilon_{31}}{\varepsilon_{33}}\right)\partial_x - \left(\varepsilon_{22} - \frac{\varepsilon_{23}\varepsilon_{32}}{\varepsilon_{33}}\right)\partial_y, \tag{45c}$$

$$\mathcal{A}^c_{22} = \frac{\varepsilon_{23}}{\varepsilon_{33}}, \tag{45d}$$

$$\begin{bmatrix} D_1 \\ D_2 \end{bmatrix} = \begin{bmatrix} \mathcal{A}^c_{11} & \mathcal{A}^c_{12} \\ \mathcal{A}^c_{21} & \mathcal{A}^c_{22} \end{bmatrix} \begin{bmatrix} \varphi \\ D_3 \end{bmatrix}. \tag{46}$$

F. Operator matrix entries for the $\mathcal{S}_c-$form

$$\mathcal{L}^c_{11} = -\frac{\varepsilon_{31}}{\varepsilon_{33}}\partial_x - \frac{\varepsilon_{32}}{\varepsilon_{33}}\partial_y, \tag{47a}$$

$$\mathcal{L}^c_{12} = -\frac{1}{\varepsilon_{33}}, \tag{47b}$$

$$\mathcal{L}^c_{21} = -\partial_x\mathcal{A}^c_{11} - \partial_y\mathcal{A}^c_{21}, \tag{47c}$$

$$\mathcal{L}^c_{22} = -\partial_x\mathcal{A}^c_{12} - \partial_y\mathcal{A}^c_{22}, \tag{47d}$$

$$\begin{bmatrix} \mathcal{L}^c_{11} & \mathcal{L}^c_{12} \\ \mathcal{L}^c_{21} & \mathcal{L}^c_{22} \end{bmatrix} \begin{bmatrix} \varphi \\ D_3 \end{bmatrix} + \begin{bmatrix} 0 \\ \rho \end{bmatrix} = \partial_z \begin{bmatrix} \varphi \\ D_3 \end{bmatrix}. \tag{48}$$

REFERENCES

[1] A. R. Baghai-Wadji, ''3D diagonalization and supplementation of Maxwell's equations in fully bi-anisotropic and inhomogeneous media, Part I: Proof of existence by construction,'' ACES Journal, this issue.

[2] A. R. Baghai-Wadji, ''3D diagonalization and supplementation of Maxwell's equations in fully bi-anisotropic and inhomogeneous media, Part II: Relative proof of consistency,'' ACES Journal, this issue.

[3] A. R. Baghai-Wadji, ''3-D electrostatic charge distribution on finitely thick busbars in micro acoustic devices: Combined regularization in the near- and far-field,'' IEEE Transactions on Ultrasonics, Ferroelectrics, and Frequency Control (UFFC), vol. 62, no. 6, June 2015, pp. 1132-1144.

Alireza Baghai-Wadji: For a biography, please refer to the accompanying paper, [1], in this issue.

ACES JOURNAL, Vol. 34, No. 2, February 2019

Mode Tracking for Parametrized Eigenvalue Problems in Computational Electromagnetics

Philipp Jorkowski
FG Theoretische Elektrotechnik
Technische Universität Berlin
Berlin, Germany
philipp.jorkowski@tu-berlin.de

Rolf Schuhmann
FG Theoretische Elektrotechnik
Technische Universität Berlin
Berlin, Germany
rolf.schuhmann@tu-berlin.de

***Abstract*—An algorithm to perform a mode tracking for parameter dependent eigenvalue problems in computational electromagnetics is presented. It is based on a Taylor expansion using the derivatives of the eigenvalue and the eigenvector and allows distinguishing between intersection and touching points in the eigenvalue curves. The method is applied to discretizations with both the finite integration technique (FIT) and the finite element method (FEM), leading to simple and generalized eigenvalue problems, respectively. The applications include the calculation of the Brillouin diagram for a periodic structure and the variation of a material parameter in a filter structure.**

***Keywords*—Eigenvalue Derivatives, Finite Element Method, Finite Integration Technique, Mode Tracking, Parametrized Eigenvalue Problems.**

I. Introduction

Within the last decades a number of efficient algorithms for the solution of eigenvalue problems (EVP) in electromagnetic field simulation have been proposed. A particular class are EVP with a dependency of one or more parameters such as material constants, geometric properties, or the phase shift of Floquet modes [1] in periodic structures. In most cases, we can assume a continuous relation between the parameter and the eigenmodes, and it is desirable to reflect this fact also in the solution approach, i.e., to provide algorithms which are able to track an eigenvalue along the variation of the parameter within a certain range. As a special challenge for such a mode tracking method it should be able to follow the eigenvalue curves also in the vicinity of intersection and touching points, where the curves of two eigensolutions come close to each other.

In this paper, we present a mode tracking algorithm for parametrized EVP which uses the sensitivity of eigenvalues *and eigenvectors* w.r.t. the parameter, described by their derivatives. It is applied to two generic types of applications given by a traveling wave tube with periodic boundary conditions and a dielectric filter with a sweep of the permittivity in a specific part of the structure.

A first efficient method for the calculation of eigenvalue and eigenvector derivatives has been published by Nelson in 1976 [2] and was extended for non-simple eigenvalues by Dailey in 1989 [3]. A simple sensitivity analysis of a waveguide has been calculated in [4]. In [5] it was shown how to extend this method to higher-order derivatives and it was applied to periodic structures, where the parameter is defined by the phase advance between two boundaries. A related mode tracking technique for the calculation of band structures in photonic crystals has been presented in [6].

The new mode tracking algorithm presented in this paper combines all these ideas and can be applied to a general parameter dependency of an EVP. It is based on a point by point sampling using Taylor expansions, and a correlation factor is introduced to distinguish the different eigenmodes near intersection and touching points. To broaden the application range of the method, an extension for generalized eigenvalue problems (GEVP) is shown.

The paper is organized as follows: In Sect. II a short overview of the basic formulas and an extension for the eigenvalue and eigenvector derivatives of GEVP is given, followed by the introduction of the mode tracking algorithm in Sect. III. In Sect. IV we introduce the physical background of our eigenvalue formulations and discuss the numerical results for two different applications: The Brillouin diagram of a periodic structure is based on a model using the finite integration technique (FIT), leading to mode tracking for a simple EVP. In the second example the eigenmodes in a dielectric filter are calculated for a variation of some permittivity values. Here, we use a finite element (FEM) model, resulting in the mode tracking algorithm for a GEVP. Finally, a conclusion and outlook for further improvements are given in Sect. V.

II. Eigenvalue Derivatives

A. Simple Eigenvalue Problems

We start with the left and right EVP,

$$\mathbf{y}^H(\mathbf{A}-\lambda\mathbf{I})=0, \qquad (\mathbf{A}-\lambda\mathbf{I})\,\mathbf{x}=0, \tag{1}$$

where $\mathbf{I}$ is the identity matrix, and the matrix $\mathbf{A}$ as well as the eigensolution $\{\mathbf{x},\mathbf{y}^H,\lambda\}$ depend on the parameter p. The eigenvectors fulfill the relation $\mathbf{y}^H\mathbf{x}=1$. Differentiating n times w.r.t. the parameter p and applying some algebraic

Submitted On: September 30, 2018
Accepted On: October 3, 2018

transformations yields the n-th order eigenvalue derivative (denoted by $.^{(n)}$, for details of this derivation see [5]):

$$\lambda^{(n)} = \mathbf{y}^H \mathbf{A}^{(n)} \mathbf{x} + \sum_{k=1}^{n-1} \binom{n}{k} \mathbf{y}^H \left(\mathbf{A}^{(n-k)} - \lambda^{(n-k)} \mathbf{I} \right) \mathbf{x}^{(k)}. \quad (2)$$

Note, that for the n-th order derivative in (2) all previous derivatives of the eigenvalue, eigenvector and system matrix are required. However, once this information is available, the formula can be evaluated with very little effort just by matrix vector multiplications.

The n-th order eigenvector derivative is given by a similar formula:

$$(\mathbf{A} - \lambda \mathbf{I}) \mathbf{x}^{(n)} = - \sum_{k=0}^{n-1} \binom{n}{k} \left(\mathbf{A}^{(n-k)} - \lambda^{(n-k)} \mathbf{I} \right) \mathbf{x}^{(k)}. \quad (3)$$

Here, a linear system with rank defect has to be solved, appropriate techniques are given, e.g., in [2], [3]. Since the matrix to be inverted in (3) remains the same for each n, a matrix decomposition technique is efficient if higher order derivatives are required. Further, such techniques can be combined with model order reduction for a faster calculation as described in [5].

B. Generalized Eigenvalue Problems

To extend the formulas above to a GEVP we start again with the eigensolution $\{\mathbf{x}, \mathbf{y}^H, \lambda\}$ of the left and right GEVP,

$$\mathbf{y}^H (\mathbf{A} - \lambda \mathbf{B}) = 0, \qquad (\mathbf{A} - \lambda \mathbf{B}) \mathbf{x} = 0, \quad (4)$$

respectively, with $\mathbf{y}^H \mathbf{B} \mathbf{x} = 1$. The eigensolution as well as both system matrices $\mathbf{A}$ and $\mathbf{B}$ might have a dependency of the parameter p. Differentiating the GEVP w.r.t. this parameter using the chain rule leads to some additional terms compared to the case of a simple EVP. Still, the approach is very similar to the one for simple EVP in [5]. The right GEVP is differentiated n times, and by reordering the terms we obtain the formula for the eigenvector derivative as:

$$(\mathbf{A} - \lambda \mathbf{B}) \mathbf{x}^{(n)} = - \sum_{k=1}^{n} \binom{n}{k} \left(\mathbf{A}^{(k)} - \sum_{j=0}^{k} \binom{k}{j} \lambda^{(j)} \mathbf{B}^{(k-j)} \right) \mathbf{x}^{(n-k)}. \quad (5)$$

Multiplying from the left with the left eigenvector y^H the highest order derivative of the eigenvector vanishes, and by reordering the terms we find the derivative of the eigenvalue:

$$\lambda^{(n)} = \sum_{k=1}^{n-1} \binom{n}{k} \left(\mathbf{y}^H \mathbf{A}^{(k)} \mathbf{x}^{(n-k)} - \left[\sum_{j=0}^{k-1} \binom{k}{j} \lambda^{(j)} \mathbf{y}^H \mathbf{B}^{(k-j)} \mathbf{x}^{(n-k)} + \lambda^{(k)} \mathbf{y}^H \mathbf{B} \mathbf{x}^{(n-k)} \right] \right) + \mathbf{y}^H \mathbf{A}^{(n)} \mathbf{x} - \sum_{j=0}^{n-1} \binom{n}{j} \lambda^{(j)} \mathbf{y}^H \mathbf{B}^{(n-j)} \mathbf{x}. \quad (6)$$

Again, this long formula only contains matrix vector multiplications and can therefore be calculated with little effort. As a cross check, (6) simplifies to (2) if $\mathbf{B} = \mathbf{I}$ and $\mathbf{B}^{(i)} = 0$ $(\forall i > 0)$ are chosen as in the case of a simple EVP. The same holds for (5) compared to (3). Moreover, and analogously to the simple EVP in (3), the matrix to be inverted in (5) remains the same for each order n, allowing similar techniques for an efficient implementation as described above.

C. Polynomial and Nonlinear Eigenvalue Problems

With its extension to GEVP, there is also the possibility to apply this algorithm to polynomial eigenvalue problems (PEVP), where higher powers of the eigenvalue λ appear in the formulation. Such PEVP (quadratic, cubic, etc.) arise, e.g., from discrete models including dispersive materials (with rational functions in ω for the permittivity) or a perfectly matched layer (PML) boundary condition in its classical form. A couple of such problems are described in [7]. In principle, a PEVP can always be transformed into a GEVP with larger dimension, which allows its solution using the presented mode tracking algorithm. However, more efficient approaches without doubling the matrix dimensions may exist.

The next step of generalization are *nonlinear* EVP with an arbitrary, non-polynomial dependency of the eigenvalue in the formulation. Such problems appear, e.g., for models with a special radiation boundary condition for waveguide problems and have been briefly discussed in [8]. Of course a general expression for the eigenvalue derivative of such formulations is not available. However, they may be tackled using linearization approaches in an expansion point with a limited range of validity, which again makes the method presented here a candidate for mode tracking. However, the general properties of such non-linear EVP can be quite different from the standard case, and thus this scenario still needs to be tested.

III. Mode Tracking Algorithm

The mode tracking algorithm can best be explained by Fig. 1. First a starting point is chosen at an arbitrary $p \in [p_{min}, p_{max}]$. In this point, the EVP is solved and the mode k for the tracking is selected. (For simplicity, the index k for the chosen mode is omitted in most of the following formulas.)

As an initialization step, the derivatives of the system matrices $\mathbf{A}^{(i)}, \mathbf{B}^{(i)}$ of the EVP as well as the derivatives of the eigensolution $\{\mathbf{x}^{(i)}, \lambda^{(i)}\}$ are required. Note that for some simulation models the matrix derivatives can be computed analytically (such as in our first example in Fig. 2, see below). If no analytical formulas are available, some additional computational effort is necessary to calculate the matrix derivatives numerically, using, e.g., a simple finite difference approach (such as for our second example, Fig. 4). Once the derivatives of the system matrices are available, formulas (2) and (3) for the simple EVP, or (6) and (5) for the GEVP, respectively, can be evaluated.

In the next step, a step width Δp is determined, depending on the derivatives of the eigenvalue and eigenvector. The smaller the derivatives are, the larger the step width can be

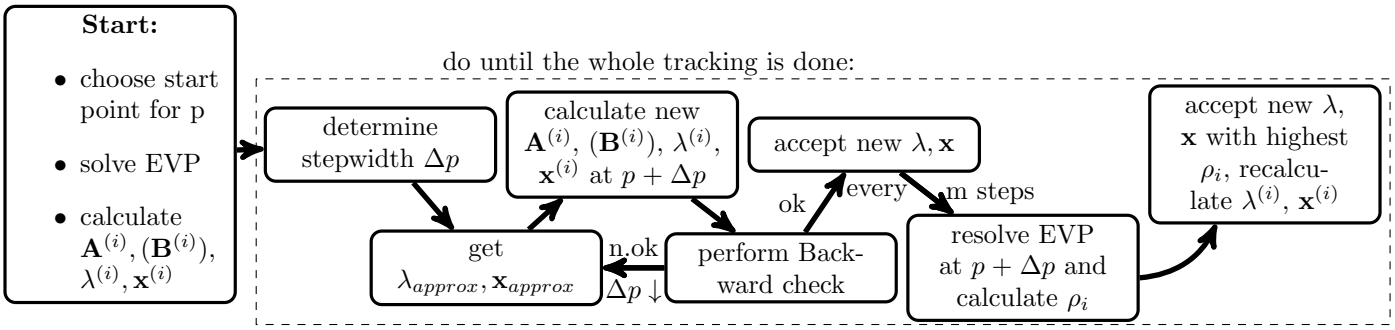

Fig. 1. Flowchart of the mode tracking algorithm.

chosen and vice versa. This step width control is important to prevent errors due to a too high step width at intersection or touching points, where the eigenvector derivatives are typically huge. On the other hand, a too small step width can considerably increase the numerical effort.

After the step width Δp has been chosen, approximations λ_{approx} of the eigenvalue and $\mathbf{x}_{approx}$ of the eigenvector at the point $p + \Delta p$ are computed, using the eigensolutions at p and the Taylor expansions:

$$\lambda_{approx} = f\left(p, \lambda, ..., \frac{\partial^n}{\partial p^n}\lambda\right), \tag{7}$$

$$\mathbf{x}_{approx} = f\left(p, \mathbf{x}, ..., \frac{\partial^n}{\partial p^n}\mathbf{x}\right). \tag{8}$$

Using these approximations, the new derivatives of this eigenpair at $p + \Delta p$ can be calculated. To do so, the new matrix derivatives at $p + \Delta p$ have to be computed first as explained above.

To control the quality of the approximations involved, a backward check is performed (see, e.g., [6]): A Taylor expansion at the new expansion point $p + \Delta p$ is evaluated for the previous point p using the new derivatives at $p + \Delta p$. The deviation between the previous eigenvalue $\lambda(p)$ and the backward approximated eigenvalue $\lambda_{approx,backward}$ from $p+\Delta p$ has to be smaller than some predefined tolerance. When the difference is small enough, the eigenpair approximation as well as their derivatives are considered to be correct, and the point $p + \Delta p$ is used as a new starting point p to continue the tracking procedure. If the backward check for the eigenpair approximation (and their derivatives) fails, i.e., the backward approximated eigenvalue is not close to the original eigenvalue, the step width Δp needs to be corrected. Using a new, smaller step width, the previous steps are repeated until the backward check succeeds.

Up to this point, the algorithm works in a purely recursive manner, and small deviations in every step may sum up to an error which at some point can no longer be tolerated. A suitable indicator to check the quality of the solutions is the residual of the eigenpair at each p. Since no corrector equation is not used here to decrease this error, every couple of steps of this algorithm the EVP has to be solved newly to eliminate this error. Here, the main challenge is to identify the proper eigenmode from this new solution. At some points within the parameter range, a couple of eigenvalues can be very close to each other or may even coincide. To identify the correct eigenpair a correlation factor,

$$\rho_k = \frac{\mathbf{x}_k^H \mathbf{x}_{approx}}{||\mathbf{x}_k|| \, ||\mathbf{x}_{approx}||}, \tag{9}$$

is introduced as the normalized scalar product between the approximated eigenvector and the eigenvectors from the recalculated EVP. This factor is computed for all candidates from the recalculated solution of the EVP, and the eigenmode with the highest ρ_k is accepted as the proper mode. The new eigenpair is also used as a new starting point for the tracking procedure, and the corresponding derivatives are calculated. In this way, the recursive error is eliminated every couple of steps.

This tracking procedure is repeated until the end of the interval of parameters p is reached. This completes the mode tracking, and solutions for each calculated point on the eigenvalue curve are available. In contrast to the standard procedure with a simple parameter sweep, the number of full EVP solutions can be considerably reduced.

IV. Numerical Results

A. Traveling Wave Tube (TWT)

The first example to test this algorithm is a so-called traveling wave tube (TWT), taken from the library of application examples of the commercial tool CST Microwave Studio [9], see Fig. 2.

The discrete model consists of a small longitudinal section of this TWT, and periodic boundary conditions are used at the front and the back plane. A predefined phase lead for the tangential fields at these boundaries defines the eigenmodes of the model to be 'macroscopic' waves, and the eigenvalues their (squared) angular frequency. Varying this phase angle between 0 and 180 degrees, the correlation of the phase advance and the eigenfrequency defines the dispersion diagram (or Brillouin diagram) of each mode. Additionally, the electric fields (the eigenvectors) are of interest, e.g., to analyze their interaction with charged particles within the TWT.

The standard procedure to compute the Brillouin diagram is to solve the EVP many times for a number of phase angles.

Here, however, we interpret the phase angle as the parameter of a parametrized EVP and apply our mode tracking algorithm.

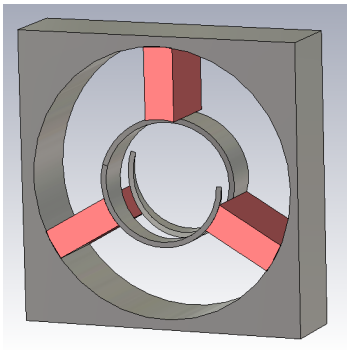

Fig. 2. Simulation setup with periodic boundaries at the front and back plane.

The model is discretized using the finite integration technique (FIT, [1]) on a Cartesian computational grid. The state variables in the FIT are the grid voltages $\widehat{\mathbf{e}}$ and $\widehat{h}$, defined as the line integrals of the electric field and the magnetic fields along the edges of the primary and the dual Grid $G, \tilde{G}$, respectively. Using these definitions, FIT transforms Maxwell's curl equations in frequency domain (for linear, isotropic and non-dispersive materials, and without currents and space charges):

$$\operatorname{curl} \mathbf{E} = -j\omega\mu\mathbf{H}, \qquad \operatorname{curl} \mathbf{H} = j\omega\varepsilon\mathbf{E}, \tag{10}$$

(with ω the angular frequency, $\mathbf{E}, \mathbf{H}$ the electric and magnetic fields, ε, μ the permittivity and the permeability, and j the imaginary unit) into matrix-vector equations, the so-called Maxwell's Grid Equations:

$$\mathbf{C}\widehat{\mathbf{e}} = -j\omega\mathbf{M}_\mu\widehat{\mathbf{h}}, \qquad \mathbf{C}^T\widehat{\mathbf{h}} = j\omega\mathbf{M}_\varepsilon\widehat{\mathbf{e}}, \tag{11}$$

Here, $\mathbf{C}$ denotes the discrete curl operator, and $\mathbf{M}_\varepsilon$ and $\mathbf{M}_\mu$ are the discrete material matrices. For a Cartesian grid with n_p grid points the discrete field vectors have approximately $3n_p$ components, and the dimension of the matrices is approximately $3n_p \times 3n_p$. Eliminating $\widehat{\mathbf{h}}$ in equations (11) yields the discrete electromagnetic eigenvalue problem:

$$(\mathbf{C}^T\mathbf{M}_\mu^{-1}\mathbf{C} - \omega^2\mathbf{M}_\varepsilon)\widehat{\mathbf{e}} = 0. \tag{12}$$

It's a unique property of the FIT that the material matrices $\mathbf{M}_\varepsilon$ and $\mathbf{M}_\mu$ are diagonal and can be easily inverted. Thus, (12) can be transformed into the simple EVP:

$$(\mathbf{M}_\varepsilon^{-1}\mathbf{C}^T\mathbf{M}_\mu^{-1}\mathbf{C} - \omega^2\mathbf{I})\widehat{\mathbf{e}} = 0. \tag{13}$$

The periodic phase shift between the tangential fields at the front and the back plane is described by the Floquet condition: It maps the electric field from one boundary, $\widehat{\mathbf{e}}_1$, to those at the other one, $\widehat{\mathbf{e}}_2$, multiplied by the phase shift: $\widehat{\mathbf{e}}_1 = \widehat{\mathbf{e}}_2 \exp(j\varphi)$. With this relation, the tangential electric components at one side of the mesh are no longer independent degrees of freedom and can be eliminated from the formulation. This leads to a reduced vector $\widehat{\mathbf{e}}_{red}$ with a reduced dimension.

The phase shift — the parameter p of the EVP — is formally included into the matrix formulation using a sparse matrix $\mathbf{L}_\varphi(p)$ as described in [7] or [10]. Additionally, the permittivity matrix has to be slightly modified in its dimension as well as in its values at the boundary. This leads to the parametrized EVP:

$$\Big(\underbrace{\mathbf{M}_{\varepsilon,per}^{-1}\mathbf{L}_\varphi^H(p)\mathbf{C}^T\mathbf{M}_\mu^{-1}\mathbf{C}\mathbf{L}_\varphi(p)}_{=\mathbf{A}_{cc}(p)} - \omega^2\mathbf{I}\Big)\,\widehat{\mathbf{e}}_{red} = 0, \tag{14}$$

which can be tackled by our mode tracking algorithm. Note that the parameter dependency of this formulation is concentrated in the $\mathbf{L}_\varphi$ matrices, which makes it easy to compute the matrix derivative analytically.

The example shown in Fig. 2 is discretized using $n_p = 46.787$ grid points, resulting in approximately 140.000 degrees of freedom in the eigenvalue equation. The geometric modeling is performed within the CST software, and the mesh and matrix data are imported into Matlab [11], where the periodic boundaries and the mode tracking have been implemented. The problem size of this model is still quite small, and all computations can be performed on a standard computer. (CPU times are not reported here since the implementation has not been optimized so far.)

The simulation results are shown in Fig. 3. First some modes around a target frequency are calculated using Matlab's standard eigenvalue solver, and a mode in the middle of this part of the spectrum is chosen for the mode tracking algorithm. Additionally, the plot shows some more eigenvalues which are close to the chosen mode, and of course there exist a large number of further eigenvalues inside the spectrum. They do not affect the analysis of the targeted eigenmode and are not plotted to ensure the readability of the figure. The reference curves (in gray) in the figure are obtained by a multiple solution of the EVP for parameter values covering the phase shift between 0 and 180 degrees. The red curve is calculated from the mode tracking scheme as described above. As a first result we can state that both solutions agree very well although most of the results of the mode tracking scheme originate from Taylor expansions rather than from full EVP solutions.

A zoom of an interesting section of the dispersion diagram is shown in the bottom right corner of Fig. 3. As mentioned previously, the algorithm detects an intersection as well as a touching point and properly tracks the eigenvalue through these challenging domains. Note that such a tracking is not available from the reference solution: The standard strategy to multiply solve the EVP fails to distinguish between these intersection or touching points, although the parameter step width is very small and a correlation factor between two solutions is used. The reason is that even when the two solutions of the EVP are close to each other and the changes in the eigenvalue are quite small, the changes in the eigenvector become very high at intersection and touching points, as well as their derivatives. As a consequence, the eigenvector

correlation between two solutions can become very unstable and unable to identify the correlation between the modes.

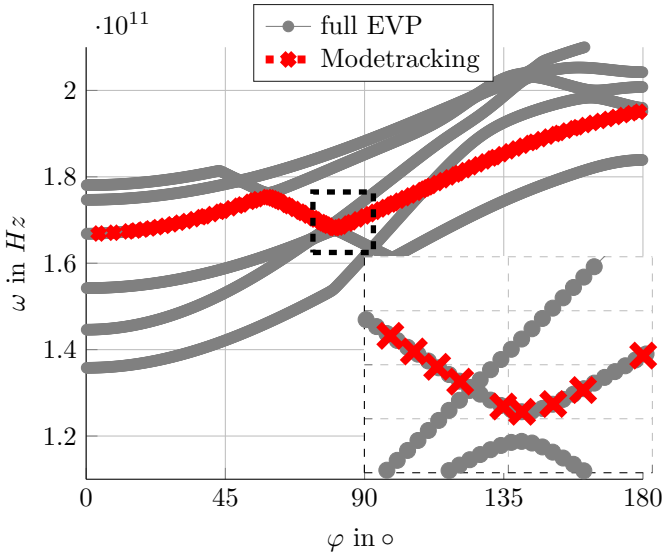

Fig. 3. Mode tracking of a chosen mode of the periodic structure within the spectrum with a zoom on the black marked section of interest.

The correlation factor ρ introduced in the previous section, however, does not show this weakness, since it does not rely on two nearby vector solutions calculated separately, but on the solution at one point and the approximation of this solution which is obtained from the previous one. This method is very robust in detecting the proper eigenmode.

B. Dielectric Filter

The second example is a dielectric filter which has been reported in many publications so far and may serve as a quasi-standard application for the simulation of highly-resonant microwave devices. Here we do not calculate the transfer behavior related to the two input/output ports, but only the relevant eigenmodes which are dominated by two dielectric rings with high permittivity. More details of the structure and all geometric dimensions are given in [12].

This example, as shown in Fig. 4, is modeled using the finite element method (FEM) on a tetrahedral mesh and first-order edge-elements $\mathbf{w}_i$. The parameter considered here is the permittivity of the ceramic resonator rings. To obtain a more challenging situation of the parameter dependency of the eigenmodes, including an intersection point, the investigated range was shifted from the original value $\varepsilon_r = 38$ to an interval around $\varepsilon_r = 57$.

The theory behind the finite element discretization is not repeated here and can be found, e.g., in [13]. The FEM model has $n_e = 130.872$ non-zero edge-elements, and the resulting EVP is a generalized one, reading:

$$\left(\mathbf{A} - \omega^2 \mathbf{B}\right)\ (E_i) = 0, \tag{15}$$

where the electric field $\mathbf{E}(\mathbf{r}) = \sum_i E_i \mathbf{w}_i(\mathbf{r})$ is represented by the degrees of freedom (E_i) with $i = 1 \ldots n_e$. The matrix $\mathbf{A}$ denotes the stiffness matrix and $\mathbf{B}$ the so-called mass matrix, respectively, with entries as reported in [13]. The main difference to the FIT formulation is that in FEM the matrix $\mathbf{B}$ holding the permittivity information is not a diagonal matrix and thus can not be efficiently inverted. Therefore the extended mode tracking variant for GEVP has to be used here.

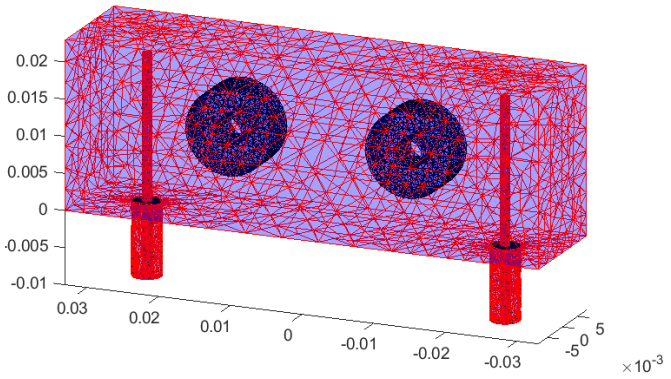

Fig. 4. Simulation setup of the dielectric filter, with different permittivity for the inner rings.

The derivatives of the matrix $\mathbf{A}$ and $\mathbf{B}$ are calculated numerically using a finite different (FD) approach. This results in a slightly increased computational effort compared to the case of matrix derivatives which are available analytically. Note, however, that the way these matrix derivatives are calculated does not play an important role in our mode tracking algorithm. Also, the algorithm is not limited to a specific kind of discretization technique.

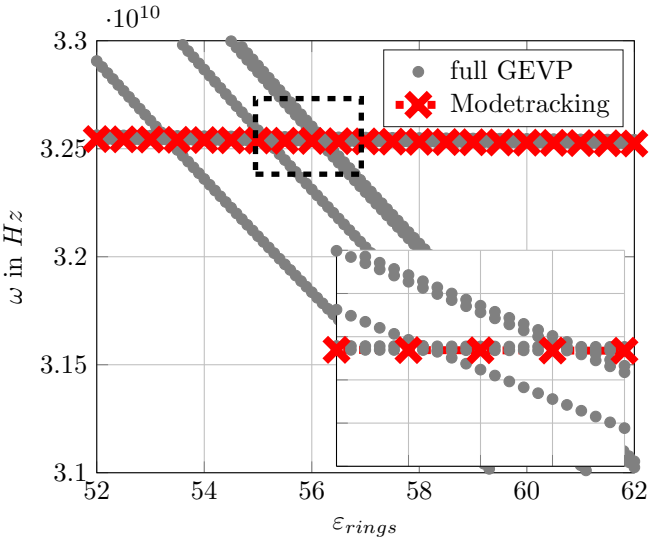

Fig. 5. Mode tracking of a chosen mode of the dielectric filter within the spectrum with a zoom on the black marked section of interest.

The results of the mode tracking algorithm for the dielectric filter are shown in Fig. 5. A mode with some candidates for intersection or touching points inside the parameter range is chosen for the analysis. As for the previous example, only a

small part of the eigenvalue spectrum is plotted for readability. Again, on the right bottom of Fig. 5 a zoom of the black dashed section is depicted. In contrast to the first example, the modes in the dielectric filter interact only weakly with each other due to the more separated geometric distribution of the corresponding fields. Thus, the eigenvector changes do not become as large as in the first example in the intersection points, and a larger step width can be chosen by the algorithm. Again, the intersection points are handled properly by the algorithm also in this case.

V. Conclusion and Outlook

A mode tracking algorithm for parametrized eigenvalue problems in computational electromagnetics has been presented. It can be used for simple as well as generalized EVP and thus be applied to discrete models from different discretization methods such as the finite integration technique or the finite element method.

A significant advantage of the new algorithm is its ability to handle intersection and touching points within eigenvalue curves without any additional post-processing, which is often necessary for comparable approaches. Furthermore, the presented algorithm is not limited to periodic structures with varying phase shift or changes in the permittivity, and it has been successfully tested with other parameter dependent problems like geometric variations. The presented formulas for generalized eigenvalue problems open the path to tackle also nonlinear EVP using a linearization as described in Sect. II-C. A next step could be to find a formulation for polynomial EVP without using linearization.

Finally, the method should also be easily extendable to mode tracking in EVP which depend on more than one parameter.

References

[1] T. Weiland, “Modes in infinitely repeating structures of cylindrical symmetry,” Proceedings of the International Linear Accelerator Conference, pp. 292–295, 1986.

[2] R. B. Nelson, “Simplified calculation of eigenvector derivatives,” AIAA Journal, vol. 14,9 pp. 1201–1205, 1976.

[3] R. L. Dailey, “Eigenvector derivatives with repeated eigenvalues,” AIAA Journal, vol. 27,4, pp. 486–491, 1989.

[4] N. Burschäpers, S. Fiege, R. Schuhmann, and A. Walther, “Sensitivity analysis of waveguide eigenvalue problems,” Adv. Radio Sci., vol. 9, pp. 85–89, 2011. doi:10.5194/asr-9-85-2011.

[5] P. Jorkowski and R. Schuhmann, “Higher-order sensitivity analysis of periodic 3-D eigenvalue problems for electromagnetic field calculations,” Adv. Radio Sci., 15, pp. 215–221, 2017. doi:10.5194/ars-15-215-2017.

[6] D. Klindworth and K. Schmidt, “An efficient calculation of photonic crystal band structures using Taylor expansions,” Commun. Comput. Phys., vol. 16,5, pp. 1355–1388, 2014. doi:10.4208/cicp.240513.260614a.

[7] B. T. Bandlow, “Zur Berechnung elektromagnetischer Eigenwertprobleme in der numerischen Simulation von Nanostrukturen mit periodischen und transparenten Randbedingungen,” Ph.D. Thesis, Univ. Paderborn, Germany, 2011. urn:nbn:de:hbz:466:2-110.

[8] C. Schenker, P. Jorkowski, K. Schmidt, and R. Schuhmann, “Solution of nonlinear eigenvalue problems in electromagnetic field computation using contour integrals,” Book of Abstracts of Kleinheubacher Tagung, 25.-27.09.2017, pp. 33–34, 2017.

[9] CST Studio Suite 2018, CST – Computer Simulation Technology GmbH, Darmstadt, Germany. http:\\www.cst.com

[10] R. Schuhmann, “Periodische Ränder mit FIT: Operatorbasierte Schreibweise,” TU Darmstadt, Internal Report, 2002.

[11] MATLAB R2017b, The MathWorks, Inc., Natick, Massachusetts, United States. http:\\www.mathworks.com

[12] J. R. Brauer and G. C. Lizalek, “Microwave filter analysis using a new 3-D finite-element modal frequency method,” IEEE Transactions on Microwave Theory and Techniques, vol. 45,5, pp. 810–818, 1997. doi:10.1109/22.575605.

[13] J.-F. Lee and R. Mittra, “A note on the application of edge-elements for modeling three-dimensional inhomogeneously-filled cavities,” IEEE Transactions on Microwave Theory and Techniques, vol. 40,9, pp. 1767–1773, 1992. doi:10.1109/22.156603.

Parametric Models for Signature Prediction and Feature Extraction

Julie Ann Jackson

Department of Electrical and Computer Engineering
Air Force Institute of Technology, Dayton, OH 45433, USA
julie.jackson@afit.edu

Abstract — This paper compares and contrasts numerical electromagnetic (EM) prediction methods and parametric scattering models for radar signature prediction and feature extraction.

Index Terms — Attributed scattering centers, radar cross section, radar feature extraction, scattering prediction.

I. INTRODUCTION

Both radar model validation and target recognition applications require accurate, and preferably fast, signature prediction methods, as illustrated in Fig. 1. Prediction methods are nonparametric (e.g., numerical electromagnetic prediction codes) and parametric (e.g., attributed scattering centers). Choice of method should be based on the trade space between model accuracy and computational efficiency. Computational efficiency includes not only the ability to quickly compute the prediction model (the forward problem) but also the complexity and feasibility to extract signatures from measured data (the inverse problem). Numerical electromagnetic (EM) prediction methods are geared toward the forward problem, while parametric models (PMs) have been developed with the inverse problem in mind. The complexity-accuracy trade space for each model type is qualitatively depicted in Fig. 2.

II. SIGNATURE PREDICTION

EM numerical prediction techniques include method of moments (MoM), differential techniques, integral equation solvers, shooting and bouncing rays (SBR) geometric/physical optics (GO/PO), and many other methods, discussed in [1-5]. Computation time varies with the electrical size of the target and is extended by the time it takes to draw/import and facetize/mesh a target model. A method to speed up the EM part of SBR is given in [6], and [7] provides a technique to extend single frequency computations over a band of frequencies. An attempt to speed the drawing portion is provided in [2], which converts a picture into a facet model. Alternatively, [2] lets users build simple targets by combining primitive shapes, which can be characterized by PMs.

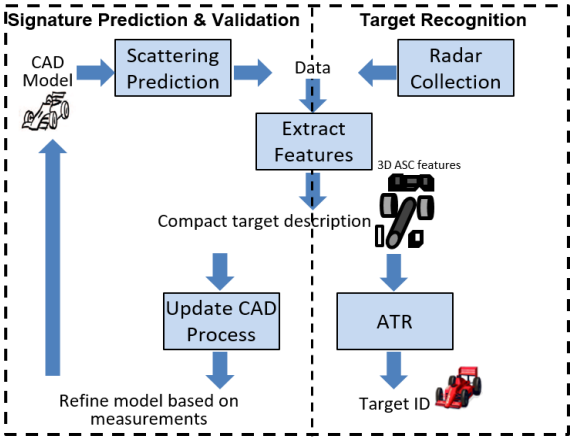

Fig. 1. Process flow diagram for signature prediction (forward problem) and signature extraction (inverse problem).

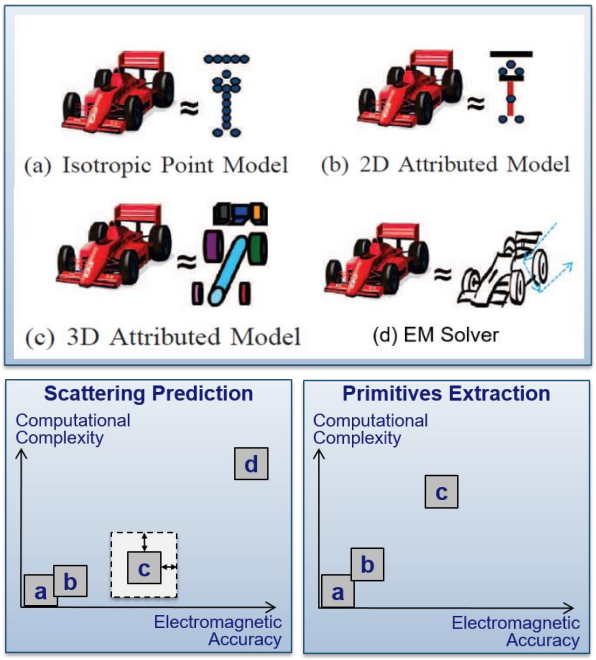

Fig. 2. Scattering models and notional complexity vs. accuracy trade space.

Submitted On: September 17, 2018
Accepted On: January 1, 2019

PMs developed for signal processing tasks may also be used for signature prediction. The isotropic point model is characterized by scatterer position and radar cross section (RCS). The isotropic point model is a key assumption in radar imaging; however, realistic scatterer persistence is typically less than 20° [8]. The monostatic 2D attributed scattering center (ASC) model [9] is parameterized by frequency, polarization, aspect (along the length of the target), and length. Other monostatic models include the Huynen and Cameron decompositions that break monostatic polarization responses into primary forms [10-12]. Bistatic canonical shape models parameterized by type, size, and orientation capture 3D physical geometry and model frequency, polarization, and azimuth and elevation aspect dependence [13]. The canonical models are built from products of planar solutions for strip, dihedral, and circular scattering mechanisms [14], [15] to approximate the 3D solution. A full analytic 3D GO/PO solution for bistatic scattering from a dihedral is given in [16]. EM predictions, PMs, and measurements of a dihedral are compared in [17]; PMs took milliseconds to compute, while MoM took hours.

PMs are extremely fast because the equations are written analytically and do not need a numerical solver like EM methods. However, accuracy is limited by underlying GO/PO and planar assumptions; edge diffraction, traveling waves, etc. are not included. Also, the dihedral and trihedral models are defined only within the interior of the corner, though plate models could be combined to model the back sides. Furthermore, PMs do not capture interactions between scatterers. Thus, a major challenge for using PMs for prediction is how to break a complex target into scattering primitives. For example, constructing a vehicle's sides with plates neglects vehicle/ground interaction, which is better modeled with dihedrals.

III. SIGNATURE EXTRACTION

Numerical EM techniques are not suited to signature extraction since each iteration in an optimization would require update to the facet model and re-run of computationally expensive prediction code. However, as shown in Fig. 1, other feature extraction methods can be used along with model refinement and EM predictions for RCS signature validation.

Parametric methods were developed with signal estimation techniques and target recognition applications in mind. Parameters may be estimated from measured data, though estimation complexity increases with model complexity. Isotropic points may be estimated using the CLEAN algorithm [18], [19]. Two-dimensional ASCs may be estimated using Prony's method or matrix pencil method [9]. Canonical shape primitives are more difficult to extract since shape selection and parameter estimation are coupled; however, an initial iterative approach is given in [20]. Other approaches to parametric model extraction include Expectation-Maximization [21], sparse dictionary techniques [22-24], and ray-tracing methods [19], [25]. Limited data from practical radar flight paths complicates the classification and estimation problem, as illustrated in [26], since objects may look similar for a narrow-angle data slice.

IV. CONCLUSION

We have provided an overview of numerical EM prediction versus PMs. While PMs are limited to simple scattering mechanisms, they are fast and well-suited to signature extraction. Numerical EM codes enable high fidelity prediction of complex targets; however, it is not computationally feasible to use EM methods for signature extraction. Thus, one should choose a signature prediction method depending on the application.

ACKNOWLEDGMENT

The views expressed in this article are those of the authors and do not reflect the official policy or position of the U.S. Air Force, Department of Defense, or the U.S. Government. Approved for public release #88ABW-2017-4831.

REFERENCES

[1] C. Uluisik, et al., "Radar cross section (RCS) modeling and simulation, Part 1: A tutorial review of definitions, strategies, and canonical examples," *IEEE Antennas Propag. Mag*., vol. 50, no. 1, pp. 115-126, Feb. 2008.

[2] G. Cakir, M. Cakir, and L. Sevgi, "Radar cross section (RCS) modeling and simulation, Part 2: A novel FDTD-based RCS prediction virtual tool for the resonance regime," *IEEE Antennas Propag. Mag*., vol. 50, no. 2, pp. 81-94, Apr. 2008.

[3] A. K. Bhattacharyya and D. L. Sengupta, *Radar Cross Section Analysis and Control*. Boston: Artech House, 1991.

[4] W. C. Chew, et al., "Fast solution methods in electromagnetics," *IEEE Trans. on Antennas Propag*., vol. 45, no. 3, pp. 533-543, Mar. 1997.

[5] J. Song, C.-C. Lu, and W. C. Chew, "Multilevel fast multipole algorithm for electromagnetic scattering by large complex objects," *IEEE Trans. on Antennas Propag*., vol. 45, no. 10, pp. 1488-1493, Oct. 1997.

[6] R. Bhalla and H. Ling, "A fast algorithm for signature prediction and image formation using the shooting and bouncing ray technique," *IEEE Trans. on Antennas Propag*., vol. 43, no. 7, pp. 727-731, July 1995.

[7] C. J. Reddy, et al., "Fast RCS computation over a frequency band using method of moments in conjunction with asymptotic waveform evaluation technique," *IEEE Trans. on Antennas Propag*., vol.

46, no. 8, pp. 1229-1233, Aug. 1998.
[8] D. E. Dudgeon, R. T. Lacoss, C. H. Lazott, and J. G. Verly, "Use of persistent scatterers for model-based recognition," in *Proc. SPIE*, vol. 2230, pp. 2230-2230-13, 1994.
[9] L. C. Potter and R. L. Moses, "Attributed scattering centers for SAR ATR," *IEEE Trans. Image Process*., vol. 6, no. 1, pp. 79-91, Jan. 1997.
[10] J. R. Huynen, "Phenomenological theory of radar targets," in *Electromagnetic Scattering*, P. L. E. Uslenghi, Ed. Academic Press, 1978.
[11] W. L. Cameron, "Feature motivated polarization scattering matrix decomposition," in *Record of the IEEE 1990 Int'l Radar Conference*, May 1990, pp. 549-557.
[12] S. R. Cloude and E. Pottier, "A reveiw of target decomposition theorems in radar polarimetry," *IEEE Trans. Geosci. Remote Sens*., vol. 34, no. 2, pp. 498-518, Mar. 1996.
[13] J. A. Jackson, B. D. Rigling, and R. L. Moses, "Canonical scattering feature models for 3D and bistatic SAR," *IEEE Trans. Aerosp. Electron. Syst*., vol. 46, no. 2, pp. 525-541, Apr. 2010.
[14] M. Gerry, "Two-Dimensional Inverse Scattering Based on the GTD Model," The Ohio State University: Ph.D. Dissertation, 1997.
[15] N. Akhter, "Far Zone Electromagnetic Scattering From Complex Shapes Using Geometrical Theory of Diffraction," The Ohio State University: Ph.D. Dissertation, 1993.
[16] J. A. Jackson, "Analytic physical optics solution for bistatic, 3D scattering from a dihedral corner reflector," *IEEE Trans. on Antennas Propag*., vol. 60, no. 3, pp. 1486-1495, Mar. 2012.
[17] A. Tempelis, M. Jussaume, and J. Jackson, "Comparison of measured and predicted bistatic scattering from a right-angle dihedral," in *IEEE Radar Conference*, May 2011, pp. 135-140.
[18] J. A. Hogbom, "Aperture synthesis with a non-regular distribution of interferometer baselines," *Astronomy and Astrophysics Supplement Series (0365-0138)*, vol. 15, no. 3, pp. 417-426, 1974.
[19] R. Bhalla and H. Ling, "Three-dimensional scattering center extraction using the shooting and bouncing ray technique," *IEEE Trans. On Antennas Propag*., vol. 44, no. 11, pp. 1445-1453, Nov. 1996.
[20] J. Jackson and R. Moses, "Synthetic aperture radar 3D feature extraction for arbitrary flight paths," *IEEE Trans. Aerosp. Electron. Syst*., vol. 48, no. 3, pp. 2065-2084, July 2012.
[21] J. A. Richards, A. S. Willsky, and J. W. Fisher III, "Expectation maximization approach to target model generation from multiple synthetic aperture radar images," *Optical Engineering*, vol. 41, no. 1, pp. 150-166, Jan. 2002.
[22] K. R. Varshney, M. Cetin, J. W. Fisher, and A. S. Willsky, "Sparse representation in structured dictionaries with application to synthetic aperture radar," *IEEE Trans. Signal Process*., vol. 56, no. 8, pp. 3548-3561, Aug. 2008.
[23] G. B. Hammond and J. A. Jackson, "Canonical feature extraction using molecule dictionaries," in *IEEE Radar Conference*, paper 5092, pp. 1-6, 29 Apr.-3 May 2013.
[24] H. Liu, et al., "Attributed scattering center extraction algorithm based on sparse representation with dictionary refinement," *IEEE Trans. On Antennas Propag*., vol. 65, no. 5, pp. 2604-2614, May 2017.
[25] Y. He, et al., "A forward approach to establish parametric scattering center models for known complex radar targets applied to SAR ATR," *IEEE Trans. on Antennas Propag*., vol. 62, no. 12, pp. 6192-6205, Dec. 2014.
[26] J. A. Jackson and R. L. Moses, "Identifiability of 3D attributed scattering features from sparse nonlinear apertures," in *Proc. SPIE*, vol. 6568, 2007, pp. 6568-6568-12.

Julie Ann Jackson is an Associate Professor of Electrical Engineering at the Air Force Institute of Technology (AFIT), where she joined the faculty in 2009. She earned the B.S.E.E. degree from Wright State University, Dayton, OH, in 2002 and the M.S. and Ph.D. degrees from The Ohio State University, Columbus, OH, in 2004 and 2009, respectively. Her graduate studies were funded with fellowships from the National Science Foundation, the Dayton Area Graduate Studies Institute, The Ohio State University, and the Ohio Board of Regents. Jackson has held internships at the Air Force Research Laboratory, Alphatech, Inc., Jacobs Sverdrup, and Bell Laboratories. She is a Senior Member of the IEEE, Member of Eta Kappa Nu and Tau Beta Pi, and Chief Advisor for the Ohio Eta Chapter of Tau Beta Pi. Jackson was elected in 2018 to the IEEE AES Society Radar Systems Panel and serves on the technical program committees of the IEEE Radar Conference and the MSS Tri-Service Radar Conference. Jackson's contributions have been recognized with multiple awards including the Air University Civilian Quarterly Award in 2018, the Southwestern Ohio Council for Higher Education (SOCHE) 2016 Faculty Excellence Award, and the 2012 Air Force Science, Technology, Engineering, and Mathematics Award for Outstanding Scientist/Engineer, Junior Civilian. Her research interests are in radar signal processing and imaging and exploitation of RF signals.

A Dual Band-Reject FSS for WI-FI Application

M. Bahadorzadeh and C. F. Bunting

School of Electrical and Computer Engineering
Oklahoma State University, Stillwater, Ok, 74075, USA
Mehdi.bahadorzadeh@okstate.edu, charles.bunting@okstate.edu

Abstract ─ A dual band FSS based on array of double square ring shaped resonators has been proposed. The proposed structure represents a wide-angle perfect the WI-FI signals and screen room applications. Simulation results show polarization independency for both rejection bands.

Index Terms ─ Dual band-rejection, wide-angle rejection, WI-FI signal blocker.

I. INTRODUCTION

A Frequency Selective Surface (FSS) is a two-dimensional frequency filter exhibiting reflection and transmission properties that are analogous to electronic frequency filters. FSS characteristics can be engineered to represent band-pass, band-stop, low-pass, or high-pass characteristics depending on design [1].

The advantage of the symmetry of the structural has been implemented to create the polarization independent resonant filter. Basically, to design a FSS, we have to maximize the rejection level at the desired frequency. It is equivalent to minimize the transmission (T) and maximizing the reflection (R) coefficients. In this paper, a planar FSS has been proposed. It rejects the electromagnetic waves at nearly 2.45 (GHz) and 5 (GHz) with rejection rate of 98% and 99%, respectively. It is observed that the structure represents Single Negative Metamaterial (SNG) behaviors at rejection resonant frequencies. FSS is polarization insensitive for both transverse electric (TE) and transvers magnetic (TM) waves. The simulation results represent good stability for different radiation angles and polarization. Many proposed FSS filters are designed for single frequency [2], and most of them do not have the simplicity in construction and rejection independent from frequency like proposed metamaterial absorbers [3].

II. DESIGN AND SIMULATION

The proposed FSS is an array of unit cell, which is considered as a double ring square shape Fig. 1.

The metallic structures on the top of the substrate are chosen as copper, the electrical conductivity and thickness are 5.8×10^7 (s/m) and 0.04 (mm), respectively. The substrate of absorber is FR4 ($\varepsilon_r = 4.38, \tan\delta = 0.025$) with 2 (mm) thickness.

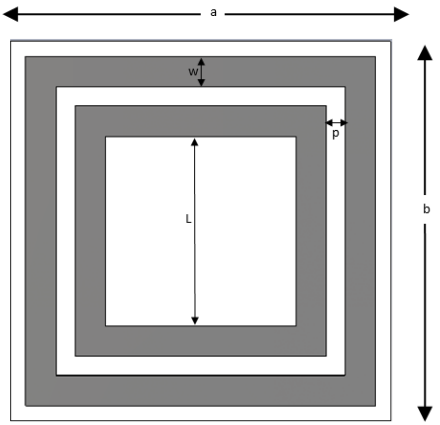

Fig. 1. Unit cell geometry and design parameters: a=b=25mm, L=12.25mm, w=2mm, and p=1mm.

The simulation is done by full wave commercial software CST [4] with periodic boundary conditions. The floquet boundary conditions perpendicular to the plane of the FSS are placed to simulate different incident angles Fig. 2.

The S_{21} and S_{11} parameters which represent the the transmission and reflection respectively are shown in Fig. 3.

The structure benefits from the symmetry so an independency of polarization and incident angle is expected. In order to investigate the influence of incident angle on the performance of the FSS, the absorption under different polarization incident wave for azimuth and elevation plane is presented in Fig. 4. The results show a good stability for different angle of incident and polarization.

Submitted On: October 9, 2018
Accepted On: October 20, 2018

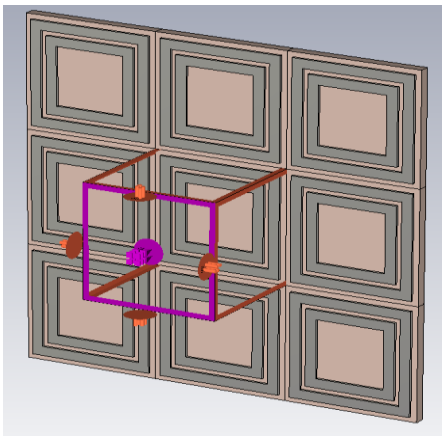

Fig. 2. The power reflection coefficient versus groove.

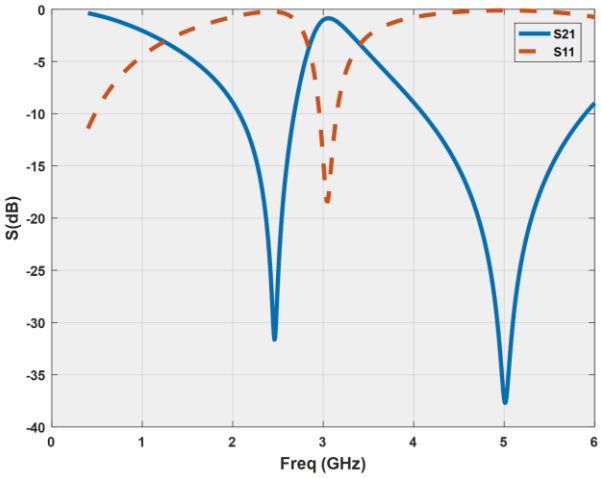

Fig. 3. Simulated reflection and transmission of the proposed metamaterial absorber

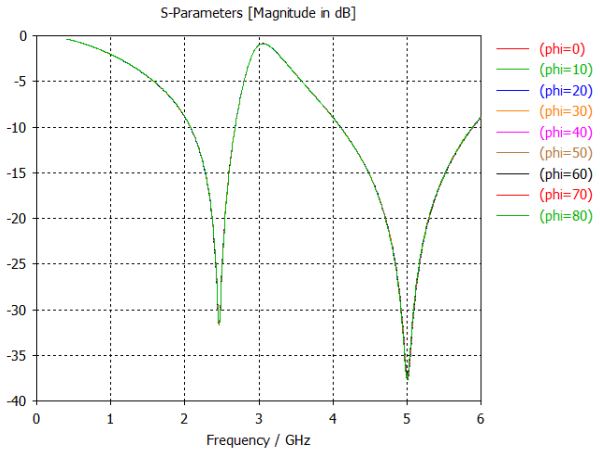

(a)

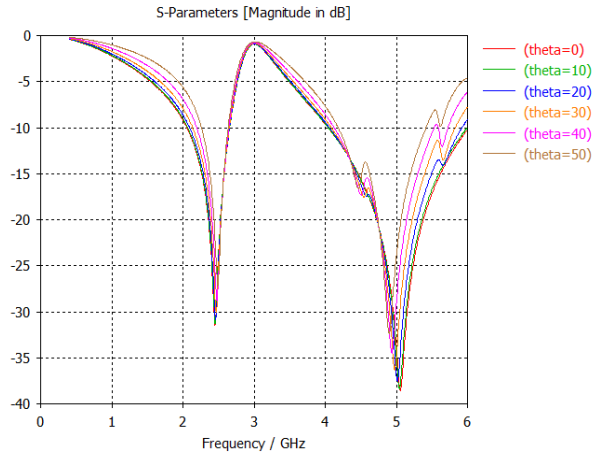

(b)

Fig. 4. Transmission at the different incident angles ranging from 0 to 80 Phi (a), and 0 for 50 Theta (b), with respect to FR4 plane.

III. THEORY

The structure shows maximum negative imaginary part of refractive index at resonant frequencies while the real part of refractive index is close to zero as shown in Fig. 5. Proposed FSS behaves like a SNG metamaterial at resonant frequencies and represents a high attenuation. Neglecting the losses, we see that when refractive index is purely imaginary at resonance frequencies the wave vector is also purely imaginary and the wave is strongly attenuated inside the slab [5]. This high attenuation constant results in a high mismatch and totally reflection of incident wave.

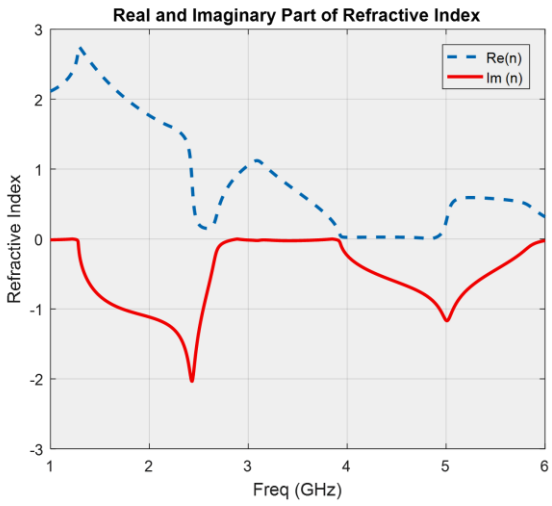

Fig. 5. Real and imaginary part of refractive index for normal incidence.

IV. CONCLUSION

The proposed symmetrical unit cell based on double square shapes represents a high level of rejection for dual WI-FI bands. Simulations demonstrated that due to the symmetry of structure the resonant frequency of rejection is independent of incident angles for a wide range both in azimuthal and elevation planes. In addition, FSS represents single negative metamaterial properties at resonance frequencies. The optimization of transmission bandwidth especially at five (GHz) can be a part of further research.

REFERENCES

[1] B. A. Munk, Frequency Selective Surfaces: Theory and Design. Wiley-Interscience Publication, April 2000.

[2] S. Choudhary and H. S. Mewara, "A band-reject frequency selective surface with stable response for WLAN applications," *Signal Processing and Communication Engineering Systems (SPACES), 2015 International Conference on*, 2-3 January 2015.

[3] M. Bahdorzadeh, N. Feiz, and H. Bolandpour, "Design amultiband perfect metamaterial absorber based on hexagonal shapes," *Applied Computational Electromagnetics (ACES), 2015 31st International Review of Progress in EM*, 2015.

[4] CST Microwave Studio, ver. 2017, Computer Simulation Technology, Framingham, MA.

[5] N. Engheta and R. W. Ziolkowski, Metamaterials Physics and Engineering Explorations. Wiley-IEEE Press, July 2006.

Mehdi Bahadorzadeh received his Ph.D. in Telecommunication Engineering - Field Theory in Science and Research Campus of Islamic Azad University in Tehran-Iran in 2009, and he started his cooperation with IAUM as Assistant Professor in 2009. As a research scholar, he has been with George Washington University ECE Department since 2015 to 2016 and he is cooperating with Oklahoma State University as a Post-Doctoral Fellow since 2017. Bahadorzadeh has researched in different area of applied electromagnetic and numerical methods. His main research area is Electromagnetic Compatibility and using new numerical method techniques for EMC problems. The author has published many papers in the international journals and conferences in the area of numerical methods in applied electromagnetic and EMC. He is a contributor to many international journals with applied electromagnetic and antenna and microwave topics. In addition, he is a Member of ACES.

Chuck Bunting received the A.A.S. degree in Electronics Technology from Tidewater Community College, Virginia Beach, VA, in 1985, and the B.S. degree in Engineering Technology from Old Dominion University, Norfolk, VA in 1989. He received the M.S. degree in 1992 and the Ph.D. degree in 1994 from Virginia Tech, Blacksburg, VA both in Electrical Engineering. Bunting is the Director of the Robust Electromagnetic Field Testing and Simulation Laboratory at Oklahoma State University where he is a Professor of Electrical and Computer Engineering. Under his leadership OSU has become an important center of EMC continuing education for the application of test methodologies for radiated emissions and susceptibility. The reverberation chamber course has been held annually in Stillwater since 2007, drawing from industry and government, providing engineers with practical training in the application of statistical methods required for proper reverberation chamber operation (over 200 attendees total). His interests include electromagnetic field penetration in aircraft structures and reverberation chamber simulation using numerical and experimental methods, engineering education, applied computational electromagnetics, statistical electromagnetics, and electromagnetic characterization and application of reverberation chambers for communication systems including RFID and UAS. He has also performed research in the development of near infrared tomography and microwave acoustic tomography for prostate cancer detection.

Mathematical Relationship of an Isotropic Point Source and the Spherically Distributed Antenna Array

Kristopher Buchanan[1], Timi Adeyemi[1], Carlos Flores-Molina[1], Sara Wheeland[1], and Steven Weiss[2]
[1]Space and Naval Warfare Systems Center Pacific (SSC Pacific): Electromagnetics Technology Branch, San Diego CA, USA
[2]Adelphi Laboratory Center: Antennas and RF Technology Integration Branch, 2800 Powder Mill Rd, Adelphi, MD 20783, USA

***Abstract*—This work investigates beam pattern behavior of an isotropic point source and a collection of sources distributed amongst a spherical volume. Pattern behavior is compared to the tapering of a plane wave expansion of spherical waves demonstrating self-adjoint characteristics. Beampatterns of atomic like orbitals and Zernike polynomials are provided as connections to common applications.**

***Index Terms*—Distributed beamforming.**

I. Introduction

Circular and spherical random arrays were first analyzed by Panicali and Lo mainly by using the variance, mean and correlation between elements [1]. A more insightful analysis was considered by [2] approximately a decade later with further examinations of circular [3]–[4] and spherical [5]–[10] array geometry.

This work presents a derivation of the exact and approximate array factor and mean-valued radiation pattern for spherically and circularly distributed random arrays from [11]–[12].

II. Formulation of the Exact Array Factor

The exact array factor can be shown as:

$$F\left(\theta,\phi\middle|R_n\right)=\frac{1}{N}\sum_{n=1}^{N}e^{jkR_n}=\frac{1}{N}\sum_{n=1}^{N}e^{jkr\sqrt{1+x^2-2x\cos\psi_n}},\ x=r_n/r \quad (1)$$
$$\cos\theta\equiv\cos\psi_n=\sin\theta\sin\theta_n\cos\left(\phi-\phi_n\right)+\cos\theta\cos\theta_n=\hat{r}\cdot\hat{r}_n$$

Since r is not a part of the integration it is placed into the term β (eqn. 4, [11]) such that $\beta = 2\pi\Delta fr/c$. Next, integration is done over the spherical volume of an isotropic point source located on the z axis by (2), and (3) [1]–[12]. Due to the change of variables ($x = r_n / r$) one obtains the multiplication of r^3 in (4), which reduces to (5) over its circularly symmetric ϕ integration:

$$\cos\theta\equiv\left(\cos\psi_n\middle|\theta_n=0°\right)=\hat{r}\cdot\hat{r}_n=\cos\theta, \quad (2)$$

$$\int_0^{r_n}\int_0^{\pi}\int_0^{2\pi}\exp\left[-j\beta\sqrt{1+\left(r_n/r\right)^2-2\left(r_n/r\right)\cos\theta}\right]r_n^2dr_n\sin\theta d\theta d\phi, \quad (3)$$

$$r^3\int_0^{A/r}\int_0^{\pi}\int_0^{2\pi}\exp\left[-j\beta\sqrt{1+x^2-2x\cos\theta}\right]x^2dxd\Omega, \quad (4)$$

$$2\pi r^3\int_0^{x'}\int_0^{\pi}\exp\left[-j\beta\sqrt{1+x^2-2x\cos\theta}\right]x^2dx\sin\theta d\theta \quad (5)$$
$$d\Omega=\sin\theta d\theta d\phi, x=r_n/r, dx=dr_n/r, \{r\equiv R_A, x'\equiv A/r\}$$

Substituting $u = [1+x^2 - 2x \cos \theta]^{½}$, $u\,du = x \sin\theta\, d\theta$ into the θ integration simplifies (5) to (6) and further reduces to (7) [12]:

$$2\pi r^3\int_0^{x'}xdx\int_{|1-x|}^{1+x}\exp\left[-j\beta u\right]udu, \quad (6)$$

$$\pi r^3\int_0^{x'}xdx\left\{e^{\left(-j\beta(1+x)\right)\left[1+j\beta(1+x)\right]}-e^{\left(-j\beta|1-x|\right)\left[1+j\beta|1-x|\right]}\right\}\Big/\beta^2. \quad (7)$$

The final integration is divided into two regions due to the absolute value of (8) and reduces to (9) for $x' > 1$ and $\theta = \beta x'$:

$$\frac{\pi r^3}{\beta^2}\left(\begin{array}{l}\int_0^{1}xdx\left\{e^{\left(-j\beta(1+x)\right)\left[1+j\beta(1+x)\right]}-e^{\left(-j\beta|1-x|\right)\left[1+j\beta|1-x|\right]}\right\}+\\ \int_1^{x'}xdx\left\{e^{\left(-j\beta(1+x)\right)\left[1+j\beta(1+x)\right]}-e^{\left(-j\beta|1-x|\right)\left[1+j\beta|1-x|\right]}\right\}\end{array}\right), \quad (8)$$

$$\bar{F}_{x'>1}=4\pi j\left(r/\beta\right)^3e^{-j\theta}\left\{\begin{array}{l}2e^{j\theta}j\theta+\\ \left(1+j\theta-\theta^2/2\right)\left(\cos\beta-3\mathrm{sinc}\beta\right)+\\ \theta^2\left(\cos\beta-\mathrm{sinc}\beta\right)/2\end{array}\right\}. \quad (9)$$

For $x' < 1$ the term $|1 - x|$ simplifies to $(1 - x)$ and provides:

$$\bar{F}_{x'<1}=2\pi r^3\left(2je^{-j\beta}/\beta^3\right)\left\{\begin{array}{l}\sin\theta\left[\theta^2/\beta-j-3/\beta\right]+\\ \theta\cos\theta\left(j+3/\beta\right)\end{array}\right\}. \quad (10)$$

In the two-extremes of large and small x′, (10) reduces to (11) and (10) to (12), respectively:

$$\bar{F}_{x'\gg1}=6\sqrt{\left(\theta-\sin\theta\right)^2+\left(1-\theta^2/2-\cos\theta\right)^2}\Big/\theta^3, \quad (11)$$

$$\bar{F}_{x'\ll1}=\frac{-3\Psi\cos\left(\Psi\right)+3\sin\left(\Psi\right)}{\left(\Psi\right)^3}=3\mathrm{tinc}\left(\Psi\right), \quad (12)$$

where $\Psi = \theta = \beta x' = \beta A/r = k A$, is taken over all angular space (θ, ϕ). This validates Fig. 5 of [10] and yields a

Submitted On: October 1, 2018
Accepted On: October 20, 2018

graphical solution of 1.815, and agree with analysis provided in Fig. 3 of [2]. Expansions of this work in the Fresnel region were investigated in [5]–[6].[1]

We diverge by the approximation since we do not take an integral over the exact space of R_n, but its expansion of (1).

What is odd about this solution is the lack of pattern multiplication. No pattern multiplication exists due to a substitution from angular space to Ψ – space.

A sphere is composed of two symmetries a ball and a shell. The ball describes a azimuthal planar distribution in the x an y axes. The shell describes elevation symmetry in the z axis.

In addition, a sphere is composed of two types of symmetry a ball containing the interior of the sphere and rings comprising the outer shell of the sphere [5]–[10].

Compound random variables explains the true solution of a spherically distributed array. Pattern multiplication of the symmetries differs from historical works of [14]–[15]. We also note corrections to works of [3], [4] and [10] in Figs. 17–21 and Figs. 41–42 of [9].

A second method of deriving (12) is provided in [9] where integration of a plane wave is expanded as a sum of spherical waves in a spherically-symmetric volume:

$$\begin{aligned}&\frac{1}{V}\int_0^1\int_0^{2\pi}\int_0^{\pi} e^{j\vec{K}\cdot\vec{r}} = \frac{1}{V}\int_0^1\int_0^{2\pi}\int_0^{\pi} e^{jkAr(\hat{n}\cdot\hat{r})}\\ &= \frac{1}{V}\sum_{l=0}^{\infty}\int_0^1\int_0^{2\pi}\int_0^{\pi} (j)^l(2l+1)j_l(kr)P_l(\cos\psi)r^2\sin\theta d\theta d\phi\\ &V = 3/4\pi,\quad \vec{K} = kA\cos\psi,\ \cos\psi = (\hat{n}\cdot\hat{r})\\ &\hat{n} = \hat{r}(\theta_0,\phi_0) = \sin\theta_0\cos\phi_0\hat{x} + \sin\theta_0\sin\phi_0\hat{y} + \cos\theta_0\hat{z}\\ &\hat{r}(\theta,\phi) = \sin\theta\cos\phi\hat{x} + \sin\theta\sin\phi\hat{y} + \cos\theta\hat{z}.\end{aligned} \tag{13}$$

The spherical Hankel function of order zero h_0 (l=0) represents the spherically symmetric wave field. Hence, upon integration of a spherically uniform distribution one obtains the zeroth order mode:

$$\begin{aligned}&\frac{3}{4\pi}\int_0^1\int_0^{2\pi}\int_0^{\pi}(j)^0(2l+1)j_0(kAr)P_0(\cos\psi)r^2\sin\theta d\theta d\phi\\ &= 3\mathrm{Tinc}(kA).\end{aligned} \tag{14}$$

III. Mean Valued Radiation Pattern

The expected beampattern for any geometrically bound topology has been shown in [1] by taking the expected value of the array factor $|\bar{F}(\Psi)^2|$ across the unit interval [-1, 1]. Hence, for a volumetric random variable x this provides the characteristic functions (1), which are orthogonal in all three axes and uncorrelated. Hence, the analysis involves the characteristic functions of the aperture distribution [9], [10] and [14]:

$$\bar{U} = \frac{1}{N} + \left(1-\frac{1}{N}\right)\Lambda|u|^2\,\Lambda|v|^2\,\Lambda|w|^2 = \frac{1}{N} + \left(1-\frac{1}{N}\right)\Lambda|\vec{\Psi}|^2. \tag{15}$$

[1]Reciprocity applies to (12) such that the near field of a receiving array equals the far field of a transmit array.

The square magnitude of the characteristic function describes the main-lobe behavior of the array and, analysis of the radiation characteristics of random arrays relies on finding the characteristic functions of the aperture distribution. An example of (15) is applied to a spherical distribution of radiators as illustrated in Fig. 1. Verification of the pattern is obvious as a spherical distribution is remains consistency in its pattern behavior in both; θ and ϕ-cut planes and when scanned.

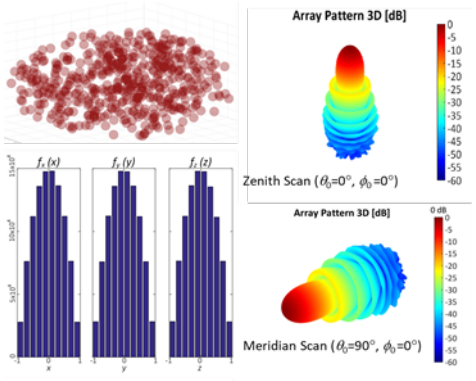

Fig. 1. Mean radiation pattern and cartesian coordinate distribution functions of a volumetric antenna array scanned from zenith to the meridian elevation angle.

IV. Physical Explanation

Taking the expected value of a random array is analogous to taking the average over all realizations of possible element placement. Mathematically, one may sample any topology using the inhomogeneous wave equation with point sources:

$$\nabla^2\psi + k^2\psi = \sum\delta\left(\vec{r} - \vec{r}_n'\right). \tag{16}$$

For the reference element the solution is:

$$\psi = \frac{e^{-jkr}}{4\pi r}. \tag{17}$$

Otherwise the solution becomes an offset from the origin as:

$$\psi = \sum_{n=1}^{N}\frac{e^{-jk|r-r_n|}}{4\pi|r-r_n|}. \tag{18}$$

The solution of (18) is approximated using a binomial expansion assuming equal path loss (19). For N elements, we find (20):

$$\psi = \sum_{n=1}^{N} e^{jkr_n(\cos\psi_n)}, \tag{19}$$

$$\psi \simeq \left(\frac{e^{-jkr}}{4\pi r}\right)\sum_{n=1}^{N} e^{jkr_n(\cos\psi_n)}, \cos\psi_n = \hat{r}_n\cdot\left(\hat{r}(\theta,\phi)\right). \tag{20}$$

The solution of the n^{th} element is out of phase by the angle ψ_n. Beamsteering is achieved by imposing the linear steering factor, cos ψ_{n0}. We obtain $e^{jkr_n(\hat{r}_n\cdot(\hat{r}(\theta,\phi)-\hat{r}(\theta_0,\phi_0)))}$. Upon phase

correction these sources are now isotropic with equal amplitudes and propagate waves that intersect at alternating maxima and minima as shown in Fig. 2. A Fourier Transform pair describes the superposition of the constructive destructive interference of the particle nature of the wave, which is easy to visualize in the Fraunhofer region.

As the number of sources grows to infinity ($N\to\infty$) the discrete pattern converges to a continuous aperture solution. However, when N does not approach infinity the solution is the expected value and is illustrated in Fig. 3. The difference in relations yields a convergence factor of ($1/N$) between the aperiodic array and continuous aperture where the former is the characteristic function on a pedestal ($1/N$).

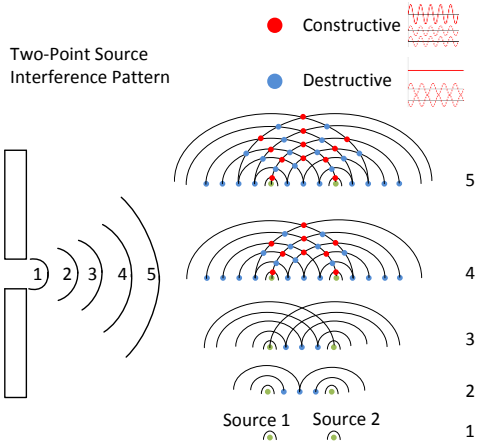

Fig. 2. Representation of constructive and destructive interference.

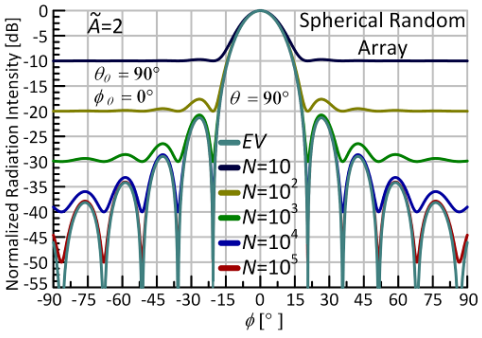

Fig. 3. Superposition diagram (top) converges to a continuous aperture distribution (*EV*) as $N\to\infty$ (bottom).

A. Spherical Waves in Unbounded Space

The characteristic modes of the spherical harmonics are derived from the fundamental solution of the Helmholtz equation (21) in unbounded space,

$$\left(\nabla^2+k^2\right)G_k=-\delta\left(\vec{r}-\vec{r}\,'\right)=-\frac{\delta(r-r')\delta(\theta-\theta')\delta(\phi-\phi')}{rr'\sin\theta} \quad (21)$$

$$G_k\left(\vec{r},\vec{r}\,'\right)=G_k\left(\vec{r}-\vec{r}\,'\right)=jh_0^{(1)}\left(jk\left|r-r'\right|\right)/4\pi=G_k\left(\vec{r}\,',\vec{r}\right)$$

Thus, the fundamental solution (21) is a point source and implies the self-adjointness property such that $G_k\left(\vec{r},\vec{r}\,'\right)=G_k\left(\vec{r}\,',\vec{r}\right)$. In other words, a spherical wave converges to a plane wave in the far field and vice versa.

An expansion of (21) as a scalar plane wave composed of scalar spherical waves can also be written as (22). From the orthogonality property of the spherical harmonics, outgoing waves are composed from multipole coefficients derived from the pattern multiplication of spherical Hankel, Bessel and spherical harmonics (23):

$$G\left(\vec{r}_1,\vec{r}_2\right)=jk\sum_{l=0}^{\infty}\begin{Bmatrix} j_l(kr_1)h_l^{(1)}(kr_2)\ \left[r_1<r_2\right] \\ j_l(kr_2)h_l^{(1)}(kr_1)\ \left[r_1>r_2\right]\end{Bmatrix}\sum_{m=-l}^{l}Y_l^m\left(\theta_1,\phi_1\right)Y_l^{m*}\left(\theta_2,\phi_2\right), \quad (22)$$

$$G\left(\vec{r},\vec{r}\,'\right)=jk\sum_{l=0,\infty}j_l\left(kr_<\right)h_l^{(1)}\left(kr_>\right)\sum_{m=-l,+l}Y_{lm}^*\left(\theta',\phi'\right)Y_{l,m}\left(\theta,\phi\right)$$
$$-\oint Y_{lm}^*\left(\theta,\phi\right)G\left(\vec{r},\vec{r}\,'\right)d\Omega=jkh_l^{(1)}\left(kr\right)j_l\left(kr'\right)Y_{lm}^*\left(\theta',\phi'\right) \quad (23)$$

In the far field the term $|\vec{r}-\vec{r}\,'|\approx r'-\vec{n}\cdot\vec{r}$, where $\vec{n}$ is a unit vector pointing in the direction of $\vec{r}\,'$. $h_l^{(1)}\left(kr\right)$ can be reduced in its asymptotic form such that:

$$\frac{e^{j\vec{k}\cdot\vec{r}}}{4\pi r}e^{-j\vec{k}\cdot\vec{r}\,'}=jk\frac{e^{jkr}}{kr}\sum_{l=0}^{\infty}(-j)^{l+1}j_l\left(kr'\right)\sum_{m=-l,+l}Y_{lm}^*\left(\theta',\phi'\right)Y_{l,m}\left(\theta,\phi\right) \quad (24)$$

The scalar plane wave expansion (25) is obtained by canceling the factor $\exp(jkr)/r$, taking the complex conjugate, and rewriting via the well-known addition theorem (26):

$$e^{j\vec{k}\cdot\vec{r}\,'}=4\pi\sum_{l=0}^{\infty}j^l j_l\left(kr'\right)\sum_{m=-l,+l}Y_{lm}^*\left(\theta',\phi'\right)Y_{l,m}\left(\theta,\phi\right), \quad (25)$$

$$e^{j\vec{k}\cdot\vec{r}\,'}=\sum_{l=0}^{\infty}j^l\left(2l+1\right)j_l\left(kr'\right)P_l\left(\cos\psi\right)$$
$$=\sum_{l=0}^{\infty}j^l\sqrt{4\pi\left(2l+1\right)}j_l\left(kr'\right)Y_{l0}\left(\psi\right), \quad (26)$$
$$Y_{l0}\left(\psi\right)=P_l\left(\cos\psi\right)\sqrt{\left(2l+1\right)/4\pi},\psi=\hat{r}\cdot\hat{r}'$$

Higher order moments do contribute to our overall pattern, but have a neglible impact.

B. Zernike Polynomials and Spherical Harmonics

It is possible to create patterns with multiple beams using complex orthogonal phase variations. A nominal example in *UV-space* is provided in Fig. 4.

Distributed orthogonality of this behavior is applied to the plane wave expansion of ψ and angular (θ, ϕ) spaces of Fig. 5 and Fig. 6, respectively. Fig. 5 demonstrates *ψ-spaces* with rotationally symmetric attributes, whereas Fig. 6 demonstrates the self-adjoint properties of spherically distributed arrays (SDA). For example, a spherical wave converges to a plane wave as the modal order increases while the point source converges to a spherical wave.

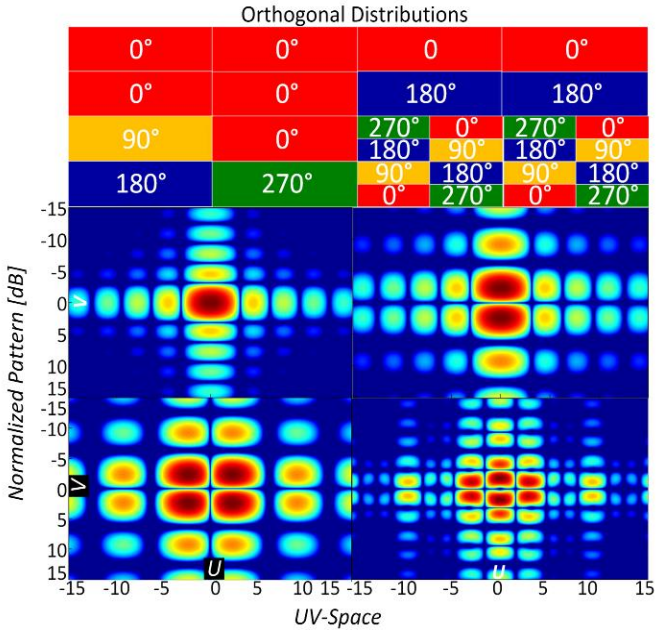

Fig. 4. Multiple beam patterns and distributed orthogonality.

The Legendre polynomials, which are orthogonal to the L^2 inner product on the interval $-1 \le x \le 1$, are the eigenfunctions of the Hermitian differential operator. They arise naturally in multipole expansions analogous to the monopole, dipole and higher moments of the spherical harmonic solutions, yielding the beampattern characteristics in Fig. 7. Furthermore, achievable pattern behavior is verified from HFSS simulations using 32 monopole element radiators steered at the meridian elevation angle in a normalized spherical aperture, A/λ=2.78 for select orbital distributions.

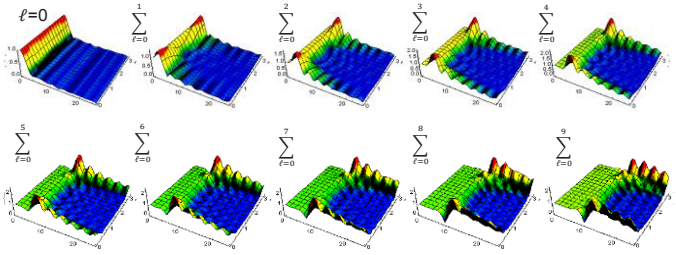

Fig. 5. Plane wave expansion in UV – space.

The three-dimensional Zernike polynomials are likewise composed of angular solutions of an orthogonal sequence defined on the unit sphere. In two-dimensional space, Zernike polynomials are commonly used in optics to describe aberrations of the cornea or lens from the nominal spherical shape (resulting in refraction errors). Examples include a circularly distributed array (CDA) as illustrated in Fig. 7. Closed form solutions of the patterns are provided in [9]. Lastly, they can represent properties of an image with no overlap of information between their moments as illustrated by Fig. 8. A final illustration of the beampatterns generated from the atomic like orbitals is shown in Fig. 9 as these distributions apply to the spherical zone of probability describing an electron's location.

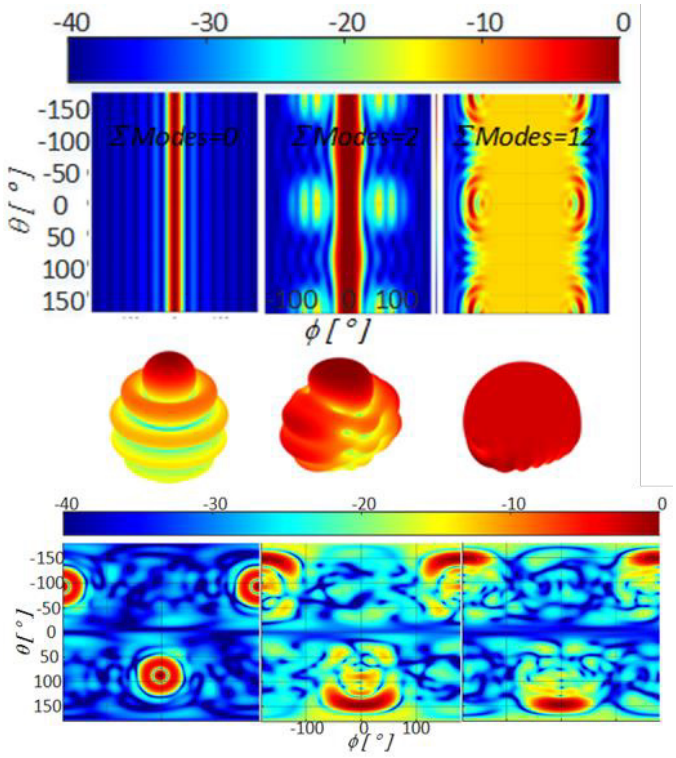

Fig. 6. Comparison of the modal summation of (25) applied to a point source in angular space, top and SDA, bottom.

V. Conclusion

The decomposition of (21) can be used to obtain the individual moments of the field at a given distance away from the source. These solutions formulate a series of basis functions for determining the array factor such that:

1. Monopole moments in the Fraunhofer region ($R>2D^2/\lambda$);
2. Monopole + Dipole moments in the Fresnel region with the first two spherical Hankel functions;
3. Monopole + Dipole + Quadrupole + Higher order modes in the near reactive field region;

and for a spherically distributed antenna array we reduce the number of basis functions of the pyramid of Fig. 8 and apply the spherical addition theorem (n as the n^{th} element) by:

$$P_l\left(\cos\psi = \hat{r}\cdot\hat{r}_n\right) = \frac{4\pi}{2l+1}\sum_{m=-l}^{l} Y_{lm}^{*}\left(\theta_n,\phi_n\right)Y_{lm}\left(\theta_{n0},\phi_{n0}\right). \quad (27)$$

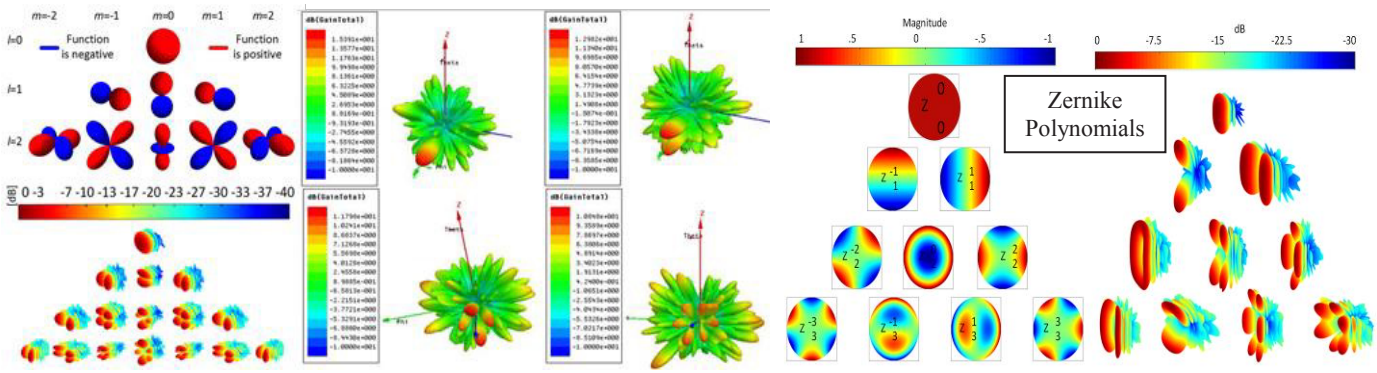

Fig. 7. Spherical harmonic distributions $Y_{mn,}$ top-left; modal beampatterns bottom-left; simulated patterns Y_{00}, Y_{01}, Y_{02}, and Y_{03}, center; Zernike distributions and modal beampatterns right.

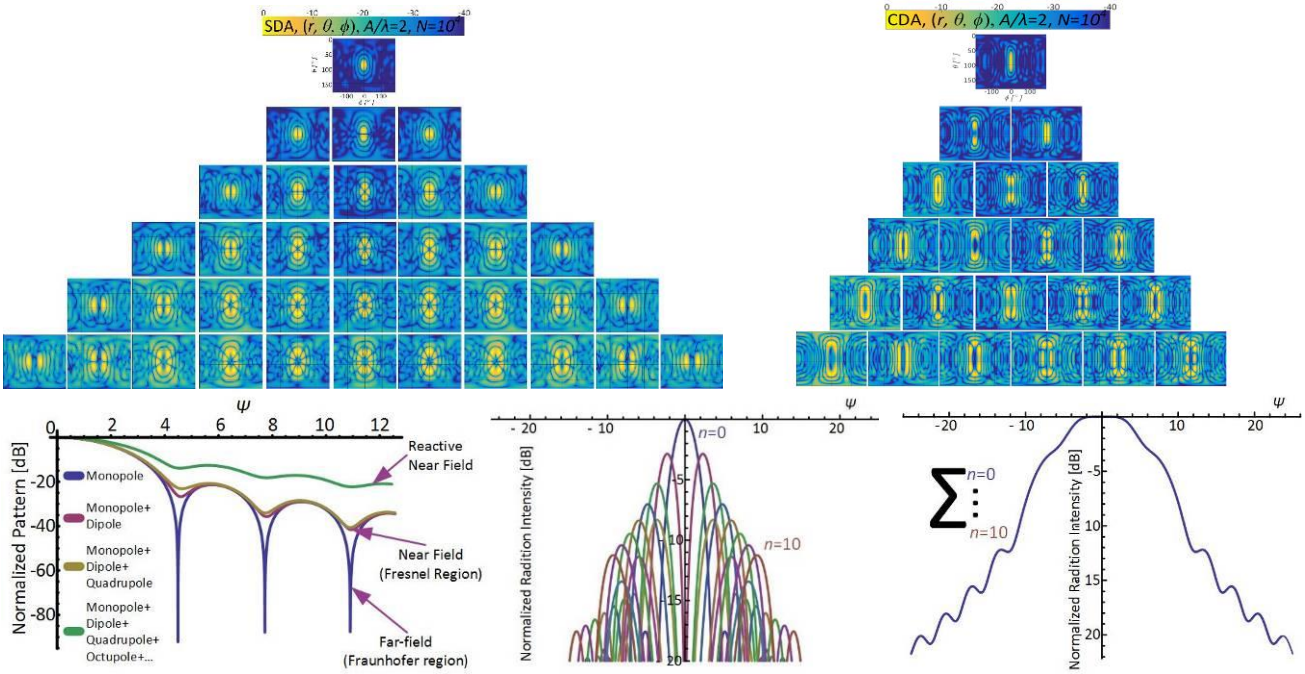

Fig. 8. Characteristic modes of the Zernike and spherical harmonic polynomials; topographical – top. Atomic orbital relationship of the superposition of spherical waves to a plane wave (bottom left). Zernike descending characteristic functions (bottom middle), characteristic function superposition (bottom right).

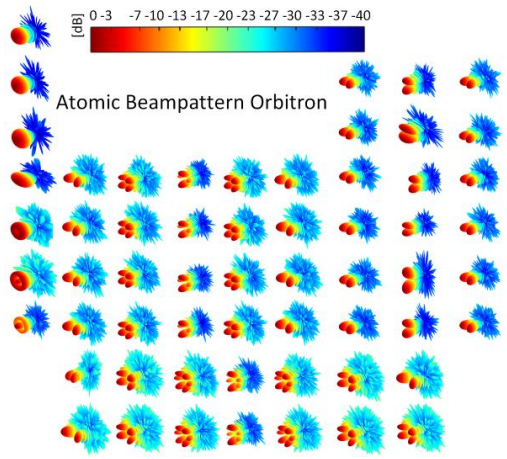

Fig. 9. Atomic like orbital beampatterns.

REFERENCES

[1] A. Panicali and L. Yuen, "A probabilistic approach to large circular and spherical arrays," IEEE Trans. Antennas Propag., vol. 17, pp. 514-522, July 1969.

[2] T. A. Dzekov and R. S. Berkowitz, "Parameters of a spherical random antenna array," in Electron. Lett., vol. 14, no. 16, pp. 495-496, Aug. 1978.

[3] H. Ochiai, "Collaborative beamforming for distributed wireless ad hoc sensor networks," IEEE Trans. Signal Process., vol. 53, pp. 4110, Nov. 2005.

[4] M. F. A. Ahmed and S. A. Vorobyov, "Collaborative beamforming for wireless sensor networks with Gaussian distributed sensor nodes," IEEE Trans. on Wireless Commun., vol. 8, pp. 638-643, Feb. 2009.

[5] K. Buchanan, O. Sternberg, S. Wheeland, and J. Rockway, "Examination of the near field response of circular antenna arrays," in United States National Committee of URSI National Radio Science Meeting (USNC-URSI NRSM), Boulder, CO, Jan. 2017, pp. 1-2.

[6] K. Buchanan, C. Flores-Molina, O. Sternberg, D. Overturf, S. Wheeland, and N. Johnson, "Near-field receive beamforming analysis

using circularly distributed random arrays," in IEEE Antennas and Propag. Int. Symp., San Diego, CA, 2017, pp. 1591-1592.

[7] D. Overturf, K. Buchanan, J. Jensen, C. Flores-Molina, S. Wheeland and G. H. Huff, "Investigation of beamforming patterns from volumetrically distributed phased arrays," in IEEE Military Communications Conference (MILCOM), Baltimore, MD, Oct. 2017, pp. 817-822.

[8] K. Buchanan and G. Huff, "A comparison of geometrically bound random arrays in Euclidean space," in IEEE Antennas and Propag. Soc. Int. Symp., Spokane, WA, July 2011, pp. 3-8.

[9] K. R. Buchanan, "Theory and applications of aperiodic (random) phased arrays," Ph.D. dissertation, Dept. Elect. & Com. Eng., Texas A&M University, TX, 2014.

[10] K. Buchanan and G. Huff, "A stochastic mathematical framework for the analysis of spherically bound random arrays," IEEE Trans. Antennas Propag., vol. 62, pp. 3002-3011, June 2014.

[11] D. Yavuz, "Frequency response and bandwidth of a spherical random array," in Electron. Lett., vol. 15, no. 11, pp. 314-315, May 1979.

[12] L. Lewin, "Comment analytic expression for the frequency response and bandwidth of a spherical random array," in Electron. Lett., vol 15. no. 19, pp. 585-586, Sept. 1979.

[13] K. Buchanan, C. Flores, S. Wheeland, J. Jensen, D. Grayson, and G. Huff, "Transmit beamforming for radar applications using circularly tapered random arrays," in IEEE Radar Conference (RadarConf), Seattle, WA, 2017, pp. 0112-0117.

[14] B. D. Steinberg, Principles of Aperture & Array System Design. New York: Wiley, 1976.

[15] Y. Lo, "A mathematical theory of antenna arrays with randomly spaced elements," IEEE Trans. Antennas Propag., vol. 12, pp. 257-268, May 1964.

Multiband Antenna for Wireless Applications Including GSM/UMTS/LTE and 5G Bands

Amirreza Jalali Khalilabadi, Student Member IEEE, and Ata Zadehgol, Sr. Member IEEE
Department of Electrical and Computer Engineering
University of Idaho, Moscow, ID, USA
jala9498@vandals.uidaho.edu, azadehgol@uidaho.edu

***Abstract*—A simple ultra thin multiband antenna is introduced. The proposed antenna with four bands covers many wireless applications. The proposed antenna has simple configuration including two open L-shaped slots to create resonat mode at GSM and GPS bands and also two rectangular slots on the radiating element for creating multi resonant modes to meet the specifications of mentioned frequency bands. According to the simple, small and planar configuration, the proposed antenna design is inexpensive and can easily be integrated with the other microwave circuit boards. The proposed antenna has the small size of 10 mm and the total size of 120 mm × 60 mm × 0.5 mm, promising to be used widely in compact and ultra slim handsets.**

***Index Terms*—multiband antenna, planar configuration, wireless applications, wireless handset.**

I. Introduction

Owing to development of mobile communication systems, the design of modern antennas with compact size, multiband operation, and integrability with other microwave circuits has attracted much attention. As a result, various types of multiband antennas have been reported [1]–[3]; however, by having two or three bands, most existing antennas are unable to cover more bands with one structure.

In this paper, we introduce a four–band slot antenna for the GSM (890–960 MHz), Galileo (1563–1591 MHz), GPS (1575.42 ± 5 MHz), Glonass (1602–1615.5 MHz), DCS (1710–1880 MHz), PCS (1850–1990 MHz), UMTS (1920–2170 MHz), LTE2300 (2305–2400 MHz)/LTE2500 (2500–2690 MHz), WLAN (2.4–2.484/5.15–5.35/5.7–5.8 GHz), and WiMAX (2.5–2.7/3.4–3.7/5.2–5.8 GHz) applications. Also the proposed antenna is able to cover some suggested bands of 5G systems including 3.3–3.8 GHz, 4.8–4.99 GHz, 5.150–5.925 GHz, 5.925–7.025 GHz, 7.235–7.25 GHz, and 7.750–8.025 frequency ranges [4]. The proposed antenna covers several applications which are narrowband and also provides the essential bandwidth for higher data rate applications.

II. Antenna Configuration

Fig. 1 shows the structure of the proposed antenna. The antenna is fabricated on a low-loss FR-4 substrate with dielectric constant of 4.3, thickness of 0.5 mm and loss tangent of 0.02. The antenna with a simple structure consists of a rectangular radiation patch, an open L-shaped slot for 900 MHz band, a horizontal open slot for GPS band and two rectangular slots

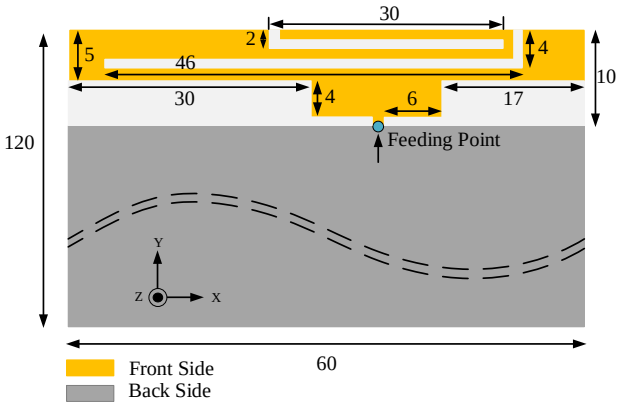

Fig. 1. Configuration of the proposed antenna (unit: mm).

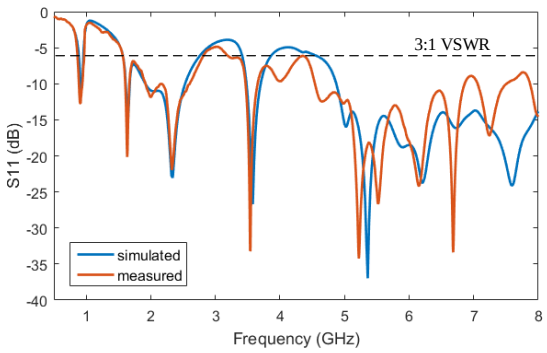

Fig. 2. Comparison between the HFSS (version 15) simulated and measured result of reflection coefficient.

for generating multi resonant modes to meet the specifications of desirable frequency bands. It is notable that an open-end slot can generate a quarter-wavelength resonant mode. Also, a wide slot can create several resonance modes, and by merging nearby resonance modes a wider bandwidth can achieved. The proposed antenna occupies an area of 10 mm × 60 mm, while the ground plane has an area of 110 mm × 60 mm which is a typical system board of mobile devices. A comparison between usage of lumped elements, structure, antenna size and

Submitted On: September 25, 2018
Accepted On: January 5, 2019

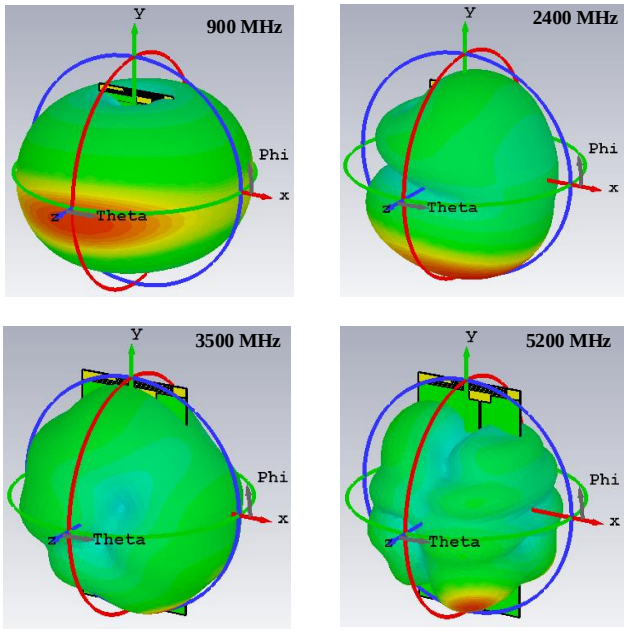

Fig. 3. Radiation patterns of the proposed antenna at different frequencies simulated by CST STUDIO SUITE 2017 Software.

TABLE I
COMPARISON OF THE PROPOSED ANTENNA WITH RECENT WORKS

[Ref] (year)	[1] (2013)	[2] (2014)	[3] (2015)	Proposed
Lumped Element	No	No	Yes	No
Structure	Planar	Planar	3D	Planar
Antenna size (mm×mm×mm)	78×0.6 ×18	115×0.5 ×15	120×0.8 ×8	120×0.5 ×10
-6 dB bandwidth (MHz)	890–960 1570–2500 ——— ———	790–1061 1650–2775 3132–6382 ———	800–1150 1700–2580 ——— ———	860-970 1560–2820 3180–4350 4400–8000

bandwidth of the proposed antenna with some recent studies is illustrated in Table I. It is notable that simultaneously covering all mentioned frequency bands with one structure is difficult, somehow none of the antenna in [1]–[3] can achieve this goal.

III. RESULTS AND DISCUSSIONS

To validate the simulation results, the designed antenna is fabricated and tested. The measured reflection coefficient S_{11} is compared to the simulated result in Fig 2. It is seen that the bandwidths for $|S_{11}| < -6$ dB (or VSWR > 3) are 12.02% (860-970 MHz) for the 900-MHz band, 57.53% (1.56-2.82 GHz) for the 2-GHz band, 31.07% (3.18-4.35 GHz) for the 3.5-GHz band, and 58.06% (4.4-8 GHz) for the 5.5-GHz band. Note that the $|S_{11}| < -6$ dB as the specification of the impedance matching bandwidth is widely acceptable for practical internal antennas [1], [3], [5], [6].

TABLE II
SIMULATED GAIN AND RADIATION EFFICIENCY RESULTS

Frequency [MHz]	CST [Gain (dB)–Efficiency (%)]	HFSS [Gain (dB)–Efficiency (%)]
900	0.8–69.18	-0.7–76
2400	3.64–61.65	4.08–77
3500	1.14–45.7	0.99–49
5200	3.79–46.7	2.86–55

The simulated peak gain and radiation efficiency values of the proposed antenna at different frequencies are presented at Table II. The results which have been obtained from the HFSS and CST softwares are almost close together and acceptable for mobile devices.

Fig. 3. demonstrates the simulated radiation patterns of the proposed antenna at 900 MHz, 2.4 GHz, 3.5 GHz, and 5.2 GHz. It can be observed that the radiation pattern of the proposed antenna at 900 MHz is dipole-like radiation pattern which shows that the radiation characteristic is stable at lower frequency [5]. Moreover, the simulated radiation patterns are almost omni-directional in the X-Z plane (with respect to position of the proposed antenna in the Cartesian coordinate) which are desired for the practical communication applications [1].

IV. CONCLUSION

In this paper, a simple planar multiband antenna for GSM, Galileo, GPS, Glonass, DCS, PCS, UMTS, LTE2300/LTE2500, WLAN (2.4–5.2–5.8 GHz), WiMAX (2.5–3.5–5.5 GHz) and 5G applications is presented and discussed. The antenna has small, ultra thin, and simple structure. We show that by inserting different slots with proper size in the truncated radiation patch, good multiband features can be achieved. It is also shown that the suggested antenna has good radiation characteristics such as stable radiation patterns, high radiation efficiency, and also acceptable gain values.

REFERENCES

[1] K. C. Lin, C. H. Lin, and Y. C. Lin, "Simple printed multiband antenna with novel parasitic-element design for multistandard mobile phone applications," IEEE Trans. Antennas Propag., vol. 61, no. 1, pp. 488–491, Jan. 2013.

[2] Z. Liang, Y. Li, and Y. Long, "Multiband monopole mobile phone antenna with circular polarization for GNSS application," IEEE Trans. Antennas Propag., vol. 62, no. 4, pp. 1910–1917, Jan. 2014.

[3] D. Wu, S. W. Cheung, and T. I. Yuk, "A compact and low-profile loop antenna with multiband operation for ultra-thin smartphones," IEEE Trans. Antennas Propag., vol. 63, no. 6, pp. 2745–2750, Jun. 2015.

[4] 5G Spectrum Recommendations, 5G Americas, Seattle, WA, USA, 2017. [Online]. Available: http://www.5gamericas.org/files/9114/9324/1786/5GA_5G_Spectrum_Recommendations_2017_FINAL.pdf

[5] Y. L. Ban, J. H. Chen, S. Yang, J. Li, and Y. J. Wu, "Low-profile printed octa-band LTE/WWAN mobile phone antenna using embedded parallel resonant structure," IEEE Trans. Antennas Propag., vol. 61, no. 7, pp. 3889–3894, Apr. 2013.

[6] Y. L. Ban, Y. F. Qiang, Z. Chen, K. Kang, and J. H. Guo, "A dual-loop antenna design for hepta-band WWAN/LTE metal-rimmed smartphone applications," IEEE Trans. Antennas Propag., vol. 63, no. 1, pp. 48–58, Jan. 2015.

Enhancement of Parameters of Slotted Waveguide Antennas Using Metamaterials

Minu Valayil [1] and Kent Chamberlin [2]

[1] SI2 Technologies; mvalayil@si2technologies.com
[2] University of New Hampshire, Dept. of ECE; kent.chamberlin@unh.edu

Abstract - An approach to increasing the gain of a slot-array antenna through the use of metamaterials is presented. The specific array antenna used in this study is a 2x4 resonant, slotted-waveguide array, although the results presented should be applicable to most arrays with slot radiators. To achieve increased gain, a metamaterial structure comprised of a split-ring resonator in conjunction with a wire structure was placed above the radiating slots. Modeled results for this configuration predicted an increase in directivity of 49%, and this result was subsequently validated by fabricating and performing measurements on antenna arrays incorporating the metamaterials. The increase in directivity also resulted in increased efficiency and sidelobe depth and yet did not degrade return loss. The measured results show that the maximum gain enhancement of antennas with metamaterials increased by up to 58% with respect to the control antenna which did not employ metamaterials.

Index Terms - antenna measurement, antenna modeling, beamwidth, metamaterials, slotted antenna, split-ring resonator.

I. INTRODUCTION

In the work reported here, metamaterial structures were placed above the radiating slots in a slotted waveguide antenna (SWA) array to increase the gain of the array without increasing its physical size. The results, both measured and modeled, show that a modest increase in gain is achievable by using metamaterials.

In an approach similar to the one presented here, Nicholson et al. [1] explored the use of split-ring resonators (SRR), which behave as metamaterial structures, to couple energy through a resonant slot in the waveguide. Their work was based on simulations, and they reported that the approach showed potential improvement in gain. However, their focus was to achieve improvement of structural properties by reducing the slot length through the use of a single SRR for each slot [1]. Although the approach presented here is similar to the approach of Nicholson, et al., there are two significant differences. One is that the metamaterial used here includes a wire structure in addition to the SRR. The other difference lies in the placement of the metamaterial structure. Specifically, their SRR was positioned in the radiating slot, while the metamaterial used here was positioned above the slot. The likely advantages to this revised metamaterial placement are that it will be less complicated to assemble, and it will provide greater bandwidth. Another recent paper introduced three split resonators inside the waveguide to yield high gain and front-to-back radiation ratio [17]. Again, this is also another application of the SRRs inside a waveguide but not on the outside of slotted waveguide antenna. Our application of SRRs on the outside of the slotted waveguide enhanced the directivity and gain compared to that of a conventional slotted waveguide antenna.

Computer modeling results using the metamaterial structure and placement described above predicted an increase in directivity [2]. To validate those modeled results, and to explicitly evaluate the effects of metamaterials on array performance, three 2x4 slot arrays were modeled, fabricated and measured. One was a conventional resonant-slot antenna, used as a control. The other two antennas were slot arrays of nearly identical design, having metamaterial structures positioned above their slots in an orientation that maximized the coupling between the metamaterial and the slot. That maximum coupling occurs when the metamaterial structure is either parallel to the slot or at right angles to it. As is detailed below, there were small variations in the slot dimensions and location for the three antenna arrays, and those variations were necessary to make the antennas identical electrically in terms of slot impedance.

The agreement between measured and modeled data was reasonable for the three configurations, and those results show an increase in directivity and concomitant decrease in beamwidth for both of the metamaterial orientations. The modeling software, High Frequency Structure Simulator (HFSS) by Ansys, showed a gain equal to directivity since the waveguide was modeled using Perfect Electric Conductor (PEC) boundaries. Because of this, the modeled directivity, rather than the modeled gain, is used in this study. The antennas were optimized using the model to achieve best directivity, return loss and lower sidelobes.

II. MATERIALS AND METHODS

2.1 Resonant Slot Array Antenna

All three arrays studied used a half-height WR-90

Submitted On: August 15, 2018
Accepted On: December 24, 2018

(0.9in x 0.2 in) rectangular waveguide as their input, with wall thickness of 0.050in. They were designed to be operational over the frequency band of 9.3 to 9.7GHz. The 8 slots were $\lambda_g/2$ apart with shorted ends and thus perform as linear, resonant, slotted-waveguide antenna arrays. The control antenna, the one without the metamaterials, is shown in Fig. 1 and was designed using Elliott's technique [3], although a computer model was used to fine tune slot impedances.

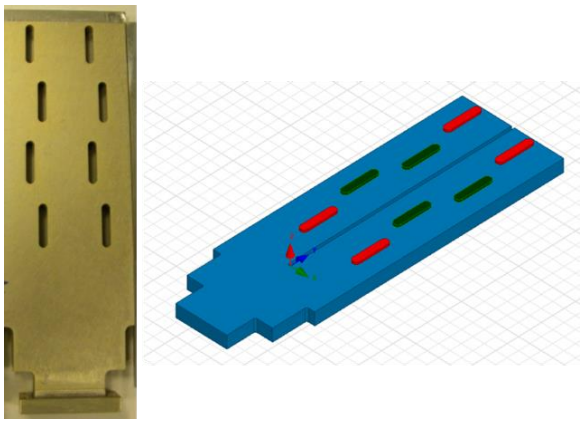

Fig. 1. The control antenna is a conventional 2x4 slot-array design without metamaterial structures: the array is pictured on the left and the array as modeled in HFSS is shown on the right.

The waveguide used to feed the arrays has an "a" dimension of 0.864in and a "b" dimension of 0.2in. As seen in Fig. 1, the slots are placed on the broadside of the waveguide and are separated by a distance compatible with TE_{10} mode operation. The offsets and slot dimensions were optimized using HFSS to minimize return loss. Minimal return loss will occur when the admittance of each slot is purely real and the total admittance is equal to characteristic impedance of the waveguide [4]. The slot dimensions for the finalized design of the control antenna are given in Table 1.

Table 1: Dimensions for the control slotted-waveguide array

Dimension	Offset (in)	Length (in)
Slot 1	0.08	0.610
Slot 2	0.09	0.615
Slot 3	0.09	0.615
Slot 4	0.08	0.610
Short distance	0.374	
Slot width	0.126	
Guide wavelength (λ_g)	0.894	

2.2 *Metamaterial Resonant Slot Array Design*

Metamaterial Design: In 1964 Veselago introduced the possibility of negative-refractive-index materials that had no known existence in nature [5] at that time. He proposed the possibility of configuring materials so as to create a structure with a negative refractive index [5]. Several practical designs employing metamaterial structures exist today: Zhang and Deng [6] introduced a metamaterial transmission line structure with split-ring resonators (SRRs) along with complimentary split-ring resonators (CSRRs). Smith et al. demonstrated that a SRR in conjunction with a wire structure would introduce negative permeability and negative permittivity [7].

The metamaterial structure used in this work, referred to as a unit cell and depicted in Fig. 2, follows the work by Smith by including both a SRR and a wire structure to create the metamaterial. The dimensions for the components comprising the unit cell were adjusted to achieve resonance at 9.5GHz as described below.

Unit cells can be joined with other unit cells to increase the physical size of the metamaterial and for the work presented, three co-linear unit cells where shown to provide the best results.

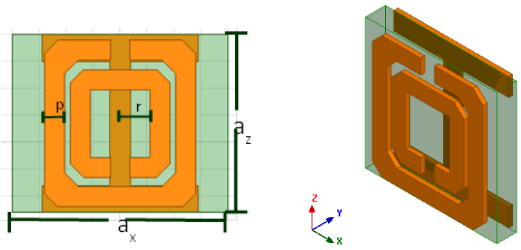

Fig. 2. A single unit cell of metamaterial structure used for this application, consisting of a SRR on the top layer of the substrate and the wire structure on the bottom layer.

The overall size of the unit cell SRR and the wire structure is 3.31mm x 3.31mm x 0.5mm and was fabricated on RO5880 substrate. The dimensions were determined using the Lorentz model for a SRR and the Drude model for the wire structure [8]. Dimensions for the unit cell structures can also be calculated using equations published by Engheta et al. [9].

Using the dimensions from the models given above, the unit cell was modeled in HFSS to assess its performance characteristics as described below. Achieving resonance at the desired frequencies required iterating the design with HFSS, and the dimensions identified in that process are given in Table 2.

Table 2: The unit cell dimensions to achieve resonance at 9.5GHz; rough values were calculated using the Drude and Lorentz models, and those values were refined using a computer model to yield the results given above

Variables	Dimensions (mm)
p	0.375
r	0.83
a_x	3.31
a_y	3.31

The configuration used to model the unit cell in HFSS is shown in Fig. 3, where the input and output ports are created using the software's waveport function; those ports are shown on the left and right faces of the computational space given in Fig. 3. In this particular configuration, the Poynting vector will flow parallel to both the SRR and wire structure, with the fields oriented as shown in Fig. 3. The effect of the unit cell on the excitation is given by the waveport's S parameters, which are plotted in Fig. 4.

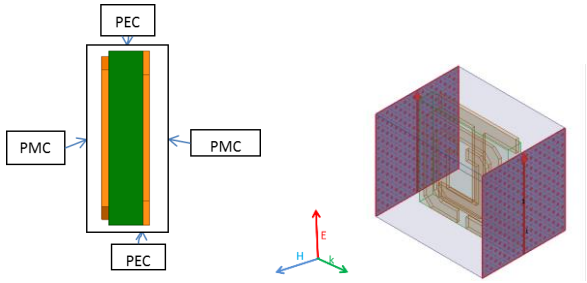

Fig. 3. Unit cell configuration modeled in HFSS: side view (left) and a projection of the 2-port waveport excitation set-up.

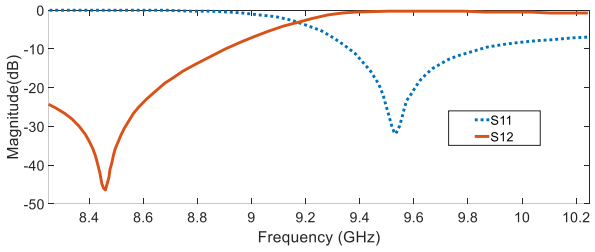

Fig. 4. HFSS S-parameter plot of the unit cell.

The modeled unit-cell S-parameters are plotted in Fig. 4, showing a magnetic-field resonant frequency of approximately 8.5GHz and a resonance frequency at 9.5GHz [8, 10]. Referring to Fig. 4, the closest impedance match appears to be in the range of 9.4 to 9.7GHz, which is coincident with the slotted waveguide antenna resonant frequency. The following section uses the data in Fig. 4 to extract the effective permittivity and permeability, showing that they are both negative within the frequency range of interest.

The orientation of the unit cell with respect to the excitation source as shown in Fig. 3 is analogous to positioning the unit cell at right angles to the plane of the slot. This orientation for the unit cell is one of the orientations investigated in this study. The other is where the unit cell is rotated 90° such that the plane of the cell is parallel with the right face. This rotated configuration was modeled as well and provided nearly identical results to the orientation of Fig. 3, and the enhancement to antenna performance was also nearly the same for both orientations.

Metamaterial Characterization: The objective of this section is to show that the unit cell used in this study behaves as a metamaterial. This is accomplished using the S-parameters plotted in Fig. 4 to determine the cell's effective permittivity and permeability.

A number of approaches exist in the literature to extract electromagnetic properties of a medium: (1) field averaging (2) curve-fitting (3) the dispersion equation and (4) S parameters [11]. The S-parameter method is commonly used for this purpose.

Several methods of S-parameter extraction techniques have been developed to characterize metamaterial structures. Those include (1) Nicholson-Ross-Weir (NRW) method (2) Bloch-Floquet Theorem method. Ziolkowski uses NRW method in his paper to retrieve effective medium parameters [8]. However, the paper by Nicholson et al. shows some limitations regarding the usage of the method for narrow bandwidth [6]. Consequently, the Bloch-Floquet method is used here to retrieve the essential parameters. The fundamental mode, TE_{10}, is the only mode considered here.

Palandoken et al. describes the Bloch-Floquet method used for extracting the parameters plotted below [13]; calculated effective permeability (μ_{eff}) and effective permittivity (ϵ_{eff}) are given in Figs. 5 and 6, respectively. As seen in Fig. 5, the real part of the permeability is negative in the frequency range between the magnetic resonance at 9.18GHz and the plasma frequency at about 11GHz. The permeability curve shows that the highest magnetic loss is close to the magnetic resonance frequency of 8.5GHz.

The magnetic resonance seen at 8.46GHz in Fig. 4 is coincident with the resonance in the permeability and permittivity curves shown in Figs. 5 and 6, respectively. The imaginary part of the effective permittivity shown in Fig. 6 is negative in the frequency range of about 8.25GHz to9.1 GHz. The Drude type response is seen to be in the frequency range of around 8.5 to 9.2GHz as is

expected for a wire structure [14]. This response agrees well with the results published by Liu et al. [15].

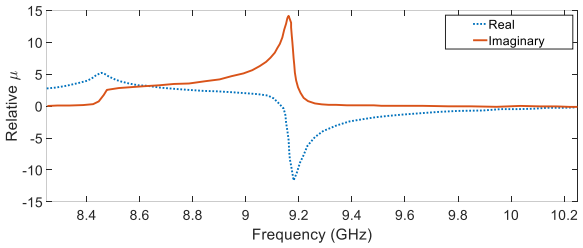

Fig. 5. The real and imaginary part of the effective permeability of the unit cell.

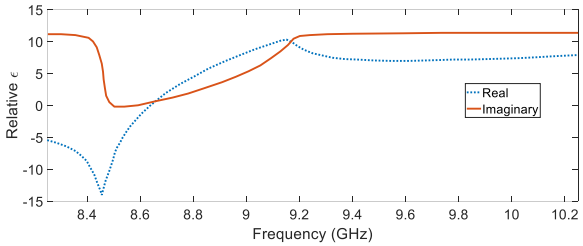

Fig. 6. The real and imaginary part of the effective permittivity of the unit cell.

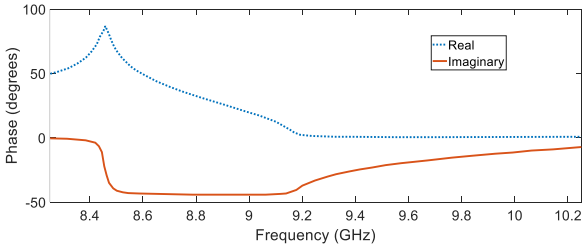

Fig. 7. The real and imaginary part of the phase of the unit cell.

Based upon the effective permittivity and permeability plots above, the unit cell in this paper can be represented as a Lorentz-Drude model [15]. The phase diagram, given in Fig. 7, shows the bandgap region in the same frequency range where the real part of permittivity is negative and the real part of the permeability is positive [10]. This bandgap region is also evident in the S-parameter result in Fig. 4.

As seen in Figs. 6 and 7, the combination of the SRR and wire structure has a clearly defined frequency range where both the permittivity and permeability are negative. Smith, et al. [16] has shown that this characteristic defines metamaterials, and hence it can be concluded that the structure used in this study behaves as a metamaterial.

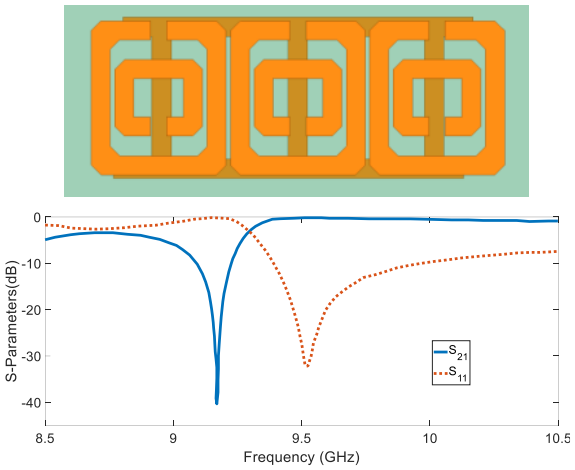

Fig. 8. Top: array of three elements used for the application. Bottom: the HFSS S-parameter results of metamaterial array.

As stated above, multiple unit cells can be added together to create a metamaterial of larger area. For this study, three elements, as shown in Fig. 8, proved to be of sufficient size to interact with the array slots. Modeled results using four elements together showed distortion in the radiation pattern and hence the use of a larger number of unit cells was not explored further.

The gap between the individual unit cell structures is crucial, and modeling results showed the optimal gap size to be 0.004". This gap size was used in the fabrication of the cells. The dimension of the SRR and the wire is the same as that of the unit cells. The wire structure on either side of the middle SRR is offset by about 0.001" since this proved to yield the greatest directivity in simulations. The array was fabricated on a 3.1 mil Rogers 5880 substrate with ϵ_r of 2.2 and dielectric loss tangent of 0.0009. The thickness of the copper deposition is 1 oz. on both sides of the substrate. When compared to the S-parameter results of a single unit cell in Fig. 4, the results for the three-unit-cell configuration show the S_{21} resonance at 8.46GHz is shifted to 9.17GHz, closer to the desired resonance frequency at 9.5GHz. These two resonances, the electric and the magnetic, reappear in the S-parameter results of the array as shown in Fig. 10. Those resonances occur at approximately 8.75GHz and 9.6GHz, respectively.

The array three-unit-cell metamaterial structure was evaluated by orienting it two different ways, one vertical with respect to the slots and the other horizontal to the slots. Either orientation appears to give approximately the same benefits in terms of increasing gain, directivity and narrowing the beamwidth.

2.3 Orienting the Metamaterial Structures Vertically with Respect to the Slots

In the vertically-oriented configuration, the three-unit-cell metamaterial structure was positioned over each of the radiating slots as shown in Figs. 9 (a) and 9 (b), where the plane of the cell is at right angles to the plane of the slot. The middle SRR of the array of metamaterial structures is located at the center of the slots. The height of the metamaterial structures was optimized to give the maximum gain.

Introduction of the metamaterial structure over the slots changed the impedance of the slots. To compensate for those changes, the computer model was used to estimate slot dimensions that would be matched for this particular slot-metamaterial configuration. By optimizing slot match, the return loss was also minimized. Those new dimensions are given in Table 3 and were used in fabricating the antenna array for the vertically-oriented metamaterial tests.

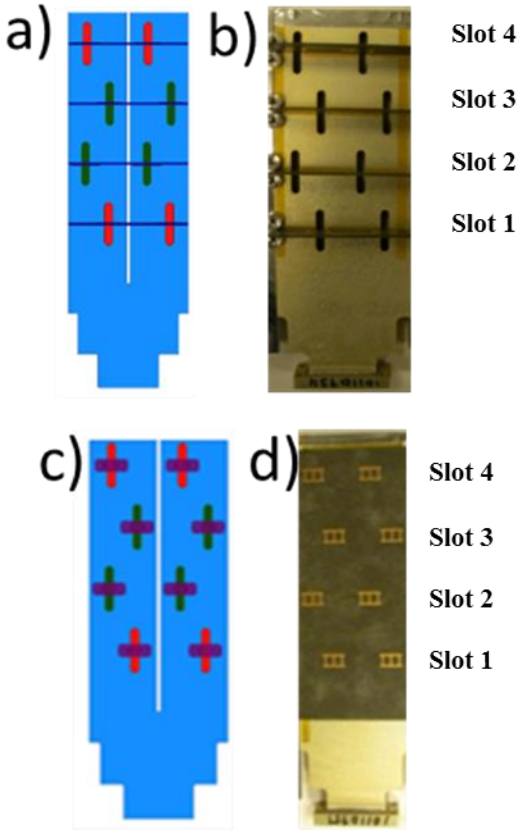

Fig. 9. (a) HFSS model representation of slotted waveguide with metamaterial structures mounted vertically, (b) picture of fabricated prototype of the vertically mounted metamaterial structure, (c) HFSS model of the horizontally-mounted metamaterial on top of the array slots, and (d) picture of fabricated prototype of horizontally mounted metamaterial structures

Table 3: Array dimensions to achieve matched slots for the vertically-mounted and horizontally-mounted metamaterial structure

	Vertically Mounted		Horizontally Mounted	
Dimension	Offset (in)	Length (in)	Offset (in)	Length (in)
Slot 1	0.16	0.64	0.16	0.665
Slot 2	0.18	0.65	0.18	0.675
Slot 3	0.18	0.65	0.18	0.675
Slot 4	0.16	0.64	0.16	0.66
Short distance	0.44		0.36	
Slot width	0.12		0.11	
Distance of SRR structures from slot	0.135		0.15	
Guide wavelength (λ_g)	0.894		0.894	

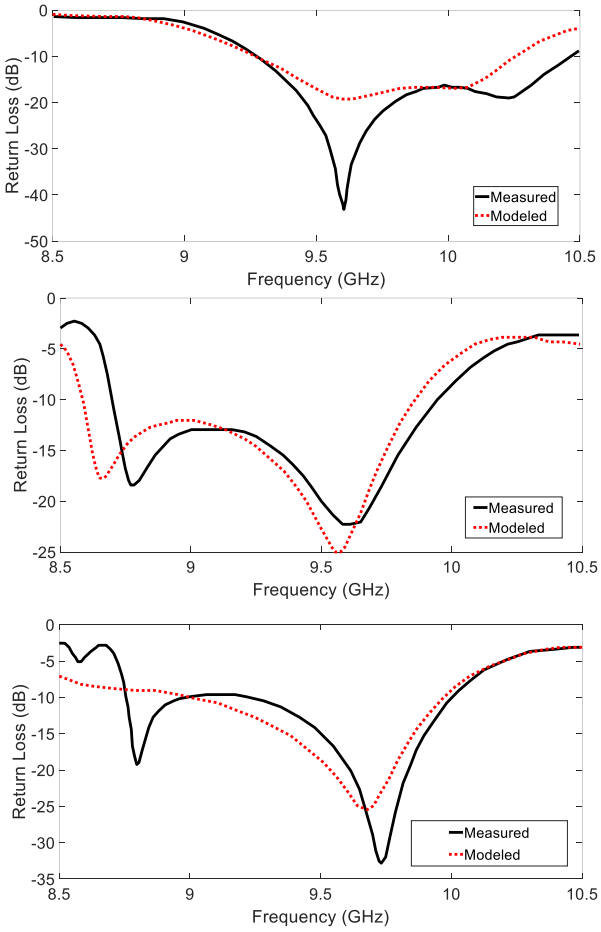

Fig. 10. Measured and modeled return loss for: control antenna (top), metamaterial mounted vertically (middle) and metamaterial mounted horizontally (bottom).

2.4 Orienting the Metamaterial Structures Horizontally with Respect to the Slots

In the horizontally-oriented configuration, the same three-unit-cell metamaterial structure was used, although its physical orientation was rotated by 90° as shown in Figs. 9 (c) and 9 (d). This configuration was optimized to minimize return loss, resulting in the array dimensions

given in Table 3. As with the vertically-oriented metamaterial configuration, the middle SRR of the array of metamaterial structures was located at the center of the slots. The height of the metamaterial structures was optimized to give the maximum gain.

III. RESULTS

The three antenna arrays described above were manufactured at Cobham Advanced Electronic Solutions, Exeter, NH to validate the modeled results. Those arrays were fabricated using the design parameters described above.

The far-field measurements were collected in a near-field anechoic chamber with NSI test set-up using a cylindrical scanner in a manner consistent with industry standards.

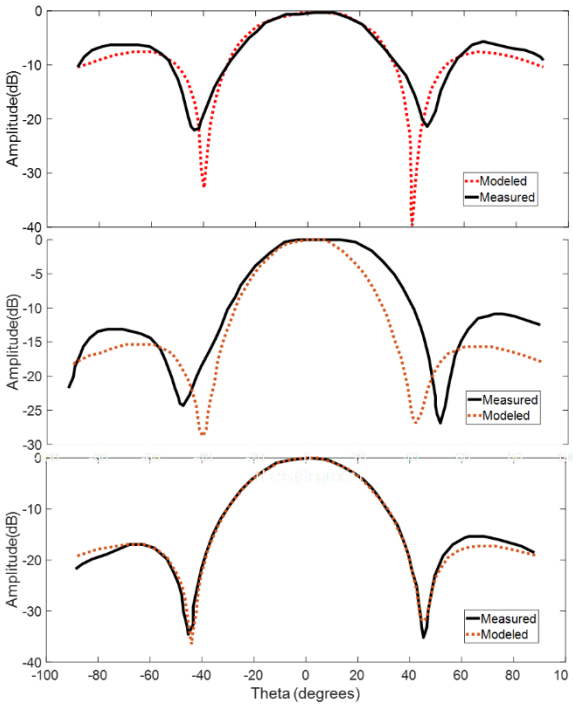

Fig. 11. E-Field radiation patten for the three antenna array configurations: control (top), vertical (middle) and horizontal at 9.6GHz.

3.1 Measured and Modeled Return Loss

The return-loss graphs for the three antenna arrays, given in Fig. 10 show reasonable agreement between the simulated and measured data for the frequencies of interest (9.3 to 9.7GHz). A conclusion that can be drawn from the S-parameter data in those figures is that all three arrays are viable from an impedance match perspective.

The return loss measurements for all three antennas showed the best match at 9.6GHz, and thus the radiation patterns were measured at that frequency.

3.2 Measured and Modeled Radiation Patterns

The modeled and measured radiation pattern data for the E-plane and H-plane at 9.6GHz for the three antennas are plotted in Figs. 11 and 12. As seen in the figure, there is reasonable agreement between the model and measurements for the three configurations. The sidelobes of the metamaterial antennas are suppressed more than the control antenna by 10dB.

There is an anomaly in the results that should be noted here. The vertically-oriented metamaterial antenna has a somewhat distorted pattern when compared to the simulated in E-plane as can be seen in Fig. 11. The assumed reason for this difference is that the metamaterial structure is flexible and was observed to be slightly curved during the test. A close examination of Fig. 3 (a) appears to confirm this assumption. Consequently, it is reasonable to assume that both metamaterial structure orientations will provide identical results if the metamaterial structures are mounted correctly.

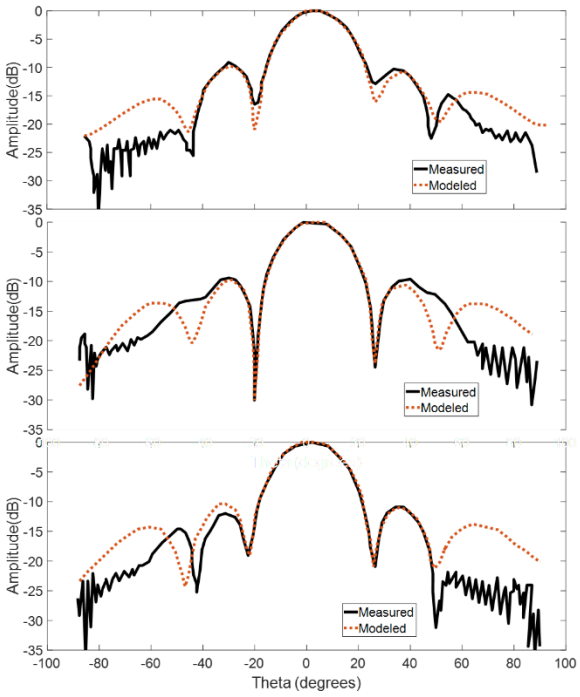

Fig. 12. H-Field radiation patten for the three antenna array configurations: control (top), vertical (middle) and horizontal at 9.6GHz.

3.3 Array Gain and Efficiency

The gain versus frequency plot of Fig. 13, which was generated using measured data, shows the variation in gain over the frequency range of 8.5 to 10.5GHz. The gain of the control array is seen to be greater than 14dB in the frequency range of 9.4 to 9.9GHz. This value increases to 14.9dB in the range of 9.9 to 10.5GHz, resulting in a bandwidth of 1100MHz. The array with the hor-

izontally-oriented metamaterial also shows a gain greater than 14dB in the frequency range of 8.9 to 10.3GHz, resulting in a bandwidth of 1400MHz, or about 300MHz more than the control antenna. The array with the vertically-oriented metamaterial shows nearly the same bandwidth as the array with the horizontally-oriented metamaterial.

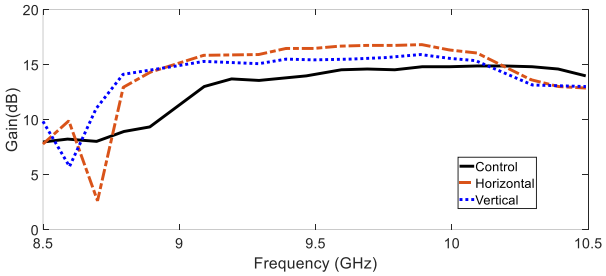

Fig. 13. Plot of gain versus frequency, calculated using measured data.

Referring to Fig. 13, the gain difference between the control array and the array with the horizontally-oriented metamaterial is approximately 2dB and this difference exists over a frequency span of nearly 1000MHz. Also evident in Fig. 13 is a gain difference of 0.9dB between the array with the vertically-oriented metamaterial and the array with the horizontally-oriented metamaterial due to some axial deformation in the metamaterial structure as described above. Based on the efficiency plot shown below in Fig. 14 proves that the efficiency of both the horizontal and the vertical mounted metamaterial antenna is better than the conventional slotted waveguide antenna.

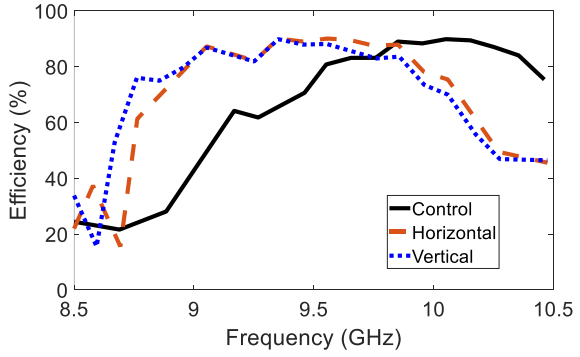

Fig. 14. Plot of efficiency versus frequency calculated using measured data.

IV. DISCUSSION AND CONCLUSIONS

The finding of the work described above is that a modest, approximately 2 dB over a wide bandwidth, increase in gain can be achieved by placing a metamaterial structure over the radiating slots in a slotted-array antenna. This can be achieved without increasing the physical size of the antenna, and the cost to include the metamaterial design presented here in the final product should be minimal.

There appears to be several mechanisms at play that cause the metamaterials to bring about the increased gain. One is that the metamaterial structure increases coupling through the slots by placing them in the reactive near-field of the slots.

Another explanation for the increased gain is that the negative index of refraction of the metamaterials compensates for the diffraction that occurs as the wave exits the waveguide slots. If diffraction compensation does occur, it would likely enhance coupling through the slot and bring about the lesser reflection mentioned in the previous paragraph. Diffraction compensation would also tend to provide a lens-like focusing of the energy which would increase directivity as reported in [7].

V. PATENTS

M. Valayil, inventor; Continental Microwave & Tool Co., Inc dba Cobham Advanced Electronic Solutions, assignee. Slotted waveguide antenna with metamaterial structures. US patent 9,595,765B1. 2017 March 14.

ACKNOWLEDGMENT

This work is funded by Cobham Advanced Electronic Solutions, Exeter, NH. Special thanks to Peter Beaulieu, Dr. Yun-Li Hou, James Skladany, Dr. Mahesh Kumar and Dan Wall at Cobham for insightful discussion on this topic.

REFERENCES

[1] K. Nicholson, W. Rowe, and P. Callus, "Split-ring resonator loaded slot array," Proceedings of the Asia-Pacific Microwave Conference, pp. 1338-1341, 2011.

[2] M. Valayil and K. Chamberlin, "Enhancement of antenna parameters of slotted waveguide antenna using metamaterials," IEEE APS-URSI, 2014.

[3] W. Zhang, Y. Zhao, and M. Zhang, "The synthesis of a longitudinal slot array on a rectangular waveguide," IEEE, vol. 12, pp. 202-205, 2012.

[4] M. Orefice and R. S. Elliott, "Design of waveguide-fed series slot arrays," IEEE PROC., vol. 129, August 1982.

[5] V. G. Veselago, "The electrodynamics of substances with simultaneously negative values of ϵ and μ," Sov. Phys., vol. 10, pp. 509-514, January 1968.

[6] Y. Zhang and L.-L. Deng, "Metamaterial transmission lines based on split-ring resonators (SRRs) and complementary split ring resonators (CSRRs)," ICMMT 2010 Proceedings, pp. 2075-2077, 2010.

[7] D. R. Smith, D. Shurig, and J. B. Pendry, "Negative refraction of modulated electromagnetic waves," Applied Physics Letters, vol 81, 2713, 2002.

[8] R. W. Ziolkowski, "Design, fabrication, and testing of double negative metamaterial," Antennas and Prop. IEEE, vol. 51, 2003.

[9] N. Engheta and R. W.Ziolkowski, "A positive future for double-negative metamaterials," IEEE Trans. Microwave Theory and Tech., vol. 53, 2005.

[10] V. Varadan and A.Tellakula, "Effective properties of split-ring

resonator metamaterials using measured scattering parameters: Effect of gap orientation," Journal of Applied Physics, vol. 100, 2006.

[11] S. Arslanagic, T. V Hansen, N. A Mortensen, A. H Gregersen, O. Sigmund, R. W. Ziolkowski, and O. Breinbjerg, "A review of the scattering parameter extraction method with clarification of ambiguity issues in relation to metamaterial homogenization," IEEE A&P Magazine 55(2), 91-106, 2013.

[12] A. M. Nicolson and G. F. Ross, "Measurement of the intrinsic properties of materials by time domain techniques," IEEE Trans. Instrum. Meas., vol. IM-19, pp. 377-382, Nov. 1970.

[13] M. Palandoken and H. Henke, "Fractal spiral resonator as magnetic metamaterial," IEEE, 09, 2009.

[14] D. R. Smith, "Analytic expressions for the constitutive parameters of magnetoelectric metamaterials," Physical Review, vol. 81, 2010.

[15] R. Liu, T. J. Cui, B. Zhao, D. Huang, and D. R. Smith, "Description and explanatin of electromagnetic behaviors in artificial metamaterials based on effective medium theory," Phys. Rev., vol. 76, 2007.

[16] D. R. Smith, S. Schultz, P. Markos, and C. M. Soukoulis, "Determination of negative permittivity and permeability of metamaterials from reflection and transmission coefficients," Phys. Rev. B, 65, 2002.

[17] A. Chandra and S. Das, "Application of SRR to achieve performance improvement and multiband characteristics in aperture antennas," IET Microwaves, Antennas & Propogation, vol. 11, pp. 990-996, 2017.

Minu Valayil is a Principal Engineer at SI2 Technologies, where she is focused on antenna design and development of new antenna technologies. She has 9 years of experience in the field of Electrical Engineering as an Microwave/RF Engineer, with 2 years of Antenna Engineering experience. Valayil's work at SI2 has been focused on the design and development of broadband, electrically small, and structurally integrated antennas and arrays. Prior to joining SI2, Valayil worked as a RF/Microwave Engineer at Cobham Integrated Electronic Solutions (CIES), in Exeter, NH. She received Sir Alan Cobham Bronze Award for Innovation for her development of metamaterial application on slotted waveguide antenna systems.

Valayil received her M.S. in Electrical Engineering from University of New Hampshire with a concentration on metamaterial antennas and BS degrees in Electrical Engineering and Biomedical Engineering from Letourneau University, Longview, TX.

Kent Chamberlin is the Chair and a Professor in the Department of Electrical and Computer Engineering. In his more than thirty-five years in academia, he has performed research for more than twenty sponsors, including the National Science Foundation. He has received two Fulbright awards, including the Fulbright Distinguished Chair, which he served in Aveiro, Portugal. He has also served as an Associate Editor for the Institute for Electrical and Electronics Engineers, and he continues to be active in performing and publishing in a range of research areas.

A Novel Design of Non-Uniform Reflectarrays with Symbolic Regression and its Realization using 3-D Printer

Peyman Mahouti [1], Filiz Güneş [1], Mehmet A. Belen [2], and Alper Çalışkan [1]

[1] Department of Electronics and Communication Engineering
University of Yıldız Technical, Istanbul, TURKEY
pmahouti@yildiz.edu.tr, gunes@yildiz.edu.tr, acaliskan@yildiz.edu.tr

[2] Department of Electric and Electronic Engineering
University of Artvin Çoruh, Artvin, TURKEY
mehmetalibelen@artvin.edu.tr

Abstract ─ Herein, a novel design of an X-band Non-Uniform Reflectarray Antenna (NURA) with Symbolic Regression SR and its fabrication using 3D Printer technology are presented. A NURA is consist of simply a grounded dielectric layer with the variable thickness. Firstly, SR is employed to obtain with a great accuracy for the reflection phase characteristics of a grounded dielectric layer in the analytical form within the continuous domain of $1 \le \varepsilon_r \le 6$ and thickness $0.1 \le h \le 3$ mm for the X-band. For this purpose, SR is trained and validated by the 3D CST Microwave Studio data. Then, for the design purpose of NURA, a special fine reflection calibration characteristic is built up again by SR with the sufficient reflection phase range of the 3D Printer's material at the operation frequency 10 GHz. In the third step, the designed NURA is then prototyped by using 3D printer technology where the material can be easily shaped and create unit cell at printing accuracy of 0.1 mm per layer. Thus, by this mean the prototyping cost of non-uniform Reflectarray design can be reduced drastically both in means of time and ease of manufacturing. In the final step, mismatching and radiation properties of the prototyped NURA are measured.

Index Terms ─ 3D printer, antenna design, microstrip reflectarrays, reflection phase modelling, symbolic regression.

I. INTRODUCTION

A Microstrip Reflectarray Antenna (MRA) is a design that being a hybrid of a reflector antenna and a planar phased array antenna which uses a suitable phasing scheme for its elements to reflect the incoming electromagnetic wave form a pencil beam in a specified direction (θ^0, φ^0) [1-4]. One of the very popular phasing schemes involves varying dimensions of the elements such as printed dipoles or patches around their resonant size. In the recent works of [3-4], novel multi-objective evolutionary design optimization procedures are put forward to obtain the quasilinear phasing characteristic for the Minkowski RA s using 3D CST Microwave Studio based Multilayer Perceptron Neural Network (MLP) models with Particle Swarm and hybrid Genetic Algorithm (GA) and Nelder-Mead (NM) algorithms, respectively. In fact, MRAs are advantageous antennas having the simple structures with low profiles, light weights and no need of any complicated feeding networks. However, MRA s are inherently narrow-band radiating elements and the mutual couplings between microstrip elements printed on standard substrates are significant; in addition, the conductor and surface wave loss are severe. To reduce these shortcomings solely grounded dielectric layer with variable thickness is proposed to be used as a reflecting surface in [5]. In this Non-Uniform dielectric layer, the required phase shift is provided by determining thickness at each cell on the RA plane to produce a pencil reflected beam in a specific direction (θ^0, φ^0). Thus, a RA design with the possible simpler and more advantageous structure can be obtained than MRAs.

In this work, a novel approach for design and fabrication of Non-uniform Reflectarray Antenna (NURA) had been proposed. Firstly in the design stage, SR [6] is applied to express the reflection phase characteristics of a grounded dielectric layer in the form of an analytical expression within the domain of $1 \le \varepsilon r \le 6$ with variable thickness $0.1 \le h \le 3$ mm using the 3-D EM based data sets for X-band (8-12 GHz) applications. Then, for the design purpose, a special fine calibration characteristic is built up by SR with the sufficient reflection phase range for the 3D Printer's material PLA with $\varepsilon_r = 2.4$ at the operation frequency 10GHz. SR Eureqa is a novel regression method that performs genetic programming within the mathematical expression domain to create a model consisting of summation of

Submitted On: September 11, 2018
Accepted On: February 21, 2019

expressions that fits to a given dataset with a great accuracy [7-8]. This regression method nowadays has been used to obtain solutions for various science and engineering problems [9-12]. In the recent work [12], SR has been employed to uncover intrinsic relationships hidden within the Big Data that is derivation of a full-wave simulation based analytical expression for the characteristic impedance Z_0 of microstrip lines. In [12], Big Data is obtained from the CST Microwave Studio, in terms of the substrate dielectric constant ε, height h and strip width w within 1-10 GHz band.

Recently, 3-D printing technology has been used for the prototyping of microwave designs [13-22]. 3D printing method has many advantages compared with the traditional fabrication methods such as being easier to prototype complex designs in terms of low cost and low weight. Herein, 3D printer technology is used for prototyping of the designed NURA. One of the most recent innovation for fast and accurate prototyping is 3D printing technology.

The paper is organized as follows: The next section gives the basics of SR and application to the reflection calibration characteristics of NURA. In this section, for the purpose of training and validation, 3D CST data set is obtained for the substrates with dielectric permittivity ($1 \le \varepsilon r \le 6$) and height ($0.1\text{mm} \le h \le 3\text{mm}$) using the waveguide simulator is briefly explained and a continuous function fitted to this data set is built up using SR, finally validation will be given. The third section is devoted to the design of NURA using SR, which is made from the 3D Printer's material PLA with $\varepsilon r=2.4$ at the operation frequency 10GHz, alongside of fabrication by 3D printer. Finally, the work ends with conclusions.

II. SYMBOLIC REGRESSION AND APPLICATION TO NURA

Symbolic Regression (SR) is used to discover mathematical expressions of functions that can fit the given data based on the rules of accuracy, simplicity, and generalization. This method builds a model consisting of solely an accurate analytical expression formed recombining the ready base functions using some evolutionary algorithms such as Genetic Programming (GP) [6], Gene Expression Programming (GEP) [23], Grammatical Evolution (GE) [24], Analytic Programming (AP) [25], and some optimization problems [26-27]. The main advantage of SR is that it does not require any specific structure or parameter, instead reveals intrinsic relationships within the dataset letting its patterns. Thus this analytical model enables a designer a rapid optimization and analysis of the complicated electromagnetic devices instead using computationally inefficient commercial full wave simulators. In this work, SR in the design stage that is based on GP. Main principle of GP based SR is such that expressions (Eqs. 1-5) are represented in chromosomes like syntactic trees. The syntactic tree form of Eq. (1) is given in Fig. 1 for a better understanding. Based on GA principles, new individuals (children) whose representations are in fact new expressions which are evaluated by fitness, are created either by random generators, or by exchanging parent's parts by crossover or mutation operators. As an example for SR regression process, the expression given in Eqs. (1-2) are taken as Parents and Eqs. (3-5) are the children of these parents through cross over or mutation operations:

$$P_1 = f(a,b,c,d,e) = \sin\left(\frac{ab}{c}\right) + \sqrt{d-e} + a^2, \quad (1)$$

$$P_1 = \cos(ab) - e^c + \sqrt{\frac{d}{e}}, \quad (2)$$

$$C_1 = \sin\left(\frac{ab}{c}\right) - e^c + a^2, \quad (3)$$

$$C_2 = \cos(ab) - e^c - 17e, \quad (4)$$

$$C_3 = \sin\left(\frac{ab}{c}\right) + (d-e)^2 + a^2. \quad (5)$$

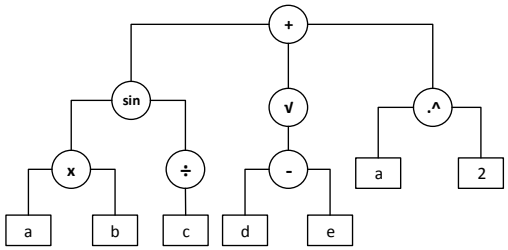

Fig. 1. An example of syntactic tree.

In Fig. 2, a typical NURA design is given in which with the variation of the height in the unit elements the reflection phase is changed and is focus on a desired direction.

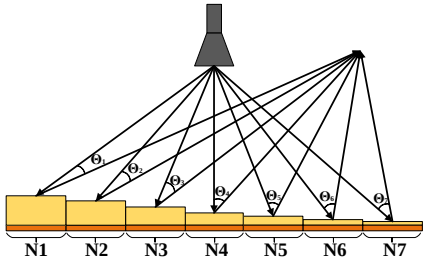

Fig. 2. Centre fed Non-Uniform Reflect Array.

The reflection phase characteristics of a grounded dielectric layer $1 \le \varepsilon_r \le 6$ with variable thickness $0.1 \le h \le 3$ mm are obtained using the H-wall simulator [2] in order to form an analytical expression for X-band (8-12 GHz) applications. For this purpose, the required training and

validation data sets of reflection phase of unit cell given in Fig. 3 are generated by the 3-D EM simulation tool CST.

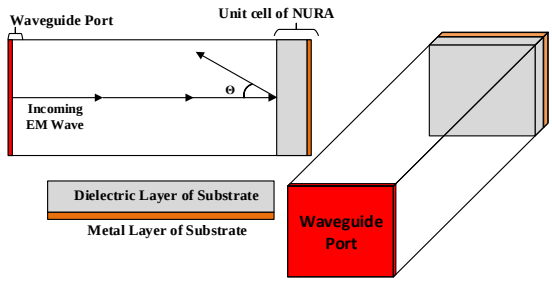

Fig. 3. Unit Cell of the NURA with its simulation setup.

The top and bottom surfaces of the H-wall waveguide simulator are perfectly electric conducting walls, while the right and left walls are perfectly magnetic field walls [2]. The vertically polarized incoming waves will be incident normally onto the element at the end of the waveguide at the broadside direction and then reflected back also at the broadside direction with a set of amplitude and phase information. A series of simulations are carried out to gather training and test data samples Tables 1 and 2 for SR search of Reflection Phase by using CST 3D EM simulation tool, respectively.

Table 1: Training data set for Reflection Phase expression

Parameter	Sample Ranges	Sample Step
Dielectric Permittivity	1-6	0.25
Substrates Height (mm)	0.3-3	0.1
Frequency (GHz)	8-12	0.5
Total	5292	

Table 2: Test data set for Reflection Phase expression

Rogers	ε_r	Height (mm)	Frequency (GHz)	Total
4003	3.55	0.305, 0.406, 0.508 0.813, 1.524	8-12	12012
4350	3.66	0.338, 0.76, 1.52	8-12	
5870	2.33	0.127*, 0.381, 0.508, 0.787, 1.575 3.175*	8-12	

*Values out of training dataset range.

The 5292 data in Table 1 are used as the training data in Eureqa environment [6] to perform SR search. The following commands are used to start the SR search:

- Use data points equally for training and validation purposes;
- Use all basic formula blocks;
- Use all exponential blocks;
- Use Mean Absolute Error as error-metric (Default).

Thus, the targeted analytical expression for Reflection Phase (RP) is obtained as a function of dielectric constant ε_r, height h, frequency f as follows:

$$RP = 541.73 - \frac{3.1\varepsilon_r^{\,2}(hf)^4}{10^6} - \frac{0.5}{h} + \frac{0.62 + 0.019(hf)^2}{0.97 + \varepsilon_r} - (45.59 + 2.68h)f \,. \quad (6)$$

The performance of the obtained expression is validated by Eureqa itself, however we also validated accuracy of the model using approximately 12.000 additionally test data belonging to the typical X-band substrates as given in Table 2, even we also tested extrapolation performance. In this analysis, the common error-metrics measures are employed which are Mean Absolute Error (MAE), Relative Mean Error (RME) and Maximum Error (MXE) as given in Eqs. (7-9) for both training and test data:

$$MAE = \frac{1}{N}\sum_{i=1}^{N}\left|T_i - P_i\right|, \quad (7)$$

$$RME = \frac{1}{N}\sum_{i=1}^{N}\frac{\left|T_i - P_i\right|}{\left|T_i\right|}, \quad (8)$$

$$MXE = \max(T_i - P_i) \,. \quad (9)$$

Table 3: Performance of Analytical Expression

Error Metric (Degree)	Training Data	Test Data
MAE	0.27	0.1027
RME	0.0006	0.0003
MXE	13.96	0.3586

Results of the performance measures of Eq. (6) are presented at Table 3 alongside of Figs. 4-5 of reflection phase versus variable substrate height for typical ε_r, f values as compared with CST values.

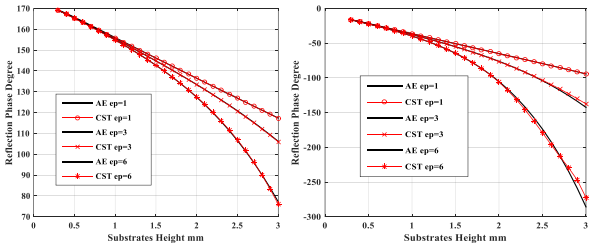

(a) (b)

Fig. 4. Reflection Phase Characteristics for variable dielectric permittivity and height for: (a) 8 GHz and (b) 12 GHz.

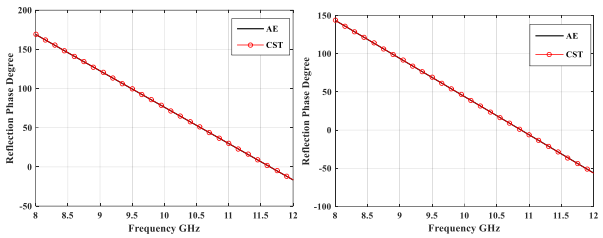

Fig. 5. Reflection Phase Characteristic for Rogers: (a) 4003 (h=0.305, ε_r =3.55), and (b) 5870 (h=1.575, ε_r =2.33).

III. 3D FABRICATION AND EXPERIMENTAL WORK

Fast and accurate prototyping process of microwave devices and antennas have an extreme importance for design process. In today's RF and microwave technology, there is an ever-increasing demand for higher level of fast, low cost and accurate prototyping. One of the most recent innovation for fast and accurate prototyping is 3D printing technology. 3D printing is a method of manufacturing in which materials, such as plastic or metal, are deposited onto one another in the form of layers to produce a three dimensional object, such as a pair of eye glasses or other 3D objects. To date, 3D printing has primarily been used in engineering to create engineering prototypes.

In this work, firstly the 3D model is exported in ".STL" file format, so that the CEL Robox® Micro [28] (Fig. 6) can create its code for printing of the prototype. Also, in case of large structure models, the model can be sliced into smaller parts, where in here, the prototyped antenna model given in Fig. 7 was sliced into smaller size parts (1/12). The material used for 3D printer is PLA "Black as Night" [29] with a dielectric constant of 2.4 and the printing accuracy (printed layer height) is chosen as 0.1 mm for the best quality printing results.

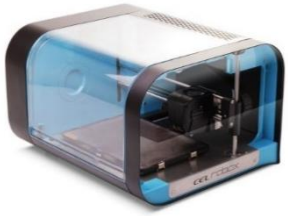

Fig. 6. CEL Robox® Micro manufacturing platform [28].

Applying the same process given in Section II, a new and simpler Reflection Calibration Characteristic having almost 360^0 phase range is obtained using SR Eureqa with the 270 CST data in Table 4 where for the substrate height variation is taken between 0.5-10 mm which is considered as 0.1 mm sample steps:

$$Phase = 1.88 + \frac{21.2}{h} - \left(0.022h^2 - 0.51h + 3.19\right)h^3 \,. \quad (10)$$

Table 4: Training data set for Limited Reflection Phase expression

Parameter	Sample Ranges	Sample Step
Substrate Height (mm)	0.5-10	0.1
Dielectric Permittivity	2.4	
Frequency (GHz)	10	
Total	270	

Since the NURA is symmetric with respect to the center, thus Table 5 gives heights of the quadratic NURA being divided 10 segments and starting from the corner point. The values given in Table 5, are necessary compensation values at each element using the Eq. (10) to convert spherical wave to the plane wave [1]. Thus, a pencil beam in the normal direction of the RA plane, is achieved by designing the height of each RA cell using the Reflection Phase Calibration Characteristic in Fig. 8, to reflect the incident wave independently with a phase compensation proportional to the distance from the phase centre of the feed-horn as well-known from the classical array theory [1].

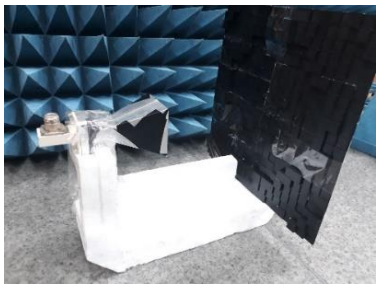

Fig. 7. Prototyped 3D printed NURA.

Table 5: Parameter values of quadratic NURA in (mm)

ID	1	2	3	4	5	6	7	8	9	10
1	1.7	1.7	1.7	2.8	3.9	5	6.3	8.7	2.4	4.4
2	1.7	1.7	2.2	3.2	4.1	5.2	6.6	9.2	2.7	4.7
3	1.7	2.2	2.9	3.7	4.6	5.7	7.3	1.7	3.3	5.1
4	2.8	3.2	3.7	4.5	5.3	6.5	8.6	1.9	4	5.7
5	3.9	4.1	4.6	5.3	6.3	7.8	1.7	3.2	4.8	6.7
6	5	5.2	5.7	6.5	7.8	1.7	2.8	4.3	5.9	8.3
7	6.3	6.6	7.3	8.6	1.7	2.8	4.2	5.5	7.3	1.7
8	8.7	9.2	1.7	1.9	3.2	4.3	5.5	7.1	1.7	3.2
9	2.4	2.7	3.3	4	4.8	5.9	7.3	1.7	3.1	4.8
10	4.4	4.7	5.1	5.7	6.7	8.3	1.7	3.2	4.8	6.4

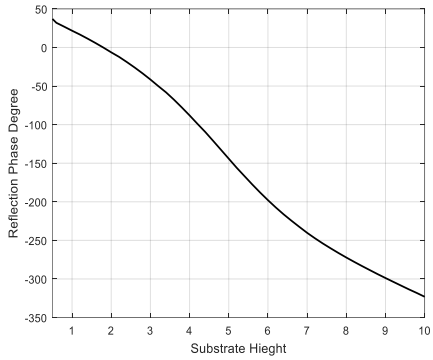

Fig. 8. Reflection phase calibration characteristic of material with dielectric permittivity of 2.4 at 10 GHz.

In Figs 9-10, the measurement results of the prototyped NURA design are presented. As it can be observed from the measurement results, the VSWR characteristics of the NURA is below 2 in all X band. Also, the design has a gain of almost 22dB at 10 GHz. The gain measurement results of NURA, show a 1 dB gain bandwidth of almost the 21% and confirm the promising characteristics of such radiating element. The feed is prime focus, positioned with an F/D = 0.66.

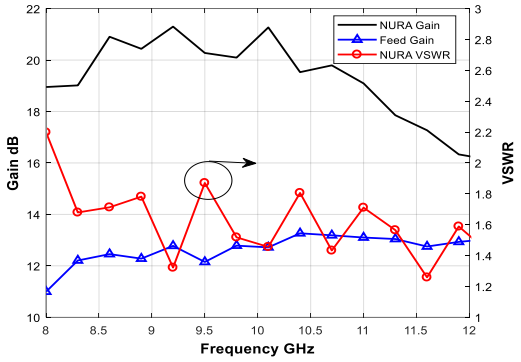

Fig. 9. Measured NURA Characteristics Gain-VSWR, over Frequency band.

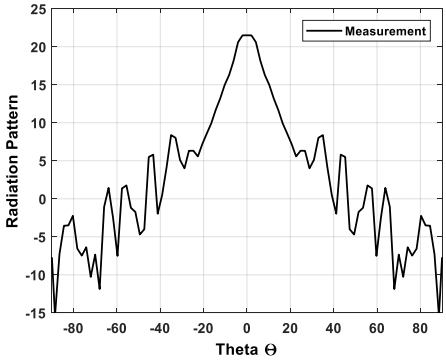

Fig. 10. Measured Far Field Gain performance of NURA at 10 GHz.

IV. CONCLUSION

In this work, a novel regression SR and prototyping method which is 3D printing is applied to the realization of the Non-Uniform Reflect-Array (NURA). As it can be seen from the results, SR is used as a successful tool for building an accurate analytical expression for the reflection phase calibration characteristic of NURA that is used in a fast design optimization and performance analysis. The required amount of training data is comparable with the counterpart regression methods [12], in spite of this, a model consisting of a solely single analytical expression is resulted revealing the intrinsic relationships of the data set using the existing data patterns. Therefore, this method can be efficiently employed in the accurate, fast modelling and design optimization of electromagnetic devices in the form of analytical expressions. The training and test data is also share publicly in [30].

In the realization step, the designed NURA is prototyped by using 3D printer technology where the PLA material can be easily shaped and create unit cell at printing accuracy of 0.1 mm per layer. Thus, by this mean the prototyping cost of NURA design can be reduced drastically both in means of time and ease of manufacturing. Measurements of the mismatching and radiation properties of the realized NURA are resulted to be agreed with the novel theoretical performances.

ACKNOWLEDGEMENT

We would like to express our special thanks of gratitude to the Research Fund of the Yildiz Technical University for founding our research under project number FAP-2018-3427, TÜBİTAK 2211/A, to Aktif Neser Elektronik, and Nutonian, Inc. for providing researcher's licenses for our use.

REFERENCES

[1] D. M. Pozar and T. A. Metzler, "Analysis of a reflect array antenna using microstrip patches of variable size," *Electronics Letters*, vol. 27, pp. 657-658, 1993.

[2] J. Huang and J. A. Encinar, *Reflect Array Antennas*. Wiley-IEEE Press, ISBN: 978–0470–08491–4, 2007.

[3] F. Güneş, S. Nesil, and S. Demirel, "Design and analysis of Minkowski reflectarray antenna using 3-D CST Microwave Studio-based neural network model with particle swarm optimization," *International Journal of RF and Microwave Computer-Aided Engineering*, vol. 23, no. 2, pp. 272-284, Mar. 2013. (DOI: 10.1002/mmce.20711).

[4] F. Güneş, S. Demirel, and S. Nesil, "A novel design approach to X-band Minkowski reflectarray antennas using the full-wave EM simulation-based complete neural model with a hybrid GA-NM algorithm," *Radioengineering*, vol. 23, no. 1, Apr. 2014.

[5] M. Moeini-Fard and M. Khalaj-Amirhosseini, "Non-

uniform reflect-array antennas," *Int. J. RF and Microwave Comp. Aid. Eng*., vol. 22, pp. 575-580, 2012.

[6] Eureqa 1.24.0 (2015). Available: http://www.nutonian.com/products/eureqa/demo/contact/

[7] J. R. Koza, *Genetic Programming*. MIT Press, ISBN 0-262-11189-6, 1998.

[8] J. R. Koza, F. H. Bennet, D. Andre, and M. Keane, *Genetic Programming III*. Morgan Kaufnamm Pub., ISBN 1-55860-543-6, 1999.

[9] M. Schmidt and M. Lipson, "Distilling free-form natural laws from experimental data," *Science*, vol. 324, no. 5923, pp. 81-85, 2009.

[10] V. Ceperic, N. Bako, and A. Baric, "A symbolic regression-based modelling strategy of AC/DC rectifiers for RFID applications," *Expert Systems with Applications*, vol. 41, iss. 16, pp. 7061-7067, 2014.

[11] M. M. Hasan, A. Sharma, F. Johnson, G. Mariethoz, and A. Seed, "Correcting bias in radar Z-R relationships due to uncertainty in point rain gauge networks," *Journal of Hydrology*, 2014. DOI: http://dx.doi.org/10.1016/j.jhydrol.2014.09.060

[12] P. Mahouti, F. Güneş, M. A. Belen, and S. Demirel, "Symbolic regression for derivation of an accurate analytical formulation using "big data": An application example," *ACES Journal*, vol. 32, no. 5, May 2017.

[13] P. Nayeri, M. Liang, R. A. Sabory-Garcia, M. Tuo, F. Yang, M. Gehm, H. Xin, and A. Z. Elsherbeni, "3D printed dielectric reflectarrays: Low-cost high-gain antennas at submillimeter waves," *IEEE Trans. Antennas Propag*., vol. 62, no. 4, pp. 2000-2008, Apr. 2014.

[14] J.-M. Floch, B. El Jaafari, and A. El Sayed Ahmed, "New compact broadband GSM/UMTS/LTE antenna realized by 3D printing," *The 9th European Conference on Antennas and Propagation*, Lisbon, Portugal, Apr. 2015.

[15] A. G. Lopez, E. L. C. Ernesto, R. Chandra, and A. J. Johansson, "Optimization and fabrication by 3D printing of a volcano smoke antenna for UWB applications," *7th European Conference on Antennas and Propagation (EuCAP)*, pp. 1471-1473, Apr. 2013.

[16] M. Mirzaee, S. Noghanian, and Y. Chang, "Low-profile bowtie antenna with 3D printed substrate," *Microw. Opt. Technol. Lett*., vol. 59, pp. 706-710, 2017.

[17] M. Ahmadloo and P. Mousavi, "Application of novel integrated dielectric and conductive ink 3D printing technique for fabrication of conical spiral antennas," *IEEE Antennas and Propagation Society International Symposium (APSURSI)*, pp. 780-781, July 2013.

[18] M. Mirzaee, S. Noghanian, L. Wiest, and Y. Chang, "Developing flexible 3D printed antenna using conductive ABS materials," *IEEE International Symposium on Antenna and Propagation and North American Radio Science Meeting 2015*, pp. 1308-1309, July 2015.

[19] B. Y. Ahn, E. B. Duoss, M. J. Motala, X. Guo, S.-I. Park, Y. Xiong, J. Yoon, R. G. Nuzzo, J. A. Rogers, and J. A. Lewis, "Omnidirectional printing of flexible, stretchable, and spanning silver microelectrodes," *Science*, vol. 323, no. 5921, pp. 1590-1593, Mar. 2009.

[20] J. J. Adams, S. C. Slimmer, J. A. Lewis, and J. T. Bernhard, "3D-printed spherical dipole antenna integrated on small RF node," *Electron. Lett*., vol. 51, no. 9, pp. 661-662, Apr. 2015.

[21] M. A. Belen and P. Mahouti, "Design and realization of quasi Yagi antenna for indoor application with 3D printing technology," *Microw Opt Technol Lett.*, 60 (9), pp. 2177-2181, 2018. https://doi.org/10.1002/mop.31319

[22] Y. C. Toy, P. Mahouti, F. Güneş, and M. A. Belen, "Design and Manufacturing of an X-Band Horn Antenna using 3-D Printing Technology," *8th International Conference on Recent Advances in Space Technologies*, İstanbul, Turkey, 19-22 June 2017.

[23] C. Ferreira, "Gene expression programming: a new adaptive algorithm for solving problems," *Complex Systems*, vol. 13, no. 2, pp. 87-129, 2001.

[24] M. O'Neill and C. Ryan, "Grammatical evolution," *IEEE Transactions on Evolutionary Computation*, vol. 5, no. 4, pp. 349-358, 2001.

[25] Z. Oplatkova and I. Zelinka, "Symbolic regression and evolutionary computation in setting an optimal trajectory for a robot," in *Proceedings of the 18th International Workshop on Database and Expert Systems Applications (DEXA '07), IEEE*, Regensburg, Germany, pp. 168-172, Sep. 2007.

[26] Y. Rahmat-Samii and E. Michielssen, *Electromagnetic Optimization by Genetic Algorithms*. John Wiley & Sons, Inc., 1999.

[27] J. M. Jeevani W. Jayasinghe, J. Anguera, D. N. Uduwawala, and A. Andújar, "Nonuniform overlapping method in designing microstrip patch antennas using genetic algorithm optimization," *International Journal of Antennas and Propagation*, vol. 2015.

[28] Robox by CEL – A micro manufacturing platform, https://www.cel-uk.com/shop/robox-by-cel-a-micro-manufacturing-platform-with-dual-nozzle-fff-head-rbx01/ [23.03.2019].

[29] PLA Filament "Black as Night," Model Number RBX-PLA-BK092.

[30] P. Mahouti, M. Ali Belen, A. Çalışkan, and F. Güneş, "Phase characterization of the nonuniform reflect arrays," *IEEE Dataport*, 2018. [Online]. Available: http://dx.doi.org/10.21227/H2BW8F. Accessed: May 28, 2018.

Asymmetric Band Structure Calculations Using the Plane Wave Expansion Method with Time-Modulated Permittivity

Adam Mock
School of Engineering and Technology
Science of Advanced Materials Program
Central Michigan University
Mount Pleasant, Michigan 48859
mock1ap@cmich.edu

***Abstract*—In this work we show how the plane wave expansion method for calculating the band structure of materials with periodic electric permittivity may be extended to calculate the band structure of periodic materials that also possess a sinusoidal time-modulation. The numerical technique is applied to a structure possessing a synthetic linear momentum which causes unidirectional bandgaps to appear in the band structure. Such devices could be of use for tunable magnet-free isolators in integrated photonics platforms.**

I. Introduction

Electromagnetic devices that allow only one-way wave propagation have many practical uses including in optical isolators [1], antennas [2] and duplexed communication transceivers [3]. Any static linear electromagnetic device is time-reversible and therefore cannot be used for unidirectional wave propagation. However, incorporating a synthetic momentum into the system via directional time-modulation can break time-reversal symmetry and induce one-way electromagnetic wave propagation [4]. Most traditional computational techniques assume static material properties. However, some recent reports have detailed methods for incorporating a sinusoidal time-modulated permittivity into computational electromagnetic tools [5]. In this work we extend the plane wave expansion method for calculating the photonic band structure of static periodic structures to materials that have harmonically time-modulated electric permittivities. With this method we show how a directional spatio-temporal modulation results in an asymmetric (in wavevector) bandstructure that produces unidirectional wave propagation in a range of frequencies.

II. Method

This work is concerned with electric permittivities of the form $\varepsilon(z,t) = \varepsilon_a(z) + \varepsilon_b(z)\cos[2\pi\Omega t + \phi]$ where $\varepsilon_a(z+\Lambda) = \varepsilon_a(z)$ and $\varepsilon_b(z+\Lambda) = \varepsilon_b(z)$ are both periodic in Λ. For one-dimensional material variation, the Maxwell equations become:

$$\frac{\partial E_x(z,t)}{\partial z} = -\mu_0 \frac{\partial H_y(z,t)}{\partial t}, \tag{1a}$$

$$-\frac{\partial H_y(z,t)}{\partial z} = -\varepsilon_0 \frac{\partial}{\partial t}[\varepsilon(z,t)E_x(z,t)]. \tag{1b}$$

If the time derivative in (1b) is expanded, one obtains:

$$-\frac{\partial H_y(z,t)}{\partial z} = -\varepsilon_0\{\varepsilon_a(z)\frac{\partial E_x(z,t)}{\partial t} + \varepsilon_b(z)\cos[\Omega t+\phi]\frac{\partial E_x(z,t)}{\partial t} - \varepsilon_b(z)\Omega\sin[\Omega t+\phi]E_x(z,t)\}.$$

The spatial periodicity motivates the use of a Bloch form, and the time-modulation motivates inclusion of harmonics $\omega + n\Omega$ for integer n. Our ansatz for solution of Eqs. 1 is:

$$E_x(z,t) = \sum_{G,n} E_x(G,n)e^{i(k+G)z}e^{-i(\omega+n\Omega)t}, \tag{2a}$$

$$H_y(z,t) = \sum_{G,n} H_y(G,n)e^{i(k+G)z}e^{-i(\omega+n\Omega)t}, \tag{2b}$$

where $G = m2\pi/\Lambda$ for m integer. Combining Eqs. 2 with Eqs. 1 produces:

$$\mu_0(\omega+n\Omega)H_y(G,n) - GE_x(G,n) = kE_x(G,n), \tag{3a}$$

$$-GH_y(G,n) + \varepsilon_0\sum_{G'}\{\varepsilon_a(G-G')(\omega_0+n\Omega)E_x(G',n) + [e^{i\phi}E_x(G',n+1) + e^{-i\phi}E_x(G',n-1)] = kH_y(G,n), \tag{3b}$$

which is an eigenvalue equation with eigenvalue k and eigenvector made up of the components $E_x(G,n)$ and $H_y(G,n)$. To obtain the bandstructure for these dynamic geometries, a range of frequency values is chosen, and for each frequency, the corresponding eigenvalue k is obtained.

III. Synthetic Momentum

To illustrate the physical properties of time-modulated periodic structures, consider the geometry shown in Fig. 1 (a). The structure consists of a repeating unit cell consisting of three layers each modulated by the same frequency but with relative phase offsets of $2\pi/3$. The phase sequence of 0, $2\pi/3$, $4\pi/3$ from left to right produces a non-zero overlap

Submitted On: September 28, 2018
Accepted On: October 12, 2018

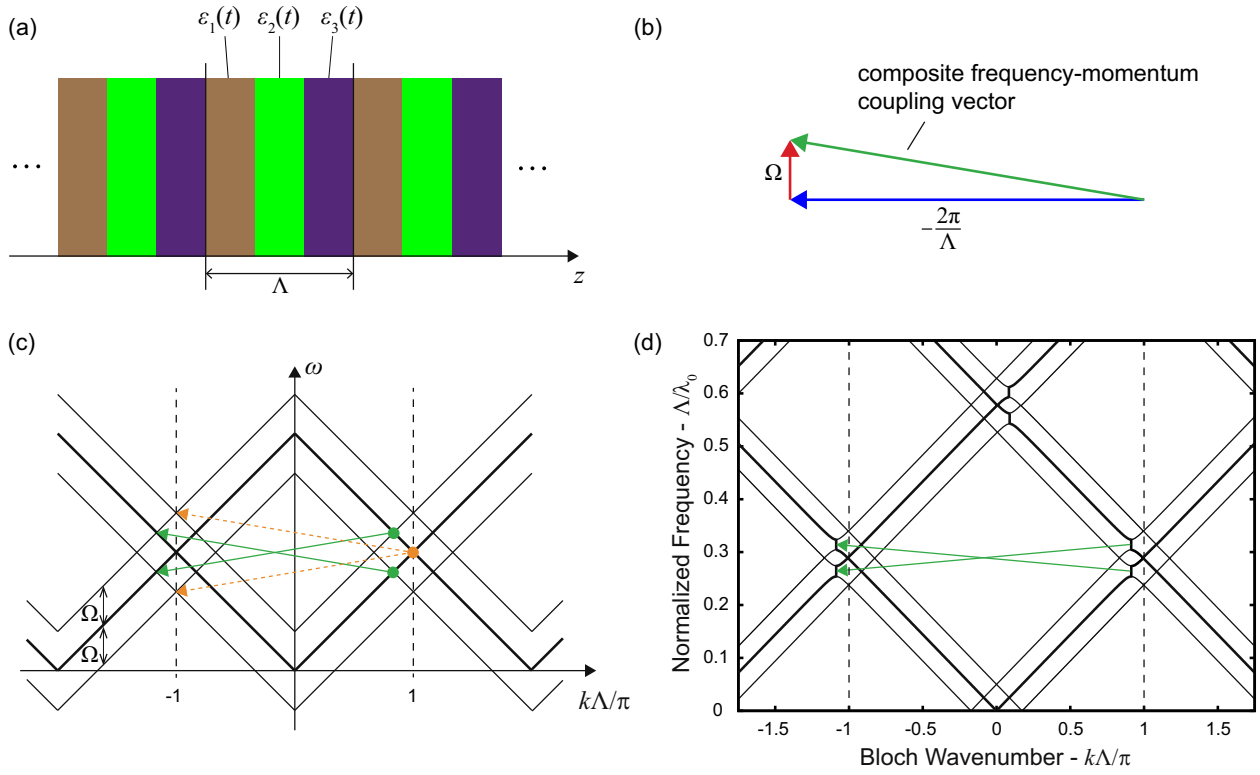

Fig. 1. (a) One-dimensional periodic structure with time-modulated permittivity. $\varepsilon_1(t) = 3.0 + 0.5\cos(\Omega t)$, $\varepsilon_2(t) = 3.0 + 0.5\cos(\Omega t + 2\pi/3)$ and $\varepsilon_3(t) = 3.0 + 0.5\cos(\Omega t + 4\pi/3)$. (b) Mode coupling vector in the spatio-temporally modulated system in (a). (c) The mode-coupling scheme in the empty lattice. The bold line is the fundamental band ($n = 0$) whereas the thin lines correspond to harmonics which is the fundamental band shifted vertically by $\pm n\Omega$ (only $n = 1$ is depicted). (d) The bandstructure of the dynamic geometry shown in (a) using the proposed numerical method.

with the continuous travelling wave modulation of the form $\cos(\Omega t + \frac{2\pi}{\Lambda} z)$ which produces a synthetic momentum pointing toward $-z$. Fig. 1 (b) shows the net momentum-frequency coupling vector. In a static periodic system, the coupling vector would be bidirectional, horizontal and of length $2\pi/\Lambda$. In the time-modulated system, it is unidirectional and tilted up by the amount Ω with concomitant length.

Fig. 1 (c) shows how the mode coupling works in this system. The empty lattice (a lattice with periodicity Λ and time-modulation frequency Ω but $\varepsilon_b \to 0$) is shown. Because of the directionality of the spatio-temporal modulation, the coupling vectors point only from right to left. The green arrows show couplings that result in photonic bandgaps. The green vectors couple band crossings that involve the fundamental band, and, therefore, bandgaps are expected to open at the green dots. The orange vectors show couplings between band crossings, but these bands belong to different order harmonics, and, therefore, no coupling occurs.

Fig. 1 (d) shows the band structure obtained using the proposed method. Indeed one sees bandgaps in the first Brillouin zone corresponding to the points highlighted in Fig. 1 (c). Specifically, there is a bandgap near $k\Lambda/\pi \lesssim 1.0$ but no bandgap near $k\Lambda/\pi \gtrsim -1.0$. This means that incident waves propagating along $+k$ at a frequency in the bandgap will be reflected; whereas, incident waves propagating along $-k$ at a frequency in the same frequency range will be transmitted as if there were no periodic perturbation to the electric permittivity at all. Due to the broken time-reversal symmetry, the band structure is clearly asymmetric in k. Technologically such a device could prove useful in tunable optical isolation particularly in magnet-free integrated photonics platforms.

In conclusion, a technique for calculating the band structure of harmonically time-modulated system is presented. We show how tailored time-modulation can impart a directional synthetic momentum to the field causing unidirectional propagation in these periodic materials.

REFERENCES

[1] D. L. Sounas and A. Alù, "Angular-momentum-biased nanorings to realize magnetic-free integrated optical isolation," ACS Photonics, vol. 1, pp. 198–204, 2014.

[2] Y. Hadad, J. C. Soric, and A. Alù, "Breaking temporal symmetries for emission and absorption," Proceedings of the National Academy of Sciences, vol. 113, no. 13, p. 34713475, 2016.

[3] N. A. Estep, D. L. Sounas, J. Soric, and A. Alù, "Magnetic-free non-reciprocity and isolation based on parametrically modulated coupled-resonator loops," Nature Physics, vol. 10, pp. 923–927, 2014.

[4] S. Taravati, N. Chamanara, and C. Caloz, "Nonreciprocal electromagnetic scattering from a periodically space-time modulated slab and application to a quasi-sonic isolator," arXiv, p. 1705.06311, 2017.

[5] Y. Shi, W. Shin, and S. Fan, "Multi-frequency finite-difference frequency-domain algorithm for active nanophotonic device simulations," Optica, vol. 3, no. 11, pp. 1256–1259, 2016.

Patch Antenna Size-Reduction Parametric Study

Randall L. Musselman [1] and James L. Vedral [2]

[1] Department of Electrical and Computer Engineering
US Air Force Academy, Colorado Springs, CO, 80840, USA
randall.musselman@usafa.edu

[2] Charles Stark Draper Laboratory, Inc. Cambridge, MA, 02139, USA
jvedral@draper.com

Abstract — Size-reduction techniques are applied to a circular UHF patch antenna, by varying parameters to better predict its desired resonant frequency. Specifically, slits are introduced into the patch, which are parametrically varied to determine the optimum slit dimensions for maximum size reduction. Further studies determine the optimum location for the probe feed, to achieve 50Ω input impedance for different slit lengths.

Index Terms — Antenna size reduction, patch antenna slits, slotted UHF antenna.

I. INTRODUCTION

Patch antennas typically resonate with dimensions that are near one-half wavelength, $\lambda/2$ [1], which can be cumbersomely large at UHF frequencies. This large size is reduced by a factor of approximately $1/\sqrt{\varepsilon_r}$ by using higher permittivity ($\varepsilon = \varepsilon_o\varepsilon_r$) material. However, the decreased bandwidth caused by higher permittivity can make this approach unattractive. In an attempt to focus on size-reduction techniques rather than exotic materials, we chose to use common FR4 printed circuit-board material for our UHF patch-antenna size-reduction analysis. FR4 has relative permittivity, ε_r of approximately 4.5 at UHF, which should reduce patch dimensions nearly 50%, if no other size-reduction techniques were used.

The addition of slits in a circular patch antenna has proven to reduce the patch radius by nearly an additional 50%, beyond the effects of permittivity alone [2,3,4]. However, the choice of slit dimensions has so far been an iterative approach. In this paper, we present the results of a parametric study of the slit dimensions in Fig. 1, in order to aid in the optimum design of size-reduced circular patch antennas.

II. SLOTTED PATCH DESIGN

To compare the results of the parametric study, an ordinary circular patch, without slits, was simulated in ANSYS Electromagnetic Desktop, a commercial finite element solver (i.e., HFSS). The patch was simulated with a radius, r of 4.5cm; dielectric thickness of 1.7mm; dielectric constant, ε_r of 4.5; and was probe fed at a distance of 0.45cm from the center of the patch. The theoretical resonant frequency can be calculated by:

$$f = \frac{1.8412c}{2\pi r\sqrt{\varepsilon_r}}. \quad (1)$$

where f, is the resonant frequency, and c is the speed of light [1]. Equation 1, along with the previously defined parameters, predicts resonance at 921MHz; HFSS simulations showed the resonance to be 914MHz.

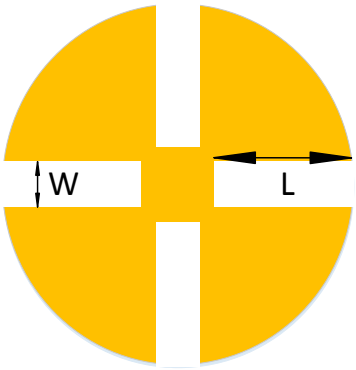

Fig. 1. Mask of the slotted circular patch antenna. L is the slit length and W is the slit width.

III. SLIT DIMENSION OPTIMIZATION

The length, L and width, W of the slits in Fig. 1 were incrementally changed in HFSS, in an attempt to estimate their effects on the resonant frequency. These two parameters were considered independently to determine if each could be fine-tuned for different purposes, even though their combined dimensions add to the increased effective circumference of the circular patch. As expected, increasing both L and W decreased the resonance frequency. However, the input impedance, at a particular feed point, appeared to change unpredictably as both W and L were increased. When the width, W was held at

Submitted On: September 28, 2018
Accepted On: October 12, 2018

a constant 1*mm* and the slit length, *L* was increased, the resonant frequency monotonically decreased. This statement is equivalent to stating that for a fixed resonant frequency, the patch antenna can be reduced in size as the slit lengths increased. The input impedance also changed as the slit dimensions changed; however, we found that it could be fine-tuned, by simply changing the location of the feed point.

For the first parametric study, we fixed the location of the feed point, in order to avoid introducing too many degrees of freedom at once, thus isolating the effects of the slit length and width. The corresponding reduction in the patch radius, as *L* increased, can be seen in Fig. 2, indicating that the only limit to the size-reducing benefit of increasing slit length, *L* is the physical radius itself, i.e., increasing *L* continued to reduce the physical size of the antenna until *L* nearly equaled the radius, *r*. Of course at that point, the patch would be separated into two halves. The data in Fig. 2 suggests that the original patch radius, which resulted in a resonant frequency of 914*MHz*, can be made resonant at 470*MHz* by the addition of slits that almost meet in the center of the patch, i.e., 98% of the radius, *r*. Without these slits, the circular patch antenna would require a radius of 8.8cm in order to be resonant at 470*MHz*, instead of 4.5cm (51% of 8.8*cm*).

As previously suggested, the slit width, *W* can also be increased, in order to decrease the patch radius for a desired resonant frequency. To explore the effects of changing slit width, *W*, the next parametric study held the slit length, *L* at a constant 95% of the radius, *r*.

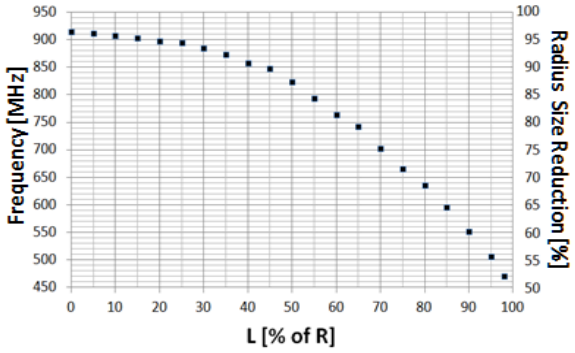

Fig. 2. Change in resonant frequency/size reduction vs. change in slot length, *L*.

One pair of slits were removed, as shown in Fig. 3, simply to allow the width of the slits to increase without interfering with the orthogonal pair, and thus cutting the patch into four quadrants. The symmetric pair of vertical slits, depicted in Fig. 1, are only necessary for circular polarization. In fact, for certain unique applications, a second resonant mode could be created by making one pair of slits different lengths than their orthogonal counterparts. However, the polarization for this second resonant mode would be orthogonal to the first.

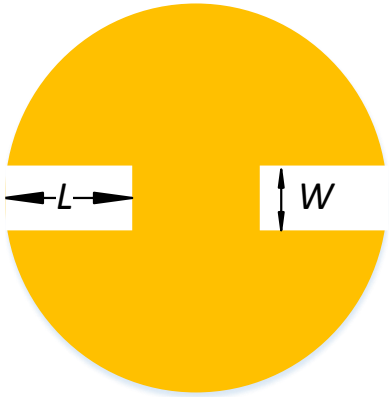

Fig. 3. Two-slit patch allows *W* to vary with fewer restrictions.

The size-reducing benefit of increasing slit width, *W* while holding *L* constant, is evident in Fig. 4, due to the fact that the resonant frequency decreased as the slit width increased. However, this is not without some design limitations. Four orthogonally oriented slits shown in Fig. 1 are required for circular polarization, which limit the relationship between *L* and *W*, in order to prevent the slits from touching one another. Also, the input impedance changes significantly with changes in *W*, when the feed-point location is held constant. In order to counteract this impedance variation, one would need to find the optimal feed point for each *L*/*W* combination, in order to achieve a desirable input impedance. Although time consuming, finding the optimal feed point can be done using known methods [5,6]. These methods are constrained only by the available area to place the feed point. Various combinations of *W* and *L* were simulated in HFSS, with the geometry depicted in Fig. 1, in order to find a predictable pattern [7]. The results, shown in Fig. 5, indicate that as *W* was varied for several different values of *L*, a well-behaved relationship emerged for small values of *W*/*L*, i.e., $W < 0.05L$. As *W* exceeded 0.05*L*, the effects of *L* appear to dominate that of *W*, i.e., diminishing returns for increasing *W* beyond 0.05*L*.

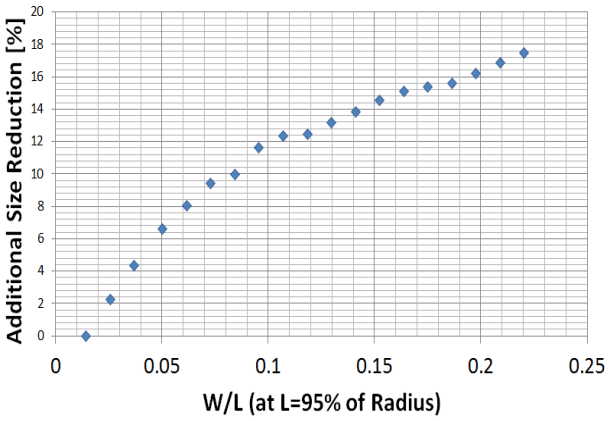

Fig. 4. Size-reducing benefit of increasing width, *W*. *L*=95% of patch radius, *r*.

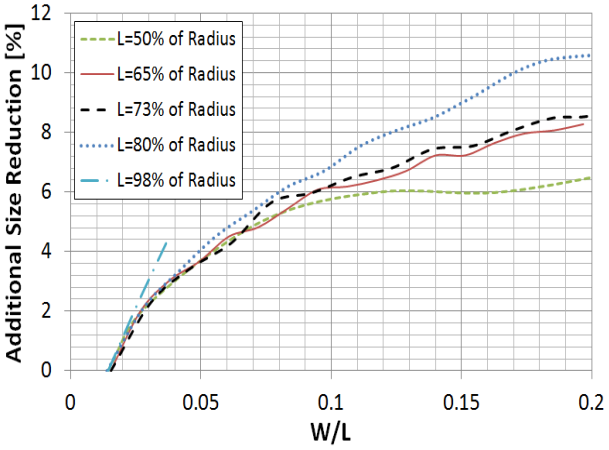

Fig. 5. Size reducing benefit of increasing width, *W* for *L* = 50%, 65%, 73%, 80%, and 90% of radius, *r*.

IV. FEED LOCATION

As previously stated, a desired impedance match can be found for each slit-length/width combination, by relocating the probe feed point. To find a trend in the feed location that would aid in the design of circular patches with slits, we explored the optimum feed-point location as a percentage of patch radius, for successively longer slits. The slit width of the circular patch was fixed at 1.37% of the radius (0.62mm). Using HFSS, the antenna feed point was relocated along the dashed radial line in Fig. 6, for successively longer slit lengths, *L* in order to achieve a matched input impedance of 50Ω. Figure 7 plots the relationship between the probe-feed location and the slit length, both normalized to the patch radius.

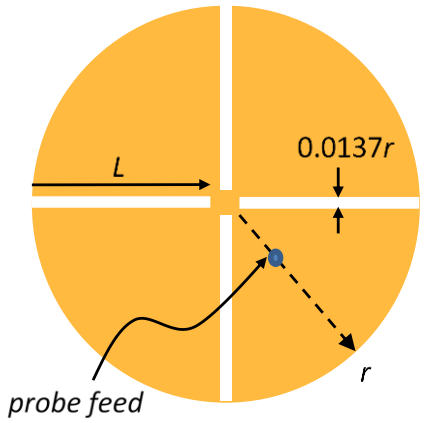

Fig. 6. Probe feed relocated along dashed radial line, to match input impedance to 50Ω, for each successively longer length, *L* for fixed width, *W* = 0.0137*r*.

It is clear by the nearly linear trend shown in Fig. 7 that the probe feed must be relocated closer to the center of the patch, as the slit length increases, i.e., for maximum size reduction [8]. If the slit length is 98% of the radius, the patch antenna must be probe fed at 14.5% of the radius, from the center of the patch. In this case, the slit width-to-length ratio is 0.014. From the results in Fig. 5, increasing the slit width up to 0.03*L* would result in beneficial patch-size reduction. Therefore, the optimum slit width should be set to 0.03*r*, for a slit length of 0.98*r*. The simulated S_{11} parameter for this design is shown in Fig. 8. The radiation pattern is shown in Fig. 9.

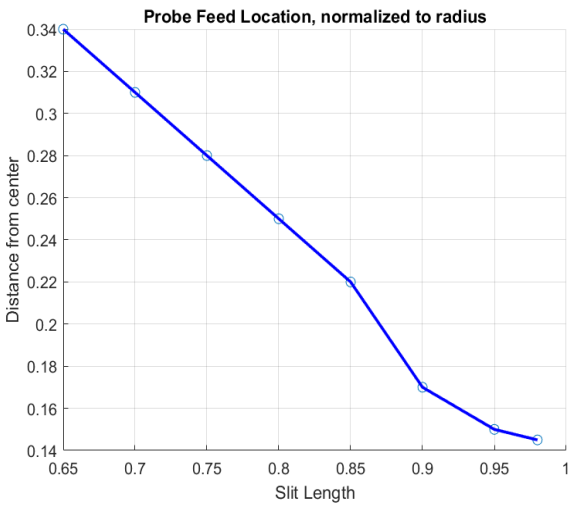

Fig. 7. Probe-feed location vs. slit length, *L* both normalized to the patch radius, *r*.

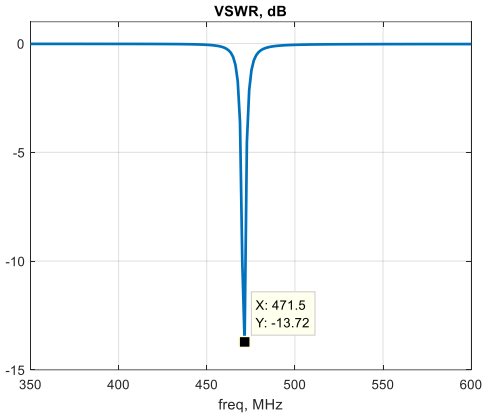

Fig. 8. S_{11} parameter, of the slotted circular patch, with radius r = 4.5*cm*, simulated with HFSS.

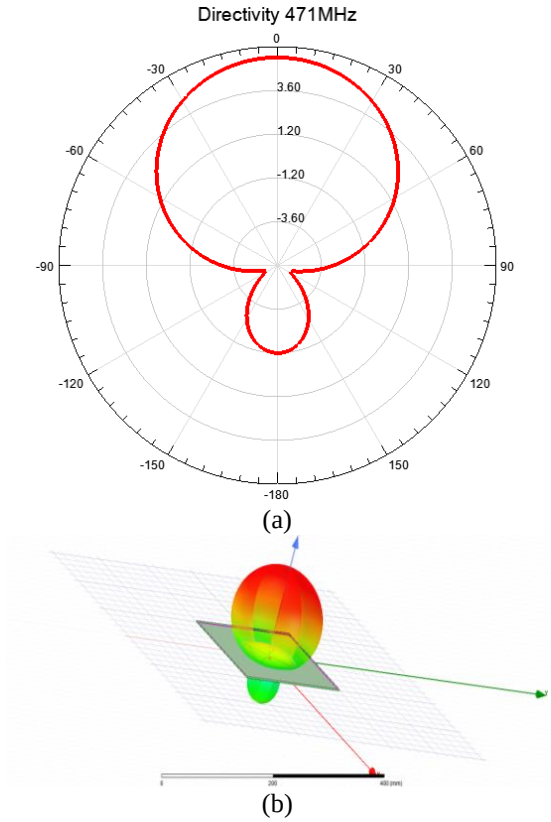

Fig. 9. Patch antenna radiation pattern: (a) E-plane and (b) 3D plot.

V. CONCLUSION

A parametric study of slit dimensions in a circular patch antenna was performed in order to characterize the size-reduction benefits of these slits. It was shown that as the slit length and width increase, the resonant frequency of the patch decreases. However, as the slit width reaches approximately 5% of its length, the slit length tends to dominate the size-reducing benefits. Near optimum size reduction can be achieved by making the slit lengths as close to the radius as possible, without actually touching, while the slit width is less than 5% of its length. This will maximize the available patch area, in order to locate the feed point for minimum *SWR*.

Another parametric study was conducted, in order to find the optimum probe-feed location for various slit lengths. The slit width was set to 1.37% of the radius, while the slit length was varied. The trend was linear, until the feed point approached very close to the center of the patch. This nearly linear trend showed that for increasing slit lengths, the optimum feed point should be located closer to the center of the patch, in order to achieve a matched 50Ω input impedance.

Summarizing the results of these parametric studies, the best results for reducing the physical size of circular patch antennas can be obtained by (1) making the slit length as long as physically possible, i.e., 98% of the radius; (2) setting the slit width to 3% of the radius (increasing the slit width any further provides diminishing returns and makes impedance matching more difficult); and (3) locating the probe feed at approximately 14% of the radius, from the center of the patch. By following these design rules, a 9-cm diameter, circular-patch antenna was made to resonate at 471*MHz*, with a 50Ω input impedance. That frequency would require a 17.6-cm diameter, i.e., nearly twice the diameter, without slits. This represents a size reduction of approximately 50%, beyond the effects of permittivity alone.

REFERENCES

[1] C. A. Balanis, *Antenna Theory Analysis and Design*. New York, Harper & Row, 1982.

[2] R. L. Musselman, et al., "Adaptive null-steered interference-rejection for a mobile satellite receiver," *IEEE Int'l. Symp. on Phased Array Syst. and Tech.*, Boston, Oct. 2010.

[3] R. L. Musselman, et al., "Circular array for satcom interference rejection," *IEEE Int'l. Conf. on Wireless Inf. Tech. and Syst.*, Maui, Nov. 2012.

[4] R. L. Musselman and J. L. Vedral, "Circular patch antenna size-reduction technique." *17th Biennial IEEE Conf. on Electromagnetic Field Computation*, Miami, 2016.

[5] P. C. Sharma and K. C. Gupta, "Analysis and optimized design of single feed circularly polarized microstrip antennas," *IEEE Trans. on Antennas Propag.*, vol. 31, no. 11, Nov. 1983.

[6] F. Raval, J. Makwana, and P. T. Patel, "Optimization of resonance frequency of circular patch antenna at 5 GHz using particle swarm optimization," *International Journal of Advances in Engr. & Tech.*, May 2011.

[7] R. L. Musselman and J. L. Vedral, "Patch antenna size-reduction parametric study," *International Applied Computational Electromagnetics Society*

(*ACES*) *Symposium*, Firenze, Italy, Mar. 2017.

[8] R. L. Musselman and J. L. Vedral, "Size-reduced patch-antenna feedpoint parametric study" *International Applied Computational Electromagnetics Society (ACES) Symposium*, Denver, CO, Mar. 2018.

Patch Antenna with Triangular Slitted Corners

Anıl Elakaş, Gürhan Ali Irmak, and Mert Şencan
Department of Electrical & Electronics Engineering
Istanbul Commerce University
Istanbul, Turkey

Ş. Taha Imeci
Department of Electrical & Electronics Engineering
Int. University of Sarajevo, Bosnia and Herzegovina

Tahsin Durak
Department of Technology, NSU, Norfolk, VA

***Abstract*—In this paper, a microstrip patch antenna with triangular slits was designed, simulated, fabricated and tested. The proposed patch antenna, with operating frequency of 9.5 GHz, is targeted. Simulation is carried out using Sonnet Suites. Antenna has 9.68 dB gain at 9.5 GHz with corresponding reflection coefficient of -19 dB. Proposed antenna introduces size reduction for patch antennas. The measurements of the fabricated patch antenna well corroborate the simulation results.**

Keywords*—Asymmetric triangular slit, gain, microstrip patch antenna.

I. INTRODUCTION

Microstrip patch antennas (MPAs) have sparked tremendous research efforts with great prospects and they have been widely integrated into many wireless applications. The salient features of MPAs have made them the ultimate candidates for applications, such as space born systems, radar or satellite systems, where lightweight and cost-effective antennas with low-profile and simple geometrical structure for ease of fabrication and installation are required. With the ever-increasing need for mobile communication and the emergence of many systems, it is important to design broadband antennas to cover a wide frequency range. The design of an efficient wide band small size antenna, for recent wireless applications, is a major challenge. Microstrip patch antennas have found extensive application in wireless communication system owing to their advantages such as low profile, conformability, low-cost fabrication and ease of integration with feed networks [1].

A factor that influences the performance of an antenna is the structure of the patch. At present is a predictable necessitate for a packed in scrap aerial having a most favorable geometrical construction which is effortlessly to make and gives a towering aerial gain point. The corners were truncated square microstrip antenna is mainly used for single patch designs. In his work, Gokten obtained the compactness of the proposed circular polarization design because of inserting four slits of equal lengths at the corners [2].

A solitary nourish spherical schism procedure of the corners shortened square microstrip antenna is mainly used in single patch designs and array designs [3].

Microstrip patch antennas are usually designed to eliminate the imaginary part of the input impedance. Edge fields are also important and they bring an additional length to the antenna. This length depends on the relative permittivity of the dielectric, dielectric height and patch width [4].

A microstrip patch antenna is made up of a radiating patch on one side of dielectric substrate while has a ground plane on the other side [5]. Substrate is located over a large metallic sheet called ground plane [6]. The suitable substrate is the one with a low dielectric constant, a large thickness compared to the operating wavelength and low loss (low tan δ) because in the realization of microwave circuits, the goal is to minimize the radiation of the line in free space and therefore have a substrate which the electromagnetic energy is concentrated in the dielectric (more precisely in the cavity formed by the metal strip and the ground plane). So a thick substrate increases the power radiated by the antenna, reduces losses by Joule effect and improves the bandwidth of the antenna. Permittivity of substrate is a critical parameter in controlling band width, efficiency, and radiation pattern of patch antenna. However, higher dielectric constant also reduces bandwidth and radiation efficiency [7].

The Wireless communication is mainly concentrated on the antenna size. The reduced antenna size results in small sensor node and low power consumption [8]. So the antenna can be a low profile, low powered and high frequency micro strip antenna. The antenna size is proportional to $1/\sqrt{\xi}r$ [9]. Small antenna concept is the one which uses planar antenna and by adjusting the electrical size the desired center frequency can be obtained [10].

The operation frequency of the reference antenna is 2.285 GHz. The size of the antenna is 80 mm × 80 mm. The coaxial probe feeding technique is used. Reference antenna has a parasitic element strip under the main part and antenna has 4 asymmetric triangular slits [11].

In this paper, the parasitic element strip in the reference antenna was removed, the number of slits was reduced from 4 to 2 and the feed position was moved to the middle of the antenna with input impedance of about 50 Ω. The size of the antenna is reduced to 21.6 mm × 21.6 mm and simulation air thickness is 10 mm. As a result of the analysis, operation frequency is 9.5 GHz. Slits angle and feeding point were changed to optimize the maximum gain, lowest return loss and smaller antenna dimensions.

The rest of this paper is organized as follow: the design steps are described in Section II, results and conclusion are presented

Submitted On: September 29, 2018
Accepted On: October 13, 2018

in Section III of the paper.

II. Design Steps

The geometrical shape of the triangular microstrip patch antenna with triangular slits design in the first step is as shown in Fig. 1. The size of the antenna is 43 mm × 42.5 mm and the box size is 700 mm × 700 mm. Initial design didn't achieve targeted center frequency of 9.5GHz.

In the second stage, the design in Fig. 2 was created by optimizing triangular slit measurements and determining the feed point location. So many iterations of simulation were carried out to achieve optimization. As a result of optimized simulation, S11 value was measured as -10.06 dB at 2.3 GHz and -19.56 dB at 4.7 GHz, antenna gain was measured as 4.82 dB at 2.3 GHz and 7.30 dB at 4.7 GHz. Yet, this design didn't achieve targeted center frequency of 9.5GHz as well.

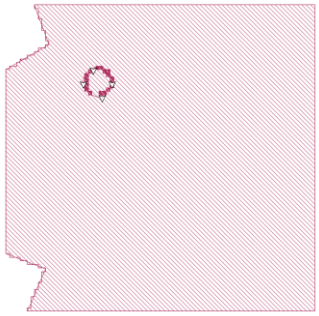

Fig. 1. First design.

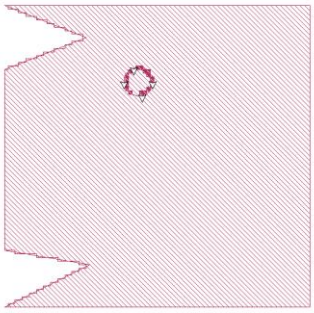

Fig. 2. Second design.

At the third step, the final design in Fig. 3 was created by reducing the antenna size and changing the feed position. The proposed patch antenna with triangular slits is designed using RT/duroit 6002 substrate with dielectric constant of 2.94, thickness *h=0.76mm* and loss tangent of 0.0012.

As a result of successive iteration of simulations, the S11 value is measured as -19.65 dB and the antenna gain is measured as 9.68 dB at 9.5 GHz, and the reverse polarity value is measured as -6.03 dB. All dimensions are provided in Fig. 3. Optimized antenna was fabricated and carried out the measurements. Fabricated antenna is shown in Fig. 4.

The S11 value obtained as a result of the final design is shown in Fig. 5. Simulation S11 is -19.65 dB but measured S11 is -11 dB. Correlation of input impedance between measured and simulation is acceptable, both in good agreement at resonant frequency. Although simulation shows -19 dB input impedance, it is difficult to achieve such input impedance from manufactured patch antenna.

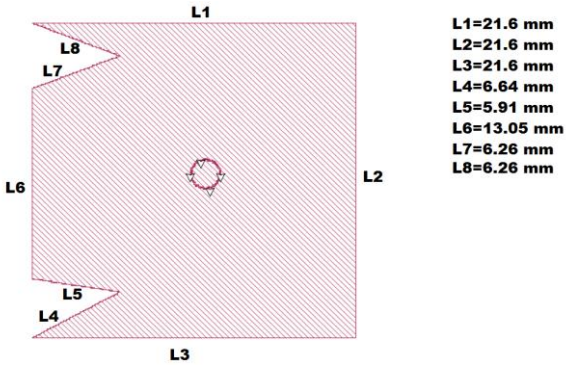

Fig. 3. Final design.

Fig. 4. Fabricated and measured antenna.

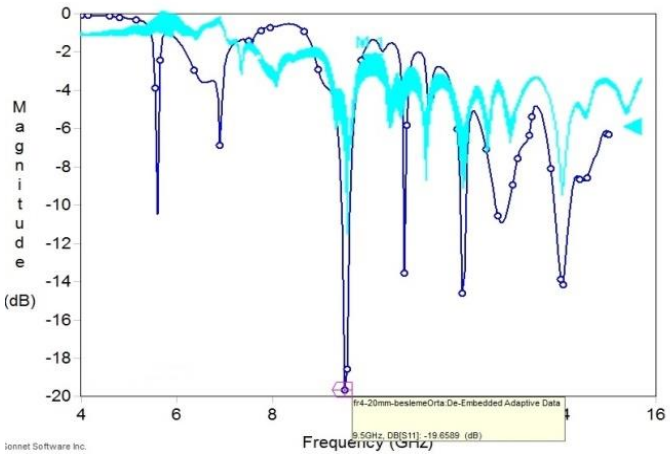

Fig. 5. Input match (|S11|) of the proposed antenna.

III. Results and Conclusion

A comprehensive parametric study of a triangular shaped double-slit microstrip patch antenna has been carried out to understand the effects of various triangular slits. The simulations results are performed using Sonnet software [12]. The frequency range of Sonnet simulation was between 0-15 GHz. Studied antenna resonance frequency is 9.5 GHz. As a result of studies and numerous simulations on the geometry of the slit, optimum dimensions have been determined. When results of simulations made by taking air thickness 10 mm and insulation thickness 1.6 mm, simulated and measured S11 were matched well at the resonance frequency of 9.5 GHz, where measured S11 is slightly lower than -11 dB and gain is 9.68 dB. Smaller antenna size was achieved due to triangular slits.

Gain of the antenna (E Theta - E Phi) radiation diagram occurred at resonance frequency at 9.5 GHz is given in Fig. 6. As seen in this graph, cross-polarization level is less than -7 dB and co-polarization has nice wide beamwidth.

Measurement is carried out in Yeditepe Universities testing facility. Measurement setup is shown in Fig. 7.

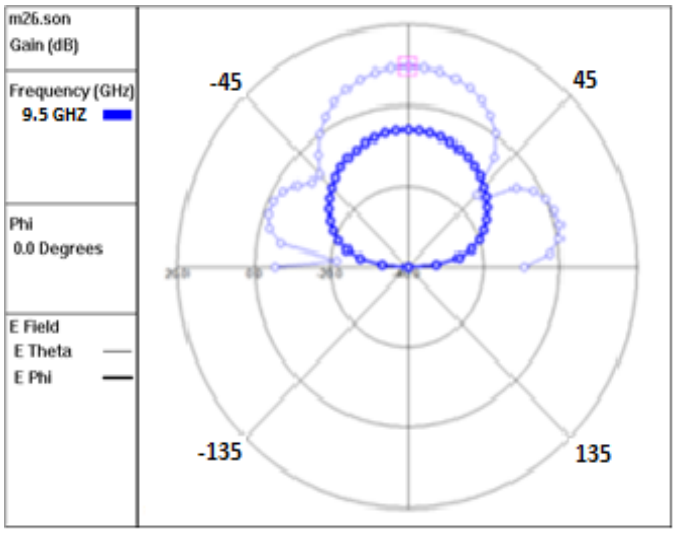

Fig. 6. E Theta – E Phi radiation pattern of patch antenna at 9.5 GHz.

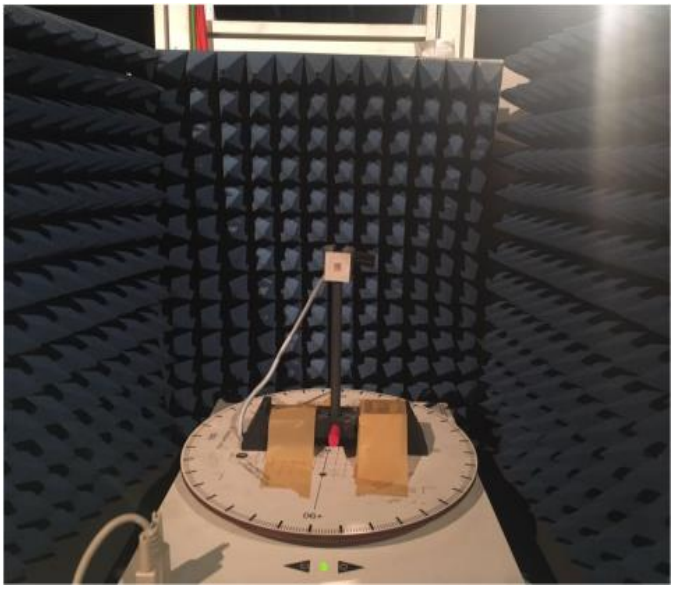

Fig. 7. Measurement setup.

The flux density at 9.5 GHz is given in Fig. 8. It is clear that current is crowded near the discontinuities of two triangular slits and around the feeding point as expected. Furthermore, color pattern shows an approximate wavelength of the antenna.

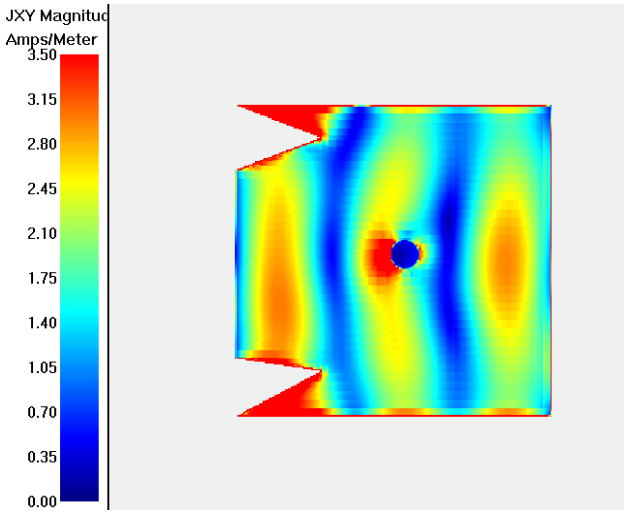

Fig. 8. The current distribution at 9.5 GHz.

ACKNOWLEDGMENT

We would like to thank Sonnet Software and Yeditepe University for their services.

REFERENCES

[1] C. A. Balanis, Antenna Theory Analysis and Design. 2nd edition, John Wiley & Sons, Inc., 1997.

[2] M. Gokten, F. Altunkilic, and H. Son, "Compact Circularly Polarized Patch Antenna," Department of 26th Annual Review of Progress in Applied Computational Electromagnetics April 26-29, 2010 - Tampere, Finland ©2010 ACES Electrical Engineering and Computer Science, Syracuse University, NY, Spring 2002.

[3] T. Imeci and A. Saral, "Corners Truncated Microstrip Patch Antenna," Halic University, Department of Electronics and Communication Engineering, ACES, Tampere, Finland, 2010.

[4] R. E. Munson, "Conformal microstrip antennas and microstrip phased arrays," IEEE Trans. Antennas Propagation, vol. AP-22, pp. 74-78, Jan. 1974.

[5] R. K. Sharan, S. K. Sharma, A. Gupta, and R. K. Chaoudhary, "An edge tapered rectangular patch antenna with parasitic stubs and slot for wideband applications," Wirel. Pers. Commun., 86, pp. 1213-1220, 2016.

[6] O. Mahmoodian, "Enhancing microstrip patch antenna performance by using high impedance surfaces (HIS)," Bull. Env. Pharmacol. Life Sci., 5(6), pp. 11-14, 2016.

[7] A. Bendaoudi and Z. Mahdjoub, "Comparative study of patch antenna loaded with slot split-ring resonators on different substrate materials," Photon Network Communication, vol. 35, pp. 195-203, 2018.

[8] D. M. Pozar, "Microstrip antenna coupled to microstripline," Electron Lett., vol. 21, no. 2, pp. 49-50, Jan. 1995.

[9] C. G. Kakoyiannis, G. Stamatiou, and P. Constantinou, "Small square meander-line antennas with reduced ground plane size for multimedia WSN nodes," Antennas and Propagation, 2009, EuCAP 2009, 3rd European Conference on, IEEE, 2009.

[10] P. M. Shanmugam and M. A. M. Mohamed, "A CPW Fed Star Shaped Patch Antenna for WSN Applications," Second International Conference on Electrical and Communication Technology, 2016, pp. 182-187.

[11] M. T. Islam, M. Cho, M. Samsuzzaman, and S. Kibria, "Compact antenna for small satellite applications," IEEE Antennas and Propagation Magazine, vol. 57, no. 2, pp. 30-36, Apr. 2015.

[12] Sonnet Suites, ver. 17.52, www.sonnetsoftware.com

Anıl Elakaş completed B.Sc. degree in Electrical and Electronics Engineering, Istanbul Commerce University, Istanbul, Turkey. His current research areas are, microwave antennas and embedded circuits.

Gürhan Ali Irmak completed B.Sc. degree in Electrical and Electronics Engineering, Istanbul Commerce University, Istanbul, Turkey. His current research areas are, microwave antennas and control circuits.

Mert Şencan completed B.Sc. degree in Electrical and Electronics Engineering, Istanbul Commerce University, Istanbul, Turkey. His current research areas are, microwave antennas and wireless communications.

Şehabeddin Taha İmeci received the B.Sc. degree in Electronics and Communications Engineering from Yildiz Technical University, Istanbul, Turkey in 1993, and the M.S.E.E. and Ph.D. degrees from Syracuse University, Syracuse, NY in 2001 and 2007, and Associate Professorship degree from Istanbul Commerce University, Istanbul Turkey in 2014, respectively. Imeci was appointed as Full Professor in Int. Univ. of Sarajevo in Nov. 2017. He is working as Vice-Rector in Sarajevo. He was with Anaren Microwave Inc., East Syracuse, NY from 2000 to 2002, and Herley Farmingdale, New York from 2002 to 2003, and PPC, Syracuse, NY from 2003 to 2005, and Sonnet Software Inc., Liverpool, NY from 2006 to 2007. He was a Teaching Assistant in the Department of Electrical Engineering and Computer Science at Syracuse University from 2005 to 2006. He authored two books and published more than 150 papers. His current research areas are, microwave antennas and electromagnetic theory.

Tahsin Durak received his B.Sc. degree in Electrical and Electronics Engineering from Gazi University, Ankara, Turkey in 1992, his first M.S degree in Electrical Engineering from Fairleigh Dickinson University, NJ, USA in 1998, his second M.S. and Ph.D. degrees in Electrical Engineering from Syracuse University, NY, USA in 2001 and 2008 respectively. From 2000 until 2001, he was with Philips Broadband Networks, Manlius, NY, USA. He was a Teaching Assistant in the Department of Electrical Engineering and Computer Science at Syracuse University from 2001 to 2004. He joined Norfolk State University, Norfolk, VA, in 2010 as an Assistant Professor. Since 2014, he has been working in industry as a Staff Engineer, Electrical Engineering Manager and Engineering Director. He continues to teach at local universities as an Adjunct Faculty. He has several US patents in the area of Microwave, RFID and IIOT. His current research areas are microwave antennas, RFID technologies, IIOT solutions, industrial automations, remote controls, industrial machine to machine communication techniques and protocols. Durak has been a Member of the IEEE.

Patch Antenna with Multiple Slits and Circular Shaped

Furkan Atalah
Department of Electrical & Electronics Engineering
Istanbul Commerce University, Istanbul, Turkey

S. Taha Imeci
Department of Electrical & Electronics Engineering
Int. University of Sarajevo, Bosnia and Herzegovina

Mustafa Imeci
Department of Electrical & Electronics Engineering
Yildirim Beyazit University, Ankara, Turkey

Tahsin Durak
Department of Technology, NSU, Norfolk, VA

Oguzhan Gungor
Department of Electrical & Electronics Engineering
Selcuk University, Konya, Turkey

***Abstract*—In this paper, a circular shaped ground-fed patch antenna is designed, simulated, built and tested. The operating antenna frequency is 14.6 GHz with -15.68 dB input and 8.14 dB gain. Furthermore, the antenna have multiple slits in a circular main body, and also supported with triangle and rectangle shapes. The measurements of the fabricated patch antenna matches the simulation results.**

***Keywords*—Circular shaped antenna, microstrip patch antenna, single resonance.**

I. INTRODUCTION

The recent revolution in electronic circuits pressured the antenna designers to come up with small, lightweight and low cost radiating structures. This requirement led to the invention of several antenna structures, of which, printed microstrip antenna received a lot attention in recent years [1].

Due to their low-profile and conformable geometry, they are widely used as embedded antennas in handheld wireless devices and military equipment [2]. However, intensive research is required to improve the inherent disadvantages of this antenna, such as: narrow bandwidth, low efficiency, spurious feed radiation, poor polarization purity and limited power capacity [3].

A microstrip patch antenna is made up of a radiating patch on one side of dielectric substrate while has a ground plane on the other side [4]. Substrate is located over a large metallic sheet called ground plane [5]. The suitable substrate is the one with a low dielectric constant, a large thickness compared to the operating wavelength and low loss because in the realization of microwave circuits, the goal is to minimize the radiation of the line in free space and therefore have a substrate which the electromagnetic energy is concentrated in the dielectric (more precisely in the cavity formed by the metal strip and the ground plane). So a thick substrate increases the power radiated by the antenna, reduces losses by Joule effect and improves the bandwidth of the antenna. Permittivity of substrate is a critical parameter in controlling band width, efficiency, and radiation pattern of patch antenna. However, higher dielectric constant also reduces bandwidth and radiation efficiency [6].

Microstrip patch antennas are usually designed to eliminate the imaginary part of the input impedance. Edge fields are also important and they bring an additional length to the antenna. This length depends on the relative permittivity of the dielectric, dielectric height and patch width [7].

Microstrip patch antennas are versatile structures which can be modified by adding simple slots either “parallel to radiation edges” or “parallel to resonance edges” in the design structure to overcome selected limitations of conventional patch antennas. The antenna can provide improved bandwidth enhancement, under certain conditions, while maintaining many of the desirable features of conventional patches. However, it is difficult to determine or predict resonant frequencies and bandwidths especially when the changes in terms of position of slots and the widths of slots are relatively small. As a result, machine algorithms can be applied to interpret the relationship between inputs and outputs of the system. Depending on the problem, the appropriate algorithms can be selected to estimate the outputs [8].

During the design process, the motivations involved in selecting different antenna components are as follows: Microstrip antennas can be incorporated in various geometries, such as: rectangular, circular, triangular, annular patches and others [9].

Circular patch is the second most popular shape and can be easily analyzed and modified to produce a range of impedance values, radiation patterns and frequencies of operation. Among the four most popular feed techniques, coax-fed method has low spurious feed radiation and is easy to match [10].

Organization of this paper is as follows: the design steps are described in Section II, results and conclusion are presented in Section III of the paper.

Submitted On: September 30, 2018
Accepted On: October 13, 2018

II. Design Steps

The size of the antenna is 20 × 31 mm. Substrate material is FR- 4 and the thickness is 1 mm (ε_r = 4.4, dielectric loss tangent = 0.0018 mm). The thickness of air in simulation is taken 3 times of the thickness of the FR-4, (3 mm). The top view of the antenna is in Fig. 1, and Table I shows the antenna parameters and the values.

TABLE I. Antenna Parameters and Values

Dimension	Length
A	*1.5mm*
B	*6mm*
C	*4.3mm*
D	*11mm*
E	*2.5mm*
F	*5mm*
G	*5.8mm*
H	*8.3mm*
I	*1.2mm*
J	*19.3mm*
K	*8mm*

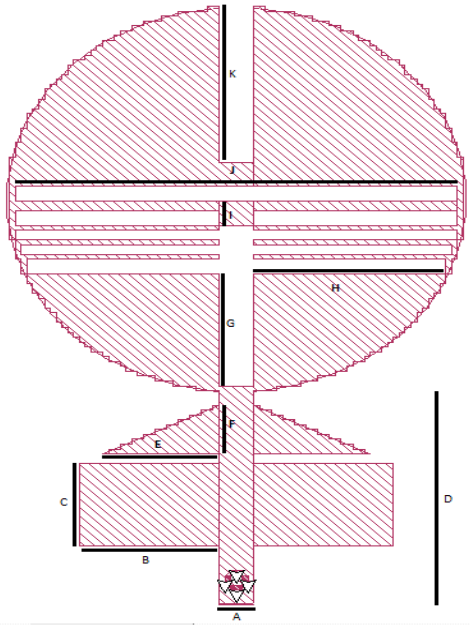

Fig. 1. Top view of the simulated circular antenna.

III. Simulation and Parametric Study

In the initial design, we had circular shape and a standard port, there was almost no gain with -35 dB reflection coefficient at 14.6 GHz. Later, triangular sections and square sections are added. Then we added some slits in circular shape, as a result of successive iteration of simulations, changing the feeding location and relocating the triangular and rectangular shapes to design, we optimized the antenna. As a result of optimization, lower input matches and high gains are maintained. In Fig. 2, input reflection coefficient, S_{11} is shown at 14.6 GHz, and -15.69 dB magnitude was found as simulation and -13.9 dB as measurement. In Fig. 3, gain graph is shown and +8.14 dB simulated and 6.1 dB measured result was found at 14.6 GHz. Fig. 4 has the manufactured antenna. Table II shows variations of gap between slits.

Measurement is carried out in Yeditepe Universities testing facility. Measurement setup is shown in Fig. 5.

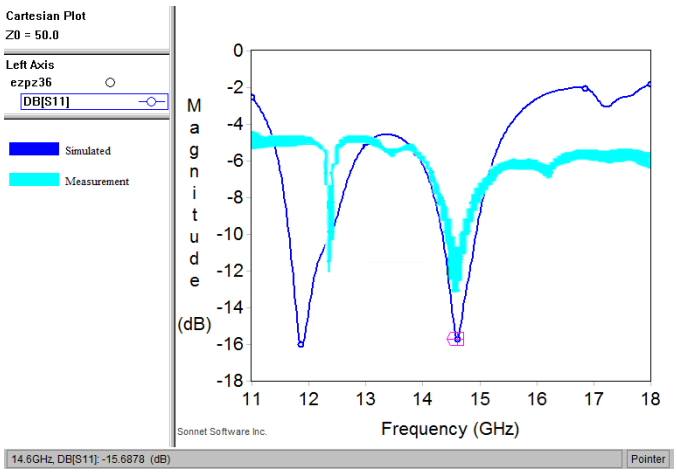

Fig. 2. S11 graph.

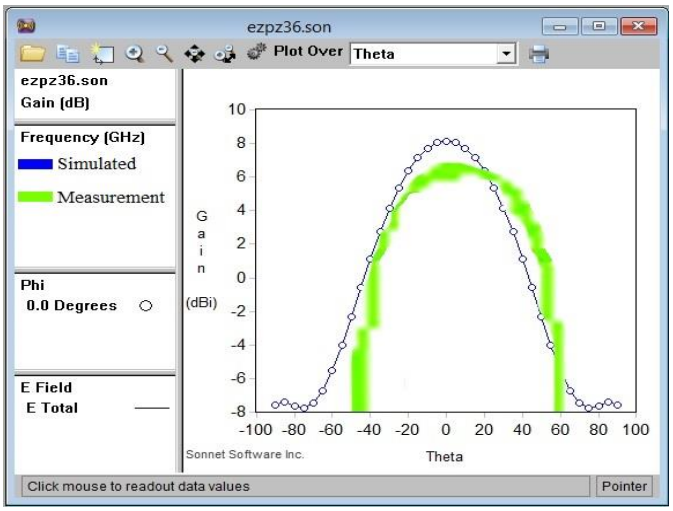

Fig. 3. Radiation pattern (gain) graph.

Fig. 4. Top view of the produced antenna.

TABLE II. FREQUENCY-GAIN-INPUT MATCH WITH MODIFIED GAP

Gap between Slits	Frequencies	Gain (dB)	Input Match (dB)
0.25	*10.5 GHz*	*6.35*	*–16.8*
	11.3 GHz	*7.22*	*–14.72*
0.5	*10.7 GHz*	*6.68*	*–15.77*
	11.9 GHz	*7.32*	*–10.5*
0.75	*11.9 GHz*	*6.88*	*–8.5*
	14.6 GHz	*8.14*	*–15.69*
1	*12.7 GHz*	*5.33*	*–8.45*
	13.5 GHz	*5.77*	*–9.25*
	14.44 GHz	*6.11*	*–18.22*

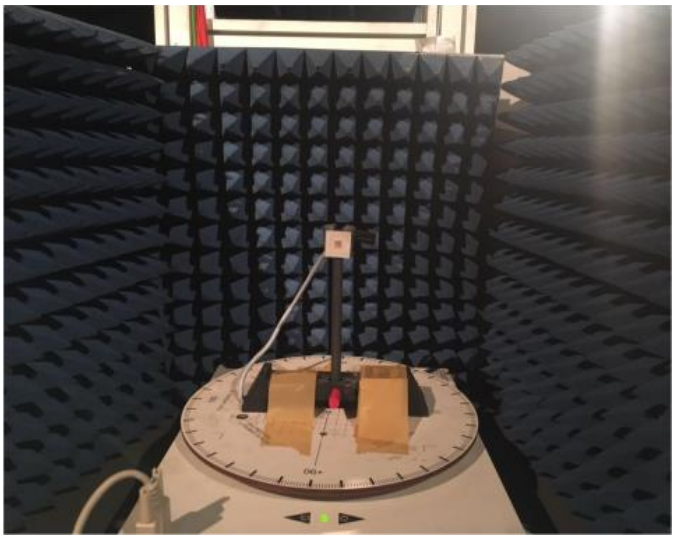

Fig. 5. Measurement setup.

IV. CONCLUSION

Our aim is to find higher gain values for fabrication of circular shaped patch antenna for single band operations by simulating with different geometrical values mentioned in the article. A comprehensive parametric study has been carryout out. Throughout our design steps in this conclusion part of this project we can say that designing circular ring shaped antenna is not easy due to limitations, dielectric material type, gain - frequency relation, feeding type and technique. Even small changes on the antenna may have drastic outcomes, these changes have to be noted each time and avoid being applied again to cause further confusion during design. It should also be noted that in circular ring shaped patch antennas making slits, gaps inside of circular ring and pincering current to the sides by increasing the length of slits and gaps increases gain.

By varying the thickness, different parameters of the designed antenna can be optimized. Proposed antenna can be used in different applications such as in wireless communication and S band applications.

The simulations results are performed using Sonnet software [11].

ACKNOWLEDGMENT

We would like to thank Sonnet Software and Yeditepe University for their services.

REFERENCES

[1] A. Dalli, L. Zenkouar, and S. Bri, “Comparison of circular sector and rectangular patch antenna arrays in C-Band,” Journal of Electromagnetic Analysis and Applications, vol. 4, no. 11 pp. 457-467, 2012.

[2] S. Malisuwan, J. Sivaraks, N. Madan, and N. Suriyakrai, “Design of microstrip patch antenna for Ku-band satellite communication applications,” International Journal of Computer and Communication Engineering, vol. 3, no. 6, Nov. 2014.

[3] A. Thakur, M. Chauhan, and M. Kumar, “Effect of substrate relative dielectric constant on bandwidth characteristics of line feed rectangular patch antenna,” International Journal of Engineering Science Invention Research & Development, vol. 1, iss. 10, e-ISSSN: 2349-6185, Apr. 2015.

[4] R. K. Sharan, S. K. Sharma, A. Gupta, and R. K. Chaoudhary, “An edge tapered rectangular patch antenna with parasitic stubs and slot for wideband applications,” Wirel. Pers. Commun., 86, pp. 1213-1220, 2016.

[5] O. Mahmoodian, “Enhancing microstrip patch antenna performance by using high impedance surfaces (HIS),” Bull. Env. Pharmacol. Life Sci., 5(6), pp. 11-14, 2016.

[6] A. Bendaoudi and Z. Mahdjoub, “Comparative study of patch antenna loaded with slot split-ring resonators on different substrate materials,” Photon Network Communication, vol. 35, pp. 195-203, 2018.

[7] R. E. Munson, “Conformal microstrip antennas and microstrip phased arrays,” IEEE Trans. Antennas Propagation, vol. AP-22, pp. 74-78, Jan. 1974.

[8] M. A. Layegh, C. Ghobadi, and J. Nouriia, “The optimization design of a noval slotted microstrip patch antenna with multi-bands using adaptive network-based fuzzy interference system,” MDPI Technologies, vol. 5, pp. 174-185, Apr. 2017.

[9] A. Deshmukh, V. Pandit, R. Colaco, and R. Doshi “Dual band dual polarized modified circular microstrip antenna,” International Conference on Circuits, Systems, Communication and Information Technology Applications (CSCITA), 2014.

[10] R. Garg, P. Bhatia, I. Bhal, and A. Ittipibon, Microstrip Antenna Design Handbook. Artech House, 2001.

[11] Sonnet Suites, ver. 17.52, www.sonnetsoftware.com

Furkan Atalah completed B.Sc. degree in Electrical and Electronics Engineering, Istanbul Commerce University, Istanbul, Turkey. His current research areas are, microwave antennas and circuits design.

Mustafa Imeci completed B.Sc. degree in Electrical and Electronics Engineering, Yildirim Beyazit University, Ankara, Turkey. His current research areas are, microwave antennas and digital signal processing.

Oguzhan Salih Gungor is pursuing his B.Sc. degree in Electrical and Electronics Engineering, Selcuk University, Konya, Turkey. His current research areas are, microwave antennas and couplers.

Şehabeddin Taha İmeci received the B.Sc. degree in Electronics and Communications Engineering from Yildiz Technical University, Istanbul, Turkey in 1993, and the M.S.E.E. and Ph.D. degrees from Syracuse University, Syracuse, NY in 2001 and 2007, and Associate Professorship degree from Istanbul Commerce University, Istanbul Turkey in 2014, respectively. Imeci was appointed as Full Professor in Int. Univ. of Sarajevo in Nov. 2017. He is working as Vice-Rector in Sarajevo. He was with Anaren Microwave Inc., East Syracuse, NY from 2000 to 2002, and Herley Farmingdale, New York from 2002 to 2003, and PPC, Syracuse, NY from 2003 to 2005, and Sonnet Software Inc., Liverpool, NY from 2006 to 2007. He was a Teaching Assistant in the Department of Electrical Engineering and Computer Science at Syracuse University from 2005 to 2006. He authored two books and published more than 150 papers. His current research areas are, microwave antennas and electromagnetic theory.

Tahsin Durak received his B.Sc. degree in Electrical and Electronics Engineering from Gazi University, Ankara, Turkey in 1992, his first M.S degree in Electrical Engineering from Fairleigh Dickinson University, NJ, USA in 1998, his second M.S. and Ph.D. degrees in Electrical Engineering from Syracuse University, NY, USA in 2001 and 2008 respectively. From 2000 until 2001, he was with Philips Broadband Networks, Manlius, NY, USA. He was a Teaching Assistant in the Department of Electrical Engineering and Computer Science at Syracuse University from 2001 to 2004. He joined Norfolk State University, Norfolk, VA, in 2010 as an Assistant Professor. Since 2014, he has been working in industry as a Staff Engineer, Electrical Engineering Manager and Engineering Director. He continues to teach at local universities as an Adjunct Faculty. He has several US patents in the area of Microwave, RFID and IIOT. His current research areas are microwave antennas, RFID technologies, IIOT solutions, industrial automations, remote controls, industrial machine to machine communication techniques and protocols. Durak has been a Member of the IEEE.

Probe Feed E-Shaped Patch Antenna at 4.87 GHz

Ezgi Kucuk and Burak Bayram
Department of Electrical & Electronics Engineering
Istanbul Commerce University
Istanbul, Turkey
Ezgikucuk1994@gmail.com, brk.bayrm@gmail.com

S. Taha Imeci
Department of Electronical Engineering, International University of Sarajevo, Sarajevo, Bosnia and Herzegovina
simeci@ius.edu.ba

Tahsin Durak
Department of Technology, NSU, Norfolk, VA
tahsind@gmail.com

***Abstract*—In this paper, E-shape microstrip patch antenna for wireless communication is designed, simulated, built and tested. The operating frequencies of antenna are 2.97 GHz and 4.85 GHz, the substrate FR4 is used for proposed antenna with dielectric constant 4.01 and 1.7mm thickness. Two parallel slots are cut to perturb the surface current path to achieve dual resonance. The E-shape has return loss of -28 dB and -14.03 dB at operating frequencies 2.97 GHz and 4.85 GHz respectively. Designing and simulation of this antenna has been done by the help of Sonnet Software. This antenna is fed by a co-axial probe feeding. In this paper, the effects of length difference among antenna legs has been studied.**

***Keywords*—Co-axial feed antenna, compact wireless antenna, E-shaped antenna, microstrip patch antenna, patch antenna, U slot antenna.**

I. INTRODUCTION

In the recent world, the demand for low weight, cheap, low profile and efficient antennas is increasing microstrip patch antenna and are more popular for meeting these requirement in several applications. The main problem encountered with these such kind of patch antennas is high value of return loss and smaller impedance bandwidth, but theses problem can be solved by using some new designing approaches [1].

The microstrip patch antenna offers the advantages of low profile, ease of fabrication, and compatibility with integrated circuit technology. They can be designed to operate over a large range of frequencies (1- 40 GHz) and easily combine to form linear or planar arrays [2].

The current wireless communication systems have to fulfill the demands such as high data rates, increased capacity, high quality, and high reliability for different applications. Multiple-input-multiple-output (MIMO) systems provide the suitable technology for these requirements without the necessity of additional bandwidth or transmit power by spreading multiple antennas, with sufficient element spacing, the correct number of elements, and appropriate array geometry or topology [3–5].

A microstrip patch antenna is type of antennas that offers a low profile, i.e., thin and easily manufacture ability, which provides great advantages over traditional. An E-shaped patch antenna is easily formed by cutting two slots from a rectangular shape. By cutting the slots from a patch, gain, return loss and bandwidth of microstrip antenna can be improved. The increased development of wireless communications, the urgency to design low volume, compact, low profile planar configuration and wideband multi-frequency planar antennas become highly desirable. Narrow bandwidth is a serious limitation of these microstrip patch antennas. Different techniques are used to overcome this narrow bandwidth limitation. These techniques include increasing the thickness of the dielectric substrate, decreasing dielectric constant and using parasitic patches [6].

For the E-shaped patch antenna, two parallel slots are incorporated to introduce a second resonant mode, resulting in a dual band antenna. If the feed point is located at the tip of the center arm as in [6–8], the second resonant mode will be introduced at a lower frequency than the fundamental resonant mode [7].

Various methods have been studied and analyzed for suppression of mutual coupling and improvement of the isolation between the antennas, including the neutralization technique [9, 10], using electromagnetic band gap (EBG) structures [11–13] or etching slots or slits from the ground and forming defected ground structures (DGSs) [14, 15]. In neutralization technique, an additional coupling is introduced by connecting the two antennas with a thin metal strip. This additional coupling cancels out the coupling between the antennas by properly adjusting the length of the metal strip, and the isolation between the two input ports can be significantly enhanced. In the DGS method, even if the DGS adds an extra degree of freedom in the design, the removal of the metal strip from the PEC or some portions of the substrate require precise micromachining techniques, and otherwise, performance degradation can occur. Also, the DGS itself is a slot antenna, which causes an increase in back lobe radiation [16].

Research on microstrip antenna in the 21st century aims at size reduction, increasing gain, wide bandwidth, multiple functionality and system-level integration. Significant research work has been reported on increasing the gain and bandwidth of microstrip antennas [6-8]. In this paper, an attempt has been

Submitted On: September 30, 2018
Accepted On: November 4, 2018

made to design a single band microstrip antenna without any geometrical complexities [8].

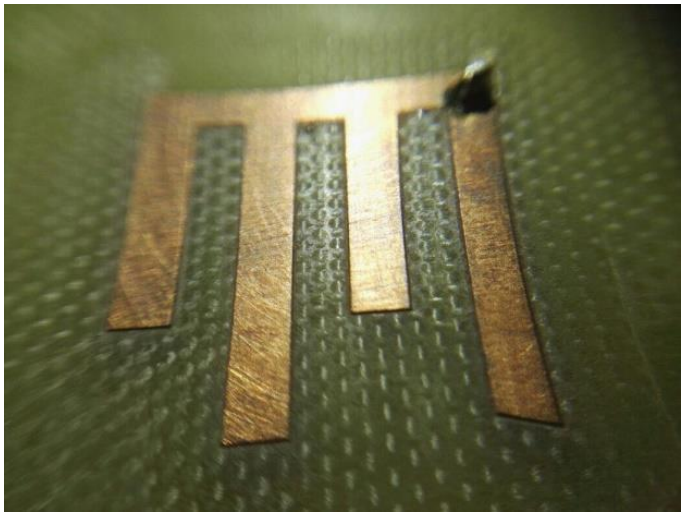

Fig. 1. Top view of the fabricated circular antenna.

II. Design Steps

The size of the antenna is 17.0 × 18.0mm. Substrate material is FR- 4 and the thickness of it is 1 mm (εr = 4.01, dielectric loss tangent = 0.0018). The thickness of air is taken as 3 times of the thickness of the FR-4, (3 mm). Top view of the fabricated and measured antenna is shown in Fig. 1.

III. Simulation and Parametric Study

Analyses were performed using Sonnet software [17]. The frequency range is between 1 - 10 GHz. In two different frequency values, -10dB or lower magnitude values were obtained. When the magnitude of S11 is -15.35 dB, gain is +7.27 dB at 2.97 GHz. In second analysis, frequency was 4.87 GHz and S11 was -12.65 dB and gain is +8.86 dB. Results are provided in Table I. When compared with the first antenna, the size of the antenna is changed from 15.0 × 16.8 mm to 17.0 × 18.0 mm. Also change the port position. In Fig. 2, gain-frequency graph is shown and +8.79 gain is found at 4.85 GHz. In Fig. 3, S11 graph is shown and at 4.85 GHz, -14.03 dB magnitude was found. A prototype of this antenna is tested by using an HP8720D network analyzer. Fig. 3 shows the comparison between simulated and measured S-parameters' results of the proposed antenna. It is noticed that there are some difference between the simulation and measurement results. These differences can be considered acceptable as long as its effect on the resonant frequency is not high and the frequency band does not shift much. The discrepancies are mostly due to the insertion loss of SMA connectors, surrounding environment that influences on wave reflection, or the fabrication tolerances.

IV. Conclusion

In this work, E type patch antenna was designed, simulated and fabricated. Compared to the first analysis, in the second analysis there was an increase in the gain value. So, when the frequency is at 2.97 GHz, S11 is -15.35 dB and the gain value is found as +7.27 dB. In the second analysis when the frequency is at 4.85 GHz, S11 is -14.03 dB and the gain is found as +8.79 dB. By adjusting antenna leg lengths, it is possible to achieve different resonance frequencies and gain. Two different analyses were compared in this article. We are also in the process of measuring the fabricated antenna for further studies on single band operations.

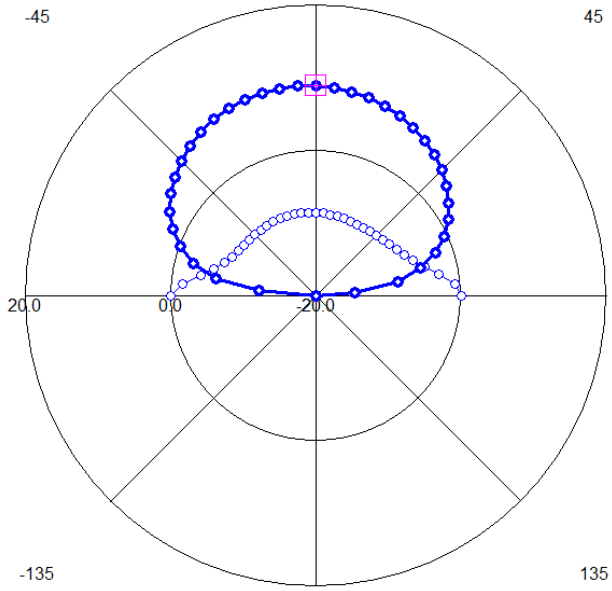

Fig. 2. Radiation pattern at 4.85 GHz.

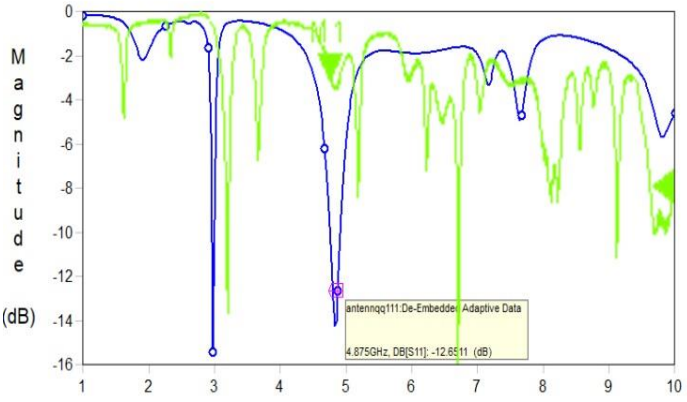

Fig. 3. Input match (S11).

TABLE I. Results and Comparisons

Frequency	S11	Gain
4.87 GHz	-12.65 dB	8.86 dB
2.97 GHz	-15.35 dB	7.27 dB
4.0 GHz	-0.92 dB	6.91 dB
6.22 GHz	-1.80 dB	4.93 dB

Acknowledgment

We would like to thank Sonnet Software for their services.

REFERENCES

[1] International Journal of Scientific Research Engineering & Technology (IJSRET).

[2] R. Divya and M. Priya, "Design and characterization of E-shape microstrip patch antenna for wireless communication," International Journal of Advanced Trends in Computer Science and Engineering, vol. 2, no. 2, Mar. 2013.

[3] W. C. Y. Lee, Mobile Communications Engineering. Wiley, New York, NY, USA, 1982.

[4] R. G. Vaughan and J. B. Anderson, "Antenna diversity in mobile communicaions," IEEE Transactions on Vehicular Technology, vol. 36, no. 4, pp. 149-172, 1987.

[5] J. S. Colburn, Y. Rahmat-Samii, M. A. Jenson, and G. J. Pottie, "Evaluation of personal communications dual-antenna hand-set diversity performance," IEEE Transactions on Vehicular Technology, vol. 47, no. 3, pp. 737-746, 1998.

[6] A. Yadav, B. Chauhan, and A. Jain, "Microstrip symmetrical E-shape patch antenna for the wireless communication systems," International Journal of Emerging Technology and Advanced Engineering, vol. 2, iss. 12, Dec. 2012.

[7] B.-K. Ang and B.-K. Chung, "A wideband E-shaped microstrip patch antenna for 5-6 GHz wireless communications," Faculty of Engineering Multimedia University, Cyberjaya, Malaysia, 2007.

[8] P. Tomar, J. K. Bhutto, and S. Rankawat, "Effect of feed position for same E-type microstrip patch antenna," International Journal of Electronics and Communication Engineering, vol. 7, no. 1, 2014.

[9] A. Diallo, C. Luxey, P. Le Thuc, R. Staraj, and G. Kossiavas, "Enhanced two-antenna structures for universal mobile telecommunications system diversity terminals," IET Microwaves, Antennas & Propagation, vol. 2, no. 1, pp. 93-101, 2008.

[10] C.-H. Lee, S.-Y. Chen, and P. Hsu, "Integrated dual planar inverted-F antenna with enhanced isolation," IEEE Antennas and Wireless Propagation Letters, vol. 8, pp. 963-965, 2009.

[11] F. Yang and Y. Rahmat-Samii, "Microstrip antennas integrated with electromagnetic band-gap (EBG) structures: a low mutual coupling design for array applications," IEEE Transactions on Antennas and Propagation, vol. 51, no. 10, pp. 2936-2946, 2003.

[12] Z. Iluz, R. Shavit, and R. Bauer, "Microstrip antenna phased array with electromagnetic bandgap substrate," IEEE Transactions on Antennas and Propagation, vol. 52, no. 6, pp. 1446-1453, 2004.

[13] F. Caminita, S. Costanzo, G. Di Massa, et al., "Reduction of patch antenna coupling by using a compact EBG formed by shorted strips with interlocked branch-stubs," IEEE Antennas and Wireless Propagation Letters, vol. 8, pp. 811-814, 2009.

[14] Y. Yu, L. Yi, X. Liu, and Z. Gu, "Mutual coupling reduction of dual-frequency patch antenna arrays," ACES Journal, vol. 31, no. 9, pp. 1092-1099, 2016.

[15] L. H. Weng, Y. C. Guo, X. W. Shi, and X. Q. Chen, "An overview on defected ground structure," Progress In Electromagnetics Research B, vol. 7, pp. 173-189, 2008.

[16] R. G. S. Alsultan and G. O. Yetkin, "Mutual coupling reduction of E-shaped MIMO antenna with matrix of C-shaped resonators," Hindawi International Journal of Antennas and Propagation, vol. 2018

[17] Sonnet Suites, ver. 17.52, www.sonnetsoftware.com

Ezgi Kucuk completed B.Sc. degree in Electrical and Electronics Engineering, Istanbul Commerce University, Istanbul, Turkey. His current research areas are, microwave antennas and embedded circuits.

Burak Bayram completed B.Sc. degree in Electrical and Electronics Engineering, Istanbul Commerce University, Istanbul, Turkey. His current research areas are, microwave antennas and control circuits.

Şehabeddin Taha İmeci received the B.Sc. degree in Electronics and Communications Engineering from Yildiz Technical University, Istanbul, Turkey in 1993, and the M.S.E.E. and Ph.D. degrees from Syracuse University, Syracuse, NY in 2001 and 2007, and Associate Professorship degree from Istanbul Commerce University, Istanbul Turkey in 2014, respectively. Imeci was appointed as Full Professor in Int. Univ. of Sarajevo in Nov. 2017. He is working as the Dean of FENS (Faculty of Engineering and Natural Sciences) in Sarajevo. He was with Anaren Microwave Inc., East Syracuse, NY from 2000 to 2002, and Herley Farmingdale, New York from 2002 to 2003, and PPC, Syracuse, NY from 2003 to 2005, and Sonnet Software Inc., Liverpool, NY from 2006 to 2007. He was a Teaching Assistant in the Department of Electrical Engineering and Computer Science at Syracuse University from 2005 to 2006. His current research areas are, microwave antennas and electromagnetic theory.

Tahsin Durak received his B.Sc. degree in Electrical and Electronics Engineering from Gazi University, Ankara, Turkey in 1992, his first M.S degree in Electrical Engineering from Fairleigh Dickinson University, NJ, USA in 1998, his second M.S. and Ph.D. degrees in Electrical Engineering from Syracuse University, NY, USA in 2001 and 2008 respectively. From 2000 until 2001, he was with Philips Broadband Networks, Manlius, NY, USA. He was a Teaching Assistant in the Department of Electrical Engineering and Computer Science at Syracuse University from 2001 to 2004. He joined Norfolk State University, Norfolk, VA, in 2010 as an Assistant Professor. Since 2014, he has been working in industry as a Staff Engineer, Electrical Engineering Manager and Engineering Director. He continues to teach at local universities as an Adjunct Faculty. He has several US patents in the area of Microwave, RFID and IIOT. His current research areas are microwave antennas, RFID technologies, IIOT solutions, industrial automations, remote controls, industrial machine to machine communication techniques and protocols. Durak has been a Member of the IEEE.

Multiple Rectangular Slotted Patch Antenna with Roof-top Shaped at 15.3 GHz

Melis Ecem Koca
Department of Electrical & Electronics Engineering
Istanbul Commerce University, Istanbul, Turkey
melis.koca@hotmail.com

Tahsin Durak
Department of Technology, NSU, Norfolk, VA
tahsind@gmail.com

S. Taha Imeci
Department of Electrical & Electronics Engineering
Int. University of Sarajevo, Bosnia and Herzegovina
simeci@ius.edu.ba

***Abstract*—In this paper, a compact sized, high frequency microstrip patch antenna with probe feeding is designed, simulated, built and tested. The patch of the antenna is diamond shaped which has a rectangular slot in the upper-center. Main contribution of the paper is to perturb the side edges of the patch and to add a rectangular slot. Parametric study of that two-substrate change was investigated. The proposed structures were simulated by using the Sonnet Suites, a planar 3-D electromagnetic simulation software which gave S11 value of -13.82 dB and gain value of 6.33 dB at 15.3 GHz.**

Keywords—Mobile equipment, rectangular slot, roof shaped, single band, wireless communication.

I. INTRODUCTION

With the advancements of mobile and wireless technologies, the consumer market is demanding compact size handsets with multiple functions. Microstrip antennas are a suitable candidate for these applications due to their inherent properties including low weight, low manufacturing cost, conformability and low profile in comparison to conventional antennas [1].

Pentagonal geometry is one of the various shapes for microstrip antennas capable of circular polarization operation that has been reported in literature, but it can be also used for linear polarization [2]. Electrically thick dielectrics increase bandwidth, but also introduce impedance matching challenges [3].

Slotted microstrip antenna possesses better bandwidth, return loss, gain and directivity when compared with non-slotted microstrip patch antenna [4]. The limitations of MSA such as narrow bandwidth, low gain and low efficiency can be minimized by selecting a proper substrate material, as permittivity of substrate is the critical parameter to control bandwidth, radiation pattern, and efficiency of patch antenna [5].

Furthermore, Multiband microstrip antennas are in demand, because they can reduce the cost and size of the communication systems. They are used in lots of applications such as wireless local area network (WLAN), satellite communications and global system for mobile (GSM) [6]. In addition, different types of dual band microstrip patch antennas are presented in literatures such as dual band microstrip antenna with single patch [7] and stacked patches [8] and using two separate antennas which are connected to by a shorting pin [9] and using metamaterial branch-line coupler [10].

The Wireless communication is mainly concentrated on the antenna size. The reduced antenna size results in small sensor node and low power consumption [11]. So the antenna can be a low profile, low powered and high frequency micro strip antenna. The antenna size is proportional to $1/\sqrt{\xi}r$ [12]. Small antenna concept is the one which uses planar antenna and by adjusting the electrical size the desired center frequency can be obtained [13].

Microstrip patch antennas are usually designed to eliminate the imaginary part of the input impedance. Edge fields are also important and they bring an additional length to the antenna. This length depends on the relative permittivity of the dielectric, dielectric height and patch width [14].

Embedded microstrip antennas have been used therapeutically for a number of applications including cardiac ablation, balloon angioplasty and cancer treatment using hyperthermia. Designers of antennas for sensing or therapy capitalize on some of the problems that plague embedded antennas for communication antennas are inherently sensitive to their environment and inherently deposit large amounts of power in the near field of the antenna, particularly when it is embedded in a lossy material, thus becoming good therapeutic tools [15].

The rest of this paper is organized as follow: the design steps are described in Section II, simulation and parametric study in Section III, and results and conclusion are presented in Section IV of the paper.

II. DESIGN STEPS

The size of the antenna is 6.4 × 6.4mm. Substrate material is Rogers RT6002 and the thickness of it is 0.762 mm (ε_r= 2.94, dielectric loss tangent = 0.0012). The thickness of air is taken

Submitted On: September 30, 2018
Accepted On: October 8, 2018

as 3 times of the thickness of the Rogers RT6002, (3 mm). Probe feeding technique is adopted in this antenna design. Feed point can be moved to any desired location on patch to achieve input impedance. Fig. 1 shows the picture of the fabricated antenna.

III. Simulation and Parametric Study

A comprehensive parametric study of a triangular shaped double-slit microstrip patch antenna has been carried out to understand the effects of various triangular slits. Analyses were performed using a commercial software. The frequency range is between 10 - 20 GHz. In two different frequency values, obtained magnitude values were -10dB below. When the magnitude of S11 is -14.12 dB, gain is 6.33 dB at 15.3 GHz. In second analysis, frequency was 14.7 GHz and S11 was -24.5 dB and the antenna's gain is 4.18 dB. A prototype of this antenna is tested by using an HP8720D network analyzer. Fig. 2 shows the comparison between simulated and measured S-parameters' results of the proposed antenna. It is noticed that there are some difference between the simulation and measurement results. These differences can be considered acceptable as long as its effect on the resonant frequency is not high and the frequency band does not shift much. The discrepancies are mostly due to the insertion loss of SMA connectors, surrounding environment that influences on wave reflection, or the fabrication tolerances. S11-frequency graph is shown and -13.82 dB magnitude is found at 15.3 GHz. In Fig. 3, gain-frequency Graph is shown and +6.33 gain is found at 15.3 GHz. Note that cross-polarization level is less than -17 dB. Fig. 4 has the simulated antenna with changed parameters. Table I provides the list of variables changed and their values and Table II provides frequency gain input match verses modified gap. Variables B, C and E has great effect on antenna gain. Highest gain is achieved when B is 0.1mm.

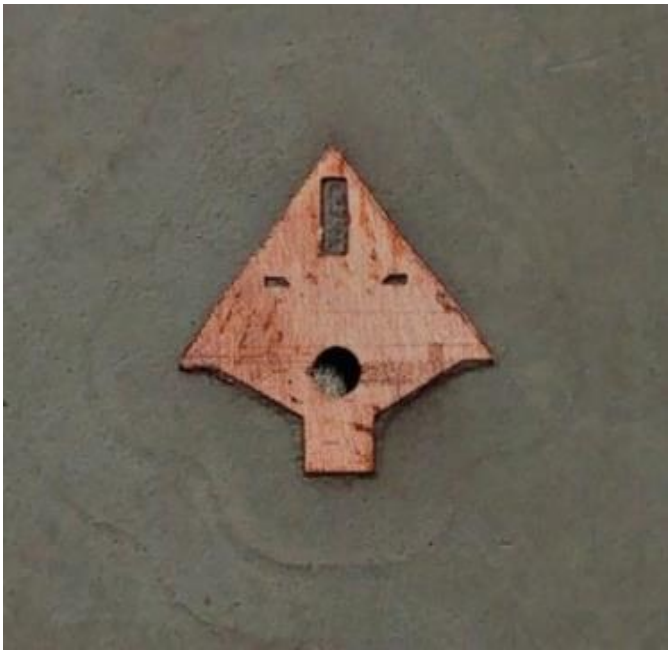

Fig. 1. Picture of the fabricated antenna.

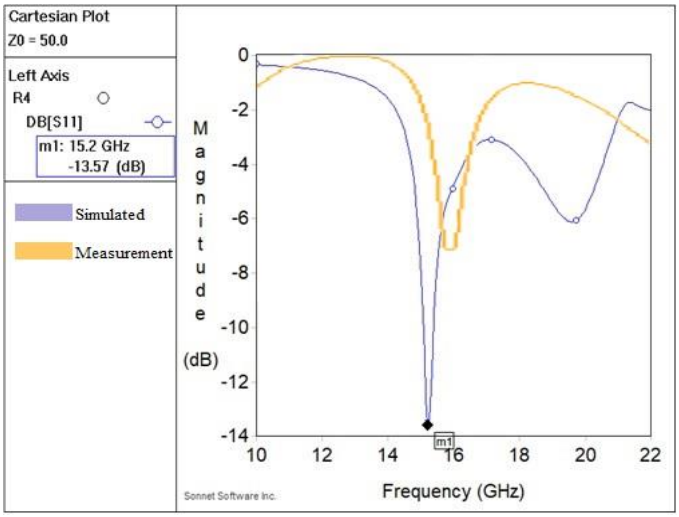

Fig. 2. S11 graph.

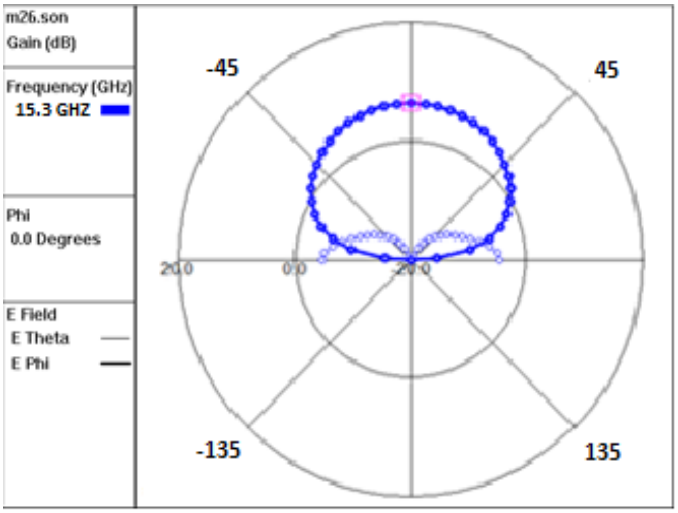

Fig. 3. Radiation pattern (gain) graph.

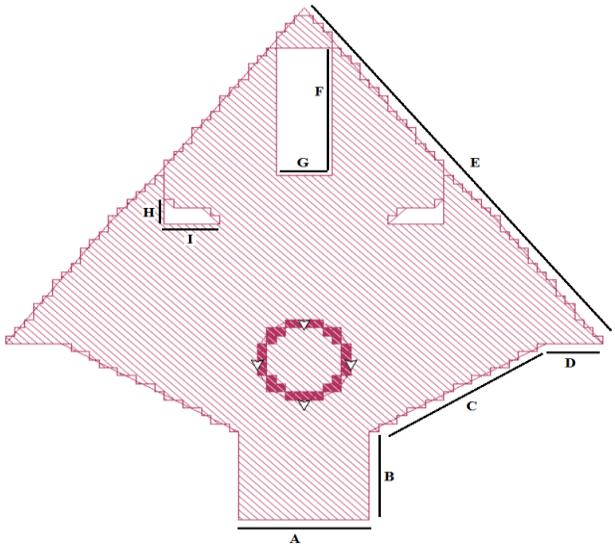

Fig. 4. Top view of the simulated antenna and its parameters.

TABLE I. CHANGING PARAMETERS

Variable	Value
A	1.4 mm
B	1.1 mm
C	2.2 mm
D	0.6 mm
E	5.3 mm
F	1.6 mm
G	0.6 mm
H	0.3 mm
I	0.6 mm

TABLE II. FREQUENCY-GAIN-INPUT MATCH WITH MODIFIED GAP

Variable	Freq. (GHz)	S11 (dB)	Gain (dB)
B = 2.1mm	22.7	-18.7	1.92
B = 0.1mm	20.2	-12.0	6.27
C = 2.7mm	16.6	-16.15	6.11
D = 1.6mm	23.4	-18.6	3.92
E = 5.8mm	25.2	-23.3	4.24

IV. CONCLUSION

A comprehensive parametric study has been carryout out on perturbed pentagonal cross-slotted patch antenna. Throughout our design steps in this conclusion part of this project we can say that designing roof shaped rectangular shaped antenna is not easy to optimize due to limitations, dielectric material type, gain - frequency relation, feeding type and technique. Compared to the first analysis, in the second analysis there was a decrease in the gain value. So, when the frequency is at 15.3 GHz, S11 is -13.82 dB and the gain value is found as + 6.33 dB. In the second analysis when the frequency is at 14.7 GHz, S11 value is -24.5 dB and the gain is found as +4.18 dB.

By varying the thickness, different parameters of the designed antenna can be optimized. Proposed antenna can be used in different applications such as in wireless communication and S band applications.

Two different analyses were compared in this article. We are also in the process of measuring the fabricated antenna for further studies on single band operations.

The simulations results are performed using Sonnet software [16].

ACKNOWLEDGMENT

We would like to thank Sonnet Software and Yeditepe University for their services.

REFERENCES

[1] B. Sharma, V. Sharma, D. Bharadwaj, K. B. Sharma, V. K. Saxena, J. S. Saini, and D. Bhatnagar, "Broadband dual frequency pentagonal microstrip antenna for wireless communication systems," Proceedings of International Conference on Microwave - 08, 2008.

[2] M. Tecpoyotl-Torres and J. G. Vera-Dimas, "Dual band pentagonal microstrip antenna for Wi-Fi applications," 2010 IEEE Electronics, Robotics and Automotive Mechanics Conference, pp. 255, 2010.

[3] R. Garg, P. Bhartia, I. Bahl, and A. Ittipiboon, Microstrip Antenna Design Handbook. Artech House, 2001.

[4] M. John, B. Manoj, and S. Rodrigues, "Design of slotted rectangular microstrip patch antenna operated in ISM band using RT-Duroid substrate," International Conference on Electrical, Electronics, and Optimization Techniques (ICEEOT), 2016.

[5] S. D. Mahamine, R. S. Parbat, S. H. Bodake, and M. P. Aher, "Effects of different substrates on rectangular microstrip patch antenna for S-band," 2016 International Conference on Automatic Control and Dynamic Optimization Techniques (ICACDOT), 2016.

[6] Z. N. Chen, Antennas for Portable Devices. John Wiley & Sons, 2007.

[7] K. P. Yang and K. L. Wong, "Dual-band circularly polarized square microstrip antenna," IEEE Trans. Antennas Propag., vol. 49, no. 3, pp. 377-382, Mar. 2001.

[8] J. Y. Jan and K. L. Wong, "A dual-band circularly polarized stacked elliptic microstrip antenna," Microw. Opt. Technol. Lett., vol. 24, no. 5, pp. 354-357, Mar. 2000.

[9] S. H. S. Esfahlani, A. Tavakoli, and P. Dehkhoda, "A Compact single-layer dual-band microstrip antenna for satellite applications," IEEE Antennas Wireless Propag. Lett., vol. 10, 2011.

[10] Y. K. Jung and B. Lee, "Dual-band circularly polarized microstrip RFID reader antenna using metamaterial branch-line coupler," IEEE Antennas Wireless Propag. Lett., vol. 10, 2011.

[11] D. M. Pozar,"Microstrip antenna coupled to microstripline," Electron Lett., vol. 21, no. 2, pp. 49-50, Jan. 1995.

[12] C. G. Kakoyiannis, G. Stamatiou, and P. Constantinou, "Small square meander-line antennas with reduced ground plane size for multimedia WSN nodes," Antennas and Propagation, 2009, EuCAP 2009, 3rd European Conference on, IEEE, 2009.

[13] P. M. Shanmugam and M. A. M. Mohamed, "A CPW Fed Star Shaped Patch Antenna for WSN Applications," Second International Conference on Electrical and Communication Technology 2016, pp. 182-187.

[14] R. E. Munson, "Conformal microstrip antennas and microstrip phased arrays," IEEE Trans. Antennas Propagation, vol. AP-22, pp. 74-78, Jan. 1974.

[15] P. Soontornpipit, C. M. Furse, and Y. C. Chung, "Design of Implantable Microstrip Antenna for Communication with Medical Implants," in IEEE Transactions on Microwave Theory and Techniques, vol. 52, no. 8, Aug. 2004.

[16] Sonnet Suites, ver. 17.52, www.sonnetsoftware.com

Melis Ecem Koca completed B.Sc. degree in Electrical and Electronics Engineering, Istanbul Commerce University, Istanbul, Turkey. His current research areas are, microstrip antennas and wireless communications.

Şehabeddin Taha İmeci received the B.Sc. degree in Electronics and Communications Engineering from Yildiz Technical University, Istanbul, Turkey in 1993, and the M.S.E.E. and Ph.D. degrees from Syracuse University, Syracuse, NY in 2001 and 2007, and Associate Professorship degree from Istanbul Commerce University, Istanbul Turkey in 2014, respectively. Imeci was appointed as Full Professor in Int. Univ. of Sarajevo in Nov. 2017. He is working as Vice-Rector in Sarajevo. He was with Anaren Microwave Inc., East Syracuse, NY from 2000 to 2002, and Herley Farmingdale, New York from 2002 to 2003, and PPC, Syracuse, NY from 2003 to 2005, and Sonnet Software Inc.,

Liverpool, NY from 2006 to 2007. He was a Teaching Assistant in the Department of Electrical Engineering and Computer Science at Syracuse University from 2005 to 2006. He authored two books and published more than 150 papers. His current research areas are, microwave antennas and electromagnetic theory.

Tahsin Durak received his B.Sc. degree in Electrical and Electronics Engineering from Gazi University, Ankara, Turkey in 1992, his first M.S degree in Electrical Engineering from Fairleigh Dickinson University, NJ, USA in 1998, his second M.S. and Ph.D. degrees in Electrical Engineering from Syracuse University, NY, USA in 2001 and 2008 respectively. From 2000 until 2001, he was with Philips Broadband Networks, Manlius, NY, USA. He was a Teaching Assistant in the Department of Electrical Engineering and Computer Science at Syracuse University from 2001 to 2004. He joined Norfolk State University, Norfolk, VA, in 2010 as an Assistant Professor. Since 2014, he has been working in industry as a Staff Engineer, Electrical Engineering Manager and Engineering Director. He continues to teach at local universities as an Adjunct Faculty. He has several US patents in the area of Microwave, RFID and IIOT. His current research areas are microwave antennas, RFID technologies, IIOT solutions, industrial automations, remote controls, industrial machine to machine communication techniques and protocols. Durak has been a Member of the IEEE.

Optimizing Scattering Coefficients of Disordered Metamaterials Using the Finite-Difference Time-Domain Method

Adam Mock and Sheldon Hewlett
School of Engineering and Technology
Science of Advanced Materials Program
Central Michigan University
Mount Pleasant, Michigan 48859
mock1ap@cmich.edu

***Abstract*—A technique based on the finite-difference time-domain method is presented for calculating optical transmission and reflection of disordered nanoparticle stacks. The approach is used to optimize a nanoparticle stack exhibiting greater than 98% average absorption over the visible spectrum.**

I. Introduction

Most electromagnetic metamaterials consist of a repeating unit cell with sub-wavelength features designed to impart a specific scattering response in a particular frequency range [1]. Metamaterials can be designed to achieve permittivities and permeabilities not found in natural materials, and these exotic material parameters can then be used to design metalenses, cloaks, mirrors and absorbers. For the case of highly absorbing metamaterials, many applications require low reflection and transmission over a broad wavelength range and over a wide range of incident angles. However, ordered metamaterials typically provide high absorption over only a limited wavelength range and over a limited range of incident angles. Alternatively, the use of disordered metamateirals has become an interesting alternative for achieving high absorption over extremely large bandwidths and incident angles [2]. However, the lack of long range order makes their analysis and design more challenging. In this work we describe our progress on obtaining reflection and transmission coefficients in disordered metamaterials consisting of dense agglomerations of gold nanoparticles using the finite-difference time-domain method (FDTD) [3], [4].

II. Dense Nanoparticle Stacks

In addition to impressive absorption, disordered metamaterials are amenable to low-cost solution-based fabrication techniques. Our approach begins with synthesis of gold nanoparticles in solution using the Turkevitch method in which nanoparticle size is controllable. In our work diameters between 5 nm and 45 nm are used. A single drop of the nanoparticle solution is deposited in a glass well using a micropipette and allowed to dry. Then a second drop is applied and allowed to dry, and this process is repeated until an opaque layer is formed, which typically requires 15-20 drops. This process is schematically shown in Fig. 1 (a), and fabricated samples are shown in Fig. 1 (b). After each drop, the reflection and absorption is measured using the configuration shown in Fig. 1 (c).

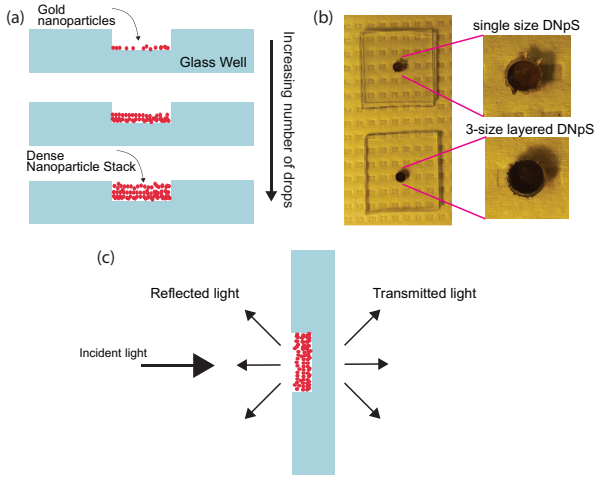

Fig. 1. (a) Experimental process for fabricating layer-by-layer dense nanoparticle stacks. The substrate is borosilicate glass, and the red spheres represent gold nanoparticles. (b) Photographs of fabricated samples. Single size DNpS indicates that nanoparticles of only a single size were used (diameter = 18 nm); whereas 3-size DNpS indicates that nanoparticles of three different sizes were used to construct the DNpS (diameters = 12, 18 and 48 nm). (c) Experimental arrangement for measuring reflection and transmission.

III. Numerical Approach

To gain further insight into the electromagnetics of our metamaterials, the reflection and transmission coefficients were determined numerically using FDTD. If the nanoparticles had been placed in an ordered arrangement, then a minimum-sized repeating unit cell can be employed to minimize computational demands. However, in our disordered materials, this approach cannot be applied directly. Therefore, we defined a unit cell that contained a large set of randomly distributed particles, and then applied periodic boundary conditions on this disordered supercell. The scheme is depicted in Figs. 2 (a)-(b).

Submitted On: September 28, 2018
Accepted On: October 12, 2018

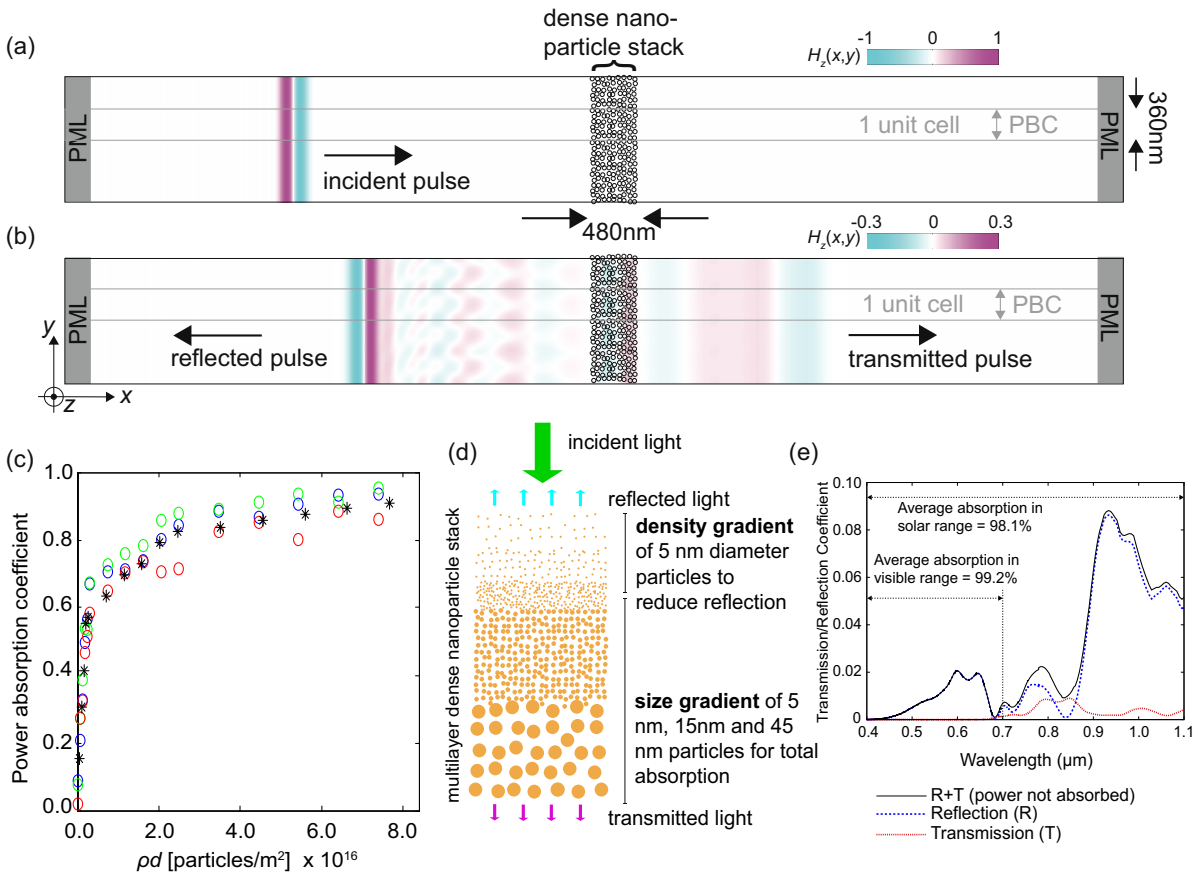

Fig. 2. (a) Computational domain depicting incident pulse on a dense nanoparticle stack. Periodic boundary conditions (PBC) are implemented along the y-direction. Four unit cells are depicted concatenated along y. The boundaries along the x-direction are terminated with perfectly matched layer (PML) absorbing boundary conditions. (b) Same as (a) but at a later time when the pulse has scattered from the dense nanoparticle stack. Reflected and transmitted field is visible. (c) Comparison between numerically calculated and experimentally measured absorption as a function of ρd where ρ is particle density and d is sample thickness. (d) Particle arrangement for structure optimized for greater than 98% absorption. (e) Numerically calculated scattering spectra for optimized structure. Coefficients in (c) and (e) are unitless power coefficients. (c)-(e) reproduced from [4], with the permission of AIP publishing.

A two-dimensional implementation of FDTD was used, so the gold nanoparticles are actually infinitely long cylinders. We deliberately used the TM_z polarization, so that the electric field would be perpendicular to the axis of the cylinder. In this sense, one can consider a cylindrical scattering cross section σ_c per unit length of cylinder along z. Then in order to obtain the approximate scattering cross section for a cylinder of finite length l, multiply σ_c by l. In order to compare the 2D FDTD results to the three-dimensional experimental results, we assume $\sigma_s \approx \sigma_c 2r\delta$ where σ_s is the spherical cross section of the nanoparticles, r is their radius, and δ is an empirical fitting factor. Fig. 2 (c) shows a comparison between the absorption measured experimentally and calculated using our 2D approach with a fitting factor of $\delta = 0.29$. The agreement is very good.

The data shown in Fig. 2 (c) corresponds to a sample with engineered disorder. We intentionally deposited nanoparticles of three different sizes with the largest particles at the exit side of the sample, and the smallest particles on the incident side. Intuitively, the small nanoparticles scatter less, so small particles on the front of the sample will reduce reflection while larger particles at the back will reduce transmission. The photograph in Fig. 1 (b) shows that the 3-size layered DNpS is indeed darker to the naked eye than the single size DNpS.

This gradient approach was further explored using our numerical approach in which we incorporate both a density gradient and a size gradient as depicted in Fig. 2 (d). Our optimized structure exhibits better than 98% absorption averaged over the entire visible spectrum as shown in Fig. 2 (e).

REFERENCES

[1] N. I. Landy, S. Sajuyigbe, J. J. Mock, D. R. Smith, and W. J. Padilla, "Perfect metamaterial absorber," Physical Review Letters, vol. 100, no. 20, p. 207402, 2008.

[2] M. K. Hedayati, F. Faupel, and M. Elbahri, "Review of plasmonic nanocomposite metamaterial absorber," Materials, vol. 7, pp. 1221–1248, 2014.

[3] S. Hewlett and A. Mock, "Plasmonic metamaterial absorbers from dense gold nanoparticle stacks," Plasmonics, vol. 12, no. 2, pp. 419–425, 2016.

[4] ——, "Engineering metamaterial absorbers from dense gold nanoparticle stacks," Journal of Applied Physics, vol. 122, no. 9, p. 093103, 2017.

Wideband Dielectric Resonator Antenna Excited by a Closed Circular Loop GCPW Slot for WLAN 5.5 GHz Applications

Wei-Chung Weng [1], Min-Chi Chang [1], and Min-Sian Chen [2]

[1] Department of Electrical Engineering
National Chi Nan University, 301, University Rd., Puli, Nantou 54561, Taiwan
wcweng@ncnu.edu.tw, s100323910@mail1.ncnu.edu.tw

[2] R&D Department
Master Wave Technology Co., Ltd., Zhubei City, 302, Taiwan
minsian.chen@masterwave.com.tw

Abstract ─ A dielectric resonator antenna is designed for WLAN 5.5 GHz band applications in this study. The dielectric resonator antenna is fabricated on a cheap FR4 substrate with grounded CPW (GCPW) structure. A new closed circular loop GCPW slot structure is employed to obtain wideband impedance matching. Results of the designed dielectric resonator antenna show that good agreement between simulated and measured reflection coefficients, radiations, and antenna gains is observed. The measured -10 dB bandwidth of the dielectric resonator antenna is 1.6 GHz (28.5%, 4.8 – 6.4 GHz), which covers the WLAN 5.5 GHz band.

Index Terms ─ Dielectric resonator, DRA, GCPW, wideband, WLAN.

I. INTRODUCTION

Dielectric resonators [1-3] have the advantages of no conductor loss, low quality factor, and high dielectric constant; hence, they are widely used for designing dielectric resonator antennas (DRAs). Theoretical analyses for first few resonant modes in an isolated cylindrical dielectric resonator have been done [4-6]. DRAs have many advantages such as compact size, wideband, and high efficiency. Different excitation mechanisms such as coaxial probe [6, 7], slot-microstrip [8], microstrip [9, 10] and slot-coplanar waveguide (CPW) can excite the dielectric resonator [3]. Apparently, the excitation mechanism of using slot-microstrip outperforms the coaxial probe since coaxial probe fed are not easy to adjust the optimal feeding position to obtain good impedance matching. DRAs also can be fed by CPW lines [11, 12]. However, CPW fed structure without a ground plane on the backside has a drawback that decreases the antenna gain and efficiency due to backside radiations. To overcome this drawback, a grounded CPW (GCPW) structure can be used. The GCPW structure has an additional ground plane on the bottom layer of the substrate to block the backside radiations. Also, the ground plane can create an extra image radiator to improve the gain of the DRA.

In this study, a wideband DRA excited by a GCPW line with slot-CPW fed structure is proposed. The designed DRA operates at the WLAN 5.5 GHz (5.15 – 5.85 GHz) band. The proposed DRA has characteristics of wideband, high gain, and wide beamwidth. Details of the proposed DRA design are described. Results of the prototype are presented and discussed as well.

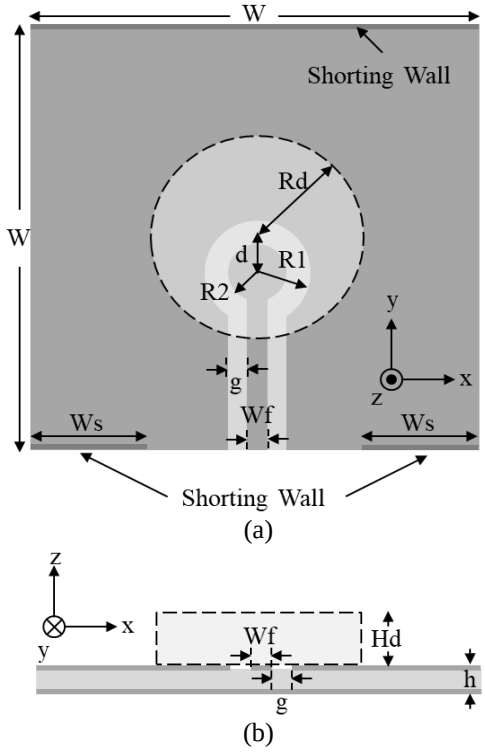

Fig. 1. The geometry of proposed wideband GCPW fed DRA: (a) top view and (b) side view.

Submitted On: September 27, 2018
Accepted On: November 4, 2018

II. ANTENNA DESIGN

Figure 1 shows the geometry of the proposed wideband DRA. The full-wave EM simulator, HFSS [13] is used to analyze the prototype of the DRA. The proposed antenna is to be fabricated on an FR4 substrate with a thickness (h) of 0.8 mm, dielectric constant of 4.4, and loss tangent of 0.02. The square size of the DRA is 60.0 mm (W) by 60.0 mm. The shorting walls are applied in the y-direction to block surface waves in the substrate. Wf is the width of the central fed line. g is the gap between the edge of the central fed line and the edge of the ground plane on the top layer of the FR4 substrate. The GCPW fed line becomes a closed circular loop line at the end. The closed circular loop GCPW slot line consists of a circular patch and a circular slot. They are concentric. The radii of the outer and inner edge of the circular slot are R1 and R2, respectively. The distance from the center of the cylindrical dielectric resonator to the center of the circular patch is d. This closed circular loop GCPW slot excites a ring of magnetic current. The magnetic current $\vec{M}$ can be determined by:

$$\vec{M} = -\hat{n} \times \vec{E} \ , \tag{1}$$

where $\vec{E}$ is the electric fields between the edges of the slot and $\hat{n}$ is the direction normal to the plane of the fed line. Figure 2 demonstrates the magnetic currents flow along the closed circular loop GCPW slot. The magnetic currents are obtained by HFSS at 5.7 GHz. The circular loop magnetic current is equivalent an electric dipole source, which then excites the cylindrical dielectric resonator [2]. By properly adjusting the orientation of the cylindrical dielectric resonator and dimensions of the closed circular loop GCPW slot structure, the desired hybrid $\mathrm{HEM}_{11\delta}$ mode can be excited. Meanwhile, wideband impedance matching of the DRA can be obtained [3]. The resonant frequency of dominant hybrid $\mathrm{HEM}_{11\delta}$ mode can be determined by [14]:

$$f_r = \frac{c}{2\pi \mathrm{Rd}} \frac{6.324}{\sqrt{\varepsilon_r + 2}} \left[0.27 + 0.36 \left(\frac{\mathrm{Rd}}{2\mathrm{Hd}} \right) + 0.02 \left(\frac{\mathrm{Rd}}{2\mathrm{Hd}} \right)^2 \right], \tag{2}$$

where c is light speed in free space and ε_r is the dielectric constant of resonator. To achieve wider bandwidth, ε_r of resonator should be kept low. Hence, we choose an available cylindrical dielectric resonator with a height (Hd) of 4.2 mm, a radius (Rd) of 14.9 mm, ε_r of 9.8, and loss tangent of 0.01 applied in this antenna design. The resonant frequency f_r of dominant $\mathrm{HEM}_{11\delta}$ mode determined by (2) is 5.73 GHz, which is closed to the center of the operating band. Simulated electric and magnetic fields at 5.7 GHz are shown in Fig. 3. The electric fields are more concentrated on the surface close to the top of the cylindrical dielectric resonator while the magnetic fields are more concentrated at the center of the cylindrical dielectric resonator. The directions of electric fields and magnetic fields are orthogonal each other, which demonstrate the dielectric resonator operating at the dominate $\mathrm{HEM}_{11\delta}$ mode. Here, $\mathrm{HEM}_{11\delta}$ is the lowest resonant frequency.

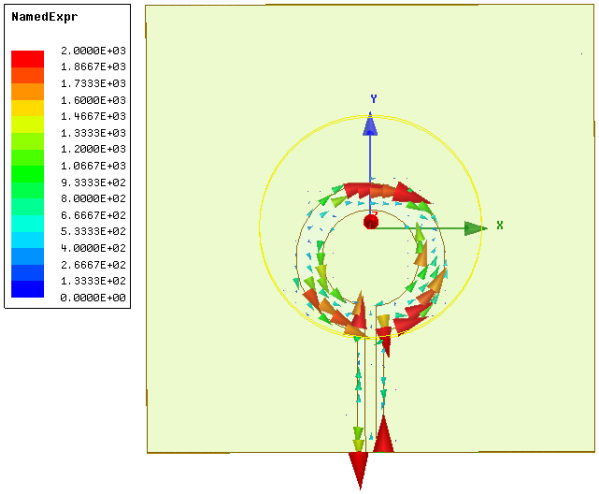

Fig. 2. The magnetic currents flow along the closed circular loop GCPW slot line. The magnetic currents are obtained by HFSS EM simulator at 5.7 GHz.

Parametric study is performed to reveal the influence of the magnitude of reflection coefficients (|S11|) by key parameters, R1, R2, and d. Other dimensions are fixed at values as shown in Table 1 when the parameter is investigated. In Fig. 4 and Fig. 5, |S11| is much sensitive in the variation of R2 than that of R1 and d. The variation of d slightly affects the |S11| as can be seen in Fig. 6. Based on the results, when designing the proposed DRA, we suggest firstly adjust the value of R2 to obtain wideband impedance matching at the desired band. The next step is to slightly adjust R1 and d to achieve better |S11| performance of the DRA.

Detailed dimensions of the designed wideband DRA are listed in Table 1 as well. A prototype has been physically realized. Figure 7 shows the pictures of the designed wideband DRA without and with the cylindrical dielectric resonator.

Table 1: Dimensions of the proposed dielectric resonator antenna (Unit: mm)

Parameter	**Size**	**Parameter**	**Size**
W	60.0	R1	10.0
Wf	2.52	R2	6.5
g	1.0	d	4.0
h	0.8	Rd	14.9
Hd	4.2	Ws	12.0

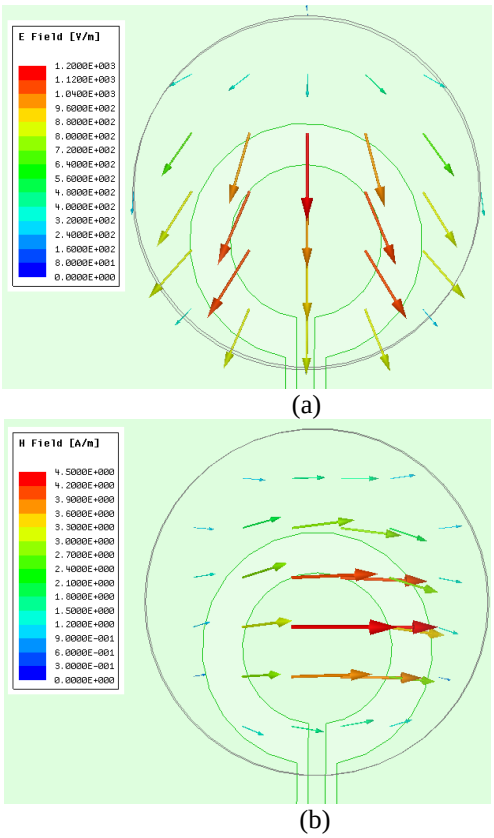

Fig. 3. Simulated top view field distributions at 5.7 GHz. (a) E-Fields close to the top surface of the dielectric resonator, and (b) H-Fields on the cross section at the center of the dielectric resonator.

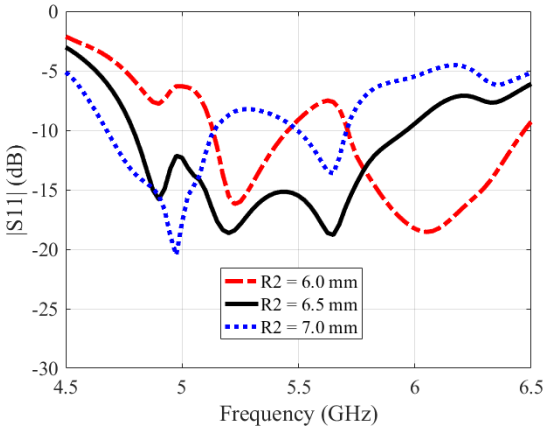

Fig. 4. Simulated reflection coefficients of the proposed DRA with varying of R2.

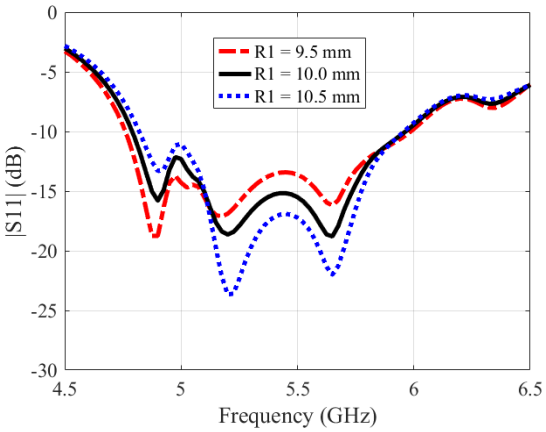

Fig. 5. Simulated reflection coefficients of the proposed DRA with varying of R1.

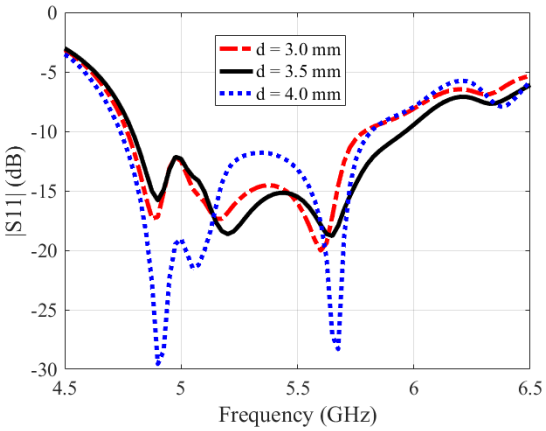

Fig. 6. Simulated reflection coefficients of the proposed DRA with varying of d.

Fig. 7. The pictures of the proposed wideband DRA: (a) without the cylindrical dielectric resonator, and (b) with the cylindrical dielectric resonator.

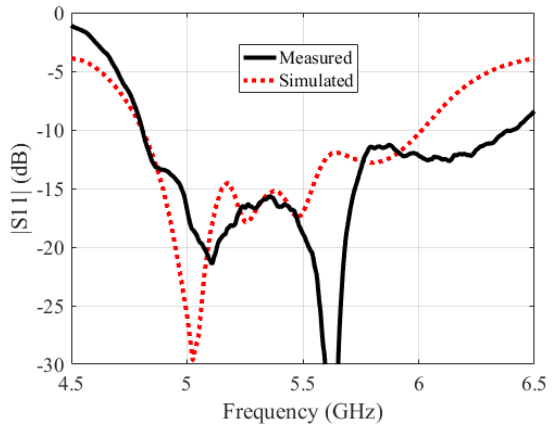

Fig. 8. The reflection coefficients of the proposed DRA.

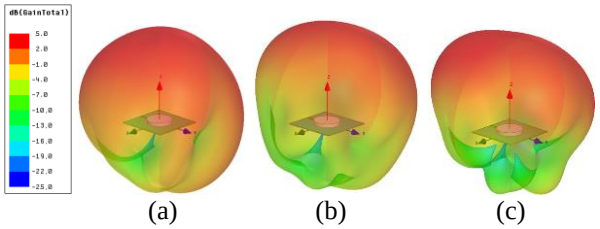

Fig. 9. Simulated 3-D radiation gain patterns of the proposed DRA at frequencies of: (a) 5.15 GHz, (b) 5.5 GHz, and (c) 5.85 GHz.

III. RESULTS AND DISCUSSIONS

The prototype of the proposed wideband DRA is measured by an Agilent's N5230A vector network analyzer (VNA) to obtain measured |S11|. The simulated and measured |S11| of the proposed DRA are shown together in Fig. 8. The simulated |S11| agrees with the measured one. The measured -10 dB impedance bandwidth is 1.6 GHz (28.57%, 4.8-6.4 GHz), which covers the WLAN 5.5 GHz band and can be considered a wideband impedance matching. Figure 9 shows simulated 3-D radiation gain patterns of the proposed DRA at frequencies of 5.15 GHz, 5.5 GHz, and 5.85 GHz. The gain patterns reveal broadside radiations. Gain patterns are similar each other at the three frequencies and near omnidirectional in the +z direction with small back lobe levels. Measured radiation properties of the proposed DRA are obtained by an MVG SG-24 antenna measurement system. Figure 10 shows the normalized far-field radiation patterns of the DRA in the y-z and x-z planes at 5.15 GHz, 5.5 GHz, and 5.85 GHz, respectively. The DRA has broadside radiations with wide beamwidths. Good agreement between simulated and measured radiation patterns is observed. It shows the validity of the simulation. The measured 3 dB beamwidths in the y-z plane are larger than those in the x-z plane. The beamwidth is around 84 degrees in the x-z plane at 5.5 GHz. Cross-polarized patterns show more than 20 dB isolation from the peak. It indicates excellent linearly polarized radiation along the broadside direction. Figure 11 shows the peak gains of the proposed DRA. The measured peak gain is 3.64 dBi at 5.5 GHz and 4.77 dBi at 5.9 GHz. Measured radiation properties of the proposed DRA at 5.15, 5.5, and 5.85 GHz are summarized in Table 2. The DRA has high gain, wide beamwidth, and good front-to-back (F/B) ratio. Based on the results of reflection coefficients and radiation properties, the designed DRA has good performance and is suitable for operating at the WLAN 5.5 GHz band.

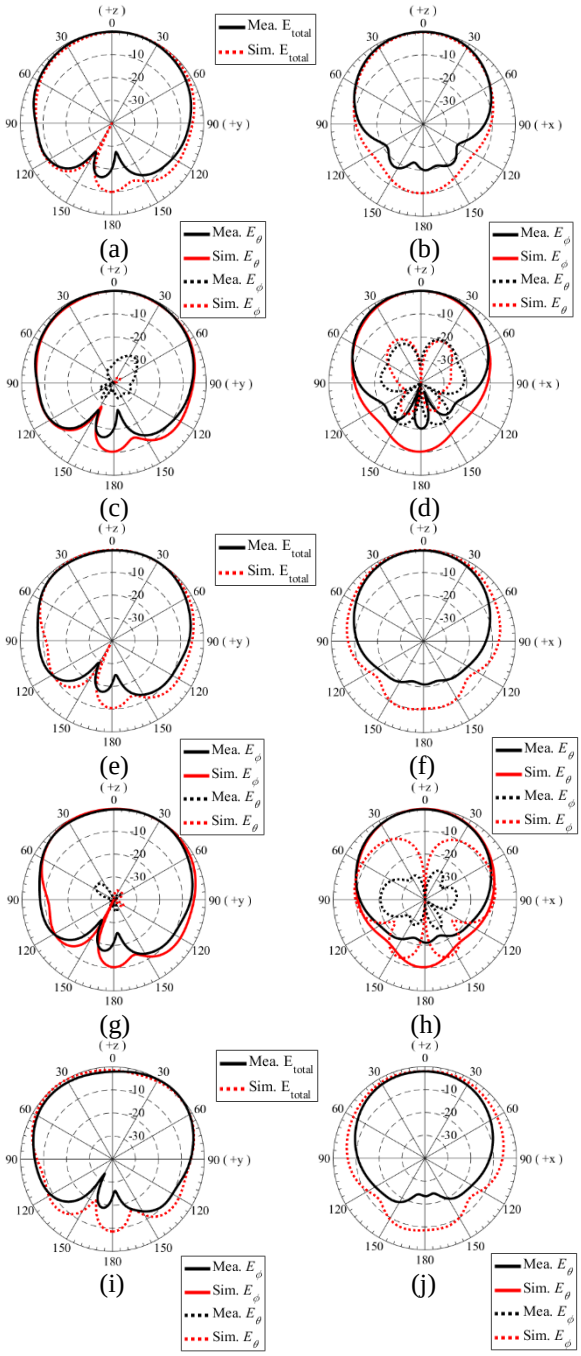

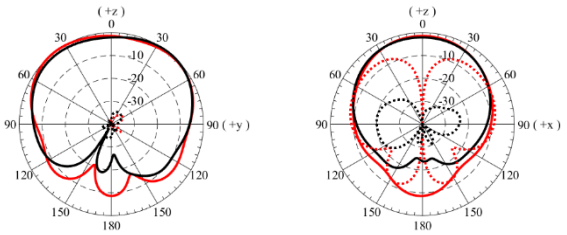

(k) y-z plane (l) x-z plane

Fig. 10. Radiation patterns (normalized) of the proposed DRA. (a), (b), (c), and (d) at 5.15 GHz. (e), (f), (g), and (h) at 5.5 GHz. (i), (j), (k), and (l) at 5.85 GHz.

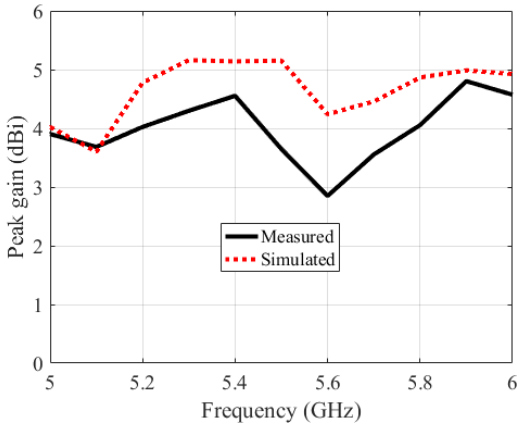

Fig. 11. The measured and simulated peak gains of the proposed antenna.

Table 2: Measured radiation properties of the proposed DRA at 5.15, 5.5, and 5.85 GHz

Frequency (GHz)	**5.15**	**5.5**	**5.85**
Gain (dBi)	3.26	3.64	4.24
Efficiency (%)	50.4	53.3	55.7
3 dB beamwidth in the y-z plane (Deg.)	124	130	138
3 dB beamwidth in the x-z plane (Deg.)	84	84	102
F/B ratio (dB)	20.08	20.67	21.34

VI. CONCLUSION

A wideband dielectric resonator antenna has been designed in this study. The proposed DRA used a closed circular loop GCPW slot line to excite the cylindrical dielectric resonator. Numerical experiments and measurements have shown the antenna's good characteristics. Antenna design and discussion have been given. Results made on the proposed wideband dielectric resonator antenna have shown a very promising performance that can be practically and effectively applied to WLAN communication systems.

ACKNOWLEDGMENT

This work was supported in part by the MOST under Grant 106-2918-I-260-002.

REFERENCES

[1] S. A. Long, M. W. McAllister, and L. C. Shen, "The resonant cylindrical dielectric cavity antenna," *IEEE Trans. Antennas Propag.*, vol. 31, pp. 406-412, May 1983.

[2] A. Petosa, *Dielectric Resonator Antenna Handbook*. 1st ed., Norwood, MA, USA: Artech-House, 2007.

[3] A. A. Kishk and Y. M. M. Antar, "Dielectric resonator antennas," *in Antenna Engineering Handbook*, J. Volakis, Ed., 4th ed., ch. 17, New York: McGraw-Hill, 2007.

[4] A. W. Glisson, D. Kajfez, and J. James, "Evaluation of modes in dielectric resonators using a surface integral equation formulation," *IEEE Trans. Microw. Theory Tech.*, vol. 31, no. 12, pp. 1023-1029, Dec. 1983.

[5] D. Kajfez, A. W. Glisson, and J. James, "Computed modal field distributions for isolated dielectric resonators," *IEEE Trans. Microw. Theory Tech.*, vol. 32, no. 12, pp. 1609-1616, Dec. 1984.

[6] Y. Zhang, A. A. Kishk, A. B. Yakovlev, and A. W. Glisson, "FDTD analysis of a probe-fed dielectric resonator antenna in rectangular waveguide," *ACES Journal*, vol. 21, no. 1, pp. 37-44, Mar. 2006.

[7] D. Guha, A. Banerjee, C. Kumar, and Y. M. M. Antar, "Higher order mode excitation for high-gain broadside radiation from cylindrical dielectric resonator antennas," *IEEE Trans. Antennas Propag.*, vol. 60, no. 1, pp. 71-77, Jan. 2012.

[8] D. Guha, P. Gupta, and C. Kumar, "Dualband cylindrical dielectric resonator antenna employing $HEM_{11\delta}$ and $HEM_{12\delta}$ modes excited by new composite aperture," *IEEE Trans. Antennas Propag.*, vol. 63, no. 1, pp. 433-438, Jan. 2015.

[9] G. Almpanis, C. Fumeaux, and R. Vahldieck, "Novel broadband dielectric resonator antennas fed through double-bowtie-slot excitation scheme," *ACES Journal*, vol. 22, no. 1, pp. 97-104, Mar. 2007.

[10] F. Z. Abushakra, A. S. Al-Zoubi, and D. F. Hawatmeh, "Design and measurements of rectangular dielectric resonator antenna linear arrays," *ACES Journal*, vol. 33, no. 4, pp. 380-387, Apr. 2018.

[11] R. A. Kranenburg, S. A. Long, and J. T. Williams, "Coplanar waveguide excitation of dielectric resonator antennas," *IEEE Trans. Antennas Propag.*, vol. 39, pp. 119-122, Jan. 1991.

[12] Y. Gao, Z. Feng, and L. Zhang, "Compact CPW-fed dielectric resonator antenna with dual polarization," *IEEE Antennas and Wireless Propagation*

Letters, vol. 10, pp. 544-547, May 2011.

[13] Ansoft High Frequency Structure Simulation (HFSS), ver. 10, Ansoft Corporation, Pittsburgh, PA, 2005.

[14] R. K. Mongia and P. Bhartia, "Dielectric resonator antennas—A review and general design relations for resonant frequency and bandwidth," *Int. J. Microw. Millimeter-Wave Comput.-Aided Eng*., vol. 4, no. 3, pp. 230-247, 1994.

Wei-Chung Weng received the B.S. degree in Electronic Engineering from National Changhua University of Education, Changhua, Taiwan, in 1993, the M.S. degree in Electrical Engineering from I-Shou University, Kaohsiung, Taiwan, in 2001, and the Ph.D. degree in Electrical Engineering from The University of Mississippi, MS, USA, in 2007.

In 2008, he joined the Department of Electrical Engineering, National Chi Nan University, Puli, Taiwan, where he is currently an Associate Professor. From 2017 to 2018, he was a Visiting Scholar at the Department of Electrical Engineering, Colorado School of Mines, Golden, CO, USA. From 2004 to 2007, he was a Graduate Research Assistant in the Department of Electrical Engineering, The University of Mississippi. From 1993 to 2004 and 2007 to 2008, he was a Teacher in the Department of Computer Engineering, Kaohsiung Vocational Technical School, Kaohsiung City, Taiwan. He has authored over 50 journal articles and conference papers and a book entitled *Electromagnetics and Antenna Optimization Using Taguchi's Method* (Morgan & Claypool, 2007). His research interests include antennas and microwave circuits design, computational electromagnetics, electromagnetic compatibility, and optimization techniques in electromagnetics.

Weng has served many journals as a Reviewer for years. He is a Member of the Applied Computational Electromagnetic Society, a Senior Member of IEEE, and a Life Member of the Institute of Antenna Engineers of Taiwan (IAET). He was the recipient of Outstanding Teaching Award of National Chi Nan University in 2013 and 2016, respectively.

Min-Chi Chang Min-Chi Chang was born in Yunlin, Taiwan. He received the B.S. degree in Electrical Engineering from National United University, Miaoli, Taiwan, in 2009. He is currently working toward the Ph.D. degree in the Department of Electrical Engineering, National Chi Nan University, Puli, Taiwan. His research interests focus on antenna design, computational electromagnetics, and optimization techniques in electromagnetics.

Min-Sian Chen was born in Miaoli, Taiwan. He received the M.S. degrees in Electrical Engineering from National Chi-Nan University, Nantou, Taiwan, in 2015. Since October 2016, he has been an Antenna Design Engineer in the R&D Department of Masterwave Technology Co., Zhubei, Taiwan. His research interests include designing, fabricating, and testing for WiFi and LTE antennas for wireless products, as well as high-gain antenna arrays for 5G communication systems and outdoor applications.

Multi-Bandwidth CPW-Fed Open End Square Loop Monopole Antenna for Energy Harvesting

Nermeen Eltresy[1,2], Dalia Elsheakh[3], Esmat Abdallah[2], and Hadia Elhenawy[1]

[1]Electronics and Communication Engineering Dept., Faculty of Engineering, Ain Shams University, Cairo, Egypt
[2]Microstrip Dept., Electronics Research Institute, El-Tahrir St., Dokki, Giza, Egypt
[3]Hawaii Center for Advance Communication, Hawaii Univesity, Honolulu, Hawaii, USA
Nermeen@eri.sci.eg, daliaelsheakh@eri.sci.eg, dalia8@hawaii.edu

***Abstract*—Compact CPW-fed open end square loop monopole antenna is presented. The antenna can harvest ambient power at different radio frequencies of 1.8, 1.9, 2.4 and 5.2 GHz. The multi-band coplanar waveguide antenna (MCPW) is designed and fabricated on a very thin and low-profile substrate. The proposed antenna is used to measure the ambient spectrum in two different places. One of them is indoor and the other is outdoor, in order to see the effect of the place on the proposed energy harvesting system. A multi-band rectifier circuit is designed and integrated with the proposed antenna. The maximum simulation efficiency is 60.98% at 1.9 GHz and -1 dBm input power. The maximum measured efficiency is 60.57% at 2.5 GHz and -1 dBm RF received power. Also, the proposed rectenna has 53.1% measured efficiency at 2.5 GHz and RF received power of -5 dBm.**

***Keywords*—Bandwidth, Coplanar waveguide antenna, Energy Harvesting, RF (radio frequency), Matching circuit.**

I. INTRODUCTION

The basic requirement for sustaining our life is the energy, because it exists in each and every one of our activities. The energy is required in household applications, industrial applications, transportation, electric power generation, and agriculture. In the near future it will be hard to satisfy our requirements of the energy, because increasing energy demand puts restrictions on the current available energy sources. As a result of that, searching for new sources specially the renewable energy sources are a recent trend. The renewable energy is the energy which can be extracted from the natural sources and is not exhausted, such as the sunlight, wind, flowing water. The conversion of this wasted energy into a useful electricity is known as the energy harvesting [1]. Ambient energy sources are widely used as a clean energy source. The ambient energy is one of the environment friendly energy sources. It can be used for the production of electric energy. Ambient energy sources use different energy harvesting methods [2], such as mechanical, optic, thermal energy extraction, and wireless energy harvesting [3-5].

Wireless energy harvesting has proven to be one of the most promising solutions because of its simplicity, ease of implementation, and availability. The ability to harvest RF energy from ambient or dedicated sources enables the wireless charging of low power devices. The wireless energy harvesting system consists of three main subsystems. The first one is the receiving antenna, which is used to capture ambient radio frequency energy which will be converted to DC power. The second subsystem is the matching network between the antenna and the rectifier. The third subsystem is the rectification circuitry, which converts the input RF power into DC output power. An output DC filter (post rectification filter) is used to provide a DC to the load by separating the high-frequency components from the DC signal [6]. When the antenna is integrated with the rectifier, the system is called rectenna [7].

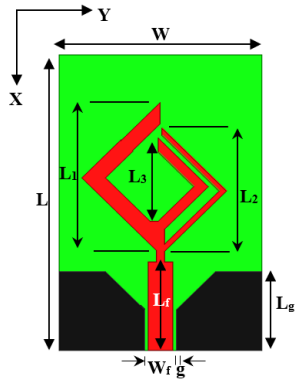

Fig. 1. The geometry of the proposed antenna.

In recent years the wireless technology became the main subject for the rapid enormous changes in frequency allocation, policies and procedures of operations, and techniques to enhance the wireless system performance. Many of wired systems are converted into wireless, for example wired LAN is converted into a wireless. As a result of that an increased demand for multiple antennas covering different wireless communication bands on the same platform increased extremely. This makes the antenna more important day by day, specially the multi-bandwidth antenna. As a result of that a multiband and broadband fractal patch antenna is presented in [8]. Four different planar multi-band antennas are designed, modeled, fabricated, and measured in [9]. A meandered planar inverted-F antenna introduced in [10] for

Submitted On: September 20, 2018
Accepted On: October 1, 2018

LTE/GSM/UMTS multi band operation. In [11], reconfigurable and multiband antenna is introduced for wireless and radar applications. Printed inverted F-antenna (PIFA) is a type of compact antenna. The design of compact multiband and environmental isolation for mobile phones is presented in [12] using planar inverted-F antenna (PIFA).

This paper presents a multi bandwidth antenna with a good response at 1.8 GHz, 1.9 GHz, 2.4 GHz and 5.2 GHz. The antenna consists of multi arm and each arm is responsible for a specific resonant frequency. A multi band rectifier circuit with high efficiency operating at three frequencies of 1.8, 1.9, and 2.4 GHz is designed for converting the received RF power into DC power. The antenna is fabricated and measured. The ambient RF spectrum is measured using the antenna. Then the antenna is integrated with the rectifier and the rectenna is measured. This paper is organized as follows. Section II presents antenna structure and geometry. The antenna design is given in section III. Section IV introduces the multiband rectifier circuit. The implementation and measured results are given in section V, while conclusion is presented in section VI.

II. Antenna Structure and Geometry

The antenna is designed using thin and flexible substrate of ROGERS (RO3003) with dielectric constant ε_r=3, dielectric loss tangent of 0.04 and thickness 130 µm. The antenna is coplanar waveguide (CPW) fed. The detailed structure of the antenna is shown in Fig. 1. The antenna has area of $L\times W$=60×40 mm^2. Feeding line with width of W_f=5mm and length of L_f=18 mm is used to feed the antenna. The separation gap between the feeding line and the ground plane is g=0.3 mm. The ground plane has length of L_g=16 mm.

III. Antenna Design

A. Design Steps Procedure

The design steps of the CPW antenna is shown in Fig. 2. The first assumed design is indicated in Fig. 2 (a) which consists of a one arm CPW antenna, the arm length is L_1=29 mm that gives one resonant band at 1.8 GHz. Then another arm with length of L_2= 22 mm has been added to give resonance at 1.8 GHz, as shown in Fig. 2 (b). After that a third arm with length L_3=18.5 mm is added between the previous two arms, which drive resonance at 2.4 GHz.

Finally, a modified etched rectangular ground plane with angle $\alpha = 45^o$ is used to improve the impedance matching at the higher bands specially 5.2 GHz. The final design is shown in Fig. 2 (d). Fig. 3 indicates response of the design steps of the multiband proposed antenna which has the following impedance bandwidth (1.58-2.1 GHz), (2.35-2.48 GHz) and (4.6-5.8 GHz) according to -6dB reflection coefficient as a reference.

B. Antenna Current Distribution and Radiation Pattern

The current distribution on the flexible multi-bandwidth CPW fed antenna at frequencies of 1.8, 1.9, 2.4, and 5.2 GHz is shown in Fig. 4, which indicates that each arm is responsible for a specific resonant frequency. This means that the largest arm gives 1.8 GHz resonant and the smallest arm gives 2.4 GHz resonant, as mentioned before in the design antenna procedure. The current distribution on the antenna at 5.2 GHz indicates that the etched ground plane in a tapered shape improves the antenna matching. The antenna radiation patterns at different frequencies in E-plane and H-plane are shown in Fig. 5. The antenna has a high gain at frequencies 1.8, 1.9, and 5.2 GHz.

IV. Multi Band Rectifier Circuit

A multi-band rectifier circuit is designed in order to rectify the received RF power at three frequencies of 1.8, 1.9, and 2.4 GHz. The schematic diagram of proposed circuit is shown in Fig. 6. The circuit consists of matching circuit and rectifier circuit. The matching circuit composites of short ended stub, 1 PF capacitor and 10 nH inductor. The rectifier circuit is a simple wave rectifier which uses a single Schottky SMS7630 diode, smoothing capacitor and load resistance. The SMS 7630 has a very low turn on voltage [13], which is suitable with the low values of received ambient power. The circuit is fabricated on low cost FR-4 substrate with dielectric constant of 4.5, loss tangent =0.025, and thickness of 0.8 mm. A comparison between simulated and measured reflection coefficient variation with frequency for the multi-band rectifier circuit is shown in Fig. 7 which indicates that the circuit is matched at more than one frequency. The rectifier efficiency can be calculated using the output power from the circuit divided by its corresponding RF input power. Equations (1) and (2) are used to calculate the rectifier efficiency [14]. The simulated rectifier efficiency variation versus different levels of the input RF power at three different frequencies of 1.8, 1.9, and 2.4 GHz is shown in Fig. 8 (a), which indicates that the maximum efficiency for the circuit is achieved at -1 dBm RF input power for the three frequencies. Fig. 8 (b) introduces the effect of the load value on the efficiency of the circuit. It can be seen that the maximum efficiency is achieved at specific load value which is approximately 550 Ohm for the three frequencies:

$$\eta = \frac{p_{out(DC)}}{p_{input\,(RF)}}, \tag{1}$$

$$\eta = \frac{V_{o(DC)}^2}{p_{input\,(RF)\times R_L}}. \tag{2}$$

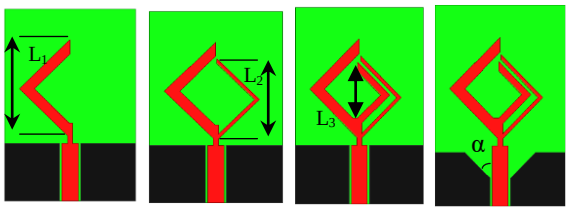

Fig. 2. Design steps of the antenna.

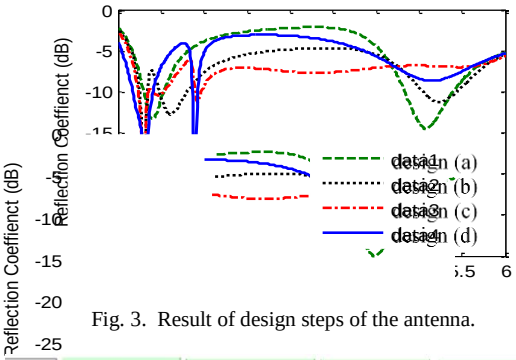

Fig. 3. Result of design steps of the antenna.

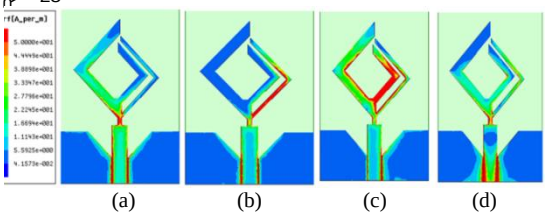

Fig. 4. The current distribution at 1.8GHz, 1.9GHz, 2.4GHz, and 5.2GHz.

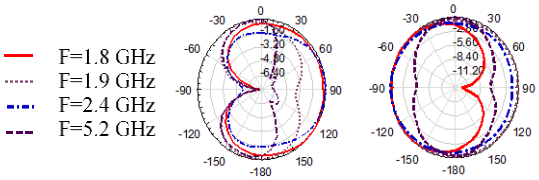

Fig. 5. The radiation pattern of the antenna in E-plane, and H-plane at different frequencies 1.8, 1.9, 2.4, and 5.2 GHz.

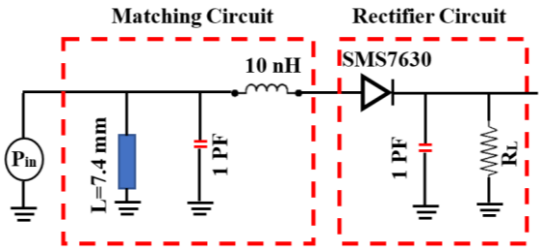

Fig. 6. Schematic diagram of multi-band rectifier circuit.

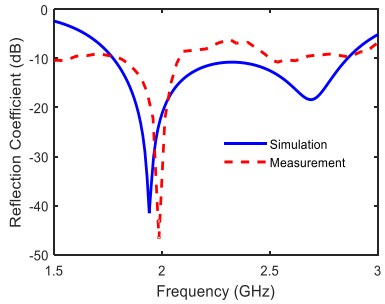

Fig. 7. Simulation and measured reflection coefficient variation versus frequency for the rectifier circuit.

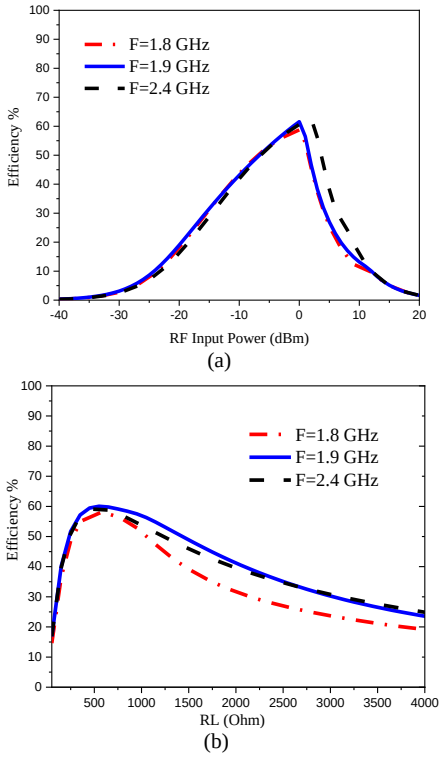

Fig. 8. Efficiency variation at frequencies of 1.8, 1.9, 2.4 GHz versus different values of: (a) RF input power and (b) load resistance.

V. Implementation and Measured Results

A. Antenna Fabrication and Spectrum Measurememt

The antenna is fabricated and tested. The fabricated antenna photo is shown in Fig. 9 (a). A comparison between the simulated and measured result for the antenna reflection coefficient variation versus frequency is indicated in Fig. 9 (b), which indicates a good agreement between CST [15], HFSS [16], and measured results.

A survey on the RF spectrum was done in order to understand the conditions of the harvesting system in Egypt RF spectrum. This survey is performed in two places one of them is outdoor measurements in the street and the other is indoor in our Electronics Research Institute (ERI) buildings. The proposed antenna is used to

measure the ambient RF spectrum at frequency band of 1.5 to 3 GHz. The Agilent Technology N9918A is used to measure the spectrum. Figure 10 shows a comparison between both indoor and outdoor spectrum measurement. It can be seen that the maximum peak for the indoor received power is at 2.4 GHz which is the Wi-Fi band and that is because in the Electronics Research Institute there are many hotspots which provide RF waves at 2.4 GHz band. According to the outdoor measurement, the value of the power at GSM 1800 band is the highest value comparing to other bands, which means that there was a GSM 1800 base station tower near to us during the outdoor measurements. Also, it is noticed that the value of the ambient RF power at Wi-Fi band is very low at the street comparing to the indoor measurements in the ERI. This is because the street in Egypt does not contain hot spots so that there is no Wi-Fi 2.4 GHz transmitted power outdoor and the Wi-Fi hotspots which is indoor are transmitting a power within 10-100 meter. As a result of that it is too hard to sense the Wi-Fi hotspots powers in the streets in Cairo.

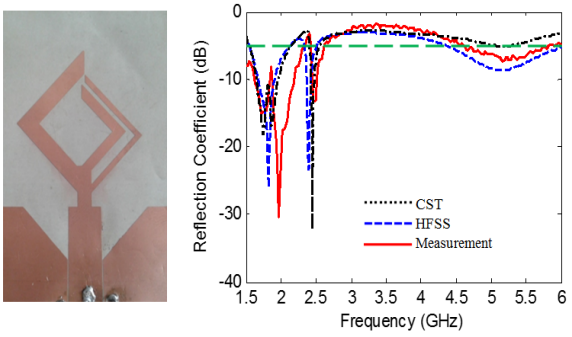

(a) (b)

Fig. 9. (a) Photo of fabricated antenna, and (b) Comparison between simulated and measured results.

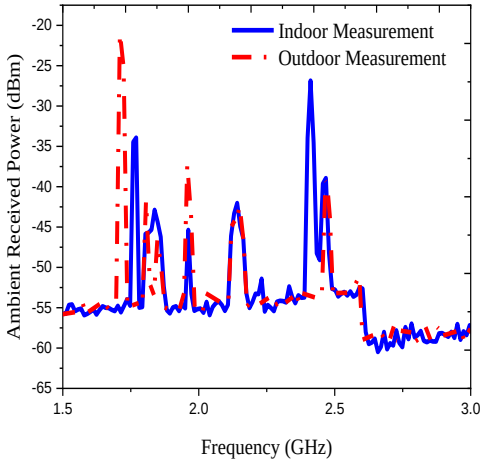

Fig. 10. Ambient RF received indoor and outdoor power by the proposed antenna.

B. System Integration and Measurement

The antenna is integrated with the multi-band rectifier as shown in Fig. 11 (a), then the overall rectenna is measured. The experimental setup for the measurement system is shown in Fig. 11 (b). Anritsu MG3697C RF signal generator is used to feed a wide band horn antenna. Two antennas are used in the measurement setup, the first one is connected with the N9918A analyzer in order to measure the received power by the antenna. The N9918A analyzer in this measurement setup is operated as a spectrum analyzer to detect the received RF power. Simultaneously to this the second antenna is integrated with the matching circuit, voltage doubler and the load resistance R_L. The output of the rectenna system is connected parallel to the Tektronix MD04104C oscilloscope to see the output DC voltage signal. This measurement setup is used each time and the results are recorded at two frequencies of F_1 =1.9 GHz, F_2=2.4, and at different RF received power by the proposed antenna. The measured rectenna efficiency variation versus RF received power using 550 Ohm load resistance is shown in Fig. 12 (a). The maximum efficiency is achieved at -1 dBm RF received power. Figure 12 (b) introduces the efficiency variation versus frequency at different received RF power of 5, -1, 05 dBm. It can be seen that the proposed rectenna has a high and stable efficiency over the frequency band of 1.8 to 2.7 GHz. Which includes GSM 1800, and Wi-Fi 2.4 GHz. The maximum efficiency is 60.57% at 2.5 GHz and RF received power of -1 dBm.

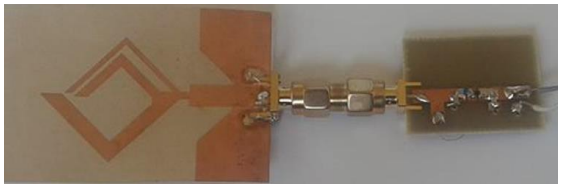

(a)

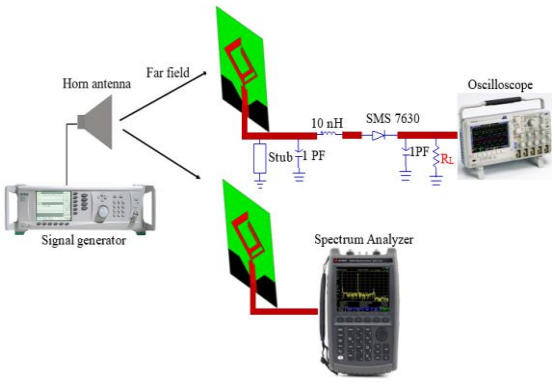

(b)

Fig. 11. (a) Photo of antenna integrated with rectifier circuit, and (b) the measurement system setup.

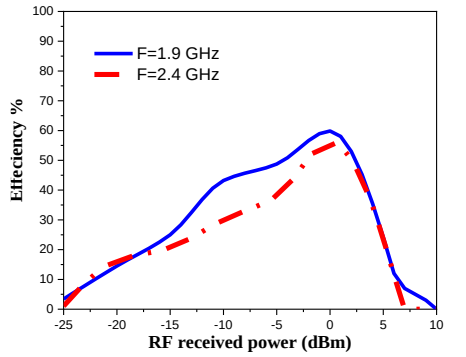

(a)

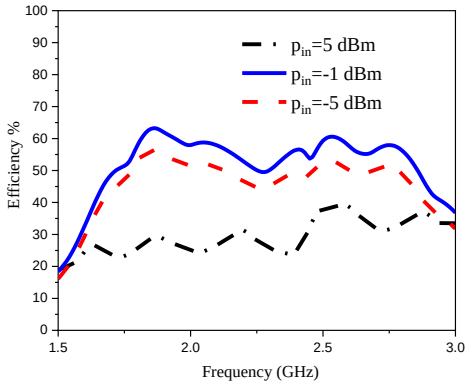

(b)

Fig. 12. The measurement efficiency variation versus: (a) RF received power and (b) frequency, R_L=550 Ohm.

VI. Conclusion

Multi bandwidth coplanar waveguide fed open end square loop monopole antenna has been designed and optimized using both CST and HFSS electromagnetic packages. The detailed steps of the design were indicated. The antenna was fabricated and measured. There is a good agreement between the simulated and measured results. A wide band rectifier circuit was designed using highly sensitive SMS7630 Schottky diode. The rectifier was fabricated and integrated with the proposed antenna. The rectenna system was measured. The maximum efficiency is achieved at 2.5 GHz, RF received power of -1 dBm, and load resistance of 550 Ohm.

Acknowledgement

This wok was supported by the National Telecommunication Regularity Authority (NTRA), Ministry of Communication and Information, Egypt.

References

[1] U. Muncuk, "Design Optimization and Implementation for RF Energy Harvesting Circuits," M.Sc. Thesis, Northeastern University, Boston, Massachusetts, July 2012.

[2] F. Yildiz, "Potential ambient energy-harvesting sources and techniques," The Journal of Technology Studies, vol. 35, no. 1, pp. 40-48, 2009.

[3] K. Ylli, D. Hoffmann, A. Willmann, P. Becker, B. Folkmer, and Y. Manoli, "Energy harvesting from human motion: Exploiting swing and shock excitations," Smart Materials and Structures Journal, pp. 1-12, Jan. 2015.

[4] M. W. Knight, H. Sobhani, P. Nordlander, and N. J. Halas, "Photodetection with active optical antennas," Science, vol. 332, pp. 702-704, May 2011.

[5] M. Arrawatia, M. Shojaei Baghini, and G. Kumar, "RF energy harvesting system from cell towers in 900MHz band," National Conference on Communications (NCC), 2011, Bangalore, India, 28-30 Jan. 2011.

[6] Z. Harouni, L. Osman, and A. Gharsallah "Efficient 2.45 GHz rectenna design with high harmonic rejection for wireless power transmission," IJCSI International Journal of Computer Science Issues, vol. 7, no. 5, Sept. 2010.

[7] E. Khansalee, K. Nuanyai, and Y. Zhao, "A dual-band rectifier for RF energy harvesting," Engineering Journal, vol. 19, no. 5, 31 Oct. 2015.

[8] J. J. Hang, F. Q. Shan, and J. Z. She, "A novel multiband and broadband fractal patch antenna," Progress In Electromagnetics Research Symposium, Cambridge, USA, Mar. 26-29, 2006.

[9] A. Cáp, Z. Raida, E. H. Palmero, and R. L. Ruiz. "Multi-band planar antennas: A comparative study," Radioengineering, vol. 14, no. 4, pp. 11-20, Dec. 2005.

[10] Y. Hong, J. Tak, J. Baek, B. Myeong, and J. Choi, "Design of a multiband antenna for LTE/GSM/UMTS band operation," International Journal of Antennas and Propagation, vol. 2014, pp. 1-9, 2014.

[11] N. Haider, D. Caratelli, and A. G. Yarovoy, "Recent developments in reconfigurable and multiband antenna technology," International Journal of Antennas and Propagation, vol. 2013, pp. 1-14, 2013.

[12] H. Tamaoka, H. Hamada, and T. Ueno, "A multiband antenna for mobile phones," Furukawa Review, no. 26, pp. 12-16, 2004.

[13] https://datasheet.octopart.com/SMS7630-040LF-Skyworks-Solutions-datasheet-8832283.pdf

[14] X. Yang, C. Jiang, A. Z. Elsherbeni, F. Yang, and Y.-Q. Wang, "A novel compact printed rectenna for data communication systems," IEEE Transactions on Antennas and Propagation, vol. 61, no. 5, pp. 2532-2539, May 2013.

[15] CST Microwave Studio, http://www.cst.com/

[16] High Frequency Structure Simulator Software (HFSS), Ver.14.02, Ansoft corporation, Canonsburg, PA.

Efficient Modeling of Antennas with Finite Conductivity using Calderón Preconditioning

Michiel Gossye, Dries Vande Ginste, Daniël De Zutter, and Hendrik Rogier
IDLab/Electromagnetics Group, Department of Information Technology
Ghent University/imec, Belgium
Michiel.Gossye@UGent.be

***Abstract*—A Calderón preconditioner for a novel single-source integral equation, which allows the simulation of high dielectric contrasts and lossy conductors, is introduced. It is shown that this preconditioner avoids breakdown when simulating scattering problems including high permittivities. This is corroborated by a numerical example of a receiving copper dipole antenna.**

I. Introduction

In recent research, Calderón preconditioners (CPs) were developed to resolve dense mesh breakdown problems that occur when solving boundary integral equations (BIEs). This preconditioner is based on the self-regularization effect of the electric field integral operator (EFIO) [1]. In [2], such a preconditioner was developed for the Poggio-Miller-Chang-Harrington-Wu-Tsai (PMCHWT) equation, resolving the dense mesh breakdown of this operator. However, for high dielectric contrasts, this preconditioner is not able to stabilize the system matrix [3]. Therefore, the accurate simulation of high contrasts including lossy conductors still remains an active research topic. In this contribution, a Calderón preconditioner for a novel single-source equation is introduced that resolves dense mesh breakdown at high dielectric contrasts. In Section II, the theoretical framework and spectral analysis of this method are described. These results are then validated by a numerical example of a lossy dipole antenna in Section III.

II. Theory

Assume a homogeneous object (characterized by ε', μ' and k'), embedded in a homogeneous background medium (characterized by ε, μ and k), as shown in Fig. 1 (a). An incident time-harmonic ($e^{j\omega t}$ time dependence) electromagnetic field $(\mathbf{E}^{in}, \mathbf{H}^{in})$ impinges on this object, generating a scattered field $(\mathbf{E}^{sc}, \mathbf{H}^{sc})$. Consider next the equivalent situation in Fig. 1 (b), where the material inside the object is replaced by that of the external region. Furthermore, a magnetic virtual current $\mathbf{m}$ residing on the boundary of the object is introduced. This current, which is to be determined, must generate the same scattered fields as in the original problem. After introduction of the Poincaré-Steklov operator $\mathcal{P}$, satisfying the property $\mathcal{P}(-\hat{\boldsymbol{n}} \times \boldsymbol{e}) = \hat{\boldsymbol{n}} \times \boldsymbol{h}$, and by imposing continuity of the electromagnetic fields on the object boundary Γ, we find the following single-source matrix equation:

$$\begin{bmatrix} \mathcal{K} + \frac{1}{2} & -1 \\ \frac{\mathcal{T}}{\eta} & -\mathcal{P} \end{bmatrix} \cdot \begin{bmatrix} \boldsymbol{m} \\ -\boldsymbol{u}_n \times \boldsymbol{E} \end{bmatrix} = \begin{bmatrix} \boldsymbol{u}_n \times \boldsymbol{E}^{in} \\ -\boldsymbol{u_n} \times \boldsymbol{H}^{in} \end{bmatrix}, \quad (1)$$

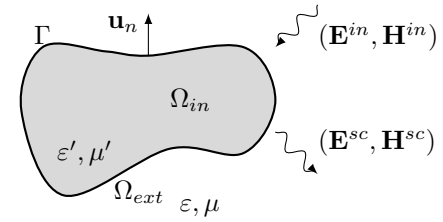

(a) Original problem

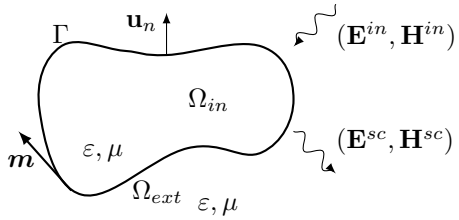

(b) Equivalent problem

Fig. 1. In (a), a homogeneous object Ω_{in} is embedded in a homogeneous background medium Ω_{ext}. Interaction of the incident field $(\boldsymbol{E}^{in}, \boldsymbol{H}^{in})$ results in a scattered field $(\boldsymbol{E}^{sc}, \boldsymbol{H}^{sc})$. In (b), the object is filled with the medium of Ω_{ext} and a surface current density $\mathbf{m}$, generating $(\boldsymbol{E}^{sc}, \boldsymbol{H}^{sc})$, is introduced on Γ.

with $\mathcal{T}$ and $\mathcal{K}$ the electric and magnetic field integral operator of Ω_{ext} [2], $\eta = \sqrt{\mu/\varepsilon}$ the impedance of Ω_{ext}, and $\boldsymbol{u}_n \times \boldsymbol{E}$ the total tangential electric field on the boundary. Next, we left multiply (1) with the following Calderón preconditioner:

$$\begin{bmatrix} 1 & 0 \\ 0 & -\eta' \mathcal{T}' \end{bmatrix}, \quad (2)$$

with η' and $\mathcal{T}'$ the impedance and the EFIO of Ω_{int}, respectively. This results, after discretization, in:

$$\begin{bmatrix} K + \frac{1}{2}G & -G \\ -\frac{\eta'}{\eta} T' \cdot (-G^T)^{-1} \cdot T & K' + \frac{1}{2}G \end{bmatrix} \cdot \begin{bmatrix} \boldsymbol{M} \\ \boldsymbol{E}_t \end{bmatrix} = \begin{bmatrix} \boldsymbol{E}_t^i \\ \eta' T' (-G^T)^{-1} \boldsymbol{H}_t^i \end{bmatrix}. \quad (3)$$

The vectors $\boldsymbol{M}$ and $\boldsymbol{E_t}$ in (3) collect the coefficients after expanding $\boldsymbol{m}$ and $-\boldsymbol{u}_n \times \boldsymbol{E}$ in Rao-Wilton-Glisson (RWG) functions. Furthermore, T and $\boldsymbol{H}_t^i$ are tested with rotated RWG basis functions, while K, K', $\boldsymbol{E}_t^i$ and the Gramian matrix G are tested with rotated Buffa-Christiansen (BC) [4] functions. T' is expanded and tested with BC and rotated BC functions, respectively.

Submitted On: August 22, 2018
Accepted On: September 29, 2018

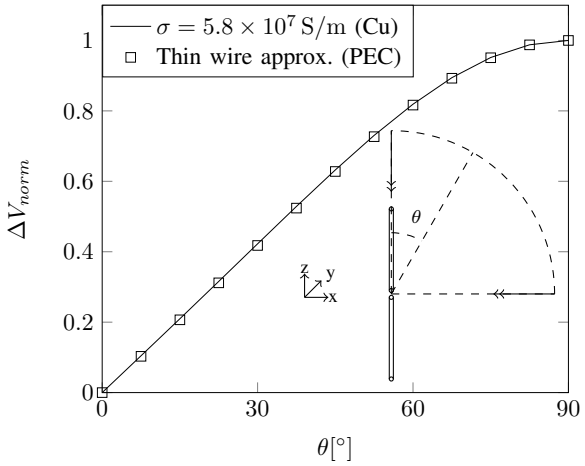

Fig. 2. Normalized voltage difference between the terminals of a copper dipole antenna with axis along the z-axis, at a frequency of 100 MHz. The antenna has a total length of $\lambda/2$, a radius of $\lambda/100$, a terminal gap of $\lambda/150$ and 2552 mesh elements. The incident wave is given by $\boldsymbol{E}^{in} = (cos(\theta)\boldsymbol{u}_x - sin(\theta)\boldsymbol{u}_z)e^{jk(sin(\theta)x+cos(\theta)z)}$ (as depicted in the schematic inset). The data are compared to the analytical approximation of a perfectly conducting thin wire antenna.

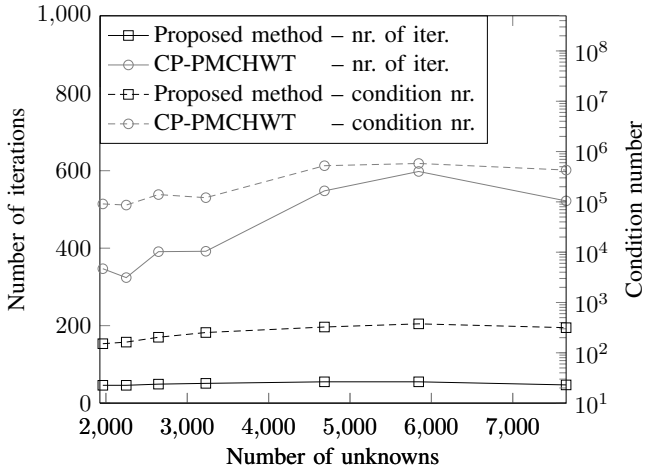

Fig. 3. Iterations until convergence (left y-axis) and condition number (right y-axis) as a function of the number of unknowns for the copper dipole antenna of Fig. 2 for an incident field $\boldsymbol{E}^{in} = \boldsymbol{u}_x e^{jkz}$, for the proposed method and for the CP-PMCHWT equation.

The convergence time of the iterative solution of (3) depends on the eigenvalue distribution of the system matrix [5]. It can be proven [6] that the eigenvalue accumulation points of the system matrix in (3) are given by:

$$\lambda_{1,\pm} = \frac{1}{2} \pm \frac{1}{2}\sqrt{\frac{\varepsilon}{\varepsilon'}}j, \tag{4}$$

and

$$\lambda_{2,\pm} = \frac{1}{2} \pm \frac{1}{2}\sqrt{\frac{\mu'}{\mu}}j. \tag{5}$$

If non-magnetic materials are assumed, one observes that the accumulation points only tend to zero or infinity when $\varepsilon \to 0$ or $\varepsilon \to -1$. Hence, in most practical engineering situations such as antenna design, which includes modeling of high dielectric contrast and conductive media, this formulation is well-conditioned.

III. Example

As a numerical validation of the formulation in (3), we consider a copper dipole antenna at a frequency of 100 MHz (inset of Fig. 2). The antenna has a total length of $\lambda/2$ and a radius of $\lambda/100$. The gap between the rods equals $\lambda/150$. In Fig. 2, the simulated voltage difference between the terminals is shown as a function of the angle of incidence of the incoming plane wave. This result is validated by the analytical thin wire approximation. The open-circuit voltage of the copper dipole shows a root mean square (rms) difference of $0.3\,\%$ compared to this reference solution.

In Fig. 3, the number of iterations until convergence (rms error $< 10^{-10}$) and the condition number of the system matrix are given as a function of the number of unknowns for both the method proposed in this paper and for the CP-PMCHWT equation. On the one hand, it can be seen that the number of iterations (≈ 50) and the condition number (≈ 300) of the proposed method remain at a stable low value for an increasing number of unknowns, validating the claim that dense mesh breakdown does not occur. The CP-PMCHWT method on the other hand suffers from ill-conditioning, resulting in longer convergence times.

IV. Conclusion

In this paper, a Calderón preconditioner for a novel single-source method that resolves the breakdown problem at high dielectric contrasts is presented. A receiving, copper dipole antenna is considered. The results demonstrate the practical applicability of the proposed method to antenna design and other scattering problems.

Acknowledgment

The authors thank the Research Foundation Flanders (FWO) for supporting this research.

References

[1] F. P. Andriulli, K. Cools, H. Bağci, F. Olyslager, A. Buffa, S. Christiansen, and E. Michielssen, "A multiplicative Calderón preconditioner for the electric field integral equation," IEEE Trans. Antennas Propag., vol. 56, no. 8, pp. 2398–2412, Aug. 2008.

[2] K. Cools, F. P. Andriulli, and E. Michielssen, "A Calderón multiplicative preconditioner for the PMCHWT integral equation," IEEE Trans. Antennas Propag., vol. 59, no. 12, pp. 4579–4587, Dec. 2011.

[3] P. Ylä-Oijala and S. P. Kiminki, "Challenges in developing efficient Calderón preconditioners for resonating or high material contrast penetrable objects," J. Comput. Appl. Math., vol. 289, pp. 296–305, Dec. 2015.

[4] A. Buffa and S. H. Christiansen, "A dual finite element complex on the barycentric refinement," Math. Comput., vol. 76, no. 260, pp. 1743–1769, Oct. 2007.

[5] P. Ylä-Oijala and M. Taskinen, "Application of combined field integral equation for electromagnetic scattering by dielectric and composite objects," IEEE Trans. Antennas Propag., vol. 53, no. 3, pp. 1168–1173, Mar. 2005.

[6] M. Gossye, M. Huynen, D. Vande Ginste, D. De Zutter, and H. Rogier, "A Calderón preconditioner for high dielectric contrast media," IEEE Trans. Antennas Propag., vol. 66, no. 2, pp. 808–818, Feb. 2018.

Directional of Arrival Tag Response for Reverse RFID Localization

Allee D. Zarrini
Department of Electrical Engineering
Colorado School of Mines
Golden, CO 80401 USA
adzarrini@mines.edu

Atef Elsherbeni
Department of Electrical Engineering
Colorado School of Mines
Golden, CO 80401 USA
aelsherb@mines.edu

Jürgen F. Brune
Mining Engineering Department
Colorado School of Mines
Golden, CO 80401 USA
jbrune@mines.edu

***Abstract*—A positioning system implemented with RFID technology is explored for a GPS-denied environment such as an underground mine or tunnel. A new method of two-dimensional localization is developed based on the angles of arrival of three tag's responses that are located at known positions. This method reduces the error when the localization process is based on the received signal strength from an RFID tag signal. Passive tags are placed in predefined locations with known information about their coordinates. An RFID reader attached to a robot with a directive antenna is used to get the AOA of the signals received from the tags. The AOA information is then used for triangulating the position of a reader's location (reverse localization).**

Keywords—Localization, RFID.

I. INTRODUCTION

Respirable dust is a known health hazard in underground mines and tunnels as well as in surface quarries and construction sites. To better track respirable dust exposure, a dust monitor with geolocating capabilities can be used to map dust exposure in spatial-temporal environment to improve engineering and management solutions for mines and industrial plant dust control.

For surface mines or other outdoor applications, the dust monitor can be equipped with a global positioning system (GPS). GPS is easily applicable, but it does not work in underground mine or tunnel environments. In such GPS-denied conditions, RFID locating technology can be used instead. RFID has been gaining popularity for its low cost compared to other locating methods. For this project, a systematic approach to locating an RFID reader using the signal strength and direction of three independent tags is developed.

II. LOCALIZATION USING DISTANCE APPROXIMATIONS

A. Mathematical Theory

The 2-D position of an unknown point can be discovered by knowing the position (x and y coordinates) of 3 different points and the distances to each of these points. Fig. 1 shows 3 circles whose radii correspond to the signal travel distance from the RFID tag to the unknown reader location. The intersections of any two circles determines the possible positions, usually 2, of the point with unknown coordinates. The intersection of all three circles then defines the exact coordinates of the unknown location. The x_1, y_1, x_2, y_2, x_3, y_3 are the known coordinates of points 1, 2, and 3 with r_1, r_2, and r_3 being the known distances away from point P with unknown coordinates x, y and z:

$$(x-x_1)^2+(y-y_1)^2=r_1^2,\quad (x-x_2)^2+(y-y_2)^2=r_2^2,\quad (x-x_3)^2+(y-y_3)^2=r_3^2.$$

As an example, consider the set of points P1, P2, P3 with coordinates (1,1), (6,3), (0,9) that are at distances of r_1 = 7.2, r_2 = 4.1, r_3 = 5.4 units away from the unknown point P. The unknown coordinates of point P can be found from the intersection of the circles as shown in Fig. 1 to be at location (5,7).

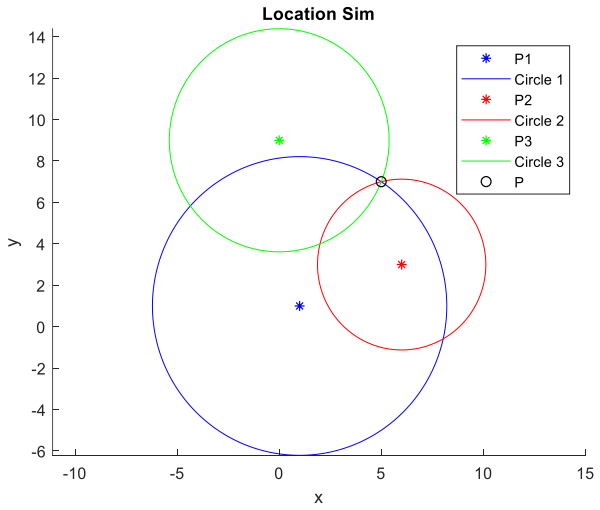

Fig. 1. A set of points P1, P2, P3 with known coordinates and the interesecting circles determining the coordinate of point P.

B. RFID Implementation

In this project, ultra-high frequency (UHF) passive RFID tags are placed at known locations as reference tags to locate the RFID reader position. The reader uses an omnidirectional antenna that will record the received signal from a tag in terms of the received signal strength (RSS). Distances between the reader and the tags can be calculated from RSS values via a generated empirical function. The reader will continuously scan all nearby tags for a predetermined amount of time. Multiple readings from each tag are averaged to reduce error from extraneous readings. If echoes from more than three tags are received, the three tags with the greatest signal strengths are chosen for the coordinate triangulation.

Submitted On: October 10, 2018
Accepted On: October 21, 2018

C. Errors and Limitations

As Fig. 2 shows, even in a clean laboratory environment the RSS-distance relation is not smooth and will produce calculation errors. Note that this data set will not result in a function because there exist many instances where a single RSS value corresponds to more than one distance.

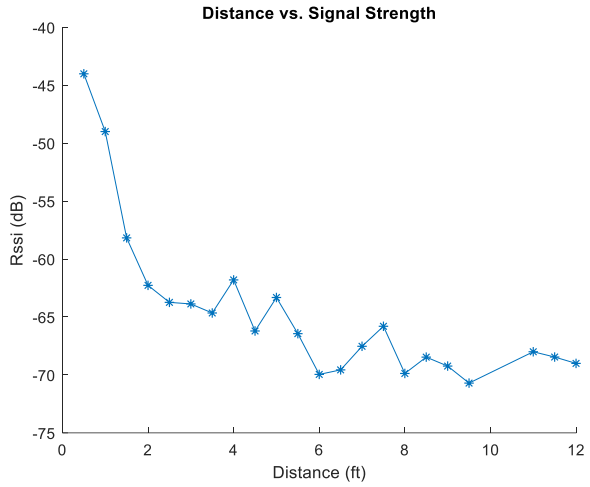

Fig. 2. Sample data showing how RSS varies greatly relative to distance.

In an underground mine environment, there may be metallic objects and electromagnetic noise that could create further interference and echoes that further distort the direct line of sight, RSS-distance relationship. Initial laboratory tests showed that location through RSS alone would not provide the desired level of accuracy. The authors decided to refine the triangulation algorithm and to improve its accuracy by recording the angle of arrival (AOA) of the received signal along with the RSS.

III. Localization using Angle of Arrival

A. Mathematial Theory

The directional algorithm similarly requires a minimum of 3 readings from the three known position tags to properly locate the unknown position of the reader. Instead of using the distance information, the reader records the AOA of the strongest signal from the known position tags. The reader must be equipped with a directional antenna which typically has a higher gain compared to the traditional omni-directional antennas, to improve the read range.

Fig. 3 illustrates the AOA from the three tags, the coordinates of the three tags and other parameters to use for solving for the unknown distances r_1, r_2, and r_3 using the following 9 equations:

$$\frac{d_{21}}{\sin(a_{21})}=\frac{r_1}{\sin(a_2)},\quad \frac{d_{21}}{\sin(a_{21})}=\frac{r_2}{\sin(a_1)},\quad \frac{d_{32}}{\sin(a_{32})}=\frac{r_2}{\sin(b_3)},$$

$$\frac{d_{32}}{\sin(a_{32})}=\frac{r_3}{\sin(b_2)},\quad \frac{d_{13}}{\sin(a_{13})}=\frac{r_3}{\sin(c_1)},\quad \frac{d_{13}}{\sin(a_{13})}=\frac{r_1}{\sin(c_3)},$$

$$d_{32}^2=d_{21}^2+d_{13}^2-2d_{21}d_{13}\cos(a_1+c_1),\quad d_{13}^2=d_{32}^2+d_{21}^2-2d_{32}d_{21}\cos(b_2+a_2),$$

$$d_{23}^2=d_{13}^2+d_{21}^2-2d_{13}d_{21}\cos(c_3+b_3).$$

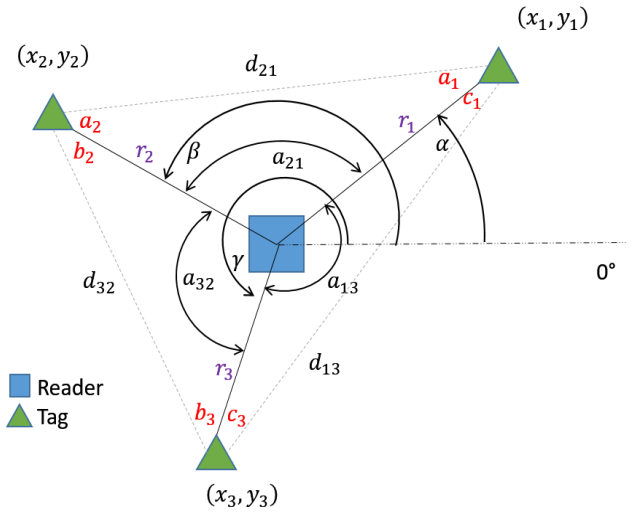

Fig. 3. The known variables in this system. α, β, γ are angles measured from the coordinate system zero axis represented by the dashed line.

Using r_1, r_2, and r_3 locating the unknown position of the reader can be achieved by the triangulation method described in Section II. For example, given a set of points P1, P2, P3 with coordinates (3,0), (12,1), (5,8) that are at angle of α = 213°, β = 351°, γ = 99°, the unknown reader position can be found from the intersection of the circles to be at location (6,2).

B. Implementation

The algorithm based on the AOA estimation requires the use of a rotating directional antenna. The antenna will rotate 360 degrees at a fixed angular velocity while recording RSS values of all tags it finds. AOA values will be registered where the strongest signals (RSS values) are obtained along with the corresponding, calculated antenna direction. The triangulation algorithm will be applied to the three strongest readings to determine the reader location.

IV. Conclusion

This implementation will be less susceptible to RSS variability caused by signal reflections off surrounding objects. Even though the reader will continue to detect those readings, the maximum RSS will be obtained from a direct line of sight with the tag which will be the strongest signal reflected from the tag. Thus, the accuracy of determining the distances is greatly enhanced. Further advantage of this process is the use of a directive antenna which will have a much greater range than an omni-directional antenna. This will also minimize the number of tags that are required and maximize the area in which the reader can detect itself. The biggest limitation however, for this algorithm is coordinates of the unknown reader position need to be within the triangle that is made by the three tags with known positions. However, for the localization of operators inside mines carrying a portable RFID reader, this special condition will not exist, hence this procedure would be applicable.

EIT Images of Human Inspiration and Expiration using a D-bar Method with Spatial Priors

Melody Alsaker
Department of Mathematics
Gonzaga University
Spokane, Washington 92258
alsaker@gonzaga.edu

Jennifer L. Mueller
Department of Mathematics
School of Biomedical Engineering
Colorado State University
Fort Collins, Colorado 80523
mueller@math.colostate.edu

***Abstract*—The inclusion of a spatial prior in the high-frequency regime of the scattering transform for the 2-D D-bar method for electrical impedance tomography is studied for use with human subject data. The effects and balance of the two regularization parameters for the inverse problem are studied. Results on data from human volunteers reveal improved spatial resolution when compared to inspiratory and expiratory CT scans.**

I. Introduction

The inverse problem of electrical impedance tomography (EIT) is modeled by the generalized Laplace equation,

$$\nabla \cdot (\sigma(x,y)\nabla u(x,y)) = 0, \quad (x,y) \text{ in } \Omega, \tag{1}$$

where $\sigma(x,y)$ is the conductivity distribution to be reconstructed from boundary data represented by the Dirichlet-to-Neumann (DN) map,

$$\Lambda_\sigma : u|_{\partial\Omega} \mapsto \sigma \frac{\partial u}{\partial \nu}\Big|_{\partial\Omega}, \tag{2}$$

which physically takes boundary voltages to current densities on the boundary. It was established in [1] that for $\sigma \in C^2(\Omega)$, the DN map Λ_σ uniquely determines σ.

Cross-sectional EIT images of the chest have applications in bedside monitoring of patients with acute respiratory distress syndrome (ARDS), detection of pulmonary edema, atelectasis, and pneumothorax, since the heterogeneity characterizing these disorders is well-represented in a 2-D slice in a patient lying down. The references [2], [3] provide surveys of clinical pulmonary applications of EIT.

The inverse problem of EIT is severely ill-posed, and hence highly sensitive to measurement noise and modeling errors. As a result, EIT reconstructions tend to suffer from low spatial resolution. The use of prior information in the reconstruction process is a classic approach in inverse problems to regularize and improve spatial resolution. Iterative reconstruction methods include *a priori* information about the conductivity distribution in the chest in the regularization term (see, for example, [4]–[15].) In this work, the conductivity is computed using a direct (non-iterative) method known as the *D-bar* method.

D-bar reconstruction methods are based on special functions known as complex geometrical optics (CGO) solutions, which satisfy a direct relationship to the unknown conductivity, and through the computation of the CGO solutions from measured EIT data, the inverse problem can be solved directly (non-iteratively). A real-time implementation of the D-bar method was given in [16], and the D-bar method has been used as the reconstruction method in a study to estimate regions of air trapping in cystic fibrosis patients [17] and in a study of EIT-derived measures of spirometry [18]. Patients with cystic fibrosis receive a CT scan approximately every three years (more often if clinically indicated). This offers the opportunity to use some information about the patient's anatomy from the CT scan as priors in the reconstruction algorithm. A method for including a spatial prior in the D-bar reconstruction algorithm was first proposed in [19] and tested on simulated data. In [20] a method for optimizing the spatial prior was presented for use with experimental tank data. In this work we demonstrate the effectiveness of that method on data collected on several patients with cystic fibrosis during tidal breathing. CT scans of the patients' chests were available as part of their regular clinical visit and were used to construct the priors.

II. Methods

A. Outline of the D-bar Method (No Priors)

The D-bar method applied here is based on the global uniqueness proof for the 2-D inverse conductivity problem [1] and subsequent implementation and development (see [21] and the references therein). The CGO solutions are special solutions to the Schrödinger equation, which arises from the change of variables in (1) $\tilde{u} = \sqrt{\sigma}u$ and $q = \sigma^{-1/2}\Delta\sigma^{1/2}$:

$$(-\Delta + q(x,y))\tilde{u}(x,y) = 0, \quad (x,y) \in \Omega. \tag{3}$$

Introducing a a non-physical complex frequency k in (3), extending the equation to $(x,y) \in \mathbb{R}^2$, and identifying a point in the complex plane $z = x + iy$ with the spatial point (x,y), the CGO solutions $\psi(z,k)$ satisfy,

$$(-\Delta + q(z))\psi(z,k) = 0, \quad z \in \mathbb{R}^2. \tag{4}$$

The related CGO solution $\mu(z,k)$ is defined by $\mu \equiv e^{ikz}\psi(z,k)$. The CGO solution $\psi(z,k)$ is related to the DN map, and hence the measured data, through the boundary integral equation,

$$\psi(z,k)|_{\partial\Omega} = e^{ikz}|_{\partial\Omega} - \int_{\partial\Omega} G_k(z-\zeta)(\Lambda_\sigma - \Lambda_1)\psi(\cdot,k)ds,$$

Submitted On: October 4, 2018
Accepted On: October 21, 2018

where G_k is the Faddeev's Green's function for the Laplacian operator [22], and Λ_1 denotes the DN map corresponding to $\sigma \equiv 1$ in Ω. The conductivity can be directly computed from knowledge of $\mu(z,k)$ in the interior of Ω through,

$$\sigma(z) = \mu^2(z,0).$$

To compute μ in the interior, the scattering transform $\mathbf{t}(k)$ of the conductivity is needed, and an integral equation is solved for μ:

$$\mu(z,k) = 1 + \frac{1}{(2\pi)^2}\int_{\mathbb{R}^2} \frac{\mathbf{t}(k')}{\overline{k'}(k-k')}\, e^{-i(kz+\bar{k}\bar{z})}\overline{\mu(z,k')}dk',$$

where the scattering transform is a nonphysical nonlinear Fourier transform of q defined by,

$$\mathbf{t}(k) := \int_\Omega e^{i\bar{k}\bar{z}} q(z)\psi(z,k)dz. \tag{5}$$

Since q is unknown, in practice the scattering transform is computed from the data via the formula,

$$\mathbf{t}(k) = \int_{\partial\Omega} e^{i\bar{k}\bar{z}}(\Lambda_\sigma - \Lambda_1)\psi(z,k)ds. \tag{6}$$

Difference images from a reference frame in which the voltage on each electrode was averaged over all of the frames in the data collection sequence can be computed using $\mathbf{t}^{\exp}_{\mathrm{dif}}(k)$, introduced in [23], where the CGO solution $\psi(z,k)$ is replaced by its asymptotic behavior e^{ikz} in the scattering transform. This approximation is denoted by $\mathbf{t}^{\exp}_{\mathrm{dif}}(k)$ and is given by,

$$\begin{aligned}\mathbf{t}^{\exp}_{\mathrm{dif}}(k) &\equiv \int_{\partial\Omega} e^{i\bar{k}\bar{z}}(\Lambda_\sigma - \Lambda_1)e^{ikz}ds(z)\\ &- \int_{\partial\Omega} e^{i\bar{k}\bar{z}}(\Lambda_{\mathrm{ref}} - \Lambda_1)e^{ikz}ds(z),\\ &= \int_{\partial\Omega} e^{i\bar{k}\bar{z}}(\Lambda_\sigma - \Lambda_{\mathrm{ref}})e^{ikz}ds(z)\end{aligned}$$

where Λ_{ref} is the DN map corresponding to the averaged data.

B. Outline of the D-bar Method with Spatial Priors

Since the computation of the scattering transform blows up in the presence of noise outside $|k| \le R_1$ for some R_1, as in [19] the scattering transform is extended to a larger k disk by computing it for the noise-free case of a known conductivity and by using the definition of the scattering transform (5), rather than the equation utilizing the data (6); this scattering transform is denoted $\mathbf{t}_{\mathrm{pr}}$. This leads to a piecewise-defined scattering transform $\mathbf{t}_{\mathrm{pw}}$, where the prior information is encoded in the method in the high-frequency components of the scattering transform through $\mathbf{t}_{\mathrm{pr}}$:

$$\mathbf{t}_{\mathrm{pw}}(k) := \begin{cases}\mathbf{t}^{\exp}_{\mathrm{dif}}(k), & |k| \le R_1\\ \mathbf{t}_{\mathrm{pr}}(k), & R_1 < |k| \le R_2\\ 0, & |k| > R_2\end{cases}. \tag{7}$$

The prior information is included in a second location in the computations as well. Denoting the CGO solution computed for the noise-free case of a known conductivity by,

$$\mu_{\mathrm{int}}(z) := \frac{1}{\pi R_2^2}\int_{|k|\le R_2} \mu_{\mathrm{pr}}(z,k)dk, \tag{8}$$

we solve a modified integral equation:

$$\begin{aligned}\mu_{R_2,\alpha}(z,k) &= \alpha + (1-\alpha)\mu_{\mathrm{int}}(z)\\ &+ \frac{1}{(2\pi)^2}\int_{|k|\le R_2} \frac{\mathbf{t}_{\mathrm{pw}}(k')}{\bar{k}'(k-k')} e_{-k'}\overline{\mu_{R_2,\alpha}(z,k')}\, dk',\end{aligned} \tag{9}$$

where the weighting parameter α is used to control the influence of the term μ_{int} upon the resulting reconstruction.

C. Construction of the Spatial Prior

The prior consists of a simple phantom representative of known features of the true conductivity distribution with assigned conductivity values. In this work, the inspiratory and expiratory CT scans best representing the slice of the chest in the plane of the electrodes were chosen to construct two sets of priors – one for inspiration and one for expiration. The boundaries of the chest shape, lungs, and heart, were approximated from the CT scans by importing the images into MATLAB and using the tool for exporting selected coordinates (r_n, θ_n) in the image to a text file. Fourier series approximations to the chest shape and the organ boundaries are represented by the function $r(\theta)$:

$$r(\theta) = a_0 + \sum_{i=1}^{N} a_i\cos(\theta) + b_i\sin(\theta),$$

where $\{a_i\}_{i=0}^N$ and $\{b_j\}_{j=1}^N$ are chosen so as to minimize the root mean squares error $\|r(\theta_n) - r_n\|$ over all the selected coordinates (r_n, θ_n).

Denoting the vector of conductivity values in each of the regions (heart, left lung, right lung, and background) by $\mathbf{c}$, we seek to find a $\mathbf{c}$ that minimizes the difference between the scattering transform computed from the measured data $\mathbf{t}^{\mathrm{vec}}$ and the scattering transform computed from the prior $\mathbf{t}^{\mathrm{vec}}_{\mathrm{pr}}$. We define the objective function,

$$J(\mathbf{c}) := \|\mathbf{t}^{\mathrm{vec}}_{\mathrm{pr}}(\mathbf{c}) - \mathbf{t}^{\mathrm{vec}}\|^{\mathbf{2}}_{\mathbf{2}}, \tag{10}$$

and solve the constrained nonlinear minimization problem,

$$\underset{\mathbf{c}\in\mathbb{R}^{\mathbf{n}}}{\text{minimize}}\ J(\mathbf{c}) \ \text{ subject to } \ell \le \mathbf{c} \le u, \tag{11}$$

where ℓ and u are n-vectors of lower and upper bounds, using the Interior Point Algorithm in MATLAB's Optimization Toolbox.

III. Results and Discussion

This data was collected with the ACE1 EIT system [24] as part of a larger study conducted in accordance with the amended Declaration of Helsinki. Data were collected at Children's Hospital Colorado, Aurora, CO under the approval of the Colorado Multiple Institutional Review Board (COMIRB) (approval number COMIRB 14-0652). Informed

written parental consent and children's informed assent was obtained from the subjects. The data used in this paper are from a 6 year old human male cystic fibrosis patient (referred to here as Subject 1) and a 12 year old human female cystic fibrosis patient (referred to here as Subject 2). The CT scans were performed as part of the subject's standard care, and the EIT data was collected immediately prior to the CT scan.

Pediatric EKG electrodes (Phillips 13951C) of height 33 mm and width 23 mm were placed around the perimeter of the subject's chest with an additional electrode on the shoulder as ground. The number of electrodes used was the maximum number that would fit around the circumference with no electrodes touching. For Subject 1, this was 22 electrodes, and for Subject 2 this was 24 electrodes. Alternating currents with frequency 125 kHz were applied at approximately 4 mA, peak-to-peak using pairwise adjacent excitation patterns. After the EIT data was collected, fiducial markers were placed at the center of each electrode, so that their locations could be noted in the CT scans. The expiratory CT scan with the most electrodes in the plane of the scan was chosen for creating the boundary and prior for full expiration, and the inspiratory scan at the level closest to the chosen expiratory CT scan was chosen for creating the boundary and prior for full inspiration. It should be noted that the expiratory CT scans are 4 cm apart in the Z (caudal-cranial) direction, while the inspiratory scans are 0.5 mm apart in the Z-direction.

Approximate organ boundaries and the outer boundary were visually extracted from the CT scan, and the domain was divided into four regions: background, heart, left lung, and right lung. The spatial priors for Subject 1 for inspiration and expiration are found in Fig. 2, and the spatial priors for Subject 2 for inspiration and expiration are found in Fig. 5. Initial guesses for the conductivity in each of the four regions were chosen from a preliminary reconstruction, and the constrained optimization problem (11) was solved to obtain values for the prior in each of the four regions. The scattering transform $\mathbf{t}_{\rm pr}$ was then computed, and the scattering transform (7) was used for the final reconstruction. Figs. 9 and 10 show the real and imaginary parts of the scattering transforms $\mathbf{t}_{\rm pr}$, which are computed from equation (5) using the spatial priors with the optimized organ values, and the real and imaginary parts of the scattering transforms $\mathbf{t}_{\rm pw}$, which are computed from equation (7), which pieces together $\mathbf{t}_{\rm dif}^{\rm exp}$ computed from the data and $\mathbf{t}_{\rm pr}$. All plots are on $|k| \leq 6$ (i.e., $R_2 = 6$ for $\mathbf{t}_{\rm pw}$), and it is evident that there is some mismatch in amplitude and features of $\mathbf{t}_{\rm dif}^{\rm exp}$ with $\mathbf{t}_{\rm pw}$. A more thorough study of the effect of this mismatch is a topic of future work.

The CT scan slices at inspiration and expiration from the two subjects are shown in Figs. 1 and 4 in the standard DICOM orientation, in which the subject's left is on the viewer's right. The expiratory CT scan for the 6 year old subject includes some diaphragm in the subject's right lung, which raises the question of whether the diaphragm is expected to be visible in the EIT images.

The EIT reconstructions effectively compute the conductivity within a 3-D slice of the body with a thickness equal

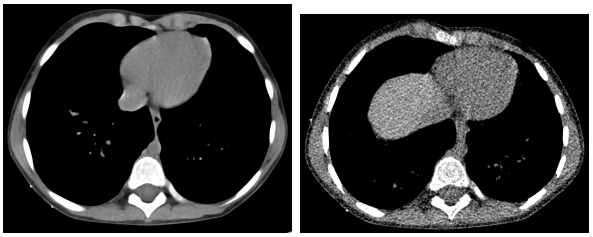

Fig. 1. Inspiratory (left) and expiratory (right) CT scans of a 6-year old male subject used to construct the boundary shape and organs for the spatial priors.

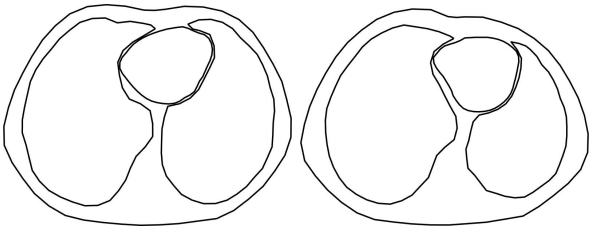

Fig. 2. Inspiratory (left) and expiratory (right) approximate organ boundaries used in the *a priori* D-bar method for a 6-year old male subject.

to that of the electrodes in the cross-section defined by the placement of the row of electrodes. The thickness of the slice is approximate, since in the clinical setting the centers of the electrodes are not aligned perfectly in a plane, and the slice that they define may well be a skew from the CT scan slices. Furthermore, the induced currents will flow out of the plane of the electrodes and affect the reconstructions. The effect of out-of-plane currents on EIT images has been analyzed in, for example, [25]–[28], and the influence of out-of-plane inhomogeneities is dependent on the conductivity of the inhomogeneities and their radial distance from the electrodes, with the least influence in the center of the slice [25]. One rule of thumb is that out-of-plane objects lying a vertical distance within 1/2 the radius R of the domain may influence the voltage measurements [28]. Approximating R by $P/(2\pi)$, where P is the perimeter of the subject in the plane of the majority of the electrodes, which for this subject was $P = 62$ cm, $R/2 = P/(4\pi) \approx 4.9$ cm. While the CT scan slice at $Z = 141$ mm contains the most fiducial markers, several markers can also be seen in the slice in Fig. 1, which is at $Z = 161$ mm, and so the effect of the diaphragm on the reconstructed images is inconclusive from this analysis. Another point to consider is the fact that the position of the diaphragm changes when a patient is supine, as is the case in the CT scanner, versus when they are sitting up, as is the case when the EIT data was collected [29]. In [29] MRI images were collected on 10 healthy men in both the sitting and supine positions, and it was found that the movement of the diaphragm (known as the diaphragmatic excursion) was greater in the supine position than in the sitting position. Since these factors do not point strongly to an influence of the presence of the diaphragm on the reconstructions, the diaphragm was not included in the prior in this study.

Reconstructions from inspiratory and expiratory data of

Subjects 1 and 2 are shown in Figs. 3 and 6, respectively. Regions of high relative conductivity are shown in red, and regions of low relative conductivity are plotted in blue. To demonstrate the effects of the parameters R_2 and α on the reconstructions, comparison plots for the inspiratory scans from both subjects are shown in Figs. 7 and 8. For all reconstructions here, $R_1 = 5$, so a prior with $R_2 = 6$ is fairly weak. Note that a stronger prior (indicated by larger R_2 or smaller α) does not necessarily improve the reconstruction further, and may in fact introduce artifacts. This is likely due to increased mismatch between the *a priori* scattering transform $\mathbf{t}_{\text{pr}}$ and the scattering transform computed from the measured data.

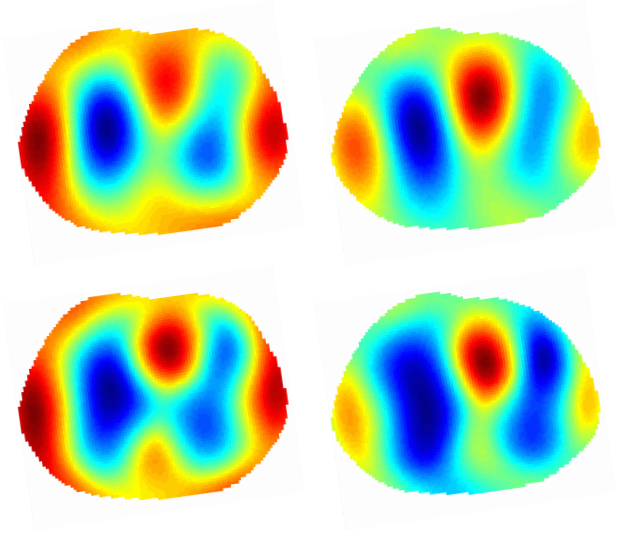

Fig. 3. Top: Standard D-bar reconstructions of data collected during inspiration (left) and expiration (right) for a 6-year-old male subject. Bottom: Corresponding D-bar reconstructions with optimized prior.

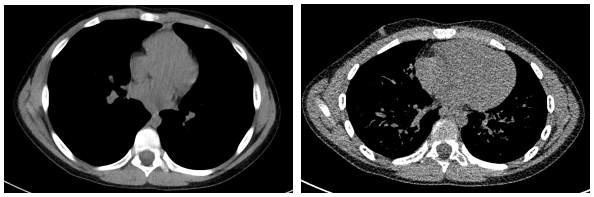

Fig. 4. Inspiratory (left) and expiratory (right) CT of 12-year old female subject used to construct the boundary shape and organs for the spatial priors.

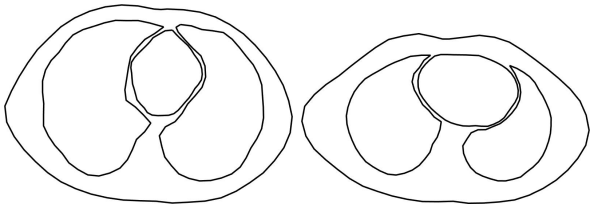

Fig. 5. Inspiratory (left) and expiratory (right) approximate organ boundaries used in the *a priori* D-bar method for a 12-year old female subject.

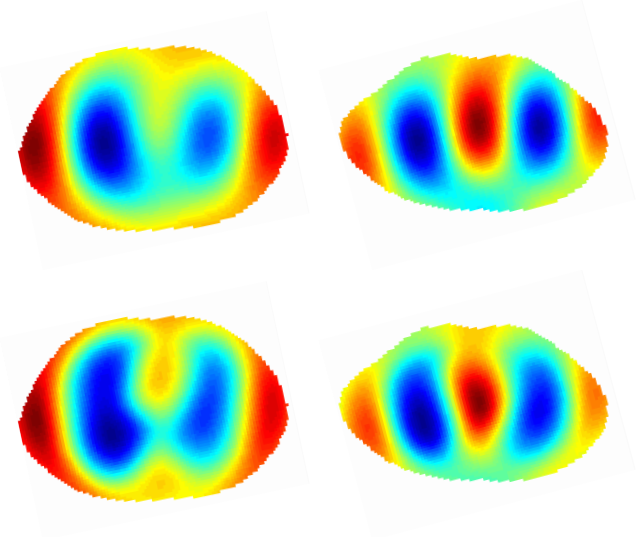

Fig. 6. Top: Standard D-bar reconstructions of data collected during inspiration (left) and expiration (right) for a 12-year-old female subject. Bottom: Corresponding D-bar reconstructions with optimized prior.

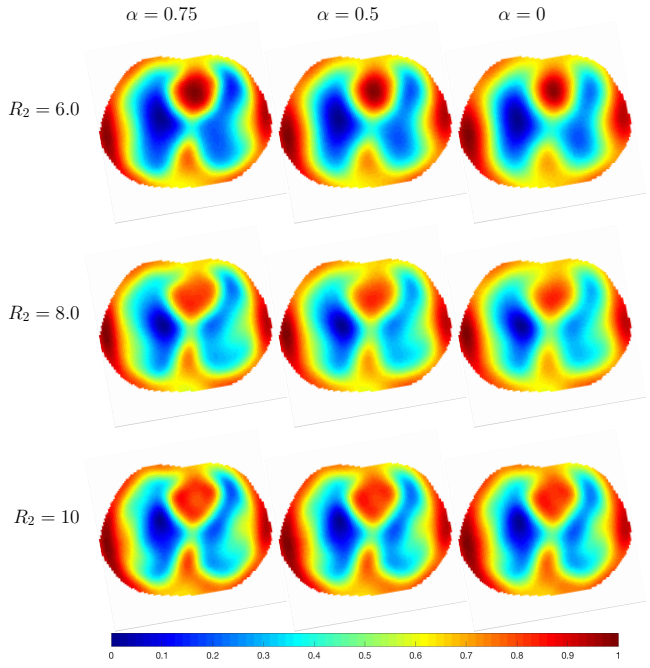

Fig. 7. A comparison of D-bar reconstructions of inspiratory data from a 6-year-old male subject using a prior with various values of R_2 and α.

IV. Conclusion

Spatial resolution of the EIT images reconstructed by the D-bar method is improved through the use of simple spatial priors. Further research is needed to determine their clinical value and whether they aid in detecting pathologies.

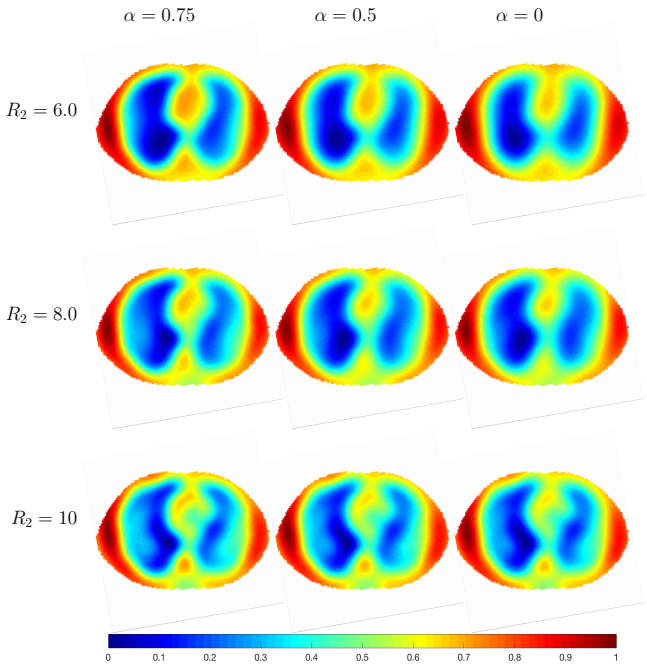

Fig. 8. A comparison of D-bar reconstructions of inspiratory data from a 12-year-old female subject using a prior with various values of R_2 and α.

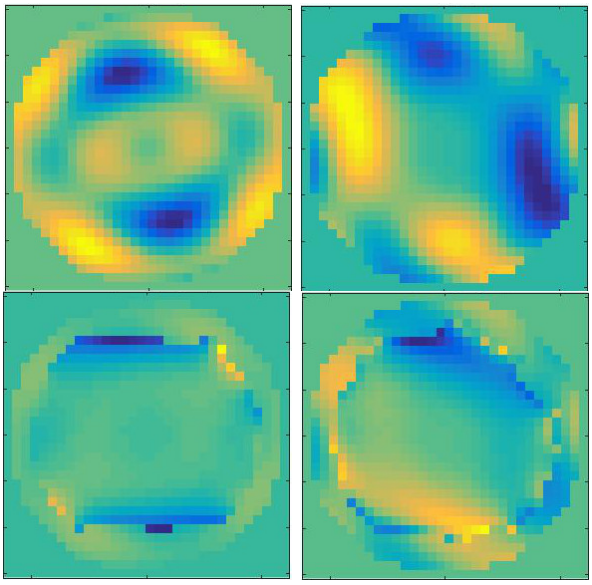

Fig. 9. Top: Plots of the real (left) and imaginary (right) parts of the *a priori* scattering transform $\mathbf{t}_{\mathrm{pr}}$ using truncation radius $R_2 = 6$, for an inspiratory frame from a 6-year-old male subject. Bottom: Real and imaginary parts of the corresponding piecewise-defined scattering transform $\mathbf{t}_{\mathrm{pw}}$.

ACKNOWLEDGMENT

This project was supported by award 1R21EB016869-01 from the NIBIB. The content is solely the responsibility of the authors and does not necessarily represent the official view of the NIBIB or NIH.

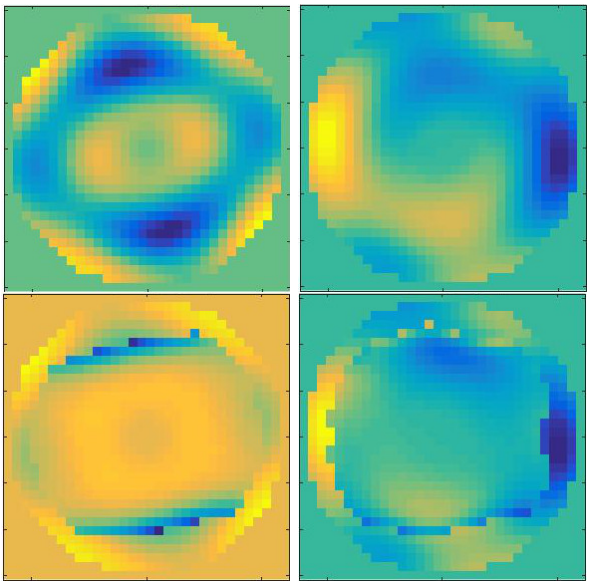

Fig. 10. Top: Plots of the real (left) and imaginary (right) parts of the *a priori* scattering transform $\mathbf{t}_{\mathrm{pr}}$ using truncation radius $R_2 = 6$, for an inspiratory frame from a 12-year-old female subject. Bottom: Real and imaginary parts of the corresponding piecewise-defined scattering transform $\mathbf{t}_{\mathrm{pw}}$.

REFERENCES

[1] A. I. Nachman, "Global uniqueness for a two-dimensional inverse boundary value problem," Ann. Math., vol. 143, no. 1, pp. 71–96, 1996.

[2] E. Costa, R. Gonzalez Lima, and M. Amato, "Electrical impedance tomography," in Intensive Care Medicine (J. Vincent, ed.), pp. 394–404, Springer, New York, 2009.

[3] D. Nguyen, J. C. Thiagalingam, and A. A. McEwan, "A review on electrical impedance tomography for pulmonary perfusion imaging," Physiol. Meas., vol. 33, no. 5, pp. 695–706, 2012.

[4] N. J. Avis and D. C. Barber, "Incorporating a priori information into the Sheffield filtered backprojection algorithm," Physiol. Meas., vol. 16, no. 3A, pp. A111–A122, 1995.

[5] U. Baysal and B. M. Eyüboglu, "Use of a priori information in estimating tissue resistivities - a simulation study," Phys. Med. and Biol., vol. 43, no. 12, pp. 3589–3606, 1998.

[6] E. D. L. B. Camargo, "Development of an absolute electrical impedance imaging algorithm for clinical use," PhD thesis, University of São Paulo, 2013.

[7] H. Dehghani, D. C. Barber, and I. Basarab-Horwath, "Incorporating a priori anatomical information into image reconstruction in electrical impedance tomography," Physiol. Meas., vol. 20, no. 1, pp. 87–102, 1999.

[8] D. C. Dobson and F. Santosa, "An image-enhancement technique for electrical impedance tomography," Inverse Probl., vol. 10, no. 2, pp. 317–334, 1994.

[9] D. Ferrario, B. Grychtol, A. Adler, J. Sola, S. H. Bohm, and M. Bodenstein, "Toward morphological thoracic EIT: Major signal sources correspond to respective organ locations in CT," IEEE T. Med. Imaging, vol. 59, no. 11, pp. 3000–3008, 2012.

[10] D. Flores-Tapia and S. Pistorius, "Electrical impedance tomography reconstruction using a monotonicity approach based on a priori knowledge," in Engineering in Medicine and Biology Society (EMBC), 2010 Annual International Conference of the IEEE, pp. 4996–4999, Aug. 2010.

[11] J. P. Kaipio, V. Kolehmainen, M. Vauhkonen, and E. Somersalo, "Inverse problems with structural prior information," Inverse Probl., vol. 15, no. 3, p. 713, 1999.

[12] K. Y. Kim, S. I. Kang, M. C. Kim, S. Kim, Y. J. Lee, and M. Vauhkonen, "Dynamic image reconstruction in electrical impedance tomography with known internal structures," IEEE Transactions on Magnetics, vol. 38, pp. 1301–1304, Mar. 2002.

[13] F. S. Moura, J. C. C. Aya, A. T. Fleury, M. B. P. Amato, and R. G. Lima, "Dynamic imaging in electrical impedance tomography of the human chest with online transition matrix identification," IEEE Transactions on Biomedical Engineering, vol. 57, pp. 422–431, Feb. 2010.

[14] M. Soleimani, "Electrical impedance tomography imaging using a priori ultrasound data," BioMed. Eng. OnLine, vol. 5, no. 8, 2006.

[15] M. Vauhkonen, D. Vadasz, P. A. Karjalainen, E. Somersalo, and J. P. Kaipio, "Tikhonov regularization and prior information in electrical impedance tomography," IEEE T. Med. Imaging, vol. 17, no. 2, pp. 285–293, 1998.

[16] M. Dodd and J. Mueller, "A real-time D-bar algorithm for 2-D electrical impedance tomography data," Inverse Probl. Imag., vol. 8, no. 4, pp. 1013–1031, 2014.

[17] J. Mueller, P. Muller, M. Mellenthin, E. DeBoer, R. Murthy, M. Capps, M. Alsaker, R. Deterding, and S. Sagel, "A method of estimating regions of air trapping from electrical impedance tomography data," Physiological Measurement, vol. 39, no. 5, p. 05NT01, 2018.

[18] P. Muller, J. Mueller, M. Mellenthin, R. Murthy, M. Capps, B. Wagner, M. Alsaker, R. Deterding, S. Sagel, and J. Hoppe, "Evaluation of surrogate measures of pulmonary function derived from electrical impedance tomography data in children with cystic fibrosis," Physiological Measurement, vol. 39, no. 4, p. 045008, 2018.

[19] M. Alsaker and J. Mueller, "A D-bar algorithm with a priori information for 2-dimensional electrical impedance tomography," SIAM J. Imaging Sci., vol. 9, no. 4, pp. 1619–1654, 2016.

[20] M. Alsaker and J. L. Mueller, "Use of an optimized spatial prior in d-bar reconstructions of EIT tank data," In review, 2017.

[21] J. L. Mueller and S. Siltanen, Linear and Nonlinear Inverse Problems with Practical Applications. Philadelphia, PA: SIAM, 2012.

[22] L. D. Faddeev, "Increasing solutions of the schroedinger equation," Sov. Phys. Dokl., vol. 10, pp. 1033–1035, 1966.

[23] D. Isaacson, J. L. Mueller, J. C. Newell, and S. Siltanen, "Imaging cardiac activity by the D-bar method for electrical impedance tomography," Physiol. Meas., vol. 27, no. 5, pp. S43–S50, 2006.

[24] M. Mellenthin, J. Mueller, E. de Camargo, F. de Moura, T. Santos, R. Lima, S. Hamilton, P. Muller, and M. Alsaker, "The ACE1 electrical impedance tomography system for thoracic imaging," IEEE Transactions on Instrumentation and Measurement, p. to appear, 2018.

[25] B. M. Eyuboglu, B. H. Brown, and D. C. Barber, "Limitations to SV determination from APT images," in Images of the Twenty-First Century. Proceedings of the Annual International Engineering in Medicine and Biology Society, pp. 442–443 vol. 2, Nov. 1989.

[26] R. Guardo, C. Boulay, B. Murray, and M. Bertrand, "An experimental study in electrical impedance tomography using backprojection reconstruction," IEEE Transactions on Biomedical Engineering, vol. 38, pp. 617–627, July 1991.

[27] K. S. Rabbani and A. M. B. H. Kabir, "Studies on the effect of the third dimension on a two-dimensional electrical impedance tomography system," Clinical Physics and Physiological Measurement, vol. 12, no. 4, p. 393, 1991.

[28] R. S. Blue, D. Isaacson, and J. C. Newell, "Real-time three-dimensional electrical impedance imaging," Physiological Measurement, vol. 21, no. 1, p. 15, 2000.

[29] R. Takazakura, M. Takahashi, N. Nitta, and K. Murata, "Diaphragmatic motion in the sitting and supine positions: Healthy subject study using a vertically open magnetic resonance system," Journal of Magnetic Resonance Imaging, vol. 19, no. 5, pp. 605–609, 2004.

Domain Decomposition Method for Scattering from an Aircraft with Jet Engine Inlet Cavity

Miodrag S. Tasic [1], Branko M. Kolundzija [1], and Tomislav S. Milosevic [2]

[1] Department of General Electrical Engineering
University of Belgrade–School of Electrical Engineering, Belgrade, 11120, Serbia
tasic@etf.rs, kol@etf.rs

[2] Applications/Technical Support
WIPL-D d.o.o., Belgrade, 11073, Serbia
tomislav.milosevic@wipl-d.com

Abstract ─ Monostatic radar cross section (RCS) of an combat aircraft is analyzed using iterative Least Square Method weighted domain decomposition method (LSM weighted DDM). The model of the 200 wavelengths long aircraft is made of perfect electric conductor (PEC). Inlet cavity of the jet engine is included in the model. The inlet has realistic shape, whereas cavity is closed with a PEC on the outlet side. Corresponding model without the inlet is also analyzed—the inlet contour is smoothed, and then it is closed with a PEC. Method of moments (MoM) solution is used as a reference. It is shown that the LSM weighted DDM solution can provide very good solution in just a few iterations if problematic parts of the structure are extracted in separate subdomains.

Index Terms ─ Domain decomposition method, jet engine inlet, method of moments, monostatic radar cross section.

I. INTRODUCTION

It is shown that jet engines have significant influence on the monostatic radar cross section (RCS) of aircrafts. A jet engine alone is difficult for electromagnetic (EM) analysis, because its inlet cavity acts like resonant structure, and it features geometrically complex, fine details (e.g., blades). Thus, asymptotic techniques (like ray tracing) cannot provide sufficient accuracy, whereas numerically exact methods (like the Method of Moments—MoM and the Finite Element Method—FEM) are limited by their computational cost. In the last decade of 20th century different strategies were used for jet engine analysis [1]. Recently, domain decomposition methods (DDMs) coupled with accelerators such as the multilevel fast multipole algorithm (MLFMA) show as good candidates for such analysis [2].

A novel iterative DDM is introduced in [3]. The entire model is decomposed into subdomains. Solution is obtained as a linear combination of the subdomain solutions from the current iteration and from all previous iterations. Original excitation is used for the subdomain solutions in the 1st iteration, whereas the subdomains are excited with the residual error in the subsequent iterations. The weighting coefficients of the linear combination are determined in a way to minimize residual error of the MoM system of equations. It is not necessary to store or invert the entire MoM matrix, so the method is more efficient than the MoM. General theory of the Method of Moments weighted Domain Decomposition Method (MoM weighted DDM) is presented in [4]. The method in [3] is a special case of the MoM weighted DDM, and can be referred to as Least Square Method weighted Domain Decomposition Method (LSM weighted DDM).

In this paper the LSM weighted DDM method is used to obtain the monostatic RCS of the geometrically realistic aircraft model, made of perfect electric conductor (PEC). The model includes the inlet cavity, but without fan blades / non-trivial outlet terminations. The cavity is ended with a simple PEC wall. To illustrate the influence of the inlet on the convergence, we also analyzed the model without the inlet.

II. LSM WEIGHTED DDM FOR MULTIPLE EXCITATIONS

The MoM weighted DDM in [4] is presented for the single excitation case (bistatic RCS). Though multiple excitation case (monostatic RCS) can be processed as a sequence of single excitation analysis, the process can be speed up by dealing with all excitations (or a group of excitations) simultaneously. In that sense, the theory of LSM weighted DDM for multiple excitations is just a slightly adapted theory from [4], but will be presented here briefly, for completeness. More detailed explanation of the method can be found in [4].

The solution for the *j*th excitation (incident EM

Submitted On: September 28, 2018
Accepted On: October 1, 2018

plane wave), $j=1,..,N_e$, is the solution of the MoM matrix equation:

$$\mathbf{Z}\mathbf{A}^{(j)}=\mathbf{V}^{(j)}, \tag{1}$$

such that the $N\times N$ matrix $\mathbf{Z}$ is a linear operator, the $N\times 1$ matrix $\mathbf{V}^{(j)}$ is the known excitation column vector, and the $N\times 1$ matrix $\mathbf{A}^{(j)}$ is the unknown response column vector to be determined. We solve (1) iteratively, using domain decomposition strategy.

The solution space of $\mathbf{A}$ is split into M overlapping subdomains, formally using $N_l\times N$ restriction matrices E_l, $l=1,..,M$. A restriction matrix E_l has a single non-zero element in each row, such that,

$$\sum_{l=1}^{M}\mathbf{E}_l^{\mathrm{T}}\mathbf{E}_l=\mathbf{I}. \tag{2}$$

Restriction of $\mathbf{A}$ to the lth subdomain results in a column vector ($N_l\times 1$ matrix) $\mathbf{A}_l=\mathbf{E}_l\mathbf{A}$, whereas extension from the lth subdomain back to the entire domain is performed as $\mathbf{B}=\mathbf{E}_l^{\mathrm{T}}\mathbf{A}_l$. Restriction of $\mathbf{Z}$ to the lth subdomain results in a $N_l\times N_l$ matrix $\mathbf{Z}_{ll}=\mathbf{E}_l\mathbf{Z}\mathbf{E}_l^{\mathrm{T}}$.

If we know the solution for the jth excitation in the $(n-1)$th iteration, $\mathbf{A}^{(n-1,j)}$, residual vector is defined as:

$$\mathbf{V}^{(n-1,j)}=\mathbf{V}-\mathbf{Z}\mathbf{A}^{(n-1,j)},\ n>0. \tag{3}$$

To start the process, we adopt $\mathbf{A}^{(0,j)}=0$. Solution for the lth subdomain (extended to the entire domain) in the nth iteration is:

$$\mathbf{B}_l^{(n,j)}=\mathbf{E}_l^{\mathrm{T}}\left(\mathbf{E}_l\mathbf{Z}\mathbf{E}_l^{\mathrm{T}}\right)^{-1}\mathbf{E}_l\mathbf{V}^{(n-1,j)}. \tag{4}$$

We calculate vector of weighting coefficients for the jth excitation in the nth iteration, $\mathbf{C}^{(n,j)}$, as:

$$\mathbf{C}^{(n,j)}=\left(\left(\mathbf{Z}\mathbf{B}^{(n,j)}\right)^{\mathrm{H}}\left(\mathbf{Z}\mathbf{B}^{(n,j)}\right)\right)^{-1}\left(\mathbf{Z}\mathbf{B}^{(n,j)}\right)^{\mathrm{H}}\mathrm{V}^{(n,j)}, \tag{5}$$

where $\mathbf{B}^{(n,j)}$ is a matrix which columns are $\mathbf{B}_l^{(n,j)}$ from (4). Approximate solution of (1) in the nth iteration can now be calculated as:

$$\mathbf{A}^{(n,j)}=\mathbf{B}^{(n,j)}\mathbf{C}^{(n,j)}, \tag{6}$$

and the residual vector in the nth iteration is:

$$\mathbf{V}^{(n,j)}=\mathbf{V}-\mathbf{Z}\mathbf{B}^{(n,j)}\mathbf{C}^{(n,j)}. \tag{7}$$

Normalized residuum is used as a measure of the accuracy of the solution. For the jth excitation, after the nth iteration, the normalized residuum is calculated as

$$R_{\mathrm{norm}}^{(n,j)}=\frac{\left\|\mathbf{V}^{(n,j)}\right\|^2}{\left\|\mathbf{V}\right\|^2}. \tag{8}$$

Essentially, solution $\mathbf{A}^{(n,j)}$ given by (6) is a linear combination of all subdomain solutions in all previous and the current iteration, for the jth excitation. Weighting coefficients $\mathbf{C}^{(n,j)}$ minimizes residuum (8) in the least square sense.

Note that a matrix $\mathbf{E}_l\mathbf{Z}\mathbf{E}_l^{\mathrm{T}}$ is not calculated using $\mathbf{Z}$, but is obtained using a partial model for the lth subdomain. Also, $\mathbf{Z}\mathbf{B}^{(n,j)}$ in (5) is calculated using a single row (or a few rows) of $\mathbf{Z}$ at a time, and entire $\mathbf{Z}\mathbf{B}^{(n,j)}$ is then stored in order to calculate residual vector using (7), instead by using (3). In that way the entire $\mathbf{Z}$ matrix is never stored, relaxing memory demands in the case of electrically large problems.

The LSM weighted DDM is an iterative procedure, such that the nth iteration consists of three steps:

1) the subdomain solutions in the nth iteration are found using (4), subdomain by subdomain—inverted matrix for the lth subdomain is calculated once, then residual vectors for all excitations are replaced in (4),

2) The vectors of weighting coefficients are calculated using (5), excitation by excitation, and

3) the approximate solution in the nth iteration is calculated using (6), and the residual vector of the matrix equation (1) in the nth iteration is calculated using (7), both excitation by excitation.

The LSM weighted DDM iterative procedure is finished when a specified normalized residuum is reached, or a specified number of iterations is reached.

III. NUMERICAL RESULTS

The model of an aircraft is shown in Fig. 1. The model is symmetric, so only the half of the model is shown. Enlarged details of the model with and without the inlet are shown in the inset figures up. The model without the inlet has smooth inlet contour, in order to simplify meshing of the PEC cover of the cavity. The uniform automatic domain decomposition [4] results in 72 subdomains, as illustrated in the inset figure right. Since automatic domain decomposition is applied, the cavity does not belong to a single subdomain. The monostatic RCS, σ, is calculated in the symmetry plane (205 incident waves are used). The normalized monostatic RCS (σ/λ^2) is shown in the graphs. Analysis is performed at the single frequency of 4 GHz, at which the model is about 200 wavelengths long. The EM simulator WIPL-D Pro [5] is used for the MoM analysis. The MoM discretization of the model with the inlet, using higher order bases, results in 499618 unknowns. The number of unknowns for the model without the inlet is 484316.

The normalized monostatic RCS in the symmetry plane, obtained by using the MoM, for the models with and without the inlet is shown in Fig. 2. The inlet significantly changes RCS in the zone where incident waves enter the inlet cavity, whereas in the rest of the symmetry plane the RCS results for the models with and without the inlet are very similar.

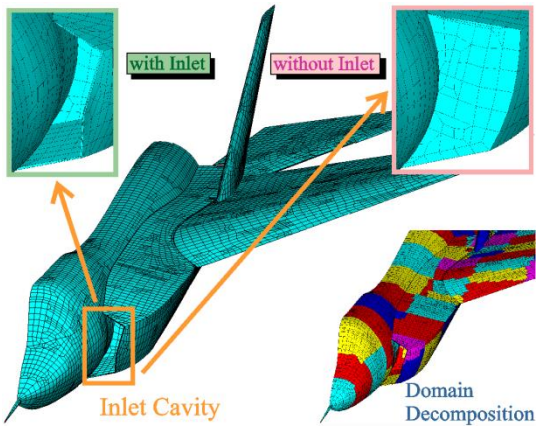

Fig. 1. A half of the symmetric aircraft model with/without inlet (inset up), and automatic domain decomposition of the model (inset right).

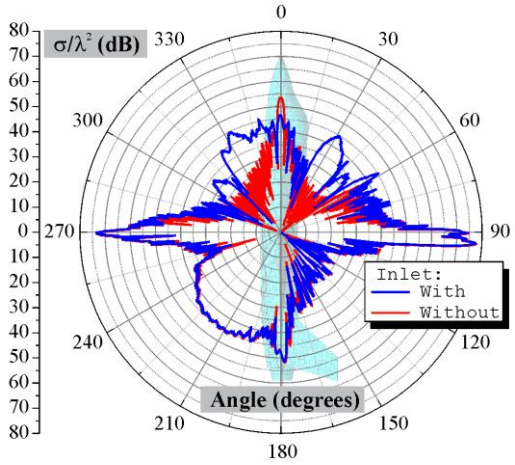

Fig. 2. Monostatic RCS, obtained by MoM, for the models with and without the inlet.

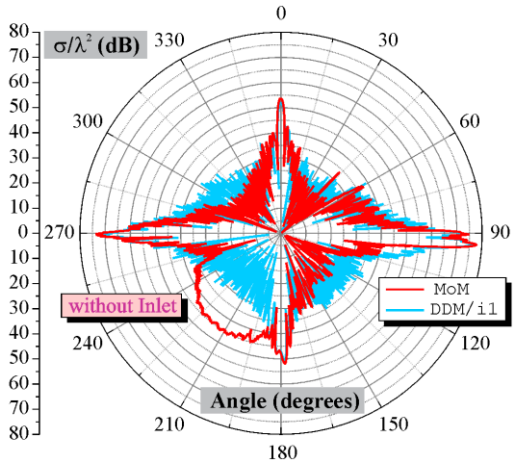

Fig. 3. Monostatic RCS for the model without the inlet, MoM vs. 1st iteration of LSM weighted DDM.

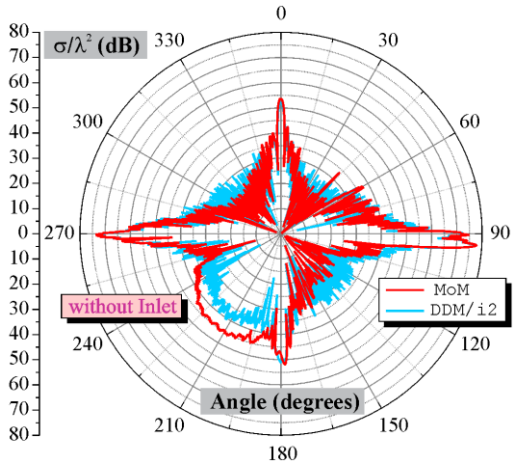

Fig. 4. Monostatic RCS for the model without the inlet, MoM vs. 2nd iteration of LSM weighted DDM.

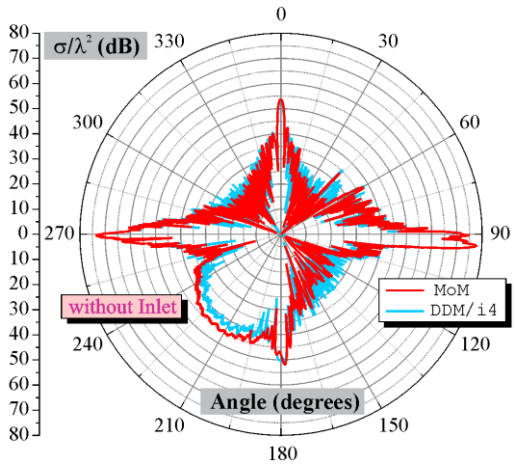

Fig. 5. Monostatic RCS for the model without the inlet, MoM vs. 4th iteration of LSM weighted DDM.

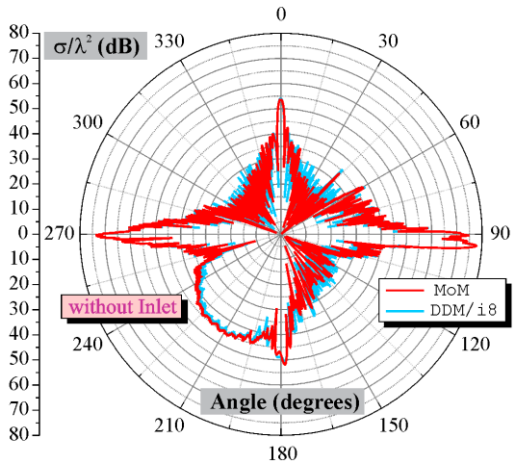

Fig. 6. Monostatic RCS for the model without the inlet, MoM vs. 8th iteration of LSM weighted DDM.

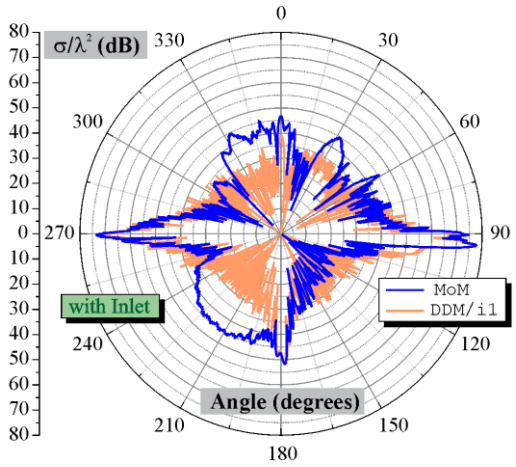

Fig. 7. Monostatic RCS for the model with the inlet, MoM vs. 1st iteration of LSM weighted DDM.

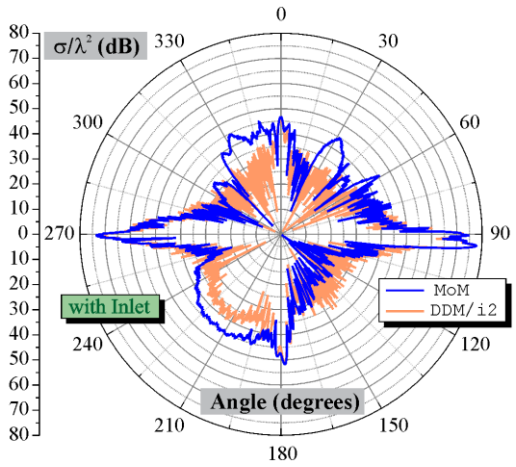

Fig. 8. Monostatic RCS for the model with the inlet, MoM vs. 2nd iteration of LSM weighted DDM.

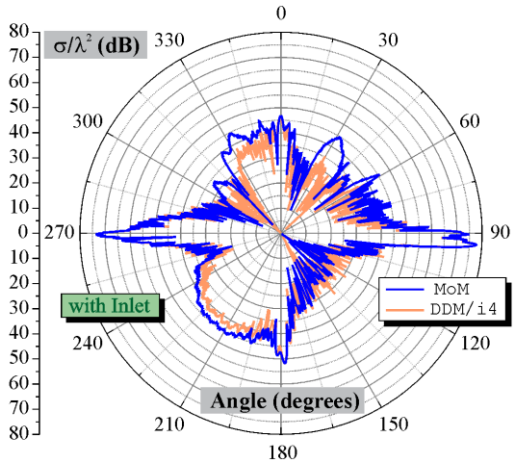

Fig. 9. Monostatic RCS for the model with the inlet, MoM vs. 4th iteration of LSM weighted DDM.

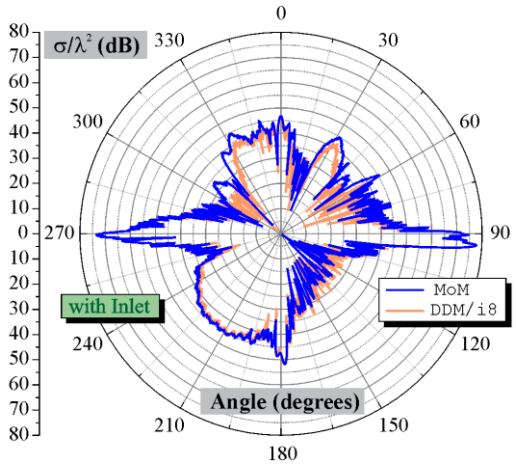

Fig. 10. Monostatic RCS for the model with the inlet, MoM vs. 8th iteration of LSM weighted DDM.

The normalized monostatic RCS for the model without the inlet, obtained by using MoM is compared to the corresponding results after 1, 2, 4, and 8 iterations of LSM weighted DDM in Figs. 3–6. Four narrow lobes (around 0, 90, 190, and 270 degrees) and one wide lobe (approximately between 195 and 240 degrees) can be distinguished. The convergence for the narrow lobes is very fast (only two iterations are needed), whereas about eight iterations are needed for the wide lobe and other zones with the low level RCS.

The normalized monostatic RCS for the model with the inlet, obtained by using MoM is compared to the corresponding results after 1, 2, 4, and 8 iterations of LSM weighted DDM in Figs. 7–10. The inlet cavity has modified RCS in the region of ±60 degrees around 0 degree (compared to the model with the inlet)—there are few lobes instead of just one, and the convergence for all of them is slower than for the narrow lobes around 90, 190, and 270 degrees. The convergence for the wide lobe between 195 and 240 degrees is essentially unchanged from the model without the inlet. The convergence in the zones with the low level RCS is similar to that of the model without the inlet.

In order to improve convergence, the inlet cavity was manually allocated to the single domain. This is done by using an auxiliary ellipsoid to extract all entities that are in the ellipsoid. Another ellipsoid is used to extract entities around junction of rear wing and the tale of the aircraft (after some numerical experiments, this part of the structure is found responsible for the slower convergence of the wide lobe between 195 and 240 degrees). Prior to the automatic domain decomposition, for each auxiliary ellipsoid a single subdomain is created from the entities that were in the ellipsoid. The rest of the structure is automatically decomposed, as in Fig. 11. In the graphs, this model is referred to as "with Inlet 2".

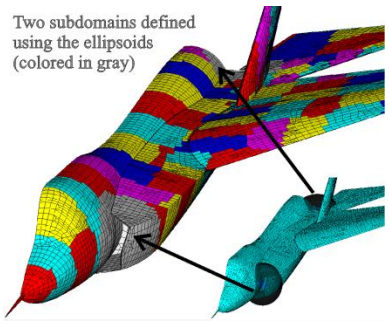

Fig. 11. Model with the inlet, combination of the automatic and manual domain decomposition.

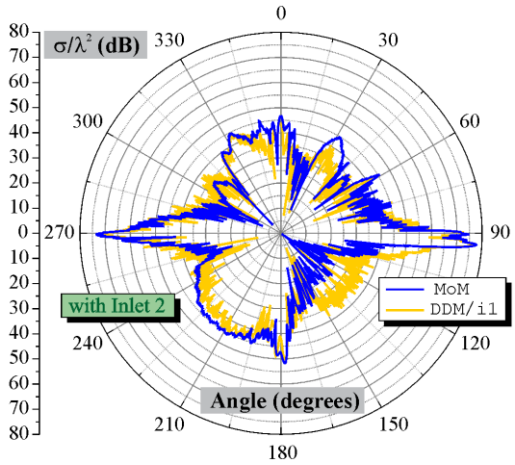

Fig. 12. The monostatic RCS for the model in Fig. 11, MoM vs. 1st iteration of LSM weighted DDM.

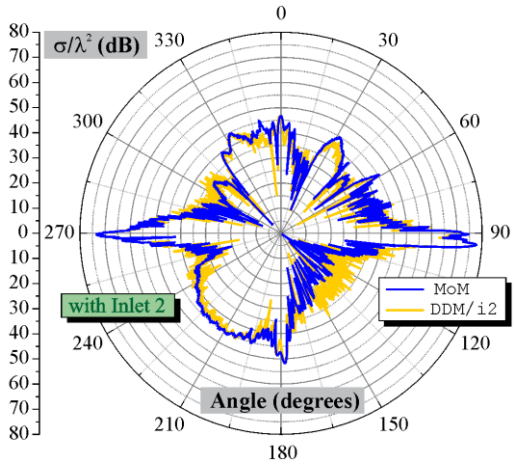

Fig. 13. The monostatic RCS for the model in Fig. 11, MoM vs. 2nd iteration of LSM weighted DDM.

The normalized monostatic RCS for the model with the inlet, obtained by using MoM is compared to the corresponding results after 1, 2, 4, and 8 iterations of LSM weighted DDM (for the model in Fig. 11) in Figs. 12–15.

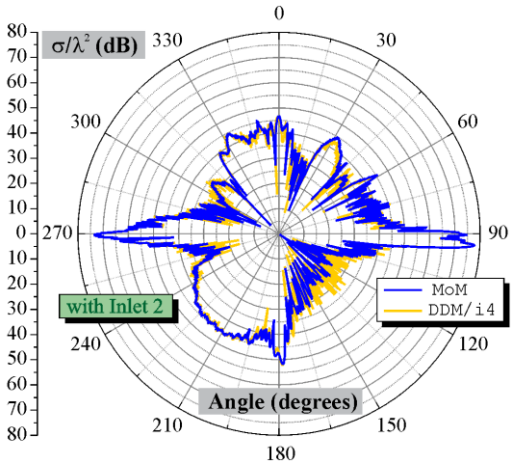

Fig. 14. The monostatic RCS for the model in Fig. 11, MoM vs. 4th iteration of LSM weighted DDM.

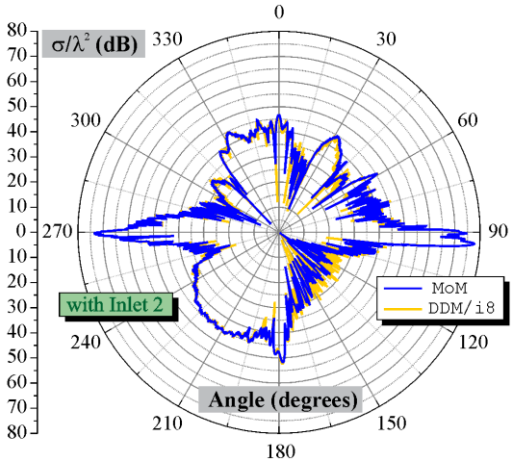

Fig. 15. The monostatic RCS for the model in Fig. 11, MoM vs. 8th iteration of LSM weighted DDM.

The convergence for the wide lobe between 195 and 240 degrees is very fast (essentially, RCS is fully stabilized after four iterations), whereas the convergence in the inlet cavity zone (±60 degrees around 0 degree) is significantly improved compared to the model without the manually defined subdomains. The convergence in the zones with the low level RCS is slightly improved compared to the model without the manually defined subdomains.

The CPU time and the storage are similar for both models. All analysis were performed using Intel(R) Xeon(R) CPU E5-2650 v4 @ 2.20 GHz (2 processors) with 256 GB RAM.

The MoM analysis CPU time / the MoM matrix storage is ~11 hours / 1860 GB. Note that MoM analysis was optimized for calculations using GPUs. Four NVIDIA GeForce GTX 1080Ti cards are used in the analysis. Estimated CPU time for the MoM analysis

without GPUs is ~250 hours.

The CPU time for the LSM weighted DDM after four iterations is ~19 hours, and after eight iterations is ~42 hours. The LSM weighted DDM matrix storage is ~53 GB per iteration. Note that LSM weighted DDM is performed independently in five different zones in the symmetry plane, in order to be able to use the concept of visibility [4]. For that reason, LSM weighted DDM matrix storage for the first iteration is about a half of 53 GB. Note also that MoM analysis is performed with the 1801 excitations (incident EM plane waves), whereas LSM weighted DDM is performed with the 205 excitations—interpolation is then used to obtain RCS for all 1801 excitations. Finally, note that LSM weighted DDM calculations were not optimized for multiple excitations analysis—the primary goal was to improve the convergence the LSM weighted DDM.

IV. CONCLUSION

LSM weighted DDM with the automatic domain decomposition is iterative technique that can be successfully applied to the monostatic RCS problems. Generally, the convergence is good, but automatically decomposed resonant cavities and/or sharp parts of the structure can cause the slower convergence. The convergence can be further improved by the extraction of problematic parts of the structure in separated subdomains, using the advantage of domain decomposition techniques. In the presented case of the aircraft this technique provides very good RCS results in just a few iterations. LSM weighted DDM provides means to solve the problems which electrical size is too large for the standard MoM. In the future work the focus will be on the optimization of the LSM weighted DDM calculations and storage techniques.

ACKNOWLEDGMENT

This work is supported by the Serbian Ministry of Education, Science, and Technological Development under grant TR-32005.

REFERENCES

[1] H. T. Anastassu, "A review of electromagnetic scattering analysis for inlets cavities and open ducts," *IEEE Antennas and Propagation Magazine*, vol. 45, no. 6, pp. 27-40, 2003.

[2] E. Garcia, C. Delgado, I. G. Diego, and M. F. Catedra, "An iterative solution for electrically large problems combining the characteristic basis function method and the multilevel fast multipole algorithm," *IEEE Trans. Antennas Propag*., vol. 56, no. 8, pp. 2363-2371, 2008.

[3] M. Tasic and B. Kolundzija, "Iterative MoM-based technique for evaluation of bistatic RCS of electrically large scatterers," *Microwave Review - Mikrotalasna Revija*, vol. 22, no. 2, Dec. 2016.

[4] M. S. Tasic and B. M. Kolundzija, "Method of moment weighted domain decomposition method for scattering from large platforms," in *IEEE Transactions on Antennas and Propagation*, vol. 66, no. 7, pp. 3577-3589, July 2018.

[5] WIPL-D, Belgrade, Serbia. (2017). WIPL-D Pro v14.0—3D EM Solver. [Online]. Available: www.wipl-d.com

Miodrag S. Tasic was born in 1972. in Belgrade, Serbia. He received the B.Sc., M.Sc., and D.Sc., degrees from the University of Belgrade, Serbia, in 1998, 2004, and 2012, respectively. He joined the School of Electrical Engineering – University of Belgrade in 2000, where at present he is a Assistant Professor in Electromagnetics and Microwave measurements. His research interests are 3D surface modeling, numerical problems in electromagnetics, and antenna measurements.

Branko M. Kolundzija was born in 1958 in Zenica, former Yugoslavia. He received the B.Sc., M.Sc., and D.Sc., degrees from the University of Belgrade, Serbia, in 1981, 1986, and 1990, respectively. He joined the School of Electrical Engineering – University of Belgrade in 1981, where at present he is a Full Professor in Electromagnetics and Antennas and Propagation. His research interests are numerical problems in electromagnetics, especially those applied to antennas and microwave components. He is the main architect of the WIPL-D software suite.

Tomislav S. Milosevic was born in 1984 in Belgrade, Serbia. He received the B.Sc. and M.Sc., degrees from the University of Belgrade, Serbia, in 2007 and 2008, respectively. In 2009, he joined WIPL-D company, where at present he works as Engineer for applications and technical support. His main research interests include modelling and simulation of various EM structures.

Modeling and Validation of a mm-Wave Shaped Dielectric Lens Antenna

David C. Mooradd, Alan J. Fenn, and Peter T. Hurst

Lincoln Laboratory, Massachusetts Institute of Technology
Lexington, Massachusetts 02421-6426, USA
mooradd@LL.MIT.EDU, ajf@LL.MIT.EDU, hurst@LL.MIT.EDU

Abstract ─ The modeling and validation of a 33 GHz shaped dielectric antenna design is investigated. The electromagnetic modeling was performed in both WIPL-D and FEKO, and was used to validate the antenna design prior to fabrication of the lens. It is shown that both WIPL-D and FEKO yield similarly accurate results as compared to measured far-field gain radiation patterns.

Index Terms ─ Antennas, FEKO, measurement, millimeter wave, shaped dielectric lens, simulations, WIPL-D.

I. INTRODUCTION

A 33 GHz uniquely shaped 50 cm diameter dielectric lens antenna has recently been developed, and it has been modeled in both WIPL-D and FEKO. The electromagnetic modeling effort was undertaken to validate the lens design prior to manufacturing. It will be shown that both models yielded similarly accurate results as compared to the final measured gain radiation patterns. The modeled antenna system shown in Fig. 1 is comprised of a Rexolite dielectric lens illuminated by a corrugated conical horn. The antenna design required dual linear polarization, an azimuth beamwidth of 1.2°, and an elevation beamwidth of 12° with a prescribed elevation beam response as shown in Fig. 2.

II. DIELECTRIC LENS

The dielectric lens shown in Fig. 1 is a composite surface design. First, using the design equations in [1], a conventional rotationally-symmetric convex-plano lens design was used to produce a 1.2º conical beam. The next step was to shape the exiting surface of the lens in the elevation plane to achieve the desired elevation beam shape shown in Fig. 2. The phase perturbation required to achieve the desired elevation beam shape was derived numerically, and this phase perturbation wat then used to the dielectric surface profile.

II. MODELING, SIMULATION, AND MEASUREMENTS

The above antenna design was modeled in both FEKO and WIPL-D. The FEKO simulation used ray launching geometrical optics to solve the full antenna system, using a spherical mode expansion of the moment method modeled corrugated horn as the illumination source of the lens. WIPL-D performed the entire simulation with the method of moments (MoM), using one symmetry plane to reduce the size of the problem. Both simulation tools yielded similar results, thus validating the antenna system design. While the modeling steps are similar in both tools, the following modeling and simulation steps are specific to WIPL-D ProCAD 2017.

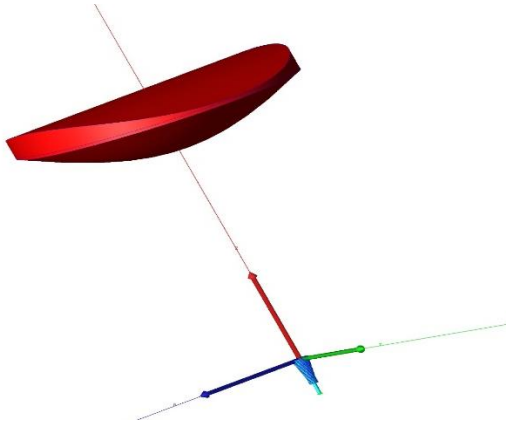

Fig. 1. Ka band corrugated horn and shaped dielectric lens as modeled in WIPL-D ProCAD.

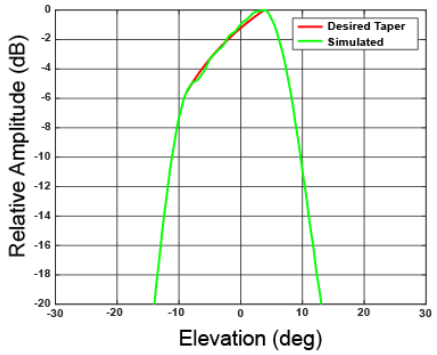

Fig. 2. Prescribed shaped beam elevation pattern.

A. Corrugated horn model & simulation

The profile of the corrugated horn was generated in Matlab, based on designs in [2], and imported into WIPL-D as a polyline. The sweep tool was used to generate the cylindrical horn, and a waveguide port was added as the excitation source. The input impedance and far-field radiation patterns were calculated, and the phase center of the horn was determined. The horn was

Approved for public release: distribution unlimited.
This material is based upon work supported under Air Force Contract No. FA8721-05-C-0002 and/or FA8702-15-D-0001. Any opinions, findings, conclusions or recommendations expressed in this material are those of the author(s) and do not necessarily reflect the views of the U.S. Air Force.

Submitted On: September 30, 2018
Accepted On: October 3, 2018

translated to place the phase center at the center of the global coordinate system.

B. Dielectric lens model

Both surface profiles of the dielectric lens were generated in Matlab and imported into WIPL-D ProCAD as polylines. The inner surface is rotationally symmetric about the central axis and was created by sweeping the polynomial about a circle. The outer surface is shaped only in the vertical (elevation) axis, and it is constant along the horizontal axis. The outer surface was created by extruding the polynomial along a horizontal line. To merge the two surfaces and create the solid lens volume, a 50 cm diameter cylinder was generated along the central axis that encapsulated the two surfaces. The three bodies (inner surface, outer surface, and cylinder) were then merged using "Boolean/ Intersect" and the unwanted portions of the structure deleted. The lens was translated along the lens axis by 50 cm to place it at the correct focal position relative to the feed. The final step was to define a dielectric domain with a relative permittivity, $\varepsilon_r = 2.54$, and assign it to the Rexolite dielectric lens structure.

C. Simulating the full antenna system

The WIPL-D and FEKO simulations were performed on different computers so a direct comparison of computational speed is not possible. The computational details of each simulation are as follows.

The WIPL-D simulations were performed on a desktop computer with two Xeon E5-2643V2 3.50 GHz processors, 64 GB RAM, a Tesla K20c GPU and six 2.65 TB solid state hard drives in RAID0 configuration for high speed scratch space. With one symmetry plane enabled, the total number of unknowns in the WIPL-D simulation was 304,240 (156,754 electric currents and 147,486 magnetic currents). Simulation time for one frequency and one polarization took 37 hours with the GPU Solver enabled.

The FEKO simulations were performed on a machine with two E5-2699 V3 2.30 GHz processors and 512 GB RAM. Approximately 91,000 moment method basis functions were used to compute the Ka-band corrugated horn spherical mode expansion functions used to illuminate the shaped lens. 65953 curvilinear triangles were used to mesh the shaped lens, which was solved for the far-field gain patterns using ray-launching geometrical optics. Total CPU time utilizing 36 cores on two CPUs was 21 hours.

The results of the FEKO and WIPL-D gain radiation pattern simulations are shown overlaid in Fig. 3. As can be seen the two simulations yield very similar results, thus validating the antenna design.

D. Comparison of simulations and measurements

Gain and radiation pattern measurements of the shaped lens antenna system were performed in a compact range anechoic chamber. The final validation is given in Fig. 4 where the WIPL-D simulated and measured antenna elevation gain radiation patterns show good agreement.

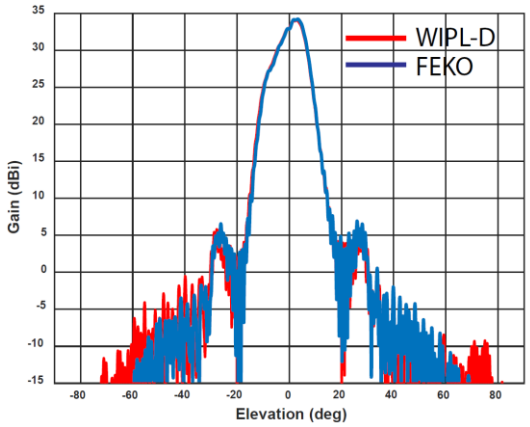

Fig. 3. Comparison of simulated elevation gain patterns for the shaped lens antenna.

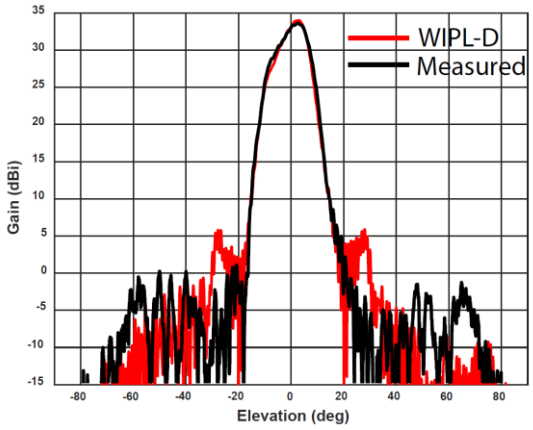

Fig. 4. Comparison of measured and WIPL-D simulated elevation gain patterns for the shaped lens antenna.

IV. CONCLUSION

A 50 cm diameter, 33 GHz, shaped beam dielectric lens antenna design was modeled in WIPL-D and FEKO. The two simulations yielded very similar results, validating design of the antenna prior to manufacturing of the lens. The simulated antenna far-field gain radiation patterns of the shaped lens antenna system also had good agreement with measured data.

REFERENCES

[1] Y. T. Lo and S. W. Lee, Antenna Handbook. Van Nostrand Reinhold Co., New York, Chapter 16, 1988.

[2] T. A. Milligan, Modern Antenna Design. McGraw-Hill, New York, 1985.

PEEC-Based Multi-Objective Synthesis of NFC Antennas in the Presence of Conductive Structures

Thomas Bauernfeind [1], Paul Baumgartner [1], Oszkar Biro [1], Christian Magele [1], Werner Renhart [1], and Riccardo Torchio [2]

[1] Institute of Fundamentals and Theory in Electrical Engineering
Graz University of Technology, Graz, 8010, Austria
t.bauernfeind@tugraz.at, paul.baumgartner@tugraz.at, biro@tugraz.at, christian.magele@tugraz.at, werner.renhart@tugraz.at

[2] Dipartimento di Ingegneria Industriale
Università degli Studi di Padova, Padova, 35131, Italy
riccardo.torchio@studenti.unipd.it

Abstract — Near Field Communication (NFC) techniques are widely used within everyday activities, e.g., contactless payment systems or authentication. Regardless of the application typically the requirements on the antenna structure are manifold. Frequently limitations in the available space make the antenna design quite challenging especially if other conductive structures are close to the NFC antenna. In the present paper we propose to synthesize the geometry of proximity integrated circuit card (PICC) antennas according to class 6 in the presence of nearby metallic structures. The optimization relies on the differential evolution strategy. The computation of the forward problem is based on the partial element equivalent circuit (PEEC) method.

Index Terms — NFC antennas, numerical optimization, partial element equivalent circuit method.

I. INTRODUCTION

Within the contactless communication technologies the NFC services have found a mass market in the last decade. Nearly all new mobile devices like smart phones or tablet PCs are equipped with NFC technologies. Although the functionality of these devices has become very complex, they tend to become smaller in size. Hence, this leads to a reduced space for the certain services. Therefore, the requirements on the NFC antenna design are increasing. Typically the antenna designer has to find a suitable structure which enables the operation of the NFC device in the three dimensional NFC operating volume (see Fig. 1) [1] which is defined by the NFC Forum.

Since the communication at the operating frequency of 13.56 MHz is established in the near field of the antennas, typically loop antennas like the one shown in Fig. 2 are utilized. Following the common design rules for the design of a PICC, the NFC transponder IC and the antenna structure should result in a resonant circuit at the operating frequency [2]. Typically the input capacitance of the NFC transponder IC is not sufficiently large to fulfill this requirement, hence an external tuning capacitor is needed [2]. In addition to the tuning to the operating frequency, also the power transmission between the NFC devices has to be taken into account which is affected by an additional matching circuitry. Especially in terms of standard compliance this behavior is essential. Typically the external matching circuit is developed subsequently to the design of the antenna structure [3], hence the NFC device does not necessarily result in an optimum design. Therefore, in the present paper we propose to optimize the antenna structure and the needed matching circuit in parallel during the numerical optimization process taking into account conductive structures which can be close to the NFC antenna. To enable this process the PEEC-method [4] is applied since it permits a direct treatment of lumped components and the discretized antenna structure in a single system of equations.

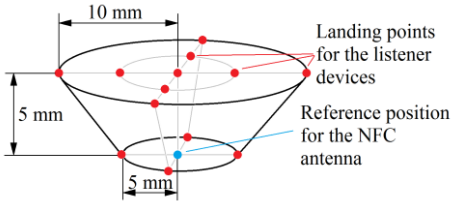

Fig. 1. NFC Operating Volume defined by the NFC Forum. Compliance tests have to be carried out at each point in the volume.

Submitted On: September 28, 2018
Accepted On: October 3, 2018

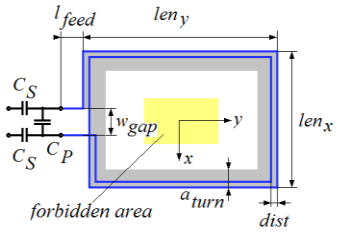

Fig. 2. Typical NFC antenna structure connected to a matching circuitry. For class 1 antennas a forbidden area is present; for class 6 no forbidden area is given.

It has been shown that stochastic optimization strategies deliver reasonable good results especially when the behavior of the objective function in the multi-dimensional parameter space is not very well known like it is the case for the present optimization task. Thus, for the present optimization task a fundamental version of the differential evolution (DE) strategy [5] has been chosen.

II. READER POWER REQUIREMENTS IN THE NFC FORUM OPERATING VOLUME

A major test criterion within the standard compliance tests is the so called reader power requirements test. According to this test the NFC device is operated in reader mode (the device acts as polling device) and should conduct the communication to the NFC listening devices in card mode. Within this test the generated field strength of the polling device is measured with three standardized so called listener devices (*Listener* 1, 3 and 6) at specific points in the NFC Forum operating volume. The field strength levels are measured in terms of voltages at specific test resistances (see Table 1). Two requirements have to be fulfilled for all listener devices: the so called H_{min}-test (the voltage at the resistance must exceed a lower limit) and the H_{max}-test (the voltage at the resistance must not exceed an upper limit). These test resistances are the load resistances of a bridge rectifier circuitry connected to the listener antennas. In order to enable a frequency domain investigation the non-linear rectifier is modeled in terms of a linear resistance. The resistance values for the six test cases summarized in Table 1 are determined based on measurements utilizing a standardized polling device and a subsequent least-squares approximation.

For the numerical optimization the NFC antennas under test as well as the listener devices have been modeled in terms of one-dimensional PEEC stick elements [4]. To take into account conductive material close to the antenna a dense grid structure is used. Figure 3 shows such test configurations. Numerical tests have shown that the strongest influence of the conductive structure is given when it has roughly the same dimensions as the antenna under test. Hence, such configurations are tested in our first investigations. The design parameters for the first test case (class 6 antenna) are $\mathbf{p}_{cl6} = [len_x, len_y, dist, a_{turn}, C_S, C_P, R_P]$. The design parameters for the antenna geometry are limited according to the corresponding ISO/IEC definitions. For the test case it is assumed that the antenna is manufactured on a FR-4 substrate material with a thickness of 1.55 mm. In the PEEC model therefore the smallest distance between the metal structure and the antenna under test is mainly defined by the thickness of the substrate. The objective set consists of the maximum current I_{IC} the NFC IC is able to deliver to the antenna, the antenna's quality factor Q_{Ant} as well as of the power levels at the listener devices computed from the voltages at the specific listener resistances ($H_{minList1}$, $H_{maxList1}$, $H_{minList3}$, $H_{maxList3}$, $H_{minList6}$, $H_{maxList6}$). Applying fuzzy functions [6] for all objectives a scalar objective function can be defined:

$$f(\mathbf{p}) = \mu\left(I_{IC}(\mathbf{p})\right) + \mu\left(Q_{Ant}(\mathbf{p})\right) + \\ + \sum_{i=1,3,6} \mu\left(H_{min}L_i(\mathbf{p})\right) + \sum_{i=1,3,6} \mu\left(H_{max}L_i(\mathbf{p})\right). \quad (1)$$

The test problems (1) are minimized by the DE strategy.

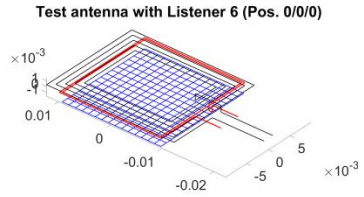

(a)

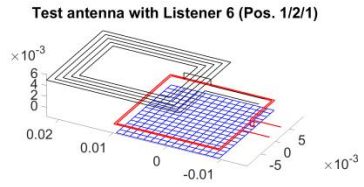

(b)

Fig. 3. PEEC-model for the numerical optimization process; Test antenna (red) with metal grid (blue) and Listener 6 antenna (black). (a) Listener 6 at position 0/0/0 according to the standard. (b) Listener 6 at position 1/2/1.

Table 1: Load resistance values and voltage levels

		Listener 1	**Listener 3**	**Listener 6**
H_{min}	R_{List} in Ω	450	300	175
	V_{Test} in V	4.1	3.14	3.79
H_{max}	R_{List} in Ω	50	35	20
	V_{Test} in V	2.85	2.5	2.23

III. RESULTS AND DISCUSSION

Due to the fact that for all points in the operating volume and for all listener devices the induced voltage has to be computed, a large number (3x14x2) of forward problems has to be solved for each individual of the population. For the class 6 test problem we have obtained a parameter set given to be $\mathbf{p}_{cl6}$ = [0.0197m, 0.0197m, 339μm, 0.0374, 368pF, 570pF, 0.7$k\Omega$]. The results have been obtained for a population size of n = 30 and it_{max} = 500 iterations. As can be seen from Fig. 4 the global minimum could not be attained. This is due to the H_{min} limit for the *Listener 1* test. Adapting (1) by introducing weighting functions could be a reasonable way to overcome this problem. Figure 5 shows the influence of the metal grid on the antenna impedance and Figs. 6 (a) and (b) show how the listener devices influence the antenna impedance due to the so called card loading effect.

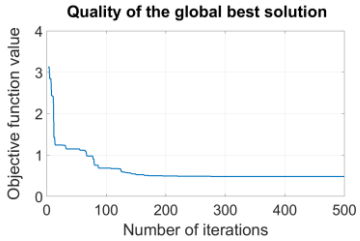

Fig. 4. Progress of the quality of the global best solution.

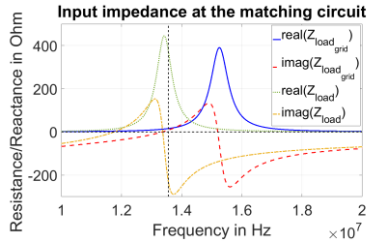

Fig. 5. Influence of the metal grid on the impedance at the matching circuit. Solid and dashed line: input impedance of the optimized antenna in presence of the conductive material. Dotted and dash-dotted line: conductive material is absent.

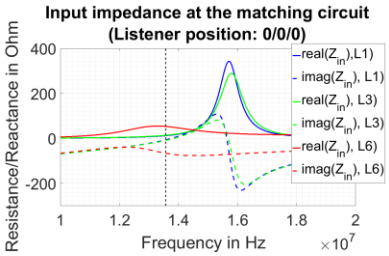

(a)

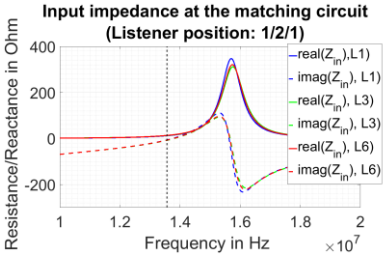

(b)

Fig. 6. Influence of the card loading on the input impedance: (a) Listeners at position 0/0/0; strongest card loading and detuning effect. (b) Listeners at position 1/2/1; reduced card loading and hardly any detuning effect.

REFERENCES

[1] M. Gebhart, R. Neubauer, M. Stark, and D. Warnez, "Design of 13.56 MHz smartcard stickers with ferrite for payment and authentication," *2011 3rd International Workshop on Near Field Communication*, Hagenberg, pp. 59-64, 2011.

[2] T. Bauernfeind, K. Preis, W. Renhart, O. Bíró, and M. Gebhart, "Finite element simulation of impedance measurement effects of NFC antennas," *IEEE Trans. Magn*., 51(3), pp. 1-4, 2015.

[3] M. Roland, H. Witschnig, E. Merlin, and C. Saminger, "Automatic impedance matching for 13.56 MHz NFC antennas," *2008 6th International Symposium on Communication Systems, Networks and Digital Signal Processing*, Graz, pp. 288-291, 2008.

[4] T. Bauernfeind, P. Baumgartner, O. Bíró, C. A. Magele, K. Preis, and R. Torchio, "PEEC-based multi-objective synthesis of non-uniformly spaced linear antenna arrays," *IEEE Trans. Magn*., 53(6), pp. 1-4, 2017.

[5] P. Alotto, "A hybrid multiobjective differential evolution method for electromagnetic device optimization," *COMPEL-The International Journal for Computation and Mathematics in Electrical and Electronic Engineering*, 30(6), pp. 1815-1828, 2011.

[6] C. Magele, G. Fürntratt, B. Brandstätter, and K. R. Richter, "Self-adaptive fuzzy sets in multi objective optimization using genetic algorithms," *Applied Computational Electromagnetics Society Journal*, 12(2), pp. 26-31, 1997.

Polarimetric Weather Radar Calibration by Computational Electromagnetics

Djordje Mirkovic
Cooperative Institute for Mesoscale Studies
National Severe Storms Laboratory (NOAA)
Norman, OK
Djordje.Mirkovic@noaa.gov

Dusan S. Zrnic
National Severe Storms Laboratory (NOAA)
Norman, OK
Dusan.Zrnic@noaa.gov

***Abstract*—The paper proposes a technique for calibrating a large polarimetric phased array weather radar The focus is on the use of computational electromagnetics. It validates the accuracy of the computations on a scaled-down antenna model and derives calibration parameters for the same model. The proposed technique is demonstrated using the WIPL-D software. The calibration is illustrated with all mathematical concepts required to carry the calibration out. The concept is adapted to use the results of numerical simulations which is part of the paper's novelty. Additionally, a roadmap of polarimetric phased array calibration is proposed and illustrated.**

Keywords—calibration, polarimetric weather radar, polarimetric weather radar calibration, radar.

I. INTRODUCTION

The current national weather radar surveillance network uses dual-polarized dish antennas. The aging network's lifetime is being extended for another twenty years through replacement of obsolete parts and inclusion of modern technology. Thus, it is expected that in about ten years a path for possible replacement should be firmed up to fall in line with typical manufacturing/procurement timeline. The new generation radar should provide the same quality weather data while serving the multifunction capability and efficiently using the allocated frequency spectrum.

Quality of the polarimetric data available from the WSR-88D radar is a benchmark for any new generation radar. Requirements on the polarimetric variables include differential reflectivity bias less than 0.1 dB, copolar correlation coefficient bias of less than 0.01 and cross-polar isolation in the antenna of more than 40 dB for the current operation mode (simultaneous horizontal H and vertical V polarization on transmission and reception). These requirements are satisfied by the WSR-88D's dish antenna whose cross-polar radiation patterns experience null collocated with the co-polar peak, while the cross-polar peaks exhibit four symmetric lobes with respect to the main beam axis. The phases of adjacent lobes are offset from each other by 180 degrees. These antenna properties are invariant with respect to the pointing directions.

Initiatives for development of new generation weather radar are multi-agency efforts aimed toward the Multifunction Phased Array Radar (MPAR) and Spectrum Efficient National Surveillance Radar (SENSR).

Both initiatives consider multiple system architectures. One radar candidate is the Planar Phased Array Radar (PPAR), a program developed jointly by the National Oceanic and Atmospheric Administration (NOAA), Lincoln Laboratory (LL), and the Federal Aviation Administration (FAA). The PPAR is chosen as one of the most mature phased array technologies due to its wide use in the military. Previously, the technology transfer has already happened with single polarization phased array radar at the National Weather Radar Testbed (NWRT) [1]. Studies on this radar proved that electronic scanning strategies of the PPAR can achieve faster, adaptive scanning and avoid mechanical wear typical for radars with dish antennas. However, this capability of the PPAR comes at the price which specifically affects the dual-pol estimates and makes the calibration of the PPAR orders of magnitude more complex than that of the dish antenna radars.

The paper is organized as follows. In the second section is the overview of existing calibration techniques and the mathematical formulation of the calibration parameters. The third section evaluates the accuracy of the computational electromagnetic (CEM) modeling for the application in PPAR calibration. The fourth section describes how to adapt CEM results to the calibration problem and finally, the fifth section presents biased radar measurements and model simulated bias.

II. CALIBRATION PROBLEM

The calibration of the PPAR has to address multiple issues related to the dependence of antenna patterns and orientation of electric fields within the beam. The main calibration issues are orthogonality and orientation of the electric fields produced by the antenna; geometrically induced cross-polar fields (geometrical coupling) [2], cross-polar (unwanted) radiation and match of the H and V beam cross-sections and pointing direction [3].

Gathering necessary calibration information may be achieved by various techniques [4]. These are based either on Far-field (FF) and Near-field (NF) measurements or simulations [4]. To our knowledge, these techniques are limited and/or not fully developed. They typically include an initial full NF antenna measurement and calibration with the placement of a near-field probe in the vicinity of the radar antenna for the antenna/probe cross-coupling measurement. Calibration is done using the initial NF measurement and cross-coupling measurement between the probe and antenna, assuming the initial NF radiation patterns. The proposed FF techniques

Submitted On: September 28, 2018
Accepted On: October 3, 2018

$$\begin{vmatrix} V_1 \\ V_2 \end{vmatrix} = C \begin{vmatrix} (s_h \cos^2\gamma + s_v \sin^2\gamma) g_1 W_1 + (s_h \cos\gamma \sin\psi + s_v \sin\gamma \cos\psi)\sqrt{g_1}\sqrt{g_2} C_T e^{j\beta} W_1 \\ (s_h \cos\gamma \sin\psi + s_v \sin\gamma \cos\psi)\sqrt{g_1}\sqrt{g_2} C_T e^{j\xi} W_1 + (s_h \sin^2\gamma + s_v \cos^2\psi) g_2 C_T C_R e^{j(\beta+\xi)} W_1 \end{vmatrix}. \quad (1)$$

require towers or drones to measure radiation patterns often enough to catch the effects of failing radiating elements [4]. These patterns are used to create the calibration matrix.

Simulation-based techniques, on the other hand, have the ability to address and evaluate issues inherent to the PPAR technology that otherwise cannot be evaluated (i.e., departure from intended polarization while beam-steering). The capability of the numerical models to precisely replicate PPAR antenna field characteristics is illustrated in the next section.

The calibration problem can be set by the voltage on reception for polarimetric PPAR (1) [3]. The Eq. 1 assumes the cross-polar radiation pattern coaxial to the copolar pattern. The cross-polar pattern may be due to cross polar sides of the patch radiator or due to the squinting of the electric field vector caused by geometry (i.e., pointing direction is out of the principal plane) [3], [5]. The effective squinting angles ψ, γ determine the orthogonal components of the electric field. This formulation yields nine calibration parameters [3], namely: antenna gains g_1, g_2; electric field squinting angles (i.e., angles of intended "horizontal" and "vertical" components with respect to the horizontal and quasi-vertical direction) ψ, γ ; radar system parameter C and calibration for port one and port two paths for same input on transmit $C_T e^{j\beta} = \frac{W_2}{W_1}$ (i.e., the ratio of transmitted voltages at ports 1 and 2); and receive $C_R e^{j\xi} = \frac{V_2}{V_1}$ (ratio of received voltages at port 1 and port 2). The thransmission differential phase β consists of the part in the transmitter and part in the antenna. Similarly ξ has two components, one from the antenna the other from the receiver. Here, we consider the antenna differential phases and differential reflectivities.

The differential reflectivity is useful for classifying precipitation type and gauging amounts [6]. Therefore it should be free of biases by the radar system. The differential phase is important for measurements of rain [7] and for identification of large hail [8]. Quantitative precipitation measurements use range derivatives of differential phase hence are not affected by the system induced bias. Nonetheless, proper unwrapping of differential phase hinges on the knowledge of the system phase. Also, the system differential phase is required to determine the differential phase on backscattering by large scatterers such as hail or biota.

In the remainder of the paper, we focus on the antenna parameters contributing to the bias in the polarimetric variables. Furthermore, we consider only calibration in the principal planes, where the cross-polar radiation is negligible, and geometrical bias is null. Nonetheless, our approach is applicable for any pointing direction for which radiation patterns are available.

III. Antenna Modeling and Validation

Achieving the strict calibration requirements set by the current WSR-88D radar is challenging for any proposed technique. In order to achieve it, the measurement, as well as the simulation results, must replicate the true antenna patterns very accurately. Here we use a single panel of the proposed PPAR demonstrator (Ten Panel Demonstrator – TPD) radar to evaluate the accuracy of the antenna modeling.

The radiating element of the TPD is a 3 layer stacked patch antenna. The precise antenna model was developed and simulated in the WIPL-D Pro software. The single antenna

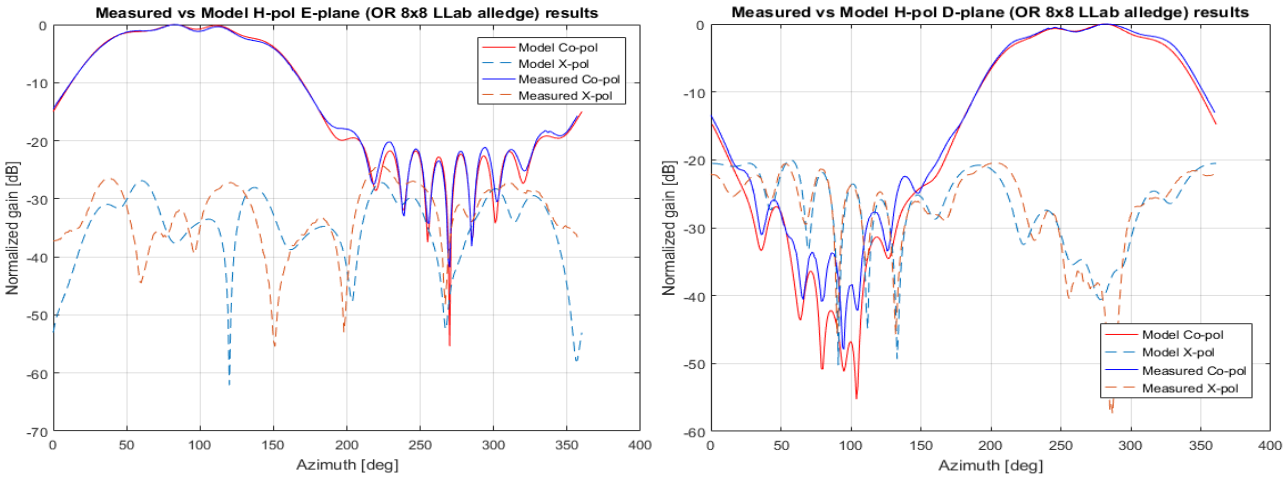

Fig. 1. Modeled and measured radiation patterns. The H-polarized element in the lover left quadrant of a single 8x8 panel is excited and the other elements terminated. Left: in the E-plane and Right: in the D-plane.

panel consists of 64 radiating elements. The panel under test uses one of four central elements for each of the polarizations (H, V, RHCP, LHCP), while others are terminated. Measurements were made at the Advanced Radar Research Center (ARRC) anechoic chamber using the Agilent network analyzer (N5222A).

The measurements include copolar and cross-polar radiation patterns as shown in Fig. 1. The patterns were obtained in the E field plane, H field plane and Diagonal plane, but for brevity, only patterns in the E and D plane are presented in Fig. 1. Very good agreement between the copolar patterns for both cuts is observed, while the cross-polar component in the E-plane shows a slight discrepancy compared to the model. In the D-plane the cross-polar components agree well. The discrepancy between the cross-polar results in the E-plane is most likely caused by the spurious reflections in the chamber.

IV. Computational Electromagnetics (CEM) as an Approach to Calibration

The CEM may be used for obtaining radiation properties of the large PPAR antenna. Yet the CEM softwares are limited by the maximal antenna size they can handle. Software packages that are currently available can exactly solve arrays which consist of a few hundred radiators, whereas the larger arrays are typically solved using some of the approximative techniques. It is not known if the accuracy of these approximative techniques is sufficient to provide polarimetric variables with acceptable errors. Some attempts have been made to evaluate the accuracy, yet a full systematic study is still pending [4]

Herein a TPD radar with an antenna consisting of 640 radiating elements is considered for CEM based calibration. This antenna size is an upper limit which may be solved in a reasonable amount of time without application of approximation techniques. The goal is to simulate patterns and develop calibration parameters that may be used to correct biased radar observations and isolate sources and causes of these biases. Evaluation of the calibration parameters follows directly from the simulation output results. Under the assumption that the antenna is oriented according to Ludwig 2 definition for radiation, or more precisely, E_φ and E_θ components of the radiated field are copolar and cross-polar components of the intended radiation. Depending on the intended polarization, the calculated fields determine the copolar or cross-polar radiation pattern of the antenna. For this case calibration parameters can be calculated as:

$$\arctan\psi = \frac{f_{hv}}{f_{vv}};\ \arctan\gamma = \frac{f_{vh}}{f_{hh}};\ Gdiff = \frac{g_1}{g_2} = \frac{|f_{hh}|^2}{|f_{vv}|^2}$$
$$\beta = \frac{\arg(f_{vv}^{Tx})}{\arg(f_{hh}^{Tx})} + K_{backend};\ \xi = \frac{\arg(f_{vv}^{Rx})}{\arg(f_{hh}^{Rx})} + K_{backend}. \quad (2)$$

Where $f_{hh}, f_{vh}, f_{hv}, f_{vv}$ are values of the voltage radiation patterns at the beam-center. The remaining C, C_T, C_R and the $K_{backend}$ parameters depend only on the back-end of the antenna and cannot be addressed by the antenna simulation. These parameters are expected to be invariant to the pointing direction of the array. Important to notice is that geometrical bias and cross-polarization bias are not included in the formulation of the problem. Nevertheless, for simulations using

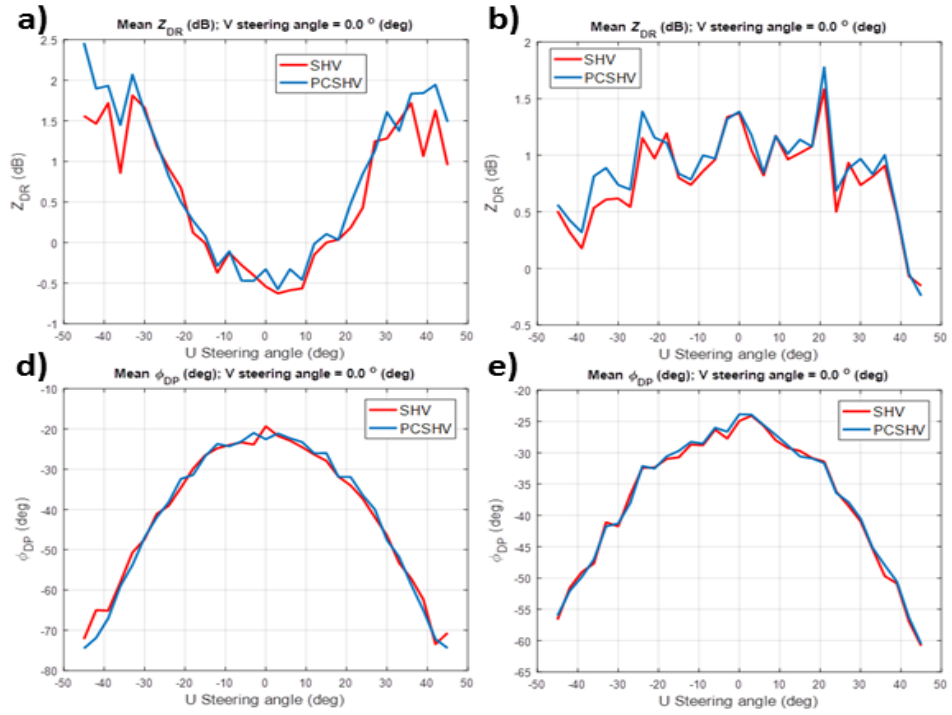

Fig. 2. Measured differential reflectivity (top) and differential phase (bottom) in light rain showing bias in the polarimetric variables when broadside is pointed at zenith angle (left) and when the principal plane is slightly off vertical (right). At zenith angle 3mm of water accumulated at the top of the radome. Water was not present (except for droplets) in the latter case. SHV denotes simultaneus transmission and reception of H and V polarization; PCSHV stands for pulse coded SHV. Coding reduces signal cross-copling and ensures minimal system bias. Figure coutery (I. Ivic).

the Ludwig 2 definition all bias sources (mechanisms) are incorporated in the E_φ and E_θ field components.

V. Radar Bias Measurements and Simulation

Observations that served as motivation for the study were collected using the TPD radar in light rain during spring 2016. The radar was operated with the beam scanning in the principal plane. In one case, the broadside was pointing at the zenith (zenith mode) and in the other, it was slightly tilted (3° to 5°) off the zenith (off zenith mode). Measurements were made in light rain as its Z_{DR} is zero at the zenith, and it is very close to zero in case of the slightly tilted principal plane. In either case, the differential phase equals the system differential phase. During the data collection in zenith mode, approximately 3 mm deep water layer accumulated on top of the radome. To avoid this water the antenna was tilted so that the principal plane was slightly off vertical thus allowing the water to drain off the radome. Two datasets revealed the effect of the thick uniform water layer on the radiation properties of the radar antenna and its effect on the calibration parameters. Here we illustrate measured differential reflectivity Z_{DR} and differential phase of the radar system (Fig. 2). In the first row (left) the radar operates in the zenith mode whereas at (right) it is off zenith. With antenna pointing at zenith (Fig. 2, left and steering angle 0°) the Z_{DR} should be zero, but it is -0.5 dB. This clearly is the system introduced bias that is increased with the pointing direction departing from the broadside to about 2 dB at about 45°. The increase of the differential reflectivity is expected due to the different nature of the H and V EM waves interaction with the radome. Namely, as the beam is steered in the H cardinal plane the H polarization has oblique incidence to the radome. At the same time, V polarization has the parallel incidence to the radome at all beam steering angles. This results in different "reductions" of the antenna gain through the radome at the twofor polarizations, thus the change in the differential gain. Another important feature is the Z_{DR} change in shape between the zenith and off zenith mode as well as the system Z_{DR} bias increase. The bias increase from about -0.5 to 1.3 dB can not be attributed to the antenna, and its origin remains to be determined.

Measurements of the differential phase Φ_{DP} are more consistent between two pointing directions than of the Z_{DR}. From the broadside value system differential phase is observed to be about 20°, whereas the electronic beam steering introduces the additional increas to 75° for zenith pointing or 55° for off zenith mode.

The next step in the calibration roadmap is the simulation of the full TPD antenna array. This is an intermediate step to the modeling of larger, operational PPARs. The TPD antenna is sufficiently "small" to be fully modeled and sufficiently large to serve as the test array in the development of the approximative techniques with sufficient accuracy for large/ full-scale operational PPAR array. This intermediate step is of utmost importance as the mathematical relationship between the various approximative techniques and the full solution can be established.

For replication of measured differential biases, we use two model setups. The first setup considers a single panel antenna with "dry" radome cover whereas the second one introduced additional water level on top of the radome ("wet" radome cover). The "wet" radome has a 3 mm thick layer of water representing the water layer on top of the radome in the zenith pointing mode. During weather surveillance, the radome would most likely be dry hence calibration for such condition is required. The situation with 3 mm uniform water film is highly unlikely for an operational radar, for which correction of the wet radome effects is applied differently].

To understand qualitatively the effects of the "wet" radome on the Z_{DR} and Φ_{DP} we chose to model beam steering on a single panel over 0 to 45° angle. The Fig. 3 shows the differential gain and differential phase of the antenna calculated at the beam peak for the case of "dry" and "wet" radome. Graphs include only steering for positive angles, as the symmetry of the calibration parameters is expected.

Simulated biases show the same trend as the biases estimated from the measured data. In both, we observe a significant difference between the "wet" and "dry" cases. Namely, the differential reflectivity bias for the radar pointing at zenith with the water layer on top of the radome has convex dependance on steering angle with Z_{DR} varying from 0.5 to 2.5 dB. The one-way differential gain in simulated data predicts a convex increase from about 0 to 6 dB; this is an overestimation most likely due to the water layer thickness. The differential gain for the dry radome has a variation of about 0.1 dB. The measurement, as aforementioned, at high elevation angle experiences concave behavior which is opposite to the simulation. This remains to be resolved.

The observed variation of the differential phase has a strong dependence on the pointing direction. Measured values show about 45° decrease of the differential phase for beam steering in zenith mode, and up to 30° when off zenith. The water layer in the simulation is overestimated. This is evident in the differential gain results (Fig. 3 (left)). This is most likely the cause of the differential phase's unexpected non-monotonic behavior. On the other hand, the results for the "dry" radome case are not just qualitatively correct but quantitatively as well. The simulation predicts approx 15° one-way (30° two way) differential phase from the antenna which agrees with the measured value if the system differential phase of about 20° is included.

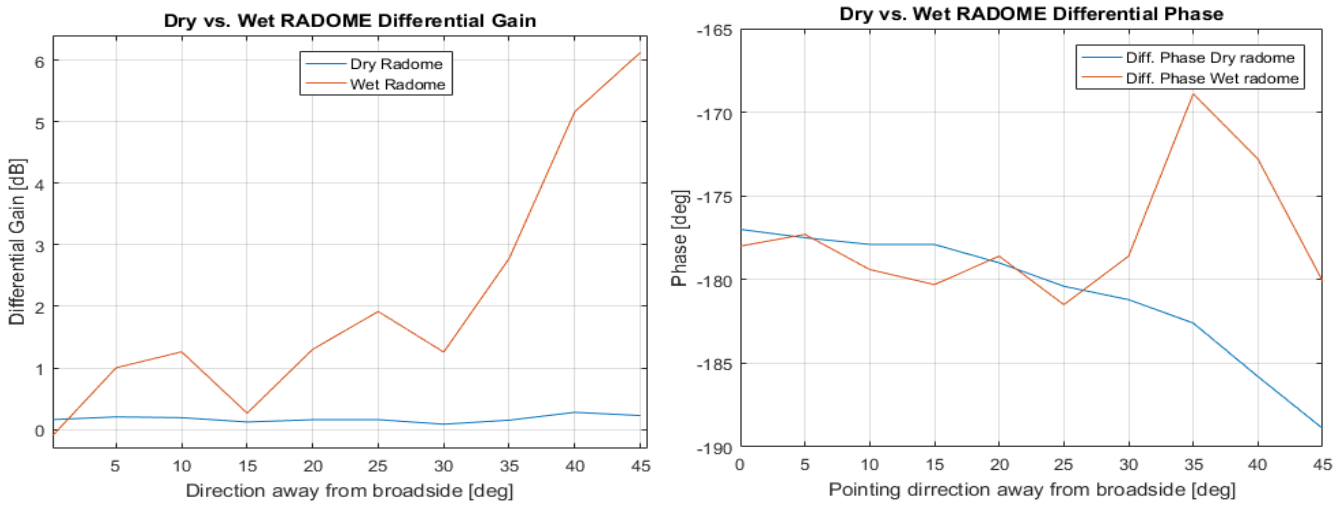

Fig. 3. The simulated differential gain (left) and differential phase(right) as polarimetric calibration parameters depicting variable bias due to the antenna and radome for "dry" and water covered(uniform 3mm layer of water) configuration. Simulated results present one-way (only transmision/reception) bias, while for the radar system this is cumulative effect of bias on transmission and reception (two-way).

VI. Conclusions

Using the CEM tools for simulation of antenna patterns is common practice, yet an application for polarimetric weather radar calibration of the antenna effects has not been made. Here we have demonstrated that the bias in differential reflectivity, in principle, can be obtained from the antenna model. We have also obtained the antenna's contribution to the offset of the system differential phase as a function of the beam pointing direction. Thus, both differential reflectivity and differential phase biases depend on the antenna pointing direction. It follows that for directions in the principal planes of the vertically oriented array (at S, C, and X bands) returns from any rain closest to the radar can be used to determine the total differential phase (i.e., contributions by the antenna and by the rest of the system). This is because the backscatter differential phase from rain is negligible at the frequencies of weather surveillance radars and thus would not influence the measurement. This is not so with differential reflectivity which depends heavily on the rain type. Therefore only light rain or drizzle with intrinsic Z_{DR} close to 0 dB is suitable for checking the total bias in Z_{DR}.

We have also identified issues in this ongoing work that need to be addressed before the final quantitative analysis can be carried out and inconsistencies in the radar observations which have to be corrected before high-quality data can be obtained. The development of the calibration procedure is expected to follow the path from a single panel model to a full-size antenna model. For large antennas, hybrid CEM methods need to be explored to find the ones that can achieve precise modeling of arrays with a few thousand elements.

VII. Acknowledgment

Authors would like to thank the MIT Lincoln Laboratory and Dr. Igor Ivic for the effort in radar design and data collection. Mr. Wasielewski was responsible for maintaining the TDP. Dr. R. Doviak comments helped to improve the manuscript. Funding was provided by NOAA/Office of Oceanic and Atmospheric Research under NOAA-University of Oklahoma Cooperative Agreement #NA11OAR4320072, U.S. Department of Commerce.

References

[1] P. L. Heinselman and S. M. Torres, "High-temporal-resolution capabilities of the national weather radar testbed phased-array radar," Journal of Applied Meteorology and Climatology, vol. 50, no. 3, pp. 579-593, 2011.

[2] G. Zhang, R. J. Doviak, D. S. Zrnic, J. Crain, D. Stainman, and Y. Al-Rashid, "Phased Array radar polarimetry for weather sensing: A theoretical formulation for bias corrections," IEEE Trans. on Geoscience and remote sensing, vol. 47, no. 11, pp. 3679-3689, 2009.

[3] D. S. Zrnic, R. J. Doviak, G. Zhang, Y. Zhang and C. Fulton, "Propagation and backscattering challenges for planar polarimetric phase array radars," in AMS Radar Conference Proceedings, Chicago, 2017.

[4] C. Fulton, J. Salazar, D. Zrnic, D. Mirkovic, I. Ivic, and R. Doviak, "Polarimetric Phased Array Calibration for Large Scale Multi-Mission Radar Applications," in Proc. IEEE Radar, Oklahoma City, 2018.

[5] L. Lei, G. Zhang, R. J. Doviak, and S. Karimkashi, "Comparison of theoretical biases in estimating polarimetric properties of precipitation with weather radar using parabolic reflector, or planar and cylindrical arrays," Trans. on Geoscience and Remote Sensing, vol. 53, no. 8, pp. 4313-4327, 2015.

[6] V. Bringi and V. Chandrasekar, Polarimetric Doppler Weather Radar: Principles and Applications. Cambridge University Press, 2001.

[7] M. Sachidananda and D. S. Zrnic, "Rain rate estimates from differential polarization measurements," J. Atmos. Oceanic Tech., vol. 4, pp. 588-598, 1977.

[8] N. Balakrishnan and D. S. Zrnic, "Use of polarization to characterize precipitation and discriminate large hail," J. Atmos. Sci., pp. 1525-1540, 1990.

[9] A. Mancini, J. Salazar, R. Lebron, and B. Leng Cheong, "A novel technique to characterize the effect of rain over a radome for radar applications," in IEEE Radar Conference 2017, Seattle, 2017.

Design and Optimization of Two-Dimensional Nano-Arrays for Directive Radiation

Aşkın Altınoklu and Özgür Ergül
Department of Electrical and Electronics Engineering
Middle East Technical University
Ankara, Turkey
ozergul@metu.edu.tr

***Abstract*—We consider design, optimization, and computational analysis of nano-arrays involving two-dimensional arrangements of nanoparticles. Similar to their counterparts used at the lower frequencies, nanoantennas can be arranged periodically to achieve directive and/or controllable radiation patterns at optical frequencies. While nanoantenna geometries are usually simple due to restrictions in nanoscale fabrications, their robust analysis still requires accurate simulation tools to model strong plasmonic interactions between particles. We use a full-wave optimization environment based on heuristic algorithms and surface integral equations to optimize two-dimensional nano-arrays and to shape their radiation patterns for diverse nano-optical applications.**

I. Introduction

Nanoantennas are well-known devices of nano-optical systems [1],[2] that are developed and used for a variety of applications, such as energy harvesting, optical communication, and sensing. Both numerical [3] and experimental [4] studies demonstrate interesting properties of nanoantennas, such as strong field enhancement, thanks to the plasmonic properties of metals at optical frequencies. Similar to their counterparts at the lower frequencies, arranging nanoantennas in array forms provides further capabilities [5],[6], such as controllability of radiation characteristics. This study is devoted to the design of nanoantenna arrays for directive radiation applications.

As presented in [6], linear arrangements of nanoparticles, such as nano-cubes, provide an ability to control scattering and radiation. For example, a well-designed array can direct the radiation of an isotropic source to desired directions, while suppressing the radiation at other directions. For the best radiation characteristics, the number of elements, their sizes, and the distances between them can be optimized. On the other hand, if a steering ability is required, two-dimensional arrays can be more suitable since they are more compact and their rotation around an isotropic source can be easier. In this work, we present the design of such two-dimensional arrays by using a full-wave simulation and optimization environment. We show that, by using very compact arrays, it is possible to control the overall radiation by directing the main beam to a desired direction, or more importantly, to multiple directions.

II. Simulation and Optimization Environment

We consider two-dimensional arrays involving nanoparticles, particularly silver (Ag) nano-cubes arranged periodically. The plasmonic properties of the metals at optical frequencies are taken into account by using surface integral equations for penetrable bodies. In the frequency domain, the permittivity values, which are typically complex numbers with negative real parts, are extracted from available measurement data. The arrays are modeled as finite (e.g., $n \times n$) three-dimensional structures that are excited by a main source (e.g., a dipole at the center) located in free space. The radiation problems are solved iteratively by using the multilevel fast multipole algorithm designed for plasmonic objects [7].

In order to design nano-arrays, we perform on/off optimization, i.e., the array elements are kept/extracted to obtain the desired radiation characteristics. An in-house implementation of genetic algorithms (GAs) is employed due to its easier usage for heuristic cost functions and multi-purpose optimization trials. The main excitation is kept in a gap at the center of the structure such that the array can be rotated to steer the created beam or beams. Once an optimal configuration for a desired radiation characteristics is found, it is further exposed to sensitivity analysis. This is particularly essential to estimate the deteriorations on the performance of an optimal structure

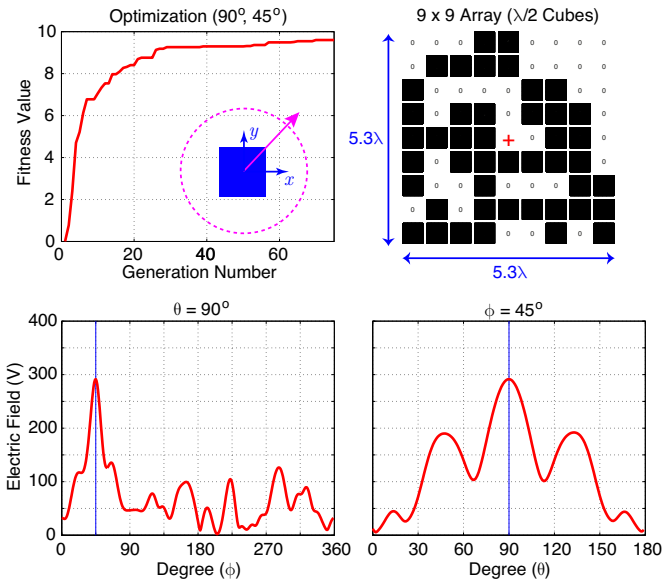

Fig. 1. The result of an optimization when the radiation is maximized at a single direction ($\theta = 90^\circ$ and $\phi = 45^\circ$).

Submitted On: October 10, 2018
Accepted On: October 21, 2018

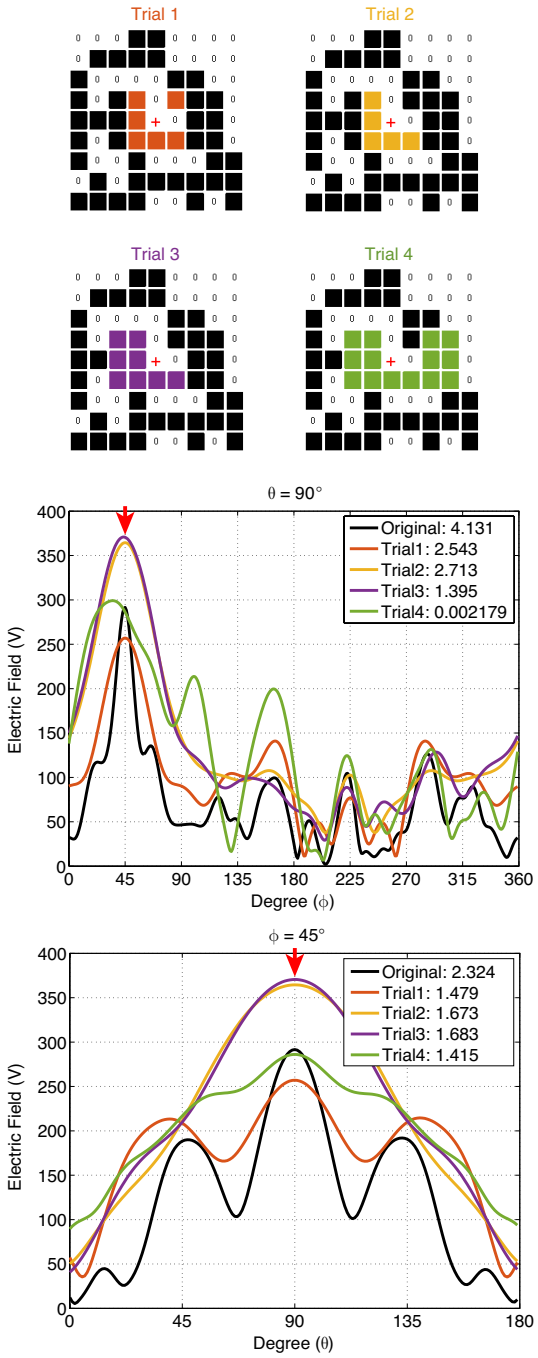

Fig. 2. Modification of the optimal nano-array shown in Fig. 1 by extracting nano-cubes. Attempts to make the nano-array compact lead to significant deteriorations in the radiation characteristics.

when it is fabricated. In addition, we perform extensive tests on the sensitivity of radiation to missing array elements in order to identify critical ones.

III. Design of Nano-Arrays

In the following, we consider two-dimensional nano-arrays involving maximum 80 Ag nano-cubes arranged as a 9×9 grid on the x-y plane. The nano-cubes have dimensions of $750 \times 750 \times 750$ nm, while the center-to-center distance is

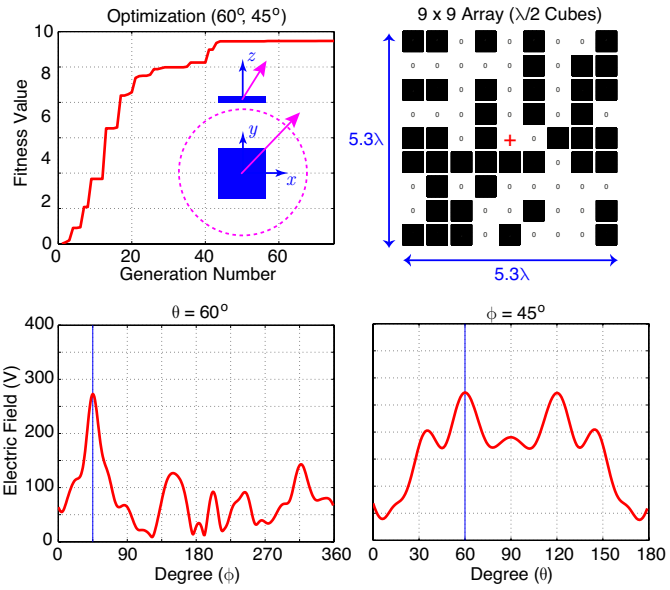

Fig. 3. The result of an optimization when the radiation is maximized at a single direction ($\theta = 60°$ and $\phi = 45°$).

900 nm. Hence, each structure fits into a box of size $7.95 \times 7.95 \times 0.75$ μm. In all results, nano-cubes are assumed to be arranged on the x-y plane. The structures are designed to operate at 200 THz, at which the cube edges correspond to $\lambda/2$ while the overall size is $5.3\lambda \times 5.3\lambda \times 0.5\lambda$. The relative permittivity of Ag at this frequency is approximately $-96 + 7.5i$. The arrays are excited by a probe modeled as a Hertzian dipole oriented in the z direction and located at the center of the array (the cube-free space). Each optimal structure is found via GAs based on less than $40 \times 80 = 3200$ (pool size $\times$ number of generations) simulations by MLFMA. The stability of the GA optimization for nano-arrays was shown in [6].

Fig. 1 presents the results of a successful optimization when the radiation is maximized at $\theta = 90°$ and $\phi = 45°$. The radiation pattern of the array is investigated on the $\theta = 90°$ and the $\phi = 45°$ planes, while the amplitude of the distance-normalized electric field intensity (E) at the desired direction is maximized with respect to the other values on these planes. Specifically, the cost function is defined as:

$$\text{CF} = \text{CF}(\theta = 90°) \times \text{CF}(\phi = 45°), \tag{1}$$

where

$$\text{CF}(\theta = 90°) = \frac{E(\theta = 90°, \phi = 45°)p(\Delta\phi)}{\text{mean}\{E(\theta = 90°, \phi \in [0, 360°])\}}, \tag{2}$$

$$\text{CF}(\phi = 45°) = \frac{E(\theta = 90°, \phi = 45°)p(\Delta\theta)}{\text{mean}\{E(\theta \in [0, 180°], \phi = 45°)\}}. \tag{3}$$

In the above, $p(\Delta s)$ represents a punishment factor, which is generally defined as $p = 1/2^{\Delta s}$, where Δs is the difference (in degrees) between the desired and realized directions for the maximum radiation. For example, if the maximum electric field intensity occurs at $10°$ away from the desired direction, the value of the cost function is drastically reduced

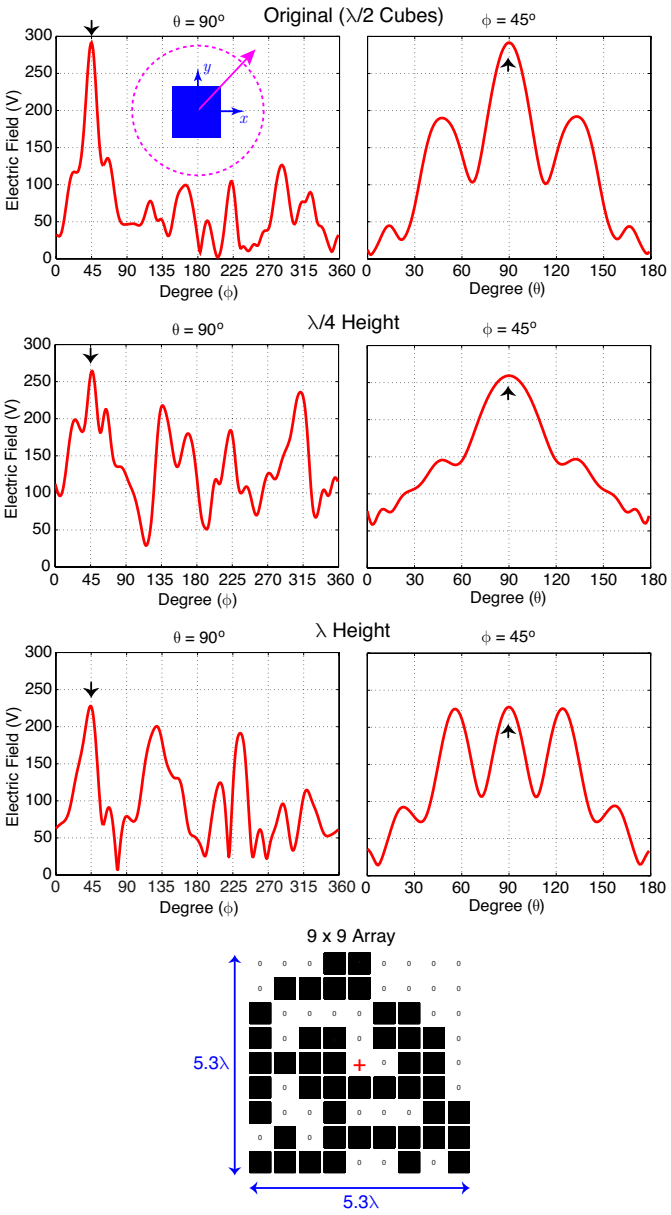

Fig. 4. Using particles with $\lambda/4$ and λ heights for the optimal arrangement in Fig. 1 found for nano-cubes. Changing the height of the particles significantly changes the performance.

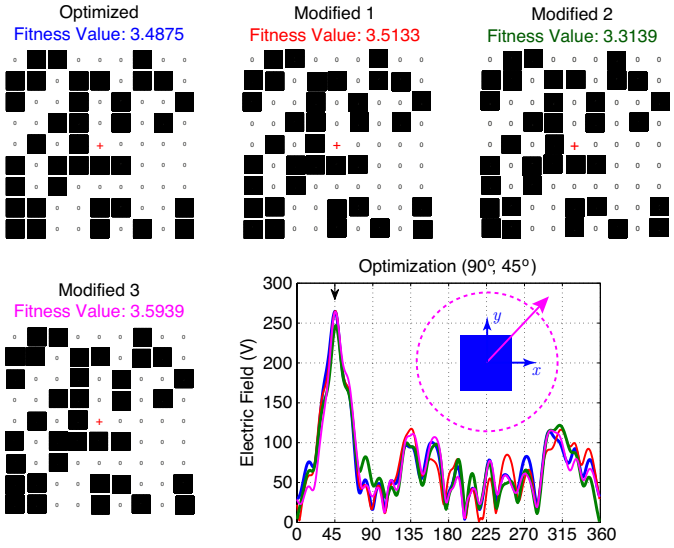

Fig. 5. Tests to demonstrate the sensitivity of a nano-array design to random particle shifts.

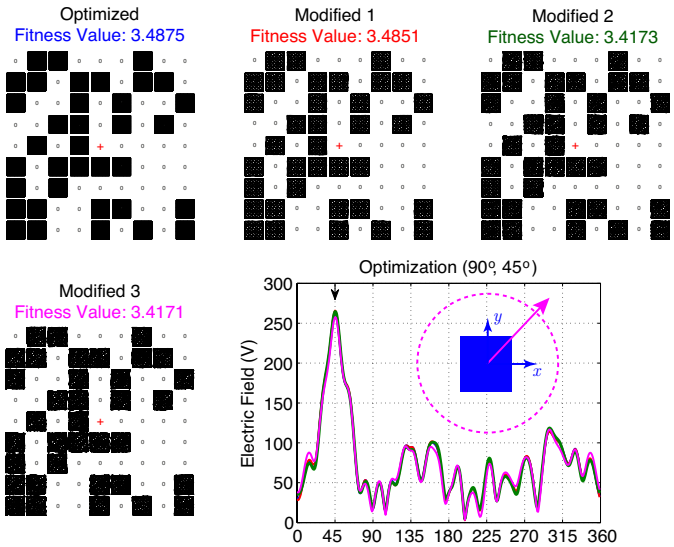

Fig. 6. Tests to demonstrate the sensitivity of a nano-array design to surface corrugations.

by $2^{10} = 1024$ times. This way, the maximum radiation is guaranteed to be in the desired direction, while it may still shift in rare cases. Fig. 1 depicts the fitness value, which is the value of the cost function for the best individual (array design) at each generation. We observe a convergence to a value of $4.131 \times 2.324 \approx 9.6$. Fig. 1 also depicts the optimal array configuration (kept nano-cubes), as well as the far-zone electric field intensity on the related planes. The maximization at the desired direction is clearly observed.

Since the designed nano-arrays have relatively complex distributions of nano-cubes (particles), one may attempt to simplify them by removing particles. This may be done based on an importance graph shown later, while the elimination of particles is not trivial. Particularly, only keeping nano-cubes that are close to the main source does not necessarily lead to good performances. As an example, Fig. 2 presents the results when the optimized nano-array shown in Fig. 1 is modified in alternative ways by extracting nano-cubes. Specifically, in these trial designs, the colored nano-cubes are kept, while all others are extracted. The corresponding far-zone electric field intensity values are also included in Fig. 2. We observe that, these attempts to make the structure more compact fail as the radiation characteristics significantly deteriorates. The best results among four nano-arrays are obtained for Trial 2 involving five nano-cubes, while the achieved value of the cost function is only $2.713 \times 1.673 \approx 4.4$. It is remarkable that adding more nano-cubes to Trial 2 (that can be

considered as the other trials) does not improve but degrades the performance, even leading to Trial 4 that generates shifted maximum on the x-y plane (hence the value of CF($\theta = 90°$) is only 0.002179 due to the punishment factor).

As the nano-arrays focused in this study involve two-dimensional arrangements of particles, they provide a higher ability for the control of the radiation pattern on the array plane. On the other hand, it is still possible to obtain good radiation characteristics in other directions. As an example, Fig. 3 presents the optimization results when the radiation is maximized at $\theta = 60°$ and $\phi = 45°$. Based on the relative value of the electric field intensity in the optimization direction with respect to those on the $(\theta = 60°, \phi \in [0, 360°])$ cone and on the $(\theta \in [0, 180°], \phi = 45°)$ plane, the achieved value of the cost function reaches 9.6. We note that this nano-array provides the same performance at $\theta = 120°$ and $\phi = 45°$.

In order to achieve better directivity out of the array plane, one may consider three-dimensional structures, while this significantly overloads the optimization mechanism that must be improved to be addressed elsewhere. Alternatively, the cubic particles may be replaced with rods to have more oscillatory patterns that may be shaped in the elevation plane. Unfortunately, this approach does not bring a significant improvement in the radiation characteristics, while the optimization must be repeated in most cases. For example, Fig. 4 presents the radiation characteristics of two nano-arrays when the optimal arrangement in Fig. 1 (found for nano-cubes) is used for different particles with $\lambda/4$ and λ heights. We observe that the modified nano-arrays cannot maintain the good radiation characteristics of the original structure.

IV. Sensitivity to Fabrication Errors

Despite rapid developments in nanotechnology, structures in small scales are prone to fabrication errors that may affect the performance of the designs in real life. When a nano-array is optimized and designed, a further analysis is required to test the feasibility of the design and to identify major performance parameters. In the case of nano-arrays considered in this study, the cubic particles may not be arranged perfectly, while the particle surfaces may not be perfectly planar. In order to demonstrate the effects of such fabrication errors on the radiation characteristics of the designed nano-arrays, Figs. 5 and 6 present two sets of numerical experiments. In both sets, a design that provides a maximum radiation at $\theta = 90°$ and $\phi = 45°$ (different from the design in Fig. 1) is considered, while its fitness value on the x-y plane is 3.4875. In Fig. 5, the cubes are randomly shifted (with Gaussian distribution) so that three different structures are obtained. We observe small changes in the radiation characteristics of the design, while the fitness value remains in the range of 3.3–3.6. In the trials shown in Fig. 6, the surfaces of nano-cubes are corrugated with 0.005λ (Modified 1), 0.015λ (Modified 2), and 0.025λ (Modified 3) limits for the protrusions/cavities. Similar to the previous cases, the design maintains its radiation characteristics with maximum radiation at the desired direction, while the corresponding fitness values are in the range of 3.4–3.5.

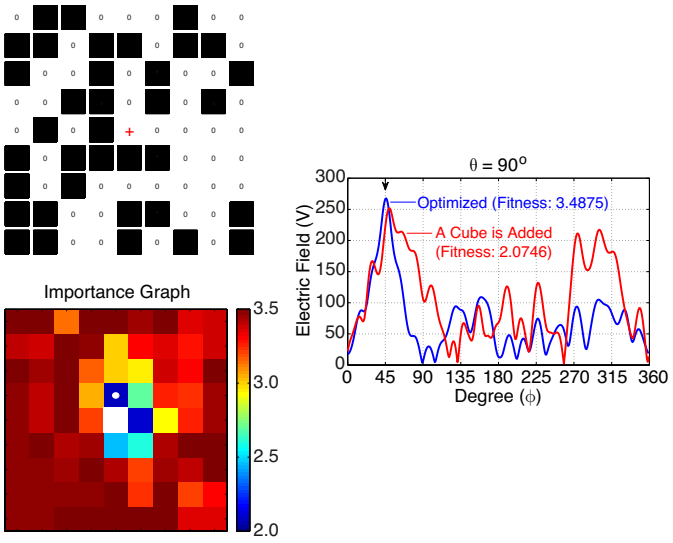

Fig. 7. The importance graph for an optimized nano-array that maximizes the radiation at a single direction. The fitness value is re-calculated when each nano-cube is added (if it was absent in the design) or extracted (if it was kept in the design).

Fig. 7 presents an extensive analysis, where the importance of each nano-cube of an optimized nano-array is investigated. The design is the same as the one considered in Figs. 5 and 6, i.e., it provides maximum radiation at $\theta = 90°$ and $\phi = 45°$. The color plot shows the value of the fitness function (originally 3.4875 for the optimized array) when each nano-cube decision is inverted (kept/extracted becomes extracted/kept) while all others remain the same. It can be observed that some of the nano-cubes are more critical; especially, two nano-cube locations close to the source location are extremely important. When these locations, which are originally empty, become filled, the fitness value significantly drops down. Fig. 3 also depicts the radiation patterns of the optimized and modified (when only one critical nano-cube is added) structures, where the deterioration of the pattern is clearly observed.

V. Multi-Direction Optimization

The developed design and optimization mechanism is particularly useful when multi-purpose optimization is required. For example, Fig. 8 presents three examples to multi-direction optimizations, i.e., when the radiation pattern of the overall structure is maximized simultaneously at two or three directions. The fitness value is defined as the mean of the far-zone electric field intensity values at these directions normalized by the values at the other directions on the same ($\theta = 90°$) plane. The designs that provide the best radiation patterns are also depicted under titles Design 1, Design 2, and Design 3. The optimization directions are shown with small arrows in the electric-field plots. We observe quite successful results with maximized radiations at the desired directions. We emphasize that once a nano-array is optimized, the same pattern can be rotated and the beams can be steered by physically rotating the array while the main source is fixed.

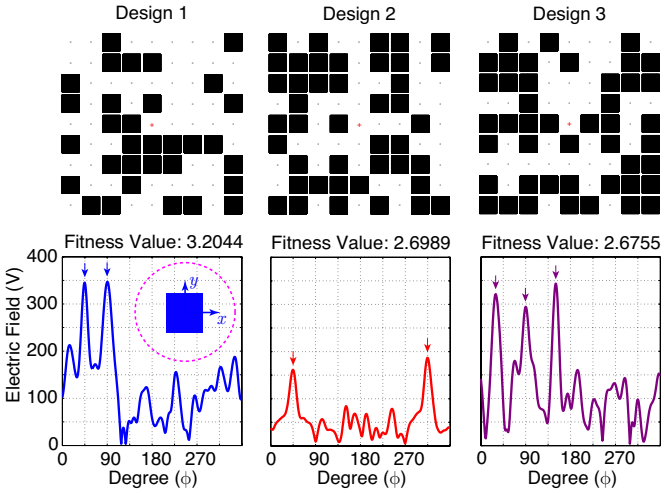

Fig. 8. Optimization results when the radiation is maximized at multiple directions.

VI. Concluding Remarks

In this study, we present the design and optimization of compact two-dimensional nano-arrays that can provide directive radiation characteristics at optical frequencies. The designs are obtained via rigorous optimization by using GAs with well-designed cost functions to maximize the radiation at desired directions. Using cubic particles, the designs are quite robust against possible fabrication errors related to the particle positioning and surface smoothness. Even when using only 80 elements, radiation patterns can be maximized simultaneously at multiple (two and three) directions. Once designed and optimized, rotation of a nano-array around an isotropic source can provide full beam-steering ability.

Acknowledgement

This work was supported by the Scientific and Technical Research Council of Turkey (TUBITAK) under the Research Grant 118E243 and by the Turkish Academy of Sciences (TUBA) in the framework of the Young Scientist Award Program.

References

[1] D. P. Fromm, et al., "Gap-dependent optical coupling of single bowtie nanoantennas resonant in the visible," Nano Lett., vol. 4, no. 5, pp. 957–961, Mar. 2004.

[2] P. J. Schuck, et al., "Improving the mismatch between light and nanoscale objects with gold bowtie nanoantennas," Phys. Rev. Lett., vol. 94, no. 017402, Jan. 2005.

[3] D. M. Solis, et al., "Optimization of an optical wireless nanolink using directive nanoantennas," Opt. Exp., vol. 21, no. 2, pp. 2369–2377, 2013.

[4] H. Chen, et al., "Design, fabrication, and characterization of near-IR gold bowtie nanoantenna arrays," Phys. Chem. C, vol. 118, no. 35, pp. 20553–20558, Aug. 2014.

[5] M. Alavirad, L. Roy, and P. Berini, "Optimization of plasmonic nanodipole antenna arrays for sensing applications," IEEE J. Sel. Top. Quantum Electron., vol. 20, no. 3, May/June 2014.

[6] A. Altınoklu and Ö. Ergül, "Computational analysis and full-wave optimizations of nanoantenna arrays for desired scattering and radiation characteristics," in Proc. URSI General Assembly and Scientific Symp. (URSI-GASS), 2017.

[7] A. Çekinmez, B. Karaosmanoğlu, and Ö. Ergül, "Integral-equation formulations of plasmonic problems in the visible spectrum and beyond," in Dynamical Systems - Analytical and Computational Techniques, M. Reyhanoglu, Ed. InTech, 2017, pp. 191–214.

Efficient Modeling of Towel Bar Antennas Using Model of Distributed Loading along Wires

Milos M. Jovicic [1], Saad N. Tabet [2], and Branko M. Kolundzija [3]

[1] WIPL-D d.o.o., Belgrade, Serbia
milos.jovicic@wipl-d.com

[2] NAVAIR, Patuxent River, MD, USA
saad.tabet@navy.mil

[3] Chair of General Electrical Engineering School of Electrical Engineering, Belgrade, Serbia
kol@etf.bg.ac.rs

Abstract — This paper presents an efficient technique to determine equivalents of towel bar antenna dielectric standoffs in the form of wires with distributed loadings using WIPL-D Pro (3-D EM solver) software. Starting from the product, we will determine its basic characteristics and propose simplifications in modeling for further analysis. Benefits of this technique are simplicity of modeling and fast, but still accurate, simulations.

Index Terms — Antenna modeling, dielectric standoff, distributed loading, WIPL-D Pro.

I. INTRODUCTION

Let us consider a simple towel bar antenna, mounted above a Perfect Electric Conductor (PEC) ground plane using dielectric standoffs, as shown in Fig. 1. The antenna is excited at one end and short-circuited to the PEC ground at the other. Hence, the antenna uses the PEC ground to operate as a loop antenna. In general, the larger the conductivity of the ground below the antenna tube is, the better the antenna efficiency will be [1].

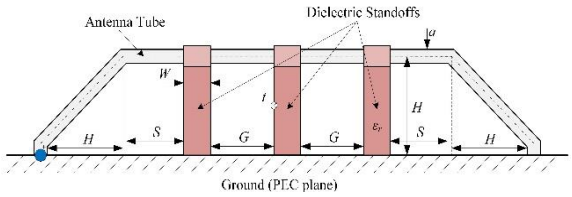

Fig. 1. Towel bar antenna mounted above a PEC ground plane.

The antenna tube is capacitively coupled to the ground. The capacitive coupling along the parts of the tube containing standoffs is different from those without standoffs. The influence of each dielectric standoff can be emulated by a loaded wire with properly determined equivalent radius. The equivalent radius and distributed loading of the wire are determined by the cross-sectional dimensions of the dielectric standoff and its electrical properties (i.e., relative dielectric constant).

In order to determine the equivalent values of the distributed loading on equivalents wires, the relative permittivity of the antenna standoffs should be determined. Capacitance per unit length of the part supported by the standoffs can be deduced from the measurements of the commercially available sample. The capacitance per unit length can be used to determine the relative permittivity of the dielectric standoff in the following way. The model of the antenna part supported by the standoffs is simulated with a variable value for the relative permittivity. The value of the capacitance per unit length is extracted from the simulations and compared to the value obtained by measurements. The relative permittivity of the standoff part is found for the case where the extracted value matches the value obtained by measurements. The capacitance per unit length is calculated using equation (1),

$$C' = \frac{1}{cZ_C}, \tag{1}$$

where c is the speed of the TEM wave propagating on the transmission line and Zc is the characteristic impedance of the line. These two parameters can be obtained from WIPL-D Pro numerical simulations.

II. EVALUATION OF CAPACITANCE PER UNIT LENGTH

If the part of the antenna supported by dielectric standoffs is set to be an eighth-wavelength long transmission line, as presented in Fig. 2, the characteristic impedance and the speed of the TEM waves can be determined using the simple transmission line equation

Submitted On: September 28, 2018
Accepted On: October 3, 2018

provided in equation (2):

$$Z(D) = Z_C \frac{Z_P + jZ_C \tan(\beta D)}{Z_C + jZ_P \tan(\beta D)}. \quad (2)$$

For the case where the length of the transmission line D is chosen to be:

$$D = \lambda / 8, \quad (3)$$

the tangent in equation (2) is equal to one, and the input impedance depends only on the transmission line termination and the characteristic impedance, as shown in equation (4):

$$Z(D) = Z_C \frac{Z_P + jZ_C}{Z_C + jZ_P}. \quad (4)$$

The choice of short and open circuit terminations can considerably simplify the calculation of the line characteristic impedance.

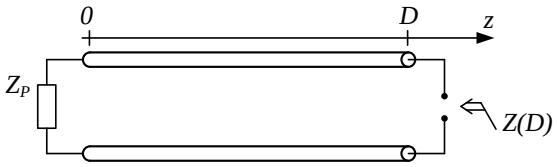

Fig. 2. Model of the transmission line section.

A. Characteristic impedance determination

For a short circuit termination, equation (4) reduces to:

$$Z_{SC}(D) = jZ_C. \quad (5)$$

On the other hand, when an eighth-wavelength transmission line is terminated in an ideal non-radiating open circuit, the input impedance becomes:

$$Z_{OC}(D) = -jZ_C. \quad (6)$$

In both cases, the magnitude of the input impedance is equal to:

$$|Z_{SC}(D)| = |Z_{OC}(D)| = Z_C. \quad (7)$$

Over a narrow frequency range, the characteristic impedance (Z_C) is determined by locating the point of intersection between the input impedance magnitude of the short circuit and open circuit termination plots, as shown in Fig. 3.

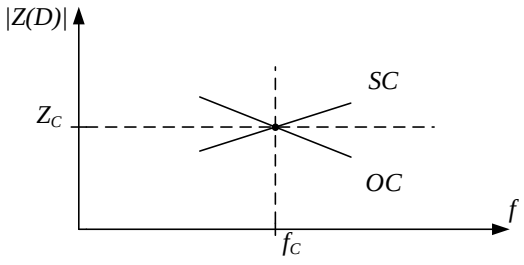

Fig. 3. Input impedance of an eighth-wavelength transmission line in a narrow frequency range for short and open circuit terminations.

B. Speed of TEM wave on transmission line

The magnitudes of the input impedance for open and short circuit terminations are equal, only when the length of the transmission line is an eighth-wavelength. Therefore, the speed of the TEM wave propagating on the transmission line can be determined from:

$$c = 8Df_C. \quad (8)$$

C. Thin wire above an infinite PEC ground plane

1) Theoretical approach

As a proof of concept for computing the per unit length equivalent capacitance, we will use the thin wire above an infinite PEC ground plane model shown in Fig. 4. This is a good benchmark, since the capacitance per unit length for this case is computable in closed form using equation (9),

$$C' = \frac{2\pi\varepsilon_0}{\ln \frac{2h}{a}}. \quad (9)$$

Some relevant dimensions used in this model are shown in Table 1.

Table 1: Model dimensions of a thin wire above an infinite PEC ground plane

Parameter [unit]	Value
a [mm]	12.7
h [mm]	609.6

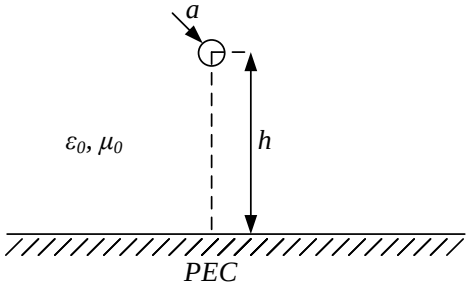

Fig. 4. Cross section of thin transmission line above the PEC infinity plane.

For the case of a thin wire above an infinite PEC ground plane with the dimensions as listed in Table 1, the capacitance per unit length is:

$$C'_{Theory} = 12{,}18 \text{ pF/m}. \quad (10)$$

2) Numerical approach

In order to illustrate the calculations of the capacitance per unit length from simulations, two separate models of an eighth-wavelength transmission line were created. The first corresponding to a short circuit termination (PEC), and the second corresponding to an open circuit termination (Perfect Magnetic Conductor - PMC). The transmission lines in both models

were 3.75 m long, with the same cross-section as the model of the thin wire above an infinite PEC ground plane discussed earlier. The narrow band frequency range of interest for both models is from 7.5 to 12.5 MHz. Both models are shown in Fig. 5.

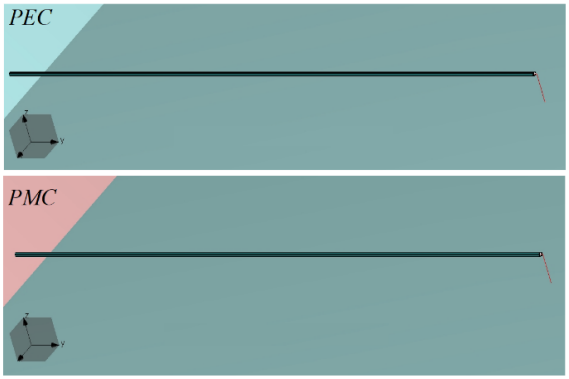

Fig. 5. Model of section of a thin wire above an infinite PEC ground plane in WIPL-D.

For short circuit termination, we used an infinite PEC plane, which forces the tangential component of the electric field to zero at the location of the PEC plane. A PMC infinite plane was used to model an ideal open circuit termination, since it forces the tangential component of the magnetic field to zero. It also enables the open circuit termination in precisely defined plane without radiation at the end.

Input impedance magnitude plots for short and open circuit termination models are shown in Fig. 6. The coordinates of their point of intersection are provided in Table 2.

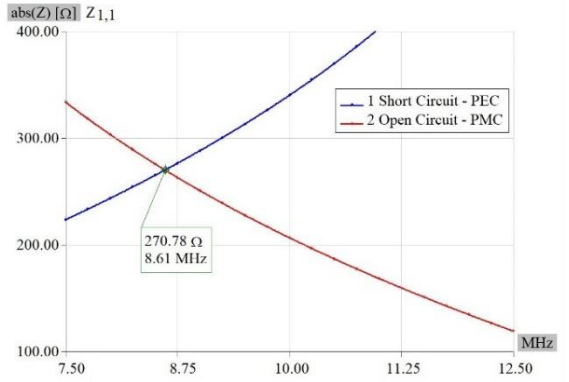

Fig. 6. Input impedance magnitude plots for short and open circuit terminations.

Table 2: Coordinates of short and open terminations point of intersection

Parameter [unit]	Value
Z_C [Ω]	270.78
f_C [MHz]	8.61

Placing the values in Table 2 into equation (8), the speed of the TEM wave in the transmission line becomes:

$$c_{WIPL-D} = 2.583 \cdot 10^8 \text{ m/s}. \quad (11)$$

The computed speed of the TEM wave in the transmission line obtained from the WIPL-D simulations is lower than the speed of light, even though the models were fully placed in vacuum. The reason for this disagreement is mainly caused by the feed region of the transmission line. Namely, instead of using plane wave excitation, we used a spatial delta generator in WIPL-D. This means that the generator is placed at one single point at the end of the feed wire, closest to the PEC plane placed below the transmission line. The total length of the conductor above the infinite PEC plane is equal to the sum of the transmission line length and the feed wire length.

If we combine the speed of the TEM wave in the transmission line obtained from equation (11), and the characteristic impedance from Table 2 into equation (1), we obtain the capacitance per unit length in equation (12) below:

$$C'_{WIPL-D} = 14.207 \text{ pF/m}. \quad (12)$$

As expected, due to the incorrect value of the speed of the TEM wave in the transmission line, the calculated value of the capacitance per unit length is also incorrect. However, if the value of the speed of light is used in equation (1), instead of the speed of the TEM wave obtained from the WIPL-D simulations, the result becomes:

$$C'_{WIPL-D\_corrected} = C'_{WIPL-D} \cdot \frac{c_{WIPL-D}}{c_0} = C'_{WIPL-D} \cdot K_{cal} = 12.23 \text{ pF/m}, \quad (13)$$

where K_{cal} represents a calibration factor defined as follows:

$$K_{cal} \triangleq \frac{c_{WIPL-D}}{c_0} = 0.86. \quad (14)$$

The relative error between the capacitance per unit length obtained from the equation and that obtained via CEM modeling is:

$$\rho = \frac{\left| C'_{Theory} - C'_{WIPL-D\_corrected} \right|}{C'_{Theory}} = 0.41\%. \quad (15)$$

III. EMULATION OF THE RELATIVE PERMITTIVITY OF THE DIELECTRIC STANDOFF

The measured capacitance per unit length of the dielectric standoff of the towel bar antenna is approximately:

$$C'_{Standoff} \cong 16.6 \text{ pF/m}. \quad (16)$$

Two new WIPL-D models representing a towel bar antenna supported by dielectric standoffs were devised in a similar fashion to the models of a thin wire above infinite PEC and PMC planes, using the dimensions

listed in Table 3. The new WIPL-D models are illustrated in Fig. 7.

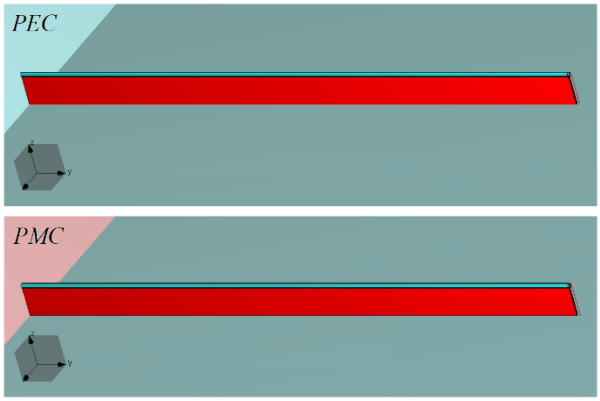

Fig. 7. Transmission line models a towel bar antenna supported by dielectric standoffs, over PEC and PMC planes, in WIPL-D Pro.

Table 3: Model dimensions for the WIPL-D models in Fig. 7

Parameter [unit]	Value
a [mm]	12.7
h [mm]	609.6
t [mm]	12.7

In order to determine the relative permittivity of the dielectric standoff, a set of simulations was run using the "Sweep" option in WIPL-D Pro. The relative permittivity value was swept from 8 to 20, in increments of 4.}. For each of the relative permittivity values analyzed, the characteristic impedance and the frequency at the point of intersection were determined. A plot showing the functional dependency of the extracted capacitance per unit length versus relative permittivity is presented in Fig. 8.

For a dielectric permittivity of 16, the extracted value of the capacitance per unit length, $C'_{Emulated} = 16.7$ pF/m, approximately equals the dielectric standoff's measured value.

Finally, when all the dimensions and the relative permittivity of the dielectric standoffs of the towel bar antenna are known, a full three-dimensional (3-D) model of the towel bar antenna can be created.

IV. MODELS OF A TOWEL BAR ANTENNA IN WIPL-D PRO

A. Metal-dielectric model of a towel bar antenna

A full 3-D metal-dielectric (M-D) model of a towel bar antenna in WIPL-D Pro is shown in Fig. 9. In order to reduce the required number of unknowns and simulation time in WIPL-D, two symmetry planes are used; PEC in the *x0y* plane and symmetry in the *y0z* plane.

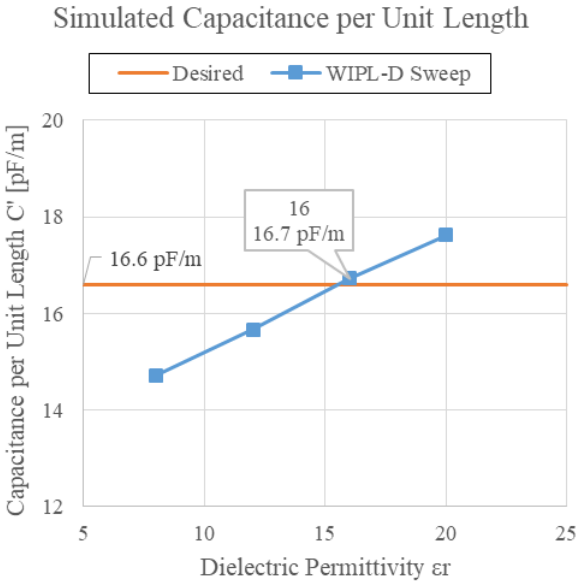

Fig. 8. Simulated capacitance per unit length.

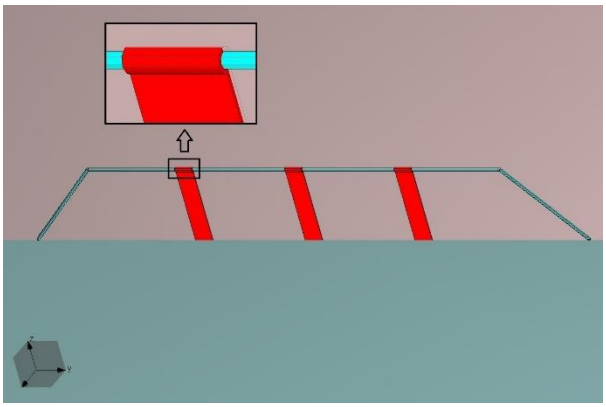

Fig. 9. Metal-dielectric model of a towel bar antenna in WIPL-D Pro.

The dimensions of the model and the electrical properties of the dielectric standoffs are provided in Table 4.

Table 4: Dimensions of the model and electrical properties of the dielectric standoffs

Parameter [unit]	Value
a [mm]	12.7
H [mm]	609.6
S [mm]	750
W [mm]	150
t [mm]	12.7
G [mm]	800
εr	**16**

B. Equivalent wire model of a towel bar antenna

An equivalent wire model of an M-D towel bar antenna, in WIPL-D Pro, is shown in Fig. 10. In this model, only PEC in the *x0y* plane is applied.

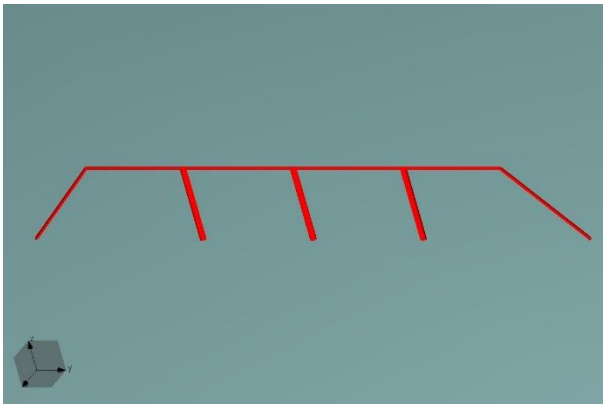

Fig. 10. Equivalent wire model of a towel bar antenna in WIPL-D Pro.

As a rule of thumb, the surface area of the cross-section of the dielectric standoff must be equal to the surface area of the cross-section of its equivalent wire. Therefore,

$$R_{equivalent} = \sqrt{\frac{W \cdot t}{\pi}}\,. \tag{17}$$

Also, the surface capacitance of the equivalent wire is related to the standoff's relative dielectric constant as shown in equation (18) below [2]:

$$C_{S,equivalent} = \frac{\varepsilon_0(\varepsilon_r - 1)R_{equivalent}}{2}\,. \tag{18}$$

V. RESULTS

The values of the equivalent radius obtained from equation (17) and the surface capacitance obtained from equation (18), respectively, are provided in Table 5. All other dimensions remained the same as those of the M-D model. It is to be noted that the equivalent wires are placed along the center of the standoffs.

A comparison of the real and imaginary components of the reflection coefficient, for the models in Figs. 9 and 10, is shown in Fig. 11.

Table 5: Equivalent radius and surface capacitance

Parameter [unit]	Value
$R_{\text{equivalent}}$ [mm]	24.625
$C_{\text{S,equivalent}}$ [pF]	1.634

Furthermore, the surface capacitance in the equivalent wire model can be manually tuned to achieve better matching to the results of the M-D model. Figures 12 and 13 show results for the reflection coefficient and radiation pattern comparisons, respectively, for the M-D model and the equivalent wire model with $C_{S,equivalent}$ = 2.452 pF.

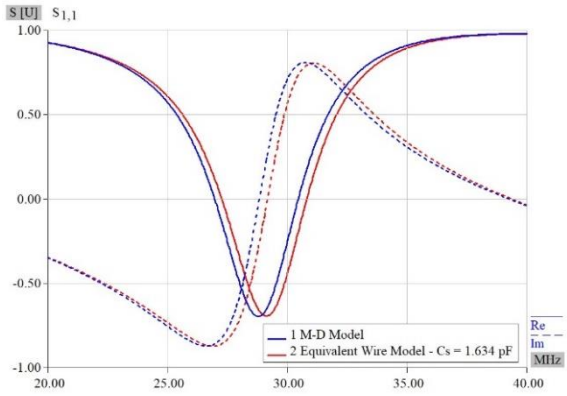

Fig. 11. Comparison of real and imaginary components of the reflection coefficient of the M-D and equivalent wire models, $C_{S,equivalent}$ = 1.634 pF.

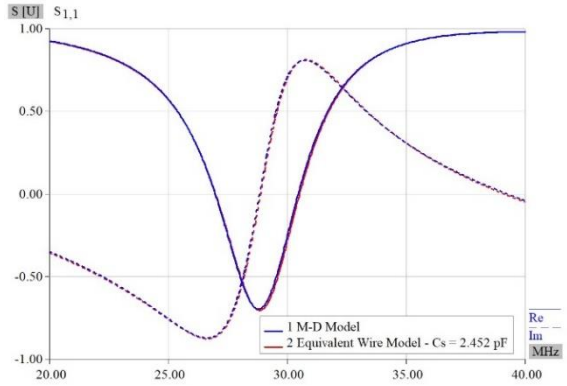

Fig. 12. Comparison of real and imaginary components of the reflection coefficient of the M-D and equivalent wire models, $C_{S,equivalent}$ = 2.452 pF.

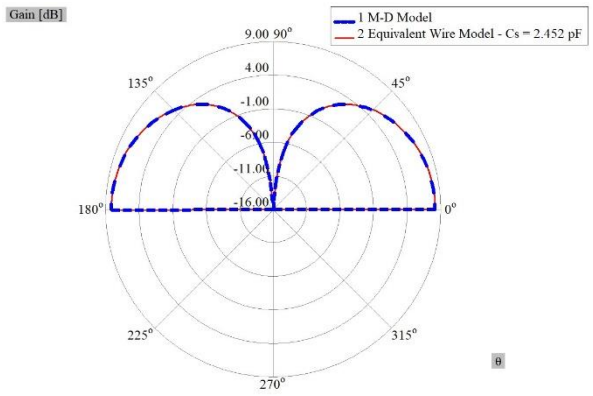

Fig. 13. Comparison of the radiation patterns of the M-D and equivalent wire models, $C_{S,equivalent}$ = 2.452 pF.

VI. SUMMARY AND CONCLUSION

The simulations of the M-D and equivalent wire models, as obtained through the provided equations, yielded very similar results. Moreover, tuning the equivalent capacitance of the equivalent wire model led to a near identical reflection coefficient and radiation pattern results when compared to those of the M-D model.

The mounting of a wire on an arbitrary platform does not require adapting the mesh of the platform, as is the case for the full 3-D M-D model. In WIPL-D Pro, the only requirement for connecting wires to a 3-D surface mesh of a platform is to properly position the wires and ensure their connectivity to the 3-D surface mesh, using non-trivial junctions at the connection points.

Moreover, the M-D model required a much larger number of unknowns, to estimate the currents over the elements, than the equivalent wire model did to approximate the axial currents along the wires. Hence, the M-D model simulation runtime far exceeded that of the equivalent wire model.

REFERENCES

[1] Towel Rail Antenna Arrays, Cobham Antenna System, 2011.

[2] WIPL-D Pro v14, Software and User's Manual, WIPL-D d.o.o., Belgrade, 2017.

Milos M. Jovicic was born in Belgrade, Serbia, in 1992. He received his BSc. degree in Electronics and MSc. degree in Microwave Techniques from the School of Electrical Engineering, Belgrade, Serbia in 2016 and 2018. Currently, he works for WIPL-D d.o.o., Belgrade, Serbia as an Application and Technical Support Engineer. His main research activities are electromagnetics modeling and simulation of various types of antennas and microwave devices.

Saad N. Tabet received his B.S., M.S. and Ph.D. in Electrical Engineering from Mississippi State University in 1982, 1984 and 1989, respectively. He has more than 30 years of experience in analytical and computational electromagnetics (CEM). For the past 20-plus years, he has been employed at Naval Air Systems Command (NAVAIR), Naval Air Station (NAS), Patuxent River, MD, USA. He currently serves as the Senior CEM Technologist and Co-Director of the Radar and CEM Modeling (RACEMM) Laboratory, which he was instrumental in creating in 2007. He leads all CEM modeling efforts, to include in-situ antenna/array radiation patterns, coupling, cosite, and link budget analyses. His in-situ modeling and analyses efforts span a score of manned and unmanned complex fixed and rotary wing aircraft, shipboard, and other application specific structures.

Branko M. Kolundzija received his B.Sc., M.Sc. and Ph.D. in Electrical Engineering from the School of Electrical Engineering, Belgrade, Serbia in 1981, 1987 and 1990, respectively. Currently, he works as a full-time Professor at the School Electrical Engineering, Belgrade, Serbia. He is the head developer of the WIPL-D software, as well as, the author of several books and scientific papers and articles in his main areas of interest: computational electromagnetics, antennas, microwaves and EMC.

Multi-Fidelity Approach for Polynomial Chaos Based Statistical Analysis of Microwave Networks

Aditi K. Prasad and Sourajeet Roy
Department of Electrical and Computer Engineering,
Colorado State University, Fort Collins, Colorado, CO 80253 USA

***Abstract* — In this paper, a novel polynomial chaos based approach for the fast statistical analysis of complex microwave structures is proposed. This approach leverages a highly efficient closed form low-fidelity model elicited from the high-dimensional model representation (HDMR) of the network. By cross-cutting the efficiency of this low-fidelity model with the accuracy of general high-fidelity simulations, the accuracy-CPU cost tradeoff for the statistical analysis can be achieved.**

I. INTRODUCTION

The generalized polynomial chaos (PC) theory is a widely accepted numerical approach for statistical analysis of circuits and systems [1]-[3]. In this approach, the uncertainty in a network response is modeled as a linear combination of polynomial basis functions of the input network parameters [1]-[3]. The coefficients of the expansion form the new unknowns of the network and can be evaluated via repeated black box solutions of the original network model [2],[3]. The main drawback with PC approaches is that the number of coefficients to be evaluated increases in a polynomial manner with the number of random parameters or dimensions. As a result, classical PC approaches are computationally prohibitive for statistical analysis of high-dimensional problems.

This paper presents a more efficient alternative to the traditional PC approaches. First, a closed form low-fidelity model of the network response is constructed using unidimensional PC expansions elicited from the first order terms of a high-dimensional model representation (HDMR). This low-fidelity model can be used to analytically emulate the network response at a fraction of the CPU costs required for a rigorous high-fidelity simulation. However, this efficiency comes at the cost of the low accuracy of the model caused by the negligence of the higher order HDMR terms. Next, a nonintrusive linear regression approach to evaluate the PC coefficients of the full-blown expansion is adopted. In this regression approach, the majority of the deterministic black box network solutions are determined by probing the closed-form low-fidelity model. In order to compensate for the lower accuracy of the low-fidelity model, only a limited number of high-fidelity simulations of the network response are added. In effect, the efficiency of the low-fidelity model is cross-cut with the accuracy of high-fidelity simulations. Notably the fraction of low-fidelity solutions to high-fidelity simulations can be easily tuned for the optimal accuracy-CPU cost tradeoff.

II. DEVELOPMENT OF PROPOSED MULTI-FIDELITY APPROACH

A general microwave network is considered where the input uncertainty is represented by n mutually uncorrelated random dimensions $\boldsymbol{\lambda}=[\lambda_1,\lambda_2,..,\lambda_n]$. Traditional PC approaches model the resultant uncertainty in the unknown current/voltage responses, $\mathbf{X}(t,\boldsymbol{\lambda})$, using a linear combination of orthogonal polynomials as

$$\mathbf{X}(t,\boldsymbol{\lambda})=\sum_{k=0}^{P}\mathbf{X}_k(t)\Phi_k(\boldsymbol{\lambda}) \tag{1}$$

where $\Phi_k(\boldsymbol{\lambda})$ is the k^{th} multivariate polynomial, $\mathbf{X}_k(t)$ is the corresponding coefficient, and the number of terms $P+1 = (n+m)!/(n!m!)$, m being the maximum degree of the expansion. In this paper, a high dimensional model representation (HDMR) of the network of (1) is considered where any response $x(t,\boldsymbol{\lambda})\in\mathbf{X}(t,\boldsymbol{\lambda})$ can be represented as a hierarchical superposition of functions describing the interactions among the random dimensions as [4]:

$$x(t,\boldsymbol{\lambda})=x_0(t)+\sum_{i=1}^{n}x_i(t,\lambda_i)+\sum_{1\le i,j\le n}x_i(t,\lambda_i,\lambda_j)+\ldots+ +x_{12..n}(t,\lambda_i..\lambda_n) \tag{2}$$

In (2), x_0 is the mean value of $x(t,\boldsymbol{\lambda})$, $x_i(t,\lambda_i)$ represents the contribution of λ_i to $x(t,\boldsymbol{\lambda})$ acting alone, $x_{ij}(t,\lambda_i,\lambda_j)$ represents the pairwise contribution of λ_i and λ_j to $x(t,\boldsymbol{\lambda})$ etc. The first order terms of (2) can be expressed using cut-HDMR [4] as

$$x_i(t,\lambda_i)=x(t,\boldsymbol{\lambda})\big|_{\boldsymbol{\lambda}^{(0)}\setminus\lambda_i}-x_0(t) \tag{3}$$

where $\boldsymbol{\lambda}^{(0)}\setminus\lambda_i$ represents the vector where all $\boldsymbol{\lambda}$ except λ_i is 0. These first order terms can now be modeled as 1D PC expansionss

$$x_i(t,\lambda_i)\approx\sum_{k=1}^{m}x_k^{(i)}(t)\phi_k(\lambda_i) \tag{4}$$

where $x_i^{(k)}(t)$ represents the k^{th} coefficient and $\boldsymbol{\phi}_k$ is the corresponding 1D basis. The coefficients of (4) can be evaluated using the pseudo-spectral collocation technique in conjunction with (3) [3]. Now, neglecting the higher order HDMR terms of (2), a low-fidleity PC representation of the response $x(t,\boldsymbol{\lambda})$ is obtained as

Submitted On: August 31, 2018
Accepted On: October 21, 2018

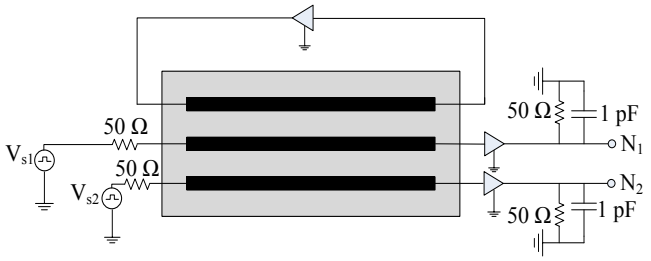

Fig. 1: Coupled transmission line network schematic

TABLE I
CHARACTERISTICS OF RANDOM PARAMETERS OF NETWORK OF FIG. 1

Random Parameters	Mean	Relative SD
ε_r (Relative permittivity of dielectric)	4.4	10%
σ (Metal conductivity)	5.8e7	
t (Thickness of metal)	5 μm	
w (Width of transmission lines)	180 μm	
h_1 (TL_1 height)	50 μm	
h_2 (TL_2 height)	70 μm	
h_3 (TL_3 height)	60 μm	
s (line spacing)	90 μm	
len (NMOS channel length)	0.1 μm	
wid (NMOS channel width)	10 μm	

$$x(t,\boldsymbol{\lambda}) \approx x_0(t) + \sum_{i=1}^{n}\sum_{k=1}^{m} x_k^{(i)}(t)\phi_k(\lambda_i) \tag{5}$$

The model of (5) is closed form in nature and can be used to analytically emulate the response instead of using a rigorous and time consuming high-fidelity simulation.

Next, to recover the coefficients of (1), the linear regression approach is chosen which typically requires $K = 2(P+1)$ black box model simulations of the network response [2]. In this paper, an iterative algorithm is used to find the fraction of K simulations performed using the low-fidelity model. This algorithm begins by initially assuming that all K simulations are performed using the low-fidelity model of (5). Thereafter, the number of high-fidelity network simulations is increased in steps of k nodes per iteration and the PC coefficients are reevaluated. The value of k is kept small enough (k = 10% of K) to minimize any overshoot beyond the optimal number of high-fidelity simulations. As the number of high-fidelity simulations increases per iteration relative to the number of low-fidelity simulations, the resultant improvement in the accuracy of the response variance is computed as

$$\eta = \frac{\int_0^{T_{\max}} \left(\sum_{i=1}^{P+1} \left(\hat{x}_i^{(r)}\right)^2 - \sum_{i=1}^{P+1} \left(\hat{x}_i^{(r-1)}\right)^2 \right) dt}{\int_0^{T_{\max}} \sum_{i=1}^{P+1} \left(\hat{x}_i^{(r)}\right)^2 dt} \tag{6}$$

where $\hat{x}$ are the computed PC coefficients and the superscript r is the iteration count. As the iteration count increases, the error in the numerator of η steadily decreases. Once the value of η falls below a prescribed tolerance, the iterations are halted.

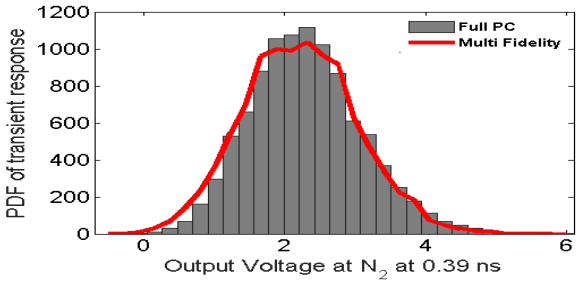

Fig. 2: Probability distribution function of transient response at node N_2 at timepoint of maximum standard deviation (t = 0.39 ns).

III. NUMERICAL RESULT AND DISCUSSION

To validate the proposed approach, the multicondutor transmission line (MTL) network of Fig. 1 is considered. The MTLs are terminated with cascode amplifiers modeled using SPICE level-49 CMOS transistors. The input waveform to lines 2 and 3 are trapezoidal pulses with rise/fall time T_r = 0.1 ns, pulse width T_w = 1 ns, and amplitude 5V. The uncertainty in the network is introduced via n = 10 random variables whose characteristics are shown in Table I. For this example, a Hermite PC expansion of degree m = 3 is required. The uncertainty quantification of the network is performed using two PC approaches – the proposed multi-fidelity approach and the traditional linear regression approach of [2]. The low-fidelity model requires only $(m+1)n+1$ = 41 SPICE simulations. In the multi-fidelity stage, only 30% of the $2(P+1)$ = 572 regression nodes (i.e., 171 nodes) requires a high-fidelity SPICE simulation translating to a speedup of more than 5 times over the traditional linear regression approach., The probability density of the transient response at N_2 evaluated at the time point when the standard deviation is maximum (0.39 ns) using the above methods and 10,000 samples is compared in Fig. 2. Despite the speedup, the proposed approach exhibits good accuracy relative to the traditional linear regression approach.

REFERENCES

[1] P. Manfredi, D. Vande Ginste, D. De Zutter and F. Canavero, "Stochastic modeling of nonlinear circuits via SPICE-compatible spectral equivalents," IEEE Trans. Circuits Syst., vol. 61, no. 7, pp. 2057–2065, Jul. 2014

[2] A. K. Prasad, M. Ahadi, and S. Roy, "Multidimensional uncertainty quantification of microwave/RF networks using linear regression and optimal design of experiments," IEEE Trans. Microwave Theory Techniques, vol. 64, no. 8, pp 2433-2446, Aug. 2016

[3] A. C. Yucel, H. Bagci, and E. Michielssen, "An ME-PC enhanced HDMR method for efficient statistical analysis of multiconductor transmission line networks," IEEE Trans. Comp., Packag. and Manuf. Technology, vol. 5, no. 5, pp. 685-696, May 2015

[4] H. Rabitz and O. F. Alis, "General formulation of high-dimensional model representations," Journal of Math. Chem., vol. 50, no. 2-3, pp. 197-233, 1999

Biomedical Magnetic Induction Tomography: An Inhomogeneous Green's Function Approach

Philippe De Tillieux and Yves Goussard

Department of Electrical Engineering
Polytechnique Montreal, Montreal, QC, H3T 1J4, Canada
louis-philippe.de-tillieux@polymtl.ca, yves.goussard@polymtl.ca

Abstract ─ Magnetic induction tomography aims to reconstruct the passive electric properties of an object by measuring its scattered magnetic field. Current state-of-the-art numerical techniques are based on differential formulations such as the finite element method. A formulation based on volume integral equations has not yet been applied to its biomedical field and could improve the reconstruction speed by reducing the number of unknowns. This paper investigates salient characteristics of the approach and offers a solution based on inhomogeneous Green's functions.

Index Terms ─ Biomedical, magnetic induction, volume integral.

I. INTRODUCTION

Biomedical magnetic induction tomography (MIT) is a novel imaging technique with applications to stroke detection, inductive measurement of wound conductivity and lung imaging [1]. Its main benefits are a very low operating and construction cost, non-ionizing interactions with matter and contactless operation. A low frequency field (in the kHz to the MHz range) is used to induce eddy currents inside an object of interest. The eddy currents depend on the passive electric properties (PEP) of the object and these in turn induce a secondary magnetic field, which can be measured at sensors outside the volume of interest. Computation of the scattered magnetic field is done through the forward model. Current state-of-the-art forward models are based on approximate, differential or surface integral equations. Here, the main challenge is to obtain accurate results while maintaining a low computation cost. The forward model may be formulated as a large linear system, which needs to be solved iteratively. While a finer discretization may yield more accurate results, it also leads to a more computationally burdensome model. For imaging purposes, the PEP of the domain of interest must be reconstructed from the known incident and scattered fields, which is referred to as the inverse problem. The inverse problem is solved iteratively by minimizing the differences between the measured scattered magnetic field and the forward model evaluation for estimated values of the PEP to which a penalty term may be added. For each iteration of the inverse solver, the forward problem must be solved, so an efficient forward model is critical. Biological tissues in the MIT frequency range may be considered as penetrable objects and volume integral equations (VIEs) can adequately model the problem. VIEs offer several advantages such as the need to discretize a much smaller domain than differential methods, a better accuracy than approximate methods and a wider range of applicability than surface integral methods. Although VIEs are commonly used in a higher frequency range (e.g., microwave tomography) and for non-destructive evaluation (NDE), specific issues plague their application to biomedical MIT. Since both permittivity and conductivity are being reconstructed (as opposed to only conductivity for NDE) and because at these frequencies biological tissues have very high dielectric properties [2], conditioning issues arise. For large domains requiring the implementation of iterative solvers, this yields a slow convergence of both the forward and the inverse solvers [1]. This paper presents and validates a model that tackles this conditioning issue arising from the high contrasts in biomedical MIT by using Green's function theory.

II. PROBLEM FORMULATION

A. Volume integral equation based model

The standard VIE is obtained by using Green's function and the volume equivalence principle to solve the wave equation [3]. Discretization is performed by the method of moments with Dirac basis functions. The scattered magnetic field at the sensors is obtained through:

$$\boldsymbol{h}^{scat}(\boldsymbol{x}) = -\tilde{\sigma}_b \boldsymbol{X}\boldsymbol{G}^R\boldsymbol{\mathcal{L}}^{-1}\boldsymbol{e}^0, \quad (1)$$

with $\boldsymbol{\mathcal{L}}^{-1} = (\boldsymbol{I} - k_b^2\boldsymbol{G}\boldsymbol{X})^{-1}$ the scattering operator, $\boldsymbol{X}$ a diagonal matrix containing the electric contrast values $X(\boldsymbol{r}) = \tilde{\sigma}(\boldsymbol{r})/\tilde{\sigma}_b - 1$, with $\tilde{\sigma}_b = \sigma - j\omega\epsilon_r\epsilon_0$ the background complex conductivity, $\boldsymbol{G} = \Delta V\left(\boldsymbol{I} + \frac{\nabla\nabla}{k_b^2}\right)g$ the dyadic Green's function, $g(\boldsymbol{r},\boldsymbol{r}') = e^{jk_b|\boldsymbol{r}-\boldsymbol{r}'|}/(4\pi|\boldsymbol{r} - \boldsymbol{r}'|)$ denotes the scalar Green's function, ΔV the

Submitted On: August 31, 2018
Accepted On: October 1, 2018

discretization volume and $\boldsymbol{e}^0$ is the incident electric field. The matrix $\boldsymbol{G}^R = \xi \nabla g$ is defined through the Levi-Civita tensor and represents the cross product of the gradient and the scalar Green's function.

The selected criterion is the L_2 norm of the differences between the measurements and the forward model evaluation. To deal with the ill-posedness of the problem, an additive regularization term is added to include *a priori* information about the domain to reconstruct. An L_2L_1 penalization term on the first differences of the contrast is chosen in order to preserve the object edges. The function $R(\boldsymbol{X}) = \lambda\sqrt{\delta^2 + t(\boldsymbol{X})^2}$ is well adapted, where t is the sum of contrast variations along each axis, δ is a hyperparameter that defines the transition between the quadratic and linear behaviors of the penalty function and λ is the regularization parameter. The cost functional to minimize is therefore: $F(\boldsymbol{X}) = \left||y - f(\boldsymbol{X})|\right|_2^2 + \lambda R(\boldsymbol{X})$. To minimize this cost functional, the L-BFGS algorithm is chosen. This quasi-Newton method offers a lower computation cost per iteration than a Newton method, while converging faster than a gradient method. The gradient of the cost functional is obtained by computing its Fréchet derivative. Straightforward computations yield $\nabla F = \boldsymbol{J}^\dagger(y - f) + \lambda R'_{HS}$ where Jacobian $\boldsymbol{J}$ can be expressed as:

$$\boldsymbol{J} = \boldsymbol{G}^R(\boldsymbol{I} - \boldsymbol{G}\boldsymbol{X})^{-\mathrm{T}}\mathrm{diag}\{\boldsymbol{e}\}. \quad (2)$$

The issue with the VIE model is that the scattering operator $\boldsymbol{\mathcal{L}}$ is ill-conditioned due to the high contrast values of biological tissues in this low frequency range. This implies a very slow convergence of the forward model. The poor conditioning of the forward model also results in a slow convergence of the inverse solver. This yields a very high computation cost, which makes the model impractical for realistic applications.

B. Inhomogeneous Green's function based model

A solution to the problem's poor conditioning and slow convergence is to perform a change of variables to a new contrast value $\boldsymbol{X}_2$, which is defined as a perturbation in an otherwise healthy tissue. Since in biomedical imaging the goal is to identify a small perturbation in a known background, this healthy tissue can be included into the background propagation medium. Two approaches may be considered. The first one is the linear embedding via Green's operator (LEGO), which makes use of the port theory to include the mutual scattering events between the background and the perturbation domain [4], but is computationally burdensome. The second one is based on the Green's function theory [5]. If one considers an inhomogeneous propagation medium including the healthy tissue, an inhomogeneous Green's function (IG) can be computed by solving $\boldsymbol{G}^{in} = \boldsymbol{\mathcal{L}}_1^{-1}\boldsymbol{G}_{12}$. Domains 1 and 2 respectively denote the inhomogeneous propagation medium and the volume of interest, which contains the contrast values $\boldsymbol{X}_2$ that are to be determined. After discretization, the forward model is given by:

$$\boldsymbol{h}^{scat}(\boldsymbol{X}_2) = \boldsymbol{G}^R\boldsymbol{X}_1(\boldsymbol{e}_1 + \boldsymbol{G}^{in}\boldsymbol{X}_2\boldsymbol{e}_2). \quad (3)$$

Here, $\boldsymbol{e}_2 = \boldsymbol{\mathcal{L}}_2^{-1}\boldsymbol{e}_{1|2}$ and $\boldsymbol{e}_1 = \boldsymbol{\mathcal{L}}_1^{-1}\boldsymbol{e}_1$ are the total fields in each domain and $\boldsymbol{e}_{1|2}$ is the total field in Domain 2 due to the inhomogeneous Domain 1. Matrices involving $\boldsymbol{X}_1$ may be computed only once so that only $\boldsymbol{e}_2$ needs to be computed at each iteration of the inverse solver. The new scattering operator $\boldsymbol{\mathcal{L}}_2^{-1}$ has a much better conditioning and convergence of both the forward and inverse problems are greatly improved. The new Jacobian is given by:

$$\boldsymbol{J} = \boldsymbol{G}^R\boldsymbol{X}_1\boldsymbol{G}^{in}(\boldsymbol{I}_2 + \boldsymbol{X}_2\boldsymbol{\mathcal{L}}_2^{-1}\boldsymbol{G}_{22})\mathrm{diag}\{\boldsymbol{\mathcal{L}}_2^{-1}\boldsymbol{e}_{1|2}\}. \quad (4)$$

III. RESULTS

The LEGO and IG models were compared to the standard VIE for a dielectric sphere emulating white matter with a layer of cerebrospinal fluid and a small blood perturbation as seen in Fig. 1 (a). The left pane of Fig. 1 (c) shows good agreement between the scattered magnetic field for the three models and the right pane shows improvement in the convergence of the inverse solver for the LEGO and IG models. In Fig. 1 (b) the reconstructed domain using the IG model is presented. The data were generated using the VIE model with 80 dB of added Gaussian noise in order to avoid the inverse crime. We notice that, although the boundaries of the perturbation are properly identified, the conductivity values are slightly underestimated, which seems to be an effect of the regularization.

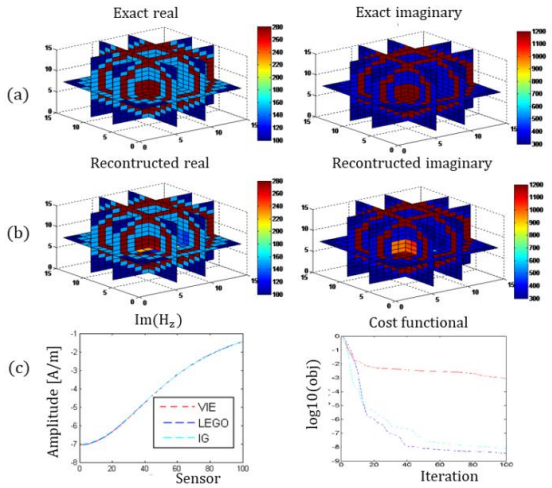

Fig. (a) Exact and (b) reconstructed domains, and (c) Im$\{H_z\}$ component of the scattered magnetic field and convergence of the cost functional for each model. The simulation domain is a cube with 20 cm edges, discretized onto a 15 X 15 X 15 Cartesian grid. It is illuminated by 15 sources (z oriented magnetic dipoles of unit amplitude) and 15 detectors are placed circularly (r = 16 cm) on three planes (z = –2:5; 0; 2:5 cm).

IV. DISCUSSION

These results indicate that, although the standard VIE model is not suitable for MIT, the alternate IG model offers considerable improvements regarding convergence of both the forward and inverse solvers. Although the proposed method shows some advantages over state-of-the-art numerical methods such as fewer unknowns and a structure well suited to parallelization, further work is required in order to reconstruct images with a lower SNR and to reduce computational cost through numerical methods such as Block algorithms and preconditioning.

REFERENCES

[1] P. De Tillieux and Y. Goussard, "A volumetric integral equation formulation for magnetic induction tomography," *Antenna Measurements & Applications (CAMA), 2016 IEEE Conference*, pp. 1-4, 2016.

[2] S. Gabriel, R. W. Lau, and C. Gabriel, "The dielectric properties of biological tissues: II. Measurements in the frequency range 10 Hz to 20 GHz," *Physics in Medicine and Biology*, 41(11), 1996.

[3] M. Pastorino, *Microwave Imaging*. vol. 208, John Wiley & Sons, 2010.

[4] V. Lancelloti, B. P. de Hon, and A. G. Tijhuis, "Scattering from large 3-D iecewise homogeneous bodies through linear embedding via Green's operators and Arnoldi basis functions," *Progress in Electromagnetics Research*, 103, pp. 305-322, 2010.

[5] C. T. Tai, "Dyadic Green functions in electromagnetic theory," *Institute of Electrical & Electronics Engineers (IEEE)*, 1994.

Philippe De Tillieux obtained his B.Eng. in Engineering Physics and M.Sc. in Electrical Engineering at Polytechnique Montreal. He is currently a Ph.D. student at the CERVO Brain Research Centre in Québec, Canada.

Yves Goussard is a Full Professor in the Department of Electrical Engineering at Polytechnique Montreal. His research interests include inverse problems, medical imaging and optimization. He obtained his engineering diploma at ENSTA and his Ph.D. at Paris XI, France.

28 GHz Propagation Channel Measurements for 5G Microcellular Environments

C. Umit Bas*, Rui Wang*, Seun Sangodoyin*, Sooyoung Hur†, Kuyeon Whang†,
Jeongho Park†, Jianzhong Zhang‡, and Andreas F. Molisch*
*University of Southern California, Los Angeles, CA, USA
†Samsung Electronics, Suwon, Korea
‡Samsung Research America, Richardson, TX, USA

***Abstract*—This paper presents results from several 28 GHz propagation channel measurement campaigns performed with a real-time channel sounder that is capable of performing directionally-resolved channel measurements in dynamic environments. We summarize the key results from three measurement campaigns; microcellular in a residential environment, stationarity region, and dynamic scatterers measurements in urban environments.**

I. Introduction

The design and deployment of any wireless system require a thorough understanding of the wireless propagation channel. Specifically for millimeter-wave (mm-wave) frequencies, due to the higher path- and penetration losses, any system operating over distances larger than a few meters will have to utilize beamforming antenna arrays [1], [2]. The statistics of the angular spectrum and their temporal variations should be taken into account when designing a system with such beamforming capabilities. However, almost all of the directional outdoor measurements for mm-wave frequencies were performed with rotating horn antenna channel sounders, which can not measure in real-time and thus are not suitable for dynamic channels [3].

In this paper, we summarize results from our recent channel sounding campaigns performed with a double-directional real-time mm-wave channel sounder [4], [5] which is described in Section II. Section III summarizes the results obtained in three measurement campaigns performed to investigate the different aspects of the microcellular environment at $28\,\mathrm{GHz}$.

II. Measurement Setup

The channel sounder used in these measurements is a real-time mm-wave channel sounder [4], [5]. By using beamforming arrays, it can perform 90° sweeps in the azimuth at the receiver (RX) and the transmitter (TX). Furthermore, TX and RX are synchronized by using GPS-disciplined Rubidium frequency references without requiring a physical connection.

Table I. Sounder Parameters Used in Measurements

Parameters	**Microcell [6]**	**Stationarity [7]**	**Dynamic [8]**
Frequency	27.85 GHz		
Bandwidth	400 MHz		
Array size	8 by 2		
Beam steering	-45° to 45°		
3dB beam width	12°		
Steering steps	5°		10°
Switching speed	$2\mu s$		
TX EIRP	57 dBm		
RX noise figure	$\leq$ 5 dB		
SISO duration	2 μs		
SISO repetition	10	10	1
Total sweep time	14.44 ms	14.44ms	0.4 ms

Thanks to the flexible design, the operation parameters of the channel sounder can be modified on a per campaign basis. Table I summarizes the parameters used in the three measurement campaigns. For the residential microcell and stationarity region measurements, we employed waveform repetition to improve RX signal to noise ratio by averaging. For the dynamic measurements, we only measured a subset of available azimuth beams to increase the snapshot repetition frequency to measure higher Doppler frequencies.

III. Measurement Campaigns

A. Residential Microcell

In [6], we investigated path-loss (PL) and delay spread in a suburban residential environment for a microcell and the impact that beamforming has on it. The obtained results also include the effects of the foliage, which is typical to a suburban street. The measurements were taken in two scenarios; first when the RX is on the same street with the TX (denoted as line-of-sight (LoS), although most of the time the direct path was blocked by foliage), and when the RX is on a crossing street and the direct path is blocked by buildings.

The estimated parameters for the PL model are summarized in Table II. The directional PL is calculated by using the power of the best TX-RX beam pair as the received power, while for the omnidirectional PL, we combine the power received via all TX-RX beams. The TX-RX distances for LoS measurements vary from $36\,\mathrm{m}$ to $400\,\mathrm{m}$, and from $130\,\mathrm{m}$ to $273\,\mathrm{m}$ for the non-LoS (NLoS). Hence the provided PL model is only applicable within these ranges. Furthermore, the median root mean square delay spreads (RMS-DS) for the omnidirectional power delay profiles were estimated as $25.63\,\mathrm{ns}$ and $67.18\,\mathrm{ns}$ for LoS and NLoS respectively.

B. Dynamic Environment

In [8], we presented the first dynamic double directional measurements for a microcell scenario. A sample measurement location is shown in Fig. 1. During this measurement, both the

Table II. Parameters of the Path Loss Models

	Data	n	P_0	$\chi\sigma$	
				σ	P-Value
Omni	LoS - ABG Model	2.82	63.47	6.44	0.975
	LoS- CI Model	2.92	61.34	6.45	0.978
	NLoS - ABG Model	4.97	29.53	2.58	0.745
	NLoS - CI Model	3.58	61.34	3.06	0.706
Directional	LoS - ABG Model	3.17	58.01	7.75	0.840
	LoS - CI Model	3.15	61.34	7.76	0.928
	NLoS - ABG Model	5.85	18.12	4.53	0.856
	NLoS - CI Model	3.96	61.34	5.06	0.958

Submitted On: September 29, 2018
Accepted On: October 1, 2018

Fig. 1. Environment for dynamic measurements.

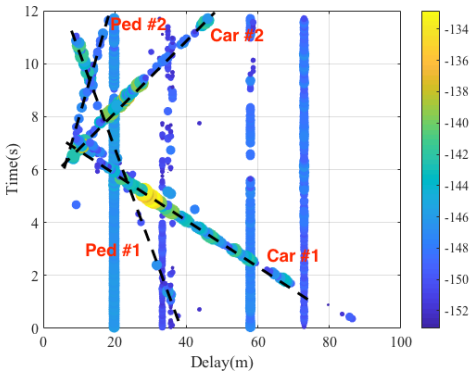

Fig. 2. Temporal evolution of the power delay profile (dB).

RX and TX are placed parallel to the road facing the same direction and perform 90° scans in the azimuth. The TX is placed at $4\,\mathrm{m}$ height, while the RX is at $1.8\,\mathrm{m}$. Along with some fixed objects, there are four moving objects; two cars and two pedestrians as indicated in Fig. 1.

Fig. 2 shows the power of the multipath components and their evolution over time. The multipath components for the four moving objects are clearly visible and their routes are marked in Fig. 2.

C. Stationarity Region

In a third campaign, we investigated the stationarity region of MIMO mm-wave channels at 28 GHz based on an outdoor measurement campaign. We analyzed results in an urban microcell LoS and LoS to NLoS transition region scenario, for the stationarity region of shadowing, power delay profile and the angular power spectrum [7].

We have found that the foliage effect can significantly alter the PL exponent even in the LoS scenario. For our measurements, this effect resulted in the proposed dual-slope PL model in Fig. 3. The propagation loss increases rapidly, about 30 dB, during the transition from LoS to NLoS. We propose to model it with a street-by-street PL model, similar to the method in [9]. More results related to the PL fitting can be found in Fig. 3. The autocorrelation distance of shadowing is 1.2 m in the LoS route, although this value might be affected by the signal variation observed in the two-path channel. It increases up to $4.8\,\mathrm{m}$ for the LoS to NLoS transition route. The average correlation distance as computed based on the similarity of the power delay profiles, is $0.9\,\mathrm{m}$ for the LoS route. It can become as high as $4\,\mathrm{m}$ at the beginning section of the transition route and drops to about $1.26\,\mathrm{m}$ afterward. The analysis based on the correlation of shadowing and PDP has suggested that mm-wave channels exhibit a smaller stationarity region compared with cm-wave channels.

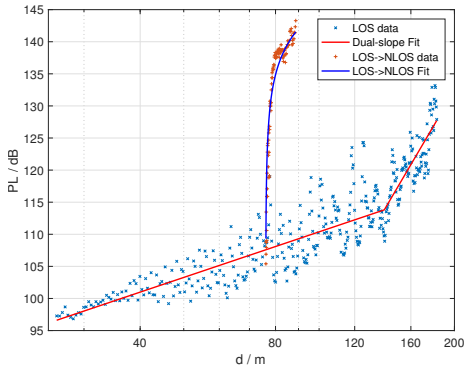

Fig. 3. The path-loss data fitting for the microcell LoS and LoS to NLoS transition region scenarios.

IV. Conclusions

This paper discusses results from various 28 GHz propagation channel measurements performed with a real-time double-directional channel sounder for three different investigations. Through extensive measurements allowed by the nature of the used channel sounder, we were able to propose statistical models for path-loss, shadowing, RMS-DS and the stationarity region. Furthermore, we presented results from the first dynamic double directional measurement campaign for microcell environment at mm-wave frequencies.

Acknowledgements

Part of this work was supported by grants from the National Science Foundation (grants CIF-1618078, CNS-1457340, ECCS-1126732) and National Institute of Standards and Technology (grant 60NANB17D317).

References

[1] F. Boccardi, R. W. Heath, A. Lozano, T. L. Marzetta, and P. Popovski, "Five disruptive technology directions for 5G," in IEEE Communications Magazine, vol. 52, no. 2, pp. 74–80, February 2014.

[2] A. F. Molisch, A. Karttunen, R. Wang, C. U. Bas, S. Hur, J. Park, and J. Zhang, "Millimeter-wave channels in urban environments," in 2016 10th European Conference on Antennas and Propagation (EuCAP), April 2016, pp. 1–5.

[3] T. S. Rappaport, G. R. Maccartney, M. K. Samimi, and S. Sun, "Wideband millimeter-wave propagation measurements and channel models for future wireless communication system design," in IEEE Transactions on Communications, vol. 63, no. 9, pp. 3029–3056, September 2015.

[4] C. U. Bas, R. Wang, D. Psychoudakis, T. Henige, R. Monroe, J. Park, J. Zhang, and A. F. Molisch, "A real-time millimeter-wave phased array MIMO channel sounder," in 2017 IEEE 86th Vehicular Technology Conference (VTC-Fall), September 2017, pp. 1–6.

[5] C. U. Bas, R. Wang, S. Sangodoyin, D. Psychoudakis, T. Henige, R. Monroe, J. Park, J. Zhang, and A. F. Molisch, "Real-time millimeter-wave MIMO channel sounder for dynamic directional measurements," arXiv preprint arXiv:1807.11921, 2018.

[6] C. U. Bas, R. Wang, S. Sangodoyin, S. Hur, K. Whang, J. Park, J. Zhang, and A. F. Molisch, "28 GHz microcell measurement campaign for residential environment," in 2017 IEEE Global Communications Conference (GLOBECOM), December 2017, pp. 1–6.

[7] R. Wang, C. U. Bas, S. Sangodoyin, S. Hur, J. Park, J. Zhang, and A. F. Molisch, "Stationarity region of mm-wave channel based on outdoor microcellular measurements at 28 GHz," in 2017 IEEE Military Communications Conference (MILCOM), October 2017, pp. 782–787.

[8] C. U. Bas, R. Wang, S. Sangodoyin, S. Hur, K. Whang, J. Park, J. Zhang, and A. Molisch, "Dynamic double directional propagation channel measurements at 28 GHz-Invited paper," in 2018 IEEE 87th Vehicular Technology Conference (VTC Spring), June 2018, pp. 1–6.

[9] A. F. Molisch, A. Karttunen, S. Hur, J. Park, and J. Zhang, "Spatially consistent pathloss modeling for millimeter-wave channels in urban environments," in 2016 10th European Conference on Antennas and Propagation (EuCAP), April 2016, pp. 1–5.

Analysis of Radio Altimeter Interference due to Wireless Avionics Intra-Communication Systems by Using Large-Scale FDTD Method -Investigation on Airbus A320 Class Passenger Aircraft-

Shunichi Futatsumori [1], Kazuyuki Morioka [1], Akiko Kohmura [1], Naruto Yonemoto [1], Takashi Hikage [2], Tetsuya Sekiguchi [2], Manabu Yamamoto [2], and Toshio Nojima [2]

[1] Surveillance and Communications Department, Electronic Navigation Research Institute
National Institute of Maritime, Port and Aviation Technology, Chofu, Tokyo 182-0025, Japan
futatsumori@mpat.go.jp, morioka@mpat.go.jp, kohmura@mpat.go.jp, yonemoto@mpat.go.jp

[2] Graduate School of Information Science and Technology
Hokkaido University, Sapporo, Hokkaido, Japan
hikage@wtemc.ist.hokudai.ac.jp, t-sekiguchi@wtemc.ist.hokudai.ac.jp, yamamoto@wtemc.ist.hokudai.ac.jp, nojima@wtemc.ist.hokudai.ac.jp

Abstract ─Radio altimeters and wireless avionics intra-communication (WAIC) systems are both operated at the frequency band 4,200 MHz–4,400 MHz. Hence, a detailed analysis is required for spectrum sharing in the same band. Firstly, a large-scale finite-difference time-domain analysis is performed to obtain the detailed characteristics of the electromagnetic field (EMF) around the three-dimensional Airbus A320 aircraft model, which assumes that a WAIC device is located inside the cabin. Then, the 4-GHz EMF propagation characteristics are evaluated based on the analyzed results. Finally, the methodology of the interference analysis is discussed based on the obtained EMF characteristics.

Index Terms ─ Aircraft, interference, large-scale finite-difference time-domain method, radio altimeter, wireless avionics intra-communication.

I. INTRODUCTION

Wireless avionics intra-communication (WAIC) systems are employed for wireless communications among sensors in an aircraft for monitoring and telemetry applications [1]. The usage scenario and the standardization of the WAIC systems have been widely studied in recent years. On the other hand, the electromagnetic compatibility (EMC) between the WAIC systems and the existing avionics systems requires to be investigated for further implementation. For WAIC systems, the frequency band 4,200–4,400 MHz is allocated. Radio altimeters are operated in the same frequency band as the WAIC systems. To investigate the EMC issues of the WAIC systems, the electromagnetic field (EMF) estimation method has been developed based on the large-scale finite-difference time-domain (FDTD) analysis [2], [3].

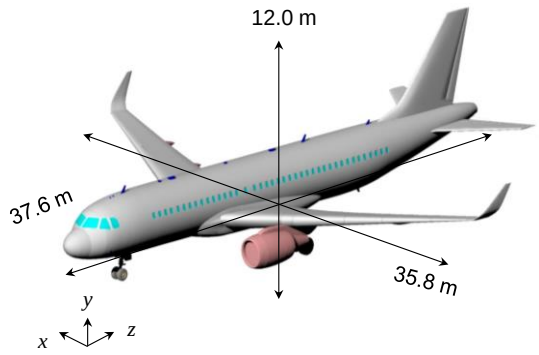

Fig. 1. Three-dimensional aircraft model based on Airbus A320-200.

In this paper, the feasibility of the 4-GHz band radio altimeter interference investigation, which is due to WAIC systems, based on the large-scale FDTD method is discussed. The 4-GHz EMF propagation characteristics around the three-dimensional (3D) model of an Airbus A320 passenger aircraft are obtained by the FDTD analysis. In addition, the desensitization criteria of the radio altimeter are discussed and the EMF distributions are analyzed.

II. LARGE-SCALE FDTD ANALYSIS AT 4 GHZ

The detailed distributions of the EMF that radiates from the WAIC device is estimated by using the FDTD analysis. The FDTD method is employed for the analysis because it is suitable to simulate complicated 3D models

Submitted On: September 30, 2018
Accepted On: October 3, 2018

with various material constants. Figure 1 and Fig. 2 show the overview of the 3D model based on Airbus A320-200 developed for analysis purposes and the cabin configurations, respectively. This model is developed based on a commercially available 3D aircraft model [3]. In addition, an in-house FDTD program is used for the analysis. As shown in the figures, the outlines and the internal structure of the model are designed to have the dimensions of the actual aircraft.

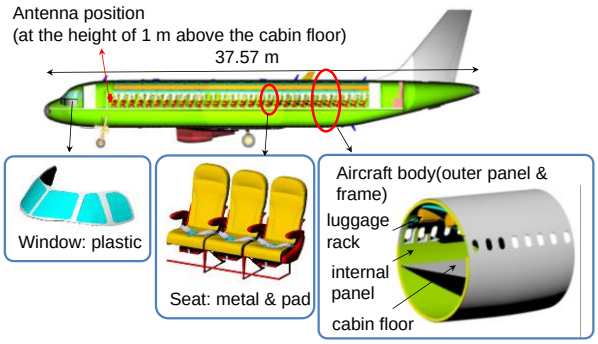

Fig. 2. Cabin configurations of the aircraft model.

Table 1: Parameters of FDTD analysis

Problem Space (mm^3)	18,125 × 12,245 × 37,625
Cell size (mm)	5
Number of cells	3,625 × 2,449 × 7,525
Frequency (GHz)	4.4
A. B. C.	CPML (10 layers)
Number of nodes	40
Required memory	6,400 GB
Antenna	1/2 dipole (0.1 W input power)

The aircraft structures such as the body, cabin partition, lavatory, galley, and ceiling luggage rack consist of a perfect electric conductor. On the other hand, some structures such as the seat ($\varepsilon_r = 2.0$, $\sigma = 3.02 \times 10^{-3}$ S/m), the cabin floor and the inside panel wall ($\varepsilon_r = 3.5$, $\sigma = 1.51$ S/m), and the windows ($\varepsilon_r = 2.25$, $\sigma = 8.34\times10^{-4}$ S/m) have limited electric conductivity [3]. This is because some materials used inside the aircraft cabin are non-flammable and have electro-magnetic lossy characteristics.

No passengers are modeled in the aircraft cabin to obtain the fundamental characteristics of the EMF propagation around the aircraft. The transmitting antenna is located at 1 m above the cabin floor as shown in Fig. 2. As this analysis is a feasibility investigation, parameters such as the antenna type, height, and input power will be varied in the future.

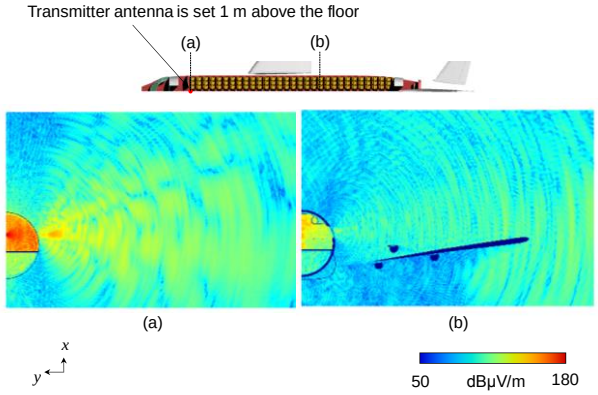

Fig. 3. Typical analyzed two-dimensional E-field strength distributions at the *xy*-plane. (a) E-field strength at the location of the antenna. (b) E-field strength at the middle of the aircraft body.

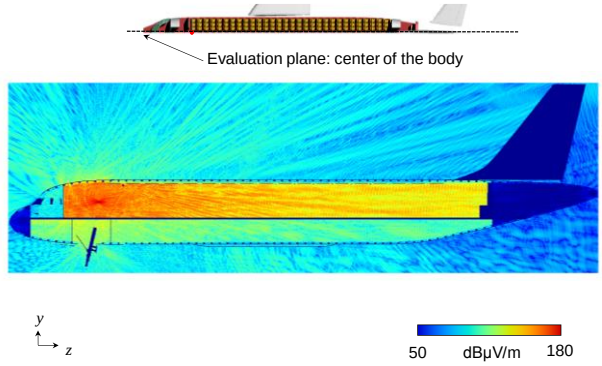

Fig. 4. Typical analyzed two-dimensional E-field strength distributions at the *yz*-plane.

III. ELECTROMAGNETIC FIELD CHARACTERISTICS

Table 1 shows the parameters used in the FDTD analysis. Uniform 5-mm cubic cells are used for the analysis. In addition, to reduce the size of the memory required for the analysis, a perfect magnetic conductor is modeled at the center of the aircraft. The numbers of cells including the 10-layer convolutional perfectly matched layer (CPML) absorbing boundary condition (ABC.) were 3,625 × 2,449 × 7,525. Assuming that the WAIC system operates at the 4-GHz band, the transmitting frequency is set as 4.4 GHz. A HITACHI SR16000 M-1 supercomputer is employed for the analysis. The number of analysis nodes and required memory are 40 nodes and 6,400 GB, respectively. Figure 3 and Fig. 4 show the typical analyzed two-dimensional electric-field (E-field) strength distributions at the *xy*-plane and *yz*-plane, respectively. As shown in the figure,

detailed EMF distributions are obtained both inside and outside the aircraft.

The desensitization criteria of the radio altimeter are defined as follows [4]:

$$N = -114dBm + 10\log\left(B_{R,IF}\right) + N_F . \quad (1)$$

Another example is as follows:

$$I_{T,IF} \geq N - 6dB, \quad (2)$$

where $B_{R,\,IF}$ is the IF bandwidth of the radio altimeter in MHz and N_F is the noise figure at the receiver input in dB, respectively. In addition, $I_{T,IF}$ is the interference power threshold at which the radio altimeter performance starts to degrade. Radio altimeter characteristics such as $B_{R,\,IF}$ and N_F are described in the [4]. The interference power can be directly calculated from the parameters of the radio altimeter antenna.

VI. CONCLUSION

The feasibility of radio altimeter interference investigation using the FDTD method were discussed. The detailed EMF propagation characteristics around the A320 class passenger aircraft at 4 GHz were obtained for analyzing the interference due to the WAIC systems. In addition, the desensitization criteria of the radio altimeter were defined for the future interference assessments based on the large-scale FDTD analysis. The sensitivity degradation of the radio altimeter by the WAIC devices will be analyzed and investigated in the future.

REFERENCES

[1] International Telecommunication Union, "Technical characteristics and operational objectives for wireless avionics intra-communications (WAIC)," Report M.2197-0, Nov. 2011.

[2] T. Hikage, K. Yahagi, M. Shirafune, T. Nojima, S. Futatsumori, A. Kohmura, and N. Yonemoto, "Numerical estimation of WAIC-band propagation characteristics in aircraft cabin using large-scale FDTD analysis," *Proceedings of the 2016 IEEE International Symposium on Antennas and Propagation and USNC-URSI National Radio Science Meeting*, TH-UB.5P.6, June 2016.

[3] K. Yahagi, M. Shirafune, T. Hikage, M. Yamamoto, T. Nojima, S. Narahashi, S. Futatsumori, A. Kohmura, and N. Yonemoto, "Large-scale FDTD analysis of 4.4 GHz-band propagation characteristics in aircraft cabin," *Proceedings of the 2016 International Symposium on Antennas and Propagation*, 3B1-3, pp. 566-567, Oct. 2016.

[4] International Telecommunication Union, "Operational and technical characteristics and protection criteria of radio altimeters utilizing the band 4 200-4 400 MHz," Report M.2059-0, Feb. 2014.

Shunichi Futatsumori received the B.E. and M.E. and Ph.D. degrees in Electronics and Information Engineering from Hokkaido University, Sapporo, Japan, in 2004, 2006 and 2009, respectively. From 2008 to 2009, he was a Research Fellow of the Japan Society for the Promotion of Science. In 2009, he joined the Electronic Navigation Research Institute (ENRI), Japan, where he has been engaged in the research of millimeter-wave radar systems and electromagnetic compatibility issues. He is currently a Chief Researcher of ENRI. Futatsumori received the Young Researcher's Award of IEICE and APMC prize, both in 2009. Futatsumori is a Member of the IEEE and IEICE.

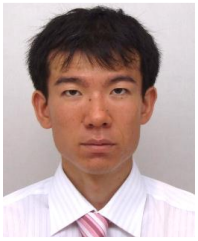

Kazuyuki Morioka received the B.Ec. from Hokkaido University, Japan in 2005 and M.E. and Ph.D. degree in Information Engineering from Shinshu University in 2010 and 2014 respectively. From 2005 to 2011, he was with Artiza Networks, Inc. From 2011 to 2012, he was a Technical Engineer at National Institute of Information and Communication Technology (NICT), Japan. He is currently a Senior Researcher at the Electronic Navigation Research Institute (ENRI), Japan. His research interest is wireless communication systems. Morioka is a Member of the IEEE, IEEJ and IEICE.

Akiko Kohmura received the B.E. and M.E. and Ph.D. degrees in Electronic Engineering from the University of Electro-Communications, Tokyo, Japan. Since 2007, she joined the Electronic Navigation Research Institute (ENRI), Japan. She is currently a Chief Researcher of ENRI. She was a Visiting Researcher of Laboratory of Electronic, Antennas and Telecommunication in France from 2011 to 2012. Her research interest are millimeter-wave radar systems and electromagnetic compatibility. Kohmura is a Member of IEEE, IEICE.

Naruto Yonemoto received the B.S. and M.S. and Ph.D. degrees from Saga University, Japan, in 1995, 1997 and 2000, respectively. He joined the Electronic Navigation Research Institute (ENRI), Japan in 2000. His carrier includes a Visiting Researcher of Laboratory of Electronic Antennas, and Telecommunications, in France from 2005 to 2006. He is also a Visiting Associate Professor of Tokyo University of Marine Science and Technology University, Japan from 2010. He is currently a Principal Researcher of ENRI. His research interest includes millimeter-wave radar systems and electromagnetic compatibility. Yonemoto is a Member of IEEE, IEICE, EuMA.

Takashi Hikage received the B.E., M.E., and Ph.D. degrees from Hokkaido University, Sapporo, Japan, in 1997, 1999, and 2002, respectively, all in Electronics and Information Engineering. From 1999 to 2003, he was with the Graduate School of Engineering, Hokkaido University. He is currently an Assistant Professor of the Graduate School of Information Science and Technology, Hokkaido University. His main research interests include experimental and numerical estimation on electromagnetic field exposure assessment, propagation for wireless communication systems, and biomedical applications, as well as implantable medical device EMI thereof.

Hikage is Member of the Institute of Electronics, Information, and Communication Engineers of Japan (IEICE), the Bioelectromagnetics Society (BEMS), and IEEE.

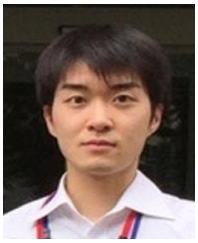

Tetsuya Sekiguchi received the B.S. degree in Engineering from National Institute of Technology, Asahikawa College, Hokkaido, Japan, in 2017. He currently belongs to the Ph.D. course at the Graduate School of Information Science and Technology, Hokkaido University, Japan. His research interest includes the development of an accurate and reliable method for estimating the propagation characteristics inside and outside aircraft cabins to advance the radio link design techniques for WAIC systems.

Manabu Yamamoto received his B.E., M.E., and Ph.D. degrees in Electronics and Information Engineering from Hokkaido University in 1993, 1995, and 1998. From 1998 to 2003, he was with the Graduate School of Engineering, and is now an Associate Professor at the Graduate School of Information Science and Technology. His research interests are analysis and design of millimeter-wave antennas and ultra-wideband antennas.

Toshio Nojima received the B.E. degree in Electrical Engineering from Saitama University, Saitama, Japan, in 1972 and the M.E. and Ph.D. degrees in Electronic Engineering from Hokkaido University, Sapporo, Japan, in 1974 and 1988, respectively. From 1974 to 1992, he was with Nippon Telegraph and Telephone (NTT) Communications Laboratories. From 1992 to 2001, he was with the Research Laboratory, NTT DoCoMo, Yokosuka, Japan. From 2002 to 2015, he was a Professor with the Graduate School of Information Science and Technology, Hokkaido University, where he conducted research on radio safety and EMC issues related to mobile radio systems as well as microwave circuit technologies. Currently, he is a professor emeritus of Hokkaido University.

Nojima is a Fellow of the Institute of Electronics, Information and Communication Engineers of Japan.

Efficient Bayesian Parameter Inversion Facilitated by Multi-Fidelity Modeling

Yaning Liu
Department of Mathematical & Statistical Sciences
University of Colorado Denver
Denver, Colorado, USA
yaning.liu@ucdenver.edu

***Abstract*—We propose an efficient Bayesian parameter inversion technique that utilizes the implicit particle filter to characterize the posterior distribution, and a multi-scale surrogate modeling method called the proper orthogonal decomposition mapping method to provide high-fidelity solutions to the forward model by conducting only low-fidelity simulations. The proposed method is applied to the nonlinear Burgers equation, widely used to model electromagnetic waves, with stochastic viscosity and periodic solutions. We consider solving the equation with a coarsely-discretized finite difference scheme, of which the solutions are used as the low-fidelity solutions, and a Fourier spectral collocation method, which can provide high-fidelity solutions. The results demonstrate that the computational cost of characterizing the posterior distribution of viscosity is greatly reduced by utilizing the low-fidelity simulations, while the loss of accuracy is unnoticeable.**

***Index Terms*—Bayesian parameter inversion, implicit particle filters, proper orthogonal decomposition mapping method, multi-fidelity modeling, surrogate modeling.**

I. Introduction

Bayesian parameter inversion (BPI) techniques are desirable for estimating model parameters, since they consider the uncertainty associated with the inversion in the form of a posterior distribution. However, BPI is computationally expensive because it involves a number of forward model simulations to sample the posterior distribution. If it is expensive to obtain the solutions to the forward model, such as the fine-resolution solutions to a physical model, the BPI can become intractable.

As a widely used BPI technique, the Markov Chain Monte Carlo (MCMC) method is robust for estimating posterior information; however, the efficiency of MCMC can be low due to its acceptance-rejection nature. The particle filtering (PF) method, as an alternative to MCMC, has many advantages, such as being "embarrassingly parallel" and applicable to high dimensional systems. Recently, a particular PF method, the implicit particle filter (IPF), was developed in [1] and [2], which can alleviate or prevent the so-called "weight collapse" phenomenon. It has been shown, by [3] for instance, that IPF can outperform state-of-the-art MCMC for some applications.

Surrogate models, also known as reduced order models, serving as efficient approximations for computationally expensive models, have been used in BPI, including IPF [3], to improve efficiency. Surrogate models are constructed in the training period, and can then be used to approximate the original models with negligible computational cost. Most surrogate modeling techniques address the approximation of the mapping from the model input parameters to a scalar model output (e.g., [4], [5]), while an efficient method that can approximate a solution field (see [6] for example) is more attractive, since the solutions of many problems in electromagnetics take the form of a field of solutions, such as the solutions to the three dimensional Maxwell equations. One particular technique, called the proper orthogonal decomposition mapping method (PODMM) [7], can approximate a fine-resolution solution from a coarse-resolution solution, which is significantly more inexpensive to obtain. The PODMM technique has been applied to climate models and shown good accuracy when used to construct surrogates.

In this paper, we consider BPI with IPF for the one-dimensional Burgers equation with stochastic viscosity. To further improve the efficiency, we couple PODMM with IPF by building a multi-scale surrogate mapping to accurately approximate the solutions to the Burgers equation required by the IPF. In the following sections, we first show the technical details of IPF and PODMM, and then present the numerical results for the stochastic Burgers equation.

II. Methodology

A. Implicit Particle Filters

Let $\boldsymbol{D}$ be the k-dimensional observations, $\boldsymbol{f}$ be the forward model and $\boldsymbol{\theta}$ be the d-dimensional unknown input parameters. They are related by:

$$\boldsymbol{D} = \boldsymbol{f}(\boldsymbol{\theta}) + \boldsymbol{\epsilon}, \tag{1}$$

where $\boldsymbol{\epsilon}$ is some random noise. In Bayesian parameter inversion, we aim to obtain the conditional probability distribution of the parameters given the observations, $p(\boldsymbol{\theta}|\boldsymbol{D})$, known as the posterior density. Combining the knowledge of the parameters prior to data being available, $p(\boldsymbol{\theta})$, the prior distribution, and the measure of how likely a set of model output values are given the parameters $p(\boldsymbol{D}|\boldsymbol{\theta})$, the likelihood function, the Bayes' theorem infers the posterior by:

$$p(\boldsymbol{\theta}|\boldsymbol{D}) \propto p(\boldsymbol{\theta})p(\boldsymbol{D}|\boldsymbol{\theta}). \tag{2}$$

In general, $p(\boldsymbol{\theta}|\boldsymbol{D})$ takes a complex form and therefore cannot be sampled directly, for instance by the inverse-transform method or the acceptance-rejection sampling method [8].

Submitted On: September 30, 2018
Accepted On: October 3, 2018

One widely used method that facilitates such sampling is importance sampling, in the framework of which, we instead sample from a new, easy-to-sample probability distribution $\pi(\boldsymbol{\theta})$, called importance distribution. The resulting N samples $\boldsymbol{\theta}_i$, $i = 1, \ldots, N$, are then weighted by:

$$w_i = \frac{p(\boldsymbol{\theta_i})p(\boldsymbol{D}|\boldsymbol{\theta_i})}{\pi(\boldsymbol{\theta}_i)}, \quad i = 1, 2, \ldots, N \tag{3}$$

to correct the bias from taking samples from the importance distribution rather than the original distribution, so that the samples and the weights collectively characterize the posterior distribution. To achieve this, a resampling procedure [9] is used to eliminate samples with small weights and obtain a set of samples that discretely represents the posterior distribution of $\boldsymbol{\theta}$. Unlike MCMC, represented by the well-known Metropolis-Hastings algorithm and Gibbs sampling, the samples in importance sampling are independent and thus can be embarrassingly parallel. Nonetheless, the importance function must be chosen carefully, or else the sampling can be inefficient due to the appearance of a large portion of samples having weights that are small enough to be negligible.

IPFs are based on importance sampling, where an importance distribution is constructed by computing the maximizer of the posterior $p(\boldsymbol{\theta}|\boldsymbol{D})$, i.e., the maximum a posteriori (MAP) of the parameters $\boldsymbol{\theta}$ given the data D, which can be found by minimizing the objective function:

$$F(\boldsymbol{\theta}) = -\log\left(p(\boldsymbol{\theta})p(\boldsymbol{D}|\boldsymbol{\theta})\right),$$

where $p(\boldsymbol{\theta})$ and $p(\boldsymbol{D}|\boldsymbol{\theta})$ are the prior distribution and the likelihood function, respectively. The idea is to construct a importance distribution so that it has large values where the posterior is large. Once the minimization problem is solved, one generates samples in the neighborhood of the minimizer $\boldsymbol{\mu} = \arg\min F$ as follows. A sequence of reference variables $\{\boldsymbol{\xi}_i\}_{i=1}^N$ are first sampled from a reference probability distribution $g(\boldsymbol{\xi})$, and subsequently each target posterior sample $\boldsymbol{\theta_i}$ is obtained by solving,

$$F(\boldsymbol{\theta}_i) - \phi = G(\boldsymbol{\xi}_i) - \gamma, \tag{4}$$

where $\phi = \min_{\boldsymbol{\theta}} F$, $G(\boldsymbol{\xi}) = -\log\left(g(\boldsymbol{\xi})\right)$ and $\gamma = \min_{\boldsymbol{\xi}} G$. The sample weights are:

$$w_i = J(\boldsymbol{\theta}_i), \tag{5}$$

where J is the Jacobian of the bijective map $\boldsymbol{\xi} \to \boldsymbol{\theta}$ [2]. Note that the sequence of samples $\boldsymbol{\theta}_i$ obtained by solving Eq. (4) are in the neighborhood of the MAP $\boldsymbol{\mu}$, since the right-hand side is small if $\boldsymbol{\xi}_i$'s are sampled close to the minimizer of G. Thus, Eq. (4) maps a likely $\boldsymbol{\xi}$ to a likely $\boldsymbol{\theta}$.

However, solving the mapping Eq. (4) is nontrivial, noting that it is in general nonlinear. One strategy, named "linear maps", is inspired by the approximation of F by its second-order Taylor expansion around the MAP $\boldsymbol{\mu}$:

$$F_0(\boldsymbol{\theta}) = \phi + \frac{1}{2}(\boldsymbol{\theta} - \boldsymbol{\mu})^T H(\boldsymbol{\theta} - \boldsymbol{\mu}), \tag{6}$$

where H is the Hessian matrix at $\boldsymbol{\mu}$. For an uncorrelated standard Gaussian reference variable, Eq. (4) is transformed to:

$$F(\boldsymbol{\theta}_i) - \phi = \frac{1}{2}\boldsymbol{\xi}_i^T\boldsymbol{\xi}_i. \tag{7}$$

Substituting $F(\boldsymbol{\theta}_i)$ in Eq. (7) with $F_0(\boldsymbol{\theta}_i)$, the mapping now takes the simple form:

$$\boldsymbol{\theta}_i = \boldsymbol{\mu} + L^{-T}\boldsymbol{\xi}_i, \tag{8}$$

where L is a lower triangular matrix obtained from the Cholesky decomposition of H. Accounting for the error of approximating the objective function F by F_0, the weights of the samples are computed as:

$$w_i \propto \exp\left(F_0(\boldsymbol{\theta_i}) - F(\boldsymbol{\theta_i})\right). \tag{9}$$

The posteriors are then represented by the ensemble of weighted samples $\{(\boldsymbol{\theta}_i, w_i)\}_{i=1}^N$.

B. Proper Orthogonal Decomposition Mapping Method

PODMM maps $\boldsymbol{g} = [g_1, \ldots, g_{\mathcal{N}_g}]^T$, the coarse-resolution solutions, to fine-resolution solutions $\boldsymbol{f} = [f_1, \ldots, f_{\mathcal{N}_f}]^T$, where $\mathcal{N}_g$ and $\mathcal{N}_f$ are the respective degrees of freedom. Suppose N coarse- and fine-resolution solutions, $\{\boldsymbol{g}_1, \ldots, \boldsymbol{g}_N\}$ and $\{\boldsymbol{f}_1, \ldots, \boldsymbol{f}_N\}$ are available for the training process. We first form the data matrix $\boldsymbol{W}^{\text{PODMM}}$ given by:

$$\boldsymbol{W}^{\text{PODMM}} = \begin{bmatrix} \boldsymbol{f}_1 - \bar{\boldsymbol{f}} & \cdots & \boldsymbol{f}_N - \bar{\boldsymbol{f}} \\ \boldsymbol{g}_1 - \bar{\boldsymbol{g}} & \cdots & \boldsymbol{g}_N - \bar{\boldsymbol{g}} \end{bmatrix},$$

where $\bar{\boldsymbol{f}}$ and $\bar{\boldsymbol{g}}$ are the averages of $\{\boldsymbol{f}_i\}_{i=1}^N$ and $\{\boldsymbol{g}_i\}_{i=1}^N$ respectively. We then determine M right singular vectors, $\boldsymbol{V} = \{\boldsymbol{v}_1, \ldots, \boldsymbol{v}_M\}$ corresponding to the M largest singular values for $\boldsymbol{W}^{\text{PODMM}}$. The proper orthogonal decomposition (POD) bases are $\boldsymbol{\xi}_i = \boldsymbol{W}^{\text{PODMM}}\boldsymbol{v}_i, i = 1, \ldots, M$. Split $\boldsymbol{\xi}_i$ into,

$$\boldsymbol{\xi}_i = \begin{bmatrix} \boldsymbol{\xi}_i^f \\ \boldsymbol{\xi}_i^g \end{bmatrix}.$$

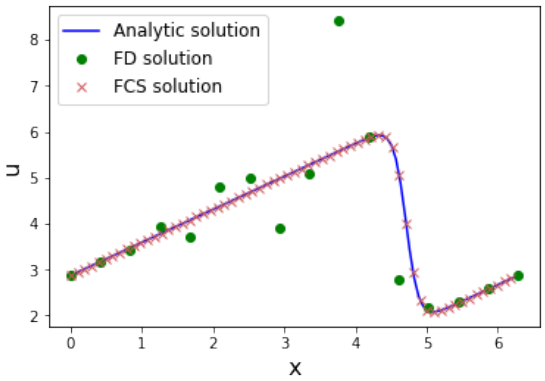

Fig. 1. Analytic, FD and FSC solutions for Burgers equation with $\nu = 0.2$.

For any given coarse-resolution $\boldsymbol{g} \notin \{\boldsymbol{g}_1, \ldots, \boldsymbol{g}_N\}$, we can predict the corresponding fine-resolution $\boldsymbol{f}$ by,

$$\boldsymbol{f} = \bar{\boldsymbol{f}} + \sum_{i=1}^{M} \gamma_i \boldsymbol{\xi}_i^f.$$

Here $\boldsymbol{\gamma} = \{\gamma_1, \ldots, \gamma_m\}$ is the solution to the least-squares problem,

$$\arg\min_{\boldsymbol{\gamma}} \left\| \boldsymbol{g} - \bar{\boldsymbol{g}} - \sum_{i=1}^{M} \gamma_i \boldsymbol{\xi}_i^g \right\|_2,$$

where

$$\|\boldsymbol{h}\|_2 = \left(\frac{1}{\mathcal{N}_h} \sum_{i=1}^{\mathcal{N}_h} h_i^2 \right)^{1/2},$$

is the root mean square for a given vector $\boldsymbol{h}$ with degree of freedom $\mathcal{N}_h$.

III. Results and Discussion

To illustrate the proposed method, we consider the one-dimensional Burgers equation,

$$\frac{\partial u}{\partial t} + \frac{1}{2}\frac{\partial u^2}{\partial x} - \nu \frac{\partial^2 u}{\partial x^2} = 0,$$

where the viscosity ν is a random variable. We consider a periodic solution with an infinite number of N-wave solutions. The analytical periodic solution we use is:

$$u = -2\nu \frac{\phi_x}{\phi}$$

$$\phi(x,t) = \frac{1}{4\pi\nu t} \sum_{n=-\infty}^{\infty} \exp -(x - 2\pi n)^2 / 4\nu t.$$

The coarse-resolution solutions are obtained from a second-order finite difference (FD) spatial discretization on a grid of 16 points, while the fine-resolution solutions are computed by a Fourier spectral collocation (FSC) method [10] with 64 spatial collocation points. The Runge-Kutta method is used for the temporal discretization in both cases.

Fig. 1 shows the analytical, FD, and FSC solutions at $t = \frac{\pi}{8}$ to the Burgers equation corresponding to $\nu = 0.2$. It can be seen that the FD solution oscillates around the shock, while the FSC solution can resolve the transition zone successfully.

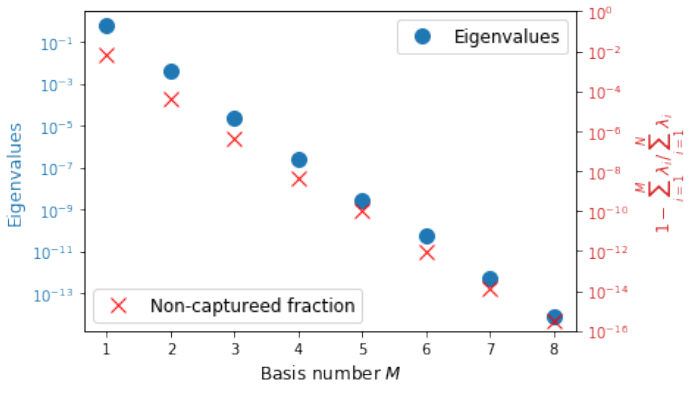

Fig. 2. Eigenvalues (left y axis) and the noncaptured fraction of the variability (right y axis) of the training data.

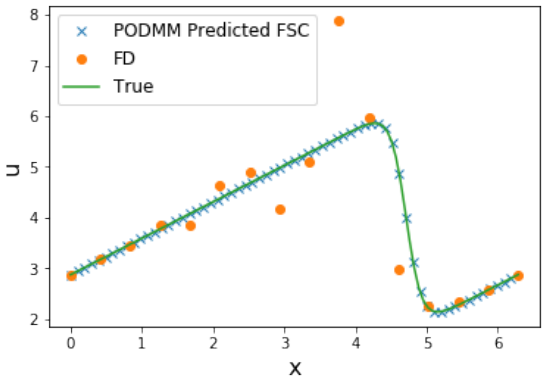

Fig. 3. Analytic, FD and PODMM predicted FSC solutions for Burgers equation with $\nu = 0.304$.

To test the performance of PODMM surrogate model in IPF, we consider a synthetic test case, where the FSC solution corresponding to $\nu = 0.2$ is perturbed by a Gaussian noise with mean 0 and 10% of the solution as the standard deviation. The prior distribution for the viscosity is also taken as Gaussian: $\mathcal{N}(0.4, 0.2^2)$. The coarse-resolution solutions $\boldsymbol{g}$'s are the FD solutions and the fine-resolution solutions $\boldsymbol{f}$'s are the FSC solutions. A set of 64 training data $\boldsymbol{g}_i, \boldsymbol{f}_i, i = 1, \ldots, 64$ is generated to construct the PODMM surrogate.

Fig. 2 exhibits the fast decay of the eigenvalues of the training data matrix $\boldsymbol{W}^{\text{PODMM}}$. For the eighth largest eigenvalue, the magnitude already drops below 10^{-13}. Also plotted is the noncaptured fraction of the variance, which is the variance not explained by using only a smaller number of eigenvalues. The noncaptured fraction also decreases very quickly. Note the noncaptured fraction can be used to determine the number of eigenvalues to be used in PODMM by prescribing a threshold value. The number will be the smallest number such that the noncaptured fraction of the total variance is smaller than the threshold. Here we will use only 8 eigenvalues, as they can capture a large enough portion of the total variance.

Fig. 3 displays the analytical, FD and PODMM predicted FSC solutions at $t = \frac{\pi}{8}$ to the Burgers equation corresponding to $\nu = 0.304$. Note that only the FD solution is computed, which is computationally inexpensive, to obtain the PODMM solution. It is demonstrated that although the FD solution does not resolve the transition zone of the shock, the PODMM-predicted FSC fine-resolution solution is in good agreement with the analytical solution. Therefore PODMM can serve as a reliable surrogate in the process of the following IPF for the characterization of the posterior distribution.

We now show the performance of PODMM in IPF. The linear map is used so that one PODMM predicted solution is needed to obtain one posterior sample. To measure the quality of the samples, we estimate the effective sample size by:

$$N_{\text{eff}} = \frac{1}{\sum_{i=1}^{N} (w_i)^2}.$$

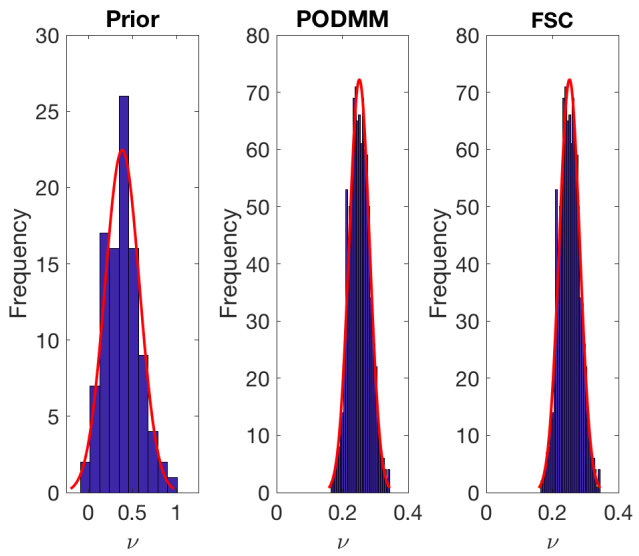

Fig. 4. Prior density and posterior densities estimated by IPF using PODMM and FSC.

The larger the estimated effective sample size is, the less severely the sample quality degenerates. In the ideal case where the weights are uniformly $1/N$, $N_{\text{eff}} = N$, which means all the samples are effective, while in the worst scenario where only one sample is weighted nonzero, $N_{\text{eff}} = 1$. In our case, the ratio of the effect sample size to the total sample size is 0.993, meaning 99.3% of the samples are effective and the IPF is very effective in alleviating sample degeneration.

The posterior distributions of ν generated by the FSC and PODMM-predicted FSC solutions in IPF are shown in Fig. 4. It can be seen that the posterior densities estimated from the samples for the two solutions are nearly indistinguishable (middle and right), indicating PODMM is capable of accurately characterizing the posterior density in IPF. Also shown is the prior normal distribution (left), which is significantly different from the posteriors. Note that the range of the posterior is also smaller compared to that of the prior distribution. To confirm it, the statistical moments of these distributions are given in Table I.

As a result, we have achieved high accuracy in estimating the posterior using the PODMM surrogate model, while saving significant computational time. The computational cost of the fine-resolution FSC solution in our example is about 10 times that of the FD solution, while the cost of PODMM prediction is negligible.

TABLE I
STATISTICAL MOMENTS OF THE PRIOR AND POSTERIOR DENSITIES

	Mean	Variance	Skewness	Kurtosis
Prior	0.4	0.04	0.0	0.0
PODMM posterior	0.2517	9.5645E-4	0.1168	2.8127
FSC posterior	0.2517	9.5645E-4	0.1168	2.8127

IV. CONCLUSIONS

In this work, we implemented an efficient Bayesian parameter inversion technique, the implicit particle filtering, to determine the stochastic viscosity of the Burgers equation. The proportion of the effective sample size from implicit particle filtering can be significantly higher than that from a traditional particle filtering method. We also demonstrated a multi-fidelity modeling technique, the proper orthogonal decomposition mapping method, can construct fine-resolution model solutions from computationally inexpensive coarse-resolution solutions. The resulting surrogate model serves as an efficient and accurate model that can lead to posterior distribution distinguishable from that obtained using the high-fidelity model.

REFERENCES

[1] A. J. Chorin and X. Tu, "Implicit sampling for particle filters," Proc. Natl. Acad. Sci. 106 (41), pp. 17249–17254, 2009.
[2] M. Morzfeld, X. Tu, E. Atkins, and A. Chorin, "A random map implementation of implicit filters," J. Comput. Phys. 231 (4), pp. 2049–2066, 2012.
[3] Y. Liu, G. S. H. Pau, and S. Finsterle, "Implicit sampling combined with reduced order modeling for the inversion of vadose zone hydrological data," Comput. Geosci., vol. 108, pp. 21–32, 2017.
[4] Y. Liu, M.Y. Hussaini, and G. Ökten, "Accurate construction of high dimensional model representation with applications to uncertainty quantification," Reliab. Eng. Syst. Safe., vol. 152, pp. 281–295, 2016.
[5] Y. Zhang, Y. Liu, G. S. H. Pau, S. Oladyshkin, and S. Finsterle, "Evaluation of multiple reduced-order models to enhance confidence in global sensitivity analyses," Int. J. Greenh. Gas Con., vol. 49 (2), pp. 217–226, 2016.
[6] Y. Liu, G. Bisht, Z. M. Subin, W. J. Riley, and G. S. H. Pau, "A hybrid reduced-order model of fine-resolution hydrologic simulations at a polygonal tundra site," Vadose Zone J., vol. 15 (2), 2016.
[7] G. S. H. Pau, C. Shen, W. J. Riley, and Y. Liu, "Accurate and efficient prediction of fine-resolution hydrologic and carbon dynamic simulations from coarse-resolution models," Water Resour. Res., vol. 52, pp. 791–812, 2016.
[8] R. Y. Rubinstein and D. P. Kroese, Simulation and the Monte Carlo Method, 3rd ed.. Wiley, 2016.
[9] M. Arulampalam, S. Maskell, N. Gordon, and T. Clapp "A tutorial on particle filters for online nonlinear/non-Gaussian Bayesian tracking," Trans. Signal. Proc., vol. 50 (2), pp. 174–188, 2002.
[10] C. Canuto, M. Y. Hussaini, A. Quarteroni, and T. A. Zang, Spectral Methods, Springer, 2006.

Robust Feed Modeling of the Asymmetric Planar Mesh Dipole-Type Antenna

Jennifer Rayno and Derek S. Linden
AWR Group, NI
El Segundo, CA 90245
jennifer.rayno@ni.com, derek.linden@ni.com

***Abstract*— This paper explores the feed method for the asymmetric planar XY-mesh dipole-type antenna and the modifications needed to prevent its exploitation by automated genetic algorithm (GA) optimization for the application of RFID tag antennas, where the antenna is optimized to the conjugate of the chip impedance. By removing certain feed parameters from the GA optimization and instead making them wavelength dependent, the goal of creating robust models which achieve accurate and matching results between various electromagnetic (EM) simulators, with a focus on the WIPL-D and Axiem EM simulators, was achieved.**

Keywords—antenna synthesis, antenna modeling, genetic algorithm.

I. Introduction

In automated antenna synthesis using genetic algorithms (GA), the antenna model needs to be created such that it is robust to the multitude of various designs that can be created and not easily exploitable with unrealistic designs. The antenna feed can be a particularly sensitive component of the model. Most antennas are initially designed using an ideal feed, since this is the fastest and simplest way. These ideal feeds should not be a key component in achieving the desired antenna performance, as they are expected to be replaced with a real feed. The purpose of the ideal feed is to provide excitation of the antenna structure and the expected port impedance. In addition, since the feed methods vary with electromagnetic (EM) simulator, setting up the feed model is very important in achieving matching results between the different EM simulators. The primary focus in this paper is achieving matching results between WIPL-D and NI AWR Axiem. Both are full-wave 3D electromagnetics solvers using the Method of Moments, however WIPL-D [1] allows arbitrary 3D modeling with finite dielectric regions, whereas Axiem [2] uses stacked planar structures and vias with infinite dielectric substrate sheets. Although the feeding methods for WIPL-D and Axiem are both gap voltage sources, in WIPL-D the feed is assigned to a wire, which must be completely inside or outside of a dielectric region, whereas in Axiem the feed is assigned to the edge of a planar conductor on the surface of a dielectric substrate sheet or in air.

This paper explores the feed method for the asymmetric planar xy-mesh dipole-type antenna and modifications needed to prevent its exploitation when used for the automated design of RFID tag antennas with an atypical desired input impedance (e.g., Z_{in} = 16 + j148Ω rather than the more typical 50Ω).

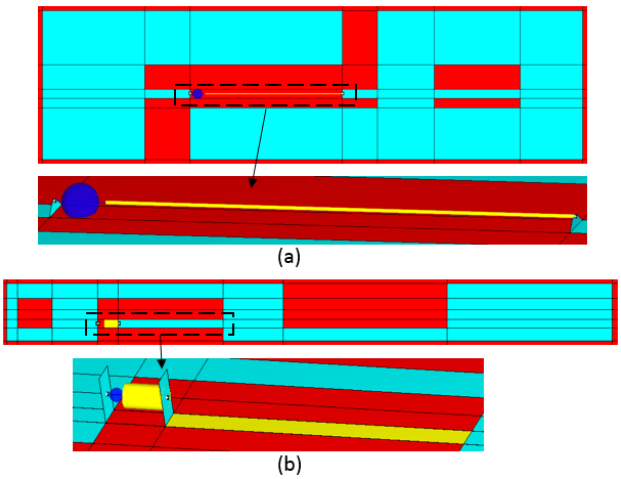

Fig. 1. Examples of WIPL-D feed models: (a) original wire and (b) final wire plus planar conducting strip.

Although the initial WIPL-D model exploited the feed wire length and diameter to meet the specifications [3], the final more robust model was also easily able to meet the specifications without needing to resort to such exploitation [4].

II. Challenges in Feed Modeling

The asymmetric planar XY-mesh dipole-type antenna in NI AWR AntSyn, a software for automated antenna synthesis, was created for use on fixed-size dielectric substrates which can simulate an environment (enviro-mesh antenna), and the capability to optimize the antenna on multiple substrates simultaneously makes it good for RFID tag applications. For RFID tag antennas, the antenna is optimized to the conjugate of the chip impedance, and a typical chip impedance value is 16 - j148Ω. This means the antenna impedance would need to have a really high inductance of j148Ω. In the initial enviro-mesh antenna WIPL-D model, the GA optimizer was easily able to exploit the feed wire to get the high inductance needed by making the feed wire really long and skinny (see Fig. 1 (a)). This did come up with a working antenna [3], however it made getting matching results in the exported Axiem model problematic, as Axiem does not use a wire feed. Fabrication would have also been more difficult. Note that other EM simulators which are able to simulate the long, skinny wire did come up with reasonably well matching results.

Submitted On: September 27, 2018
Accepted On: October 3, 2018

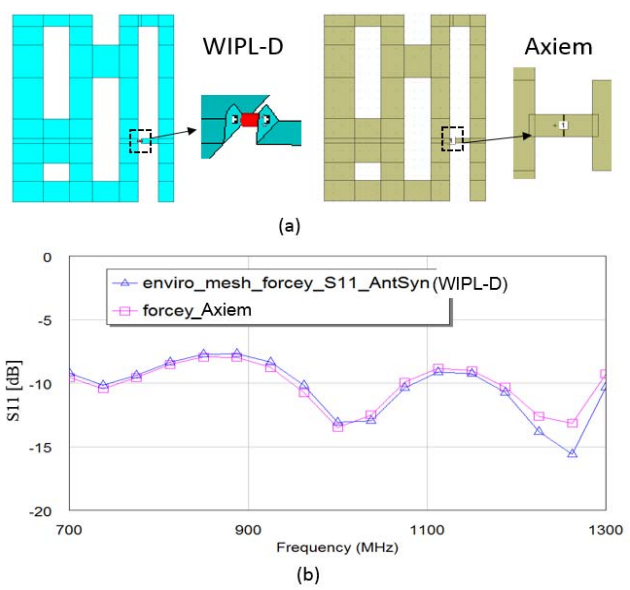

Fig. 2. Comparison of WIPL-D and Axiem for example 1 (no substrate): (a) antenna models and (b) return loss.

Several variations of feed methods in both WIPL-D and Axiem were investigated to see which would give accurate and reasonably well matching results, where an additional EM simulator was used as a tie breaker if necessary. The feed method which ended up working best utilizes a fixed, wavelength-dependent length/diameter for the feed wire in WIPL-D and an internal port with corresponding dimensions in Axiem, and the rest of the original feed was replaced by a planar conductor on the surface of the substrate, where the width is independent of the feed wire (see Fig. 1(b)). In WIPL-D, for the most accurate results with a cylindrical wire feed, the length to radius ratio should be greater than 30 [1]. Since the feed wire needs to be kept very short, this would require a much thinner wire than can be accurately represented in Axiem, as it is very hard to replicate the behavior of very thin feed wires in Axiem. The internal port in Axiem is assigned to the edge between two touching or electrically close planar conductors, and the smallest edge the mesh must represent is specified [2]. Once the internal port conductors are smaller than a certain amount, the port characteristics do not change as significantly as they would for the actual wire, and the very small edge needed to represent the very thin port conductor can significantly increase meshing time or cause errors depending on the antenna model. A tradeoff is made that achieves reasonably well matching results among the various simulators for a variety of cases. With this new WIPL-D model, the GA optimizer is not able to exploit the feed method to achieve the desired specifications but must instead work harder on the antenna design to meet tighter specifications. This new method was also able to come up with a working antenna [4].

III. Results

For comparison of the WIPL-D and Axiem results using the new feed modeling method, two enviro-mesh design examples are shown—the first without substrate and the second with various substrates. Since the purpose was to achieve matching results between the two simulators, the two antennas were not fully optimized and a 50Ω port impedance was used. Fig. 2 shows the design 1 models and return loss, whereas Fig. 3 shows the same for design 2. Both models show reasonably well matching return loss over the entire band. The design 2 results were compared on various substrate dielectrics (ε_r = 2, 4, and 8), and Fig. 3 shows the ε_r = 2 results. Reasonably well matching return loss was also achieved for the other two dielectrics with design 2. Also, the gain vs. frequency results were compared, and both design 1 and design 2 showed excellent matching between the two simulators.

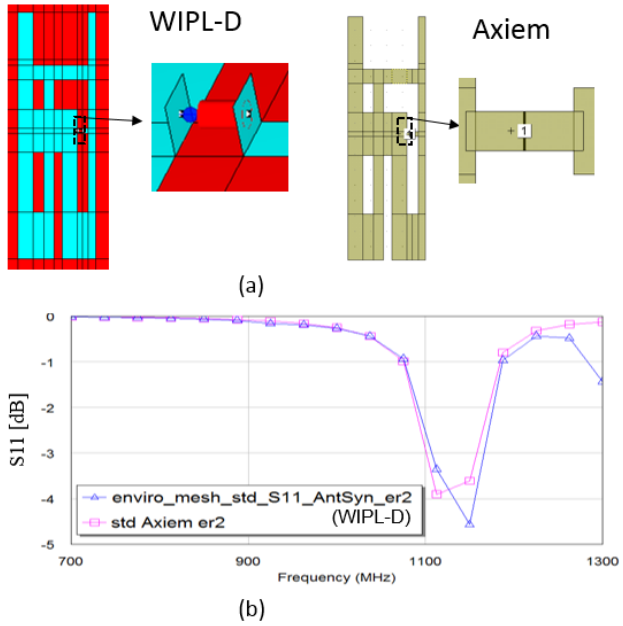

Fig. 3. Comparison of WIPL-D and Axiem for example 2 (has substrate): (a) antenna models and (b) return loss.

IV. Conclusions

The original enviro-mesh antenna model worked well and was robust for more typical 50Ω antenna impedance, however it was discovered to be easily exploitable when used with the complex impedances necessary for RFID tag antenna designs. By removing certain feed parameters from the GA optimization and instead making them wavelength dependent in addition to converting the rest of the original feed wire into a planar conducting strip, the goal of creating robust models which achieve accurate and matching results between various EM simulators, with a focus on the WIPL-D and Axiem EM simulators was achieved.

References

[1] WIPL-D Pro v11.0, Software and User's Manual, WIPL-D d.o.o., Belgrade, 2014.

[2] "Simulation and Analysis Guide," NI AWR Design Environment v13.02 Edition, 2017.

[3] D. S. Linden and J. Rayno, "Synthesis of robust UHF RFID antennas on dielectric substrates," Antenna Systems and Technology, Fall 2016, pp. 6-10.

[4] D. S. Linden and J. Rayno, "Create robust UHF RFID tag antennas on dielectric substrates," Microwaves and RF, March 2017.

Improving Millimeter-Wave Channel Models for Suburban Environments with Site-Specific Geometric Features

Yaguang Zhang [1], Soumya Jyoti [2], Christopher R. Anderson [3], Nicolo Michelusi [1], David J. Love [1], Alex Sprintson [2], and James V. Krogmeier [1]

[1] School of Electrical and Computer Engineering
Purdue University, West Lafayette, IN 47907, USA
{ygzhang, michelus, djlove, jvk}@purdue.edu

[2] Department of Electrical and Computer Engineering
Texas A&M University, College Station, TX 77843, USA
{soumyajyoti.jh, spalex}@tamu.edu

[3] Department of Electrical and Computer Engineering
United States Naval Academy, Annapolis, MD 21402, USA
canderso@usna.edu

Abstract ─ This paper proposes simple procedures to improve traditional statistical millimeter-wave channel models for suburban environments with site-specific geometric features. Blockages by buildings and vegetation were considered and existing models were verified with measurement data for an emulated microcell deployment. The results indicate that a holistic, network-level approach for channel modeling will help deal with the high dependence of millimeter waves on site-specific features.

Index Terms ─ Channel modeling, millimeter wave, site-specific geometric features, suburban environments.

I. INTRODUCTION

Millimeter wave (mm-wave) bands have become the most promising candidate for enlarging the usable radio spectrum in future wireless networks such as 5G [1]. Since frequent and location-specific blockages are expected at mm-waves, the challenge is understanding the propagation characteristics of mm-wave signals and accordingly predicting the channel state information as needed, so that the high mobility requirements of these wireless networks can be addressed in real-time.

The majority of current research has focused on urban areas with high population densities [1]–[3]. Very few measurement campaigns have been performed in suburban and rural environments. Moreover, statistical models for point-to-point links have received significant attention, but this approach ignores all or most of site-specific geometric features, which mm-waves are sensitive to due to blockages. In this paper, we explore this research gap by focusing on suburban environments and improving standard 5G channel models with site-specific geometric features.

II. MM-WAVE PROPAGATION MEASUREMENTS FOR SUBURBAN ENVIRONMENTS

An outdoor propagation measurement campaign was carried out at the United States Naval Academy (USNA) in Annapolis, Maryland. The transmitter (TX) was temporarily installed on the Mahan Hall clock tower to emulate a typical 5G suburban microcell deployment. A custom-designed broadband sliding correlator channel sounder was used as the receiver (RX) and moved around the campus to obtain path loss measurements. More details for the measurement setup can be found in [4].

III. BUILDING BLOCKAGE ANALYSIS

One approximately 200-m-long straight track was chosen for a continuous signal recording, to investigate the shadowing effect of buildings on a moving user. The resulting basic transmission losses are shown in Fig. 1 (a). The dotted lines illustrate the boundaries between the line-of-sight (LoS) area and the non-line-of-sight (NLoS) area due to blockages. As we can see, the most significant blockage was from Michelson Hall, which obstructed the southern half of the track. Rickover Hall partially blocked the track at the north end.

To estimate the path loss caused by building blockages, the knife-edge diffraction (KDE) model [3] was utilized. In our case, the Universal Transverse Mercator (UTM) coordinate system was extended with height to form a 3-dimensional (3D) space for computing

Submitted On: September 20, 2018
Accepted On: September 29, 2018

the effective height of the obstructing screen, as well as the distances between the TX, the RX, and the screen. Note that the path obstruction may occur either on a horizontal roof edge or a vertical side edge of the building. Finally, the screen height was computed as the distance between the obstruction point and the direct Euclidean path between the TX and the RX. The resulting diffraction losses were used to shift the large-scale path loss predictions from the International Telecommunication Union (ITU) site-general model for propagations over rooftops [5]:

$$PL(d,f) = 10 \cdot \alpha \cdot \log_{10}(d) + \beta + 10 \cdot \gamma \cdot \log_{10}(f) + N(0,\sigma),$$

where d is the 3D direct distance between the TX and the RX in meters and f is the operating frequency in GHz. In our case, f = 28 GHz. The parameter values α = 2.29, β = 28.6, γ = 1.96, and σ = 3.48, were chosen for the LoS propagation in a suburban environment [5], which are recommended by ITU for distances from 55 m to 1200 m at 2.2–73 GHz frequency.

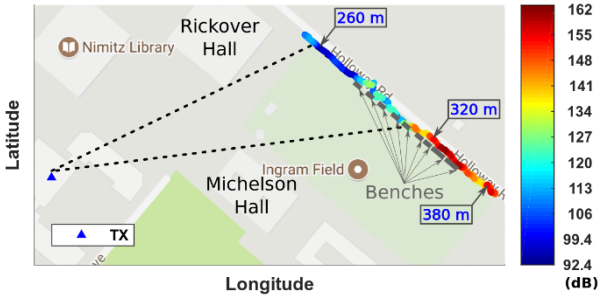

(a) Track with Basic Transmission Losses on Holloway Road

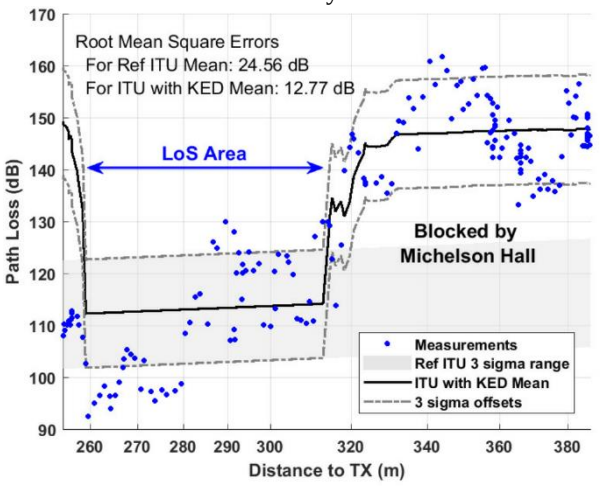

(b) Path Loss for the Modified ITU Model

Fig. 1. Considering building blockages to improve a statistical channel model. (a) Path losses on Holloway road illustrate the shadowing effect of buildings. The numbers in the boxes are distances to the TX. (b) After being shifted by diffraction losses, the ITU model closely follows the measurement results.

Figure 1 (b) shows the final results. The ITU model provides path loss predictions in the form of Gaussian variables. Accordingly, 3-sigma ranges for both the original and shifted ITU models are shown and root mean square errors (RMSEs) are computed separately according to the mean of each model. As we can see, the modified ITU predictions follow the measurement data much better than the original ones, providing a RMSE improvement of 11.79 dB. Another observation is, for distances below 280 m, the original ITU model overestimated the path loss by around 20 dB. This may be caused by some strong reflection path(s). Also, the KED model overestimated the attenuation caused by Rickover Hall. This was probably because the blockage happened at the southern vertical edge of the building, which corresponds to a very short obstructing screen, whereas the KED model applies for a screen with infinite height. Still, the KED model helped identify the path loss peak below 260 m.

IV. FOLIAGE ANALYSIS

The effect of foliage for modeling mm-wave channel is a vital consideration for suburban environments as scattering and absorption at these frequencies can significantly attenuate 0 2 4 6 8 10 12 14 16 18 Vegetation Depth (m) -20 -10 0 10 20 30 40 50 Attenuation (dB) Specific Attenuation: Slope of Fitted line = 0.0662 dB/m Measurements Fitted Weissberger ITU-R FITU-R COST235 Fig. 2. Comparison of computed and measured path loss at 28 GHz. the signal. In our measurement campaign, eleven sites had partial or total obstruction of the LoS signal from foliage, ranging from a single tree to a small grove of trees. Our measurement results were compared against four well known empirical models [6] that are valid in this frequency range: COST235, Weissberger, ITU-R and FITU-R models.

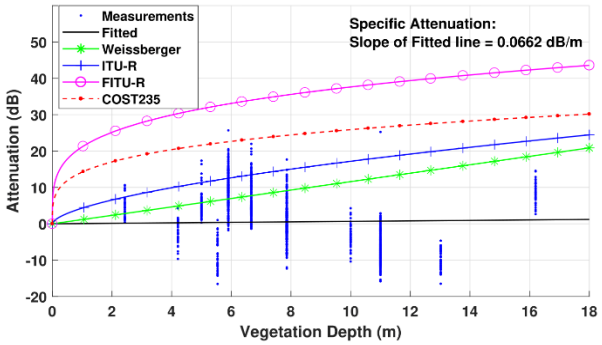

Fig. 2. Comparison of computed and measured path loss at 28 GHz.

Figure 2 illustrates our measured excess vegetation attenuation versus vegetation depth as well as existing model predictions. We can see that the mean measured value of foliage attenuation (0.07 dB/m) is significantly less than those of model-predicted values. In fact, our

measurements demonstrate a significant amount of multipath energy arriving at the receiver, likely being scattered from other objects in the environment. As a result, we recorded a greater signal strength than what would be predicted by these simple single-path attenuation models.

V. CONCLUSION

In this paper, we illustrate two measurement- and geometry-based techniques for improving existing statistical mm-wave channel models. Our approach is suitable for a holistic, network-level model that utilizes side information and the results could be updated in real-time. Our techniques demonstrate a modest, but significant, overall improvement in propagation modeling accuracy.

ACKNOWLEDGMENT

Sponsorship for this work was provided by NSF under Grant CNS-1642982.

REFERENCES

[1] T. S. Rappaport, *et al.*, "Millimeter wave mobile communications for 5G cellular: It will work!," *IEEE Access*, vol. 1, pp. 335-349, 2013.

[2] G. R. MacCartney and T. S. Rappaport, "73 GHz millimeter wave propagation measurements for outdoor urban mobile and backhaul communications in New York City," in *IEEE International Conference on Communications (ICC), 2014, IEEE*, pp. 4862-4867, 2014.

[3] T. S. Rappaport, G. R. MacCartney, S. Sun, H. Yan, and S. Deng, "Small-scale, local area, and transitional millimeter wave propagation for 5G communications," *IEEE Transactions on Antennas and Propagation*, vol. 65, no. 12, pp. 6474-6490, 2017.

[4] Y. Zhang, *et al.*, "28-GHz channel measurements and modeling for suburban environments," in *IEEE International Conference on Communications (ICC), 2018, IEEE*, pp. 1-6, 2018.

[5] ITU, "Propagation data and prediction methods for the planning of shortrange outdoor radiocommunication systems and radio local area networks in the frequency range 300 MHz and 100 GHz," Tech. Rep., June 2017. [Online]. Available: https://www.itu.int/rec/R-REC-P.1411-9-201706-I/en

[6] H. M. Rahim, C. Y. Leow, and T. A. Rahman, "Millimeter wave propagation through foliage: Comparison of models," in *2015 IEEE 12th Malaysia International Conference on Communications (MICC)*, pp. 236-240, Nov. 2015.

Yaguang Zhang received the B.Eng. degree in Telecommunications from Tianjin University, China, in 2013, and the M.S. degree in Electrical and Computer Engineering in 2015 from Purdue University. He is currently pursuing a Ph.D. degree in Electrical and Computer at Purdue University. His research focuses on GPS signal processing in agricultural applications and millimeter-wave channel modeling.

Soumya Jyoti received his B.Tech. degree in Electronics & Communication Engineering from National Institute of Technology (NIT), Rourkela, India. He is currently pursuing a Master's degree in Computer Engineering from Texas A&M University, College Station, Texas. His research interests include communication, networking and distributed systems.

Christopher R. Anderson received the B.S., M.S., and Ph.D. degrees in Electrical Engineering from Virginia Tech, Blacksburg, VA, USA, in 1999, 2002, and 2006, respectively. He joined the United States Naval Academy (USNA), Annapolis, MD, USA, as an Assistant Professor in 2007. In 2013, he was promoted to Associate Professor of Electrical Engineering. He is the Founder and Director of the USNA Wireless Measurements Group, a focused research group that specializes in spectrum, propagation, and field strength measurements in diverse environments and at frequencies ranging from 300 MHz to 60 GHz. From 2016-2018, he was a Visiting Researcher with the Institute for Telecommunication Sciences, a U.S. Government lab focused on advanced research to inform spectrum policy and solve emerging telecommunication issues. His research has produced 60 peer-reviewed conference and journal publications, several of which have been cited in current and upcoming wireless standards. He has been active in the ongoing 1755-1780 MHz Advanced Wireless Service 3 and 3.5 GHz Citizens Broadband Radio Service, both of which allow sharing of DoD spectrum with commercial wireless systems. His research interests include propagation measurements and modeling, millimeter-wave communications, and software-defined radio. He has served as an Editor of the IEEE Transactions on Wireless Communications.

Nicolò Michelusi received the B.Sc. (Hons.), M.Sc. (Hons.), and Ph.D. degrees from the University of Padova, Italy, in 2006, 2009, and 2013, respectively, and the M.Sc. degree in Telecommunications Engineering from the Technical University of Denmark in 2009, as a part of the T.I.M.E. double degree program. From 2013 to 2015, he was a Post-Doctoral Research Fellow at the Ming-Hsieh Department of Electrical Engineering, University of Southern California, CA, USA. He is currently an Assistant Professor with the School of Electrical and Computer Engineering, Purdue University, West Lafayette, IN, USA. His research interests lie in the areas of 5G wireless networks, millimeter-wave communications, stochastic optimization, and distributed optimization.

David J. Love received the B.S. (Hons.), M.S.E., and Ph.D. degrees in Electrical Engineering from the University of Texas at Austin in 2000, 2002, and 2004, respectively. Since 2004, he has been with Purdue University, where he is currently the Reilly Professor of Electrical and Computer Engineering. His research interests include the design and analysis of broadband wireless communication systems, 5G wireless systems, multiple-input multiple-output (MIMO) communications, millimeter-wave wireless, software-defined radios and wireless networks, coding theory, and MIMO array processing.

Alex Sprintson received the B.S. (summa cum laude), M.S., and Ph.D. degrees in Electrical Engineering from the Technion, Haifa, Israel, in 1995, 2001, and 2003, respectively. From 2003 to 2005, he was a Post-doctoral Research Fellow at the California Institute of Technology, Pasadena, CA, USA. He is currently a Full Professor with the Department of Electrical and Computer Engineering, Texas A&M University, College Station, TX, USA. His research interests include communication networks with a focus on wireless network coding, distributed storage, and software defined networks.

James V. Krogmeier received the B.S.E.E. degree from the University of Colorado at Boulder in 1981 and the M.S. and Ph.D. degrees from the University of Illinois at Urbana-Champaign in 1983 and 1990, respectively. In 1990, he joined the Faculty of Purdue University, West Lafayette, IN, USA, where he is currently a Professor and an Associate Head with the School of Electrical and Computer Engineering. His research interests include the application of signal processing in wireless communications, adaptive filtering, channel equalization, synchronization, precision agriculture, and intelligent transportation systems.

Electronically Steerable Radiation Pattern of Coupled Periodic Antenna Used Floquet Analysis

Ben Latifa Nader
National Engineering School of Tunis
Tunis Elmanar University
SysCom Laboratory
Tunisia, Tunis 1002
benlatifanader@yahoo.fr

Hamdi Bilel
National Engineering School of Tunis
Tunis, Tunisia
hamdibilel1985@gmail.com

Aguili Taoufik
National Engineering School of Tunis
Tunis, Tunisia

***Abstract*—In this paper we have developed a new Floquet analysis combined to MOM-CEG method to produce 3D electronically controlled antenna arrays. This approach permits to model and optimize the antenna arrays system by the sweeping of radiation beam in several directions. A parametric study on electromagnetic performance of the antenna system based on Floquet states offer a considerable advantages in 3Dsteerable radiation beam, size and directivity. Then smart periodic antenna has been constructed by placing the main beam in the desired direction.**

I. Introduction

Periodic antenna arrays are several antennas combined and arranged together to synthesize a global radiation pattern with directional beam. To modelize the proposed structure, two formulation are given in spectral and spatial domain, where the Moment method [1] combined with generalised equivalent circuit MOM-GEC [2] is applied. In this work we introduce the Floquet Approach to reduce the formulation of periodic structure to a one reference cell with periodic walls. This Floquet modal analysis introduce all possible Floquet states and group the coupling information of the overall structure. This new method is applied to generate a tree dimensional (3D) electronically controlled antenna; the sweeping of radiation beam of smart antenna are nowadays used to improve the performance of mobile and wireless communications systems. This paper is organized as follows: First it is necessary to explain the problem formulation and how to use Floquet model analysis combined with MoM-CEG method. After that we present a numerical results and we discuss the behavior of 3D steerable radiation beam and how to derive the main beam of the overall structure in the desired direction.

A. Problem Formulation: Floquet Modal Analysis Combined to MOM-CEG Method

In this section, we start with a comparison between spatial and spectral formulation of periodic system. The theoretical results show that Floquet model analysis can be applied to synthesize directional beam of infinity element and reduce spacial electromagnetic calculus to a reference cell with periodic walls [3], [4]. These artificial walls contain all coupling information of the overall structure. After that MoM-CEG method is applied to the reference cell. This new formulation

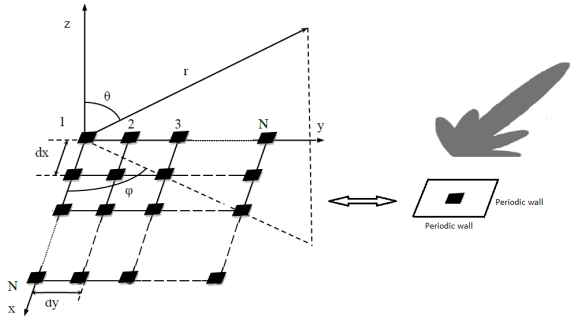

Fig. 1. Floquet modal ananysis presentation in 2-D periodic structure.

is used to achieve predictable radiation pattern and controlled beam direction. These smart antennas are common in radar and communication system. The Floquet model analysis of periodic structure are shown in Fig. 1. The formulation of MoM-CEM method is applied on this reference cell with periodic walls in modal space and α and β are the Floquet phases [5]. Based on MoM-CEM method and using impedance operator representation, we can identify the relationship between the current density and the electric field for any Floqued mode:

$$\widetilde{J}_{\alpha\beta} = \widetilde{J}_{e,\alpha\beta}; \widetilde{E}_{e,\alpha\beta} = -\widetilde{E}_{\alpha\beta} + \widetilde{Z}_{\alpha\beta} * \widetilde{J}_{e,\alpha\beta}. \quad (1)$$

The current dencity excited by the located source on the periodic structure can be computed as:

$$J(x,y) = \frac{d_x d_y}{4\Pi^2} \int\int \widetilde{J}_{\alpha\beta}(x,y) d_\alpha d_\beta. \quad (2)$$

B. Numerical Results

In this section, we present Floquet modal analysis of periodic antenna array, as an example we simulate and design a structure of 4 linear elements over matlab. We will extract all possible Floquet modes (α, β) and we will show their influence on pattern radiation:

$$\alpha_p = \frac{2\pi p}{N d_x} \text{ and } \alpha \in [\frac{-\pi}{d_x}, \frac{\pi}{d_x}].$$

Submitted On: August 23, 2018
Accepted On: October 21, 2018

TABLE I
THE DIRECTIVITY VALUE WITH STEERING ANGLE

Steering angle θ_s (deg)	0	30	45	60
Directivity (dB)	45.52	28.32	25.68	22.58

TABLE II
THE PERFORMANCE PARAMETERS OF THE PERIODIC STRUCTURE

	SLL (dB)	Peak gain (dBi)	Directivity (dB)
(α_1, β_0)	-13	-6.1	25.18
(α_0, β_0)	-23	-11.4	23.66
(α_{-1}, β_0)	-13	-6.1	25.81
(α_{-2}, β_0)	-11.5	-9.6	25.42

The behaviour of radiation pattern for all floquet modes (α_{-2}, β_0), (α_{-1}, β_0), (α_0, β_0), (α_1, β_0) and their superposition E_{tot} is shown in Fig. 3.

Fig. 2 shows a 3D surface plot of the radiation pattern of periodic antenna obtained by the supperpotion of floquet modes. The main beam can be steered to a desired direction.

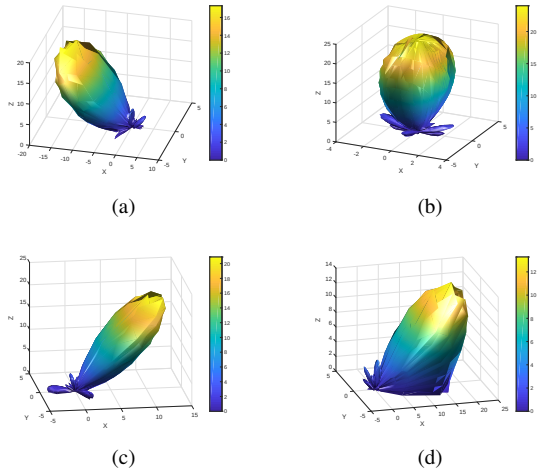

Fig. 2. 3D radiation beam pattern steering of proposed array at different angles: (a) θ_s = -45 (deg); (b) θ_s = 0 (deg); (c) θ_s = 45 (deg); (d) θ_s = 60 (deg).

Table I shows a better performance in terms of directivity at θ_s = 0 (deg).

The radiation pattern plot in Fig. 3 obtained by using Floquet modal method demonstrates the aptitude of this technique to supperpose all Floquets modes and steer the main beam to a desired direction. Table II illustrates the performance parameter (Side lobe level, Peak gain and directivity) of radiation pattern for each Floquet mode.

II. CONCLUSION

For the first time Floquet modal analysis combined to MOM-CEG method are introduced to improve the performance of smart antenna arrays. These periodic antennas are able to provide a directional beam that can be electronically

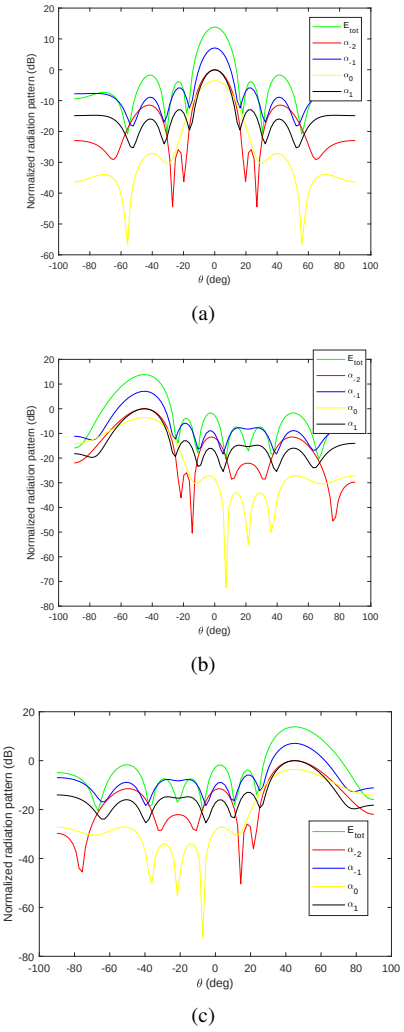

Fig. 3. Simulated 2D radiation pattern of periodic antenna en function the elevation angle theta for different steering angle: (a) θ_s = 0 (deg); (b) θ_s = -45 (deg); (c) θ_s =45 (deg).

steered. The result shows that by increasing the steering angle θ_s, lower value of directivity can be obtained and the maximum of directivity is achieved at $\theta_s = 0(deg)$.

REFERENCES

[1] H. Bilel, T. Aguili, and H. Baugrand, "Floquet modal analysis to modlize and study 2 D planar almost periodic structures in finite and infinite extend with coupled motifs," PIERS B, 2015.

[2] H. Bilel, T. Aguili, N. Ravue, and H. Baugrand, "Calculation of mutual coupling parameter and their effects in 1D almost periodic structures," PIERS B, 2014.

[3] N. Ben Latifa, H. Bilel, and T. Aguili, "Floque modal analysis to study radiation pattern for coupled almost periodic antenna array," AICCSA, TUNISIA, 2017.

[4] H. Bilel, S. Limam, and T. Aguili, "Uniform and concentric circular Antenna arrays synthesis for smart antenna systems using artificial neural network algorithm," PEARS B, 2016.

[5] Z. Mikkioui and H. Baudrand, "Bi-dimensional bi-periodic centred field microstrip leakly wave antenna analysis by a source modal decomposition in sperctal domain," IET Microwaves Antennas and Propagation, 2008.

Design of Dual Band Rectifiers for Energy Harvesting Applications

Abdullah Eroglu [1], Kowshik Dey [2], Rezwan Hussain [2], and Tunir Dey [2]

[1] Department of Electrical and Computer Engineering
North Carolina A&T State University, Greensboro, NC, 27411, US
aeroglu@ncat.edu

[2] Department of Electrical and Computer Engineering
Purdue University Fort Wayne, Fort Wayne, IN, 46805, US

***Abstract*—Design, simulation and implementation of dual band radio frequency energy harvesting (RFEH) system operating at 900MHz and 1.8GHz is introduced. In the proposed design, RF-DC conversion system is designed to passively amplify the available voltage for rectification by developing a resonator with high quality factor. Passive amplification and rectification are implemented using a combination of clamper and peak detector circuits. Harmonics presented in the rectified output voltage is eliminated by using an innovative two-section dual band transmission line matching network and filter. Energy harvesting system is designed, simulated and measured. Close agreement has been observed between analytical, simulation and measurement results.**

***Keywords*—Dual band, energy harvesting, matching network, radio frequency, rectanna, rectifier.**

I. Introduction

Wireless sensor networks (WSNs) comprise of a set of active nodes which communicate with each other and a central node. In recent years WSNs have expanded to evolvement of a new area called Internet of Things (IoT) that investigates the connectivity and exchange of data between all physical devices in the network [1]. WSNs have been used in agriculture, healthcare, earth-sensing, industry and myriads of other applications. It is not uncommon to see that the most of the time, sensor nodes are situated in hazardous locations with limited accessibility. Hence, these sensors at the nodes are typically powered by battery. Since, battery is limited form of energy source, they require periodic recharge or replacement which brings along the added cost of maintenance and replacement [2]. Disposal of battery is also a cumbersome task which is hazardous to the environment.

One way to overcome the power problem due to limited battery lifetime is to use a method called energy harvesting. Energy harvesting also known as power harvesting, or energy scavenging is the process of extracting energy from external sources using solar power, thermal energy, wind energy, salinity gradients, and kinetic energy which all can be referred as ambient energy. Energy harvester once extracts the energy in the ambient it then converts that energy to DC, rectifies the signal and powers wireless autonomous devices that might be part of larger networks [3-4]. Radio Frequency (RF) energy harvester systems have antenna, and impedance matching networks to interface the rectifier system as illustrated in Fig. 1. This system can energize any type of network that has low power requirement such as wireless sensor networks.

Submitted On: October 27, 2018
Accepted On: November 24, 2018

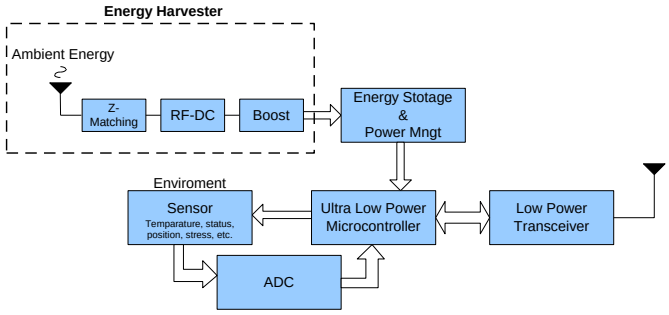

Fig. 1. Block diagram of RFEH.

In this paper, design, simulation and implementation of dual band radio frequency energy harvesting system operating at 900MHz and 1.8GHz is introduced. The proposed energy harvester has integrated impedance matching network, filter and cascaded three stage rectifier which is based on voltage doubler circuit to convert RF-DC. The system is simulated with Agilent Design System (ADS) and implemented. It has been confirmed that the analytical, simulation and measurement results are all in agreement.

II. Design of Rectifier Circuit

Clampers or DC resonators hold the peak of a waveform at the desired DC level. In other words, it clamps the waveform either in positive or negative direction using diode with a capacitively coupled signal as shown in Fig. 2. The output voltage of the clamper circuit can be expressed as:

$$V_{clamp} = 2V_p - V_{th}. \quad (1)$$

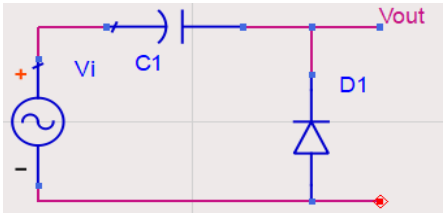

Fig. 2. Voltage clamper circuit.

Since the energy is considerably low in the ambient, we need to take into account the effect of diode threshold voltage, V_{th}. The diode should be capable of fast switching with a very low threshold voltage which is required for conduction.

To produce a steady voltage from the rectifier we incorporate peak detector with clamper circuit. A peak detector is a series connection of a diode and a capacitor outputting a DC voltage equal to the peak value of the applied sinusoidal signal. The peak detector circuit with voltage waveforms is illustrated in Fig. 3.

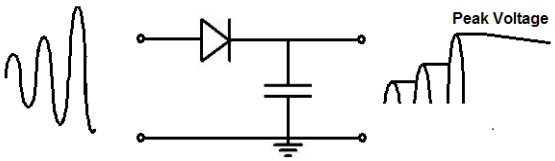

Fig. 3. Peak detector circuit.

The voltage output of the peak detector circuit is given as:

$$V_{pkDetect} = V_{clamp} - V_{th}. \quad (2)$$

The clamping and peak detector circuits can now be integrated to form single stage of the radio frequency energy harvesting (RFEH) system as shown in Fig. 4. The single stage RFEH can be cascaded to increase the amount of output voltage. In the proposed system, three stage RFEH is used to accomplish RF-DC conversion.

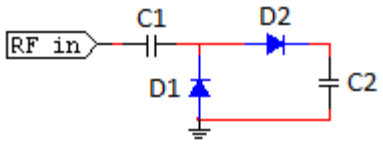

Fig. 4. Single stage of RFEH.

III. Dual Band Transmission Line Matching

To ensure maximum power is transferred from the antenna to rectifier we need to provide a matching network as shown in Fig. 5. Primary challenge of designing matching network for the proposed circuit lies in the fact that load impedance of an antenna varies with frequency due to the presence of capacitance. Another challenge is the complexity of matching circuit required to work at two different frequencies simultaneously.

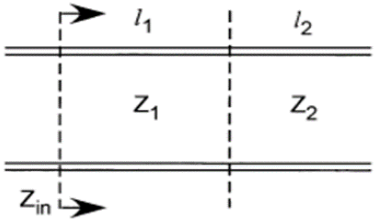

Fig. 5. Two-section dual-band transformer.

Two-section transformer which can match impedance with frequency dependent load is proposed in [5]. A practical dual-band two-section 1/3-wavelength transformer [6] that works at the fundamental frequency and its second harmonic is designed for the proposed system. Such a novel transformer is of a high interest because of the requirements for a low profile, and more efficient RF low-noise down converter, and desecration of frequency recycle in commercial and military operations.

The dual band matching network is designed as follows. Let's assume, load impedance connected to energy harvesting antenna to be Z_1 and Z_2, at the two frequencies, f_1 and f_2, respectively. f_1 and f_2 are set to be 900MHz and 1.8GHz, respectively.

The input impedance Z_{in} of the two-section transmission line shown in Fig. 5 is:

$$Z_{in}=Z_1\frac{z_L'+JZ_1\tan(\beta l_1)}{Z_1+JZ_L'tan(\beta l_1)}, \quad (3)$$

$$Z'_L=Z_2\frac{R_l+JZ_2\tan(\beta 2)}{Z_2+JR_l\tan(\beta l_2)}, \quad (4)$$

where β is the wave number. For proper impedance matching, input impedance should be equal to characteristic impedance Z_0 at the two intended frequencies $f_1$and f_2. Relating Z_{in} to Z_0 and solving for Z'_L in (3) we get,

$$\frac{Z_0-JZ_1\tan(\beta l_1))}{Z_1-JZ_0tan(\beta l_1)},$$

$$Z'_L=Z_1\frac{Z_0-JZ_1\tan(\beta l_1))}{Z_1-JZ_0\tan(\beta l_1)}. \quad (5)$$

From (4) and (5), we can write:

$$(Z_1^2-Z_2Z_0)\tan(\beta l_1)\tan(\beta l_2) = Z_2Z_0(R_l-Z_0), \quad (6)$$

n (7)

which leads to:

$$\tan(\beta l_1)\tan(\beta l_2) = \alpha = \frac{Z_2Z_0(R_l-Z_0)}{(R_lZ_1^2-Z_2^2Z_0)}, \quad (8)$$

$$\frac{\tan(\beta l_1)}{\tan(\beta l_2)} = \gamma = \frac{Z_1(Z_2^2-Z_LZ_0)}{Z_2(R_lZ_0-Z_1^2)}. \quad (9)$$

From (8) and (9), we obtain:

$$(\tan(\beta l_1))^2 = \alpha\gamma, \quad (10)$$

$$(\tan(\beta l_2))^2 = \frac{\alpha}{\gamma}. \quad (11)$$

When $f_1 = f_1$,is substituted into (10)-(11), the following equations are found:

$$(\tan(\beta_1 l_1))^2 = \alpha\gamma, \quad (12)$$

$$(\tan(\beta_2 l_1))^2 = \alpha\gamma, \quad (13)$$

$$(\tan(\beta_1 l_2))^2 = \frac{\alpha}{\gamma}, \quad (14)$$

$$(\tan(\beta_2 l_2))^2 = \frac{\alpha}{\gamma}. \quad (15)$$

The solutions of (12)-(13) give:

$$\tan(\beta_1 l_2) = \pm\tan(\beta_1 l_1). \quad (16)$$

And

$$\beta_2 l_1 \mp \beta_1 l_1 = n\pi. \quad (17)$$

Similarly, from (14) and (15), we obtain:

$$\beta_2 l_2 \mp \beta_1 l_2 = m\pi. \quad (18)$$

In (17)-(18), n and m are integers. Assuming m =n=1 and $f_2 \geq f_1$ we get a solution for the above equations as follows:

$$l_2 = l_1, \quad (19a)$$

$$l_2 = \frac{\pi}{\beta_2+\beta_1}. \quad (19b)$$

When the line lengths are calculated, α and γ can be determined by using (10) and (11) at either f_1 or f_2. For example, simplifying equation (19), using f_1 we obtain:

$$\alpha = (\tan(\beta_1 l_1))^2, \tag{20}$$

$$\gamma = 1, \tag{21}$$

so,

$$R_l Z_0 = Z_1 Z_2. \tag{22}$$

Equation (22) is valid when $Z1+Z2 \neq 0$. We can also show that:

$$R_l Z_1^2 - Z_2^2 Z_0 = \frac{R_l Z_0 (R_l - Z_0)}{\alpha}. \tag{23}$$

Using (22) and (23), we can now get either Z_1 or Z_2. Using standard means the solution for Z_1 leads to the real line impedance value:

$$Z_1 = \sqrt{\frac{Z_0}{2\alpha}(R_l - Z_0) + \sqrt{[\frac{Z_0}{2\alpha}(R_l - Z_0)]^2 + Z_0^3 R_L}}. \tag{24}$$

Z_2 can then be obtained from (22) as:

$$Z_2 = \frac{Z_0 R_l}{Z_1}. \tag{25}$$

Hence, the total length of transmission line in wavelengths can be calculated at the fundamental frequency f_1 using:

$$\frac{l_1 + l_2}{\lambda_1} = \frac{\beta_1 \lambda_1}{\beta_1 + \beta_2},$$

$$L = \frac{\beta_1 \lambda_1}{\beta_1 + \beta_2}. \tag{26}$$

IV. Simulation Results

The proposed three stage RFEH is designed and simulated as shown in Fig. 6. Harmonics are presented in the rectified output voltage. The two section matching network discussed in Section III is designed and integrated to eliminate the harmonics. The two section matching network can match impedance at two distinct frequency without causing any defficieny in the circuit. Fig. 7 shows output spectrum without harmonics after the use of two section matching network. Fig. 8 shows the simulated output power in frequency domain where harmonics is present. Without the transmission line we got some ripples at 900 MHz and 1.8 GHz. Voltage peak at 0 Hz is 146 mv.

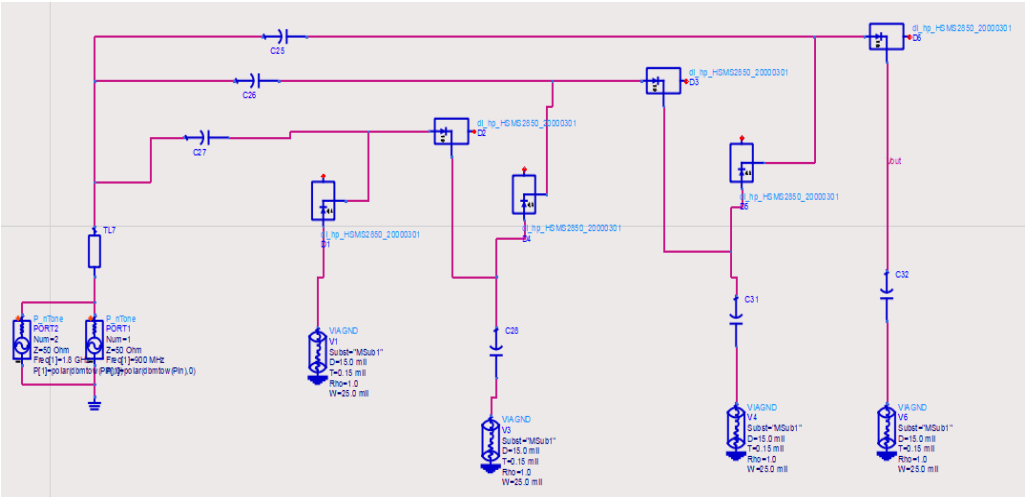

Fig. 6. The complete RFEH system.

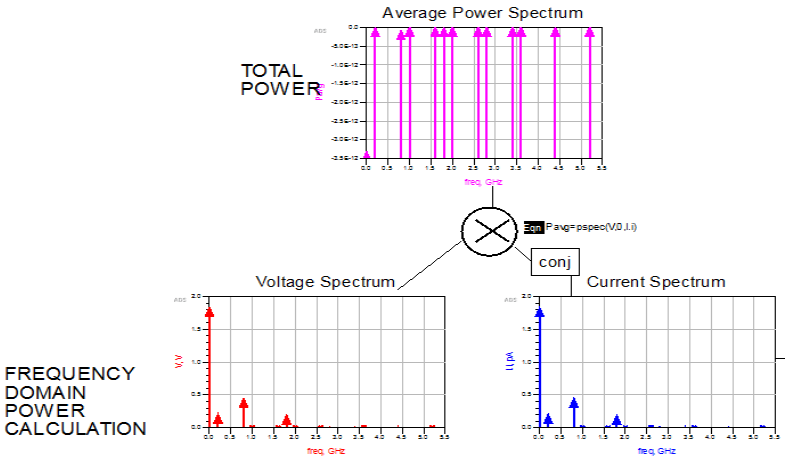

Fig. 7. Frequency Spectrum of Output power.

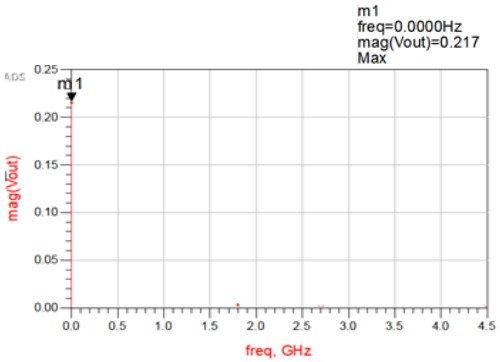

Fig. 8. Voltage spectrum showing elimination of harmonics from output with impedance matching network.

V. Measurement Results

The prototype of three sections is buit and tested. RF-35 material with dielectric constant 3.5 was used to make the prototype. The two critical components used in the design are Schottky diode HSMS 2850 from Broadcom Inc., and 56pf capacitor from Wurth Electronics. The circuit was fabricated in university lab as shown Fig. 9. Figure 9 (a) and 9 (b) shows the top and bottom view of the prototype of the rectifier, respectively

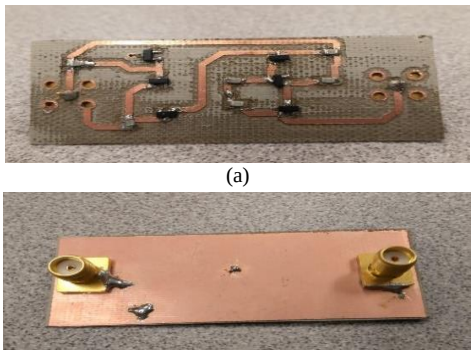

(a)

(b)

Fig. 9. (a) Top and (b) bottom view of rectifier.

The test set up of the energy harvesting system is illustrated in Fig. 10.

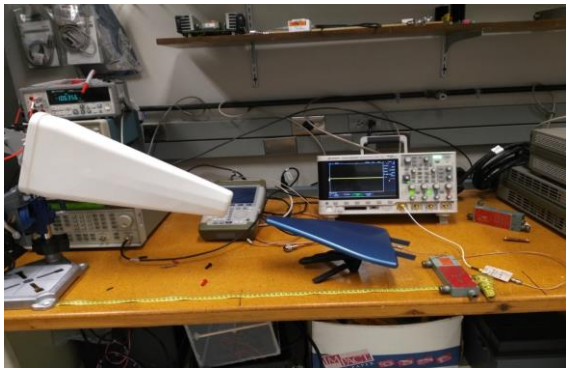

Fig. 10. The test set up for measuring rectifier output.

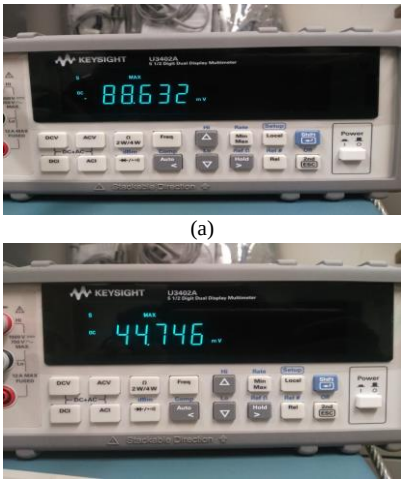

(a)

(b)

Fig. 11. The DC voltage measurement output at: (a) 900MHz and (b) 1.8 GHz.

The rectifier output at 900 MHz and at 1.8 GHz is measured to be 88.63 mV and 44.74 mV, respectively as shown in Fig. 11.

VI. Conclusion

In this paper, design, simulation and implementation of a dual band radio frequency energy harvesting (RFEH) system operating at 900MHz and 1.8GHz is introduced. The proposed harvesting system is designed, simulated and measured. It is shown that RFEH system can passively amplify the available ambient RF energy via three stage voltage doubler circuit. Passive amplification and rectification is implemented using a combination of clamper and peak detector. Harmonics presented in the rectified output voltage is eliminated by using transmission line matching network and filter. Energy harvesting system designed and simulated is then implemented and tested. Close agreement between analytical, simulation and measurement results are obtained.

References

[1] L. Tan and N. Wang, "Future Internet: The Internet of Things," in Proc. 3rd Int. Conf. Adv. Comput. Theory Eng. (ICACTE), vol. 5. Aug. 2010, pp. V5-376–V5-380.

[2] D. Carli, D. Brunelli, L. Benini, and M. Ruggeri, "An effective multi-source energy harvester for low power applications," Design, Automation & Test in Europe Conference & Exhibition (DATE), 2011, pp. 1,6, 14-18 Mar. 2011

[3] H. Li, C. Tian, and Z. D. Deng, "Energy harvesting from low frequency applications using piezoelectric materials," Applied Physics Reviews 1, 041301, 2014.

[4] R. Vyas, H. Nishimoto, M. Tentzeris, Y. Kawahara, and T. Asami, "A battery-less, energy harvesting device for long range scavenging of wireless power from terrestrial TV broadcasts," in Microwave Symposium Digest (MTT), 2012 IEEE MTT-S International , pp. 1-3, 17-22 June 2012.

[5] K. Rajawat, N. Gatsis, S. Kim, and G. B. Giannakis, "Cross-layer design of coded multicast for wireless random access networks," IEEE Journal on Selected Areas in Communications, vol. 29, no. 10, pp. 1970-1980, Dec. 2011.

[6] Y. L. Chow and K. L. Wan, "A transformer of one-third wavelength in two sections-for a frequency and its first harmonic," IEEE Microwave Wireless Comp. Lett., vol. 12, pp. 22-23, Jan. 2002.

A Study of SAR on Child Passengers and Driver Due to Cellphone Connectivity within Vehicle

Margaret J. Lyell [1] and Daniel N. Aloi [2]

[1] Explorations Minerva, LLC
Ann Arbor, MI 48113, USA
ML137@explorationsminervallc.com

[2] Department of Electrical and Computer Engineering
Oakland University, Rochester, MI 44309, USA
daloi@oakland.edu

Abstract ─In this work, SAR values in passenger and driver head and body regions due to the presence of one or more cellphones were determined via simulation for the situation in which all vehicle passengers are children. Additionally, the adult driver has access to a hands free cellphone as part of increased in-vehicle connectivity. The FEKO tool, using the Method of Moments, was utilized for simulations.

Index Terms ─ Cellphone, in-vehicle connectivity, RF, SAR, specific absorption rate.

I. INTRODUCTION

Potential adverse impacts to health due to tissue heating [1] can result from radio frequency (RF) emissions. Such emissions are becoming more ubiquitous, due to the prevalence of cellphones, connected devices and increased expectations of connectivity within a vehicle. SAR is defined as:

$$SAR = (\sigma / \rho) |E|^2, \quad (1)$$

where σ is the tissue conductivity (S/m), ρ is the tissue mass density (Kg/m^3) and E is the (rms) electric field (v) in the tissue. Limits on the SAR values (in W/Kg) allowable have been set by various regulatory jurisdictions. In the United States, this limit is 1.6 W/kg. A standard SAR value of interest is the spatial peak SAR averaged over 1 gram of tissue.

It is known that SAR values for the same level of RF can be larger in a child's brain tissue (due to increased conductivity in the brain tissue) as contrasted with that of an adult [2, 3]. Gender differences also exist; this work utilizes a male child model at ten years old, in the fiftieth percentile of growth.

An initial study [4] on the level of SAR in a vehicle from cellphones involved a driver and adult passengers; a subset of whom utilized a cellphone at frequency 900 MHz. This study was extended [5] to higher frequencies. ***Our work considers*** an in-vehicle scenario in which *all passengers are children*, each with a cellphone, and the *adult driver has the option of using a 'hands-free' cellphone.*

The paper is organized as follows. Section II presents relevant models for use in the FEKO simulation environment with the Method of Moments (MOM) technique. Section III provides (spatial) peak SAR results (head and body) of vehicle occupants for different cases of passenger loading. Conclusions are given in Section IV.

II. MODEL DEVELOPMENT

A. Adult driver and child passenger models

The shape properties for the adult driver model are (1) a sphere for the head and (2) parallelepipeds for the torso, right and left lap and right and left legs. The adult model, shown in Fig. 1, utilizes dimensions from [4, 5]. Adult dimensions include: brain radius, 0.1 m and height from bottom of leg to center of head, 0.94 m. Neither brain nor body are modeled with any internal structure, following [4, 5].

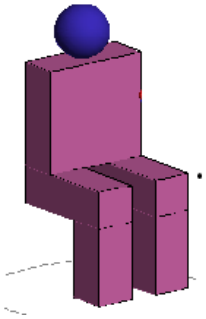

Fig. 1. Adult driver model.

Ibrani et al. [3] state that a child's head size phantom is eighty percent of an adult phantom, for children between seven and ten years old. Child body height is

Submitted On: September 5, 2018
Accepted On: October 3, 2018

approximately seventy percent of an adult's height [2]. The ten year old male child model's dimensions are: brain radius, 0.08 m and height from bottom of the leg to center of brain, 0.668 m.

Permittivity (ε_r) and conductivity (σ) values differ between adult and child models and are frequency dependent. Our simulations use 900 MHz frequency. For adult brain tissue, $\varepsilon_r = 45.81$ and $\sigma = 0.77$ S/m. For adult muscle tissue, $\varepsilon_r = 55.96$ and $\sigma = 0.97$ S/m. In child brain tissue, $\varepsilon_r = 56.01$ and $\sigma = 1.00$ S/m. In child muscle tissue, $\varepsilon_r = 58.01$ and $\sigma = 0.99$ S/m.

B. Cellphone model

The cellphone model used is that of a (λ/4) monopole antenna radiating at frequency 900 MHz, also used in [4, 5]. The S1,1 parameter value, with resonant frequency at 900 MHz, is less than -25 dB. Antenna length is 108.3 mm. Antenna ground plane is 40 mm in length and 20 mm in width.

C. Vehicle model

Figure 2 shows the vehicle structure used in [4], modified for use in this work. Red lines show the modifications; these make the vehicle boxier. The windscreen is now flat above the metal front bottom. Side windows are rectangular; additional roof surface adjacent to side windows is now glass. This results in 0.92 m^2 more glass instead of metal in the front part of the roof. Note coordinate directions in Fig. 2. Vehicle components are aluminum and untreated glass. Permittivity and conductivity values are found in [4].

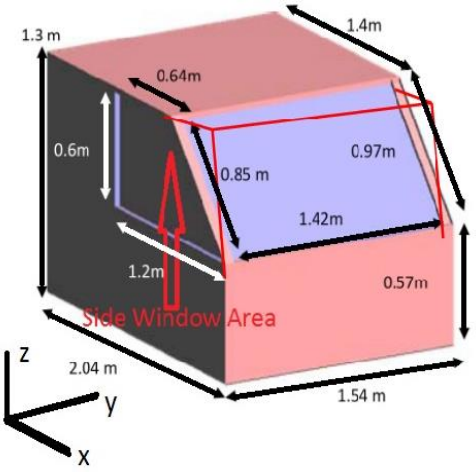

Fig. 2. Vehicle model.

D. Driver, passengers, and cellphones in vehicle

The left hand side of Fig. 3 shows the passenger layout (as in [4]). Here, each child passenger has a cellphone, indicated by a red dot. The rear seat child passengers have their torsos' back edge at x=0.167 m; the front seat child passenger's and adult driver's are at x=0.883 m. The right hand side of Fig. 3 shows the driver. The hands-free cellphone, indicated by the red dot, is located at approximately the same height as the middle of the driver's head; it is 0.72 m in front of the driver's torso's front and is at the windscreen's lateral midpoint. The front windscreen is x=0.03m beyond the cellphone placement. Windows and front windscreen are untreated glass (shown in brown).

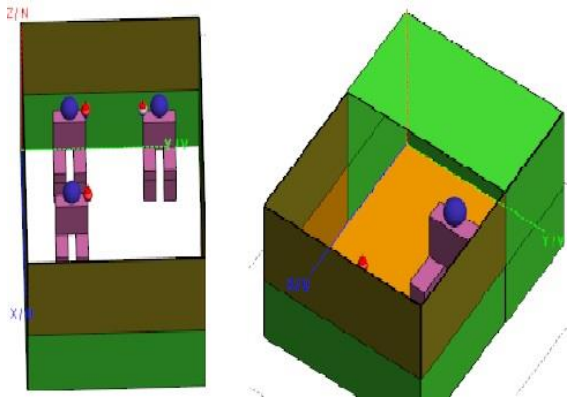

Fig. 3. Layout of child passengers (each with cellphone) and driver (with hands-free cellphone) in the vehicle.

III. SIMULATION RESULTS: SPATIAL PEAK SAR VALUES

Peak spatial SAR results for eleven different simulations developed in FEKO [6] are given in Table 1. Total power in each simulation run is 1.6 W. Note that Case 1 has one cellphone using 1.6 W power; thus, all SAR is due to radiation from one high powered cellphone.

Table 1: SAR simulation results

S	D	RF	RB	LB	HS	WHS	BS	WBS
1		X			0.845	RF	1.728	RF
2				X	0.914	LB	1.170	LB
3	X				0.014	DR	0.105	DR
4	X			X	0.596	LB	0.165	LB
5	X		X	X	0.32	LB, RB	0.573	LB
6	X		X		0.607	RB	0.843	RB
7	X	X		X	0.337	RF	0.563	LB
8	X	X			1.012	RF	1.272	RF
9	X	X		X	0.470	RF	0.755	RF
10	X	X	X		0.377	RB	0.622	RB
11	X			X	0.900	LB	1.148	LB

Keys to table abbreviations are: S=Simulation case number, D = Driver, (RF, RB, LB) = respectively, the Right Front Seat Child, Right Back Seat Child, and Left Back Seat Child, HS = Maximum Head SAR,

BS = Maximum Body SAR, WHS = Person having the Maximum Head SAR, WBS = Person having Maximum Body SAR. SAR values are given in units of W/Kg.

Note the hands-free cellphone is not used in cases 1, 2, 9 and 11.

In cases Sim9 and Sim11, the hands-free cellphone is *not* used; induced SAR in the driver is due to passenger cellphones only. Note that the driver's head SAR is roughly an order of magnitude less than the driver's body SAR. In Sim3 (hands-free cellphone utilized), body SAR is 0.105 W/kg and head SAR is 0.014 W/Kg. Maximum body SAR of passengers is found in the upper torso region, close to the cellphone location. Peak body SAR is usually greater than the peak head SAR, consistent with a passenger's cellphone location being not immediately adjacent to the ear.

VI. CONCLUSION

This work, part of a larger effort investigating SAR values in child and adult occupants when multiple RF devices are in use, provides SAR results for multiple child and driver head and body regions. The hands-free cellphone option offers increased in-vehicle connectivity as well as increased RF. Physical reflection also contributes to SAR; as metal surface area is decreased in the boxier vehicle by approximately 1 m^2 relative to that of [4], reflections are reduced.

REFERENCES

[1] Specific Absorption Rate for Cellular Telephones, US Federal Communications Agency, https://www.fcc.gov/general/specific-absorption-rate-sar-cellular-telephones [Accessed 10-11-17].

[2] M. Ibrani, L. Ahma, E. Hamiti, and J. Haxhibeqiri, "Derivation of electromagnetic properties of child biological tissues at radio frequencies," *Progress in Electromagnetics Research Letters*, vol. 25, pp. 87-100, 2011.

[3] M. Ibrani, L. Ahma, and E. Hamiti, "Comparative SAR assessment in adults and children exposed to electromagnetic fields of radio frequency devices," *WSEAS Trans. on Communications*, iss. 2, vol. 9, pp. 105-114, 2010.

[4] K. H. Chan, S. W. Leung, and Y. M. Siu, "Specific Absorption Rate evaluation for people using wireless communication device in vehicle," *2010 IEEE Symposium on Electromagnetic Compatibility*, pp. 706-711, 2010.

[5] Y. Diao, W. N. Sun, K.H. Chan, S. W. Leung, and Y. M. Siu, "Specific absorption rate evaluation for multiple wireless communication devices inside a vehicle," P*roceedings of the 2013 International Symposium on Electromagnetic Theory*, pp. 626-629, 2013.

[6] FEKO, Altair Hyperworks FEKO, Suite 7.0, Troy, MI.

Margaret J. Lyell received the B.S. degree in Mathematics from Case Western Reserve Univ., M.S. degrees in Aerospace Engineering and Computer Science, from Univ. of Southern California and Johns Hopkins Univ, respectively, and the Ph.D. degree in Aerospace Engineering from Univ. of Southern California. Her experience includes research efforts in (a) fluid dynamics, including hydrodynamic stability theory and microgravity fluid mechanics and (b) multi-agent systems technology. Work in fluid dynamics was largely performed while she was a Resident Research Associate at the Jet Propulsion Laboratory and an Associate Professor at West Virginia University. Her more recent research efforts in multi-agent systems theory and applications were largely performed while she was a Lead and Principal Scientist at The MITRE Corporation and at Intelligent Automation, Inc. Her current focus involves system aspects of Internet of Things (IoT) applications. In particular, she is focused on RF utilization and impact (including SAR) and security in IoT systems as part of her role as Principal at Explorations Minerva LLC. She is a member of AIAA, APS, SIAM and IEEE.

Daniel N. Aloi received his B.S. (1992), M.S. (1996) and Ph.D. (1999) degrees in Electrical Engineering from Ohio University, located in Athens, Ohio, USA.

He served as a Research Assistant from 1995-1999 in the Avionics Engineering Center within the School of Engineering and Computer Science at Ohio University; Summer Intern at Rockwell International in Cedar Rapids, Iowa, and Senior Project Engineer at OnStar, Incorporated, a subsidiary of General Motors from 2000-2002. He has been employed in the Electrical and Computer Engineering Department at Oakland University in Rochester, Michigan from 2002 until present. And is the Founder and Director of the Applied EMAG and Wireless Lab at Oakland University. Aloi's research interests reside in area of applied electromagnetics with emphasis on antenna measurements, antenna modeling/analysis and antenna design. He is a Member of the Institute of Navigation and is a Senior Member of the Institute of Electrical and Electronics Engineers (IEEE). He has received in excess of $4M in research funding from a variety of federal and private entities including the Federal Aviation Administration, Defense Advanced Research Program Agency (DARPA) and the National Science Foundation (NSF). He has authored/co-authored over 100 technical papers and is an inventor on 5 patents.

Estimation of 1090 MHz Signal Environment on Airport Surface by Using Multilateration System

Junichi Honda, Yasuyuki Kakubari, and Takuya Otsuyama

Surveillance and Communications Department
Electronic Navigation Research Institute (ENRI)
National Institute of Maritime, Port and Aviation Technology
Chofu, Tokyo 182-0012 Japan
j-honda@enri.go.jp

Abstract ─ This paper is concerned with an estimation of 1090 MHz signal environment on airport surface. Secondary surveillance radar and its applications share 1030 MHz and 1090 MHz. Since many aircraft emit signals with same frequency band, increasing signal amount will be saturated and result in the performance degradation. To meet the aviation requirement, it is important to manage the signal amount. In this paper, focusing on 1090 MHz, we propose an estimation method for signal amount on airport surface, by using multilateration system.

Index Terms ─ 1090 MHz, ATCRBS, Mode S, multilateration, secondary surveillance radar, signal amount.

I. INTRODUCTION

Secondary surveillance radar (SSR) has become one of main surveillance systems in the civil aviation, and multilateration (MLAT), wide area MLAT (WAM) and automatic dependent surveillance - broadcast (ADS-B) have been developed as SSR applications. In those systems, 1030/1090 MHz frequency bands are employed and shared with each other [1],[2]. Therefore, with increasing the demand of aircraft, signal environment is getting worse. In order to maintain the safety operation, signal amount and signal rate should be appropriately managed.

The purpose of this study is to estimate the current signal environment of 1030/1090 MHz to evaluate the future signal environment. In addition, we consider the environment of distorted signals which affects to the detection rate. In this paper, focusing on 1090 MHz, we propose an estimation method for analyzing signal environment on airport surface. Currently we are under the investigation of a new MLAT system by using radio-over-fiber (RoF) [3],[4]. A prototype system is deployed at Sendai airport, Japan. The proposed method to acquire signal data uses receiver units implementing to MLAT system. Comparing with the signal data between receivers, we analyze signal amount, signal rate and the amount of distorted signals on airport surface. In this paper, we firstly introduce the experimental system for collecting 1090 MHz signals and secondly discuss the estimation method of signal environment. Finally we show the signal amount and distorted signals of ATCRBS (Air Traffic Control Radar Beacon System) and Mode S of which are signal types employed in 1090 MHz [5]. We discuss the signal environment on airport surface.

II. ESTIMATION METHOD OF SIGNAL ENVIRONMENT

To obtain 1090 MHz signals, MLAT system is employed. ENRI developed a new MLAT system named as OCTPASS (Optical Fiber Connected Passive Surveillance) [3],[4], and the system is deployed at Sendai airport which is a middle size airport in Japan. OCTPASS has eight receiver units connected to a central signal processing unit by optical fiber. The received signals are transmitted to the central processing unit by RoF technology. RoF enables to transmit RF signals in the long distance by amplitude modulation in the optical region. Consequently, OCTPASS directly processes the RF signals at the central processing unit. Our method to analyze 1090 MHz signals uses its characteristics.

Figure 1 shows an experimental environment in Sendai airport. As shown in this figure, eight OCTPASS receivers are located in the airport. In addition, three transmitters exist. The first is used for the actual operation, second one is for trainees, and the final is our experimental system. Signal amount is anticipated to be larger than that of same size airports due to three transmitters.

Next, we explain the method to count the number of 1090 MHz signals. All received RF signals are transmitted to the central processing unit. The central unit makes groups as signals are collected within the arbitrary time gate. Therefore, we can count and compare the signals at the same arrival time. Statistical signal amount in the

Submitted On: October 2, 2018
Accepted On: October 20, 2018

airport is considered if a receiver unit detects a signal, even if the signals are not decoded. On the other hand, distorted signals are counted by compared with all receiver data. If a received signal is different from other received signals, we regard it as a distorted signal. Figure 2 is an example for distinguishing received signals.

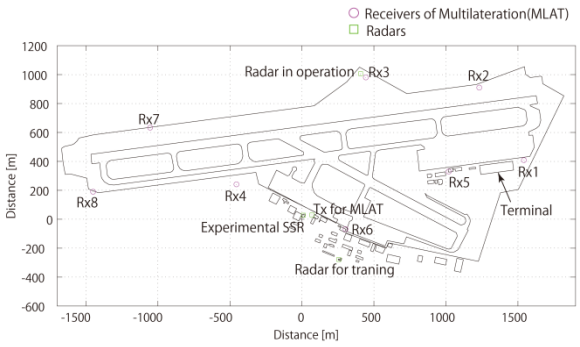

Fig. 1. Experimental environment in Sendai Airport.

Time	Receiver							
	Rx1	Rx2	Rx3	Rx4	Rx5	Rx6	Rx7	Rx8
t_1	AA11	0000	0000	AA11	AA11	0000	AA11	AA11
. . .								
t_2	0000	AB12	AB12	0000	0000	0000	AB00	0000
. . .								

Received signals
No signal
Received correct signals
Received signals, but distorted one

Note:
t_1 - "AA11" is the received signal from an aircraft.
t_2 - "AB12" is the correct signal emitted from an aircraft, but "AB00" is the distorted signal by comparing with other received signals.

Fig. 2. Distinction of received signals.

III. ESTIMATED SIGNAL AMOUNT AND DISTORTED SIGNALS

We analyzed ATCRBS and Mode S signals used in 1090 MHz. Figure 3 shows signal amount of ATCRBS. This figure indicates that the signal amount depends on the receiver position. The data is the averaged value for 10 second. The maximum value is about 3,000 per second. The largest number of signals is obtained by Rx7, and the minimum one is at Rx6. As Rx7 is relatively open area, the signal amount is large, while the value of Rx6 is small because it is located around the buildings such as hanger and shadowed by airport terminal. Figure 4 shows signal amount of Mode S. As shown in this figure, the amount is less than 1/10 of ATCRBS. The characteristic for time dependence is the almost same as that of Fig. 1.

Finally we analyzed the distorted signals. In this paper, we show the result of ATCRBS. Figure 5 is the estimated amount of distorted signals based on the idea shown in Fig. 2. As an example, we compare the signals of Rx7 at 1:00. The number of distorted signal is about 450, and the total received signal is about 1750 from Fig. 3. Therefore, the rate of distorted signals is approximately 25%. The rate of distorted signals depends on the receiver allocation, but in this airport the performance of a normal MLAT system which needs the decoded signals, might become worse in comparison with OCTPASS.

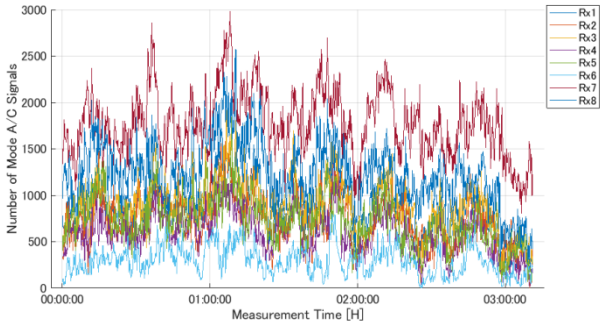

Fig. 3. Signal amount of ATCRBS.

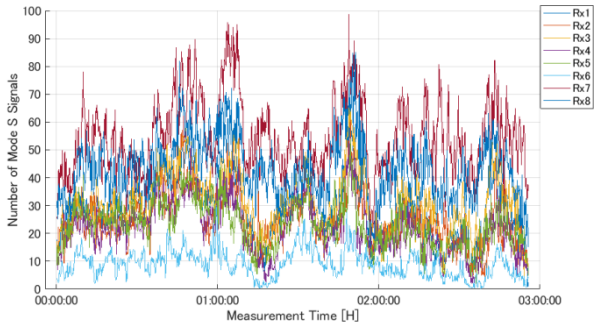

Fig. 4. Signal amount of Mode S.

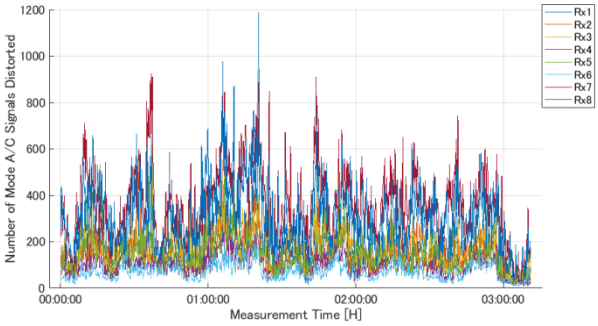

Fig. 5. Amount of distorted signals of ATCRBS.

IV. CONCLUSION

In this paper, we have introduced the estimate method for analyzing 1090 MHz signal environment in airport. The proposed method uses OCTPASS system with several receiver units deployed in airport whose receiver units are connected by the RoF. Collecting RF signals to the central processing unit, we can easily estimate the received signal amount and the number of

distorted signals. It has been found that the signal amount depends on the receiver allocation. It has been also found that the signal amount of Mode S is much less than that of ATCRBS. Moreover, we checked the rate of distorted signals at Rx7 as example. It has been demonstrated that the distorted signals were detected about 1/4 of total received signals.

We would like to analyze other experimental data, and would also like to make the expectancy value of future signal amount. We need to evaluate the performance of OCTPASS by comparing with the normal MLAT. They deserve as future studies.

ACKNOWLEDGMENT

The work was supported in part by a Grant-in-Aid for Young Scientists (B) (16K18072) from the Japan Society for Promotion of Science.

REFERENCES

[1] ICAO, Annex 10 Aeronautical Telecommunications, Volume 4 Surveillance and Collision Avoidance System, 4th edition, 2007.

[2] ICAO, Doc9924 Aeronautical Surveillance Manual, 2nd edition, 2017.

[3] T. Koga, et al., "Results of Evaluation of Multilateration with Radio on Fiber Connection," *IEICE Technical Report SANE*, vol. 106, no. 1, pp. 273-278, April 2006.

[4] Y. Kakubari, T. Koga, H. Miyazaki, H. Shimada, and S. Nihei, "Enhancement of passive surveillance system for airport surface movement," *Electronics and Communications in Japan*, vol. 97, no. 3, pp. 24-30, 2014.

[5] RTCA, Minimum Operation Performance Standards for Air Traffic Control Radar Beacon System/Mode Select (ATCRBS/Mode S) Airborne Equipment, DO-181E, March 2011.

Junichi Honda received the Ph.D. degree from Fukuoka Institute of Technology, Fukuoka, Japan, in 2011. He is a Senior Researcher in Electronic Navigation Research Institute, Japan. His main interests are in electromagnetic wave propagation characteristics, radar signal processing, and navigation systems.

Yasuyuki Kakubari received the Ph.D. degree from Tohoku University, Miyagi, Japan, in 2007. He joined Electronic Navigation Research Institute in 2008 and is currently a Senior Researcher. His main interests are in developing new multilateration system and radio-over-fiber applications.

Takuya Otsuyama received the B.E., M.E., and Ph.D. degrees from University of Electro-Communications, Japan, in 1996, 1998, and 2002, respectively. He is currently a Principal Researcher in Electronic Navigation Research Institute, Japan. His research interests include electromagnetic propagation and aeronautical surveillance system.